

**Development of a High-order Navier-Stokes Solver using Flux
Reconstruction to Simulate Three-dimensional Vortex Structures in a
Curved Artery Model**

by Christopher Cox

B.S. in Aeronautical and Mechanical Engineering, May 2003,

Rensselaer Polytechnic Institute, Troy, NY

M.S. in Aeronautics and Astronautics, March 2005,

Stanford University, Stanford, CA

A Dissertation submitted to

The Faculty of
The School of Engineering and Applied Science
of The George Washington University
in partial fulfillment of the requirements
for the degree of Doctor of Philosophy

January 19, 2018

Dissertation directed by

Michael W. Plesniak

Professor of Mechanical and Aerospace Engineering

Chunlei Liang

Associate Professor of Mechanical and Aerospace Engineering

The School of Engineering and Applied Science of The George Washington University certifies that Christopher Cox has passed the Final Examination for the degree of Doctor of Philosophy as of December 6, 2017. This is the final and approved form of the dissertation.

Development of a High-order Navier-Stokes Solver using Flux Reconstruction to Simulate Three-dimensional Vortex Structures in a Curved Artery Model

Christopher Cox

Dissertation Research Committee:

Michael W. Plesniak, Professor of Mechanical and Aerospace Engineering,
Dissertation Co-Director

Chunlei Liang, Associate Professor of Mechanical and Aerospace
Engineering, Dissertation Co-Director

Elias Balaras, Professor of Mechanical and Aerospace Engineering,
Committee Member

Philippe M. Bardet, Associate Professor of Mechanical and Aerospace
Engineering, Committee Member

H.T. Huynh, Aerospace Engineer, NASA Glenn Research Center, Committee
Member

© Copyright 2018 by Christopher Cox
All Rights Reserved

Dedication

To my parents, Michael and Lucille.

Acknowledgments

First and foremost, I want to thank my advisers Prof. Michael W. Plesniak and Prof. Chunlei Liang for giving me the opportunity to pursue doctoral research in their labs and for their constant support and guidance throughout this endeavor. I also want to thank Prof. Elias Balaras, Prof. Philippe Bardet and Dr. H.T. Huynh for their commitment serve on my dissertation committee and for their invaluable feedback. Lastly, I want to thank my lab mate M. Reza Najjari for the many fruitful academic discussions and for sharing results from his high quality PIV data, which made possible the comparison between numerical and experimental results contained in this dissertation.

This research has been financially supported under the Presidential Merit Fellowship, the Douglas L. Jones Endowed Scholarship, and the Center for Biomimetics and Bioinspired Engineering (COBRE) of The George Washington University.

Abstract

Development of a High-order Navier-Stokes Solver using Flux Reconstruction to Simulate Three-dimensional Vortex Structures in a Curved Artery Model

Low-order numerical methods are widespread in academic solvers and ubiquitous in industrial solvers due to their robustness and usability. High-order methods are less robust and more complicated to implement; however, they exhibit low numerical dissipation and have the potential to improve the accuracy of flow simulations at a lower computational cost when compared to low-order methods. This motivates our development of a high-order compact method using Huynh's flux reconstruction scheme for solving unsteady incompressible flow on unstructured grids. We use Chorin's classic artificial compressibility formulation with dual time stepping to solve unsteady flow problems. In 2D, an implicit non-linear lower-upper symmetric Gauss-Seidel scheme with backward Euler discretization is used to efficiently march the solution in pseudo time, while a second-order backward Euler discretization is used to march in physical time. We verify and validate implementation of the high-order method coupled with our implicit time stepping scheme using both steady and unsteady incompressible flow problems. The current implicit time stepping scheme is proven effective in satisfying the divergence-free constraint on the velocity field in the artificial compressibility formulation. The high-order solver is extended to 3D and parallelized using MPI. Due to its simplicity, time marching for 3D problems is done explicitly. The feasibility of using the current implicit time stepping scheme for large scale three-dimensional problems with high-order polynomial basis still remains to be seen.

We directly use the aforementioned numerical solver to simulate pulsatile flow of a Newtonian blood-analog fluid through a rigid 180° curved artery model. One of

the most physiologically relevant forces within the cardiovascular system is the wall shear stress. This force is important because atherosclerotic regions are strongly correlated with curvature and branching in the human vasculature, where the shear stress is both oscillatory and multidirectional. Also, the combined effect of curvature and pulsatility in cardiovascular flows produces unsteady vortices. The aim of this research as it relates to cardiovascular fluid dynamics is to predict the spatial and temporal evolution of vortical structures generated by secondary flows, as well as to assess the correlation between multiple vortex pairs and wall shear stress. We use a physiologically (pulsatile) relevant flow rate and generate results using both fully developed and uniform entrance conditions, the latter being motivated by the fact that flow upstream of a curved artery may not have sufficient straight entrance length to become fully developed. Under the two pulsatile inflow conditions, we characterize the morphology and evolution of various vortex pairs and their subsequent effect on relevant haemodynamic wall shear stress metrics.

Contents

Dedication	iv
Acknowledgments	v
Abstract	vi
Contents	viii
List of Figures	xiii
List of Tables	xxiv
Nomenclature	xxvi
1 Introduction	1
1.1 High-order Methods for Unstructured Grids	2
1.2 Motivation and Objective	4
1.3 Developments and Highlights	6
1.4 Outline	8
I Development of a High-order Flux Reconstruction Incompressible Navier-Stokes Solver	10
2 Governing Equations of Motion	11
2.1 Incompressible Navier-Stokes Equations with Artificial Compressibility	12
3 The Flux Reconstruction Method	18
3.1 Flux Reconstruction Formulation	19

3.1.1	One-Dimensional Formulation	19
3.1.1.1	Algorithm	26
3.1.2	Tensor Product Formulation on Quadrilaterals	29
3.1.2.1	Inviscid Numerical Flux Formulation	36
3.1.2.2	Viscous Numerical Flux Formulation	38
3.1.2.3	Algorithm	40
4	Time Integration Schemes under Artificial Compressibility	42
4.1	Explicit Pseudo Time Stepping	43
4.1.1	Total Variation Diminishing Runge-Kutta Scheme	43
4.1.2	Algorithm	44
4.2	Implicit Pseudo Time Stepping	44
4.2.1	Backward Euler Scheme with LU-SGS Iterative Smoothing .	44
4.2.2	Algorithm	50
5	Two-Dimensional Numerical Results	51
5.1	Taylor-Couette Flow	52
5.2	NACA0012 Airfoil	56
5.3	Taylor-Green Decaying Vortices	62
5.4	Double Periodic Shear Layers	65
5.4.1	Convergence	65
5.4.2	h/p Resolution	66
5.5	Cylinder	69
6	Three-dimensional Numerical Results	79
6.1	Tensor Product Formulation on Hexahedrals	80

6.1.1	Inviscid and Viscous Numerical Flux Formulation	87
6.2	Numerical Results	89
6.2.1	Sphere	89
6.3	Parallel Computing Performance	97
6.3.1	Single-Node	97
6.3.2	Multi-Node	98
7	Conclusions	101
7.1	Future Directions for Research	103
II	High-order Numerical Simulations of Pulsatile Flow through a Curved Artery Model	105
8	Steady and Pulsatile Flow in a 180° Curved Pipe	106
8.1	Introduction	107
8.2	Geometry	115
8.3	Vorticity	117
8.4	Vortex Identification Method	121
8.5	Wall Shear Stress	124
8.6	Poiseuille Entrance Condition	126
8.6.1	Initial and Boundary Conditions	126
8.6.2	Numerical Convergence	128
8.6.3	Secondary Flow	128
8.6.4	Primary Flow	132
8.6.5	Vorticity	135
8.6.6	Vortex Identification	141
8.6.7	Centrifugal and Pressure Gradient Force	142

8.7 Pulsatile Flow with Fully Developed and Uniform Entrance Condition	147
8.7.1 Numerical Pulsatile Waveform	148
8.7.2 Initial and Boundary Conditions	163
8.7.2.1 Womersley Entrance Condition	163
8.7.2.2 Uniform Entrance Condition	163
8.7.3 Numerical Convergence	164
8.7.4 Secondary Flow	166
8.7.4.1 Comparison with PIV Data	174
8.7.5 Primary Flow	176
8.7.6 Vorticity	185
8.7.7 Vortex Identification	194
8.7.7.1 Deformed/Split-Dean Vortex	194
8.7.7.2 Lyne Vortex	201
8.7.8 Deformed-Dean Vortex Splitting	203
8.8 Wall Shear Stress in Pulsatile Flow	217
8.8.1 Instantaneous Wall Shear Stress	217
8.8.2 Time-Averaged Wall Shear Stress	224
8.8.3 Oscillatory Shear Index	225
8.8.4 Relative Residence Time	230
8.8.5 Transverse Wall Shear Stress	231
9 Conclusions	234
9.1 Future Directions for Research	238
Appendix A Two-Dimensional Mapping and Basis Functions	239

A.1	4-Node Quadrilateral Element	240
A.2	8-Node Quadrilateral Element	241
A.3	12-Node Quadrilateral Element	244
Appendix B	Three-Dimensional Mapping and Basis Functions	247
B.1	8-Node Hexahedral Element	248
B.2	20-Node Hexahedral Element	250
Appendix C	Curved Pipe Entrance Condition: Fully Developed Steady (Poiseuille) Flow	254
Appendix D	Curved Pipe Entrance Condition: Fully Developed Pulsatile (Womersley) Flow	261
Appendix E	Curved Pipe Entrance Condition: Undeveloped (Uniform) Pulsatile Flow	312
Bibliography		363

List of Figures

3.1 Distribution of solution points (SP ●) and numerical flux points (FP ■) for a 4th order FR method inside a 1D reference element Ω_r	21
3.2 (a) correction functions g_2 , g_{SD} and g_{DG} and (b) correction function derivatives g'_{DG} , g'_{SD} and g'_2 for the left boundary for $p = 3$	26
3.3 Isoparametric mapping from cubic (a) physical element Ω_e to (b) reference element Ω_r . (c) physical element with 12-node orientation and (d) reference element with 12-node orientation.	31
3.4 Distribution of solution points (SP ●) and flux points (FP ■) for $p = 3$ (4th order) FR method inside a unit reference element Ω_r	34
3.5 Divergence of the flux $\hat{\nabla} \cdot \hat{\mathbf{F}}$ in 2D reference element Ω_r at solution point (●) (ξ_l, η_m) requires information from four interface flux points (■). . . .	35
3.6 Interface between reference element Ω_r and Ω_{r+1} where common numerical fluxes are computed.	36
5.1 Incompressible Taylor-Couette flow at $Re = 10$. (a) coarse grid Ω^1 , (b) azimuthal velocity $V(r)$ using $p = 3$ for Ω^3	53
5.2 Reduction in L^1 -norm of continuity and momentum pseudo residuals $\ R_\tau(\cdot)\ _1$ for $p = 3$ on Ω^3 , indicating that both RK3 and implicit LU-SGS schemes are implemented correctly under dual time stepping. (a) continuity, (b) x-momentum, (c) y-momentum.	54
5.3 NACA0012 at $Re = 1850$: mesh. (a) full, (b) zoom.	57
5.4 NACA0012 at $Re = 1850$: pressure at the leading edge (LE) (a,c,e) and sharp trailing edge (TE) (b,d,f) from implicit LU-SGS with sweep number $k_{max} = 10$ for polynomial orders $p = \{1, 2, 3\}$, indicating smoothest pressure contours for $p = 3$	59
5.5 NACA0012 at $Re = 1850$: u -velocity from implicit LU-SGS with sweep number $k_{max} = 10$ (a,c,e) for polynomial orders $p = \{1, 2, 3\}$. L^1 -norm of pseudo residual $\ \mathbf{R}_\tau\ _1$ as a function of wall clock time for various k_{max} (b,d,f) demonstrates faster convergence under implicit LU-SGS. Compared to $k_{max} = 1$, the residual can be reduced by more than an order of magnitude using $k_{max} = 10$	60

5.6 Taylor-Green at $Re = 10$: z -vorticity using polynomial order $p = 3$ with implicit LU-SGS on Ω^3 at $t = 1\text{s}$. (a) mesh, (b) z -vorticity.	63
5.7 Taylor-Green at $Re = 10$: p -convergence of L^1 - and L^2 -norm of errors $\ \epsilon\ _1$ (dashed) and $\ \epsilon\ _2$ (solid) on grids $\Omega^i \forall i = 1 \dots 4$	63
5.8 Double shear layer at $Re = 500$: z -vorticity for $p = 3$ using implicit LU-SGS from $t = 0.0\text{s}$ to $t = 1.0\text{s}$	67
5.9 Double shear layer at $Re = 10,000$: z -vorticity at $t = 1.8\text{s}$ for $p = 1$ (a-c), $p = 2$ (d-f) and $p = 3$ (g-i) for each $N_e \times N_e$ mesh, demonstrating the removal of spurious vortices through hp -refinement. The quantity in parenthesis signifies DOFs in each coordinate direction.	68
5.10 Cylinder at $Re = 100$: mesh. (a) full, (b) zoom.	70
5.11 Cylinder at $Re = 100$: z -vorticity under RK3 and implicit LU-SGS for polynomial orders $p = \{1, 2, 3\}$. The vortex shedding pattern is well-represented near $30d$ for $p = 3$, demonstrating the effectiveness of the high-order FR- g_{SD} scheme in maintaining vortices far downstream of the bluff body.	75
5.12 Cylinder at $Re = 100$: (a) C_L and (b) C_D vs. physical time predicted using $p = 2$. The discrepancy in (b) between RK3 and implicit LU-SGS is attributed to effectiveness of the implicit dual time stepping scheme in satisfying the divergence free velocity constraint (see Figures 5.13a and 5.13b).	76
5.13 Cylinder at $Re = 100$: (a) RK3, (b) implicit LU-SGS. L^1 -norm of continuity residual vs. physical time before pseudo iterations begin ($m = 0$) and after pseudo iterations end ($m = m_{max}$) predicted using $p = 2$	76
5.14 Cylinder at $Re = 100$: (a) RK3, (b) implicit LU-SGS. L^1 -norm of x -momentum residual vs. physical time before pseudo iterations begin ($m = 0$) and after pseudo iterations end ($m = m_{max}$) predicted using $p = 2$	77
5.15 Cylinder at $Re = 100$: (a) RK3, (b) implicit LU-SGS. L^1 -norm of y -momentum residual vs. physical time before pseudo iterations begin ($m = 0$) and after pseudo iterations end ($m = m_{max}$) predicted using $p = 2$	77
5.16 Cylinder at $Re = 100$: total pseudo iterations m_{max} per physical time step using implicit LU-SGS, demonstrating a $2.5x$ increase in pseudo iterations required to drop $\ \mathbf{R}_\tau\ _1$ by 10^3 if the physical and pseudo time step sizes are decreased by an order of magnitude to $\Delta\tau = \Delta t = 1\text{E-}2$. This highlights the effectiveness of the implicit LU-SGS scheme in reducing all pseudo time derivatives with large time steps.	78

6.1	Isoparametric mapping from quadrilateral (a) physical element Ω_e to (b) reference element Ω_r . (c) physical element with 20-node orientation and (d) reference element with 20-node orientation.	84
6.2	Sphere at $Re = 118$: mesh (zoom).	90
6.3	Sphere at $Re = 118$: (a) aluminum dust flow visualization by Taneda (1956) taken from Van Dyke (1982), (b) numerical solution using FR- g_{SD} with $p = 4$	91
6.4	Sphere at $Re = 118$: (a) pressure contours, (b) skin friction coefficient C_f showing separation at $\theta = 124.2^\circ$, and (c) streamlines and separation length to diameter ratio $s/d = 1.00$	92
6.5	Sphere at $Re = 300$: mesh. (a) full, (b) zoom.	94
6.6	Sphere at $Re = 300$: time series of drag and lift coefficient.	95
6.7	Sphere at $Re = 300$: isosurface of λ_2 colored by velocity magnitude showing the hairpin vortical structures shed into the wake with the original mesh superimposed; (a) xy -plane, (b) xz -plane, (c) isometric view. Results are generated using a $p = 4$ polynomial.	96
6.8	Strong scalability: speedup vs. number of processing elements with $p = 4$ on sphere mesh with 109,440 elements.	99
6.9	Weak scalability: efficiency vs. number of processing elements (problem size per processing element is 452,750 DOFs).	100
8.1	Curved pipe geometry and orientation. (a) curvature mesh, (b) cross-sections, (c) cross-section planar view, (d) top planar view.	116
8.2	Steady flow: non-dimensional secondary velocity magnitude $ \mathbf{u}_{\theta r}^* $. $Re = \{220, 430, 640, 883\}$, $\phi = \{22^\circ, 45^\circ, 90^\circ, 135^\circ\}$	130
8.3	Steady flow: non-dimensional secondary velocity vectors $\mathbf{u}_{\theta r}^*$. $Re = \{220, 430, 640, 883\}$, $\phi = \{22^\circ, 45^\circ, 90^\circ, 135^\circ\}$	131
8.4	Steady flow: non-dimensional streamwise velocity u_s^* . $Re = \{220, 430, 640, 883\}$, $\phi = \{22^\circ, 45^\circ, 90^\circ, 135^\circ\}$	133
8.5	Steady flow: non-dimensional streamwise velocity, u_s^* , profile at $z = 0$ plane of symmetry. $Re = \{220, 430, 640, 883\}$, $\phi = \{22^\circ, 45^\circ, 90^\circ, 135^\circ\}$. . .	134

8.6 Schematic of Dean (D), Deformed-Dean (DD), Split-Dean (SD) and Lyne-Type (LT) vortex pairs; the red and blue colors signify counter-clockwise and clockwise rotation of the secondary flow, respectively (when viewed from upstream).	137
8.7 Steady flow: velocity surface of u_s^* colored by non-dimensional streamwise vorticity ω_s^* visualized from three difference views: isometric, upper and inner. $Re = 883$, $\phi = \{22^\circ, 45^\circ, 90^\circ, 135^\circ\}$ ($I \equiv \text{inner}$, $O \equiv \text{outer}$, $U \equiv \text{upper}$, $L \equiv \text{lower}$).	139
8.8 Steady flow: non-dimensional streamwise velocity, u_s^* , profile at $z/r_{max} = 0.33$ plane. $Re = \{220, 430, 640, 883\}$, $\phi = \{22^\circ, 45^\circ, 90^\circ, 135^\circ\}$	140
8.9 Steady flow: non-dimensional second eigenvalue of $\mathbf{S}^2 + \mathbf{R}^2$, $\lambda_2^* < 0$. $Re = \{220, 430, 640, 883\}$, $\phi = \{22^\circ, 45^\circ, 90^\circ, 135^\circ\}$	142
8.10 Steady flow: non-dimensional pressure p^* . $Re = \{220, 430, 640, 883\}$, $\phi = \{22^\circ, 45^\circ, 90^\circ, 135^\circ\}$	145
8.11 Steady flow: balance of non-dimensional centrifugal, pressure gradient and viscous forces along the radius of curvature direction $f_c^* + f_{pg}^* + f_v^*$. $Re = \{220, 430, 640, 883\}$, $\phi = \{22^\circ, 45^\circ, 90^\circ, 135^\circ\}$	146
8.12 Flow rate Q as function of non-dimensional pulse period $t^* = t/T$ and the corresponding inlet velocity profile u as a function of pipe diameter d	149
8.13 Flow rate Q (-) “lagging” the straight pipe non-dimensional pressure gradient $-\partial p^*/\partial s^*$ (--) for Womersley number $\alpha = 4.22$. The pressure gradient from a pulsatile Poiseuille solution (--) required to produce the same flow rate is shown for comparison.	154
8.14 Reynolds number Re and Dean number κ as a function of non-dimensional pulse period t^* and non-dimensional inlet velocity profile u/\bar{u}_{mean} for Womersley entrance condition (-). The bulk velocity \bar{u} corresponds to the uniform entrance condition (---), and the parabolic profile corresponds to the Poiseuille solution (--) obtained using the same bulk flow. The Womersley number is $\alpha = 4.22$	155
8.15 Womersley entrance condition: p -convergence of $\ \boldsymbol{\tau}_w^*\ _2$ on Ω^2 during pulse acceleration and deceleration.	166
8.16 Womersley entrance condition: (a)-(c) non-dimensional secondary velocity vectors $\mathbf{u}_{\theta r}^*$ and (d)-(f) streamlines colored by magnitude at $\phi = 45^\circ$ and $0.22 \leq t^* \leq 0.24$	167

8.17 Uniform entrance condition: (a)-(c) non-dimensional secondary velocity vectors $\mathbf{u}_{\theta r}^*$ and (d)-(f) streamlines colored by magnitude at $\phi = 45^\circ$ and $0.22 \leq t^* \leq 0.24$	168
8.18 Poiseuille entrance condition: (a) non-dimensional secondary velocity vectors $\mathbf{u}_{\theta r}^*$ and (b) streamlines colored by magnitude at $\phi = 45^\circ$ and $Re = 883$. The flow rate at this steady Re corresponds to flow rate at $t^* = 0.23$ under pulsatile conditions.	168
8.19 Womersley entrance condition: (a)-(c) non-dimensional secondary velocity vectors $\mathbf{u}_{\theta r}^*$ and (d)-(f) streamlines colored by magnitude at $\phi = 90^\circ$ and $0.22 \leq t^* \leq 0.24$	170
8.20 Uniform entrance condition: (a)-(c) non-dimensional secondary velocity vectors $\mathbf{u}_{\theta r}^*$ and (d)-(f) streamlines colored by magnitude at $\phi = 90^\circ$ and $0.22 \leq t^* \leq 0.24$	170
8.21 Poiseuille entrance condition: (a) non-dimensional secondary velocity vectors $\mathbf{u}_{\theta r}^*$ and (b) streamlines colored by magnitude at $\phi = 90^\circ$ and $Re = 883$. This Re corresponds to the bulk flow at $t^* = 0.23$ under pulsatile conditions.	171
8.22 Womersley entrance condition: non-dimensional secondary velocity magnitude $ \mathbf{u}_{\theta r}^* $ at (t^*, ϕ)	172
8.23 Uniform entrance condition: non-dimensional secondary velocity magnitude $ \mathbf{u}_{\theta r}^* $ at (t^*, ϕ)	173
8.24 Womersley entrance condition: comparison of non-dimensional secondary velocity magnitude $ \mathbf{u}_{\theta r}^* $ with particle image velocimetry data from Najjari and Plesniak (2017) at $t^* = 0.25$ and $\phi = \{45^\circ, 90^\circ, 135^\circ\}$. (a)-(c) PIV, (d)-(f) CFD.	175
8.25 Womersley entrance condition: non-dimensional streamwise velocity u_s^* at (t^*, ϕ)	178
8.26 Uniform entrance condition: non-dimensional streamwise velocity u_s^* at (t^*, ϕ)	179
8.27 Womersley entrance condition: non-dimensional streamwise velocity u_s^* profile at $z = 0$ plane of symmetry for $0.14 \leq t^* \leq 0.29$ showing flow acceleration (solid) and deceleration (dash-dot). $\phi = \{22^\circ, 45^\circ, 90^\circ, 135^\circ\}$	180
8.28 Uniform entrance condition: non-dimensional streamwise velocity u_s^* profile at $z = 0$ plane of symmetry for $0.14 \leq t^* \leq 0.29$ showing flow acceleration (solid) and deceleration (dash-dot). $\phi = \{22^\circ, 45^\circ, 90^\circ, 135^\circ\}$	181

8.29 Instantaneous non-dimensional wall shear stress vectors τ_w^* with magnitude contours at $t^* = 0.19$ under (a) Womersley entrance condition and (b) Uniform entrance condition. In (b) higher wall shear stress occurs towards the inner wall where $\theta = 180^\circ$ near the entrance at $\phi = 0^\circ$ due to the shorter wall length (i.e. thinner boundary layer) and larger streamwise velocity.	183
8.30 Womersley, Uniform and Poiseuille entrance conditions: profiles of streamwise velocity normalized by bulk velocity u_s/\bar{u} at $z = 0$ for $\phi = \{22^\circ, 45^\circ, 90^\circ, 135^\circ\}$. At phases $t^* = 0.14$ and $t^* = 0.23$ the flow is accelerating and decelerating, respectively, at the same bulk velocity of $\bar{u} = 0.247$ m/s. The steady flow result at $Re = 883$ from the Poiseuille entrance condition corresponds to the same value of bulk velocity. A straight pipe Poiseuille flow result is shown to highlight profile flattening and skewness with respect to a parabolic profile, where the maximum non-dimensional velocity equals 2 at $r = 0$ when using \bar{u} as the velocity scale.	184
8.31 Womersley entrance condition: (a)-(d) vortex lines colored by streamwise vorticity ω_s^* at $\phi = 90^\circ$ and $t^* = 0.23$ showing the local direction of the three-dimensional vorticity vector ω^* associated with Split-Dean and Lyne-type regions, (e) streamwise vorticity ω_s^* , and (f) vorticity magnitude ω^*	187
8.32 Womersley entrance condition: velocity surface of u_s^* at $t^* = 0.23$ colored by non-dimensional streamwise vorticity ω_s^* visualized from three difference views: isometric, upper and inner. ($I \equiv \text{inner}$, $O \equiv \text{outer}$, $U \equiv \text{upper}$, $L \equiv \text{lower}$).	190
8.33 Uniform entrance condition: velocity surface of u_s^* at $t^* = 0.23$ colored by non-dimensional streamwise vorticity ω_s^* visualized from three difference views: isometric, upper and inner. ($I \equiv \text{inner}$, $O \equiv \text{outer}$, $U \equiv \text{upper}$, $L \equiv \text{lower}$).	191
8.34 Womersley entrance condition: non-dimensional streamwise velocity, u_s^* , profile at $z/r_{max} = 0.38$ plane for $0.14 \leq t^* \leq 0.29$ showing flow acceleration (solid) and deceleration (dash-dot). $\phi = \{22^\circ, 45^\circ, 90^\circ, 135^\circ\}$	192
8.35 Uniform entrance condition: non-dimensional streamwise velocity, u_s^* , profile at $z/r_{max} = 0.41$ plane for $0.14 \leq t^* \leq 0.29$ showing flow acceleration (solid) and deceleration (dash-dot). $\phi = \{22^\circ, 45^\circ, 90^\circ, 135^\circ\}$	193
8.36 Womersley entrance condition: non-dimensional second eigenvalue λ_2^* of $\mathbf{S}^2 + \mathbf{R}^2$, $\lambda_2^* < 0$ at (t^*, ϕ)	197
8.37 Uniform entrance condition: non-dimensional second eigenvalue λ_2^* of $\mathbf{S}^2 + \mathbf{R}^2$, $\lambda_2^* < 0$ at (t^*, ϕ)	198

8.38 Womersley entrance condition: non-dimensional pressure p^* at (t^*, ϕ) (contour levels are rescaled for each cross-section).	199
8.39 Uniform entrance condition: non-dimensional pressure p^* at (t^*, ϕ) (contour levels are rescaled for each cross-section).	200
8.40 Womersley and Uniform entrance conditions: streamlines associated with the “head” of Deformed-Dean colored by non-dimensional streamwise vorticity ω_s^* at $t^* = 0.23$, highlighting the strong helical pattern of the streamlines under WEC in comparison to UEC. Strong helical patterns of streamlines result from strong secondary flow action, which is more prevalent under a fully developed pulsatile entrance condition.	201
8.41 Womersley entrance condition: isosurfaces of $\lambda_2^* = -24$ colored by streamwise vorticity ω_s^* , highlighting cross-sectional vortex splitting of Deformed-Dean during deceleration for which $0.21 \leq t^* \leq 0.26$. Vortex splitting occurs at $t^* = 0.23$	202
8.42 Womersley entrance condition: summation of non-dimensional centrifugal, pressure gradient and viscous forces along the radius of curvature direc- tion $f_c^* + f_{pg}^* + f_v^*$ at (t^*, ϕ)	210
8.43 Uniform entrance condition: summation of non-dimensional centrifugal, pressure gradient and viscous forces along the radius of curvature direction $f_c^* + f_{pg}^* + f_v^*$ at (t^*, ϕ)	211
8.44 Non-dimensional centrifugal forces f_c^* , pressure gradient forces f_{pg}^* and viscous forces f_v^* at $\phi = 90^\circ$. Results from WEC (b,e,h,k) and UEC (c,f,i,l) are extracted from the pulsatile waveform at $t^* = 0.23$. The flow rates across PEC, WEC and UEC are equal with a bulk velocity $\bar{u} = 0.247$ m/s, corresponding to $Re = 883$. All results have been non-dimensionalized using \bar{u} as the velocity scale and contour levels for all images are equal.	212
8.45 Non-dimensional streamwise velocity u_s^* profiles in the given z/r_{max} plane at $\phi = 90^\circ$ under (a) PEC, (b) WEC and (C) UEC. Images superimposed above profiles (top to bottom) are the following: secondary velocity vectors $\mathbf{u}_{\theta r}^*$, secondary velocity magnitude $ \mathbf{u}_{\theta r}^* $, streamwise vorticity ω_s^* , λ_2^* , and force balance due to centrifugal forces, pressure gradient forces and viscous forces $f_c^* + f_{pg}^* + f_v^*$ (with contours of λ_2^*). Each superimposed image displays the position of the z/r_{max} plane from which the velocity profiles are extracted. Data in both (b) and (c) are extracted from the pulsatile waveform at $t^* = 0.23$. Flow rates of (a), (b) and (c) are equal with a bulk velocity $\bar{u} = 0.247$ m/s, corresponding to $Re = 883$. All results have been non-dimensionalized using \bar{u} as the velocity scale and contour levels for the various entrance conditions are equal for each flow variable. Inner (I) and outer (O) walls are indicated.	213

8.46 Split-Dean (red) and Deformed-Dean (blue) vortex core region trajectory during the phases $0.15 < t^* < 0.30$: (a) vortex trajectory at $\phi = 90^\circ$ of point $P(x', z', t)$ where largest negative value of $\lambda_2^* = \lambda_2 d^2/\bar{u}_{mean}^2$ occurs; (b) time evolution of estimated speed; (c) time evolution of $\lambda_2^* _P$ superimposed on top of pulsatile flow rate Q (green).	214
8.47 Split-Dean (SD) vortex trajectory above $z' = 0$: numerical data from $\lambda_2 _P$ (●), experimental data from $d_2 _P$ (+). Experimental data provided by Najjari and Plesniak (2017).	216
8.48 Curved pipe orientation and wall shear stress axis description. (a) cross-section planar view, (b) top planar view, (c) WSS axis description.	219
8.49 Instantaneous non-dimensional wall shear stress vectors τ_w^* with magnitude contours. (a)-(l) WEC, (m)-(x) UEC.	220
8.50 Non-dimensional time averaged wall shear stress $TAWSS^*$: (a) Womersley entrance condition, (b) Uniform entrance condition.	225
8.51 Oscillatory shear index OSI : (a) Womersley entrance condition, (b) Uniform entrance condition.	226
8.52 Womersley entrance condition at $t^* = 0.26$: (a) streamlines and ω_z^* in the $z = 0$ plane of symmetry, (b) superimposed $\lambda_2^* = -15$ isosurface above $z = 0$ colored by streamwise vorticity ω_s^* (red - ω_s^* points upstream, blue - ω_s^* points downstream).	227
8.53 (a) non-dimensional wall shear stress vector $\tau_w^*(\phi)$ and (b) non-dimensional wall pressure $p_w^*(\phi)$ along inner wall at $\theta = 180^\circ$ under WEC (—) and UEC (---).	229
8.54 Womersley entrance condition at $t^* = 0.26$: (a) streamlines in the $z = 0$ plane of symmetry, (b) streamlines near curve entrance, indicating region of critical points during deceleration near the inner wall, where $25^\circ < \phi < 35^\circ$. Streamlines are colored by the non-dimensional streamwise velocity u_s^*	229
8.55 Non-dimensional relative residence time RRT^* : (a) Womersley entrance condition, (b) Uniform entrance condition.	231
8.56 Non-dimensional transverse wall shear stress $TransWSS^*$: (a) Womersley entrance condition, (b) Uniform entrance condition.	233
A.1 Orientation of 4-node reference element $\Omega_r = \{\xi, \eta \mid 0 \leq \xi, \eta \leq 1\}$	240
A.2 Orientation of 8-node reference element $\Omega_r = \{\xi, \eta \mid 0 \leq \xi, \eta \leq 1\}$	242

A.3	Orientation of 12-node reference element $\Omega_r = \{\xi, \eta \mid 0 \leq \xi, \eta \leq 1\}$	244
B.1	Orientation of 8-node reference element $\Omega_r = \{\xi, \eta, \beta \mid 0 \leq \xi, \eta, \beta \leq 1\}$	248
B.2	Orientation of 20-node reference element $\Omega_r = \{\xi, \eta, \beta \mid 0 \leq \xi, \eta, \beta \leq 1\}$	250
C.1	Poiseuille entrance condition: non-dimensional vorticity magnitude $ \omega^* $. $Re = \{220, 430, 640, 883\}, \phi = \{22^\circ, 45^\circ, 90^\circ, 135^\circ\}$	256
C.2	Poiseuille entrance condition: non-dimensional centrifugal force f_c^* . $Re = \{220, 430, 640, 883\}, \phi = \{22^\circ, 45^\circ, 90^\circ, 135^\circ\}$	257
C.3	Poiseuille entrance condition: non-dimensional pressure gradient force $-f_{pg}^*$. $Re = \{220, 430, 640, 883\}, \phi = \{22^\circ, 45^\circ, 90^\circ, 135^\circ\}$	258
C.4	Poiseuille entrance condition: non-dimensional viscous force f_v^* . $Re = \{220, 430, 640, 883\}, \phi = \{22^\circ, 45^\circ, 90^\circ, 135^\circ\}$	259
C.5	Poiseuille entrance condition: non-dimensional wall shear stress magnitude $ \tau_w^* $. $Re = \{220, 430, 640, 883\}, \phi = \{22^\circ, 45^\circ, 90^\circ, 135^\circ\}$	260
D.1	Womersley entrance condition: velocity surface of u_s^* at $\theta = 22^\circ$ colored by non-dimensional streamwise vorticity ω_s^* visualized from three difference views: isometric, upper and inner. ($I \equiv inner, O \equiv outer, U \equiv upper, L \equiv lower$).	263
D.2	Womersley entrance condition: velocity surface of u_s^* at $\theta = 45^\circ$ colored by non-dimensional streamwise vorticity ω_s^* visualized from three difference views: isometric, upper and inner. ($I \equiv inner, O \equiv outer, U \equiv upper, L \equiv lower$).	267
D.3	Womersley entrance condition: velocity surface of u_s^* at $\theta = 90^\circ$ colored by non-dimensional streamwise vorticity ω_s^* visualized from three difference views: isometric, upper and inner. ($I \equiv inner, O \equiv outer, U \equiv upper, L \equiv lower$).	271
D.4	Womersley entrance condition: velocity surface of u_s^* at $\theta = 135^\circ$ colored by non-dimensional streamwise vorticity ω_s^* visualized from three difference views: isometric, upper and inner. ($I \equiv inner, O \equiv outer, U \equiv upper, L \equiv lower$).	275
D.5	Womersley entrance condition: non-dimensional vorticity magnitude $ \omega^* $ at (t^*, ϕ)	279

D.6 Womersley entrance condition: non-dimensional secondary velocity vectors $\mathbf{u}_{\theta r}^*$ at (t^*, ϕ)	282
D.7 Womersley entrance condition: non-dimensional secondary velocity magnitude $ \mathbf{u}_{\theta r}^* $ at (t^*, ϕ)	285
D.8 Womersley entrance condition: non-dimensional streamwise velocity u_s^* at (t^*, ϕ)	288
D.9 Womersley entrance condition: non-dimensional second eigenvalue λ_2^* of $\mathbf{S}^2 + \mathbf{R}^2$, $\lambda_2^* < 0$ at (t^*, ϕ)	291
D.10 Womersley entrance condition: non-dimensional pressure p^* at (t^*, ϕ) . .	294
D.11 Womersley entrance condition: non-dimensional centrifugal force f_c^* at (t^*, ϕ)	297
D.12 Womersley entrance condition: non-dimensional pressure gradient force $-f_{pg}^*$ at (t^*, ϕ)	300
D.13 Womersley entrance condition: non-dimensional viscous force f_v^* at (t^*, ϕ) .	303
D.14 Womersley entrance condition: non-dimensional centrifugal, pressure gradient and viscous forces along the radius of curvature direction $f_c^* + f_{pg}^* + f_v^*$ at (t^*, ϕ)	306
D.15 Womersley entrance condition: non-dimensional wall shear stress magnitude $ \tau_w^* $ at (t^*, ϕ)	309
E.1 Uniform entrance condition: velocity surface of u_s^* at $\theta = 22^\circ$ colored by non-dimensional streamwise vorticity ω_s^* visualized from three difference views: isometric, upper and inner. ($I \equiv inner$, $O \equiv outer$, $U \equiv upper$, $L \equiv lower$)	314
E.2 Uniform entrance condition: velocity surface of u_s^* at $\theta = 45^\circ$ colored by non-dimensional streamwise vorticity ω_s^* visualized from three difference views: isometric, upper and inner. ($I \equiv inner$, $O \equiv outer$, $U \equiv upper$, $L \equiv lower$)	318
E.3 Uniform entrance condition: velocity surface of u_s^* at $\theta = 90^\circ$ colored by non-dimensional streamwise vorticity ω_s^* visualized from three difference views: isometric, upper and inner. ($I \equiv inner$, $O \equiv outer$, $U \equiv upper$, $L \equiv lower$)	322

E.4 Uniform entrance condition: velocity surface of u_s^* at $\theta = 135^\circ$ colored by non-dimensional streamwise vorticity ω_s^* visualized from three difference views: isometric, upper and inner. ($I \equiv inner$, $O \equiv outer$, $U \equiv upper$, $L \equiv lower$).	326
E.5 Uniform entrance condition: non-dimensional vorticity magnitude $ \omega^* $ at (t^*, ϕ)	330
E.6 Uniform entrance condition: non-dimensional secondary velocity vectors $\mathbf{u}_{\theta r}^*$ at (t^*, ϕ)	333
E.7 Uniform entrance condition: non-dimensional secondary velocity magnitude $ \mathbf{u}_{\theta r}^* $ at (t^*, ϕ)	336
E.8 Uniform entrance condition: non-dimensional streamwise velocity u_s^* at (t^*, ϕ)	339
E.9 Uniform entrance condition: non-dimensional second eigenvalue λ_2^* of $\mathbf{S}^2 + \mathbf{R}^2$, $\lambda_2^* < 0$ at (t^*, ϕ)	342
E.10 Uniform entrance condition: non-dimensional pressure p^* at (t^*, ϕ)	345
E.11 Uniform entrance condition: non-dimensional centrifugal force f_c^* at (t^*, ϕ)	348
E.12 Uniform entrance condition: non-dimensional pressure gradient force $-f_{pg}^*$ at (t^*, ϕ)	351
E.13 Uniform entrance condition: non-dimensional viscous force f_v^* at (t^*, ϕ)	354
E.14 Uniform entrance condition: non-dimensional centrifugal, pressure gradient and viscous forces along the radius of curvature direction $f_c^* + f_{pg}^* + f_v^*$ at (t^*, ϕ)	357
E.15 Uniform entrance condition: non-dimensional wall shear stress magnitude $ \tau_w^* $ at (t^*, ϕ)	360

List of Tables

4.1 Size of element matrix \mathbf{M}_r as a function of polynomial order p in 2D, where $N_{eq} = 3$ and $\mathcal{N} = 2$	48
4.2 Size of element matrix \mathbf{M}_r as a function of polynomial order p in 3D, where $N_{eq} = 4$ and $\mathcal{N} = 3$	48
5.1 Taylor-Couette at $Re = 10$: order of accuracy n demonstrated by L^1 -norm and L^2 -norm of errors during h -refinement for polynomial orders $p = \{1, 2, 3\}$	55
5.2 NACA0012 at $Re = 1850$: speedup of implicit LU-SGS over RK3 for polynomial orders $p = \{1, 2, 3\}$, demonstrating largest speedup under $k_{max} = 10$	61
5.3 NACA0012 at $Re = 1850$: p -refinement convergence of C_D under implicit LU-SGS scheme.	61
5.4 Taylor-Green at $Re = 10$: order of accuracy n demonstrated by L^1 -norm and L^2 -norm of errors during h -refinement for polynomial orders $p = \{1, 2, 3\}$ under implicit LU-SGS.	64
5.5 Double Shear Layer at $Re = 500$: convergence rate obtained from L^2 -norm of errors using Richardson extrapolation at $t = 1s$ for polynomial orders $p = \{1, 2, 3\}$	67
5.6 Cylinder at $Re = 100$: Strouhal numbers and force coefficients due to pressure $C_{(\cdot),p}$ and viscosity $C_{(\cdot),v}$ predicted using polynomial orders $p = 2$ and $p = 3$. Root mean square values are signified by the superscript $(\cdot)'$. Best results are obtained using $p = 3$ and implicit LU-SGS scheme. Comparison to various incompressible flow solvers demonstrates wide agreement in results.	73
5.7 Cylinder at $Re = 100$: comparison of St , C_L and C_D obtained from the current solver using $p = 3$ and implicit LU-SGS with various incompressible solvers. Strong agreement is demonstrated between current results and those from Chan et al. (2011), who ran a compressible flow simulation at low Mach number using the spectral difference method.	74
6.1 Sphere at $Re = 118$: convergence of C_D and flow separation angle θ under p -refinement.	91

6.2 Sphere at $Re = 118$: comparison of drag coefficient due to pressure $C_{D,p}$ and viscosity $C_{D,v}$ and separation length to diameter ratio s/d with other discontinuous high-order solvers.	93
6.3 Sphere at $Re = 300$: coefficients of mean drag \bar{C}_D , mean drag fluctuation C'_D , mean side \bar{C}_L , and mean side fluctuation C'_L with comparison to various investigators.	95
6.4 Memory requirement for sphere mesh with 109,440 hexahedral elements.	97
6.5 Wall-clock time to compute $\nabla \cdot \mathbf{F}$ on Intel® Xeon® E5-1650 v3 processor, normalized by total degrees of freedom of the mesh and the number of equations.	98
 8.1 Pulsatile waveform parameters.	150
8.2 Pearson correlation coefficient $\rho_{a,b}$ of experimental secondary velocity $\mathbf{u}_{\theta r,e}^*$ and numerical secondary velocity $\mathbf{u}_{\theta r,n}^*$ and L^2 -norm of the difference $\ \mathbf{u}_{\theta r,e}^* - \mathbf{u}_{\theta r,n}^*\ _2$ at $t^* = 0.25$ and $\phi = \{45^\circ, 90^\circ, 135^\circ\}$	175
8.3 Largest negative values of $\lambda_2^* = \lambda_2 d/\bar{u}$ at $\phi = 90^\circ$ and $t^* = 0.23$ within the Deformed-Dean (DD) and Split-Dean (SD) vortex core regions under Poiseuille, Womersley and uniform entrance conditions.	207
8.4 Non-dimensional distance Δl^* between numerical and experimental trajectories of the SD vortex shown in Figure 8.47 for phases $0.21 \leq t^* \leq 0.29$	217

Nomenclature

Acronyms

FR	flux reconstruction
DG	discontinuous Galerkin
SD	spectral difference
SV	spectral volume
DOF	degrees of freedom
D	Dean vortex
DD	Deformed-Dean vortex
SD	Split-Dean vortex
LT	Lyne-type vortex
PEC	Poiseuille entrance condition
WEC	Womersley entrance condition
UEC	uniform entrance condition
WSS	wall shear stress

Indices

e	physical element
r	reference element
n	physical iteration level
m	pseudo iteration level
k	LU-SGS sweep level

Symbols

$(\cdot)^{LB}$	denotes values at left interface of Ω_r
$(\cdot)^{RB}$	denotes values at right interface of Ω_r

$(\cdot)^L$	denotes values on left side of interface
$(\cdot)^R$	denotes values on right side of interface
$(\cdot)^{com}$	denotes common values at interface between elements
(\cdot)	denotes values transformed from physical space to reference space

Variables / Parameters

β_o	artificial compressibility parameter
ν	kinematic viscosity
μ	dynamic viscosity
P	static pressure
p	static pressure P divided by density ρ
ρ	density
t	physical time
τ	pseudo/artificial time
Δt	physical time step
$\Delta \tau$	pseudo/artificial time step
x, y, z	physical coordinates
u, v, w	velocity components in x, y, z
CFL	Courant-Friedrichs-Lowy condition
\mathbf{u}	velocity vector
$\boldsymbol{\omega}$	vorticity vector
$\boldsymbol{\tau}_w$	wall shear stress vector
\mathbf{U}	solution/state vector
\mathbf{U}_g	ghost vector of state variables
\mathbf{U}^{com}	interface common solution vector
\mathbf{F}	flux vectors in x
\mathbf{G}	flux vectors in y

\mathbf{H}	flux vectors in z
\mathbf{f}_e	inviscid flux vectors in x
\mathbf{g}_e	inviscid flux vectors in y
\mathbf{h}_e	inviscid flux vectors in z
\mathbf{f}_v	viscous flux vectors in x
\mathbf{g}_v	viscous flux vectors in y
\mathbf{h}_v	viscous flux vectors in z
\mathbf{A}_e	convective flux Jacobians of \mathbf{f}_e
\mathbf{B}_e	convective flux Jacobians of \mathbf{g}_e
\mathbf{C}_e	convective flux Jacobians of \mathbf{h}_e
\mathbf{S}	physical time derivative
\mathbf{R}	residual / divergence of flux vector \mathbf{F}
\mathbf{R}_τ	pseudo/modified residual
λ_A	eigenvalues of \mathbf{A}_e
λ_B	eigenvalues of \mathbf{B}_e ,
λ_C	eigenvalues of \mathbf{C}_e
c_x	pseudo speed of sound in x
c_y	pseudo speed of sound in y
c_z	pseudo speed of sound in z
\mathbf{n}	unit normal vector
V_n	interface normal velocity
c_n	interface normal pseudo speed of sound
M_p	pseudo Mach number
\mathbf{M}_r	element matrix
ϕ_k	shape functions
\mathbf{J}	Jacobian matrix of metrics
\mathbf{C}^T	adjugate matrix of \mathbf{J}

\mathbf{s}_ξ	first row vector of \mathbf{C}^T
\mathbf{s}_η	second row vector of \mathbf{C}^T
\mathbf{s}_β	third row vector of \mathbf{C}^T
Ω	solution domain
Ω_e	physical element
Ω_r	reference element
Ω_{nb}	neighboring reference element
x_k, y_k, z_k	nodal physical coordinates in Ω_e
ξ, η, β	reference coordinates in Ω_r
K	number of nodes per element
N_e	number of elements in solution domain Ω
N_s	number of solution points per reference element Ω_r
N_f	number of flux points per reference element Ω_r
N_{eq}	number of equations
\mathcal{P}_{N_p}	Legendre polynomial
p	degree of Lagrange polynomial ℓ
δ_{ij}	Kronecker delta
ℓ	Lagrange polynomial
n	numerical order of accuracy
\mathcal{N}	dimension of solution domain Ω
$\mathbb{R}^{\mathcal{N}}$	real coordinate space of \mathcal{N} dimensions
\mathbf{I}_D	identity matrix with $\mathbf{I}_D(1, 1) = 0$
\mathbf{f}_r	continuous flux functions in Ω_r along ξ
\mathbf{g}_r	continuous flux functions in Ω_r along η
\mathbf{h}_r	continuous flux functions in Ω_r along β
\mathbf{f}_r^D	discontinuous flux functions in Ω_r along ξ
\mathbf{g}_r^D	discontinuous flux functions in Ω_r along η

\mathbf{h}_r^D	discontinuous flux functions in Ω_r along β
\mathcal{R}_{R,N_p}	right Radau polynomial
\mathcal{R}_{L,N_p}	left Radau polynomial
g_2	correction function - Huynh's lumped Lobatto
g_{SD}	correction function - modified Spectral Difference
g_{DG}	corection function - nodal discontinuous Galerkin
k	Runge-Kutta stage
a_k, b_k, c_k	coefficients of a Runge-Kutta scheme
Re	Reynolds number
κ	Dean number
α	Womersley number
St	Strouhal number
f_s	shedding frequency
r	radius
δ	curvature ratio
r_{max}	curved pipe maximum radius
d	curved pipe diameter
R	curved pipe radius of curvature
C_L	lift coefficient
C_D	drag coefficient
$C_{L,v}$	lift coefficient due to viscosity
$C_{L,p}$	lift coefficient due to pressure
$C_{D,v}$	drag coefficient due to viscosity
$C_{D,p}$	drag coefficient due to pressure
C'_L	root mean square value of lift coefficient
C'_D	root mean square value of drag coefficient
\bar{C}_L	mean value of lift coefficient

\bar{C}_D	mean value of drag coefficient
C_f	skin friction coefficient
$TAWSS$	time-averaged wall shear stress
OSI	oscillatory shear index
RRT	relative residence time
$TransWSS$	transverse wall shear stress

Chapter 1

Introduction

1.1 High-order Methods for Unstructured Grids

Low-order methods (2nd and below) are abundant in academia and ubiquitous in industry. For many flow problems, low-order numerical methods are the appropriate choice taking into account requirements in accuracy, code simplicity, and computational speed. They are robust, flexible and straightforward to implement. They are well-suited for design of high-speed aircraft in cruise [1]. However, low-order methods are too dissipative to accurately resolve unsteady vortex structures that propagate over large spatial and temporal scales.

High-order methods (3rd and above) can provide high accuracy for similar cost as low-order methods [2]. They exhibit low numerical dissipation, which is needed for accurately predicting vortex dominated flows such as those produced by high-lift systems, rotor-craft blades and flapping wings as well as large eddy simulation (LES) and direct numerical simulation (DNS) of turbulence. Another important problem that demands use of high-order methods for accurate simulation is acoustic wave propagation for Computational Aeroacoustics (CAA), which requires the modeling of high frequency waves in the near field and small amplitude waves in the far field. Tackling these types of flow problems, especially around complex geometries that demand the use of unstructured grids warrants the adoption of high-order methods. However, high-order methods are less robust and more complicated to implement than low-order methods, especially when treating irregular geometries. Also, the Courant-Friedrichs-Lowy (CFL) condition can be more restricted for high-order methods, and with the use of high-order methods comes the need for high-order mesh generation capability.

Popular discontinuous spectral/ hp element methods that have been developed to address the need for high-order accuracy are discontinuous Galerkin (DG), spectral volume (SV), spectral difference (SD), and flux reconstruction (FR). Discontinuous

Galerkin was initially developed for solving the neutron transport equation by Reed and Hill [3] and is the most widely adopted discontinuous high-order method. Over the years, much effort has been devoted to the development of DG (see Arnold et al. [4] for a unified analysis of DG methods for elliptic problems). The local DG (LDG) method by Cockburn and Shu [5], the collocation based nodal DG method by Hesthaven and Warburton [6], and the hybridized DG (HDG) by Cockburn, Gopalakrishnan and Lazarov [7] are just a few of the variants of the DG method that have gained popularity. The SV method was introduced by Wang, Zhang and Liu [8], where each element is split into multiple FV cells called control volumes. Similar to DG, the SV method is compact. The staggered grid Chebyshev multi-domain method initially pioneered by Kopriva [9] and later modified and applied to triangular and quadrilateral elements was called SD method by Liu, Vinokur and Wang [10]. The SD scheme is similar to DG but based upon the differential form of the governing equations, avoiding the need to calculate surface or volume integrals. The FR method was pioneered by Huynh [11, 12]. Like SD, it is also based on the differential form. The FR approach represents a significant development because it has the ability to recover nodal DG, SV and SD for linear problems. The lifting collocation penalty method by Wang and Gao [13] (LCP) is an indirect extension of the FR method to triangles. Haga, Gao and Wang [14] further extended LCP to tetrahedral and prismatic elements. Due to the close connection of FR and LCP, the involved authors coined the name correction procedure via reconstruction (CPR). In the SD approach, solution and flux points are arranged in a staggered fashion within each element. In FR, however, a single grid is used. As a result, FR does not require extra flux computations at locations other than interior solution points. Using this fact, Liang, Cox and Plesniak [15] showed improved computational efficiency of FR over SD for quadrilateral elements, especially when simulating viscous flows.

The FR method has seen significant development since its conception. One such

development was made by Vincent, Castonguay and Jameson [16] who identified an infinite family of energy stable high-order schemes, also known as Vincent-Castonguay-Jameson-Huynh (VCJH) schemes. These schemes provide a stable formulation for linear advection problems on triangular elements, which was shown by Castonguay et al. [17]. Following this work, Williams et al. [18] proved stability of the VCJH schemes for linear advection-diffusion problems for all orders of accuracy. Non-linear stability analysis of FR schemes was done by Jameson et al. [19], who showed that location of the solution points within each element have a significant effect on non-linear stability. This is a significant finding since linear analysis of FR schemes implies that stability is independent of solution point positioning. They show that by using an exact L^2 projection to approximate the flux as opposed to the collocation projection, aliasing driven instabilities can be eliminated. Further work on treating aliasing errors through over-integration applied to the flux reconstruction method was done by Spiegel and Huynh [20].

Discontinuous high-order methods are friendly for parallelization on multiple processing elements for both fixed and deforming meshes. The potential for convergence acceleration of discontinuous spectral/ hp methods can be realized by hp -adaptivity and hp -multigrid methods. For a comprehensive review of high-order methods, see Wang [21], Vincent and Jameson [22], and Huynh, Wang and Vincent [23]. For in depth analyses on the connection between DG and FR, see the work of De Grazia et al. [24] and Mengaldo et al. [25]

1.2 Motivation and Objective

With the development of high-order unstructured methods comes the need to achieve faster convergence, especially for solving large-scale problems using parallel computers. This demand motivates the development of time stepping techniques for

which the CFL condition is less restrictive, which is hardly the case when explicit (e.g. multi-stage Runge-Kutta) schemes are combined with high-order methods and dual time stepping. In this work, we present an implicit scheme that overcomes the time step restriction associated with explicit schemes used for solving the unsteady incompressible Navier-Stokes equations. Work done to improve convergence of unsteady incompressible flow can be seen in Liang, Chan, Liu and Jameson [26], whereby they used an SD method and Chorin's original artificial compressibility formulation (AC) [27] as well as a p -multigrid method to accelerate the convergence rate of pseudo time stepping for a particular physical time step. However, the p -multigrid method marginally improves the stiffness introduced by the artificial compressibility approach, especially for flows that require high aspect ratio elements near solid walls. As computers become equipped with larger RAM, implicit time stepping schemes are seen as effective drivers to overcome this stiffness. With these implicit schemes much larger time steps can be taken in comparison to explicit schemes, delivering the potential to improve the rate of convergence significantly.

Application of the DG method to the incompressible Navier-Stokes equations was performed by Bassi et al. [28], where artificial compressibility was introduced only at the interface flux level. Shahbazi, Fischer and Ethier [29] and Nguyen, Peraire and Cockburn [30] applied DG to these equations as well, using triangular and tetrahedral grids. However, incompressible solvers involving a Poisson solver cannot be easily parallelized according to domain decomposition of the grid. One advantage of the approach taken in our current work lies in the fact that the method is discontinuous and local; as a result, there is no global matrix to split.

In recent years, the lower-upper symmetric Gauss-Seidel (LU-SGS) scheme that was originally developed by Jameson and Yoon [31] with multiple grids for solving the unsteady Euler equations has been used within the high-order CFD community for solving compressible flow problems on unstructured grids using SD [32, 33, 34] and

SV [35] methods. When solving incompressible flows using artificial compressibility, the LU-SGS scheme is more economical because it requires the solution of only three equations in two dimensions as opposed to the four needed for compressible flow. Furthermore, with the introduction of artificial compressibility, pressure and velocity are loosely coupled and the Navier-Stokes equations take on a mixed hyperbolic/parabolic mathematical nature. Since both pressure and velocity are state variables in pseudo time, this loose coupling combined with a discontinuous numerical method paves the way for extreme scalability on parallel computers for unstructured grids. However, the feasibility of implementing the current implicit time stepping scheme for large scale three-dimensional simulations is still unclear. At this time, all 3D simulations presented in this work directly use explicit pseudo time stepping.

This work aims to bring Huynh's flux reconstruction method, which has been principally used to produce high-order accurate solutions for compressible flows, to the incompressible flow regime. Direct application of this work that is of immediate interest to us involves the study of vortex dominated viscous flows in curved artery models, which we discuss in detail in Part II of this dissertation. In this regard, the current solver is novel, especially if future implementations can be applied to moving and deforming grids needed to solve problems involving fluid-structure interaction (FSI) on massively parallel computers.

1.3 Developments and Highlights

The major contributions from this dissertation are summarized as follows:

- Developed 2D and 3D unstructured incompressible Navier-Stokes flow solvers, requiring over 45,000 lines of well-commented modules and subroutines

written in FORTRAN. Distributed memory parallelism was performed using the standardized and portable message-passing standard MPI.

- Developed over 19,000 lines of pre- and post-processing scripts using a combination of MATLAB [36], GMSH [37] and Tecplot [38].
- Implemented Huynh’s high-order flux reconstruction method for quadrilateral elements (*linear, quadratic, cubic*) and hexahedral elements (*linear, quadratic*), a Rusanov Riemann solver for calculating inviscid numerical fluxes, and a BR2-type scheme for calculating viscous numerical fluxes.
- Implemented cubic Bezier curves in 2D to handle curved boundaries.
- Demonstrated effectiveness of an implicit dual time stepping scheme with LU-SGS smoothing for solving Chorin’s formulation of steady and unsteady incompressible Navier-Stokes equations in 2D.
- Verified 2D and 3D implementation of the flux reconstruction method and compared results to both experimental and numerical work from the literature.
- Demonstrated efficient implementation of the 3D solver on parallel computers for higher polynomial orders of the flux reconstruction scheme.
- Extended the 2D solver to 3D (*explicit pseudo time stepping only*).
- Collaborated with experimentalists to simulate pulsatile flow of a blood-analog fluid through a curved artery model under physiological conditions.
- Studied the effect of both fully developed steady/pulsatile and undeveloped pulsatile uniform entrance conditions on the development of secondary flow and vortical structures, highlighting both pulsatility and curvature effects.
- Computed instantaneous wall shear stresses and metrics commonly used to assess oscillatory and multidirectional aspects of the flow.
- Described spatial and temporal evolution of three-dimensional vortex structures and the conditions under which vortex splitting occurs.
- Demonstrated a correlation between vortex structures and haemodynamic wall

shear stress metrics.

1.4 Outline

The dissertation is presented in two parts:

In Part I, we first present the governing equations under artificial compressibility and dual time stepping. We then introduce the one-dimensional formulation of Huynh's high-order flux reconstruction method and algorithm for computing the residual, followed by the extension to tensor product (quadrilateral) elements. The formulation for computing element interface inviscid and viscous numerical fluxes is given. We present both explicit and implicit time stepping schemes in the context of the flux reconstruction method and the algorithm implemented under dual time stepping. Furthermore, we verify the 2D implementation of the solver for simulating steady and unsteady viscous flow by demonstrating order of accuracy and validating solutions with well known test cases. After the 2D results, we provide the FR formulation in 3D for tensor product (hexahedral) elements and verify the implementation by simulating steady and unsteady laminar flow past a sphere. Finally, we assess the performance and efficiency of the 3D solver on single- and multi-node computers.

In Part II, we first give a brief background on steady and unsteady flow through curved pipes, highlighting the major works of the 20th century while identifying hitherto unexplored areas of research. We highlight the usefulness of the current work with regard to the study of blood flow through curved arteries and its implication on the progression of atherosclerosis. Next, we outline the geometry of the curved artery model under consideration and give background information on vorticity and vortex identification. Then, we provide detailed descriptions of flow results for three different flow conditions to the entrance of the curve: 1)

fully developed steady (Poiseuille) flow, 2) fully developed pulsatile (Womersley) flow, and 3) undeveloped (uniform) pulsatile flow. We characterize the development of secondary flows and the spatial and temporal evolution of three-dimensional vortex structures, highlighting both pulsatility and curvature effects, and compare our results to experimental data. Finally, we correlate the evolution of secondary flow structures to relevant haemodynamic wall shear stress metrics.

Part I

Development of a High-order Flux Reconstruction Incompressible Navier-Stokes Solver

Chapter 2

Governing Equations of Motion

2.1 Incompressible Navier-Stokes Equations with Artificial Compressibility

The continuity equation of an incompressible fluid

$$\nabla \cdot \mathbf{u} = 0 \quad (2.1)$$

states mathematically that the divergence of the velocity vector field \mathbf{u} is zero. Physically, this means the time rate of change of the volume of a moving fluid element, per unit volume, is zero. Numerically, this is a constraint on the solution that must be satisfied at the steady state when simulating a steady flow problem or at each physical time step for an unsteady flow problem. The unsteady momentum equations of an incompressible Newtonian fluid written in non-conservation form are

$$\frac{\partial \mathbf{u}}{\partial t} + \mathbf{u} \cdot \nabla \mathbf{u} = -\frac{1}{\rho} \nabla P + \nu \nabla^2 \mathbf{u}. \quad (2.2)$$

Together, Eqs. (2.1) and (2.2) are called the unsteady incompressible Navier-Stokes equations. The above system of equations can be expanded for a Cartesian coordinate system (x, y) as

$$\frac{\partial u}{\partial x} + \frac{\partial v}{\partial y} = 0 \quad (2.3)$$

$$\frac{\partial u}{\partial t} + \frac{\partial u^2}{\partial x} + \frac{\partial uv}{\partial y} = -\frac{1}{\rho} \frac{\partial P}{\partial x} + \nu \left(\frac{\partial^2 u}{\partial x^2} + \frac{\partial^2 u}{\partial y^2} \right) \quad (2.4)$$

$$\frac{\partial v}{\partial t} + \frac{\partial vu}{\partial x} + \frac{\partial v^2}{\partial y} = -\frac{1}{\rho} \frac{\partial P}{\partial y} + \nu \left(\frac{\partial^2 v}{\partial x^2} + \frac{\partial^2 v}{\partial y^2} \right). \quad (2.5)$$

In the above formulation, $u = u(x, y, t)$ and $v = v(x, y, t)$ are the velocity components, $P = P(x, y, t)$ is the static pressure, ρ is the density, and ν is the kinematic viscosity.

Numerical computation of the incompressible Navier-Stokes equations is

challenging because the continuity equation lacks a time-dependent term. To handle this difficulty, consider Chorin's artificial compressibility method [27] whereby Eqs. (2.3)-(2.5) are modified by adding artificial or pseudo time derivatives of pressure and velocity to the continuity and momentum equations, respectively, such that

$$\frac{1}{\beta_o} \frac{\partial p}{\partial \tau} + \frac{\partial u}{\partial x} + \frac{\partial v}{\partial y} = 0 \quad (2.6)$$

$$\frac{\partial u}{\partial \tau} + \frac{\partial u}{\partial t} + \frac{\partial u^2}{\partial x} + \frac{\partial uv}{\partial y} = -\frac{\partial p}{\partial x} + \nu \left(\frac{\partial^2 u}{\partial x^2} + \frac{\partial^2 u}{\partial y^2} \right) \quad (2.7)$$

$$\frac{\partial v}{\partial \tau} + \frac{\partial v}{\partial t} + \frac{\partial vu}{\partial x} + \frac{\partial v^2}{\partial y} = -\frac{\partial p}{\partial y} + \nu \left(\frac{\partial^2 v}{\partial x^2} + \frac{\partial^2 v}{\partial y^2} \right) \quad (2.8)$$

where the artificial terms are all derivatives with respect to an artificial or pseudo time τ . The symbol β_o represents the artificial compressibility parameter and p is the static pressure divided by the density, $p(x, y, t) = P(x, y, t)/\rho$. We can write the above system in strong conservation form as

$$\frac{\partial \mathbf{U}}{\partial \tau} + \mathbf{I}_D \frac{\partial \mathbf{U}}{\partial t} + \nabla \cdot \mathbf{F}(\mathbf{U}, \nabla \mathbf{U}) = 0. \quad (2.9)$$

The vector of state variables $\mathbf{U}(x, y, t) \in \Omega$, where $\Omega \subset \mathbb{R}^2$ and $t \geq 0$, and the vector of fluxes $\mathbf{F}(\mathbf{U}, \nabla \mathbf{U})$ are

$$\mathbf{U} = \begin{bmatrix} p \\ u \\ v \end{bmatrix}, \quad \mathbf{F}(\mathbf{U}, \nabla \mathbf{U}) = \begin{bmatrix} \mathbf{f} \\ \mathbf{g} \end{bmatrix} \quad (2.10)$$

and $\mathbf{I}_D = \text{diag}(0, 1, 1)$. The flux vector contains both inviscid terms denoted $(\cdot)_e$ and

viscous terms denoted $(\cdot)_v$ in x and y , where

$$\mathbf{f} = \mathbf{f}_e - \mathbf{f}_v \quad (2.11)$$

$$\mathbf{g} = \mathbf{g}_e - \mathbf{g}_v. \quad (2.12)$$

The inviscid fluxes for the artificial compressibility formulation are

$$\mathbf{f}_e = \begin{bmatrix} \beta_o u \\ u^2 + p \\ uv \end{bmatrix}, \quad \mathbf{g}_e = \begin{bmatrix} \beta_o v \\ uv \\ v^2 + p \end{bmatrix} \quad (2.13)$$

and the viscous fluxes are

$$\mathbf{f}_v = \begin{bmatrix} 0 \\ \nu \frac{\partial u}{\partial x} \\ \nu \frac{\partial v}{\partial x} \end{bmatrix}, \quad \mathbf{g}_v = \begin{bmatrix} 0 \\ \nu \frac{\partial u}{\partial y} \\ \nu \frac{\partial v}{\partial y} \end{bmatrix}. \quad (2.14)$$

Since the governing form of the incompressible equations has been modified to take on a mixed hyperbolic/parabolic nature due to the introduction of artificial compressibility, there exist three characteristics in 2D that can be obtained from the eigensystem of the convective flux Jacobians \mathbf{A}_e and \mathbf{B}_e

$$\mathbf{A}_e = \frac{\partial \mathbf{f}_e}{\partial \mathbf{U}} = \begin{bmatrix} 0 & \beta_o & 0 \\ 1 & 2u & 0 \\ 0 & v & u \end{bmatrix}, \quad \mathbf{B}_e = \frac{\partial \mathbf{g}_e}{\partial \mathbf{U}} = \begin{bmatrix} 0 & 0 & \beta_o \\ 0 & v & u \\ 1 & 0 & 2v \end{bmatrix}. \quad (2.15)$$

The eigenvalues of \mathbf{A}_e and \mathbf{B}_e are

$$\lambda_A = \{u - c_x, u, u + c_x\} \quad (2.16)$$

$$\lambda_B = \{v - c_y, v, v + c_y\} \quad (2.17)$$

where

$$c_x = \sqrt{u^2 + \beta_o} \quad (2.18)$$

$$c_y = \sqrt{v^2 + \beta_o} \quad (2.19)$$

are now termed the *pseudo* speed of sound in each direction. This means that pressure waves having finite speed are introduced into the fluid. However, these pressure waves die out as the solution approaches the divergence-free velocity state - this is termed the *pseudo* steady state. Note that the pseudo speed of sound is a function of both the velocity and the artificial compressibility parameter. Furthermore, the pseudo Mach number $M_p = u/c_x$ is always less than 1 for $\beta_o > 0$. This is a necessary condition in order for pressure waves to travel upstream and affect the entire flow field. More details on the eigenstructure of the incompressible Navier-Stokes equations with artificial compressibility can be found in Elsworth and Toro [39].

In true incompressible flow, the pressure field is affected instantaneously throughout the domain by any flow disturbances. However, in Chorin's modified formulation, the artificial compressibility parameter β_o , which is not a function of space or time in these simulations, introduces waves with finite speed into the fluid as a means to distribute the pressure. Consequently, the non-physical effect on the pressure field by any disturbance is delayed by some amount of time. Ideally, the value of β_o should be chosen as high as possible for a given

algorithm such that incompressibility is recovered quickly without degradation of the solution. For steady flow, the artificial compressibility formulation can be very efficient because the divergence-free constraint for the velocity field does not have to be satisfied at each iteration. Only at the steady state does the solution take physical meaning and $\nabla \cdot \mathbf{u} = 0$. Also, computational efficiency is generally better than that for compressible flow solvers at the incompressible limit. However, unsteady computations of incompressible flows are time-consuming because any change in the flow must be propagated throughout the entire flow field.

Following the description given by Kwak et al. [40], the formation of the boundary layer in viscous flows is sensitive to the streamwise pressure gradient, especially in an environment where an adverse pressure gradient can cause flow separation. If separation occurs, a pressure wave with finite speed will modify the local pressure gradient, which will ultimately affect the position of separation. This phenomenon can have a feedback effect on the pressure field. Thus, convergence issues arise if the wave does not propagate sufficiently fast. For internal flows in particular, the distribution characteristics of pressure waves within a viscous flow become rather important. To achieve reasonable convergence in this solver, β_o is typically chosen between 1 and 4. Although, general optimization of β_o to accelerate steady state convergence has been performed by a number of authors including Turkel [41] and Helenbrook [42].

The classic formulation of Chorin has been well studied by many authors. To mention just a few, Belov et al. [43] developed a fully-implicit algorithm for solving unsteady incompressible Euler and Navier-Stokes equations. Drikakis et al. [44] developed a non-linear multigrid method for accelerating convergence under explicit time stepping. For transient flows, we point out the work done by Merkle and Athavale [45], Soh and Goodrich [46], Rogers and Kwak [47], and Rogers, Kwak and Kiris [48]. A unified implicit solution procedure outlined by Kwak et al. [49]

is capable of solving low-speed compressible flows, transonic, as well as supersonic flows accurately and efficiently. Application of exact and approximate Riemann solvers to Chorin's formulation has been conducted by Elsworth and Toro [39, 50]. Detailed descriptions of high-resolution schemes and various solution methods for incompressible and low-speed flows are provided in the text by Drikakis and Rider [51].

Chapter 3

The Flux Reconstruction Method

3.1 Flux Reconstruction Formulation

3.1.1 One-Dimensional Formulation

The motivation for the development of FR was to allow for the various well known high-order schemes discussed earlier - nodal DG, SV SD - to be cast within a single unifying framework. This method uses the differential form of the governing equations and can achieve arbitrary order of accuracy. The idea is to construct a globally continuous flux function within a given domain from a piecewise discontinuous flux through weighted correction functions. This method has proven to be a significant advancement for high-order methods in terms of reduced complexity, robustness, flexibility and efficiency and is presented below. For a full presentation of the method, see the original pioneering work by Huynh [11, 12].

Consider the one-dimensional scalar conservation law

$$\frac{\partial u}{\partial t} + \frac{\partial f(u)}{\partial x} = 0 \quad (3.1)$$

where t is time and x is the spatial coordinate. The quantity $u(x, t) \in \Omega$ is a conserved scalar and $f(u)$ is the flux, where $\Omega \subset \mathbb{R}^1$ and $t \geq 0$. Let the domain Ω be partitioned into N_e non-overlapping elements denoted by $\Omega_e = \{x \mid x_e \leq x \leq x_{e+1}\}$ such that

$$\Omega = \bigcup_{e=1}^{N_e} \Omega_e. \quad (3.2)$$

Let $u^E(x, t)$ represent the exact solution of Eq. (3.1) and let $u(x, t)$ represent the global approximation to the exact solution. Furthermore, let u_e represent the approximate numerical solution in each element Ω_e of the partitioned domain. This approximate solution is defined to be a polynomial of degree p that is local to each element. Piecewise summation of u_e gives the global approximation u , which is discontinuous

across element interfaces, to the exact solution. Similarly, let f^E represent the exact flux of Eq. (3.1) and let f represent the global approximation to the exact flux. Also, let f_e represent the approximate numerical flux in each element, which is a polynomial of degree $p + 1$. The piecewise sum of f_e gives the global approximation f to the exact flux. The global approximation f is designed to be C^0 continuous between elements in order for the scheme to be conservative, and we outline Huynh's methodology for constructing f throughout the remainder of this section.

For a convenient implementation, each physical element Ω_e is transformed to a reference element $\Omega_r = \{\xi \mid 0 \leq \xi \leq 1\}$ via an isoparametric mapping of the form

$$x = \Theta_e(\xi) = (1 - \xi)x_e + \xi x_{e+1} \quad (3.3)$$

for which the inverse is

$$\xi = \Theta_e^{-1}(x) = \frac{x - x_e}{x_{e+1} - x_e}. \quad (3.4)$$

After the transformation to the reference domain, the governing equations take the form

$$\frac{\partial \hat{u}}{\partial t} + \frac{\partial \hat{f}}{\partial \xi} = 0 \quad (3.5)$$

where

$$\hat{u} = Ju_e(\Theta_e(\xi), t), \quad \hat{f} = f_e(\Theta_e(\xi), t) \quad (3.6)$$

and $J = x_{e+1} - x_e$.

In the FR approach in 1D, a Lagrange polynomial is used as the interpolating polynomial through a set of nodal points within Ω_r . These nodal points are also

referred to as solution points. The number of solution points per element $N_s|_{\Omega_r}$ is dependent upon the degree of the polynomial p and the dimension \mathcal{N} of the conservation law such that

$$N_s|_{\Omega_r} = (p + 1)^{\mathcal{N}}. \quad (3.7)$$

Also, the numerical flux points are located at the left and right interface where $\xi = 0$ and $\xi = 1$, respectively. The number of flux points per element $N_f|_{\Omega_r}$ is

$$N_f|_{\Omega_r} = 2\mathcal{N}(p + 1)^{\mathcal{N}-1}. \quad (3.8)$$

The total number of solution points in the global domain, referred to as the *degrees of freedom* (DOF), is

$$DOF|_{\Omega} = N_e N_s|_{\Omega_r}. \quad (3.9)$$

For a 4th order FR method for which $p = 3$ and $N_s = 4$, the distribution of solution points and flux points inside Ω_r along the transformed coordinate direction ξ is depicted in Figure 3.1.



Figure 3.1 Distribution of solution points (SP •) and numerical flux points (FP ■) for a 4th order FR method inside a 1D reference element Ω_r .

From this figure, we can see that the FR approach avoids the two-grid system and subsequent computational work associated with a staggered solution point/flux point framework inherent to the SD method. Using the solution at $p+1$ solution points, an

interpolating polynomial of degree p is built using the Lagrange nodal basis

$$\ell_i(\xi) = \prod_{s=1, s \neq i}^{p+1} \left(\frac{\xi - \xi_s}{\xi_i - \xi_s} \right) \quad \forall \quad i = 1 \dots p+1 \quad (3.10)$$

for which $\ell_i(\xi_s) = \delta_{is}$, where δ_{is} is the Kronecker delta. For each Ω_r , the solution and flux vectors can be reconstructed by the collocation projection

$$\hat{u}_r(\xi) = \sum_{i=1}^{p+1} \hat{u}_{r|i} \ell_i(\xi) \quad (3.11)$$

$$\hat{f}_r^D(\xi) = \sum_{i=1}^{p+1} \hat{f}_{r|i}^D \ell_i(\xi) \quad (3.12)$$

where $\hat{u}_{r|i} = \hat{u}_r(\xi_i)$ are the nodal coefficients of the solution in Ω_r , which represent the value of the approximate solution polynomial \hat{u}_r evaluated at the set of $p+1$ solution points. The nodal coefficients $\hat{f}_{r|i}^D = \hat{f}_r(\xi_i)$ of the discontinuous flux \hat{f}_r^D are computed from $\hat{u}_{r|i}$.

Following the description from Huynh [12], reconstruction of the C^0 continuous flux \hat{f}_r for each element involves the jump in flux at each interface. Using this disparity, corrections are made to the discontinuous flux function \hat{f}_r^D given by Eq. (3.12) in order to define a flux function that is continuous. Following Huynh's 1D formulation, let the polynomial \hat{f}_r represent a continuous flux function in Ω_r that accounts for data interaction among adjacent elements by taking on common flux values at the two interfaces. The discontinuous flux function \hat{f}_r^D is then corrected in the following manner

$$\hat{f}_r(\xi) = \hat{f}_r^D(\xi) + \left[\hat{f}_{r-\frac{1}{2}}^{com} - \hat{f}_r^D(0) \right] g_r^{LB}(\xi) + \left[\hat{f}_{r+\frac{1}{2}}^{com} - \hat{f}_r^D(1) \right] g_r^{RB}(\xi) \quad (3.13)$$

where $(\cdot)^{LB}$ and $(\cdot)^{RB}$ signify functions used to apply corrections to the left and right boundary interfaces of Ω_r . This formulation provides two corrections to \hat{f}_r^D in 1D

- one correction due to a jump in flux at the left boundary of Ω_r , $\hat{f}_{r-\frac{1}{2}}^{com} - \hat{f}_r^D(0)$, and a second correction due to a jump in flux at the right boundary, $\hat{f}_{r+\frac{1}{2}}^{com} - \hat{f}_r^D(1)$. The term \hat{f}^{com} is the common flux evaluated between elements at the interface that can be computed using an appropriate Riemann solver, and $g_r(\xi)$ is a function of degree $p+1$ required to apply the corrections. The jump in flux at the interface results in a correction to \hat{f}_r^D evaluated at all solution points. For the left boundary, the general correction function in 1D is defined as

$$g_r^{LB}(\xi) = \alpha \mathcal{R}_{R,p+1}(\xi) + (1 - \alpha) \mathcal{R}_{R,p}(\xi) \quad (3.14)$$

where $\mathcal{R}_{R,p+1}(\xi)$ represents the right Radau polynomial

$$\mathcal{R}_{R,p+1}(\xi) = \frac{(-1)^{p+1}}{2} \left(\mathcal{L}_{p+1}(\xi) - \mathcal{L}_p(\xi) \right) \quad (3.15)$$

of degree $p+1$ for $p > -1$, where a shifted Legendre polynomial $\mathcal{L}(\xi)$ of degree $p+1$ on the interval $\{\xi \mid 0 \leq \xi \leq 1\}$ is determined by

$$\mathcal{L}_{p+1}(\xi) = \frac{2p+1}{p+1} \left(2\xi - 1 \right) \mathcal{L}_p(\xi) - \frac{p}{p+1} \mathcal{L}_{p-1}(\xi) \quad (3.16)$$

for which $\mathcal{L}_{-1}(\xi) = 0$ and $\mathcal{L}_0(\xi) = 1$. Choosing $\alpha = 1$ for the correction function in Eq. (3.14) recovers the collocation based nodal DG method, and we can write $g_r^{LB} = g_{DG}^{LB}$ where

$$g_{DG}^{LB}(\xi) = \mathcal{R}_{R,p+1}(\xi). \quad (3.17)$$

Alternatively, choosing $\alpha = (p+1)/(2p+1)$ recovers a modified SD method, and we can

write $g_r^{LB} = g_{SD}^{LB}$ where

$$g_{SD}^{LB}(\xi) = \frac{p+1}{2p+1} \mathcal{R}_{R,p+1}(\xi) + \frac{p}{2p+1} \mathcal{R}_{R,p}(\xi). \quad (3.18)$$

This scheme was proven stable by Huynh [11] using von Neumann stability analysis. The original SD scheme was proven linearly stable by Jameson [52]. As mentioned earlier, the difference between the FR method that uses g_{SD} and the original SD scheme is that the latter approach uses a staggered grid for each element while the current approach uses a single grid. A comparison of computational efficiency between SD and FR when solving the compressible Euler and Navier-Stokes equations was performed in Liang, Cox and Plesniak [15]. These authors demonstrated the improved efficiency of FR over SD, especially when simulating viscous flows.

A third type of scheme can be obtained by setting $\alpha = p/(2p+1)$, which gives the g_2 scheme identified by Huynh [11] and written as

$$g_2^{LB}(\xi) = \frac{p}{2p+1} \mathcal{R}_{R,p+1}(\xi) + \frac{p+1}{2p+1} \mathcal{R}_{R,p}(\xi). \quad (3.19)$$

This scheme is also referred to as $g_{Lump,Lo}^{LB}$ due to the inherent feature of the correction function to lump corrections to the left boundary by choosing the solution points to be the Lobatto points, where the derivatives of the correction function are zero.

The expression for a correction to the right boundary is denoted $g_r^{RB}(\xi)$ and obtained simply by reflection of $g_r^{LB}(\xi)$, so that $g_r^{RB}(\xi) = g_r^{LB}(1-\xi)$ on the interval $\Omega_r = \{\xi \mid 0 \leq \xi \leq 1\}$. The correction functions for left and right boundaries must take

on the values

$$g_r^{LB}(0) = 1, \quad g_r^{LB}(1) = 0 \quad (3.20)$$

$$g_r^{RB}(0) = 0, \quad g_r^{RB}(1) = 1. \quad (3.21)$$

As stated before, the discontinuous flux function \hat{f}_r^D is of degree p . However, both g_r^{LB} and g_r^{RB} are of degree $p+1$. Therefore, the continuous function \hat{f}_r is designed to be of degree $p+1$ and takes on the two common flux values at the interface

$$\hat{f}_r(0) = \hat{f}_{r-\frac{1}{2}}^{com} \quad (3.22)$$

$$\hat{f}_r(1) = \hat{f}_{r+\frac{1}{2}}^{com}. \quad (3.23)$$

This ultimately ensures C^0 continuity of the approximate flux across interfaces. Once suitable correction functions for g_r^{LB} and g_r^{RB} have been defined for Ω_r , a derivative of the continuous flux function can be computed using

$$\frac{\partial \hat{f}_r(\xi_l)}{\partial \xi} = \sum_{i=1}^{p+1} \hat{f}_{r|i}^D \frac{d\ell_i(\xi_l)}{d\xi} + [\hat{f}_{r-\frac{1}{2}}^{com} - \hat{f}_r^D(0)] \frac{dg_r^{LB}(\xi_l)}{d\xi} + [\hat{f}_{r+\frac{1}{2}}^{com} - \hat{f}_r^D(1)] \frac{dg_r^{RB}(\xi_l)}{d\xi} \quad (3.24)$$

at the solution nodes ξ_l where $l = 1 \dots p+1$, after which the solution can then be advanced in time with an appropriate time stepping scheme. A derivative of the discontinuous flux function $\partial \hat{f}_r^D / \partial \xi$ is computed from the Lagrange polynomial or the chain-rule. We use the former method in the current implementation, which is demonstrated in Eq. (3.24).

The current choice of correction function for all Ω_r is $g_r = g_{SD}$ from Huynh [11, 12] where the solution points are located at the Legendre-Gauss quadrature points, which are the roots of the equation $\mathcal{L}_{p+1}(\xi) = 0$. This type of correction function is seen as a trade-off between stability and accuracy when considering other choices such as g_2 and g_{DG} . The reason for this trade-off lies in the relative steepness of

the correction function g_{SD} - its steepness is greater than that of g_2 but less than g_{DG} (see Figure 3.2). This corresponds to a correction strength between g_2 and g_{DG} , since ultimately we require derivatives of g_r to compute spatial derivatives of the transformed flux in Eq. (3.5).

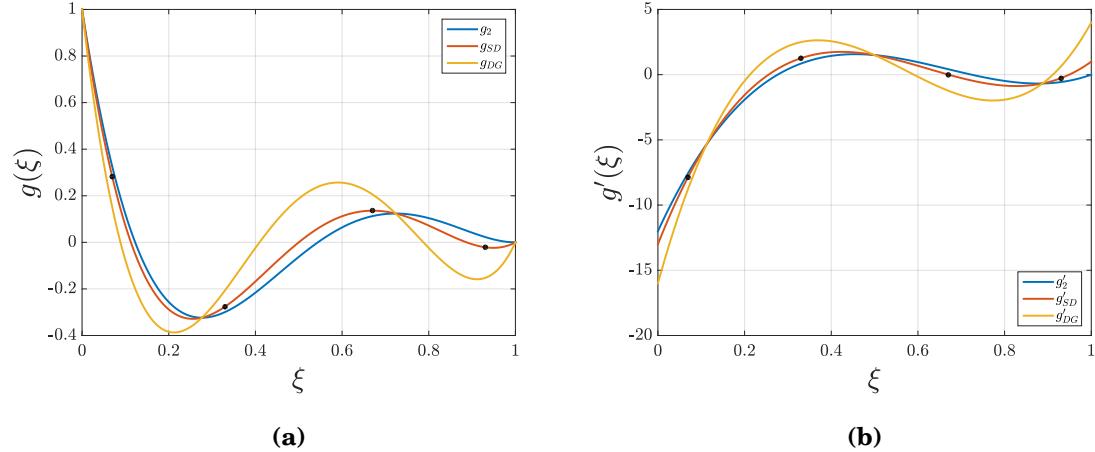
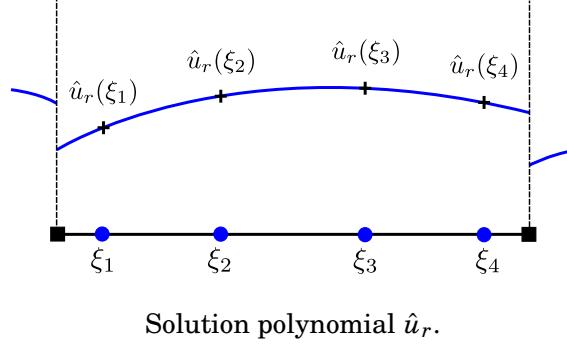


Figure 3.2 (a) correction functions g_2 , g_{SD} and g_{DG} and (b) correction function derivatives g'_2 , g'_{SD} and g'_{DG} for the left boundary for $p = 3$.

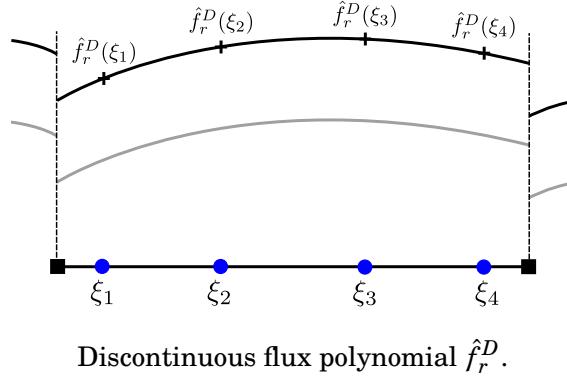
3.1.1.1 Algorithm

In summary, the algorithm used to compute $\partial\hat{f}/\partial\xi$ at each solution point ξ_l for $l = 1 \dots p + 1$ for each reference element can be described in five major stages:

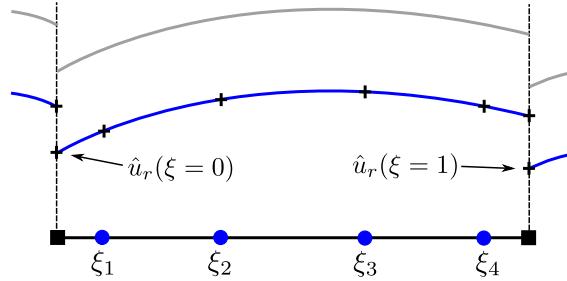
1. Construct the solution polynomial \hat{u}_r , using the solution at $p + 1$ points and a degree p polynomial ℓ_i built from a Lagrange basis.



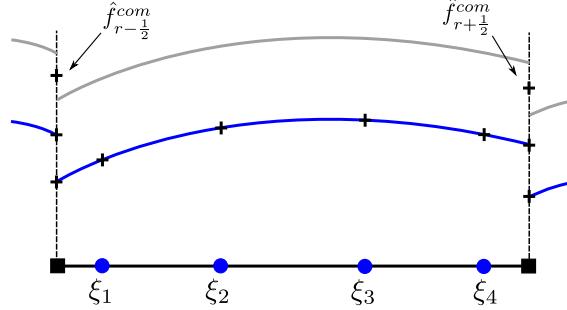
2. Construct the discontinuous flux polynomial \hat{f}_r^D of degree p from the solution at $p+1$ points.



3. Reconstruct the solutions \hat{u}_r and the discontinuous fluxes \hat{f}_r^D along the edges of Ω_r from Eqs. (3.11)-(3.12) and compute the common numerical fluxes \hat{f}^{com} from a Riemann solver.

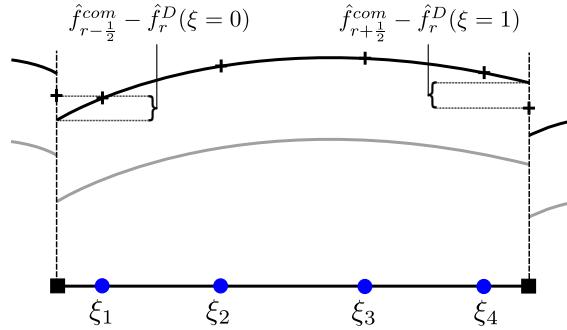


Reconstruction solution \hat{u}_r at the left and right interfaces.

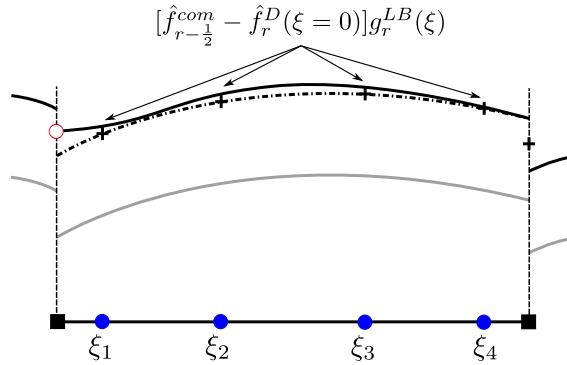


Common numerical flux \hat{f}_r^{com} evaluated by Riemann solver.

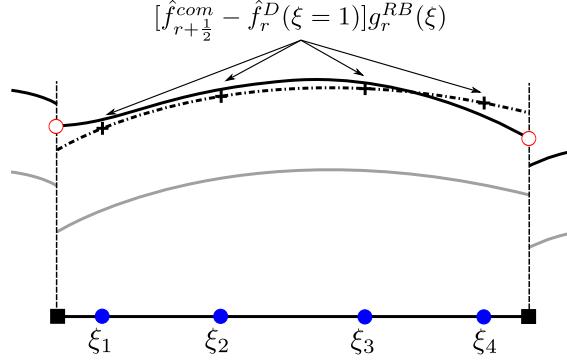
4. Construct the continuous flux polynomial \hat{f}_r of degree $p+1$ by adding flux corrections based upon the jump in flux along the left and right edges of Ω_r by using correction functions g_r^{LB} and g_r^{RB} of degree $p+1$. In the current implementation, we use only one type of correction function; namely $g_r = g_{SD}$.



Jump in flux at the left and right interfaces.

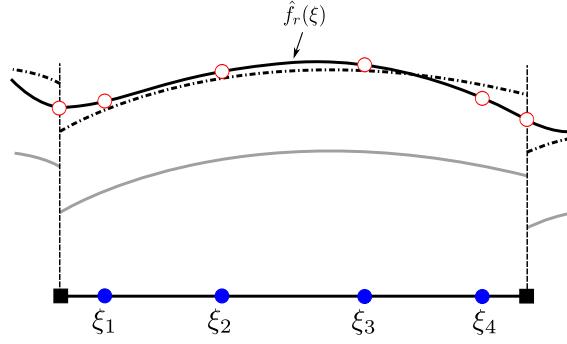


Add first correction to discontinuous flux \hat{f}_r^D due to jump in flux at left interface.



Add second correction to discontinuous flux \hat{f}_r^D due to jump in flux at right interface.

5. Evaluate $\partial\hat{f}_r/\partial\xi$ at each solution point ξ_l within Ω_r using Eq. (3.24).



Evaluate flux derivative $\partial\hat{f}_r/\partial\xi$ at each solution point.

3.1.2 Tensor Product Formulation on Quadrilaterals

To use the FR method to simulate viscous flow on an unstructured quadrilateral mesh, consider the strong conservation form of the two-dimensional incompressible Navier-Stokes equations with artificial compressibility previously defined in Eq. (2.9) as

$$\frac{\partial \mathbf{U}}{\partial \tau} + \mathbf{I}_D \frac{\partial \mathbf{U}}{\partial t} + \nabla \cdot \mathbf{F}(\mathbf{U}, \nabla \mathbf{U}) = 0 \quad (3.25)$$

within an arbitrary solution domain $\Omega \subset \mathbb{R}^2$, which is partitioned into N_e non-overlapping, conforming, quadrilateral elements, each denoted by Ω_e such that

$$\Omega = \bigcup_{e=1}^{N_e} \Omega_e, \quad \bigcap_{e=1}^{N_e} \Omega_e = \emptyset. \quad (3.26)$$

In considering non-uniformity of the solution domain, one is motivated to transform each physical element Ω_e into a reference element $\Omega_r = \{\xi, \eta \mid 0 \leq \xi, \eta \leq 1\}$. The transformation from a physical domain to a computational domain can be achieved through an isoparametric mapping

$$x(\xi, \eta) = \sum_{k=1}^K x_k \phi_k(\xi, \eta) \quad (3.27)$$

$$y(\xi, \eta) = \sum_{k=1}^K y_k \phi_k(\xi, \eta) \quad (3.28)$$

where K is the number of nodes per element Ω_e , (x_k, y_k) are nodal Cartesian coordinates, and $\phi_k(\xi, \eta)$ are the shape functions, which are provided in Appendix A for linear, quadratic and cubic elements. For the case where Ω_e is a cubic quadrilateral element, whose nodal orientation is depicted in Figure 3.3, $K = 12$ and node 1 is located at $(\xi, \eta) = (0, 0)$. Alternatively, to capture general curvature of boundaries in complex geometries, the current two-dimensional implementation of the solver uses Bezier curves, similar to those used in Gao, Wang and Liu [53]. The Bezier curve implementation here uses the two end points of a boundary face along with two interior control points whose locations are defined based upon the geometry of neighboring boundary faces; therefore, these Bezier curves are designed to be cubic.

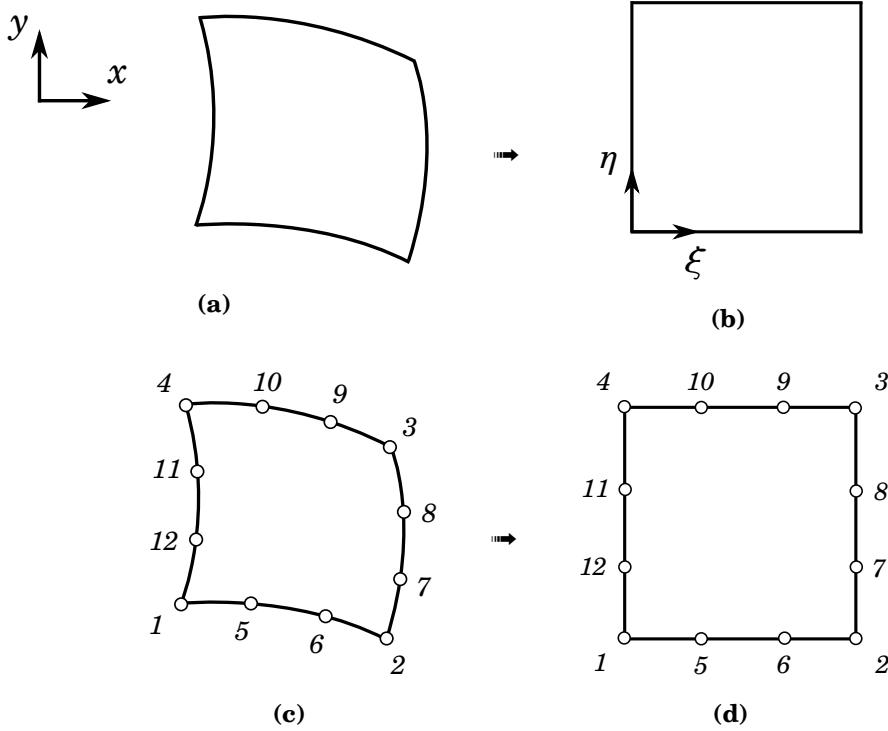


Figure 3.3 Isoparametric mapping from cubic (a) physical element Ω_e to (b) reference element Ω_r . (c) physical element with 12-node orientation and (d) reference element with 12-node orientation.

After transformation into the computational domain, the governing equations in Eq. (3.25) can be re-written in the form

$$\frac{\partial \hat{\mathbf{U}}}{\partial \tau} + \mathbf{I}_D \frac{\partial \hat{\mathbf{U}}}{\partial t} + \hat{\nabla} \cdot \hat{\mathbf{F}} = 0 \quad (3.29)$$

where

$$\hat{\mathbf{U}} = |\mathbf{J}| \mathbf{U}, \quad \hat{\mathbf{F}} = \begin{bmatrix} \hat{\mathbf{f}} \\ \hat{\mathbf{g}} \end{bmatrix} = |\mathbf{J}| \mathbf{J}^{-1} \begin{bmatrix} \mathbf{f} \\ \mathbf{g} \end{bmatrix}. \quad (3.30)$$

In the above equations, $(\hat{\cdot})$ represents values in transformed, reference space. For example, the operator $(\hat{\nabla})$ represents a gradient in the reference element Ω_r , whereas

previously (∇) was a gradient in the physical element Ω_e . For a stationary grid, the metric Jacobian \mathbf{J} is independent of time and can be computed along with its inverse for each 2D reference element as

$$\mathbf{J} = \begin{bmatrix} \frac{\partial x}{\partial \xi} & \frac{\partial x}{\partial \eta} \\ \frac{\partial y}{\partial \xi} & \frac{\partial y}{\partial \eta} \end{bmatrix}, \quad \mathbf{J}^{-1} = \begin{bmatrix} \frac{\partial \xi}{\partial x} & \frac{\partial \xi}{\partial y} \\ \frac{\partial \eta}{\partial x} & \frac{\partial \eta}{\partial y} \end{bmatrix} \quad (3.31)$$

where the metrics of the Jacobian are obtained from the relationship between the non-uniform physical element and the reference element in Eqs. (3.27)-(3.28). In this implementation of the high-order flux reconstruction scheme, \mathbf{J} is stored at each solution and flux point depicted in Figure 3.4 in Chapter 3. From the expression of the transformed fluxes in Eq. (3.30), we can write

$$\mathbf{C}^T = |\mathbf{J}| \mathbf{J}^{-1} \quad (3.32)$$

where \mathbf{C}^T is the transpose of the cofactor matrix of the Jacobian matrix \mathbf{J} and is also known as the adjugate of \mathbf{J} . The entries of \mathbf{C}^T represent the local face areas of a mesh element associated with each node projected in the x and y directions. For simplicity, we rewrite the transpose of the cofactor matrix as

$$\mathbf{C}^T = |\mathbf{J}| \begin{bmatrix} \frac{\partial \xi}{\partial x} & \frac{\partial \xi}{\partial y} \\ \frac{\partial \eta}{\partial x} & \frac{\partial \eta}{\partial y} \end{bmatrix} = \begin{bmatrix} \mathbf{s}_\xi \\ \mathbf{s}_\eta \end{bmatrix}. \quad (3.33)$$

Expanding Eq. (3.29) gives

$$\frac{\partial \hat{\mathbf{U}}}{\partial \tau} + \mathbf{I}_D \frac{\partial \hat{\mathbf{U}}}{\partial t} + \frac{\partial \hat{\mathbf{f}}}{\partial \xi} + \frac{\partial \hat{\mathbf{g}}}{\partial \eta} = 0 \quad (3.34)$$

and

$$\frac{\partial \hat{\mathbf{U}}}{\partial \tau} + \mathbf{I}_D \frac{\partial \hat{\mathbf{U}}}{\partial t} + \frac{\partial}{\partial \xi} (s_{\xi,1} \mathbf{f} + s_{\xi,2} \mathbf{g}) + \frac{\partial}{\partial \eta} (s_{\eta,1} \mathbf{f} + s_{\eta,2} \mathbf{g}) = 0. \quad (3.35)$$

Alternatively, Eq. (3.29) can be written in the more compact form

$$\frac{\partial \hat{\mathbf{U}}}{\partial \tau} + \hat{\mathbf{S}} + \hat{\mathbf{R}} = 0 \quad (3.36)$$

where $\hat{\mathbf{S}}$ represents the physical time derivative and $\hat{\mathbf{R}}$ is the divergence of the flux vector, also known as the residual. These two terms combined we call the pseudo residual

$$\hat{\mathbf{R}}_\tau = \hat{\mathbf{S}} + \hat{\mathbf{R}}. \quad (3.37)$$

The distribution of solution points in the unit square reference element is shown in Figure 3.4 for a FR method for which the polynomial order is $p = 3$. The number of solution points per element is $N_s = (p+1)^2 = 16$. Using the solution at $p+1$ solution points, a p degree Lagrange polynomial in each reference direction ξ and η can be built using

$$\ell_i(\xi) = \prod_{s=1, s \neq i}^{p+1} \left(\frac{\xi - \xi_s}{\xi_i - \xi_s} \right) \quad \forall \quad i = 1 \dots p+1 \quad (3.38)$$

$$\ell_j(\eta) = \prod_{s=1, s \neq j}^{p+1} \left(\frac{\eta - \eta_s}{\eta_j - \eta_s} \right) \quad \forall \quad j = 1 \dots p+1 \quad (3.39)$$

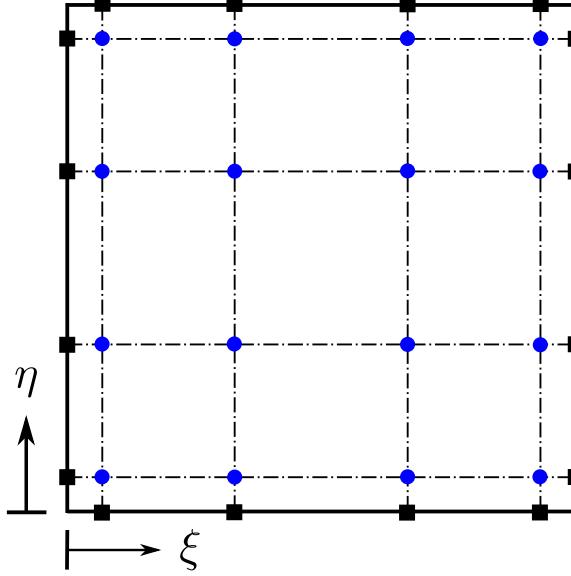


Figure 3.4 Distribution of solution points (SP •) and flux points (FP ■) for $p = 3$ (4th order) FR method inside a unit reference element Ω_r .

for which $\ell_i(\xi_s) = \delta_{is}$ and $\ell_j(\eta_s) = \delta_{js}$. The solution and flux vectors can be reconstructed within Ω_r through tensor products of the two one-dimensional polynomials ℓ_i and ℓ_j by

$$\hat{\mathbf{U}}_r(\xi, \eta) = \sum_{j=1}^{p+1} \sum_{i=1}^{p+1} \hat{\mathbf{U}}_{r|i,j} \ell_i(\xi) \ell_j(\eta) \quad (3.40)$$

$$\hat{\mathbf{f}}_r^D(\xi, \eta) = \sum_{j=1}^{p+1} \sum_{i=1}^{p+1} \hat{\mathbf{f}}_{r|i,j}^D \ell_i(\xi) \ell_j(\eta) \quad (3.41)$$

$$\hat{\mathbf{g}}_r^D(\xi, \eta) = \sum_{j=1}^{p+1} \sum_{i=1}^{p+1} \hat{\mathbf{g}}_{r|i,j}^D \ell_i(\xi) \ell_j(\eta) \quad (3.42)$$

where $\hat{\mathbf{U}}_{r|i,j} = \hat{\mathbf{U}}_r(\xi_i, \eta_j)$ are the nodal coefficients of the solution in Ω_r , which represent the value of the approximate solution polynomial $\hat{\mathbf{U}}_r$ evaluated at the set of solution points. The nodal coefficients $\hat{\mathbf{f}}_{r|i,j}^D = \hat{\mathbf{f}}_r(\xi_i, \eta_j)$ and $\hat{\mathbf{g}}_{r|i,j}^D = \hat{\mathbf{g}}_r(\xi_i, \eta_j)$ of the discontinuous fluxes $\hat{\mathbf{f}}_r^D$ and $\hat{\mathbf{g}}_r^D$ are computed from $\hat{\mathbf{U}}_{r|i,j}$.

Following the methodology presented for the one-dimensional formulation in

Section 3.1.1, the continuous flux functions defined along ξ and η directions are

$$\hat{\mathbf{f}}_r(\xi, \eta) = \hat{\mathbf{f}}_r^D(\xi, \eta) + [\hat{\mathbf{f}}_{r-\frac{1}{2}}^{com} - \hat{\mathbf{f}}_r^D(0, \eta)] g_r^{LB}(\xi) + [\hat{\mathbf{f}}_{r+\frac{1}{2}}^{com} - \hat{\mathbf{f}}_r^D(1, \eta)] g_r^{RB}(\xi) \quad (3.43)$$

$$\hat{\mathbf{g}}_r(\xi, \eta) = \hat{\mathbf{g}}_r^D(\xi, \eta) + [\hat{\mathbf{g}}_{r-\frac{1}{2}}^{com} - \hat{\mathbf{g}}_r^D(\xi, 0)] g_r^{LB}(\eta) + [\hat{\mathbf{g}}_{r+\frac{1}{2}}^{com} - \hat{\mathbf{g}}_r^D(\xi, 1)] g_r^{RB}(\eta) \quad (3.44)$$

and the corresponding derivatives of the continuous flux functions at the solution nodes (ξ_l, η_m) where $l = 1 \dots p+1$ and $m = 1 \dots p+1$ are

$$\begin{aligned} \frac{\partial \hat{\mathbf{f}}_r(\xi_l, \eta_m)}{\partial \xi} &= \sum_{j=1}^{p+1} \sum_{i=1}^{p+1} \hat{\mathbf{f}}_{r|i,j}^D \frac{d\ell_i(\xi_l)}{d\xi} \ell_j(\eta_m) \\ &\quad + [\hat{\mathbf{f}}_{r-\frac{1}{2}}^{com} - \hat{\mathbf{f}}_r^D(0, \eta_m)] \frac{dg_r^{LB}(\xi_l)}{d\xi} + [\hat{\mathbf{f}}_{r+\frac{1}{2}}^{com} - \hat{\mathbf{f}}_r^D(1, \eta_m)] \frac{dg_r^{RB}(\xi_l)}{d\xi} \end{aligned} \quad (3.45)$$

$$\begin{aligned} \frac{\partial \hat{\mathbf{g}}_r(\xi_l, \eta_m)}{\partial \eta} &= \sum_{j=1}^{p+1} \sum_{i=1}^{p+1} \hat{\mathbf{g}}_{r|i,j}^D \ell_i(\xi_l) \frac{d\ell_j(\eta_m)}{d\eta} \\ &\quad + [\hat{\mathbf{g}}_{r-\frac{1}{2}}^{com} - \hat{\mathbf{g}}_r^D(\xi_l, 0)] \frac{dg_r^{LB}(\eta_m)}{d\eta} + [\hat{\mathbf{g}}_{r+\frac{1}{2}}^{com} - \hat{\mathbf{g}}_r^D(\xi_l, 1)] \frac{dg_r^{RB}(\eta_m)}{d\eta}. \end{aligned} \quad (3.46)$$

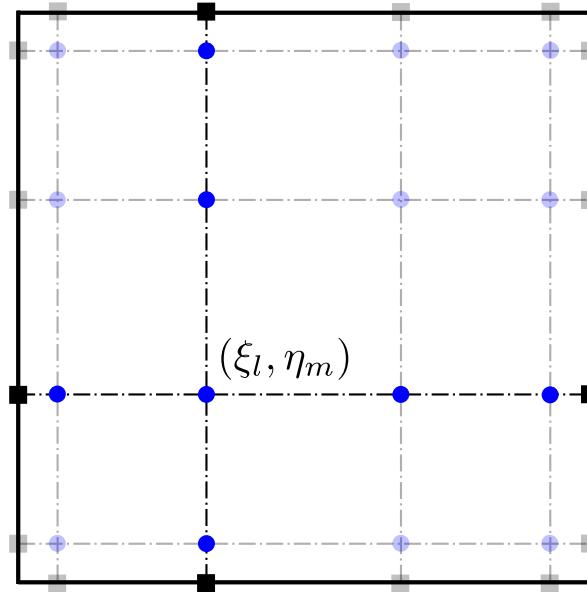


Figure 3.5 Divergence of the flux $\hat{\nabla} \cdot \hat{\mathbf{F}}$ in 2D reference element Ω_r at solution point (\bullet) (ξ_l, η_m) requires information from four interface flux points (\blacksquare).

The solution can then be advanced in time with an appropriate time stepping scheme. Following the one-dimensional formulation, the derivatives $\partial \hat{\mathbf{f}}_r^D / \partial \xi$ and $\partial \hat{\mathbf{g}}_r^D / \partial \eta$ of the discontinuous flux functions are computed from the Lagrange polynomial.

3.1.2.1 Inviscid Numerical Flux Formulation

Since the mathematical nature of the governing equations for incompressible flow has been modified due to the introduction of artificial compressibility, common inviscid fluxes $\hat{\mathbf{f}}_e^{com}$ and $\hat{\mathbf{g}}_e^{com}$ at an interface between elements in the reference space, depicted in Figure 3.6, can be computed using an approximate Riemann solver.

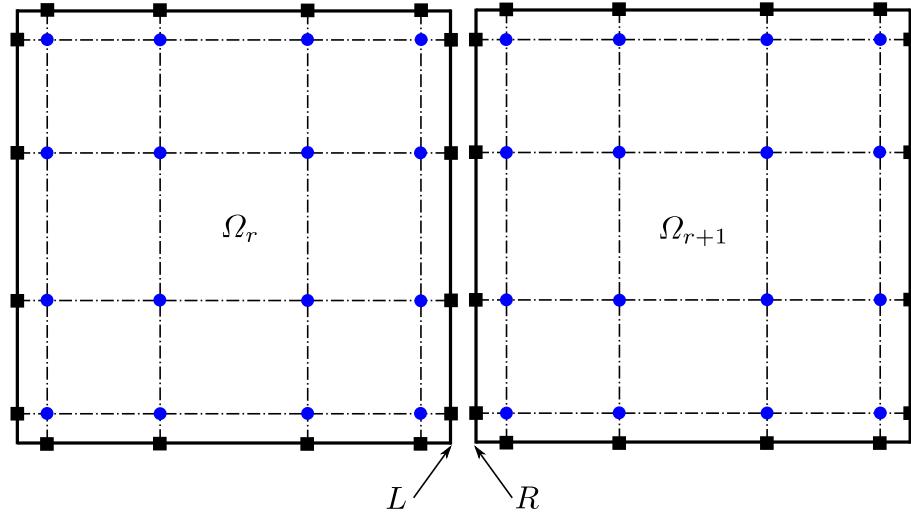


Figure 3.6 Interface between reference element Ω_r and Ω_{r+1} where common numerical fluxes are computed.

Here, we use a Rusanov Riemann solver [54], where the flux is expressed in the ξ and η directions

$$\hat{\mathbf{f}}_e^{com} = \frac{1}{2} \left[\hat{\mathbf{F}}_e^R + \hat{\mathbf{F}}_e^L - \hat{\lambda}_{max} (\mathbf{U}^R - \mathbf{U}^L) \right] \quad (3.47)$$

$$\hat{\mathbf{g}}_e^{com} = \frac{1}{2} [\hat{\mathbf{G}}_e^R + \hat{\mathbf{G}}_e^L - \hat{\lambda}_{max} (\mathbf{U}^R - \mathbf{U}^L)] \quad (3.48)$$

where

$$\hat{\mathbf{F}}_e = s_{\xi,1} \mathbf{f}_e + s_{\xi,2} \mathbf{g}_e \quad (3.49)$$

$$\hat{\mathbf{G}}_e = s_{\eta,1} \mathbf{f}_e + s_{\eta,2} \mathbf{g}_e. \quad (3.50)$$

Alternatively, the above transformed common fluxes can be written in the form

$$\hat{\mathbf{f}}_e^{com} = \frac{1}{2} [(\mathbf{F}_e^R + \mathbf{F}_e^L) \cdot \mathbf{n}_\xi - \lambda_{max} (\mathbf{U}^R - \mathbf{U}^L)] |\mathbf{s}_\xi| \quad (3.51)$$

$$\hat{\mathbf{g}}_e^{com} = \frac{1}{2} [(\mathbf{F}_e^R + \mathbf{F}_e^L) \cdot \mathbf{n}_\eta - \lambda_{max} (\mathbf{U}^R - \mathbf{U}^L)] |\mathbf{s}_\eta| \quad (3.52)$$

where

$$\mathbf{F}_e = \begin{bmatrix} \mathbf{f}_e \\ \mathbf{g}_e \end{bmatrix} \quad (3.53)$$

is the convective flux vector. The vectors normal to the interfaces associated with the ξ and η directions are

$$\mathbf{n}_\xi = \frac{\mathbf{s}_\xi}{|\mathbf{s}_\xi|} \quad (3.54)$$

$$\mathbf{n}_\eta = \frac{\mathbf{s}_\eta}{|\mathbf{s}_\eta|}. \quad (3.55)$$

Terms written as $(\cdot)^R$ and $(\cdot)^L$ denote right and left states of an interface associated with the ξ direction when evaluating $\hat{\mathbf{f}}_e^{com}$ and η direction when evaluating $\hat{\mathbf{g}}_e^{com}$.

The maximum eigenvalue

$$\lambda_{max} = \max_k |\lambda_k| = |V_n| + c_n \quad (3.56)$$

evaluated along these directions falls out of an eigensystem analysis of the convective flux Jacobian \mathbf{A}_n , where

$$\mathbf{A}_n = \frac{\partial(\mathbf{F}_e \cdot \mathbf{n})}{\partial \mathbf{U}} = \begin{bmatrix} 0 & \beta_o n_1 & \beta_o n_2 \\ n_1 & 2un_1 + vn_2 & un_2 \\ n_2 & vn_1 & un_1 + 2vn_2 \end{bmatrix}. \quad (3.57)$$

The velocity normal to the interface is defined as

$$V_n = u^* n_1 + v^* n_2 \quad (3.58)$$

where $(\cdot)^*$ indicates quantities averaged from the right and left states. The pseudo speed of sound at the interface now takes the form

$$c_n = \sqrt{V_n^2 + \beta_o}. \quad (3.59)$$

The implementation of boundary conditions follows that which is provided in Krivodonova and Berger [55], where ghosts states \mathbf{U}_g along the boundary are constructed at interfacial flux points and the Riemann problem is solved to satisfy the type of boundary condition specified.

3.1.2.2 Viscous Numerical Flux Formulation

The common viscous fluxes at the interface can be computed using the first procedure of Bassi and Rebay (BR1) [56], Compact Discontinuous Galerkin (CDG) [57], Local Discontinuous Galerkin (LDG) [58], or the second procedure of Bassi and Rebay (BR2) [59]. In order to guarantee compactness of the stencil in multiple dimensions, we use the popular BR2 scheme. To compute these terms, the derivative of $\hat{\mathbf{U}}$, is

needed to evaluate the viscous part of the discontinuous flux function derivatives $\partial \hat{\mathbf{f}}_r^D / \partial \xi$ and $\partial \hat{\mathbf{g}}_r^D / \partial \eta$. Following the flux reconstruction concept in Huynh [12] and connecting it with the BR2 scheme, the gradient of the common solution is

$$\frac{\partial \hat{\mathbf{U}}_{r+\frac{1}{2}}^{com}}{\partial \xi} = \frac{1}{2} \left[\frac{\partial \hat{\mathbf{U}}_r^{RB}(1, \eta)}{\partial \xi} + \frac{\partial \hat{\mathbf{U}}_{r+1}^{LB}(0, \eta)}{\partial \xi} \right] \quad (3.60)$$

where

$$\hat{\mathbf{U}}_r^{RB}(\xi, \eta) = \hat{\mathbf{U}}_r(\xi, \eta) + \left[\hat{\mathbf{U}}_{r+\frac{1}{2}}^{com} - \hat{\mathbf{U}}_r(1, \eta) \right] g_r^{RB}(\xi) \quad (3.61)$$

$$\hat{\mathbf{U}}_{r+1}^{LB}(\xi, \eta) = \hat{\mathbf{U}}_{r+1}(\xi, \eta) + \left[\hat{\mathbf{U}}_{r+\frac{1}{2}}^{com} - \hat{\mathbf{U}}_{r+1}(0, \eta) \right] g_{r+1}^{LB}(\xi) \quad (3.62)$$

$$\hat{\mathbf{U}}_{r+\frac{1}{2}}^{com} = \frac{1}{2} \left[\hat{\mathbf{U}}_r(1, \eta) + \hat{\mathbf{U}}_{r+1}(0, \eta) \right]. \quad (3.63)$$

Therefore,

$$\begin{aligned} \frac{\partial \hat{\mathbf{U}}_{r+\frac{1}{2}}^{com}}{\partial \xi} &= \frac{1}{2} \left[\frac{\partial \hat{\mathbf{U}}_r(1, \eta)}{\partial \xi} + \frac{\partial \hat{\mathbf{U}}_{r+1}(0, \eta)}{\partial \xi} + \left(\hat{\mathbf{U}}_{r+\frac{1}{2}}^{com} - \hat{\mathbf{U}}_r(1, \eta) \right) \frac{dg_r^{RB}(1)}{d\xi} \right. \\ &\quad \left. + \left(\hat{\mathbf{U}}_{r+\frac{1}{2}}^{com} - \hat{\mathbf{U}}_{r+1}(0, \eta) \right) \frac{dg_{r+1}^{LB}(0)}{d\xi} \right]. \end{aligned} \quad (3.64)$$

Similarly, in the η direction

$$\begin{aligned} \frac{\partial \hat{\mathbf{U}}_{r+\frac{1}{2}}^{com}}{\partial \eta} &= \frac{1}{2} \left[\frac{\partial \hat{\mathbf{U}}_r(\xi, 1)}{\partial \eta} + \frac{\partial \hat{\mathbf{U}}_{r+1}(\xi, 0)}{\partial \eta} + \left(\hat{\mathbf{U}}_{r+\frac{1}{2}}^{com} - \hat{\mathbf{U}}_r(\xi, 1) \right) \frac{dg_r^{RB}(1)}{d\eta} \right. \\ &\quad \left. + \left(\hat{\mathbf{U}}_{r+\frac{1}{2}}^{com} - \hat{\mathbf{U}}_{r+1}(\xi, 0) \right) \frac{dg_{r+1}^{LB}(0)}{d\eta} \right]. \end{aligned} \quad (3.65)$$

Note that Eq. (3.64) and Eq. (3.65) require data from elements r and $r+1$ only. As a result, the computational stencil in 2D involves five elements. This compactness ultimately allows for a more economical integration of an implicit time stepping scheme. Furthermore, this stencil lends itself towards a more straightforward implementation on massively parallel computers.

3.1.2.3 Algorithm

In summary, the algorithm used to compute the residual $\hat{\mathbf{R}}$ for a tensor product element can be described in six major stages:

1. Construct the solution polynomial $\hat{\mathbf{U}}_r$ using the solution at $p+1$ points and the one-dimensional Lagrange polynomials ℓ_i and ℓ_j of degree p .
2. Construct the discontinuous flux polynomials $\hat{\mathbf{f}}_r^D$ and $\hat{\mathbf{g}}_r^D$ of degree p from $\hat{\mathbf{U}}_r$ at the solution points.
3. Reconstruct the solutions and discontinuous fluxes along the edges of Ω_r from Eqs. (3.40)-(3.42) and compute the common numerical fluxes $\hat{\mathbf{f}}^{com}$ and $\hat{\mathbf{g}}^{com}$ from a Riemann solver.
4. Use the results from stage 3 to form common values $\hat{\mathbf{U}}_{r+1/2}^{com}$ and $\hat{\nabla}\hat{\mathbf{U}}_{r+1/2}^{com}$ needed to compute viscous numerical fluxes.
5. Construct the continuous flux polynomials $\hat{\mathbf{f}}_r$ and $\hat{\mathbf{g}}_r$ of degree $p+1$ by adding flux corrections based upon the jump in flux along interfaces of Ω_r by using correction functions g_r^{LB} and g_r^{RB} of degree $p+1$. For all simulations in this work, we set $g_r = g_{SD}$.
6. Evaluate the residual $\hat{\nabla} \cdot \hat{\mathbf{F}}$ at each solution point (ξ_l, η_m) within Ω_r using Eqs. (3.45)-(3.46).

Once the above procedure is complete, a dual time stepping algorithm can be used to march the solution forward in time. The details of the dual time stepping algorithm are provided in Chapter 4. We use a second-order backward Euler scheme to discretize the physical time derivative. Also, we implement an implicit backward Euler scheme with non-linear LU-SGS iterative smoothing to march the solution in pseudo time to drive the pseudo residual $\hat{\mathbf{R}}_\tau$ to zero and evaluate its effectiveness in achieving a solenoidal velocity field for each physical time step. Results are compared

to those from pseudo time marching with an explicit scheme such as Shu and Osher's total variation diminishing (TVD) three-stage third-order Runge-Kutta scheme [60] (RK3). The implementation of explicit time marching in pseudo time follows the general idea from the dual time stepping technique performed by Jameson [61].

Chapter 4

Time Integration Schemes under Artificial Compressibility

4.1 Explicit Pseudo Time Stepping

4.1.1 Total Variation Diminishing Runge-Kutta Scheme

The popular TVD RK3 scheme of Shu and Osher [60] when applied to pseudo time stepping can be written as

$$\hat{\mathbf{U}}_k^{n+1,m} = a_k \hat{\mathbf{U}}_0^{n+1,m} + b_k \hat{\mathbf{U}}_{k-1}^{n+1,m} - c_k \Delta\tau \left[\hat{\mathbf{S}}_{k-1}^{n+1,m} + \hat{\mathbf{R}}_{k-1}^{n+1,m} \right] \quad (4.1)$$

$\forall k = 1, \dots, 3, m = 1, \dots, m_{max}$

where m represents the number of RK3 pseudo iterations. At the start of each round of pseudo iterations, when $k = 1$ and $m = 1$, $\hat{\mathbf{U}}_0^{n+1,1}$ is the solution from the previous physical time step. However, for $m > 1$, $\hat{\mathbf{U}}_0^{n+1,m}$ represents the solution from the previous pseudo time step. Discretization of the physical time derivative $\hat{\mathbf{S}}$ is done using a second-order backward difference scheme (BDF2), which is both A -stable and L -stable, and exists under dual time stepping as a source term written as

$$\hat{\mathbf{S}}_{k-1}^{n+1,m} = \frac{\mathbf{I}_D}{2\Delta t} (3\hat{\mathbf{U}}_{k-1}^{n+1,m} - 4\hat{\mathbf{U}}^n + \hat{\mathbf{U}}^{n-1}). \quad (4.2)$$

The index k signifies different stages of the Runge-Kutta scheme for which the coefficients a_k , b_k and c_k are defined as

$$k = 1 \rightarrow a_1 = 1, b_1 = 0, c_1 = 1$$

$$k = 2 \rightarrow a_2 = \frac{3}{4}, b_2 = \frac{1}{4}, c_2 = \frac{1}{4}$$

$$k = 3 \rightarrow a_3 = \frac{1}{3}, b_3 = \frac{2}{3}, c_3 = \frac{2}{3}$$

Initially, to start the physical iterations when $n = 1$ we set $\hat{\mathbf{U}}^0 = \hat{\mathbf{U}}^1 = \hat{\mathbf{U}}(x, y, z, t = 0)$, where $\hat{\mathbf{U}}(x, y, z, t = 0)$ is the initial condition.

4.1.2 Algorithm

Algorithm 1 Explicit Pseudo Time Stepping

```

do  $n = 1 \rightarrow n_{max}$  !physical iterations

do  $m = 1 \rightarrow m_{max}$  !pseudo iterations

do  $k = 1 \rightarrow 3$  !Runge-Kutta stages

    compute  $\hat{\mathbf{S}}_{k-1}^{n+1,m}(\hat{\mathbf{U}}_{k-1}^{n+1,m}, \hat{\mathbf{U}}^n, \hat{\mathbf{U}}^{n-1})$ 

    compute  $\hat{\mathbf{R}}_{k-1}^{n+1,m}(\hat{\mathbf{U}}_{k-1}^{n+1,m})$ 

    compute  $\hat{\mathbf{U}}_k^{n+1,m}$ 

end do  $k$ 

if  $\|\hat{\mathbf{R}}_\tau\|_1^m / \|\hat{\mathbf{R}}_\tau\|_1^0 < tol$  !check criterion

    exit  $m$  !proceed to  $n + 1$ 

end if

end do  $m$ 

end do  $n$ 

```

4.2 Implicit Pseudo Time Stepping

4.2.1 Backward Euler Scheme with LU-SGS Iterative Smoothing

In order to relax the restriction on time step size and drive the pseudo residual $\hat{\mathbf{R}}_\tau$ closer and faster to zero to achieve steady state, we use an implicit time stepping scheme. The cost associated with the solution of coupled non-linear equations at each time step motivates linearization of the residual in the governing equations. This resulting linear system of equations is then solved *element-by-element* using a

non-linear LU-SGS iterative smoother. For each element r , we can rewrite Eq. (3.36) as

$$\frac{\partial \hat{\mathbf{U}}_r}{\partial \tau} + \hat{\mathbf{S}}_r + \hat{\mathbf{R}}_r = 0. \quad (4.3)$$

The linearized set of equations is formulated below, where r and nb represent the current and neighboring quadrilateral elements Ω_r and Ω_{nb} , respectively, and n and m represent physical and pseudo iteration indices, respectively. The pseudo time derivative is discretized with a first-order backward Euler scheme

$$\frac{\hat{\mathbf{U}}_r^{n+1,m+1} - \hat{\mathbf{U}}_r^{n+1,m}}{\Delta \tau} + \hat{\mathbf{S}}_r^{n+1,m+1} + \hat{\mathbf{R}}_r^{n+1,m+1} = 0. \quad (4.4)$$

We can rewrite Eq. (4.4) as

$$\begin{aligned} & \frac{\hat{\mathbf{U}}_r^{n+1,m+1} - \hat{\mathbf{U}}_r^{n+1,m}}{\Delta \tau} + \hat{\mathbf{S}}_r^{n+1,m+1} - \hat{\mathbf{S}}_r^{n+1,m} + \hat{\mathbf{R}}_r^{n+1,m+1} - \hat{\mathbf{R}}_r^{n+1,m} \\ &= -\hat{\mathbf{R}}_r^{n+1,m} - \hat{\mathbf{S}}_r^{n+1,m} \end{aligned} \quad (4.5)$$

where a second-order backward difference scheme (BDF2) is used for the physical time derivative,

$$\hat{\mathbf{S}}_r^{n+1,m+1} = \frac{\mathbf{I}_D}{2\Delta t} (3\hat{\mathbf{U}}_r^{n+1,m+1} - 4\hat{\mathbf{U}}_r^n + \hat{\mathbf{U}}_r^{n-1}). \quad (4.6)$$

Correspondingly, for pseudo time level m the discretization is

$$\hat{\mathbf{S}}_r^{n+1,m} = \frac{\mathbf{I}_D}{2\Delta t} (3\hat{\mathbf{U}}_r^{n+1,m} - 4\hat{\mathbf{U}}_r^n + \hat{\mathbf{U}}_r^{n-1}). \quad (4.7)$$

Gathering terms

$$\begin{aligned} \left(\frac{\mathbf{I}}{\Delta\tau} + \frac{3\mathbf{I}_D}{2\Delta t} \right) (\hat{\mathbf{U}}_r^{n+1,m+1} - \hat{\mathbf{U}}_r^{n+1,m}) &+ \hat{\mathbf{R}}_r^{n+1,m+1} - \hat{\mathbf{R}}_r^{n+1,m} \\ &= -\hat{\mathbf{R}}_r^{n+1,m} - \hat{\mathbf{S}}_r^{n+1,m} \end{aligned} \quad (4.8)$$

and then linearizing the residual while dropping the $n+1$ index for convenience

$$\hat{\mathbf{R}}_r^{m+1} - \hat{\mathbf{R}}_r^m \approx \frac{\partial \hat{\mathbf{R}}_r}{\partial \hat{\mathbf{U}}_r} \Delta \hat{\mathbf{U}}_r + \sum_{nb \neq r} \frac{\partial \hat{\mathbf{R}}_r}{\partial \hat{\mathbf{U}}_{nb}} \Delta \hat{\mathbf{U}}_{nb} \quad (4.9)$$

the following expression is obtained

$$\left(\frac{\mathbf{I}}{\Delta\tau} + \frac{3\mathbf{I}_D}{2\Delta t} + \frac{\partial \hat{\mathbf{R}}_r}{\partial \hat{\mathbf{U}}_r} \right) \Delta \hat{\mathbf{U}}_r^{m+1} = -\hat{\mathbf{R}}_r^m - \hat{\mathbf{S}}_r^m - \sum_{nb \neq r} \frac{\partial \hat{\mathbf{R}}_r}{\partial \hat{\mathbf{U}}_{nb}} \Delta \hat{\mathbf{U}}_{nb}. \quad (4.10)$$

To avoid computation and storage of $\partial \hat{\mathbf{R}}_r / \partial \hat{\mathbf{U}}_{nb}$ we can perform another linearization similar to the one done in Kannan [62] and apply the LU-SGS algorithm by replacing m with k on the left hand side of Eq. (4.10), where k now represents one forward/backward sweep through the grid, and introducing (\star) to signify the most recently computed solution. With this modification, Eq. (4.10) becomes

$$\left(\frac{\mathbf{I}}{\Delta\tau} + \frac{3\mathbf{I}_D}{2\Delta t} + \frac{\partial \hat{\mathbf{R}}_r}{\partial \hat{\mathbf{U}}_r} \right) \Delta \hat{\mathbf{U}}_r^{k+1} = -\hat{\mathbf{R}}_r^m - \hat{\mathbf{S}}_r^m - \sum_{nb \neq r} \frac{\partial \hat{\mathbf{R}}_r}{\partial \hat{\mathbf{U}}_{nb}} \Delta \hat{\mathbf{U}}_{nb}^\star \quad (4.11)$$

and $\partial \hat{\mathbf{R}}_r / \partial \hat{\mathbf{U}}_{nb}$ is eliminated in the following manner:

$$\begin{aligned} \hat{\mathbf{R}}_r^m + \sum_{nb \neq r} \frac{\partial \hat{\mathbf{R}}_r}{\partial \hat{\mathbf{U}}_{nb}} \Delta \hat{\mathbf{U}}_{nb}^\star &= \hat{\mathbf{R}}_r(\hat{\mathbf{U}}_c^m, \hat{\mathbf{U}}_{nb}^m) + \sum_{nb \neq r} \frac{\partial \hat{\mathbf{R}}_r}{\partial \hat{\mathbf{U}}_{nb}} \Delta \hat{\mathbf{U}}_{nb}^\star \\ &\approx \hat{\mathbf{R}}_r(\hat{\mathbf{U}}_c^m, \hat{\mathbf{U}}_{nb}^\star) \\ &\approx \hat{\mathbf{R}}_r(\hat{\mathbf{U}}_c^\star, \hat{\mathbf{U}}_{nb}^\star) - \frac{\partial \hat{\mathbf{R}}_r}{\partial \hat{\mathbf{U}}_r} \Delta \hat{\mathbf{U}}_r^\star. \end{aligned} \quad (4.12)$$

Substituting Eq. (4.12) into Eq. (4.11), we can obtain the final form

$$\begin{aligned} \left(\frac{\mathbf{I}}{\Delta\tau} + \frac{3\mathbf{I}_D}{2\Delta t} + \frac{\partial \hat{\mathbf{R}}_r}{\partial \hat{\mathbf{U}}_r} \right) \delta \hat{\mathbf{U}}_r^{k+1} = & -\hat{\mathbf{R}}_r \left(\hat{\mathbf{U}}_r^*, \hat{\mathbf{U}}_{nb}^* \right) - \hat{\mathbf{S}}_r \left(\hat{\mathbf{U}}_r^m, \hat{\mathbf{U}}_r^n, \hat{\mathbf{U}}_r^{n-1} \right) \\ & - \left(\frac{\mathbf{I}}{\Delta\tau} + \frac{3\mathbf{I}_D}{2\Delta t} \right) \Delta \hat{\mathbf{U}}_r^* \end{aligned} \quad (4.13)$$

where

$$\delta \hat{\mathbf{U}}_r^{k+1} = \Delta \hat{\mathbf{U}}_r^{k+1} - \Delta \hat{\mathbf{U}}_r^* \quad (4.14)$$

and

$$\Delta \hat{\mathbf{U}}_r^{k+1} = \hat{\mathbf{U}}_r^{k+1} - \hat{\mathbf{U}}_r^m \quad (4.15)$$

$$\Delta \hat{\mathbf{U}}_r^* = \hat{\mathbf{U}}_r^* - \hat{\mathbf{U}}_r^m. \quad (4.16)$$

The above linear system is solved element-by-element with direct LU decomposition and the solution is updated with

$$\hat{\mathbf{U}}_r^{k+1} = \hat{\mathbf{U}}_r^* + \delta \hat{\mathbf{U}}_r^{k+1}. \quad (4.17)$$

After a maximum number of sweeps k_{max} through the grid, the solution reaches pseudo time level $m+1$, and after a maximum number of pseudo iterations m_{max} the solution reaches physical time level $n+1$; at this time the fictitious pressure waves introduced into the fluid by artificial compressibility disappear and the solution $\hat{\mathbf{U}}_r$ takes physical meaning. It is important to note the size of the element matrix \mathbf{M}_r , which consists of terms inside the brackets on the left-hand side of Eq. (4.13). The size of this matrix is shown in Eq. (4.18) and is a function of the number of equations

to solve N_{eq} , number of solution points $p+1$ per Ω_r in 1D, and dimension \mathcal{N} of Ω

$$\text{Size of } \mathbf{M}_r = \left[N_{eq} \cdot (p+1)^{\mathcal{N}} \right] \times \left[N_{eq} \cdot (p+1)^{\mathcal{N}} \right]. \quad (4.18)$$

Table 4.1 shows the size of \mathbf{M}_r as a function of polynomial order p , where $N_{eq} = 3$ and $\mathcal{N} = 2$. For increasingly higher orders of accuracy, the size of this matrix produces a higher memory requirement and increases the total number of operations, rendering the system more computationally expensive to solve.

p	1	2	3	4
\mathbf{M}_r	12x12	27x27	48x48	75x75

Table 4.1 Size of element matrix \mathbf{M}_r as a function of polynomial order p in 2D, where $N_{eq} = 3$ and $\mathcal{N} = 2$.

p	1	2	3	4
\mathbf{M}_r	32x32	108x108	256x256	500x500

Table 4.2 Size of element matrix \mathbf{M}_r as a function of polynomial order p in 3D, where $N_{eq} = 4$ and $\mathcal{N} = 3$.

The element Jacobian $\partial\hat{\mathbf{R}}_r/\partial\hat{\mathbf{U}}_r$ is computed numerically [33] at every physical iteration n by applying a perturbation ϵ to each state variable,

$$\frac{\partial\hat{\mathbf{R}}_r}{\partial\hat{\mathbf{U}}_r}\Big|_n = \frac{\hat{\mathbf{R}}_r\left(\hat{\mathbf{U}}_r^n + \epsilon, \hat{\mathbf{U}}_{nb}^n\right) - \hat{\mathbf{R}}_r\left(\hat{\mathbf{U}}_r^n, \hat{\mathbf{U}}_{nb}^n\right)}{\epsilon} \quad (4.19)$$

where ϵ is typically $\sqrt{\epsilon_{machine}}$. Ultimately, the cost per iteration factors are the following:

1. Frequency of computing the element Jacobian - $\partial\hat{\mathbf{R}}_r/\partial\hat{\mathbf{U}}_r$

2. Degree of Lagrange polynomial - p
3. Number of pseudo iterations - m
4. Number of LU-SGS sweeps - k

To help improve convergence rates, however, the computation of $\partial\hat{\mathbf{R}}_r/\partial\hat{\mathbf{U}}_r$ can be frozen without degrading the solution. In other words, this term can be recomputed every 1-5 physical iterations, depending on time step size. In 3D, Table 4.2 shows that for a 5th order scheme where $p = 4$ the size of \mathbf{M}_r is 500x500, motivating the need for a fast, non-stationary iterative method to solve Eq. (4.13). As a result, practical use of this time stepping scheme with high-order spatial discretizations for large scale three-dimensional simulations still remains to be seen.

4.2.2 Algorithm

Algorithm 2 Implicit Pseudo Time Stepping

```

do  $n = 1 \rightarrow n_{max}$  !physical iterations

do  $m = 1 \rightarrow m_{max}$  !pseudo iterations

    compute  $\hat{\mathbf{S}}^{n+1,m}(\hat{\mathbf{U}}^{n+1,m}, \hat{\mathbf{U}}^n, \hat{\mathbf{U}}^{n-1})$ 

    do  $k = 1 \rightarrow k_{max}$  !LU-SGS sweeps

        do  $r = 1 \rightarrow N_r$  !forward sweep

            compute  $\hat{\mathbf{R}}_r^{n+1,m}(\hat{\mathbf{U}}_r^\star, \hat{\mathbf{U}}_{nb}^\star)$ 

            solve  $\delta\hat{\mathbf{U}}_r^{n+1,m}$ 

            update  $\hat{\mathbf{U}}_r^{n+1,m+1}$ 

        end do  $r$ 

        do  $r = N_r \rightarrow 1$  !backward sweep

            compute  $\hat{\mathbf{R}}_r^{n+1,m}(\hat{\mathbf{U}}_r^\star, \hat{\mathbf{U}}_{nb}^\star)$ 

            solve  $\delta\hat{\mathbf{U}}_r^{n+1,m}$ 

            update  $\hat{\mathbf{U}}_r^{n+1,m+1}$ 

        end do  $r$ 

    end do  $k$ 

    if  $\|\hat{\mathbf{R}}_\tau\|_1^m / \|\hat{\mathbf{R}}_\tau\|_1^0 < tol$  !check criterion

        exit  $m$  !proceed to  $n + 1$ 

    end if

    end do  $m$ 

end do  $n$ 

```

Chapter 5

Two-Dimensional Numerical Results

5.1 Taylor-Couette Flow

Proper implementation of the numerical method was verified by comparing results to the exact solution for steady incompressible Taylor-Couette flow [63]. The analytical expression for azimuthal velocity $\tilde{V}(r)$ in this problem is

$$\tilde{V}(r) = r_i \omega_i \frac{\left(\frac{r_o}{r} - \frac{r}{r_o}\right)}{\left(\frac{r_o}{r_i} - \frac{r_i}{r_o}\right)} + r_o \omega_o \frac{\left(\frac{r}{r_i} - \frac{r_i}{r}\right)}{\left(\frac{r_o}{r_i} - \frac{r_i}{r_o}\right)} \quad (5.1)$$

where $r_i = 1$ and $r_o = 2$ are the inner and outer radius and ω_i and ω_o are the inner and outer cylinder angular speeds, respectively. The inner cylinder spins clockwise at a rate $\omega_i = 1$ while the outer cylinder is stationary. At $t = 0$, initial u and v velocity conditions are given based upon the analytical expression, and cubic Bezier curves are implemented for curved boundaries, where no-slip velocity conditions are satisfied through specification of exact flux. The Reynolds number $Re = r_i \omega_i d / \nu$ is 10, where $d = r_o - r_i$ is the gap distance between the inner and outer walls. Refinement is done uniformly from the coarsest grid Ω^1 shown in Figure 5.1a down to the finest grid Ω^4 . The L^p -norm of azimuthal velocity error $\|\epsilon\|_p$ for $p = \{1, 2, 3\}$ is computed by Eq. (5.2)

$$\|\epsilon\|_p = \left(\frac{1}{DOF} \sum_{k=1}^{DOF} |\epsilon_k|^p \right)^{\frac{1}{p}} \quad (5.2)$$

where $\epsilon(r) = \tilde{V}(r) - V(r)$ and $V(r)$ is the azimuthal velocity obtained numerically. Total degrees of freedom are denoted by DOF, which represents the total number of solution points in Ω . The subsequent orders of accuracy n achieved are computed

by Eq. (5.3)

$$n_{L^p} = \frac{\log \left[\frac{\|\epsilon\|_p(\Omega^i)}{\|\epsilon\|_p(\Omega^{i+1})} \right]}{\log \left[\frac{h(\Omega^i)}{h(\Omega^{i+1})} \right]} \quad (5.3)$$

where the sub/superscript $p = \{1, 2\}$ represents the different norms and

$$h(\Omega^i) = \frac{1}{\sqrt[N]{DOF}} \quad (5.4)$$

for $\Omega^i \subset \mathbb{R}^N$. For this benchmark test case, $i = \{1, 2, 3, 4\}$ represents four uniformly refined domains with number of elements 48, 192, 768 and 3072, respectively. For this two-dimensional benchmark test, $N = 2$.

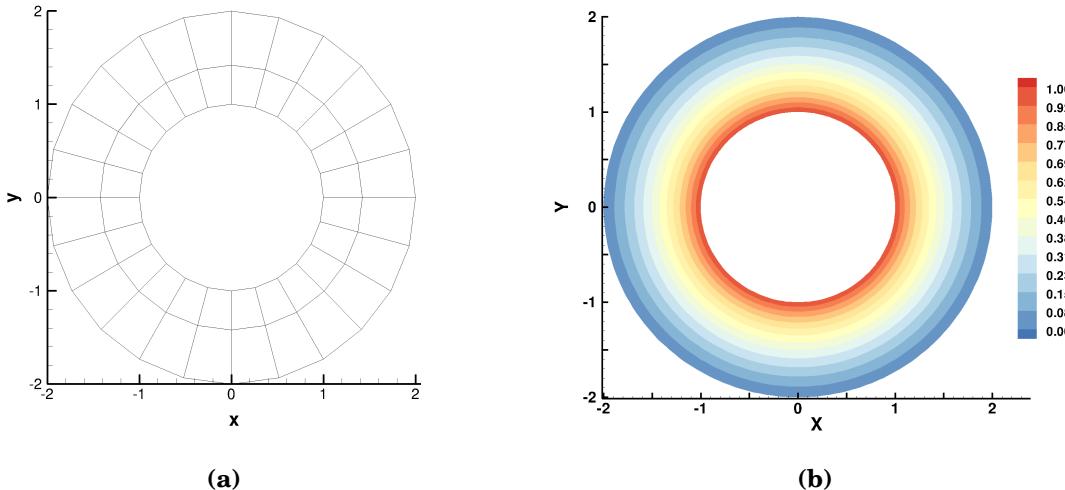


Figure 5.1 Incompressible Taylor-Couette flow at $Re = 10$. (a) coarse grid Ω^1 , (b) azimuthal velocity $V(r)$ using $p = 3$ for Ω^3 .

The profile of azimuthal velocity $V(r)$ obtained numerically using $p = 3$ on Ω^3 is shown in Figure 5.1b and reductions in L^1 -norm and L^2 -norm of the error are tabulated in Table 5.1, giving the expected order of accuracy n for various p . On

average, $n = 2.11$ for $p = 1$, $n = 2.85$ for $p = 2$, and $n = 4.23$ for $p = 3$. These accuracy results are obtained exactly using both explicit and implicit pseudo time stepping, with and without inclusion of the source term from physical time discretization \hat{S} . Since this is an internal flow problem, the order of accuracy is dependent upon how well the curvature of the solid boundary is resolved.

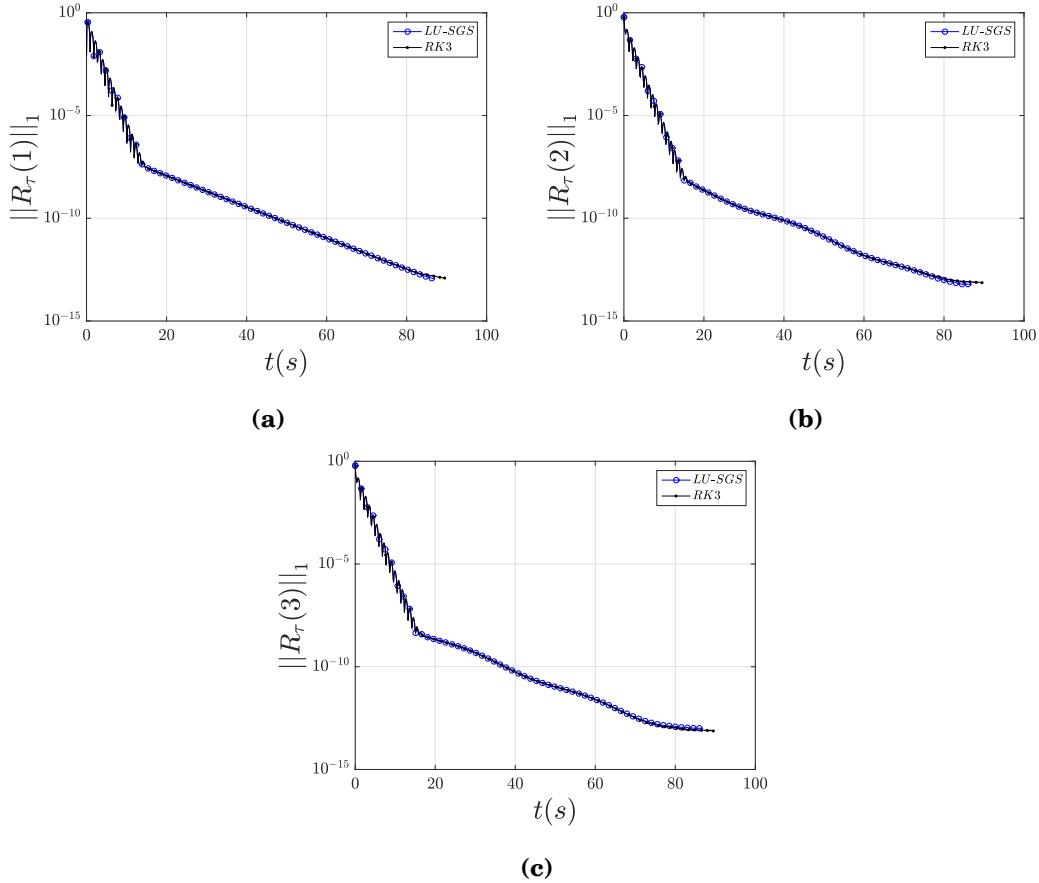


Figure 5.2 Reduction in L^1 -norm of continuity and momentum pseudo residuals $\|R_\tau(\cdot)\|_1$ for $p = 3$ on Ω^3 , indicating that both RK3 and implicit LU-SGS schemes are implemented correctly under dual time stepping. (a) continuity, (b) x-momentum, (c) y-momentum.

<i>Domain</i>	<i>Elements</i>	DOF	$\ \epsilon\ _1$	n_{L^1}	$\ \epsilon\ _2$	n_{L^2}
Ω^1	48	192	7.97E-2	-	9.55E-2	-
Ω^2	192	768	1.74E-2	2.20	2.16E-2	2.14
Ω^3	768	3072	3.98E-3	2.13	5.05E-3	2.10
Ω^4	3072	12288	9.26E-4	2.10	1.19E-3	2.08

(a) $p = 1$

<i>Domain</i>	<i>Elements</i>	DOF	$\ \epsilon\ _1$	n_{L^1}	$\ \epsilon\ _2$	n_{L^2}
Ω^1	48	432	6.94E-3	-	8.99E-3	-
Ω^2	192	1728	6.45E-4	3.42	8.81E-4	3.35
Ω^3	768	6912	8.45E-5	2.93	1.07E-4	3.04
Ω^4	3072	27648	2.01E-5	2.07	2.40E-5	2.16

(b) $p = 2$

<i>Domain</i>	<i>Elements</i>	DOF	$\ \epsilon\ _1$	n_{L^1}	$\ \epsilon\ _2$	n_{L^2}
Ω^1	48	768	1.64E-3	-	1.93E-3	-
Ω^2	192	3072	6.80E-5	4.59	8.16E-5	4.56
Ω^3	768	12288	3.71E-6	4.20	4.57E-6	4.16
Ω^4	3072	49152	2.22E-7	4.06	2.89E-7	3.98

(c) $p = 3$ **Table 5.1** Taylor-Couette at $Re = 10$: order of accuracy n demonstrated by L^1 -norm and L^2 -norm of errors during h -refinement for polynomial orders $p = \{1, 2, 3\}$.

Convergence of the L^1 -norm of pseudo residuals $R_\tau(\cdot) = \hat{R}_\tau(\cdot)/|\mathbf{J}|$ on Ω^3 from the continuity and momentum equations are plotted against physical time t in Figure 5.2 using $p = 3$. The same physical and pseudo time step sizes are used for both RK3 and implicit LU-SGS time stepping schemes and $\|\mathbf{R}_\tau\|_1$ is required to decrease one

order of magnitude within each physical iteration. As expected, the results from both schemes overlap each other and the level to which each residual drops is 10^{-13} . This analysis verifies that both RK3 and implicit LU-SGS are implemented correctly under dual time stepping. Although both schemes perform well in computing this steady flow, the explicit scheme exhibits difficulty in addressing stiffness introduced by artificial compressibility in the modified continuity equation for unsteady flow. This fact is highlighted in Section 5.5, where we compare results between the explicit and implicit schemes for unsteady flow past a cylinder and show the latter scheme to be a promising choice.

5.2 NACA0012 Airfoil

In order to demonstrate performance of implicit dual time stepping on a highly non-uniform grid, numerical results were obtained for steady flow past a NACA0012 airfoil at zero angle of attack at $Re = 1850$ and unit chord length. The grid used for this simulation, shown in Figure 5.3, contains a total of 8114 linear quadrilateral elements with 100 of these representing the profile of the airfoil, which exhibits a sharp trailing edge. Curvature of the airfoil is captured using our cubic Bezier curve implementation. The blockage in y caused by the presence of the airfoil in the 40×40 domain is 0.3%. Initial conditions are set to $[p, u, v]^T = [1, 1, 0]^T$. At the inlet boundary, freestream velocity conditions are given while at the outlet, only pressure is specified. Far field boundary conditions are applied to the top and bottom boundaries of the domain. The no-slip velocity condition is applied to the airfoil surface. We obtain results using polynomial orders $p = 1$, $p = 2$ and $p = 3$, which correspond to 32456, 73026 and 129824 degrees of freedom, respectively. Since we seek a steady state solution, we can remove dual time stepping and ignore the term $\hat{\mathbf{S}}$ resulting from physical time discretization. To demonstrate the

effectiveness of sweeping within the implicit LU-SGS scheme in driving $\nabla \cdot \mathbf{u}$ to zero and ultimately the residual $\hat{\mathbf{R}}_\tau$ to zero, we run multiple scenarios for the sweep count k_{max} . The various sweep counts used in this study are $k_{max} = \{1, 3, 6, 10\}$, where one forward/backward movement through the grid constitutes one full sweep.

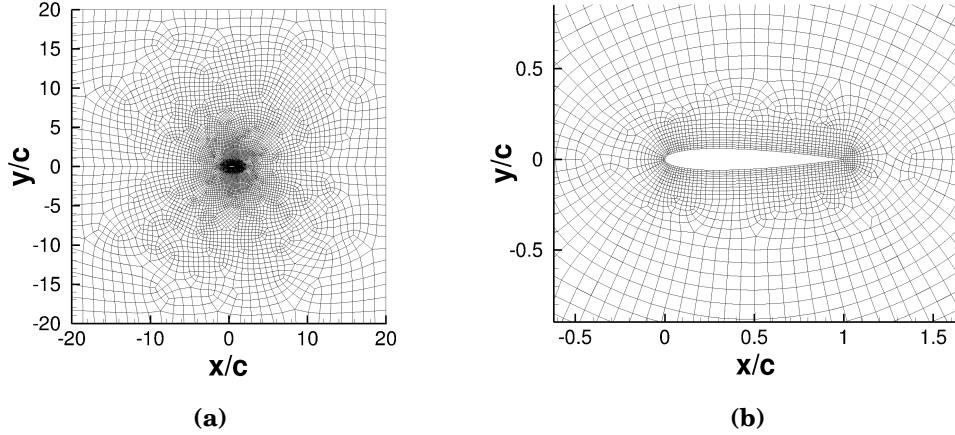


Figure 5.3 NACA0012 at $Re = 1850$: mesh. (a) full, (b) zoom.

The implicit scheme offers increased stability and permits highly accelerated convergence to the steady state. We accomplish this by setting the initial maximum CFL at $m = 0$ to 0.5 and increasing it exponentially [35] at every pseudo iteration with $CFL|_m = CFL|_{m=0} \cdot a^m$, where the factor a is set to 1.2. Using this function and the definition for CFL , this equates to increasing $\Delta\tau$ exponentially towards ∞ . Figure 5.4 shows steady state pressure contours around the leading and sharp trailing edge for various polynomial orders. As expected, improvements in contour shape can be seen with higher orders of accuracy. Contours for u -velocity and convergence rates of $\|\mathbf{R}_\tau\|_1$ are shown in Figure 5.5 for all sweep count numbers. The fast reduction in residual using the implicit LU-SGS scheme due to the increased pseudo time step can be seen in this figure. Maximum CFL numbers using RK3 for $p = 1$, $p = 2$ and $p = 3$ are 0.16, 0.14 and 0.07, respectively. This figure also shows the

effectiveness of LU-SGS sweeping in dropping the steady state residual by an order of magnitude, from $k_{max} = 1$ to $k_{max} = 10$. Speedup factors for different values of p with the various sweep counts are tabulated in Table 5.2 and are computed at the point where $\|\mathbf{R}_\tau\|_1 = 1.0E-5$. Results show that minimum wall clock times have been achieved for $k_{max} = 10$. For all LU-SGS simulations in this test case, the element Jacobian $\partial \hat{\mathbf{R}}_r / \partial \hat{\mathbf{U}}_r$ is computed every five iterations. Slightly faster convergence can be achieved through optimization of this incremental value. Convergence of the drag coefficient obtained through p -refinement is shown in Table 5.3, with a converged value of $C_D = 0.0867$.

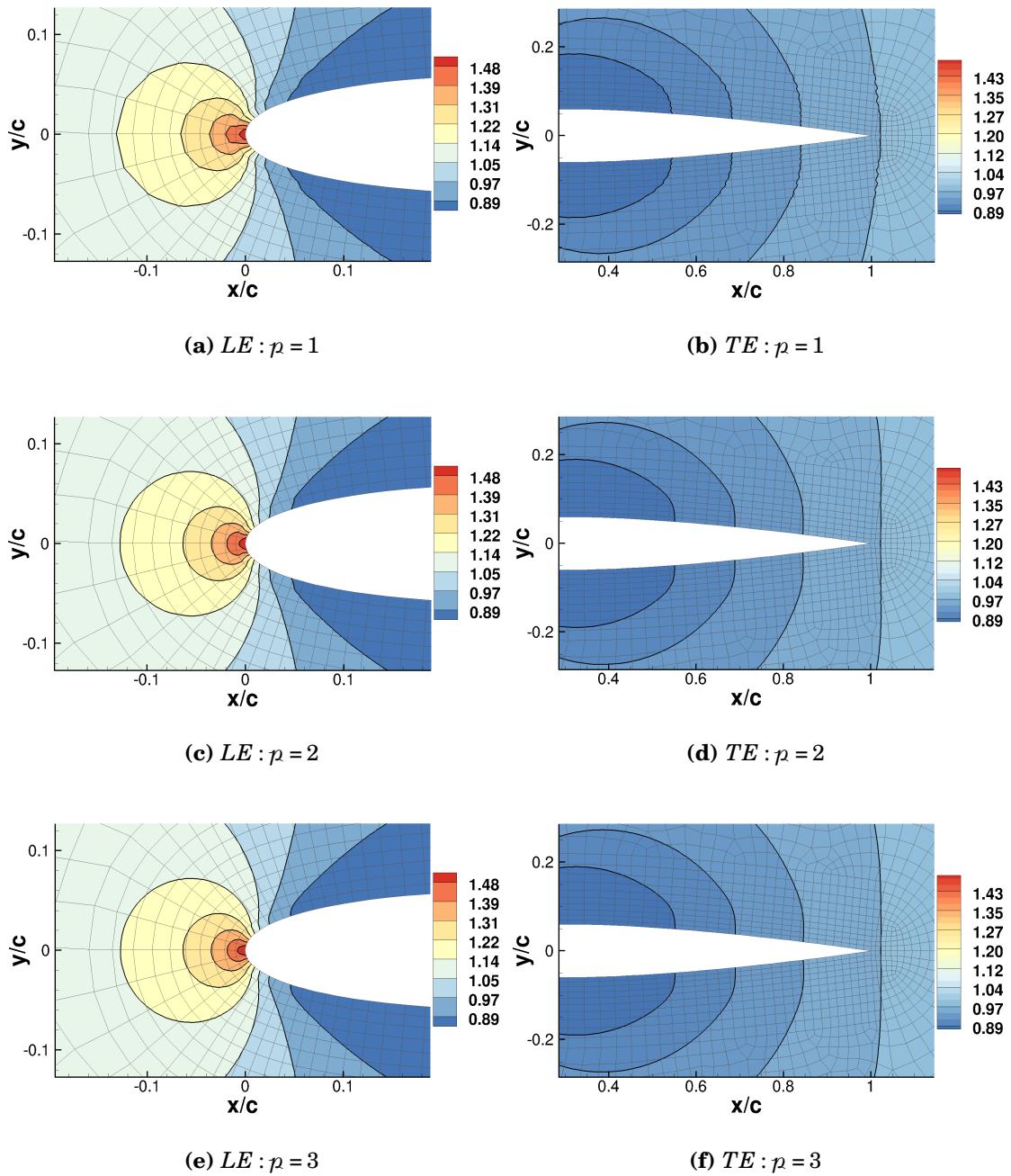


Figure 5.4 NACA0012 at $Re = 1850$: pressure at the leading edge (LE) (a,c,e) and sharp trailing edge (TE) (b,d,f) from implicit LU-SGS with sweep number $k_{max} = 10$ for polynomial orders $p = \{1, 2, 3\}$, indicating smoothest pressure contours for $p = 3$.

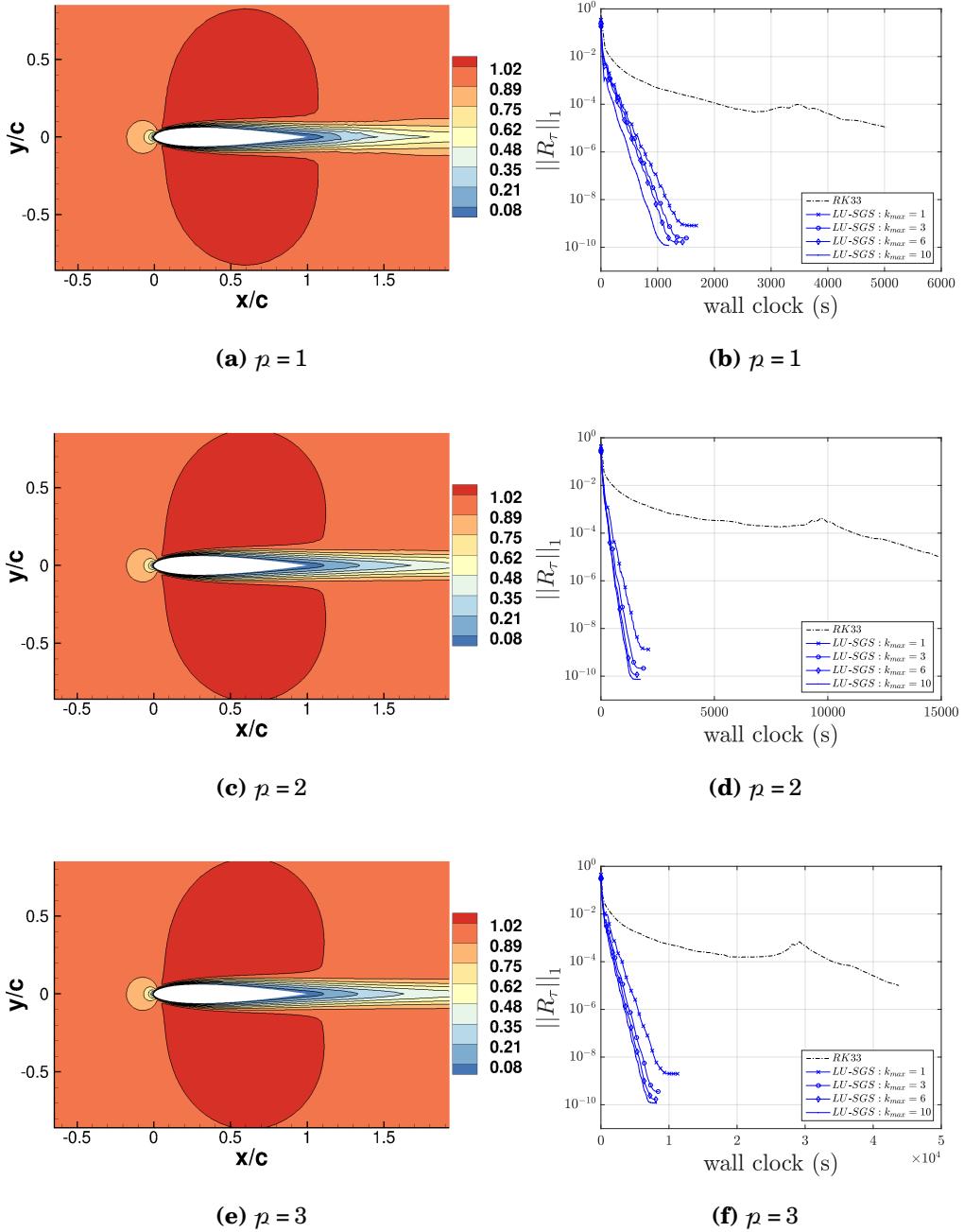


Figure 5.5 NACA0012 at $Re = 1850$: u -velocity from implicit LU-SGS with sweep number $k_{max} = 10$ (a,c,e) for polynomial orders $p = \{1, 2, 3\}$. L^1 -norm of pseudo residual $\|R_\tau\|_1$ as a function of wall clock time for various k_{max} (b,d,f) demonstrates faster convergence under implicit LU-SGS. Compared to $k_{max} = 1$, the residual can be reduced by more than an order of magnitude using $k_{max} = 10$.

	RK3	LU-SGS		
k_{max}	-	1	3	6
$Speedup$	1	9.0	10.1	10.9
		(a) $p = 1$		

	RK3	LU-SGS		
k_{max}	-	1	3	6
$Speedup$	1	19.8	25.6	28.4
		(b) $p = 2$		

	RK3	LU-SGS		
k_{max}	-	1	3	6
$Speedup$	1	10.5	13.9	14.6
		(c) $p = 3$		

Table 5.2 NACA0012 at $Re = 1850$: speedup of implicit LU-SGS over RK3 for polynomial orders $p = \{1, 2, 3\}$, demonstrating largest speedup under $k_{max} = 10$.

p	C_D
1	0.08157
2	0.08735
3	0.08675
4	0.08670

Table 5.3 NACA0012 at $Re = 1850$: p -refinement convergence of C_D under implicit LU-SGS scheme.

5.3 Taylor-Green Decaying Vortices

The Taylor-Green decaying vortex problem with periodic boundary conditions is commonly used to verify a numerical method for simulation of unsteady incompressible flow. The periodic conditions help to remove influence from boundaries of the domain on the accuracy of the method. We solve the unsteady Navier-Stokes equations on a square domain $\{x, y \mid 0 \leq x, y \leq 2\pi\}$ at $Re = 10$. We set the initial condition to the exact solution

$$p(x, y, t) = -\frac{\cos(2qx) + \cos(2qy)}{4} \exp\left(\frac{-4q^2t}{Re}\right) \quad (5.5)$$

$$u(x, y, t) = -\cos(qx) \sin(qy) \exp\left(\frac{-2q^2t}{Re}\right) \quad (5.6)$$

$$v(x, y, t) = \sin(qx) \cos(qy) \exp\left(\frac{-2q^2t}{Re}\right) \quad (5.7)$$

at $t = 0$, where $q = 1$ is the Taylor array number. Similar to Section 5.1, h -refinement is done uniformly from the coarsest grid Ω^1 (4x4) down to the finest grid Ω^4 (32x32); however, to render the elements slightly more irregular a perturbation of 10% is applied to the mesh nodes based on h . The L^p -norms are computed using u -velocity. A small constant time step of $\Delta t = 1E-4$ is chosen to ensure that spatial accuracy does not degrade due to errors resulting from time discretization. At this small time step, the maximum number of pseudo iterations is set at $m_{max} = 20$ and the sweep count at $k_{max} = 3$.

The vorticity field obtained numerically for $p = 3$ and using implicit LU-SGS on Ω^3 is shown in Figure 5.6, and the L^p -norm of the errors are tabulated in Table 5.4 at $t = 1s$. On average, the results demonstrate that the order of accuracy $n = 2.30$ for $p = 1$, $n = 3.41$ for $p = 2$, and $n = 4.16$ for $p = 3$. Comparing results in Table 5.4b for Ω^3 and Table 5.4c for Ω^2 , we can see that by increasing the polynomial order from $p = 2$ to $p = 3$ similar levels of $\|\epsilon\|_1$ and $\|\epsilon\|_2$ can be achieved with less than half the

number of DOFs. Furthermore, order enrichment results gathered from Table 5.4 and plotted in Figure 5.7 demonstrate exponential rate of convergence.

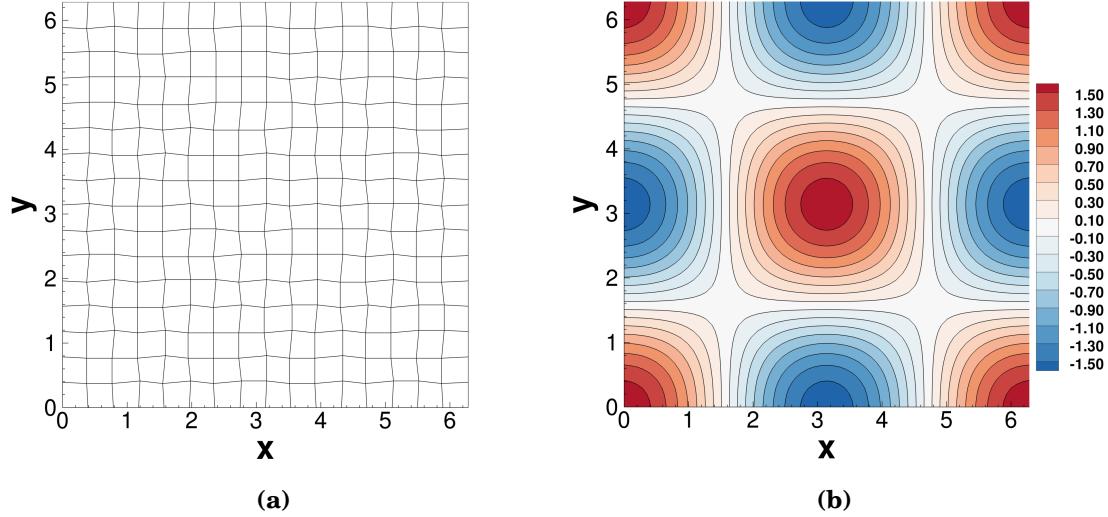


Figure 5.6 Taylor-Green at $Re = 10$: z -vorticity using polynomial order $p = 3$ with implicit LU-SGS on Ω^3 at $t = 1$ s. (a) mesh, (b) z -vorticity.

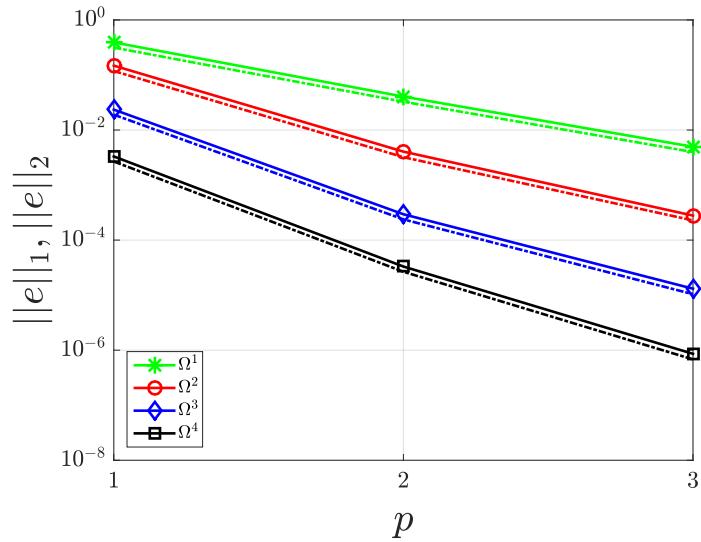


Figure 5.7 Taylor-Green at $Re = 10$: p -convergence of L^1 - and L^2 -norm of errors $\|\epsilon\|_1$ (dashed) and $\|\epsilon\|_2$ (solid) on grids $\Omega^i \forall i = 1 \dots 4$.

<i>Domain</i>	<i>Elements</i>	DOF	$\ \epsilon\ _1$	n_{L^1}	$\ \epsilon\ _2$	n_{L^2}
Ω^1	16	64	3.15E-1	-	3.91E-1	-
Ω^2	64	256	1.18E-1	1.42	1.48E-1	1.40
Ω^3	256	1024	1.90E-2	2.63	2.35E-2	2.66
Ω^4	1024	4096	2.68E-3	2.83	3.31E-3	2.83

(a) $p = 1$

<i>Domain</i>	<i>Elements</i>	DOF	$\ \epsilon\ _1$	n_{L^1}	$\ \epsilon\ _2$	n_{L^2}
Ω^1	16	144	3.27E-2	-	4.05E-2	-
Ω^2	64	576	3.21E-3	3.35	4.05E-3	3.32
Ω^3	256	2304	2.38E-4	3.75	2.95E-4	3.77
Ω^4	1024	9216	2.66E-5	3.16	3.31E-5	3.16

(b) $p = 2$

<i>Domain</i>	<i>Elements</i>	DOF	$\ \epsilon\ _1$	n_{L^1}	$\ \epsilon\ _2$	n_{L^2}
Ω^1	16	256	3.98E-3	-	4.96E-3	-
Ω^2	64	1024	2.28E-4	4.12	2.79E-4	4.15
Ω^3	256	4096	1.04E-5	4.46	1.30E-5	4.42
Ω^4	1024	16384	6.80E-7	3.93	8.59E-7	3.92

(c) $p = 3$ **Table 5.4** Taylor-Green at $Re = 10$: order of accuracy n demonstrated by L^1 -norm and L^2 -norm of errors during h -refinement for polynomial orders $p = \{1, 2, 3\}$ under implicit LU-SGS.

5.4 Double Periodic Shear Layers

5.4.1 Convergence

The second unsteady test case presented is a double periodic pair of horizontal shear layers with a small vertical perturbation in a square domain $\{x, y \mid 0 \leq x, y \leq 1\}$ with periodic boundary conditions. This problem was introduced by Bell, Colella and Glaz [64] to test convergence properties of their projection method and later studied by Minion and Brown [65] to assess the effect of grid resolution on the behavior of various difference approximations for the unsteady incompressible Navier-Stokes equations. This is considered a “thick” shear layer problem with initial conditions given by

$$u = \begin{cases} \tanh[(y - 0.25) / \rho], & \text{if } y \leq 0.5 \\ \tanh[(0.75 - y) / \rho], & \text{if } y > 0.5 \end{cases} \quad (5.8)$$

$$v = \delta \sin(2\pi x) \quad (5.9)$$

where $\rho = 1/30$ represents shear layer thickness (smaller ρ produces thinner shear layers) and $\delta = 0.05$ the amplitude of the initial perturbation. This prescribes the initial u -velocity to be $u(y=1) = -1$, $u(y=0.5) = 1$ and $u(y=0) = -1$. The vorticity solution at various times can be seen in Figure 5.8. Each shear layer evolves into a periodic arrangement of large symmetric vortices, with the shear layer being thinned by the large straining flow field. The thinning shear layers eventually roll up with the large vortices. To test the convergence of our solver, we compute the solution at $t = 1$ s using 32×32 , 64×64 and 128×128 grids, similar to the grid shown in Figure 5.6a. The initial Reynolds number based on the length of the box is $Re = 500$ ($\nu = 0.002$) and physical and pseudo time steps are $1.0E-4$. Max pseudo iterations were set to

$m_{max} = 20$ and the sweep count to $k_{max} = 3$. For polynomial orders $p = 1$, $p = 2$ and $p = 3$, the convergence rates are estimated in the same manner as Minion and Brown [65] using a procedure based on Richardson extrapolation and provided in Table 5.5.

5.4.2 h/p Resolution

To illustrate the performance of our high-order FR method with implicit pseudo time stepping in resolving this shear layer at higher Reynolds number, we increase the Reynolds number to $Re = 10,000$ ($\nu=1.0\text{E-}4$) and march the solution to $t = 1.8\text{s}$ on 32×32 , 64×64 and 128×128 regular grids. As the larger physical vortices develop and the shear layer thins, non-physical vortices originate in the shear layer due to insufficient grid and/or order resolution. These vortices are further stretched as they wrap around the larger ones. The spurious nature of these vortices is confirmed by observing their elimination from the solution during h - and p -refinement. This fact can be seen in Figure 5.9, which shows existence of spurious vortices using $p = \{1, 2, 3\}$ on a 32×32 grid and using $p = 1$ on a 64×64 grid. Furthermore, comparing results in Figures 5.9b and 5.9g, which both use 128 DOFs in each direction, we can conclude that the performance of $p = 3$ is better than $p = 1$ in attempting to remove the spurious vortices. If we refine these grids further to contain $\text{DOFs} \geq 256$ we can appropriately resolve the flow field and eliminate any non-physical numerical artifact.

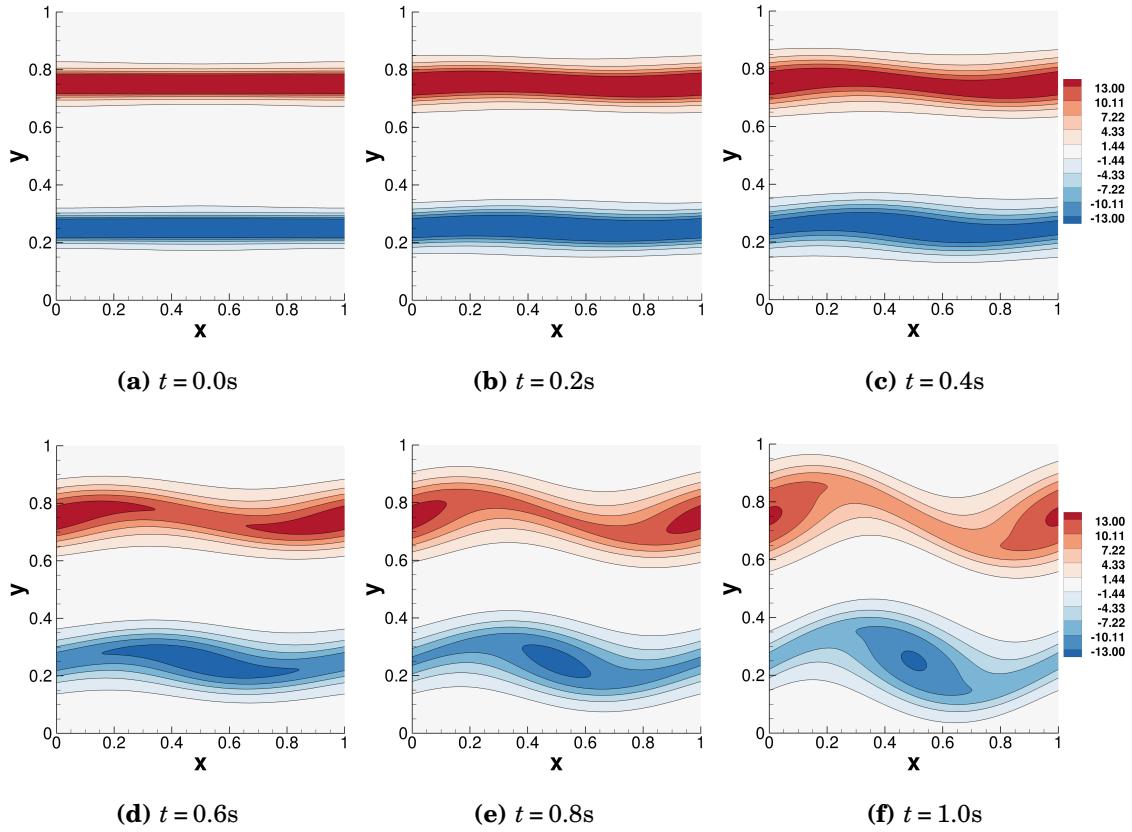


Figure 5.8 Double shear layer at $Re = 500$: z -vorticity for $p = 3$ using implicit LU-SGS from $t = 0.0\text{s}$ to $t = 1.0\text{s}$.

	$p = 1$	$p = 2$	$p = 3$
$\ u_{\Omega^1} - u_{\Omega^2}\ _2$	2.263E-2	2.569E-3	1.367E-4
$\ u_{\Omega^2} - u_{\Omega^3}\ _2$	6.374E-3	3.817E-4	1.053E-5
<i>Richardson Rate</i>	1.83	2.75	3.70

Table 5.5 Double Shear Layer at $Re = 500$: convergence rate obtained from L^2 -norm of errors using Richardson extrapolation at $t = 1\text{s}$ for polynomial orders $p = \{1, 2, 3\}$.

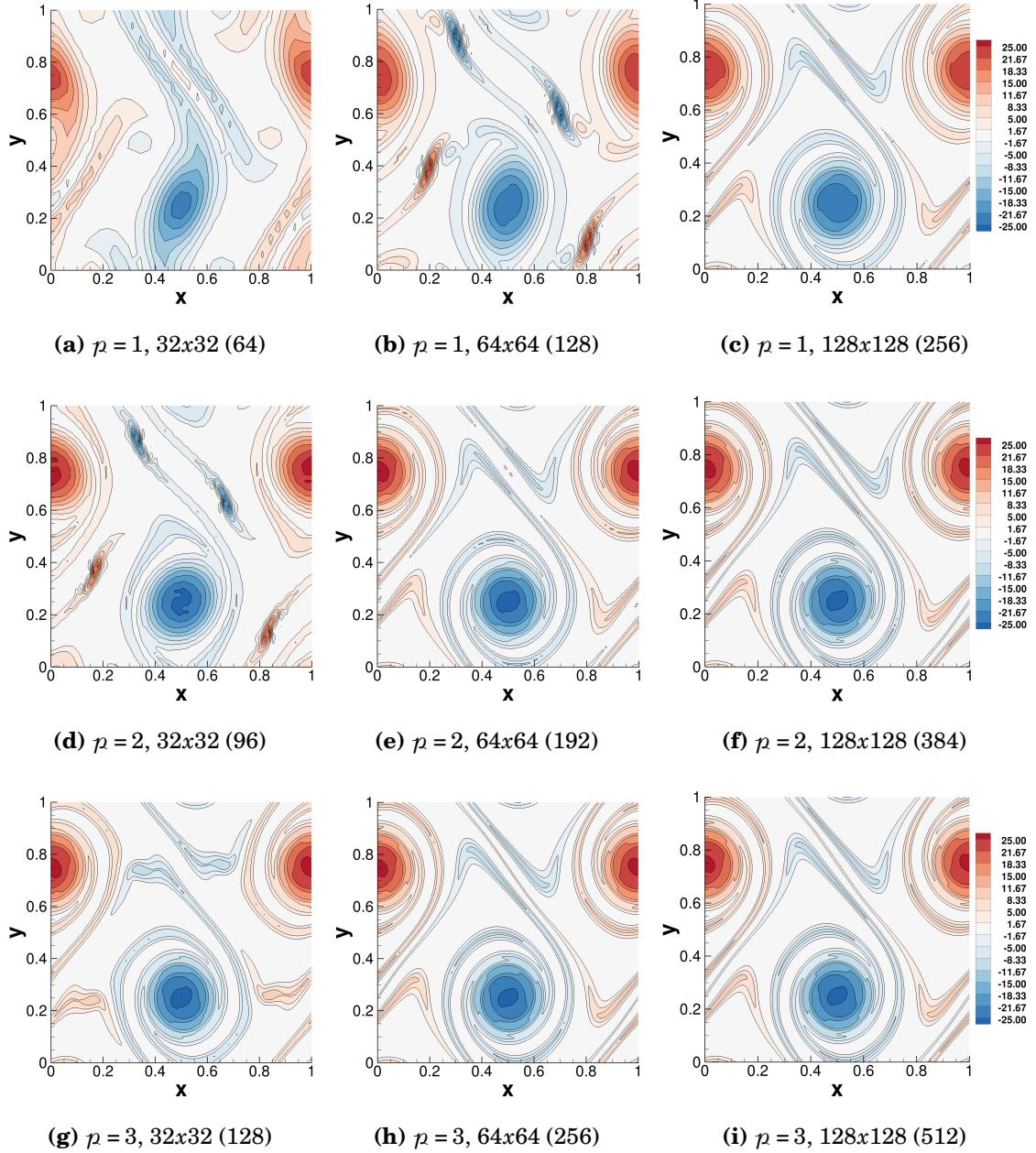


Figure 5.9 Double shear layer at $Re = 10,000$: z -vorticity at $t = 1.8s$ for $p = 1$ (a-c), $p = 2$ (d-f) and $p = 3$ (g-i) for each $N_e \times N_e$ mesh, demonstrating the removal of spurious vortices through hp -refinement. The quantity in parenthesis signifies DOFs in each coordinate direction.

5.5 Cylinder

One of the goals of this work is the design of an implicit dual time stepping scheme for the high-order FR method to predict unsteady flow in complex geometries. In this section, we report numerical results for unsteady laminar flow at $Re = 100$ past a stationary cylinder with diameter $d = 1$. The grid for this test case is shown in Figure 5.10 and contains 4371 linear quadrilateral elements with 48 elements along the wall of the cylinder, which is represented by our cubic Bezier curves. The blockage in y caused by the presence of the cylinder in the 50×40 domain is 2.5%. The initial and boundary conditions applied to the NACA0012 airfoil were also applied to this geometry. As before, we obtain results for $p = 1$, $p = 2$ and $p = 3$, which correspond to 17484, 39339 and 69936 degrees of freedom in Ω , respectively.

The pseudo time step taken by the implicit scheme is chosen to be $100x$ larger than that afforded by the explicit scheme. Furthermore, increased stability offered by the implicit LU-SGS implementation can permit a $100x$ larger physical time step, while still capturing the transient process. The pseudo and physical time step size used by the explicit scheme is $\Delta\tau^{RK3} = \Delta t^{RK3} = 1.0E-3$ for $p = 2$ and $\Delta\tau^{RK3} = \Delta t^{RK3} = 6.0E-4$ for $p = 3$. Cost per physical iteration is higher for the implicit scheme and mainly depends upon four factors: (1) the frequency of computing the element Jacobian $\partial\mathbf{R}_r/\partial\mathbf{U}_r$, (2) size of the element matrix \mathbf{M}_r (i.e. polynomial order), (3) number of pseudo iterations, and (4) number of sweeps through the mesh. For unsteady flow calculations, a criterion is used during each physical iteration, whereby the pseudo residual is evaluated at the end of each pseudo iteration to determine if the continuity equation has been satisfied. The criterion for pseudo steady state convergence per physical time step requires that $\|\mathbf{R}_\tau\|_1$ drop by a factor of 10^3 . If this value is not reached, the maximum number of pseudo iterations for explicit and implicit schemes is set to $m_{max}^{RK3} = 20$ and $m_{max}^{LU-SGS} = 200$. The value for

m_{max}^{LU-SGS} is made larger by an order of magnitude to account for the increased time step size associated with this scheme. Larger $\Delta\tau$ and Δt cause the element matrix \mathbf{M}_r to be less diagonally dominant and result in more pseudo iterations to achieve convergence to the pseudo steady state than smaller time step sizes. The LU-SGS sweep count number is set to $k_{max} = 3$. In this unsteady flow problem, $\partial\hat{\mathbf{R}}_r/\partial\hat{\mathbf{U}}_r$ is computed at every single physical iteration.

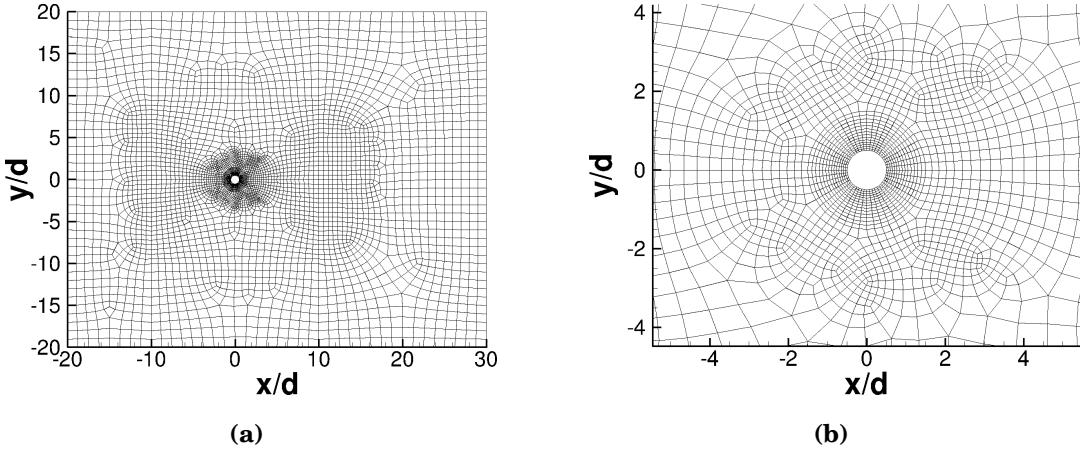


Figure 5.10 Cylinder at $Re = 100$: mesh. (a) full, (b) zoom.

Instantaneous z -vorticity contours at approximately $t = 360$ s for $p = 1$, $p = 2$ and $p = 3$ can be seen in Figure 5.11 for both RK3 and implicit LU-SGS schemes. Figures 5.11a-5.11b demonstrate that the current grid is inadequate for a $p = 1$ to maintain the integrity of the vortex shedding downstream of the bluff body. Figures 5.11c-5.11d and 5.11e-5.11f demonstrate that higher order polynomials have the ability to capture the vortex shedding properly, with the latter set of figures from $p = 3$ displaying the smoothest contours of vorticity.

Plots of force coefficients C_L and C_D generated using $p = 2$ are shown in Figure 5.12 for roughly 32 vortex shedding cycles. These plots show a visual comparison between RK3 and implicit LU-SGS, with the former exhibiting a slightly

larger amplitude for C_L (1.6%) and larger mean value for C_D (0.15%). Values for Strouhal number and various force coefficients are tabulated in Table 5.6 using data collected from approximately 60 data points per shedding cycle over 50 cycles. A fast Fourier transform was performed to capture the shedding frequency f_s needed to compute the Strouhal number $St = f_s d/U_\infty$. Coefficients of lift and drag due to pressure ($C_{L,p}, C_{D,p}$) and viscosity ($C_{L,v}, C_{D,v}$) are shown and compared to data from Park, Kwon and Choi [66] and Sharman et al. [67]. The former authors employed the fractional step method of Choi and Moin [68] while the latter authors utilized the SIMPLE algorithm [69]. Results from Posdziech and Grundmann [70] are reported as well. Root mean square (RMS) values are indicated by $(\cdot)'$. For $p = 3$ and implicit LU-SGS, the RMS of lift coefficient ($C'_L = 0.23$) exactly matches the values obtained by Park et al. and Sharman et al., while the RMS of drag coefficient ($C'_D = 0.0063$) is smaller by approximately 1.5% but exactly equal to the value reported by Posdziech et al. Additionally, amplitudes of C_L and C_D are provided in Table 5.7 along with results from different authors such as Chan et al. [71], Liu et al. [72], Ding et al. [73], [74] and Williamson [75]. We compute C_L by taking an average of peak values and we compute C_D by averaging all values over the 50 shedding cycles. The uncertainty in drag is calculated by averaging the differences between all peak values and the mean value. Note that the current incompressible 4th order results using implicit LU-SGS agree extremely well with the result from Chan, who used a low speed compressible flow solver with a 4th order spectral difference method. Values for Strouhal number $St = 0.164$ are consistent across the board of numerical results and match the experimental result from Williamson.

Side-by-side comparisons of reduction in $\|R_\tau(1)\|_1$, $\|R_\tau(2)\|_1$ and $\|R_\tau(3)\|_1$ between RK3 and implicit LU-SGS are plotted in Figures 5.13, 5.14 and 5.15, respectively, during the physical time interval $340 \leq t \leq 440$. These plots display the level of pseudo residuals for all three equations before pseudo iterations begin ($m = 0$)

and after pseudo iterations end ($m = m_{max}$) per physical iteration over multiple shedding cycles. Also, the number of pseudo iterations required for convergence per physical time step for implicit LU-SGS is shown in Figure 5.16. The flat line for RK3 in this plot demonstrates that the criterion for $\|\mathbf{R}_\tau\|_1$ is consistently not satisfied due to the inability of the explicit scheme to further improve the divergence of velocity field through rather restricted pseudo time stepping, which is evident in the overlapping lines in Figure 5.13a. This fact points to the stiffness associated with pressure. In Figure 5.13b, however, we see that the implicit LU-SGS scheme is capable of reducing $\|\mathbf{R}_\tau(1)\|_1$, which is required to more accurately satisfy the continuity equation. This reduction is attributed to the larger pseudo time step afforded by the implicit scheme. Though, at the same time, some accuracy in $\|\mathbf{R}_\tau(2)\|_1$ and $\|\mathbf{R}_\tau(3)\|_1$ is given up under the assigned criterion, as illustrated in Figures 5.14 and 5.15. To assess the effect of time step size on the number of pseudo iterations when using implicit LU-SGS, we reduce the time step by an order of magnitude from $\Delta\tau^{LUSGS} = \Delta t^{LUSGS} = 0.1$ to $\Delta\tau^{LUSGS} = \Delta t^{LUSGS} = 0.01$, and plot maximum pseudo iterations per physical time step in Figure 5.16. These results demonstrate that we require approximately $2.5x$ more pseudo iterations to drop $\|\mathbf{R}_\tau\|_1$ by the same criterion of 10^3 using this smaller time step. So, to simulate the same amount of physical time, the smaller pseudo time stepping requires $25x$ more CPU time. Therefore, we can conclude that the increased stability offered by large implicit pseudo time stepping improves the convergence rate.

Analysis of this unsteady laminar flow problem highlights that the explicit scheme is not as effective in satisfying the divergence-free constraint on the velocity field as the implicit scheme. The implicit scheme for pseudo time stepping is well suited for accurately solving unsteady incompressible flow using the artificial compressibility method. Within the context of the present high-order FR framework, the restrictions on both pseudo and physical time step sizes experienced by the

combination of RK3 and BDF2 for dual time stepping can be effectively alleviated by an implicit backward Euler scheme with non-linear LU-SGS.

	Current			Park et al. [66]	Sharman et al. [67]	Posdziech et al. [70]
	RK3	LU-SGS	RK3	LU-SGS		
Blockage	2.5%	2.5%	2.5%	2.5%	1.0%	2.0%
Elements	4371	4371	4371	4371	~39000	14441
p	2	2	3	3	-	-
St	0.164	0.164	0.164	0.164	0.165	0.164
C_L	± 0.320	± 0.316	± 0.331	± 0.325	± 0.332	± 0.325
C'_L	0.227	0.223	0.234	0.230	0.23	0.23
$C'_{L,p}$	0.200	0.197	0.205	0.202	0.21	0.20
$C'_{L,v}$	0.031	0.030	0.031	0.031	0.030	0.031
C_D	1.344	1.342	1.342	1.339	1.33	1.33
$C_{D,p}$	1.002	1.000	1.000	0.997	0.99	0.99
$C_{D,v}$	0.342	0.342	0.342	0.342	0.34	0.34
C'_D	0.0066	0.0062	0.0068	0.0063	0.0064	0.0064
$C'_{D,p}$	0.0060	0.0056	0.0064	0.0058	0.0058	0.0058
$C'_{D,v}$	7.13E-4	6.50E-4	7.50E-4	6.58E-4	7.00E-4	4.00E-4

Table 5.6 Cylinder at $Re = 100$: Strouhal numbers and force coefficients due to pressure $C_{(\cdot),p}$ and viscosity $C_{(\cdot),v}$ predicted using polynomial orders $p = 2$ and $p = 3$. Root mean square values are signified by the superscript $(\cdot)'$. Best results are obtained using $p = 3$ and implicit LU-SGS scheme. Comparison to various incompressible flow solvers demonstrates wide agreement in results.

	Method	St	C_L	C_D
Current	Artificial Compressibility + FR- g_{SD} ($p = 3$, implicit LU-SGS)	0.164	± 0.325	1.339 ± 0.009
Park et al. [66]	Fractional Step	0.165	± 0.332	1.33 ± 0.009
Sharman et al. [67]	SIMPLE	0.164	± 0.325	1.33 ± 0.009
Chan et al. [71]	SD ($p = 3$, Mach=0.1)	0.164	± 0.325	1.338 ± 0.009
Castonguay [76]	FR- g_{SD} ($p = 5$, Mach=0.2)	0.16457	± 0.32729	$1.3578 \pm 9.1468\text{E-}3$
Liu et al. [72]	Artificial Compressibility + RANS	0.165	± 0.339	1.350 ± 0.012
Ding et al. [73]	Hybrid FD	0.164	± 0.280	1.325 ± 0.008
Ding et al. [74]	Hybrid FD	0.166	± 0.287	1.356 ± 0.010
Williamson [75] (experiment)	-	0.164	-	-

Table 5.7 Cylinder at $Re = 100$: comparison of St , C_L and C_D obtained from the current solver using $p = 3$ and implicit LU-SGS with various incompressible solvers. Strong agreement is demonstrated between current results and those from Chan et al. (2011), who ran a compressible flow simulation at low Mach number using the spectral difference method.

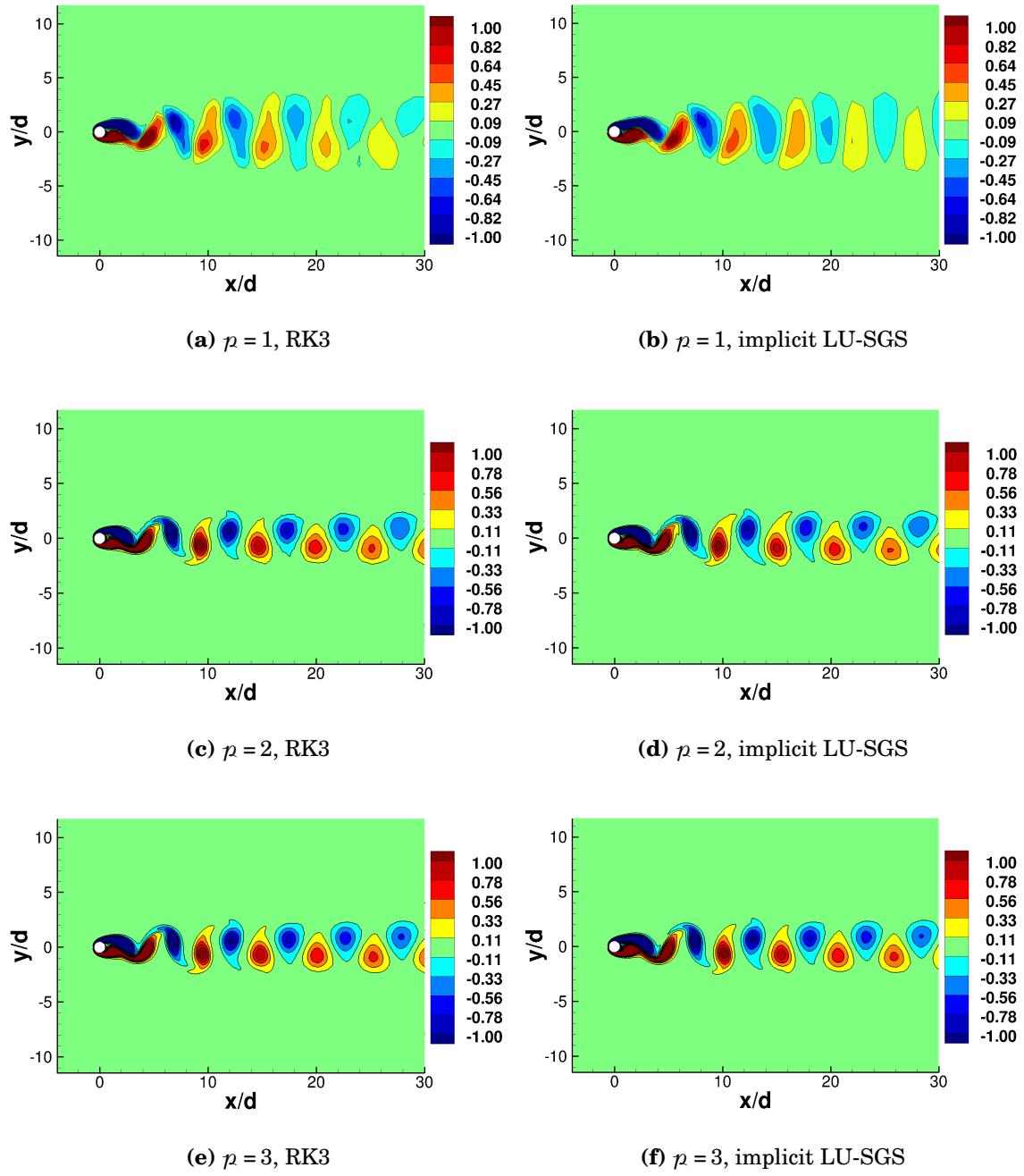


Figure 5.11 Cylinder at $Re = 100$: z -vorticity under RK3 and implicit LU-SGS for polynomial orders $p = \{1, 2, 3\}$. The vortex shedding pattern is well-represented near $30d$ for $p = 3$, demonstrating the effectiveness of the high-order FR-g_{SD} scheme in maintaining vortices far downstream of the bluff body.

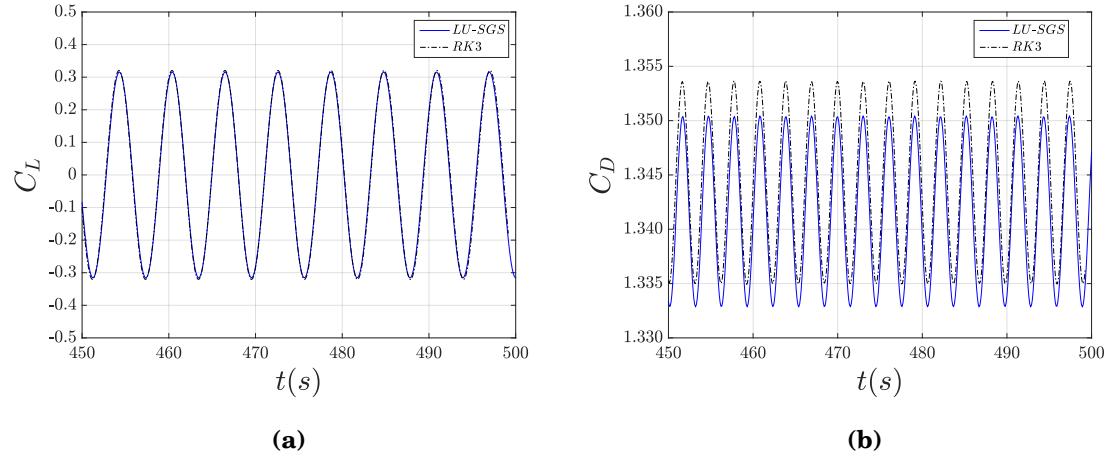


Figure 5.12 Cylinder at $Re = 100$: (a) C_L and (b) C_D vs. physical time predicted using $p = 2$. The discrepancy in (b) between RK3 and implicit LU-SGS is attributed to effectiveness of the implicit dual time stepping scheme in satisfying the divergence free velocity constraint (see Figures 5.13a and 5.13b).

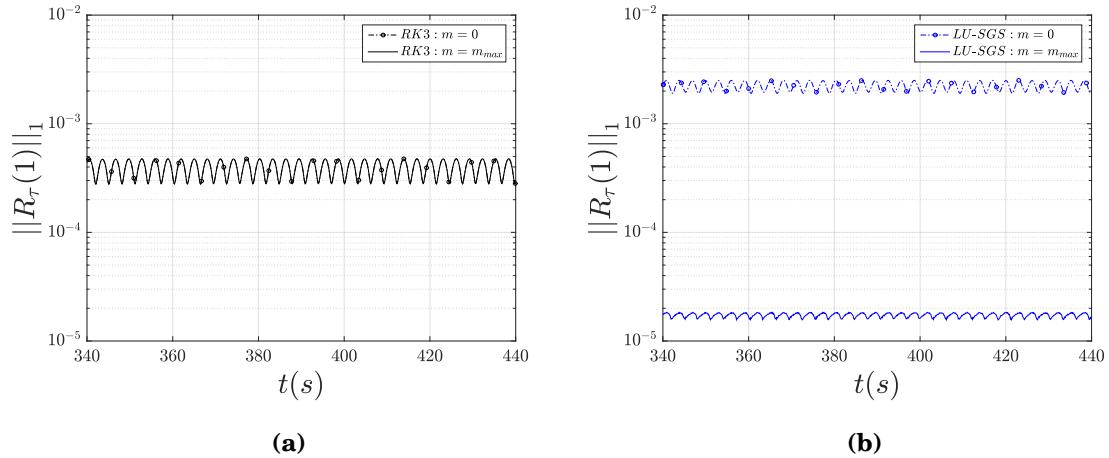


Figure 5.13 Cylinder at $Re = 100$: (a) RK3, (b) implicit LU-SGS. L^1 -norm of continuity residual vs. physical time before pseudo iterations begin ($m = 0$) and after pseudo iterations end ($m = m_{max}$) predicted using $p = 2$.

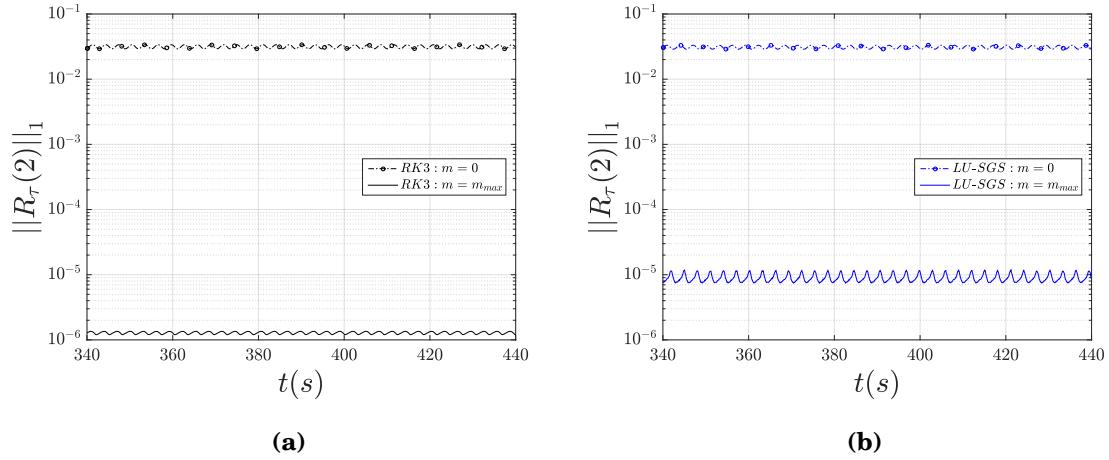


Figure 5.14 Cylinder at $Re = 100$: (a) RK3, (b) implicit LU-SGS. L^1 -norm of x -momentum residual vs. physical time before pseudo iterations begin ($m = 0$) and after pseudo iterations end ($m = m_{max}$) predicted using $p = 2$.

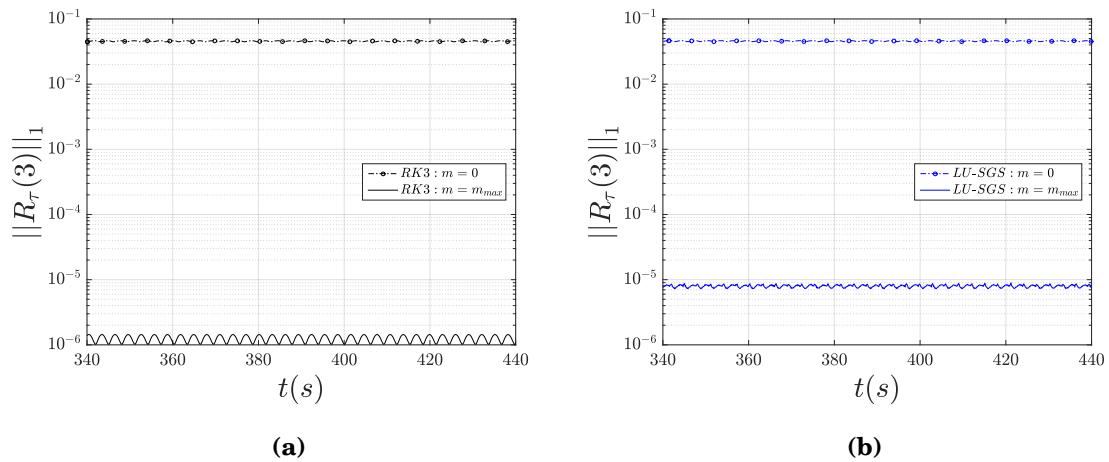


Figure 5.15 Cylinder at $Re = 100$: (a) RK3, (b) implicit LU-SGS. L^1 -norm of y -momentum residual vs. physical time before pseudo iterations begin ($m = 0$) and after pseudo iterations end ($m = m_{max}$) predicted using $p = 2$.

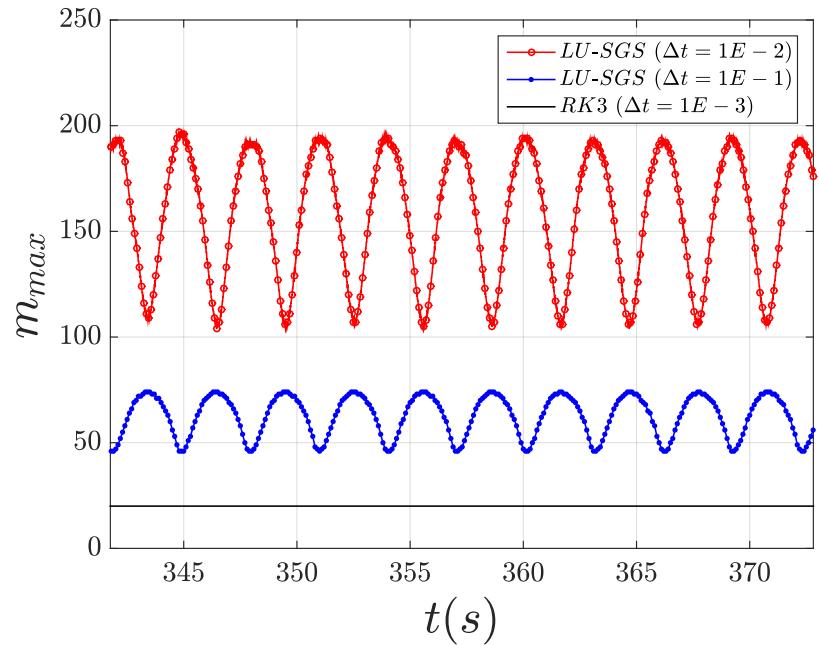


Figure 5.16 Cylinder at $Re = 100$: total pseudo iterations m_{max} per physical time step using implicit LU-SGS, demonstrating a $2.5x$ increase in pseudo iterations required to drop $\|\mathbf{R}_\tau\|_1$ by 10^3 if the physical and pseudo time step sizes are decreased by an order of magnitude to $\Delta\tau = \Delta t = 1E-2$. This highlights the effectiveness of the implicit LU-SGS scheme in reducing all pseudo time derivatives with large time steps.

Chapter 6

Three-dimensional Numerical Results

6.1 Tensor Product Formulation on Hexahedrals

Consider the three-dimensional unsteady incompressible Navier-Stokes equations with artificial compressibility for a Cartesian coordinate system (x, y, z)

$$\frac{1}{\beta_o} \frac{\partial p}{\partial \tau} + \frac{\partial u}{\partial x} + \frac{\partial v}{\partial y} + \frac{\partial w}{\partial z} = 0 \quad (6.1)$$

$$\frac{\partial u}{\partial \tau} + \frac{\partial u}{\partial t} + \frac{\partial u^2}{\partial x} + \frac{\partial uv}{\partial y} + \frac{\partial uw}{\partial z} = -\frac{\partial p}{\partial x} + \nu \left(\frac{\partial^2 u}{\partial x^2} + \frac{\partial^2 u}{\partial y^2} + \frac{\partial^2 u}{\partial z^2} \right) \quad (6.2)$$

$$\frac{\partial v}{\partial \tau} + \frac{\partial v}{\partial t} + \frac{\partial vu}{\partial x} + \frac{\partial v^2}{\partial y} + \frac{\partial vw}{\partial z} = -\frac{\partial p}{\partial y} + \nu \left(\frac{\partial^2 v}{\partial x^2} + \frac{\partial^2 v}{\partial y^2} + \frac{\partial^2 v}{\partial z^2} \right) \quad (6.3)$$

$$\frac{\partial w}{\partial \tau} + \frac{\partial w}{\partial t} + \frac{\partial wu}{\partial x} + \frac{\partial wv}{\partial y} + \frac{\partial w^2}{\partial z} = -\frac{\partial p}{\partial z} + \nu \left(\frac{\partial^2 w}{\partial x^2} + \frac{\partial^2 w}{\partial y^2} + \frac{\partial^2 w}{\partial z^2} \right). \quad (6.4)$$

We can write the above system in strong conservation form as

$$\frac{\partial \mathbf{U}}{\partial \tau} + \mathbf{I}_D \frac{\partial \mathbf{U}}{\partial t} + \nabla \cdot \mathbf{F}(\mathbf{U}, \nabla \mathbf{U}) = 0. \quad (6.5)$$

The vector of state variables $\mathbf{U}(x, y, z, t) \in \Omega$, where $\Omega \subset \mathbb{R}^3$ and $t \geq 0$, and the vector of fluxes $\mathbf{F}(\mathbf{U}, \nabla \mathbf{U})$ are

$$\mathbf{U} = \begin{bmatrix} p \\ u \\ v \\ w \end{bmatrix}, \quad \mathbf{F}(\mathbf{U}, \nabla \mathbf{U}) = \begin{bmatrix} \mathbf{f} \\ \mathbf{g} \\ \mathbf{h} \end{bmatrix} \quad (6.6)$$

where $\mathbf{I}_D = \text{diag}(0, 1, 1, 1)$. The flux vector contains both inviscid terms denoted $(\cdot)_e$ and viscous terms denoted $(\cdot)_v$ in x, y and z , where

$$\mathbf{f} = \mathbf{f}_e - \mathbf{f}_v \quad (6.7)$$

$$\mathbf{g} = \mathbf{g}_e - \mathbf{g}_v \quad (6.8)$$

$$\mathbf{h} = \mathbf{h}_e - \mathbf{h}_v. \quad (6.9)$$

Under artificial compressibility, the three inviscid fluxes vectors are

$$\mathbf{f}_e = \begin{bmatrix} \beta_o u \\ u^2 + p \\ uv \\ uw \end{bmatrix}, \quad \mathbf{g}_e = \begin{bmatrix} \beta_o v \\ vu \\ v^2 + p \\ vw \end{bmatrix}, \quad \mathbf{h}_e = \begin{bmatrix} \beta_o w \\ wu \\ wv \\ w^2 + p \end{bmatrix} \quad (6.10)$$

and the viscous flux vectors are

$$\mathbf{f}_v = \begin{bmatrix} 0 \\ \nu \frac{\partial u}{\partial x} \\ \nu \frac{\partial v}{\partial x} \\ \nu \frac{\partial w}{\partial x} \end{bmatrix}, \quad \mathbf{g}_v = \begin{bmatrix} 0 \\ \nu \frac{\partial u}{\partial y} \\ \nu \frac{\partial v}{\partial y} \\ \nu \frac{\partial w}{\partial y} \end{bmatrix}, \quad \mathbf{h}_v = \begin{bmatrix} 0 \\ \nu \frac{\partial u}{\partial z} \\ \nu \frac{\partial v}{\partial z} \\ \nu \frac{\partial w}{\partial z} \end{bmatrix}. \quad (6.11)$$

As stated before in Section 2.1, ν is the kinematic viscosity, $u = u(x, y, z, t)$, $v = v(x, y, z, t)$ and $w = w(x, y, z, t)$ are the velocity components, β_o is the artificial compressibility parameter, and $p = p(x, y, z, t) = P(x, y, z, t)/\rho$ is static pressure P divided by density ρ . In three dimensions under artificial compressibility, there are four characteristics obtained from the eigensystem of the following convective flux

Jacobians \mathbf{A}_e , \mathbf{B}_e and \mathbf{C}_e

$$\mathbf{A}_e = \frac{\partial \mathbf{f}_e}{\partial \mathbf{U}} = \begin{bmatrix} 0 & \beta_o & 0 & 0 \\ 1 & 2u & 0 & 0 \\ 0 & v & u & 0 \\ 0 & w & 0 & u \end{bmatrix}, \quad \mathbf{B}_e = \frac{\partial \mathbf{g}_e}{\partial \mathbf{U}} = \begin{bmatrix} 0 & 0 & \beta_o & 0 \\ 0 & v & u & 0 \\ 1 & 0 & 2v & 0 \\ 0 & 0 & w & v \end{bmatrix}$$

$$\mathbf{C}_e = \frac{\partial \mathbf{h}_e}{\partial \mathbf{U}} = \begin{bmatrix} 0 & 0 & 0 & \beta_o \\ 0 & w & 0 & u \\ 0 & 0 & w & v \\ 1 & 0 & 0 & 2w \end{bmatrix}. \quad (6.12)$$

The eigenvalues of \mathbf{A}_e , \mathbf{B}_e and \mathbf{C}_e are

$$\lambda_A = \{u - c_x, u, u, u + c_x\} \quad (6.13)$$

$$\lambda_B = \{v - c_y, v, v, v + c_y\} \quad (6.14)$$

$$\lambda_C = \{w - c_z, w, w, w + c_z\} \quad (6.15)$$

where the pseudo speed of sound in each direction is

$$c_x = \sqrt{u^2 + \beta_o} \quad (6.16)$$

$$c_y = \sqrt{v^2 + \beta_o} \quad (6.17)$$

$$c_z = \sqrt{w^2 + \beta_o}. \quad (6.18)$$

The arbitrary solution domain Ω is partitioned into N_e non-overlapping, conforming, hexahedral elements, each denoted by Ω_e such that

$$\Omega = \bigcup_{e=1}^{N_e} \Omega_e, \quad \bigcap_{e=1}^{N_e} \Omega_e = \emptyset. \quad (6.19)$$

Each three-dimensional physical element Ω_e is mapped to a reference element $\Omega_r = \{\xi, \eta, \beta \mid 0 \leq \xi, \eta, \beta \leq 1\}$ through an isoparametric mapping

$$x(\xi, \eta, \beta) = \sum_{k=1}^K x_k \phi_k(\xi, \eta, \beta) \quad (6.20)$$

$$y(\xi, \eta, \beta) = \sum_{k=1}^K y_k \phi_k(\xi, \eta, \beta) \quad (6.21)$$

$$z(\xi, \eta, \beta) = \sum_{k=1}^K z_k \phi_k(\xi, \eta, \beta) \quad (6.22)$$

where K is the number of nodes per element Ω_e , (x_k, y_k, z_k) are nodal Cartesian coordinates, and $\phi_k(\xi, \eta, \beta)$ are the shape functions.

For the case where Ω_e is a quadratic hexahedron as depicted in Figure 6.1, $K = 20$ and node 1 is located at the origin of Ω_r where $(\xi, \eta, \beta) = (0, 0, 0)$. This figure shows the nodal orientation used to perform the mapping of the physical element to the reference element. The shape functions are provided in Appendix B for both linear and quadratic hexahedral elements. The extension to cubic elements is straightforward.

After transformation into the computational domain, the governing equations in Eq. (6.5) can be re-written in the form

$$\frac{\partial \hat{\mathbf{U}}}{\partial \tau} + \mathbf{I}_D \frac{\partial \hat{\mathbf{U}}}{\partial t} + \nabla \cdot \hat{\mathbf{F}} = 0 \quad (6.23)$$

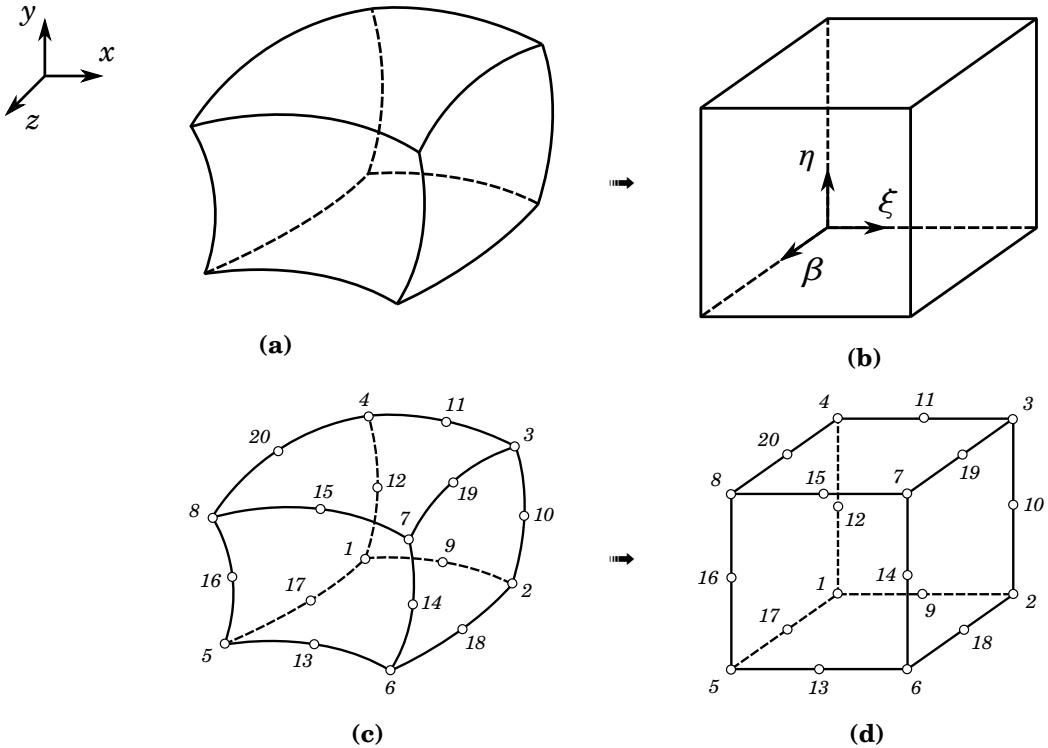


Figure 6.1 Isoparametric mapping from quadrilateral (a) physical element Ω_e to (b) reference element Ω_r . (c) physical element with 20-node orientation and (d) reference element with 20-node orientation.

where

$$\hat{\mathbf{U}} = |\mathbf{J}| \mathbf{U}, \quad \begin{bmatrix} \hat{\mathbf{f}} \\ \hat{\mathbf{g}} \\ \hat{\mathbf{h}} \end{bmatrix} = |\mathbf{J}| \mathbf{J}^{-1} \begin{bmatrix} \mathbf{f} \\ \mathbf{g} \\ \mathbf{h} \end{bmatrix}. \quad (6.24)$$

For a stationary grid, we compute the metric Jacobian \mathbf{J} and its inverse as

$$\mathbf{J} = \begin{bmatrix} \frac{\partial x}{\partial \xi} & \frac{\partial x}{\partial \eta} & \frac{\partial x}{\partial \beta} \\ \frac{\partial y}{\partial \xi} & \frac{\partial y}{\partial \eta} & \frac{\partial y}{\partial \beta} \\ \frac{\partial z}{\partial \xi} & \frac{\partial z}{\partial \eta} & \frac{\partial z}{\partial \beta} \end{bmatrix}, \quad \mathbf{J}^{-1} = \begin{bmatrix} \frac{\partial \xi}{\partial x} & \frac{\partial \xi}{\partial y} & \frac{\partial \xi}{\partial z} \\ \frac{\partial \eta}{\partial x} & \frac{\partial \eta}{\partial y} & \frac{\partial \eta}{\partial z} \\ \frac{\partial \beta}{\partial x} & \frac{\partial \beta}{\partial y} & \frac{\partial \beta}{\partial z} \end{bmatrix} \quad (6.25)$$

at every solution and flux point for each 3D reference element, where the metrics of the Jacobian are obtained from the relationship between the physical hexahedron and the reference cube in Eqs. (6.20)-(6.22). Rewriting the transpose of the 3D cofactor matrix as

$$\mathbf{C}^T = |\mathbf{J}| \begin{bmatrix} \frac{\partial \xi}{\partial x} & \frac{\partial \xi}{\partial y} & \frac{\partial \xi}{\partial z} \\ \frac{\partial \eta}{\partial x} & \frac{\partial \eta}{\partial y} & \frac{\partial \eta}{\partial z} \\ \frac{\partial \beta}{\partial x} & \frac{\partial \beta}{\partial y} & \frac{\partial \beta}{\partial z} \end{bmatrix} = \begin{bmatrix} \mathbf{s}_\xi \\ \mathbf{s}_\eta \\ \mathbf{s}_\beta \end{bmatrix} \quad (6.26)$$

and expanding the governing equations in transformed space

$$\frac{\partial \hat{\mathbf{U}}}{\partial \tau} + \mathbf{I}_D \frac{\partial \hat{\mathbf{U}}}{\partial t} + \frac{\partial \hat{\mathbf{f}}}{\partial \xi} + \frac{\partial \hat{\mathbf{g}}}{\partial \eta} + \frac{\partial \hat{\mathbf{h}}}{\partial \beta} = 0 \quad (6.27)$$

we obtain the formulation

$$\begin{aligned} \frac{\partial \hat{\mathbf{U}}}{\partial \tau} + \mathbf{I}_D \frac{\partial \hat{\mathbf{U}}}{\partial t} + \frac{\partial}{\partial \xi} (s_{\xi,1} \mathbf{f} + s_{\xi,2} \mathbf{g} + s_{\xi,3} \mathbf{h}) \\ + \frac{\partial}{\partial \eta} (s_{\eta,1} \mathbf{f} + s_{\eta,2} \mathbf{g} + s_{\eta,3} \mathbf{h}) \\ + \frac{\partial}{\partial \beta} (s_{\beta,1} \mathbf{f} + s_{\beta,2} \mathbf{g} + s_{\beta,3} \mathbf{h}) = 0. \end{aligned} \quad (6.28)$$

The distribution of solution points in a unit cube can be interpreted by the distribution in a unit square shown in Figure 3.4 for a FR method for which the polynomial order is $p = 3$. The number of solution points per element is $N_s = (p+1)^3 = 64$. Using the solution at $p+1$ solution points, a p degree Lagrange polynomial in each ξ , η and β direction can be built using

$$\ell_i(\xi) = \prod_{s=1, s \neq i}^{p+1} \left(\frac{\xi - \xi_s}{\xi_i - \xi_s} \right) \quad \forall \quad i = 1 \dots p+1 \quad (6.29)$$

$$\ell_j(\eta) = \prod_{s=1, s \neq j}^{p+1} \left(\frac{\eta - \eta_s}{\eta_j - \eta_s} \right) \quad \forall \quad j = 1 \dots p+1 \quad (6.30)$$

$$t_k(\beta) = \prod_{s=1, s \neq k}^{p+1} \left(\frac{\beta - \beta_s}{\beta_k - \beta_s} \right) \quad \forall \quad k = 1 \dots p+1 \quad (6.31)$$

for which $\ell_i(\xi_s) = \delta_{is}$, $\ell_j(\eta_s) = \delta_{js}$ and $\ell_k(\beta_s) = \delta_{ks}$. The solution and flux vectors can be reconstructed with Ω_r through tensor products of the three one-dimensional polynomials ℓ_i , ℓ_j and ℓ_k by

$$\hat{\mathbf{U}}_r(\xi, \eta, \beta) = \sum_{k=1}^{p+1} \sum_{j=1}^{p+1} \sum_{i=1}^{p+1} \hat{\mathbf{U}}_{r|i,j,k} \ell_i(\xi) \ell_j(\eta) \ell_k(\beta) \quad (6.32)$$

$$\hat{\mathbf{f}}_r^D(\xi, \eta, \beta) = \sum_{k=1}^{p+1} \sum_{j=1}^{p+1} \sum_{i=1}^{p+1} \hat{\mathbf{f}}_{r|i,j,k}^D \ell_i(\xi) \ell_j(\eta) \ell_k(\beta) \quad (6.33)$$

$$\hat{\mathbf{g}}_r^D(\xi, \eta, \beta) = \sum_{k=1}^{p+1} \sum_{j=1}^{p+1} \sum_{i=1}^{p+1} \hat{\mathbf{g}}_{r|i,j,k}^D \ell_i(\xi) \ell_j(\eta) \ell_k(\beta) \quad (6.34)$$

$$\hat{\mathbf{h}}_r^D(\xi, \eta, \beta) = \sum_{k=1}^{p+1} \sum_{j=1}^{p+1} \sum_{i=1}^{p+1} \hat{\mathbf{h}}_{r|i,j,k}^D \ell_i(\xi) \ell_j(\eta) \ell_k(\beta) \quad (6.35)$$

where $\hat{\mathbf{U}}_{r|i,j,k} = \hat{\mathbf{U}}_r(\xi_i, \eta_j, \beta_k)$ are the nodal coefficients of the solution in Ω_r , which represent the value of the approximate solution polynomial $\hat{\mathbf{U}}_r$ evaluated at the set of solution points. The nodal coefficients $\hat{\mathbf{f}}_{r|i,j,k}^D = \hat{\mathbf{f}}_r(\xi_i, \eta_j, \beta_k)$, $\hat{\mathbf{g}}_{r|i,j,k}^D = \hat{\mathbf{g}}_r(\xi_i, \eta_j, \beta_k)$ and $\hat{\mathbf{h}}_{r|i,j,k}^D = \hat{\mathbf{h}}_r(\xi_i, \eta_j, \beta_k)$ of the discontinuous fluxes $\hat{\mathbf{f}}_r^D$, $\hat{\mathbf{g}}_r^D$ and $\hat{\mathbf{h}}_r^D$ are computed from $\hat{\mathbf{U}}_{r|i,j,k}$.

Following the methodology presented for the one-dimensional formulation in Section 3.1.1, the continuous flux functions defined along ξ , η and β directions are

$$\hat{\mathbf{f}}_r(\xi, \eta, \beta) = \hat{\mathbf{f}}_r^D(\xi, \eta, \beta) + [\hat{\mathbf{f}}_{r-\frac{1}{2}}^{com} - \hat{\mathbf{f}}_r^D(0, \eta, \beta)] g_r^{LB}(\xi) + [\hat{\mathbf{f}}_{r+\frac{1}{2}}^{com} - \hat{\mathbf{f}}_r^D(1, \eta, \beta)] g_r^{RB}(\xi) \quad (6.36)$$

$$\hat{\mathbf{g}}_r(\xi, \eta, \beta) = \hat{\mathbf{g}}_r^D(\xi, \eta, \beta) + [\hat{\mathbf{g}}_{r-\frac{1}{2}}^{com} - \hat{\mathbf{g}}_r^D(\xi, 0, \beta)] g_r^{LB}(\eta) + [\hat{\mathbf{g}}_{r+\frac{1}{2}}^{com} - \hat{\mathbf{g}}_r^D(\xi, 1, \beta)] g_r^{RB}(\eta) \quad (6.37)$$

$$\hat{\mathbf{h}}_r(\xi, \eta, \beta) = \hat{\mathbf{h}}_r^D(\xi, \eta, \beta) + [\hat{\mathbf{h}}_{r-\frac{1}{2}}^{com} - \hat{\mathbf{h}}_r^D(\xi, \eta, 0)] g_r^{LB}(\beta) + [\hat{\mathbf{h}}_{r+\frac{1}{2}}^{com} - \hat{\mathbf{h}}_r^D(\xi, \eta, 1)] g_r^{RB}(\beta) \quad (6.38)$$

and the corresponding derivatives of the continuous flux functions at the solution

nodes (ξ_l, η_m, β_n) where $l = 1 \dots p+1$, $m = 1 \dots p+1$ and $n = 1 \dots p+1$ are

$$\begin{aligned} \frac{\partial \hat{\mathbf{f}}_r(\xi_l, \eta_m, \beta_n)}{\partial \xi} &= \sum_{k=1}^{p+1} \sum_{j=1}^{p+1} \sum_{i=1}^{p+1} \hat{\mathbf{f}}_{r|i,j,k}^D \frac{d\ell_i(\xi_l)}{d\xi} \ell_j(\eta_m) \ell_k(\beta_n) \\ &\quad + \left[\hat{\mathbf{f}}_{r-\frac{1}{2}}^{com} - \hat{\mathbf{f}}_r^D(0, \eta_m, \beta_n) \right] \frac{dg_r^{LB}(\xi_l)}{d\xi} \\ &\quad + \left[\hat{\mathbf{f}}_{r+\frac{1}{2}}^{com} - \hat{\mathbf{f}}_r^D(1, \eta_m, \beta_n) \right] \frac{dg_r^{RB}(\xi_l)}{d\xi} \end{aligned} \quad (6.39)$$

$$\begin{aligned} \frac{\partial \hat{\mathbf{g}}_r(\xi_l, \eta_m, \beta_n)}{\partial \eta} &= \sum_{k=1}^{p+1} \sum_{j=1}^{p+1} \sum_{i=1}^{p+1} \hat{\mathbf{g}}_{r|i,j,k}^D \ell_i(\xi_l) \frac{d\ell_j(\eta_m)}{d\eta} \ell_k(\beta_n) \\ &\quad + \left[\hat{\mathbf{g}}_{r-\frac{1}{2}}^{com} - \hat{\mathbf{g}}_r^D(\xi_l, 0, \beta_n) \right] \frac{dg_r^{LB}(\eta_m)}{d\eta} \\ &\quad + \left[\hat{\mathbf{g}}_{r+\frac{1}{2}}^{com} - \hat{\mathbf{g}}_r^D(\xi_l, 1, \beta_n) \right] \frac{dg_r^{RB}(\eta_m)}{d\eta} \end{aligned} \quad (6.40)$$

$$\begin{aligned} \frac{\partial \hat{\mathbf{h}}_r(\xi_l, \eta_m, \beta_n)}{\partial \beta} &= \sum_{k=1}^{p+1} \sum_{j=1}^{p+1} \sum_{i=1}^{p+1} \hat{\mathbf{h}}_{r|i,j,k}^D \ell_i(\xi_l) \ell_j(\eta_m) \frac{d\ell_k(\beta_n)}{d\beta} \\ &\quad + \left[\hat{\mathbf{h}}_{r-\frac{1}{2}}^{com} - \hat{\mathbf{h}}_r^D(\xi_l, \eta_m, 0) \right] \frac{dg_r^{LB}(\beta_n)}{d\beta} \\ &\quad + \left[\hat{\mathbf{h}}_{r+\frac{1}{2}}^{com} - \hat{\mathbf{h}}_r^D(\xi_l, \eta_m, 1) \right] \frac{dg_r^{RB}(\beta_n)}{d\beta}. \end{aligned} \quad (6.41)$$

6.1.1 Inviscid and Viscous Numerical Flux Formulation

Inviscid numerical fluxes $\hat{\mathbf{f}}_e^{com}$, $\hat{\mathbf{g}}_e^{com}$ and $\hat{\mathbf{h}}_e^{com}$ computed at the interface between elements in the reference space are computed using an approximate Rusanov Riemann solver

$$\hat{\mathbf{f}}_e^{com} = \frac{1}{2} \left[\hat{\mathbf{F}}_e^R + \hat{\mathbf{F}}_e^L - \hat{\lambda}_{max} (\mathbf{U}^R - \mathbf{U}^L) \right] \quad (6.42)$$

$$\hat{\mathbf{g}}_e^{com} = \frac{1}{2} \left[\hat{\mathbf{G}}_e^R + \hat{\mathbf{G}}_e^L - \hat{\lambda}_{max} (\mathbf{U}^R - \mathbf{U}^L) \right] \quad (6.43)$$

$$\hat{\mathbf{h}}_e^{com} = \frac{1}{2} \left[\hat{\mathbf{H}}_e^R + \hat{\mathbf{H}}_e^L - \hat{\lambda}_{max} (\mathbf{U}^R - \mathbf{U}^L) \right] \quad (6.44)$$

where

$$\hat{\mathbf{F}}_e = s_{\xi,1} \mathbf{f}_e + s_{\xi,2} \mathbf{g}_e + s_{\xi,3} \mathbf{h}_e \quad (6.45)$$

$$\hat{\mathbf{G}}_e = s_{\eta,1} \mathbf{f}_e + s_{\eta,2} \mathbf{g}_e + s_{\eta,3} \mathbf{h}_e \quad (6.46)$$

$$\hat{\mathbf{H}}_e = s_{\beta,1} \mathbf{f}_e + s_{\beta,2} \mathbf{g}_e + s_{\beta,3} \mathbf{h}_e. \quad (6.47)$$

Alternatively, we can write the transformed common inviscid fluxes computed at each flux point located at the interface as

$$\hat{\mathbf{f}}_e^{com} = \frac{1}{2} \left[(\mathbf{F}_e^R + \mathbf{F}_e^L) \cdot \mathbf{n}_\xi - \lambda_{max} (\mathbf{U}^R - \mathbf{U}^L) \right] |\mathbf{s}_\xi| \quad (6.48)$$

$$\hat{\mathbf{g}}_e^{com} = \frac{1}{2} \left[(\mathbf{F}_e^R + \mathbf{F}_e^L) \cdot \mathbf{n}_\eta - \lambda_{max} (\mathbf{U}^R - \mathbf{U}^L) \right] |\mathbf{s}_\eta| \quad (6.49)$$

$$\hat{\mathbf{h}}_e^{com} = \frac{1}{2} \left[(\mathbf{F}_e^R + \mathbf{F}_e^L) \cdot \mathbf{n}_\beta - \lambda_{max} (\mathbf{U}^R - \mathbf{U}^L) \right] |\mathbf{s}_\beta| \quad (6.50)$$

where the convective flux vector is

$$\mathbf{F}_e = \begin{bmatrix} \mathbf{f}_e \\ \mathbf{g}_e \\ \mathbf{h}_e \end{bmatrix}. \quad (6.51)$$

The normal vectors to the interfaces associated with the ξ , η and β directions are

$$\mathbf{n}_\xi = \frac{\mathbf{s}_\xi}{|\mathbf{s}_\xi|} \quad (6.52)$$

$$\mathbf{n}_\eta = \frac{\mathbf{s}_\eta}{|\mathbf{s}_\eta|} \quad (6.53)$$

$$\mathbf{n}_\beta = \frac{\mathbf{s}_\beta}{|\mathbf{s}_\beta|}. \quad (6.54)$$

The maximum eigenvalue λ_{max} in each ξ , η and β direction is computed from the 3D convective flux Jacobian \mathbf{A}_n , where

$$\mathbf{A}_n = \frac{\partial(\mathbf{F}_e \cdot \mathbf{n})}{\partial \mathbf{U}} = \begin{bmatrix} 0 & \beta_o n_1 & \beta_o n_2 & \beta_o n_3 \\ n_1 & 2un_1 + vn_2 + wn_3 & un_2 & un_3 \\ n_2 & vn_1 & un_1 + 2vn_2 + wn_3 & vn_3 \\ n_3 & wn_1 & wn_2 & un_1 + vn_2 + 2wn_3 \end{bmatrix}. \quad (6.55)$$

The velocity normal to the interface is

$$V_n = u^* n_x + v^* n_y + w^* n_z. \quad (6.56)$$

As before, the terms denoted by $(\cdot)^*$ indicate quantities averaged from the right and left states, and the pseudo speed of sound is

$$c_n = \sqrt{V_n^2 + \beta_o}. \quad (6.57)$$

The extension of the viscous numerical fluxes in three dimensions follows in a straightforward manner from Section 3.1.2.2.

6.2 Numerical Results

6.2.1 Sphere

Steady flow at $Re = 118$

To verify implementation of the flux reconstruction method for the three-dimensional

Navier-Stokes equations, we simulate steady flow past a sphere at $Re = 118$. This value of Reynolds is chosen to compare current results to experimental results and to other established high-order flow solvers that use either the flux reconstruction/correction procedure via reconstruction or spectral difference method.

The mesh contains 38016 hexahedral elements with 48 elements in the xy -plane along the wall of the sphere, counting from the windward side to the leeward side and back. This produces 240 DOF for a $p = 4$ polynomial. In total, there are 864 elements along the entire surface, resulting in 21600 DOF. Far field boundaries are $30d$ away, where d is the diameter of the sphere. The near surface mesh is show in Figure 6.2.

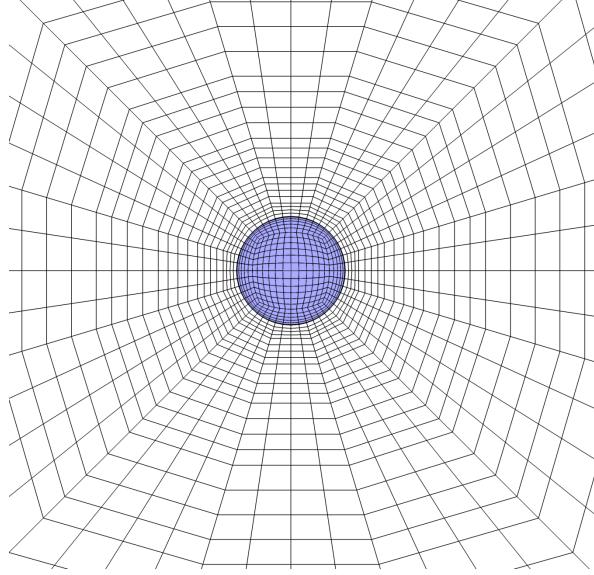


Figure 6.2 Sphere at $Re = 118$: mesh (zoom).

We perform a p -refinement from $p = 1$ to $p = 4$ and use the g_{SD} correction function for all simulations. For all 3D simulations, we use the explicit RK3 scheme of Shu and Osher [60] detailed in Section 4.1 for pseudo time stepping. We compute the components of the drag coefficient due to both pressure $C_{D,p}$ and viscosity $C_{D,v}$ and the separation angle θ measured from the windward stagnation point. Table 6.1 reports converged values of $C_{D,p} = 0.4848$ and $C_{D,v} = 0.5157$, leading to a total drag

coefficient of $C_D = 1.0005$. The angle of separation is $\theta = 124.2^\circ$.

p	$C_{D,p}$	$C_{D,v}$	C_D	θ
1	0.5110	0.4661	0.9771	129.6°
2	0.4879	0.5138	1.0017	124.4°
3	0.4850	0.5156	1.0006	124.2°
4	0.4848	0.5157	1.0005	124.2°

Table 6.1 Sphere at $Re = 118$: convergence of C_D and flow separation angle θ under p -refinement.

Visual comparison of the separation region behind the sphere using streamlines computed from the simulation are compared to aluminum dust flow visualization obtained from Taneda [77] and taken from Van Dyke [78]. Smooth pressure contours and values of skin friction C_f as a function of θ are shown in Figure 6.4 along with the separation length to diameter ratio $s/d = 1.00$. The separation angle is determined from the location where C_f turns negative.

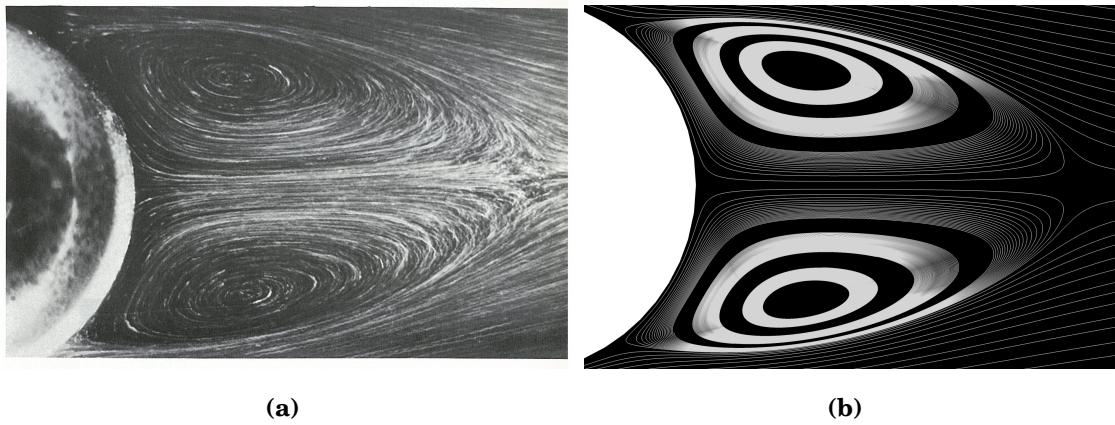


Figure 6.3 Sphere at $Re = 118$: (a) aluminum dust flow visualization by Taneda (1956) taken from Van Dyke (1982), (b) numerical solution using FR-gSD with $p = 4$.

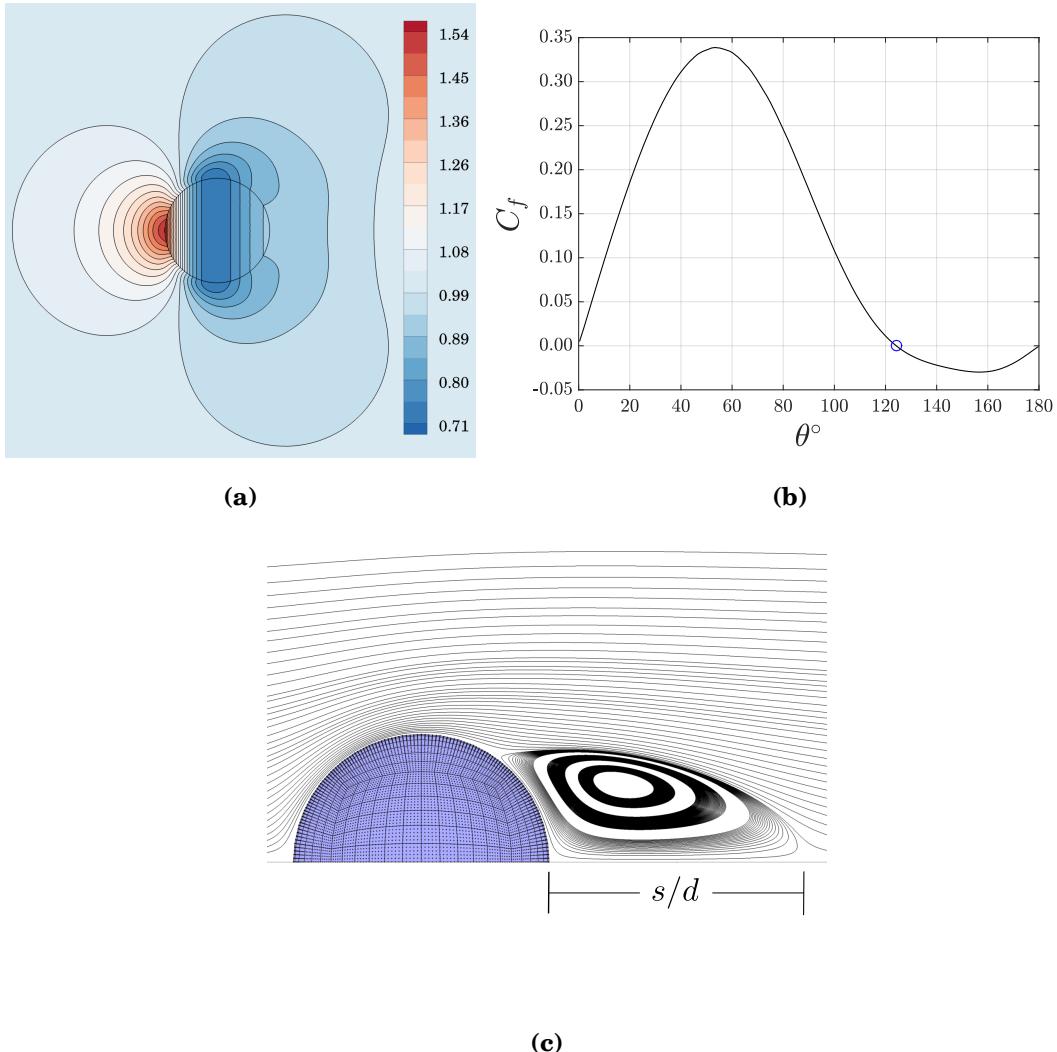


Figure 6.4 Sphere at $Re = 118$: (a) pressure contours, (b) skin friction coefficient C_f showing separation at $\theta = 124.2^\circ$, and (c) streamlines and separation length to diameter ratio $s/d = 1.00$.

Comparison to results obtained from other high-order solver are tabulated in Table 6.2. Castonguay [76] used an FR- g_{HU} scheme, Haga et al. [14] used a CPR scheme, and Sun et al. [79] used the SD method. All of these authors solved the compressible Navier-Stokes equations at Mach=0.2535 and report separation angles of either $\theta = 123.6^\circ$ or $\theta = 123.7^\circ$. The currently reported $C_{D,v}$ is equal to the results from Castonguay et al. to four significant digits, while $C_{D,p}$ is smaller by 3%.

	Method	Mach	Mesh	p	$C_{D,p}$	$C_{D,v}$	C_D	θ	s/d
Current	FR- g_{SD}	<i>inc.</i>	38016 (hex)	4	0.4848	0.5157	1.0005	124.2°	1.00
Castonguay [76]	FR- g_{HU}	0.2535	20736 (hex)	5	0.5005	0.5157	1.0162	123.7°	-
Haga et al. [14]	CPR	0.2535	24334 (mixed)	3,5	-	-	-	123.6°	-
Sun et al. [79]	SD	0.2535	6144 (hex)	3,5	-	-	-	123.6°	1.04

Table 6.2 Sphere at $Re = 118$: comparison of drag coefficient due to pressure $C_{D,p}$ and viscosity $C_{D,v}$ and separation length to diameter ratio s/d with other discontinuous high-order solvers.

Unsteady flow at $Re = 300$

To further verify implementation of the three-dimensional viscous flow solver, we simulate unsteady flow past a sphere at $Re = 300$. The mesh contains 109440 hexahedral elements with 72 elements in the xy -plane along the wall of the sphere. This gives 360 DOF for a $p = 4$ polynomial. In total, there are 1944 elements along the entire surface, resulting in 48600 DOF. The inlet, top and bottom boundaries of the mesh are $25d$ away from the sphere and the exit boundary is $50d$ downstream, where d is the diameter of the sphere. Far field boundary conditions are used for the top and bottom. At the inlet, the velocity is prescribed and the pressure is extracted from the interior of the domain. At the exit, the pressure is prescribed and the velocity is extracted. The global mesh and surface mesh are shown in Figure 6.5.

Time series of drag force coefficient C_D and side force coefficient C_L are shown in Figure 6.6. Mean values and fluctuations of the drag and side coefficients are provided in Table 6.3 along with the Strouhal number St . Results are obtained using a $p = 4$ polynomial, which gives a total of 13.68 million solution points. Statistics are

obtained over 25 shedding cycles using 200 data points per cycle and compared to results from various investigators.

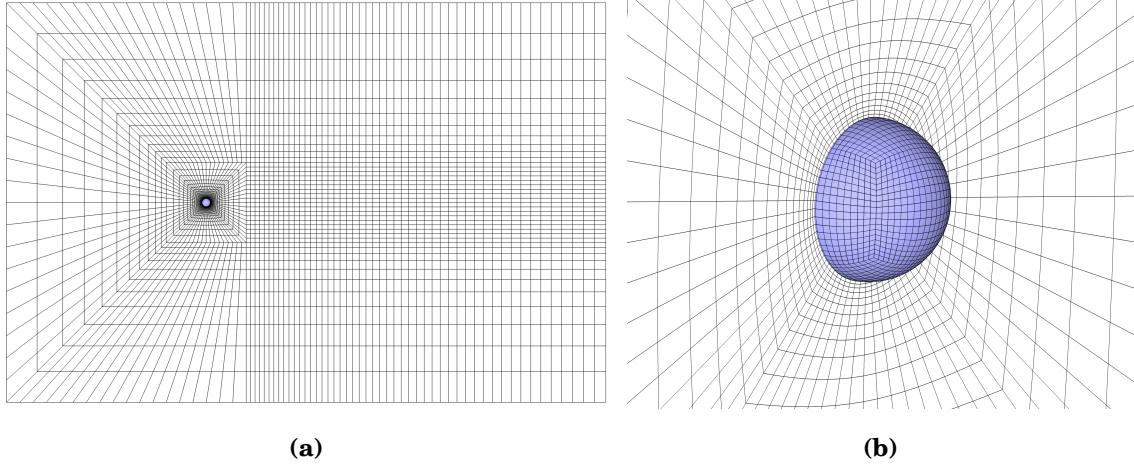


Figure 6.5 Sphere at $Re = 300$: mesh. (a) full, (b) zoom.

Both Johnson and Patel [80] and Tomboulides and Orszag [81] ran incompressible solvers, the former using a combination of central and upwind differencing (CD/UD) and the latter using a mixed spectral element/Fourier spectral method (SE/FS). The remaining authors used compressible solvers run at Mach number equal to 0.3. The value of \bar{C}_D matches the result from Johnson and Patel while \bar{C}_L and St match the results obtained from Castonguay et al., who used a FR- g_{HU} scheme with $p = 3$.

Figure 6.7 demonstrates the shedding of the hairpin vortical structures into the wake of the sphere. These structures are identified by the λ_2 -criterion of Jeong and Hussain [82] (see Section 8.4 for details of this method). Unlike the alternate two-sided shedding of vortices seen in unsteady flow past a two-dimensional cylinder, the shedding of vortices in this case is one-sided. Detailed analysis of the shedding mechanism is provided in Johnson and Patel [80].

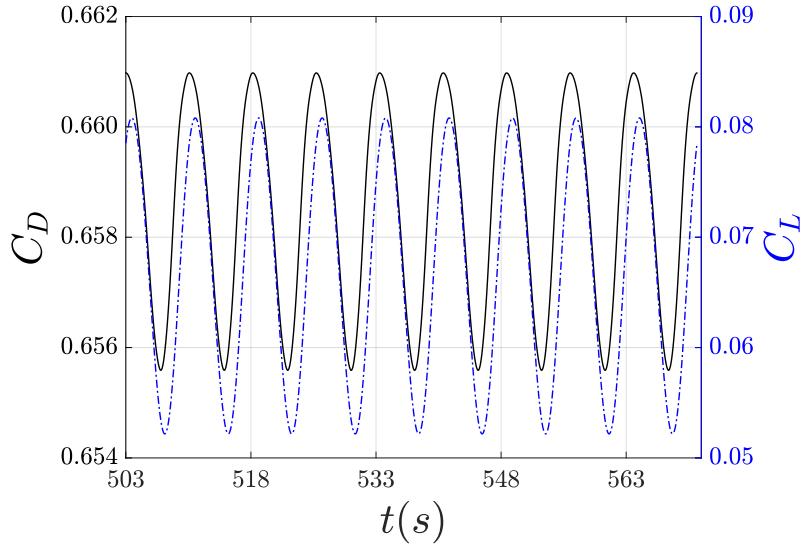


Figure 6.6 Sphere at $Re = 300$: time series of drag and lift coefficient.

	Method	Mach	Mesh	p	\bar{C}_D	C'_D	\bar{C}_L	C'_L	St
Current	FR- g_{SD}	<i>inc.</i>	109440 (hex)	4	0.6586	0.0024	0.0669	0.0140	0.1314
Johnson and Patel [80]	CD/UD	<i>inc.</i>	-	-	0.656	0.0035	0.069	0.016	0.137
Tomboulides and Orszag [81]	SE/FS	<i>inc.</i>	-	3	0.671	0.0028	-	-	0.136
Castonguay [76]	FR- g_{HU}	0.3 (mixed)	287015	3	0.6724	0.00303	0.0667	0.0150	0.1313
Haga et al. [14]	CPR	0.3 (mixed)	54312	3	0.670	0.0032	-	-	0.131
Gassner [83]	DG	0.3 (tet)	160000	3	0.673	0.0031	0.065	0.015	0.135

Table 6.3 Sphere at $Re = 300$: coefficients of mean drag \bar{C}_D , mean drag fluctuation C'_D , mean side \bar{C}_L , and mean side fluctuation C'_L with comparison to various investigators.

High-resolution results are obtained during post-processing by refining each mesh element size h by $p + 1$ and reconstructing the solution at all interior nodes based upon the tensor product formulation given in Eq. 6.32. The original mesh is superimposed on the results to demonstrate the low numerical dissipation of the high-order scheme, especially in the wake far downstream of the sphere where the mesh is more coarse.

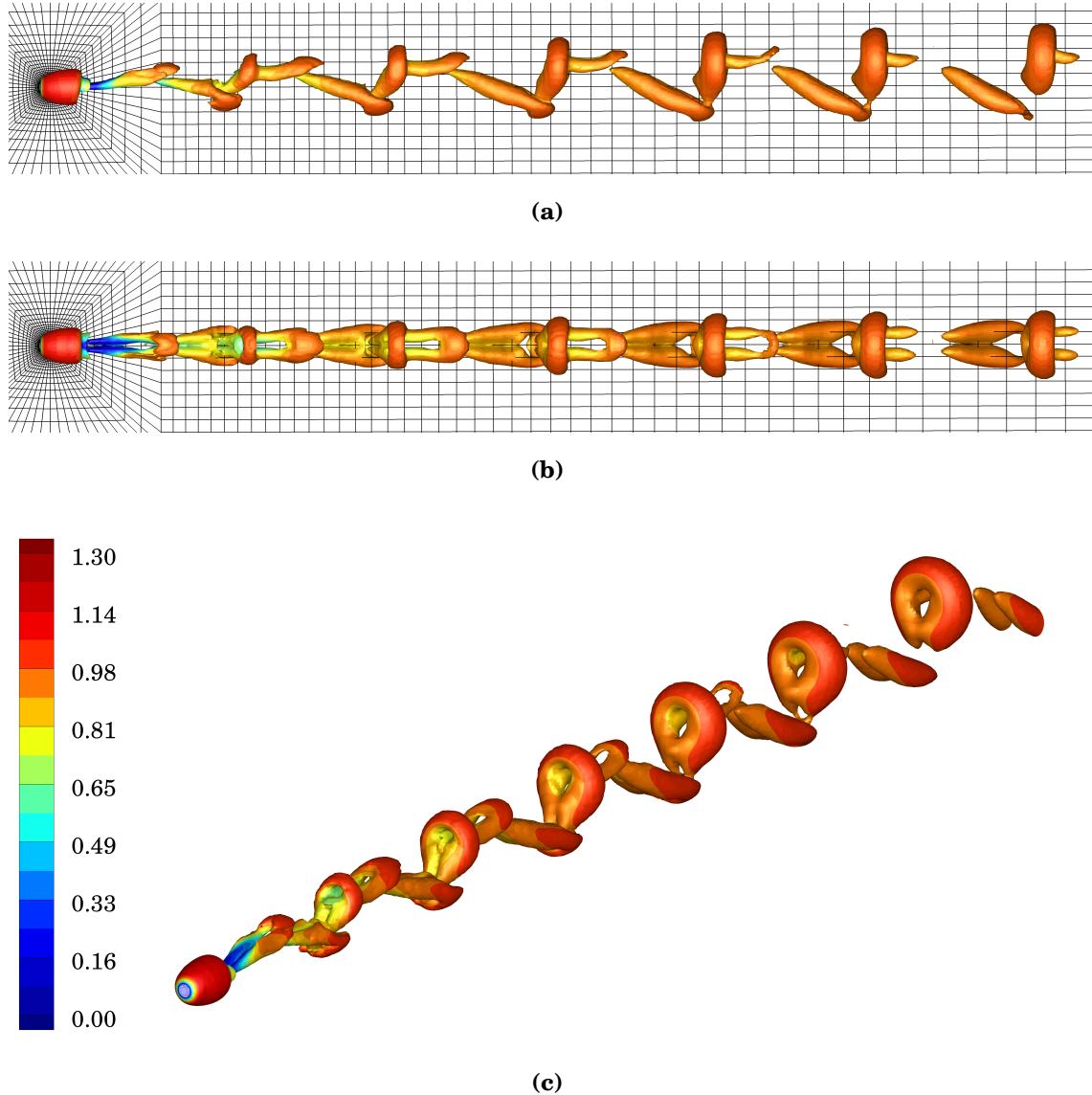


Figure 6.7 Sphere at $Re = 300$: isosurface of λ_2 colored by velocity magnitude showing the hairpin vortical structures shed into the wake with the original mesh superimposed; (a) xy -plane, (b) xz -plane, (c) isometric view. Results are generated using a $p = 4$ polynomial.

6.3 Parallel Computing Performance

6.3.1 Single-Node

Performance of the solver was measured for flow past a sphere case at $Re = 300$ on an Intel® Xeon® E5-1650 v3 Haswell processor with 6 cores (CPU family 6, Model 63, Stepping 2) running at 3.50 GHz with four 8 GB DDR4-2133 memory modules producing a maximum memory bandwidth of ~ 68 GB/s. In order to maintain this clock rate, Turbo Boost was disabled for this test. Also, Hyper-Threading was disabled. Domain decomposition was handled by METIS [84] and parallel processing by MPICH [85], which is a portable implementation of the communication protocol Message Passing Interface (MPI). The memory requirement for the sphere mesh, which consists of 109,440 hexahedral elements, is provided in Table 6.4 for various polynomial order p . This table shows the increase in required memory from polynomial order $p = 1$ to $p = 5$. From this data, we can see that the amount of memory required per degree of freedom per number of equations to solve decreases as p increases, indicating memory efficiency for higher order polynomials.

p	1	2	3	4	5
Memory (GiB)	0.86	1.90	3.80	6.73	11.44
GiB / DOF / N_{eq} ($\times 10^{-7}$)	2.46	1.61	1.35	1.23	1.21

Table 6.4 Memory requirement for sphere mesh with 109,440 hexahedral elements.

Performance of the solver was measured in terms of wall-clock time taken to compute the pseudo residual $\mathbf{R}_\tau = \nabla \cdot \mathbf{F}$ normalized by the total degrees of freedom and number of equations to solve, such that $t_{wall}^* = t_{wall}/DOF/N_{eq}$. Table 6.5 shows that, for a given mesh, as the polynomial order increases the normalized wall clock time

decreases from \sim 61 nanoseconds to \sim 34 nanoseconds. These results demonstrate the improved performance in updating the state vector at each solution node as the polynomial order increases from $p = 1$ to $p = 5$. In other words, the solver efficiency improves as the number of degrees of freedom increases, highlighting a significant benefit of using the flux reconstruction method in particular and high-order methods in general. Improved efficiency of an FR implementation with increasing p on both GPUs and CPUs was also demonstrated in the PyFR solver developed at Imperial College and reported in Witherden, Vermeire and Vincent [86].

p	DOF	t_{wall}^* (10^{-9} s)
1	875,520	60.82
2	2,954,880	41.62
3	7,004,160	37.80
4	13,680,000	35.53
5	23,639,040	33.93

Table 6.5 Wall-clock time to compute $\nabla \cdot \mathbf{F}$ on Intel® Xeon® E5-1650 v3 processor, normalized by total degrees of freedom of the mesh and the number of equations.

6.3.2 Multi-Node

Scalability of current three-dimensional high-order flux reconstruction solver was assessed on the Colonial One high performance cluster located at The George Washington University. Colonial One's CPU nodes feature dual Intel® Xeon® E5-2670 v2 Sandy Bridge processors with 8 cores running at 2.6 GHz with 128 GB of RAM. As in the previous section, domain decomposition was handled through METIS and parallel processing through Open MPI [87], which is an open source MPI implementation. Both strong and weak scalability tests were performed. A strong

test demonstrates scalability of the solver over many processing elements (PEs) for a fixed problem size. Ideally, wall clock time to compute a given number of iterations should inversely scale with the number of processing elements. In these tests, the term “processing elements” means number of processor cores. Strong scalability results shown in Figure 6.8 with $p = 4$ on the sphere mesh with 109,440 elements demonstrate a rather linear speedup up from 1 PE to 512 PEs, achieving an efficiency of 87%.

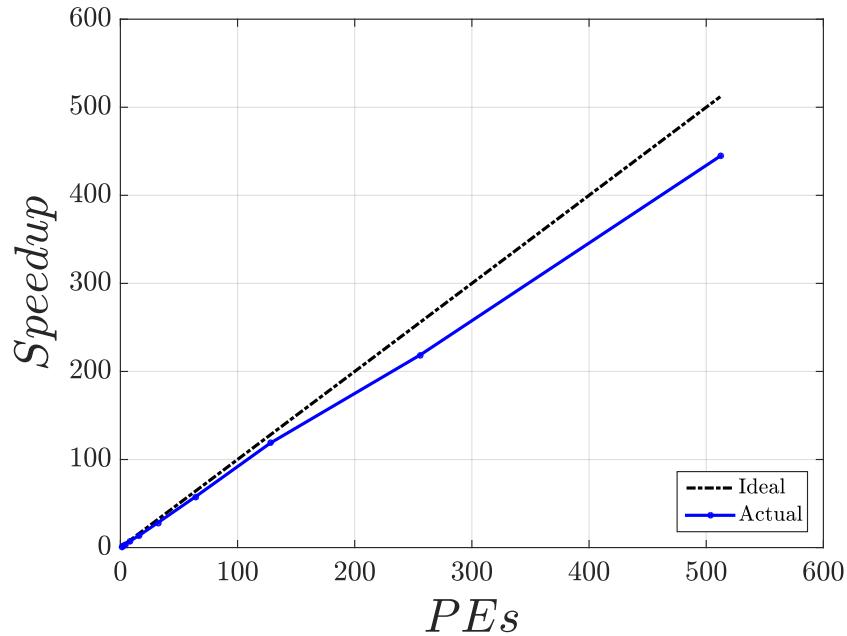


Figure 6.8 Strong scalability: speedup vs. number of processing elements with $p = 4$ on sphere mesh with 109,440 elements.

A weak test shows scalability over many PEs for a fixed problem size per processing element ratio. Under this type of test, an ideal result would show a constant compute time for various problem sizes because the number of PEs used scales with problem size. Results for weak scalability can be seen in Figure 6.9, where the problem size per PE is maintained at 452,750 DOFs. The efficiency t_1/t_{PE} represents the inverse of compute times normalized by the compute time associated

with using 1 PE. From this plot, we can see that communication overhead increases the compute time needed with 512 PEs by $\sim 13\%$

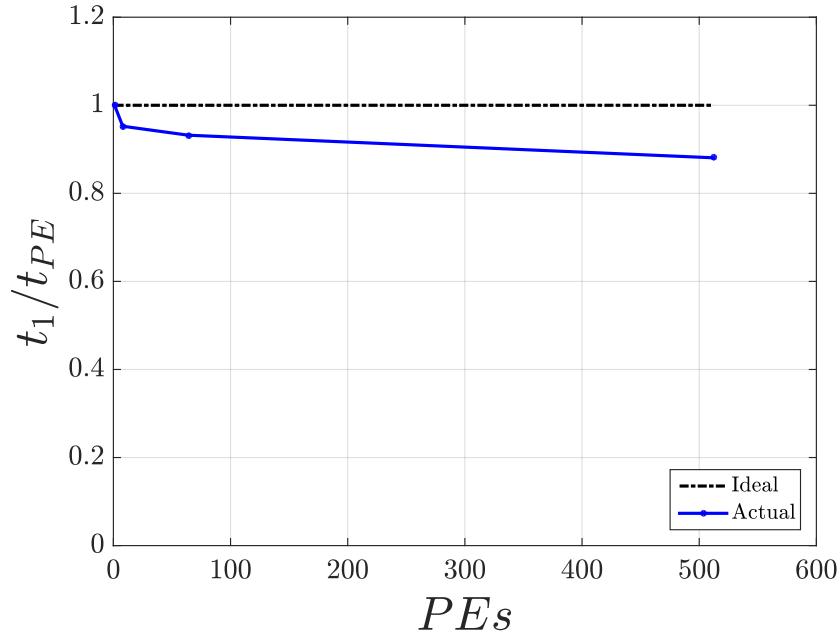


Figure 6.9 Weak scalability: efficiency vs. number of processing elements (problem size per processing element is 452,750 DOFs).

Chapter 7

Conclusions

A high-order compact flux reconstruction method for solving unsteady incompressible flows on unstructured quadrilateral grids with implicit dual time stepping has been developed. The governing equations employ Chorin's classic artificial compressibility formulation such that advanced time stepping techniques developed for solving compressible flow can be used. We implement both a total variation diminishing Runge-Kutta scheme and a backward Euler with non-linear LU-SGS smoothing scheme to handle pseudo time and a second-order backward Euler scheme for physical time. Inviscid numerical fluxes are computed using a Rusanov Riemann solver and viscous numerical fluxes are computed using the popular 2nd procedure of Bassi and Rebay. This method makes the computational stencil compact, requiring information from direct neighboring elements only and allowing for inversion of the implicit operator within the LU-SGS framework. Accuracy and convergence of this solver is shown by studying both steady and unsteady laminar flow problems. The current implicit dual time stepping scheme is proven effective in solving the unsteady incompressible Navier-Stokes equations in pseudo time in the context of a discontinuous high-order spatial method, which is limited by time step size restrictions for explicit schemes. The class of discontinuous high-order methods (e.g. SD and FR) that were designed to solve compressible flow problems can be extended to solve incompressible flows using the artificial compressibility formulation with dual time stepping. We extend development of the solver to perform parallel 3D simulations and validate implementation by simulating steady and unsteady laminar flow past a sphere using explicit pseudo time stepping. Our incompressible solver is very suitable for parallel computing that uses straightforward domain decomposition for partitioning computational elements. Furthermore, we demonstrate the improved efficiency of the 3D solver as the polynomial order p increases, highlighting a significant benefit of using the flux reconstruction method in particular and discontinuous high-order methods

in general. Similar to the implementation in Cox et al. [88], this solver can be easily extended to handle moving and deforming grids for problems involving fluid-structure interactions.

7.1 Future Directions for Research

Implicit Time Integration in 3D

The feasibility of implementing the current implicit dual time stepping scheme in 3D still remains to be seen. Since the element matrix \mathbf{M}_r in Section 4.2 with the number of equations, the polynomial order p , and the dimension of the problem, an efficient non-stationary iterative solver should be employed to achieve unsteady solutions in a practical amount of time.

Convergence Acceleration

To further improve the convergence rate in pseudo time under dual time stepping, a p -multigrid method should be implemented and direct comparisons to the results contained herein should be made. Work on p -multigrid as it relates to the discontinuous high-order SD method was presented in Liang et al. [32] for solving the steady compressible Euler equations and Liang et al. [89] for solving the unsteady incompressible Navier-Stokes equations.

Moving and Deforming Grids

To address the increasing need for the capability to solve fluid-structure interaction problems, an implementation of the current solver on moving and deforming grids should be done. An implementation of the high-order SD method for solving the incompressible Navier-Stokes equations on moving and deforming unstructured grids was done by Cox et al. [88], in which they simulated unsteady flow past an inline tube bundle of cylinders equally sized and spaced using an SD

scheme with $p = 3$. Under FR, however, the implementation would be easier and more efficient than SD due to the fact that there is no extra set of interior flux points in the FR approach that would require updating the metrics of the Jacobian matrix needed for a moving and deforming mesh.

Part II

High-order Numerical Simulations of Pulsatile Flow through a Curved Artery Model

Chapter 8

Steady and Pulsatile Flow in a 180° Curved Pipe

8.1 Introduction

Cardiovascular flows are pulsatile, incompressible flows that exist in complex geometries with compliant walls. Together, these factors produce a vortex rich environment that can affect the progression of cardiovascular disease by altering wall shear stresses. Wall shear stress is one of the most physiologically relevant factors within the cardiovascular system - it affects endothelial cells via mechanotransduction - and atherosclerotic regions are strongly correlated with curvature and branching in the human vasculature where there exists oscillatory shear stress with a low time-averaged value and spatial/temporal shear gradients [90, 91]. Additionally, multidirectionality of the flow may play an important role in the prevalence of atherosclerotic disease [92, 93, 94]. Relevant haemodynamic metrics used to assess the local variation in blood flow characteristics as it relates to atherosclerotic lesions are low *time-averaged wall shear stress* (*TAWSS*), *oscillatory shear index (OSI)* of He and Ku [95] and *relative residence time (RRT)* of Himborg et al. [96]. Although, evidence for the low temporal mean and oscillatory shear stress concept is less robust than previously assumed by the community [97]. As a result, another metric called *transverse wall shear stress* (*TransWSS*) was put forth by Peiffer et al. [94] that is designed to account for multidirectionality of the wall shear stress vector.

Human arteries often follow a path that can curve, twist, taper, bifurcate, and vary in cross-sectional shape. To locate regions where atherosclerosis progresses, many researchers perform numerical simulations using patient-specific data and geometry to study fluid flow. Other researchers adopt a more idealized approach in order to grasp the underlying flow physics without the added complexity of variable geometry. To do this, a simplified model is needed such as a curved pipe and we adopt this approach here. We model a human artery with a simple, rigid 180° curved

pipe with circular cross-section and constant curvature. This assumption is valid since healthy arteries exhibit a rather circular cross-section; therefore, segments of curved arteries can be modeled as curved pipes, neglecting effects of taper, torsion and elasticity.

The body of research on flows through curved pipes in the 20th century is vast, beginning in 1902 with Williams et al. [98] who first noticed the shift in axial velocity towards the outer wall. Shortly thereafter, Eustice [99, 100] showed the existence of secondary flow¹ through a coiled pipe. Steady fluid motion through a curved pipe consists of a pair of counter-rotating helical vortices that are symmetric with respect to the plane of symmetry separating the upper and lower halves of the pipe. A description of the secondary flow which causes these vortices is given by Singh [101]. As fluid enters a curve, a centrifugal force acts on fluid particles and away from the center of curvature towards the outer wall. As a result, a pressure gradient force sets up across the pipe cross-section and acts towards the center of curvature. For an inviscid fluid, there is no secondary action because the centrifugal force and pressure gradient force are completely balanced. On the other hand, for a viscous fluid, where the no-slip condition at a solid boundary forces the near-wall fluid to move slower than the fluid away from the wall, a smaller pressure gradient is required to balance the local centrifugal force near the wall. Consequently, the difference in these pressure gradients causes the faster-flowing fluid (away from the wall) to move outwards and the slower-flowing fluid (near the wall) to move inwards. This leads to the development of secondary flow. Also, near to the wall a balance no longer exists between centrifugal and pressure gradient forces since $\mathbf{u} \rightarrow 0$ as the fluid approaches the wall. An additional description of secondary motion offered by Soh and Berger [102] states that

¹In curved pipes, the primary flow is defined to be parallel to the pipe axis whereas the secondary flow is superimposed on and perpendicular to the primary flow.

“To maintain the momentum balance between the centrifugal force and the pressure gradient, slower-moving fluid particles must move along paths whose radii of curvature are smaller than those of faster-moving particles. This leads to the onset of a secondary flow...”

Ultimately, this means that fluid motion is not parallel to the pipe axis as it is through a straight pipe.

The mechanism of secondary flow in a curved pipe under fully developed steady flow conditions was originally put forth by Dean [103, 104], who found that fluid motion is dependent upon a parameter K referred to thereafter as the *Dean number* and expressed as

$$K = \left(\frac{ru_o}{\nu} \right)^2 \frac{2r}{R} \quad (8.1)$$

where u_o is the maximum velocity in a straight pipe of the same radius and pressure gradient. The original form of the Dean number defined in Eq. (8.1) can be written in terms of the pressure gradient G

$$K = \left(\frac{Gr^2}{4\mu} \right)^2 \frac{2r^3}{\nu^2 R}. \quad (8.2)$$

For fully developed flow, most theoretical and numerical investigators follow the form used by McConalogue and Srivastava [105], who extended Dean’s analysis to larger values of K . However, they defined the Dean number as

$$D = \frac{Gr^2}{\mu} \sqrt{\frac{2r^3}{\nu^2 R}} \quad (8.3)$$

where Gr^2/μ is four times the peak velocity in Poiseuille flow in a straight tube, driven by the same pressure gradient. Since $u_o = 2\bar{u}$ for Poiseuille flow, D and K are

related by

$$D = 4\sqrt{K} = 4Re \sqrt{\frac{2r}{R}} \quad (8.4)$$

where Re is the Reynolds number based upon bulk velocity \bar{u} and pipe diameter d . Following the analysis by Berger, Talbot and Yao [106], the Dean number can also be defined as

$$\kappa = Re \sqrt{\delta}. \quad (8.5)$$

The curvature ratio

$$\delta = \frac{r}{R} \quad (8.6)$$

is a measure of the geometric effect and extent to which centrifugal force varies in the cross-section. In this form of the Dean number, the Reynolds number Re is also defined based on bulk velocity and pipe diameter as

$$Re = \frac{\bar{u}d}{\nu} = \frac{\rho \bar{u}^2}{\mu \bar{u}/d} = \frac{\text{convective inertial forces}}{\text{viscous forces}}. \quad (8.7)$$

The right-hand-side of Eq. (8.7) shows that Re is a ratio of convective inertial forces to viscous forces. The form of the Dean number given in Eq. (8.5) is related to D and K by

$$\kappa = \frac{D}{4\sqrt{2}} = \sqrt{\frac{K}{2}}. \quad (8.8)$$

Berger, Talbot and Yao [106] point out that many investigators have used the above variants of the Dean number (K , D , κ), creating confusion in interpreting results

from the literature. However, versions of the Dean number based the on bulk velocity \bar{u} as opposed to pressure gradient are natural for experimentalists because this quantity can readily be measured and provides a more convenient characterization of the flow than the pressure gradient, which is more difficult to measure. To make our results more accessible to experimentalists, we adopt the form of the Dean number κ suggested by Berger, Talbot and Yao in Eq. (8.5). Re-writing κ as

$$\begin{aligned}\kappa &= \frac{\sqrt{\rho r \frac{\bar{u}^2}{R} \times \rho \bar{u}^2}}{\mu \frac{\bar{u}}{d}} \\ &= \frac{\sqrt{\text{centripetal forces} \times \text{convective inertial forces}}}{\text{viscous forces}}\end{aligned}\tag{8.9}$$

offers a physical interpretation of the Dean number as the ratio of centrifugal and convective inertial forces to viscous forces. Since secondary flow is induced by centrifugal forces and their interaction with viscous forces, κ is a measure of the magnitude of secondary flow. For an extensive review of the literature on steady flows in curved pipes, see Berger, Talbot and Yao [106].

Fully developed pulsatile flow was expressed analytically by Womersley [107], who provided an exact solution to the equations for a viscous fluid in a straight circular tube under a pressure gradient that is a periodic function in time. Given the concern of cardiovascular pathologists with local haemodynamic flow conditions of a specific artery, this work was a landmark achievement towards a method for calculating velocity, flow rate and shear stress under a known pressure gradient. Due to his work, pulsatile fluid motion in a tube is dependent upon a parameter α referred to as the *Womersley number* and expressed as

$$\alpha = r \sqrt{\frac{\omega}{v}}\tag{8.10}$$

where $\omega = 2\pi f$ is the angular frequency of pulsation. The dimensionless quantity

α^2 can be interpreted as the ratio of transient inertial forces to viscous forces. An alternative physical interpretation written in Doorly and Sherwin [108] is demonstrated by re-writing Eq. (8.10) as

$$\alpha = \frac{d}{2} \sqrt{\frac{2\pi}{vT}} \propto \frac{d}{\sqrt{vT}} \quad (8.11)$$

which states that the Womersley number is the ratio of pipe diameter to growth of the laminar boundary layer during the pulsatile waveform period T .

In addition to the Womersley number, which is related to physical scales in the pipe cross-section, the reduced velocity is another dimensionless quantity that introduces an axial length scale. The reduced velocity is also known as the inverse of the Strouhal number St and is written as

$$u_{red} = \frac{\bar{u}_{mean} T}{d} \quad (8.12)$$

where \bar{u}_{mean} is the mean velocity over the pulse period. The physical meaning of this quantity can be interpreted as the ratio of distance traveled by the mean flow along the pipe to the pipe diameter. The reduced velocity can be related to the Womersley number by

$$u_{red} = \frac{\pi}{2} \frac{Re_{mean}}{\alpha} \quad (8.13)$$

where Re_{mean} is the Reynolds number based on \bar{u}_{mean} .

For fully developed oscillatory flows in a curved pipe with frequency ω , Lyne [109] obtained a perturbation solution of the incompressible Navier-Stokes equations for small Dean number and large Womersley number. The large frequency value implies that viscous effects are confined to the near wall region and the core of the mainstream flow is inviscid. His result shows the flow depends on the Womersley

number and the secondary streaming Reynolds number $R_s = u_o^2 r / \omega v R$, which is a Reynolds number based upon the secondary velocity. For large Womersley number, it was shown that secondary flow in the interior of the pipe is in the opposite sense to that which is predicted by steady Dean flow. Siggers and Waters [110] also studied fully developed flow through a curved pipe of uniform curvature under an oscillatory pressure gradient. Fully developed flows driven by a pressure gradient that is sinusoidally varying in time about a non-zero mean was investigated by Smith [111]. The analysis revealed a number of pulsatile motions and the manner in which secondary motion can change its direction from inward to outward “centrifuging” at high frequencies. Sudo et al. [112] performed experimental and numerical studies of secondary flow induced by fully developed oscillatory flow in a curved pipe for a range of Dean and Womersley numbers. Their results suggested that secondary flows can be classified into five circulation patterns; Type I - Dean, Type II - Deformed Dean, Type III - Intermediate between Dean and Lyne, Type IV - Deformed Lyne, and Type V - Lyne. Boiron et al. [113] also conducted experimental and numerical studies in a 180° curved pipe, focusing on the starting effect of the fluid on secondary flow for a range of Dean and Womersley numbers. In addition, they studied the balance of centrifugal force and radial pressure gradient in the symmetry plane as it relates to the appearance of Lyne vortices. Further experimental and numerical work was done by Timit et al. [114], who studied developing pulsatile flow in a 90° curved pipe. Their results demonstrated that for increased Womersley number, the intensity of secondary flow decreased during the acceleration phase of the pulsatile waveform and increased during the deceleration phase due to the effect of reverse flow. Furthermore, they observed that the increase in secondary flow was accompanied by Lyne flow. More recently, van Wyk et al. [115] conducted numerical simulations of flow through a rigid 180° curved pipe and compared results generated using Newtonian and non-Newtonian blood-analog fluids. They used a physiological

waveform from a human carotid artery and observed small vortices located at the inner wall during the deceleration phase, similar to results that will be reported herein.

Ku [116] highlighted the fact that flow through an artery may not be fully developed as is the case when blood emanates from the heart, which functions as a large pressure reservoir. Near the heart, flow entering curved or branched arteries is not fully developed - the velocity profiles are flattened near the center, signifying a developing boundary near the wall and an inviscid core in the center.

Despite the vast amount of research in the 20th century related to fully developed and developing steady and pulsatile flows in curved pipes, there is still knowledge to be gained concerning the spatial and temporal evolution of three-dimensional vortex structures and their role in vascular flows. In light of this, we perform numerical simulations with the solver developed in Part I using three flow conditions to the entrance of the curve; 1) fully developed steady flow, 2) fully developed pulsatile flow, and 3) undeveloped pulsatile flow. Condition 1) uses a Poiseuille (parabolic) velocity profile, condition 2) uses a Womersley velocity profile, and condition 3) uses a uniform velocity profile at the inlet. Within the curve, the flow develops without any symmetry condition imposed between the upper and lower halves of the pipe. Based upon our flow results, we attempt to address the following questions in the context of laminar, incompressible, Newtonian flow in a 180° curved pipe of constant diameter and curvature ratio with zero torsion subjected to a physiological pulsatile waveform:

1. How do three-dimensional vortex structures caused by secondary flows evolve in both space and time under pulsatile inflow conditions?
2. What is the effect of the entrance condition on the development of these vortex structures?

3. What features in the flow are considered pulsatility effects? What are curvature effects?
4. What wall shear stress patterns emerge and how does the entrance condition affect these patterns?
5. What is the correlation between the spatial and temporal evolution of vortex structures and wall shear stresses?

8.2 Geometry

A model of the curved section of the pipe that we use to generate the numerical results is depicted in Figure 8.1. The origin of the Cartesian coordinate system $(x, y, z) = (0, 0, 0)$ is defined along with the diameter d , radius of curvature R , flow direction, and location of the inner (I), outer (O), upper (U) and lower (L) walls. For these studies, the curvature ratio is maintained at $r/R = 1/7$, where the radius $r = d/2$ is 6.35 mm. These parameters are chosen to match the experiments performed by Najjari and Plesniak [117, 118]. The mesh that we use to perform numerical simulations has a straight section upstream to the curve entrance of $5d$ and a straight section downstream of the curve exit of $15d$. We define $\theta = [0^\circ, 180^\circ]$ to represent the angle measured along the poloidal or azimuthal direction from the outer wall and $\phi = [0^\circ, 180^\circ]$ to represent the toroidal angle measured along the streamwise/axial direction from the inlet of the curved pipe. For the current radius of curvature measured from the origin to the pipe axis, the distance from the curve entrance at $\phi = 0^\circ$ to $\phi = 22^\circ$ is $s_{22^\circ} = 7\pi d/16$ and the distance of the whole curve is $s_{180^\circ} = 7\pi d/2$. Within the pipe curve from $\phi = 0^\circ$ to $\phi = 180^\circ$, there are 48 elements along the wall in the azimuthal direction and 160 elements along the all in the toroidal direction. A 5th order flux reconstruction method that uses a $p = 4$ Lagrange polynomial to represent the solution along each dimension (ξ, η, β) within a reference

element Ω_r produces a layer of solution points approximately $l_{sp} = 0.0239$ mm away from the wall. This distance is 0.188% of the pipe diameter.

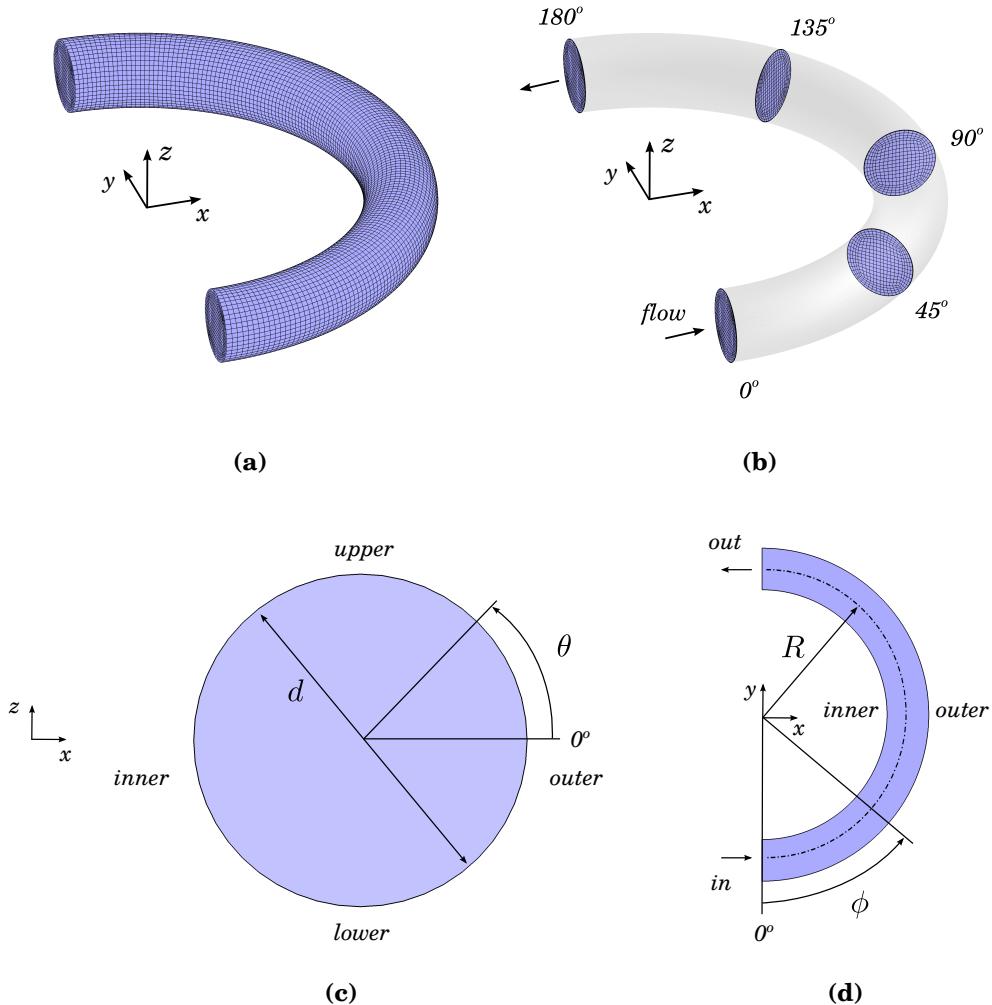


Figure 8.1 Curved pipe geometry and orientation. (a) curvature mesh, (b) cross-sections, (c) cross-section planar view, (d) top planar view.

8.3 Vorticity

Mathematically, vorticity is defined as the curl of the velocity field \mathbf{u}

$$\boldsymbol{\omega} = \nabla \times \mathbf{u} \quad (8.14)$$

and is often used to describe fluid motion. Physically, vorticity is a measure of solid-body-like rotation of fluid elements, describing how the velocity vector changes from one point in space O to another point O' an infinitesimal distance away and perpendicular to the velocity vector. Through Stokes' theorem, circulation is defined as

$$\Gamma = \oint_C \mathbf{u} \cdot d\mathbf{s} = \int_A \boldsymbol{\omega} \cdot \mathbf{n} dS \quad (8.15)$$

where \mathbf{n} is the unit normal to an elemental surface dS , which states that the circulation around a reducible² curve C is equal to the vorticity flux through the surface A bounded by the curve. From Eq. (8.15), vorticity can be interpreted as the circulation per unit area for an elemental surface that is perpendicular to the vorticity vector [119]. Kinematically, the ideas of the velocity field can be applied to the vorticity field. For example, similar to the fact that a streamline is tangent to the velocity vector, a vortex line is a line that is tangent to the local vorticity vector everywhere. These vortex lines are defined by

$$\frac{dx}{\omega_x} = \frac{dy}{\omega_y} = \frac{dz}{\omega_z}. \quad (8.16)$$

In real fluid flow around a stationary body where the no-slip condition must be satisfied, vortex lines must be tangent to the body surface (except at points of

²A curve inside the fluid is said to be reducible if it can be continuously shrunk to a point.

separation and attachment) because the component of vorticity normal to the body surface vanishes. This is true because the circulation for any closed circuit on the body is zero. The no-slip boundary condition ensures that particles are not translating. The particles are, however, undergoing rotation, and since the vorticity component perpendicular to the wall is zero, the vorticity vector lies in the wall. This also means that vortex lines are always perpendicular to wall streamlines. Away from the wall though, in general three-dimensional flow, vortex lines and streamlines are not necessarily orthogonal. Furthermore, because the vorticity is the curl of the velocity field it follows, from the vector-differential operator identity $\nabla \cdot (\nabla \times \mathbf{u}) = 0$, that the divergence of vorticity must be zero

$$\nabla \cdot \boldsymbol{\omega} = 0. \quad (8.17)$$

Since the vorticity is a solenoidal vector field, vortex lines and streamlines of an incompressible fluid obey the same laws. Thus, it is often stated that vortex tubes, defined by vortex lines passing through points of a reducible curve, cannot end within a fluid - they must either form closed curves, extend to infinity or intersect a solid boundary at a location where the vorticity is zero [120]. The term vortex tube implies that any cross-section is oval and that the vorticity vector is parallel to the tube surface everywhere, such that $\boldsymbol{\omega} \cdot \mathbf{n} = 0$ on the surface. Thus vorticity flux through any cross-section of the vortex tube is constant and equal to the circulation around any curve that encloses the tube once - this is commonly called the vortex tube strength. Regions of the fluid where the vorticity is zero do not have any vortex lines, and is said to be irrotational. A vortex filament is sometimes referred to as a vortex tube immediately surrounded by irrotational fluid and is often called a vortex. Alternatively, this term is also used to denote an infinitesimal vortex tube. However, this notion of a vortex filament requires that the fluid be ideal. In a real

fluid, viscosity diffuses vorticity. A definition of what constitutes a vortex has been widely discussed in the literature and we address this topic further in Section 8.4 as it relates to identifying vortices in pulsatile viscous flow through a curved pipe.

To further understand vorticity and its role in viscous flows, consider the dynamic equation that governs vorticity for viscous, incompressible fluids

$$\frac{D\omega}{Dt} = \boldsymbol{\omega} \cdot \nabla \mathbf{u} + \nu \nabla^2 \boldsymbol{\omega} \quad (8.18)$$

called the vorticity transport equation, derived by taking the curl of the momentum equation (neglecting body forces)

$$\frac{\partial \mathbf{u}}{\partial t} + \mathbf{u} \cdot \nabla \mathbf{u} = -\frac{1}{\rho} \nabla P + \nu \nabla^2 \mathbf{u}. \quad (8.19)$$

The term $D\boldsymbol{\omega}/Dt$ on the left-hand side of Eq. (8.18) is the material derivative of vorticity, which represents the rate of change of vorticity for a fluid particle due to unsteadiness or convection. The second term on the right-hand side $\nu \nabla^2 \boldsymbol{\omega}$ is the net rate of viscous diffusion of vorticity. From a solid wall, vorticity transport into the interior of the flow occurs by diffusion only. The distance δ to which this spreading occurs is proportional to $\sqrt{\nu t}$. Changes in wall vorticity at high Re do not have much effect on the flow field away from the wall, where vortical structures can evolve without disruption caused by the wall boundary vorticity. Also, at high Re the time scale over which diffusion occurs $t_d \approx d^2/\nu$ is much larger than the time scale for convection $t_c \approx d/\bar{u}$. At low Re , however, where the ratio t_d/t_c is smaller, viscous effects are important and vorticity diffusion plays a larger role. Finally, the first term on the right-hand side $\boldsymbol{\omega} \cdot \nabla \mathbf{u}$ can be interpreted as the rate of deforming vortex lines. In other words, generation or destruction of vorticity occurs by either stretching or turning of vortex lines. Stretching and contracting a vortex line produces and decreases vorticity, respectively. Also, turning of a vortex line can transfer vorticity in

one direction at the expense of vorticity in another direction. This stretching/turning interpretation assumes that a vortex line moves as a material line with the fluid velocity, which is true for purely inviscid flows where viscous diffusion does not exist. Alternatively, it can be stated that fluid particles on a vortex line at any instant in time will remain on that vortex line at all subsequent times. This is Helmholtz's second law [121]. For viscous flows, however, where vorticity diffusion is non-zero, this interpretation must be qualified by saying that $\boldsymbol{\omega} \cdot \nabla \mathbf{u}$ generates vorticity as though the vortex line were moving as a material line [119].

An interesting fact about Eq. (8.18) is that pressure is absent and the rate of change of vorticity is only dependent upon the instantaneous local values of velocity and vorticity. This highlights the usefulness of vorticity in interpreting viscous flow problems. As stated earlier, vorticity is an indicator of solid-body rotation of fluid particles. Shear stresses act tangential to a particle surface and, if unbalanced, generate vorticity. Pressure does not have a direct effect on the vorticity field because forces arising from pressure act through a particle's center of mass and cannot produce rotation (an exception occurs, for example, when the fluid is stratified, where the density gradient implies that a particle's center of mass does not coincide with its geometric center, thereby producing rotational motion - this is called baroclinic torque). Furthermore, the connection between net shear stresses and vorticity can be demonstrated by re-writing the viscous term in the momentum equation as

$$\mu \nabla^2 \mathbf{u} = \nabla \cdot \boldsymbol{\tau} = -\mu \nabla \times \boldsymbol{\omega}. \quad (8.20)$$

Equation (8.20) shows that shear stress and vorticity are directly related, where the fluid viscosity is the proportionality constant. Therefore, we can say that an unbalanced shear stress can only exist when the vorticity is non-zero. Alternatively, the existence of vorticity means that a fluid particle is, or was at some previous

instant in time, subjected to a net viscous force.

8.4 Vortex Identification Method

A vortex is generally referred to as a region of the flow field where the fluid exhibits a swirling motion. One intuitive definition from Lugt [122] states that

“A vortex is the rotating motion of a multitude of material particles around a common center.”

Vorticity magnitude has been widely used to represent vortex cores³, though this metric can be problematic in cases where a vortex exists but exhibits strong streamwise variation in vorticity, which would indicate separated vortices even though there is only one continuous vortex filament. On the other hand, a concentration of vortex lines does not necessarily indicate a vortex. Therefore, the existence of vorticity does not imply a vortex and is not capable of distinguishing between pure shearing and swirling motions of a vortex.

Many authors attempted to address the issue of vortex identification. The vast research on this topic ranges from Eulerian-based criteria, which make use of the velocity gradient tensor $\nabla \mathbf{u}$, to Lagrangian-based ones in search of a universal, clear definition of a vortex. Here, we choose to use a popular vortex identification method from the Eulerian-based literature developed by Jeong and Hussain [82], known as the λ_2 -criterion. We use this method to identify vortical structures created by the combined effect of pulsatility and curvature-induced secondary motion in the pipe.

³The term *vortex core* is used interchangeably with the term *vortex* and is adopted herein to refer to a vortex core *region* following the description by Jeong and Hussain [82], and should not be confused with a vortex core *axis*.

Jeong and Hussain proposed a Galilean invariant definition of a vortex for incompressible flows that makes use of the velocity gradient tensor

$$\nabla \mathbf{u} = \frac{\partial u_j}{\partial x_i} \quad (8.21)$$

which can be decomposed into symmetric and antisymmetric second-order tensors as follows

$$\nabla \mathbf{u} = \mathbf{S} + \mathbf{R}. \quad (8.22)$$

The symmetric part, known as the strain-rate tensor \mathbf{S} , is defined as

$$\mathbf{S} = \frac{1}{2} \left[\nabla \mathbf{u} + \nabla (\mathbf{u})^T \right] \quad (8.23)$$

and is responsible for pure straining motion, where line elements are extended or contracted depending on the eigenvalues associated with the eigenvectors of the strain-rate tensor - a positive or negative eigenvalue corresponds to the line element being stretched or compressed, respectively. For incompressible flow, since $\nabla \cdot \mathbf{u} = 0$, $\text{Tr}(\mathbf{S}) = 0$ and the sum of the eigenvalues of \mathbf{S} equals zero. The antisymmetric part in Eq. (8.21) is known as the rotation-rate tensor \mathbf{R} , also known as the vorticity tensor, and is defined as

$$\mathbf{R} = \frac{1}{2} \left[\nabla \mathbf{u} - \nabla (\mathbf{u})^T \right]. \quad (8.24)$$

This tensor is related to vorticity through $R_{ij} = \frac{1}{2} \epsilon_{ijk} \omega_k$.

The development of the λ_2 -criterion was motivated by the discrepancy in the pressure minimum and the vortex core. The reasoning behind using a local pressure minimum as a vortex identification criterion is that a reduction in pressure is

typically seen at the axis of a swirling motion, which exhibits a balance between the centrifugal force and pressure force. However, as Jeong and Hussain point out, this is problematic for two reasons: 1) unsteady straining can create a pressure minimum without vortical motion, and 2) viscosity can eliminate the pressure minimum in a flow with vortical motion, i.e. vortices in Stokes flow over a step where the pressure gradient is balanced by the viscous term. Therefore, the existence of a local pressure minimum is not sufficient, nor is it a necessary condition for a vortex core to exist and cannot be used as a general detection criterion. Although, the concept of a pressure minimum does give Jeong and Hussain a starting point for their definition of a vortex core, which makes use of the eigenvalues of the second-order tensor $\mathbf{S}^2 + \mathbf{R}^2$. This tensor is derived from the formulation for the pressure Hessian obtained from taking the gradient of the governing momentum equations

$$-\frac{1}{\rho} \nabla (\nabla p) = \frac{D\mathbf{S}}{Dt} + \mathbf{S}^2 + \mathbf{R}^2 + \frac{D\mathbf{R}}{Dt} + \mathbf{SR} + \mathbf{RS} - \nu \nabla^2 (\mathbf{S} + \mathbf{R}). \quad (8.25)$$

Note that the antisymmetric part of this equation

$$\frac{D\mathbf{R}}{Dt} = -\mathbf{SR} - \mathbf{RS} + \nu \nabla^2 \mathbf{R} \quad (8.26)$$

is the vorticity transport equation. Removing the vorticity transport equation from Eq. (8.25) and discarding the effects due to unsteady straining $D\mathbf{S}/Dt$, which can produce spurious local pressure minima, and viscosity $\nu \nabla^2 \mathbf{S}$, which can obscure the pressure minimum, produces the form

$$-\frac{1}{\rho} \nabla (\nabla p) = \mathbf{S}^2 + \mathbf{R}^2. \quad (8.27)$$

From this analysis, they define a vortex as a region that can be connected by two negative eigenvalues of $\mathbf{S}^2 + \mathbf{R}^2$, which corresponds to the condition that two

eigenvalues of the pressure Hessian should be positive for a local pressure minimum in a plane to occur. Although, Chakraborty et al. [123] point out that the region in which the two eigenvalues of the pressure Hessian are positive may not include the pressure minimum point in the plane if the pressure gradient does not vanish at that point in the plane. Since $\mathbf{S}^2 + \mathbf{R}^2$ is symmetric, it contains real eigenvalues only. Therefore, if λ_1 , λ_2 and λ_3 represent the eigenvalues and $\lambda_1 \geq \lambda_2 \geq \lambda_3$, Jeong and Hussain state that a vortex region is defined when $\lambda_2 < 0$ - this is the λ_2 -criterion. Note that unlike vorticity, $\mathbf{S}^2 + \mathbf{R}^2$ vanishes at a solid boundary, which eliminates the possibility of a vortex core centered at the boundary. As pointed out by Doorly et al. [124], the largest negative value of λ_2 does not necessarily correlate to the center of rotation of a vortex - it is the point corresponding to the strongest relative rotational acceleration, resulting from the \mathbf{R}^2 term.

We identify vortex cores in our flow through a curved pipe using isosurfaces of negative values of λ_2 . It is important to keep in mind that vortical structures identified by an isosurface do not strictly define the extent of the vortex core region - it merely sets a threshold for defining a vortical structure. The strain-rate tensor \mathbf{S} and rotation-tensor \mathbf{R} are directly computed from the flux reconstruction methodology shown in Section 3.1.2.2. The LAPACK subroutine DGEEV, which uses the QR algorithm, was used to solve the eigenvalue problem.

8.5 Wall Shear Stress

In this section, we quickly describe the formulation used by the high-order numerical solver to compute wall shear stress. Wall shear stress is used here in the following ways: 1) to assess numerical convergence, and 2) to compute relevant haemodynamic metrics used to assess the local variation in blood flow characteristics. These metrics are provided in Section 8.8.

Before defining a formulation for the wall shear stress, first let us define the second-order stress tensor \mathbf{T} for a Newtonian fluid to be

$$\mathbf{T} = 2\mu\mathbf{S} \quad (8.28)$$

where \mathbf{S} is the symmetric strain rate tensor defined in Eq. (8.23). This gives

$$\mathbf{T} = \mu \begin{bmatrix} 2\frac{\partial u}{\partial x} & \frac{\partial v}{\partial x} + \frac{\partial u}{\partial y} & \frac{\partial w}{\partial x} + \frac{\partial u}{\partial z} \\ \frac{\partial v}{\partial x} + \frac{\partial u}{\partial y} & 2\frac{\partial v}{\partial y} & \frac{\partial w}{\partial y} + \frac{\partial v}{\partial z} \\ \frac{\partial w}{\partial x} + \frac{\partial u}{\partial z} & \frac{\partial w}{\partial y} + \frac{\partial v}{\partial z} & 2\frac{\partial w}{\partial z} \end{bmatrix}. \quad (8.29)$$

The components of the velocity gradient tensor are computed using the flux reconstruction methodology in Section 3.1.2.2. To compute the wall shear stress vector we follow the full decomposition approach provided in John et al. [125]. We first compute the wall traction $\mathbf{T}\mathbf{n}$ vector, where the local vector \mathbf{n} is normal to the wall surface. Then, we compute the amount of traction in the wall normal direction with $[(\mathbf{T}\mathbf{n}) \cdot \mathbf{n}] \mathbf{n}$. Finally, we subtract these two terms to obtain the shear stress vector that lies in the wall

$$\boldsymbol{\tau}_w = \mathbf{T}\mathbf{n} - [(\mathbf{T}\mathbf{n}) \cdot \mathbf{n}] \mathbf{n}. \quad (8.30)$$

With this information, we can visualize the direction and magnitude of the wall shear stress under pulsatile flow. This is motivated by the various haemodynamic metrics commonly used to assess localized atherosclerotic disease in curved and branched sections of the human arterial network.

8.6 Poiseuille Entrance Condition

Steady flow results have been generated for four different Reynolds numbers - $Re = \{220, 430, 640, 883\}$ - in order to categorize different secondary flow patterns seen in the curved pipe under steady flow conditions and make comparisons to those obtained under pulsatile conditions. Specifically, $Re = 883$ was selected as a steady flow test case due to results obtained under pulsatile flow conditions in Section 8.7.7.1, where it was found that vortex splitting in the cross-sectional plane occurs at this Reynolds number during deceleration. These Reynolds numbers correspond to constant flow rates of $Q = 7.8$ mL/s, 15.2 mL/s, 22.7 mL/s, and 31.3 mL/s, respectively and Dean numbers of $\kappa = \{83, 163, 242, 334\}$ ($D = \{470, 919, 1368, 1888\}$). In the straight section of the constant diameter pipe upstream of the curve the condition is that of a fully developed Poiseuille flow; however, within the curve the flow is developing. This is designated the *Poiseuille entrance condition* (PEC). Results for secondary velocity, streamwise velocity, pressure, vorticity and vortex identification are provided in the following sections for toroidal planes of $\phi = \{22^\circ, 45^\circ, 90^\circ, 135^\circ\}$, in addition to initial and boundary conditions and numerical convergence criteria.

8.6.1 Initial and Boundary Conditions

For all steady viscous flow simulations, we set the initial velocity field to zero flow and the initial pressure field to zero such that

$$\begin{aligned}
p(x, y, z, 0) &= 0 \\
u(x, y, z, 0) &= 0 \\
v(x, y, z, 0) &= 0 \\
w(x, y, z, 0) &= 0.
\end{aligned} \tag{8.31}$$

At the inlet, we specify only the velocity field using the parabolic velocity profile obtained for laminar Poiseuille flow, and we extrapolate the pressure from the adjacent interior flux points

$$\begin{aligned}
p_g^{inlet} &= p_i^{inlet} \\
u_g^{inlet} &= 2\bar{u} \left(1 - r^2/r_{max}^2\right) \\
v_g^{inlet} &= 0 \\
w_g^{inlet} &= 0
\end{aligned} \tag{8.32}$$

where \bar{u} is the cross-sectional bulk velocity. Following Section 3.1.2.1 which provides the details for computing interfacial numerical fluxes, the indices i and g denote the interior and ghost flux point on each face of the inlet boundary $\partial\Omega^{inlet}$ where the Riemann problem is solved. The variable r represents the distance from the pipe centerline to the solution point/node and $r_{max} = d/2$ is the pipe radius (previously, r was defined as $d/2$). On the outlet boundary $\partial\Omega^{outlet}$, we extract the velocity field from the adjacent interior flux points while the pressure is set to zero for all time,

such that

$$\begin{aligned}
 p_g^{outlet} &= 0 \\
 u_g^{outlet} &= u_i^{outlet} \\
 v_g^{outlet} &= v_i^{outlet} \\
 w_g^{outlet} &= w_i^{outlet}.
 \end{aligned} \tag{8.33}$$

The solver allows for negative pressure values since only relative pressure variations are important for incompressible flow. Finally, we apply the no-slip boundary condition at the pipe wall such that

$$u = v = w = 0 \quad \text{at} \quad r = r_{max}. \tag{8.34}$$

8.6.2 Numerical Convergence

To achieve numerical convergence for the various steady flow simulations, we perform a p -convergence study of the L^2 -norm of wall shear stress $\|\boldsymbol{\tau}_w\|_2$ on the mesh from Section 8.2 using order $p = 2$, $p = 3$ and $p = 4$ such that the difference between $p = 3$ and $p = 4$ is less than 1%. To achieve the steady state in each Reynolds number case, we drive the pseudo residual $\|\boldsymbol{R}_\tau\|_2$ below a value of 1E-8. Due to the initial velocity condition being a zero flow condition, the pseudo time step used for all steady flow simulations was chosen to be small at $\Delta t = 1.25\text{E-}5$ and the artificial compressibility parameter was set to $\beta_o = 1.25$.

8.6.3 Secondary Flow

Non-dimensional secondary velocity magnitude $|\boldsymbol{u}_{\theta r}^*| = |\boldsymbol{u}_{\theta r}|/\bar{u}$, where \bar{u} is the bulk velocity, for various values of the toroidal angle ϕ is plotted in Figure 8.2 followed

by the corresponding secondary velocity vector field in Figure 8.3. From these two figures at $\phi = 22^\circ$, we see increased secondary velocities along the upper and lower walls moving inward. On the other hand, in the interior of the pipe, the secondary motion of the fluid moves outward. We see this trend of inward/outward movement in secondary flow for all values of ϕ shown. At $\phi = 45^\circ$, secondary motion is strongest and accompanied by a low velocity region near the inner wall. Inspection of the velocity vectors reveals a pair of secondary recirculation zones, one above and one below the $z = 0$ plane of symmetry. For higher Re , the center of these zones moves closer towards the inner wall as the secondary motion becomes stronger. This secondary flow pattern develops because the pressure gradient, caused by centrifugal forces, drives the slower moving fluid near the wall inward towards the inner wall and the faster moving fluid in the interior towards the outer wall. Furthermore, at $Re = 430$ and $\phi = 90^\circ$ we see the appearance of two secondary saddle points along the plane of symmetry. In this context, we should note that when a saddle point is present in secondary flow, it means that the three-dimensional velocity vector is directly aligned with the streamwise, or primary, flow direction. These secondary saddle points occur because the secondary boundary layer can no longer accept fluid, thereby preventing the boundary layer from growing. Consequently, streamlines are pushed away from the plane of symmetry near the center of the pipe, giving rise to a second and third pair of secondary recirculation zones. Additional description and definition of these zones as they relate to the streamwise vorticity field will be given in Section 8.6.5.

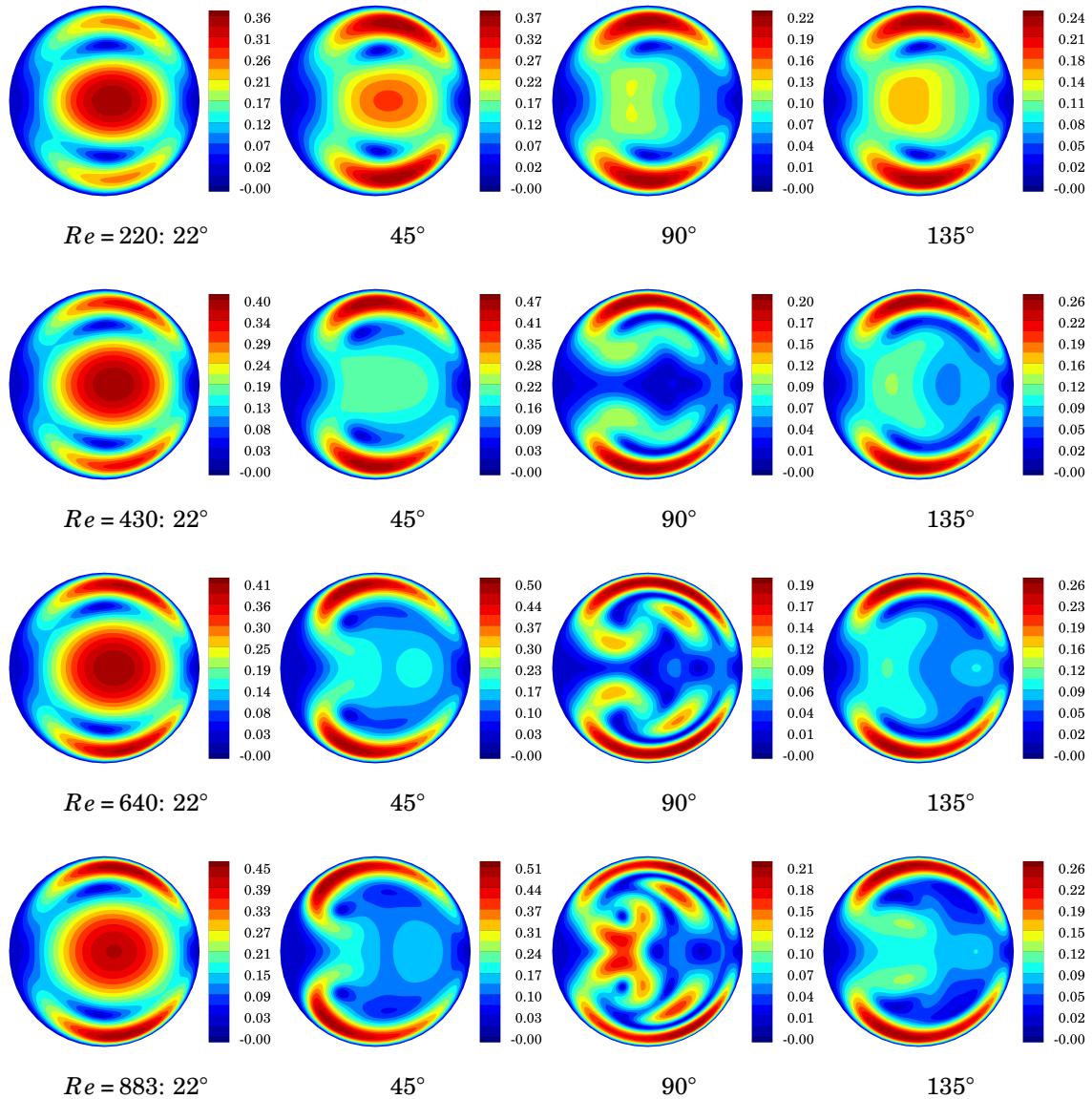


Figure 8.2 Steady flow: non-dimensional secondary velocity magnitude $|u_{\theta r}^*|$. $Re = \{220, 430, 640, 883\}$, $\phi = \{22^\circ, 45^\circ, 90^\circ, 135^\circ\}$.

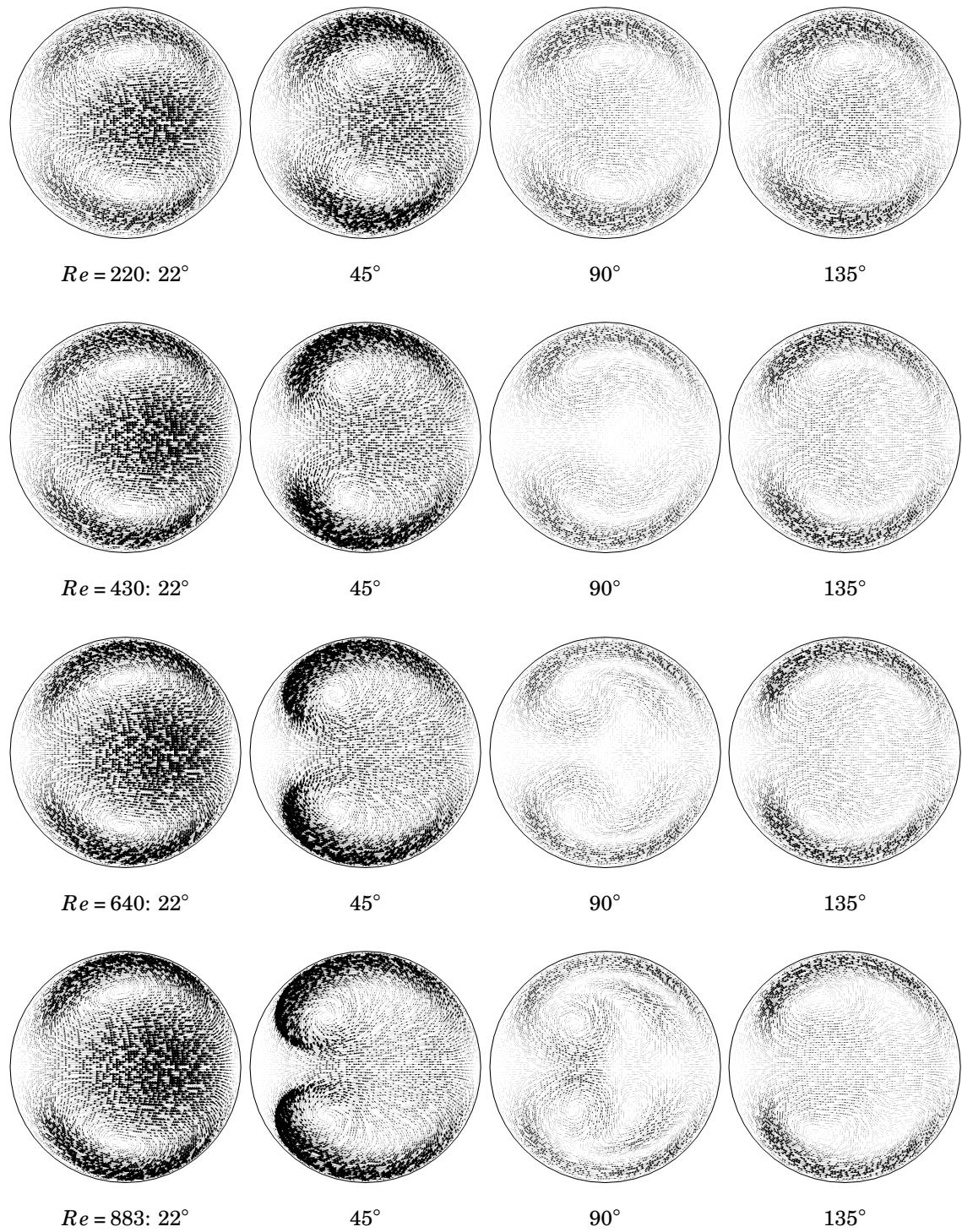


Figure 8.3 Steady flow: non-dimensional secondary velocity vectors $u_{\theta r}^*$. $Re = \{220, 430, 640, 883\}$, $\phi = \{22^\circ, 45^\circ, 90^\circ, 135^\circ\}$.

8.6.4 Primary Flow

Figure 8.4 shows the pattern of non-dimensional streamwise velocity, $u_s^* = u_s/\bar{u}$, for the various values of Re and ϕ . At $\phi = 22^\circ$, the cross-sectional pattern of contours is rather circular with low streamwise velocity near the walls and large streamwise velocity in the center, with the maximum velocity being shifted towards the outer wall, as opposed to Poiseuille flow in a straight pipe where the maximum velocity is located directly at the center. At $\phi = \{45^\circ, 90^\circ, 135^\circ\}$ the contours take on the typical crescent-like shape, which is more pronounced at higher Re . The maximum velocity is shifted even farther towards the outer wall. Streamwise velocity profiles at the plane of symmetry are shown in Figure 8.5. These profiles demonstrate the typical skewed characteristic of flow through a curvature, with larger skewness occurring at higher Re . For all Re shown, the location of maximum velocity moves farther towards the outer wall as the bulk flow moves downstream along the curve (i.e. for increasing ϕ). In all plots, the maximum non-dimensional streamwise velocity is always less than the straight pipe Poiseuille flow value of 2 and decreases along the curve. At $\phi = 45^\circ$, the profile flattens at higher Re for $r/r_{max} < 0$. At $\phi = 90^\circ$, a double peak pattern starts to form for $Re = 640$. At $Re = 883$ the double peak is even more pronounced, and the streamwise velocity reaches a local minimum near the pipe center, $r/r_{max} = 0$. At $\phi = 135^\circ$, the double peak disappears and the profile is rather linear in the region $0.6 < r/r_{max} < 0$.

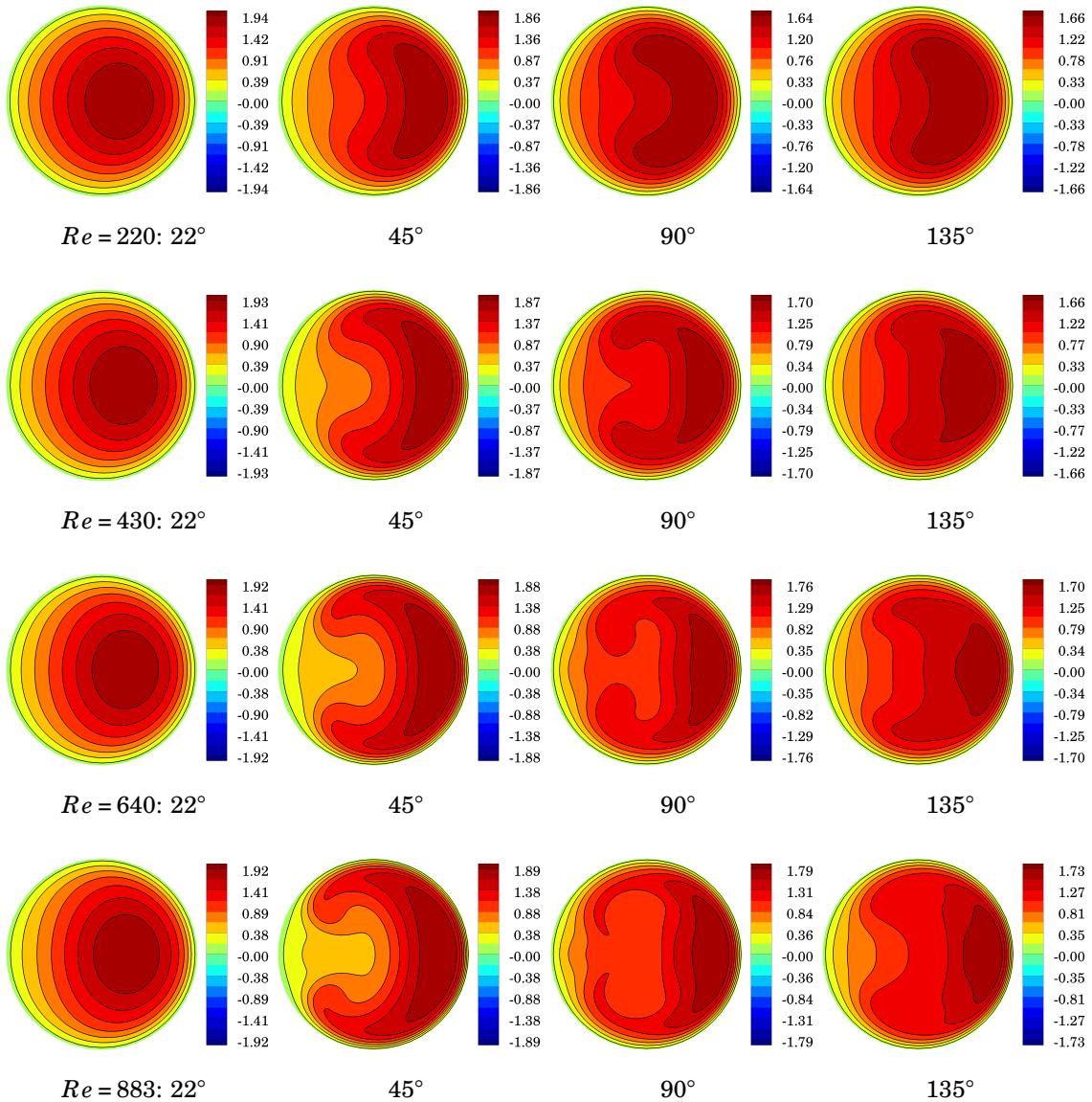
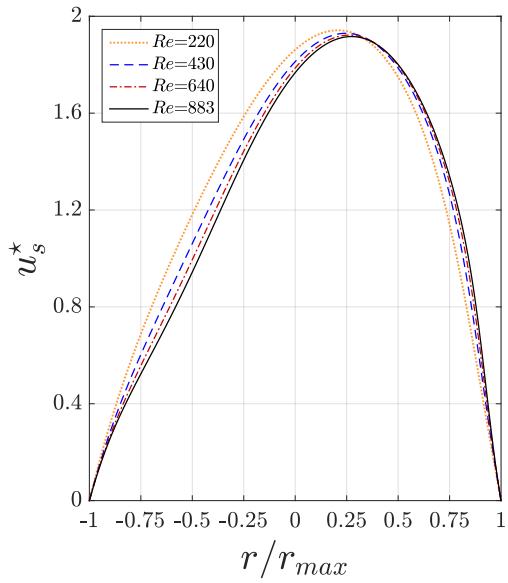
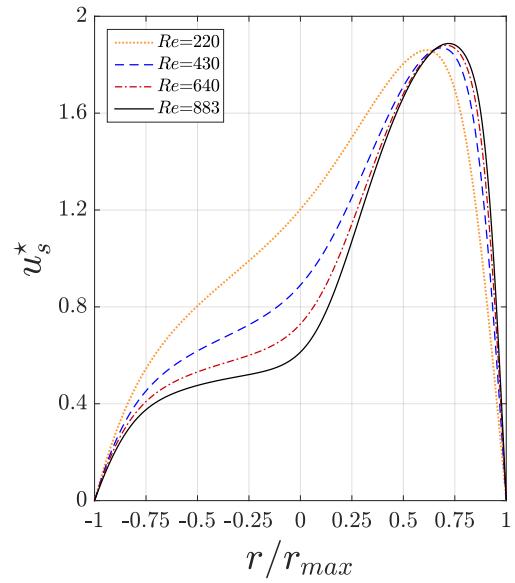


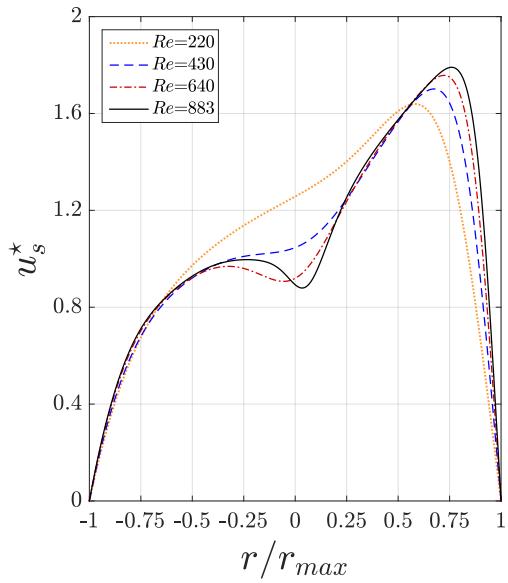
Figure 8.4 Steady flow: non-dimensional streamwise velocity u_s^* . $Re = \{220, 430, 640, 883\}$, $\phi = \{22^\circ, 45^\circ, 90^\circ, 135^\circ\}$.



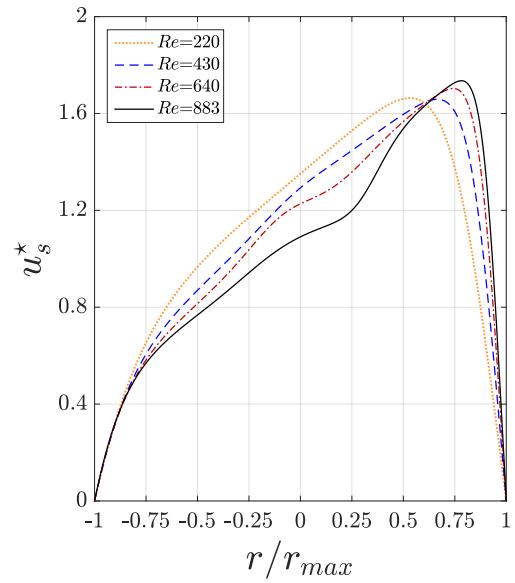
(a) 22°



(b) 45°



(c) 90°



(d) 135°

Figure 8.5 Steady flow: non-dimensional streamwise velocity, u_s^* , profile at $z = 0$ plane of symmetry. $Re = \{220, 430, 640, 883\}$, $\phi = \{22^\circ, 45^\circ, 90^\circ, 135^\circ\}$.

8.6.5 Vorticity

Vorticity can be used to further understand the underlying physics of viscous flow. In the cross-sectional views of Figure 8.7, we plot the streamwise component of non-dimensional vorticity, $\omega_s^* = \omega_s d/\bar{u}$, for various ϕ . For the purpose of cross-sectional visualization, we use the right-hand-screw rule with thumb pointing out-of-page to signify positive vorticity in all planes of ϕ . Therefore, a positive ω_s^* points upstream (in the negative streamwise direction) and negative ω_s^* points downstream (in the positive streamwise direction). This orientation is used in the following sections of this dissertation. To better understand and visualize the three-dimensional shape of the velocity profile, we plot three different views - isometric, upper and inner - of the streamwise velocity surface in Figure 8.7. Each view is colored by the streamwise vorticity and denotes the location of the inner (I), outer (O), upper (U) and lower (L) walls (see Section 8.2 for geometry and orientation definitions).

Secondary boundary layers develop along the upper and lower walls as a result of the fluid entering these layers near the outer wall and exiting at the inner wall. Berger and Talbot [106] stated that at a high Dean number, or high Reynolds number for a given curvature ratio, the centrifugal force due to the curvature leads to an increased circumferential velocity where more fluid is “sucked” into the boundary layer at the outer wall. This results in the boundary layer being thinner near the outer wall and thicker near the inner wall. As the Dean number increases, the boundary layer at the inner wall thickens further and may eventually separate. Our results confirm this description by Berger and Talbot.

In addition to the secondary boundary layers, Figure 8.7 shows two regions of oppositely-signed streamwise vorticity adjacent to the wall layer vorticity at $\phi = 22^\circ$, indicating counter rotations of the secondary motion separated by the plane of symmetry. This vorticity pattern is the result of the well known *Dean* (D) flow, which

is depicted in the schematic shown in Figure 8.6a.

At $\phi = 45^\circ$, these regions of oppositely-signed vorticity deform to produce a more “comma-like” shape (see Sudo et al. [112] for classification of various secondary flow circulations). This pattern of vorticity results from secondary flow that is designated *Deformed-Dean* (DD) circulation, produced by the saddle point described earlier that deflects the secondary flow away from the plane of symmetry. The Deformed-Dean recirculation pair is depicted in Figure 8.6b.

At $\phi = 90^\circ$, a region of streamwise vorticity opposite to that of Dean and Deformed-Dean circulation appears closer to the plane of symmetry. This effect can be partly attributed to the formation of a secondary saddle point that was first pointed out in Section 8.6.3. This second region of oppositely-signed vorticity we refer to as *Lyne-type*⁴ (LT) circulation. As pointed out by Doorly and Sherwin, the Lyne-type circulation accepts vorticity from the eruption of the secondary boundary layer at the inner wall. The Lyne-type recirculation pair is depicted in Figure 8.6c along with the Deformed-Dean pair.

Furthermore, at $\phi = 90^\circ$, the head of the comma-like Deformed-Dean forms another region of concentrated vorticity. We refer to this third recirculation region as *Split-Dean* (SD) because, as we will describe in Section 8.6.6, the “heads” of the upper and lower Deformed-Dean split off from the main comma-shaped region. To qualify when and where this splitting occurs, we use the λ_2 vortex identification criterion described in Section 8.4. At this cross-section, we now observed a total of six regions of secondary circulations - three above and three below the plane of symmetry - where the streamwise vorticity is non-zero. In conclusion, DD and SD both exhibit the same sign of streamwise vorticity above or below the plane of symmetry while LT vorticity

⁴We use this term loosely here under steady flow conditions, realizing that Lyne circulation was originally described under high-frequency oscillatory viscous flow where the viscous effects are confined to a thin layer along the wall while the interior core of the flow is inviscid [109].

is oppositely-signed. The three pairs of recirculation zones - Deformed-Dean, Lyne-type and Split-Dean - are depicted together in the schematic in Figure 8.6d.

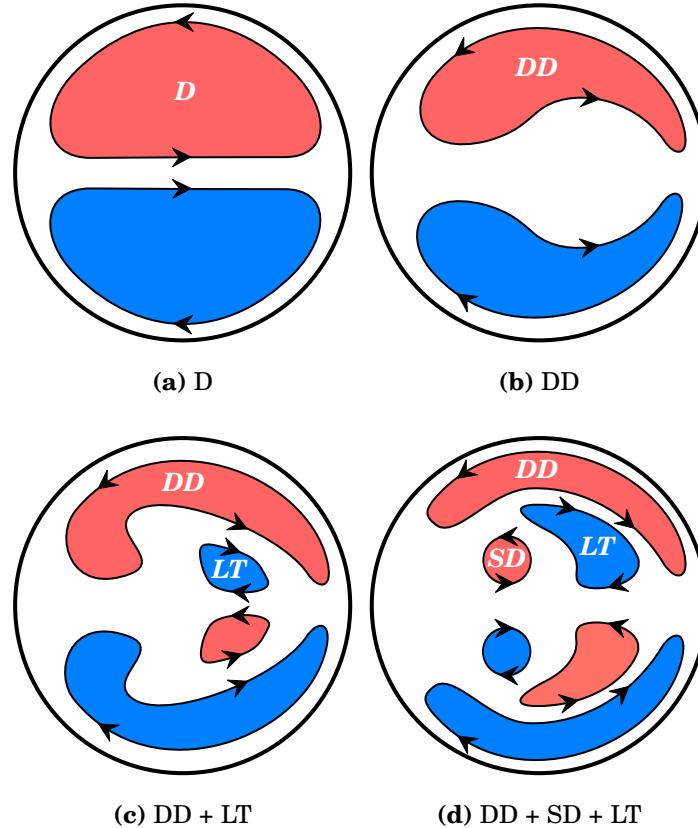


Figure 8.6 Schematic of Dean (D), Deformed-Dean (DD), Split-Dean (SD) and Lyne-Type (LT) vortex pairs; the red and blue colors signify counter-clockwise and clockwise rotation of the secondary flow, respectively (when viewed from upstream).

The isometric view in Figure 8.7 depicts the skewed velocity profile along with DD, SD and LT streamwise vorticity. This particular view shows the reduced and rather flattened streamwise velocity corresponding to SD vorticity. To see this more clearly, the non-dimensional streamwise velocity profiles at the plane $z/r_{max} = 0.33$ are plotted in Figure 8.8. This plane cuts right through SD at this Reynolds numbers and toroidal angle. In this figure, we see a double peak profile at $\phi = 45^\circ$ for $Re = \{640, 883\}$ and at $\phi = 90^\circ$ for $Re = \{430, 640, 883\}$. At $\phi = 90^\circ$ and $Re = 883$, the streamwise

velocity is indeed flattened around $r/r_{max} = -0.3$ where SD exists. The velocity then decreases to a local minimum at the $r/r_{max} = 0$ center and then increases rather linearly to a maximum around $r/r_{max} = 0.7$. The region where the profile flattens can be called the inviscid region. Recall that in Section 8.3 the existence of vorticity means that a fluid particle is subjected to a net viscous force. In the context here, this means that the non-zero SD vorticity exists in a small inviscid core region because of the viscous forces associated with DD vorticity. These figures highlight the complexity of the flow field, even under steady flow, and serve as a starting point for interpretation of the flow physics under pulsatile conditions in Section 8.7.

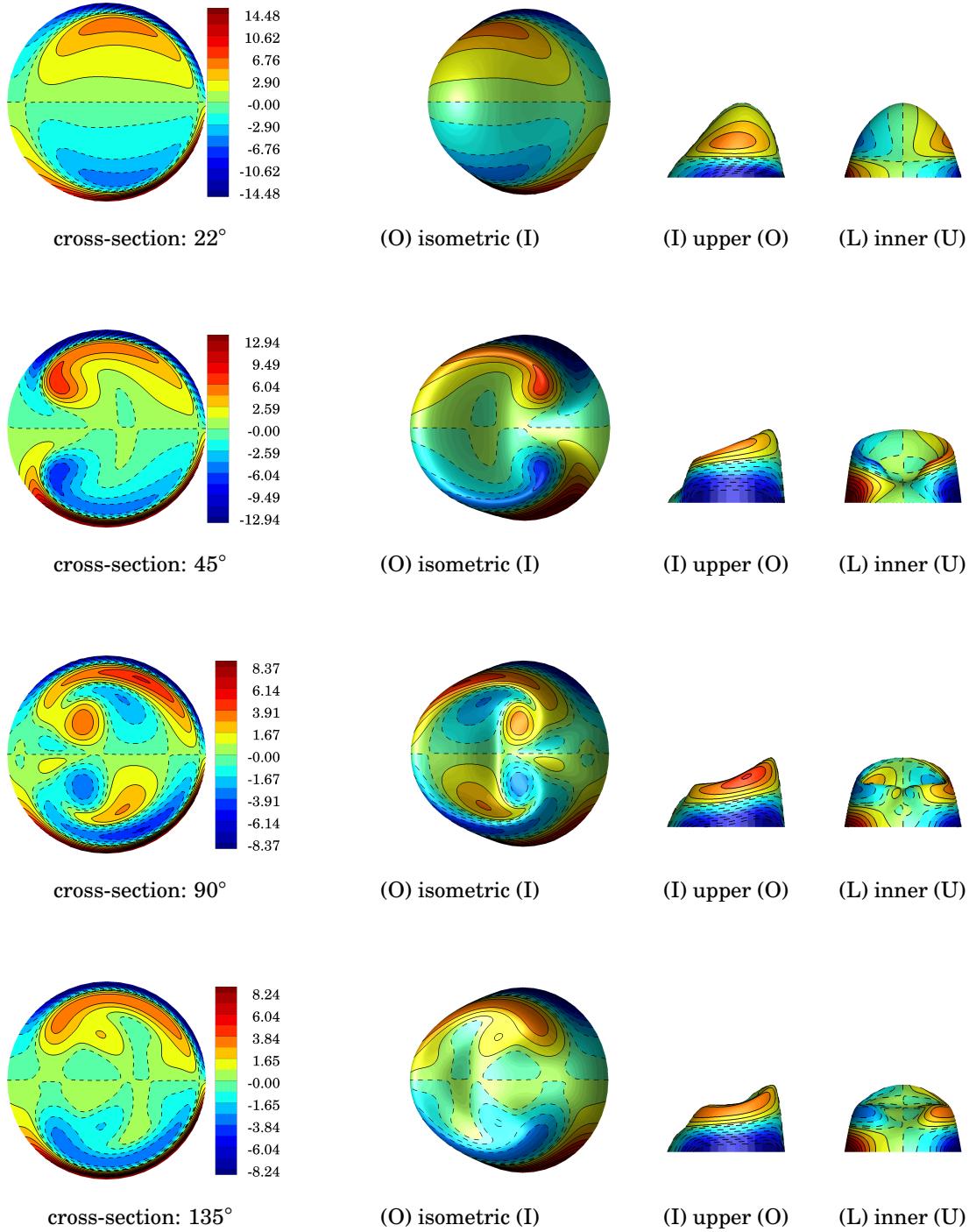


Figure 8.7 Steady flow: velocity surface of u_s^* colored by non-dimensional streamwise vorticity ω_s^* visualized from three difference views: isometric, upper and inner. $Re = 883$, $\phi = \{22^\circ, 45^\circ, 90^\circ, 135^\circ\}$ ($I \equiv inner$, $O \equiv outer$, $U \equiv upper$, $L \equiv lower$).

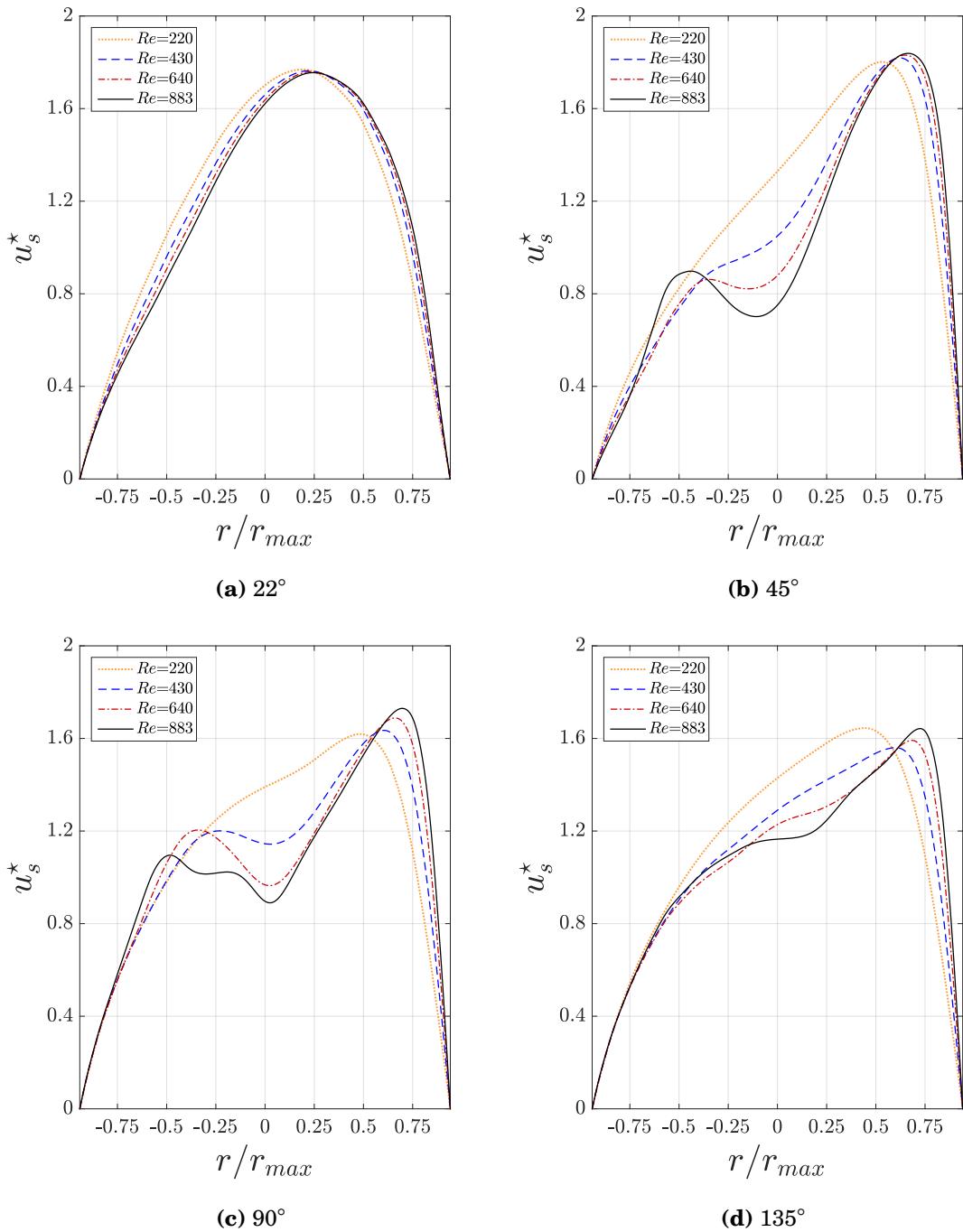


Figure 8.8 Steady flow: non-dimensional streamwise velocity, u_s^* , profile at $z/r_{max} = 0.33$ plane. $Re = \{220, 430, 640, 883\}$, $\phi = \{22^\circ, 45^\circ, 90^\circ, 135^\circ\}$.

8.6.6 Vortex Identification

In Section 8.4, the λ_2 -criterion for vortex identification by Jeong and Hussain was discussed and λ_2 results from our steady flow cases are plotted in Figure 8.9. This figure shows the second eigenvalue of $\mathbf{S}^2 + \mathbf{R}^2$ where $\lambda_2 < 0$, non-dimensionalized so that $\lambda_2^* = \lambda_2 d^2 / \bar{u}^2$. For $Re = \{220, 430\}$ across all planes of ϕ a vortex is present, corresponding to DD circulation. Hereafter, we refer to this region as the DD vortex, which is strongest at $\phi = 45^\circ$ for all Reynolds numbers. At $Re = 640$ and $\phi = 90^\circ$, a second vortex appears closer to the plane of symmetry, though with less than half the strength as the “head” of DD at this location. This region we refer to as the LT vortex. At this same toroidal location but for $Re = 883$, a third vortex appears between DD and LT vortex, which we now call the SD vortex. Of these three vortices, SD is the strongest in this plane and at least twice as large as DD and LT. At this location and Reynolds number, DD is of lower strength compared to the lower Reynolds number case of $Re = 640$. This means that the head of DD splits at $\phi = 90^\circ$ for $640 < Re < 883$, causing the two-pair vortex system present at $Re = 640$ to become a three-pair vortex system at higher Re . Furthermore, the fact that only the single pair of DD vortices exists at $\phi = 45^\circ$ and $\phi = 135^\circ$ means that SD vortex must be connected upstream and downstream to the DD vortex, which also shares the same sign of streamwise vorticity as SD. We investigate further conditions under which vortex splitting occurs under pulsatile conditions in Section 8.7.7.1.

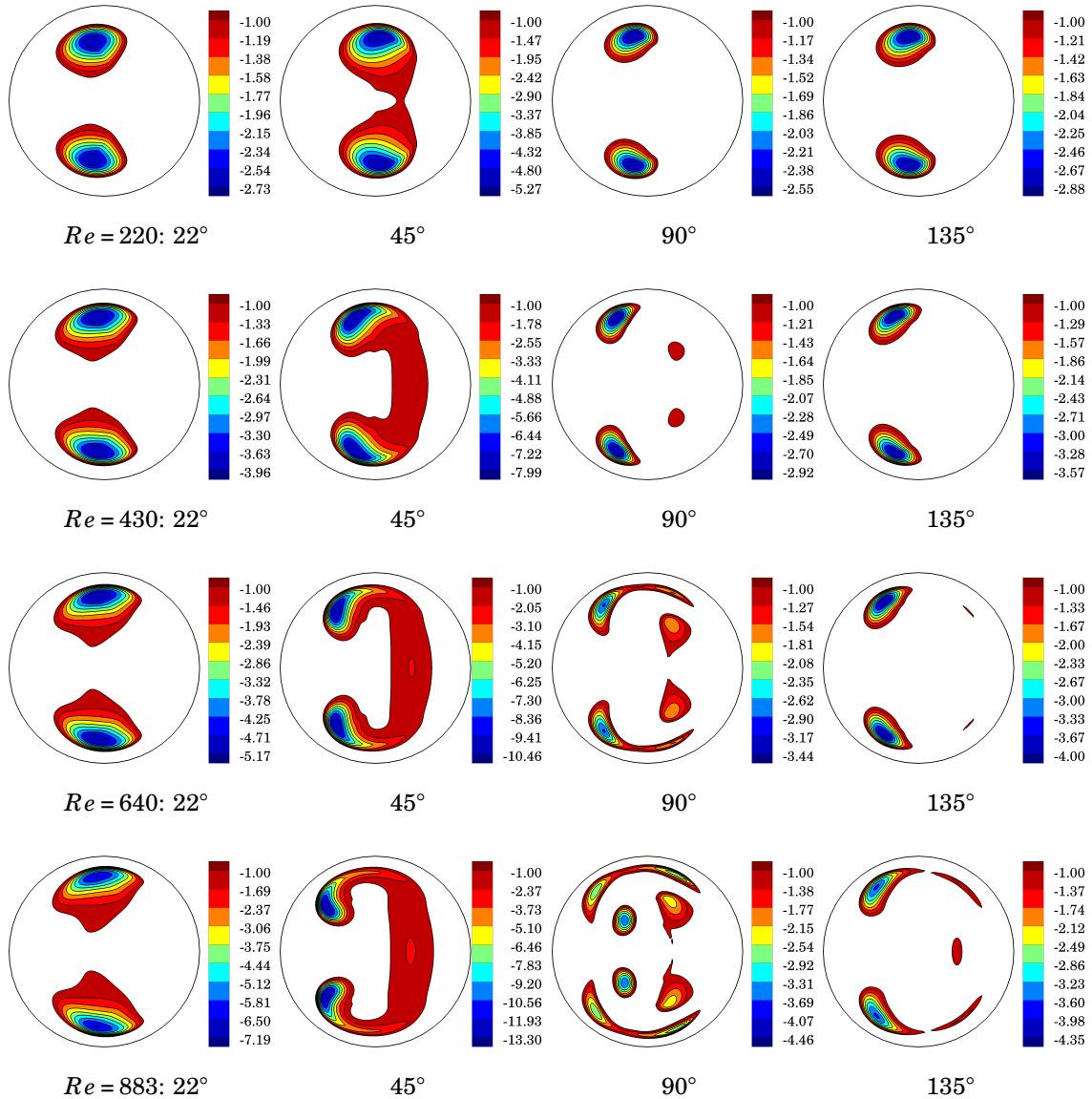


Figure 8.9 Steady flow: non-dimensional second eigenvalue of $\mathbf{S}^2 + \mathbf{R}^2$, $\lambda_2^* < 0$. $Re = \{220, 430, 640, 883\}$, $\phi = \{22^\circ, 45^\circ, 90^\circ, 135^\circ\}$.

8.6.7 Centrifugal and Pressure Gradient Force

We stated in Section 8.6.3 that secondary flow in a curved pipe occurs because centrifugal forces cause a pressure gradient along the radius of curvature that, in turn, drives the near-wall slower-moving fluid inward and the interior faster-moving

fluid outward. In this section we plot both pressure and pressure gradient. The pressure distribution within a plane of given ϕ can be seen in Figure 8.10, which shows colored contour lines of non-dimensional pressure $p^* = p/\bar{u}^2$, where p is the static pressure P divided by density ρ as previously defined in Section 2.1. Red and blue contours denote high and low pressures, respectively. Higher pressures form at the outer wall and lower pressures form at the inner wall. Also, we see a local pressure minimum associated with DD circulation. We made use of this fact to identify vortices with the λ_2 -criterion in Section 8.6.6. The balance between centrifugal force f_c pressure gradient force f_{pg} and viscous force f_v along the radius of curvature from the origin at $(x,y,z) = (0,0,0)$ is shown in Figure 8.11. The centrifugal force is

$$f_c = \frac{u_s^2}{R_{sp}} \quad (8.35)$$

where R_{sp} is the perpendicular distance from the z -axis through the origin to the solution point at which u_s is computed. The pressure gradient force along the radius of curvature is computed using the directional derivative

$$f_{pg} = -\left(s_x \frac{\partial p}{\partial x} + s_y \frac{\partial p}{\partial y} + s_z \frac{\partial p}{\partial z}\right) \quad (8.36)$$

where $\mathbf{s} = (s_x, s_y, s_z)$ is a unit vector in the direction of the radius of curvature and the viscous force is computed as

$$\begin{aligned} f_v = & s_x \nu \left(\frac{\partial^2 u}{\partial x^2} + \frac{\partial^2 u}{\partial y^2} + \frac{\partial^2 u}{\partial z^2} \right) \\ & + s_y \nu \left(\frac{\partial^2 v}{\partial x^2} + \frac{\partial^2 v}{\partial y^2} + \frac{\partial^2 v}{\partial z^2} \right) \\ & + s_z \nu \left(\frac{\partial^2 w}{\partial x^2} + \frac{\partial^2 w}{\partial y^2} + \frac{\partial^2 w}{\partial z^2} \right). \end{aligned} \quad (8.37)$$

These forces are then normalized by \bar{u}^2/d . Red/blue contours signify positive/negative forcing towards the outer/inner wall. Drawing on our description of secondary flow given in Section 8.6.3, a pressure gradient force sets up across the pipe cross-section and acts towards the center of curvature to balance the centrifugal force induced by the curvature (see Appendix C Figure C.2 for plots of centrifugal forces and Figure C.3 for plots of pressure gradient forces). Due to the effect of viscosity, the slower-moving fluid near the wall has a smaller local centrifugal force, in turn requiring a smaller pressure gradient to balance it. This difference in pressure gradients induces the secondary flow. Typically, a balance of these forces where $f_c + f_{pg} + f_v = 0$ occurs in DD regions (e.g. $Re = 220$, $\phi = 90^\circ$). A balance also occurs at $\phi = 90^\circ$ in the interior of the cross-section right at SD location for $Re = 883$, where vortex splitting has occurred at this cross-section. The SD vortex creates a local pressure gradient with respect to its core, where there is a local pressure minimum, due to its rotation. This local pressure gradient combined with the pressure gradient caused by centrifugal forcing due to positive streamwise velocity creates a force balance at the core of the SD vortex. Such a force balance analysis may help us understand the mechanism(s) by which vortex splitting occurs under pulsatile flow conditions in Section 8.7.

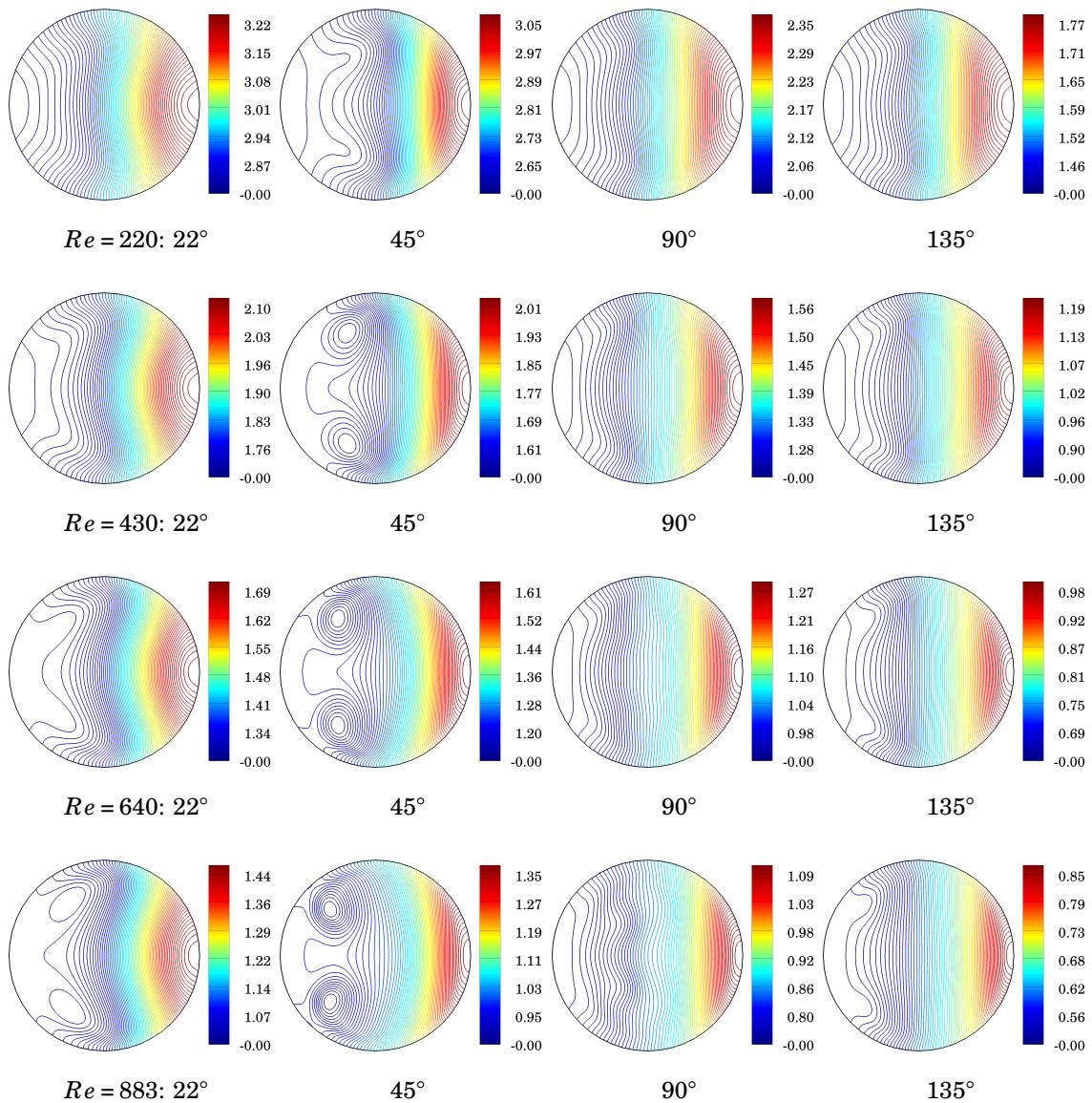


Figure 8.10 Steady flow: non-dimensional pressure p^* . $Re = \{220, 430, 640, 883\}$, $\phi = \{22^\circ, 45^\circ, 90^\circ, 135^\circ\}$.

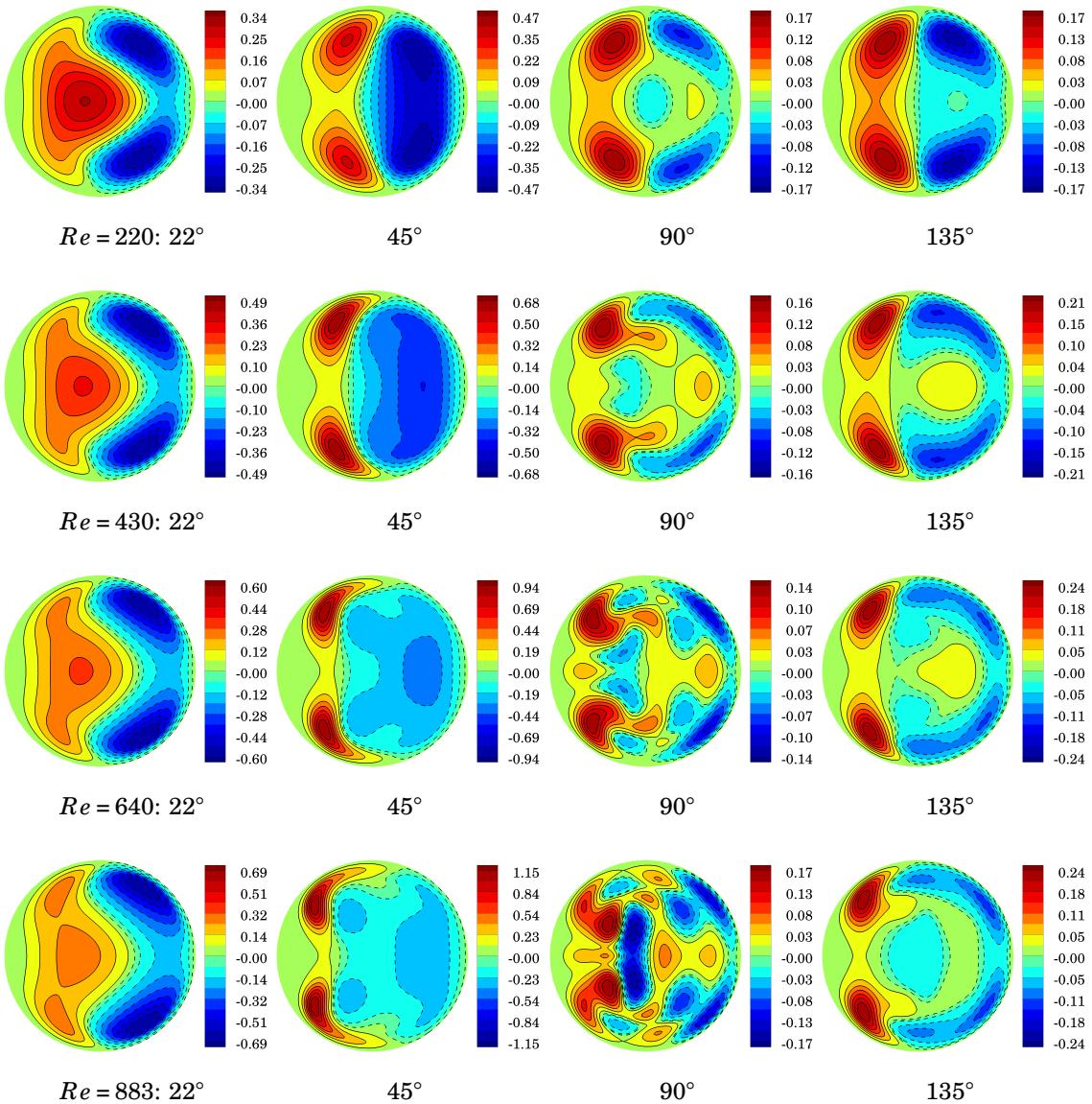


Figure 8.11 Steady flow: balance of non-dimensional centrifugal, pressure gradient and viscous forces along the radius of curvature direction $f_c^* + f_{pg}^* + f_v^*$. $Re = \{220, 430, 640, 883\}$, $\phi = \{22^\circ, 45^\circ, 90^\circ, 135^\circ\}$.

8.7 Pulsatile Flow with Fully Developed and Uniform Entrance Condition

To address the main research questions presented in Section 8.1, we performed numerical simulations of pulsatile flow through a curved pipe using two entrance conditions. First, we prescribe a fully developed pulsatile velocity profile to the inlet of the straight section of the pipe upstream to the curve entrance. This velocity profile is obtained from experimental particle image velocimetry (PIV) performed by Najjari and Plesniak [118] and is subsequently referred to as the *Womersley entrance condition* (WEC). Fully developed pulsatile flow occurs when the velocity profile does not change along the streamwise direction; the velocity can, however, be a function of both pipe radius and time. Similar to steady flow conditions shown in Section 8.6, flow within the curve is, however, developing. The integrated velocity profile produces a flow rate that matches the experiment, which uses a physiological flow rate of the human carotid artery obtained from Holdsworth et al. [126]. Under WEC, we analyze the velocity, vorticity, and pressure fields along with the vortical structures produced, highlighting both curvature and pulsatility effects. Descriptions of vortex splitting in the planar cross-section are provided with possible explanations for the underlying mechanism(s). Also, we compare our numerical velocity results near mid-deceleration to those obtained experimentally by Najjari and Plesniak [118]. Furthermore, since spatial variation of the wall shear stress is commonly believed to contribute largely to the development and progression of atherosclerosis, we calculate the wall shear stress over the entire surface of the curved pipe over the pulse period and use these instantaneous results to compute vascular metrics commonly used to assess variation in blood flow characteristics as it applies to arterial disease.

The second pulsatile entrance condition studied, motivated by the fact that

flow upstream to a curved artery may not be fully developed [116], is one which is undeveloped. We refer to this velocity condition as the *Uniform entrance condition* (UEC). Under UEC, the pulsatile flow rate is the same as that used under WEC. Under this condition, we analyze the flow field and compare results to those produced under WEC to study the effect of entrance condition on the evolution of secondary flow patterns, vortical structures and wall shear stress.

8.7.1 Numerical Pulsatile Waveform

The pulsatile flow rate waveform used in this numerical study matches that used by Najjari and Plesniak [117, 118], who experimentally measured phase averaged 2C-2D PIV data at various cross-sections of an identical curved geometry that is studied here numerically. This flow rate is shown in Figure 8.12. To perform the numerical simulations, our solver requires that a velocity field be specified at the inlet to the computational domain. This velocity field is extracted from the PIV data captured upstream of the curvature in the straight section of the pipe where the flow is fully developed pulsatile flow. The PIV data provided was obtained over a discretized set of 100 phases over the entire waveform period.

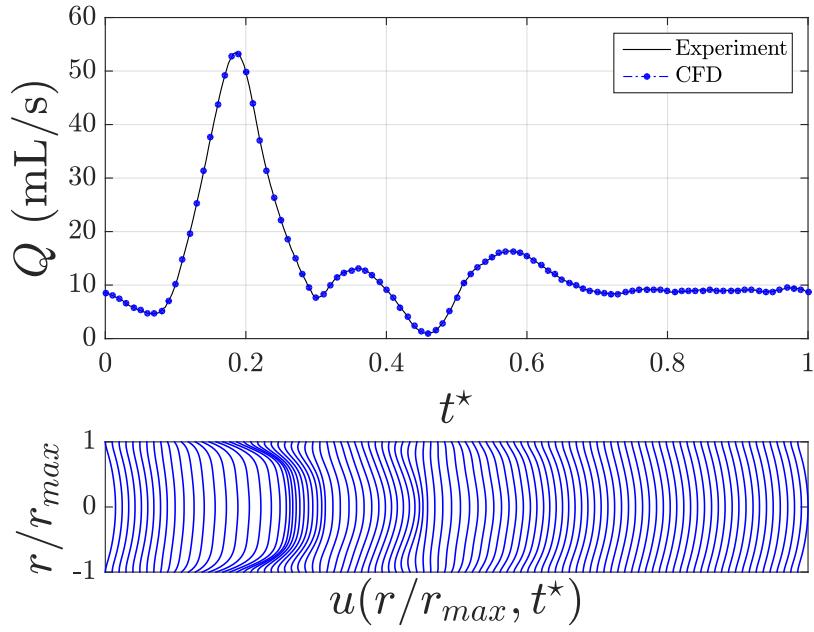


Figure 8.12 Flow rate Q as function of non-dimensional pulse period $t^* = t/T$ and the corresponding inlet velocity profile u as a function of pipe diameter d .

In order assign the velocity at an arbitrary set of spatial coordinates, we fit a 10th order polynomial to the experimental velocity profile at each phase of the waveform and interpolate between phases to prescribe a velocity field that is continuous in time. Ideally, an analytical solution of the velocity profile given as a function of both space and time should be used. However, such a solution was not available for this specific waveform at the time of performing these numerical simulations. The frequency of the waveform is $f = 0.25 \text{ s}^{-1}$ and the kinematic viscosity of the fluid matches the experiment at $\nu = 3.55\text{E-}6 \text{ m}^2/\text{s}$. Although the density ρ is not explicitly needed to run the flow solver, relevant physiological values of the wall shear stress can be obtained by setting $\rho = 1060 \text{ kg/m}^3$, which is an approximate value for the density of blood plasma. For a pipe diameter of $d = 0.0127 \text{ m}$, the Womersley number is $\alpha = 4.22$.

Parameter	Expression	Value
Q_{min}	-	1.0 mL/s
Q_{mean}	-	13.4 mL/s
Q_{max}	-	53.2 mL/s
\bar{u}_{min}	$4Q_{min}/\pi d^2$	7.8 mm/s
\bar{u}_{mean}	$4Q_{mean}/\pi d^2$	105.5 mm/s
\bar{u}_{max}	$4Q_{max}/\pi d^2$	419.6 mm/s
u_{red}	$\bar{u}_{mean} T/d$	33.2
$\bar{u}_{peak-to-mean}$	$\bar{u}_{max}/\bar{u}_{mean}$	4.0
Re_{min}	$\bar{u}_{min} d/\nu$	28
Re_{mean}	$\bar{u}_{mean} d/\nu$	377
Re_{max}	$\bar{u}_{max} d/\nu$	1501
κ_{min}	$Re_{min} \sqrt{\delta}$	10
(D_{min})	$(4\sqrt{2} \kappa_{min})$	(59)
κ_{mean}	$Re_{mean} \sqrt{\delta}$	143
(D_{mean})	$(4\sqrt{2} \kappa_{mean})$	(807)
κ_{max}	$Re_{max} \sqrt{\delta}$	567
(D_{max})	$(4\sqrt{2} \kappa_{max})$	(3209)

Table 8.1 Pulsatile waveform parameters.

These parameters are maintained constant throughout all simulations. Details of the waveform are provided in Table 8.1. The minimum, mean and maximum flow rate are 1.0 mL/s, 13.4 mL/s and 53.2 mL/s, respectively, computed from integration of the numerical velocity profile. This gives a peak-to-mean ratio of approximately 4. The corresponding Reynolds numbers are $Re = \{28, 377, 1501\}$, and the Dean numbers are $\kappa = \{10, 143, 567\}$ ($D = \{59, 807, 3209\}$). The Reynolds number is based on bulk flow velocity and pipe diameter.

The reduced velocity computed from Eq. (8.12) is $u_{red} = 33.2$, which signifies that the mean flow travels approximately 33 diameters over the pulse period. Since the length of the 180° curved section of the pipe is $7\pi d/2 \approx 11$, the distance traveled by the mean flow in one period is nearly $3x$ the length of the entire curve. High values of u_{red} such as this indicate that flow structures generated within each pulse period do not interfere with each other. This is confirmed quantitatively in a pulse period convergence study done in Section 8.7.3.

It is a well known fact that pulsatile flow through a pipe exhibits a phase lag between flow rate and pressure gradient due to the inertia of the fluid, and that this lag increases with Womersley number, with flow rate “lagging” the pressure gradient. That is to say that for a given pipe diameter and fluid viscosity, the higher the waveform frequency f and flow rate Q the more out-of-phase that flow rate and pressure gradient become. Following the description given by Zamir [127], under pulsatile flow in a straight pipe the flow rate increases gradually as the pressure gradient rises to its peak, with the peak velocity being smaller than that obtained under Poiseuille flow using a constant pressure gradient equal to the peak pressure gradient reached under the pulsatile conditions. This loss in peak flow rate increases with higher Womersley number, such that at very high frequency the fluid hardly moves. On the other hand, the phase lag between flow rate and pressure gradient decreases as the pulsatile frequency decreases, i.e. flow rate becomes more in-phase with pressure gradient if the change in pressure is slow. As the frequency approaches zero, the solution at each phase in a straight pipe approaches a steady Poiseuille flow solution. This can be called the quasi-steady Poiseuille solution or “pulsatile Poiseuille flow” [128]. In a curved pipe as $f \rightarrow 0$, the solution at each phase approaches the steady state solution for a given Dean number under a Poiseuille entrance condition, resembling the results obtained in Section 8.6.

Figure 8.13 demonstrates the phase lag between flow rate and non-dimensional

pressure gradient along the streamwise direction $-\partial p^*/\partial s^*$ under the current Womersley entrance flow condition to the curved pipe. The pressure gradient shown here is computed by our solver using the flux reconstruction methodology detailed in Part I and extracted from the straight section upstream of the curve. For comparison, in addition to the pressure gradient from fully developed pulsatile flow, we superimpose the pressure gradient from a Poiseuille flow required to produce the same flow rate. This plot shows that $-\partial p^*/\partial s^*$ is generally positive during flow rate acceleration and negative during deceleration for the Womersley number of $\alpha = 4.22$. During acceleration at $t^* = 0.14$ where the flow rate is $Q = 31.3$ mL/s, the ratio of pulsatile pressure gradient to a pressure gradient from Poiseuille flow is $(\partial p^*/\partial s^*|_W) / (\partial p^*/\partial s^*|_P) \approx 9$. Thus, for the current geometric and pulsatile flow conditions, the pressure gradient at this phase is 9x larger than the pressure gradient required under Poiseuille flow to produce the same flow rate. During deceleration at $t^* = 0.23$, where the flow rate matches that at $t^* = 0.14$, the ratio is $(\partial p^*/\partial s^*|_W) / (\partial p^*/\partial s^*|_P) \approx -6$, which is smaller in magnitude and opposite in sign to the acceleration side. Furthermore, at $t^* = 0.19$ where maximum flow rate occurs the pulsatile pressure gradient is approximately 80% of the Poiseuille value, owing to the inertia of the fluid and ultimately the decreased pressure gradient at this phase due to the lag between flow rate and pressure gradient.

Figure 8.14 shows the velocity profiles under WEC and UEC for the phases $0.14 \leq t^* \leq 0.29$, as well as the bulk (phase) velocity \bar{u} and velocity profile from a Poiseuille solution computed from the same bulk flow value. For a given phase, the parabolic Poiseuille profile corresponds to the Poiseuille pressure gradient shown in Figure 8.13. At peak flow rate, which occurs near $t^* = 0.19$ where $Re \approx 1500$ and the ratio of bulk velocity to waveform mean velocity is $\bar{u}/\bar{u}_{mean} \approx 4$, the maximum velocity achieved at the centerline clearly does not reach the maximum of the Poiseuille flow profile due to fluid inertia. However, there is a point during deceleration at which

the maximum velocity at the $r/r_{max} = 0$ centerline is approximately equal to the Poiseuille flow solution. This occurs at $t^* = 0.24$. At this phase where $Re \approx 745$, the bulk velocity to waveform mean velocity ratio is $\bar{u}/\bar{u}_{mean} \approx 2$ and the maximum velocity to mean velocity ratio is $u_{max}/\bar{u}_{mean} \approx 4$. This means that $u_{max}/\bar{u} \approx 2$, which matches the result from a Poiseuille solution. Throughout the remainder of the deceleration phase, the maximum velocity exceeds that of the Poiseuille solution. These plots demonstrate the effect of inertia inherent in the pulsatile waveform at $\alpha = 4.22$ compared to a Poiseuille solution, for which the pressure gradient and flow rate are in-phase. Note that a small region of reverse flow in the velocity profile near the pipe wall begins at $t^* = 0.22$, and that this region grows with decelerating flow. This reverse flow in the entrance condition can have an important effect on wall shear stress during deceleration, especially along the inner wall.

In later sections, we provide a matrix of cross-sectional results in the curve for non-dimensional secondary velocity, streamwise velocity, vorticity, pressure, λ_2 -criterion and wall shear stress. Comprehensive results of all variables from mid-acceleration through deceleration where $0.15 < t^* < 0.29$ and $\phi = \{22^\circ, 45^\circ, 90^\circ, 135^\circ\}$ are provided in Appendices D and E for Womersley and uniform entrance conditions, respectively. Of particular importance are the results from $0.22 < t^* < 0.26$, where the flow conditions are conducive to a vortex rich environment. Pulsatile velocities are non-dimensionalized by the bulk velocity averaged over the entire waveform period \bar{u}_{mean} so that $u^* = u/\bar{u}_{mean}$. This constant mean waveform velocity is chosen instead of the phase bulk velocity \bar{u} because of the large variation that can occur between peak profile velocity and bulk velocity. For example, if we non-dimensionalize the pulsatile velocity field by the bulk velocity at each phase, the non-dimensional result will increase as the bulk velocity, or flow rate, approaches zero. This will produce non-physical characterization of the pulsatile velocity field through time, and since we want to look at how the physical quantities change from phase to phase, we use

\bar{u}_{mean} as the velocity scale. Similarly, pressure, vorticity, and the λ_2 -criterion are non-dimensionalized such that $p^* = P/\rho\bar{u}_{mean}^2$, $\omega^* = \omega d/\bar{u}_{mean}$, $\lambda_2^* = \lambda_2 d^2/\bar{u}_{mean}^2$ and $\tau_w^* = \tau_w d/\mu\bar{u}_{mean}$.

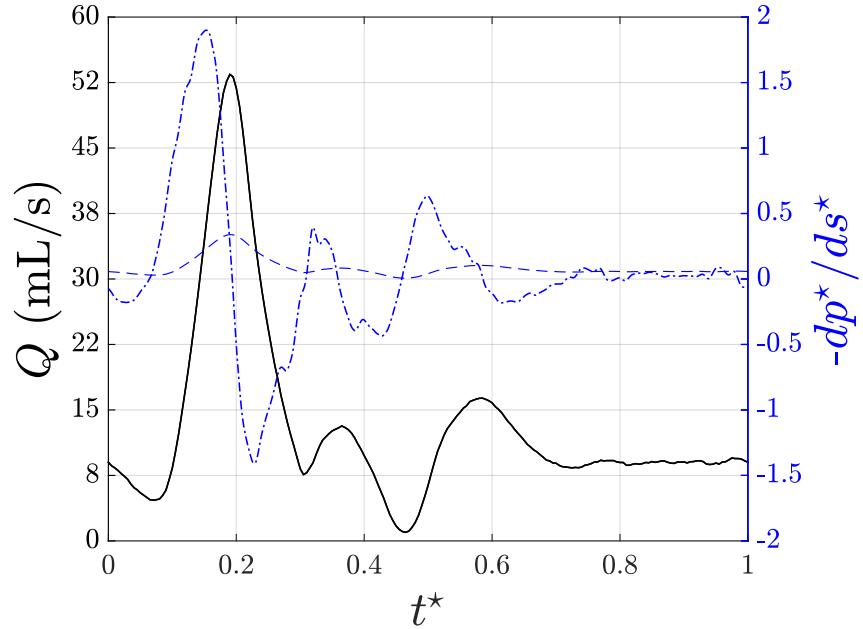


Figure 8.13 Flow rate Q (—) “lagging” the straight pipe non-dimensional pressure gradient $-\partial p^*/\partial s^*$ (---) for Womersley number $\alpha = 4.22$. The pressure gradient from a pulsatile Poiseuille solution (—) required to produce the same flow rate is shown for comparison.

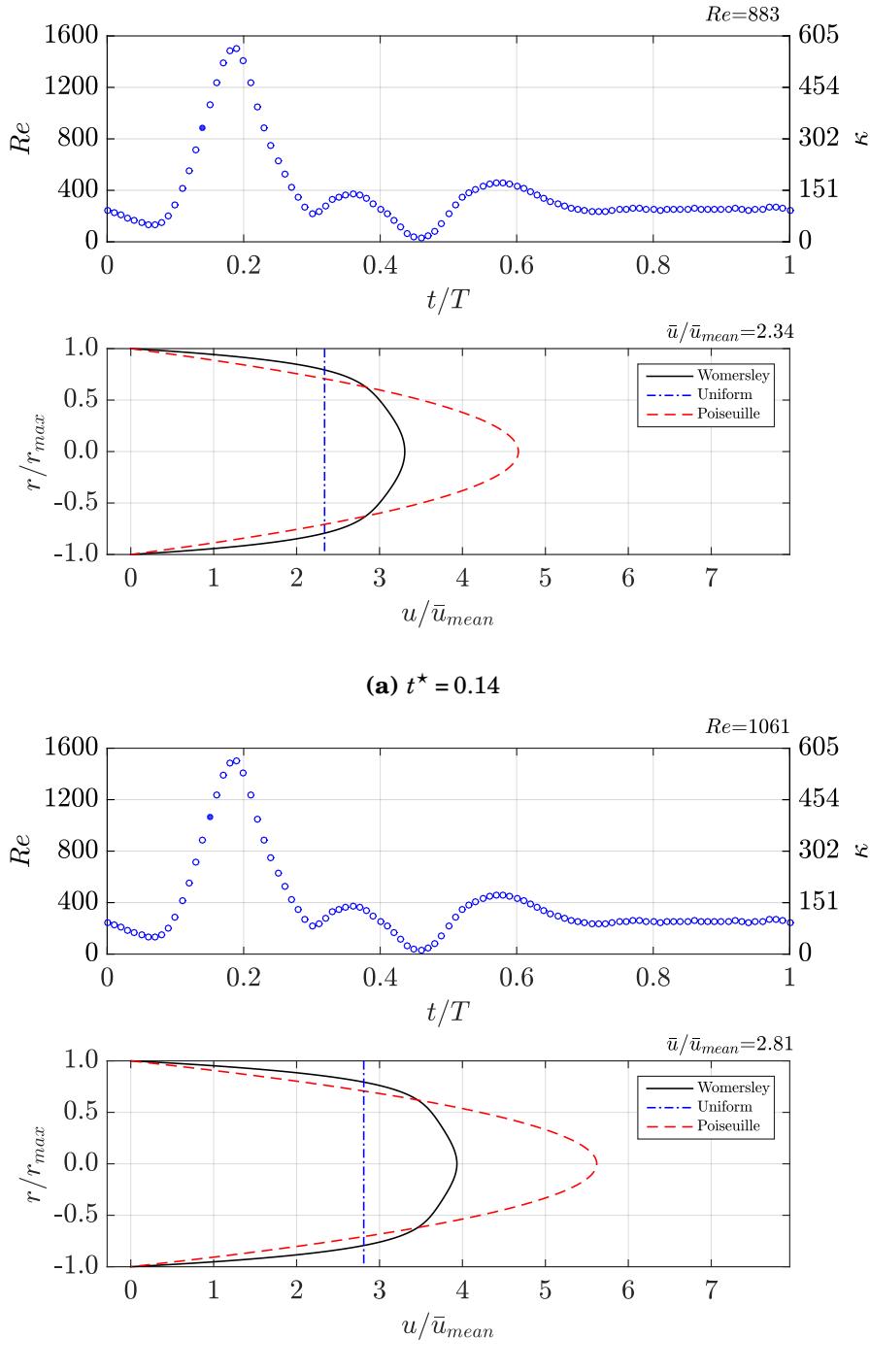
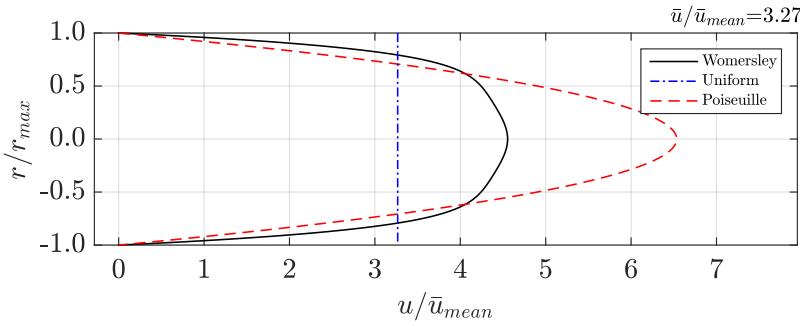
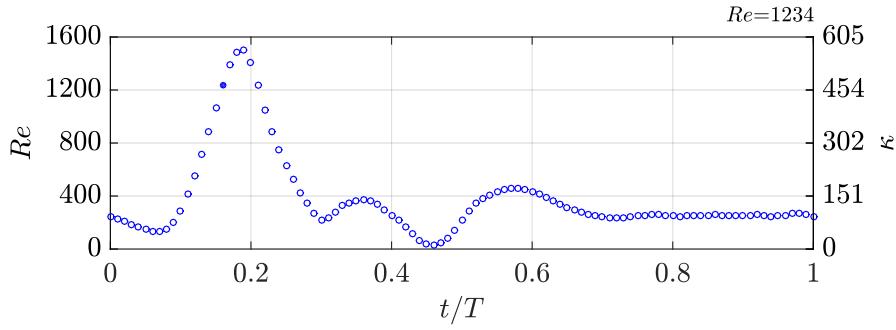
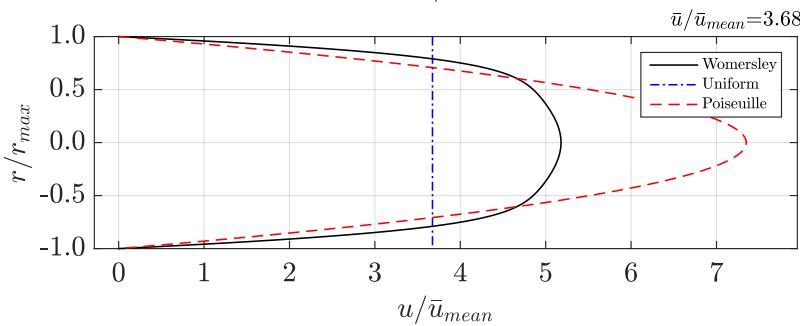
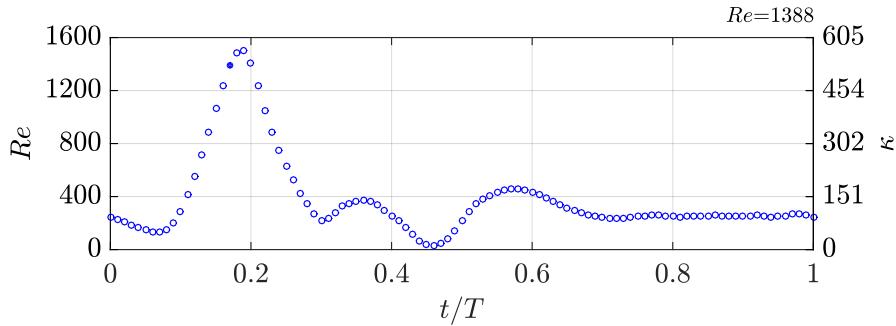


Figure 8.14 Reynolds number Re and Dean number κ as a function of non-dimensional pulse period t^* and non-dimensional inlet velocity profile u/\bar{u}_{mean} for Womersley entrance condition (—). The bulk velocity \bar{u} corresponds to the uniform entrance condition (---), and the parabolic profile corresponds to the Poiseuille solution (--) obtained using the same bulk flow. The Womersley number is $\alpha = 4.22$.

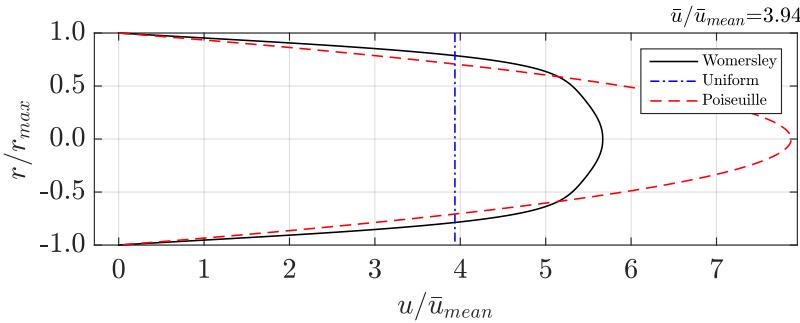
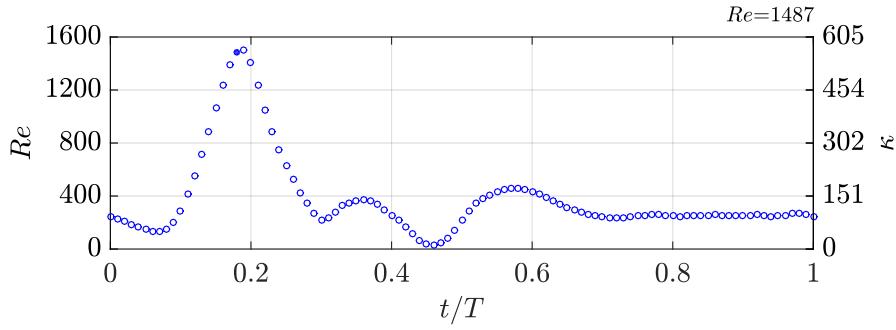


(c) $t^* = 0.16$

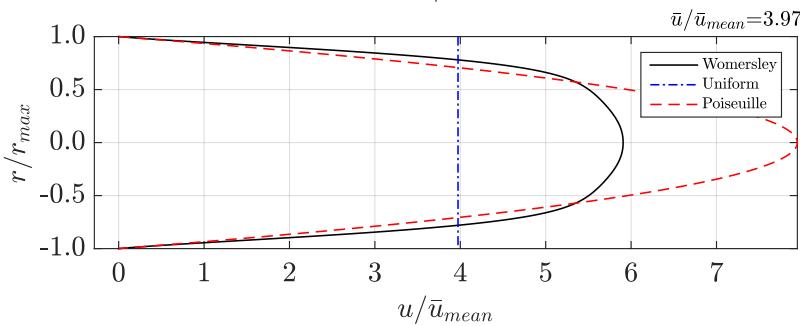
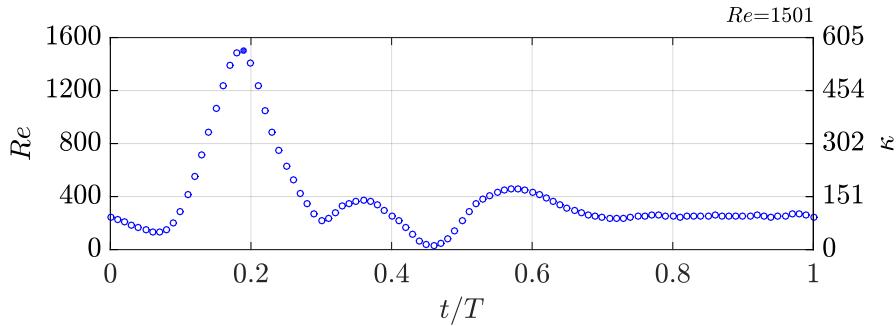


(d) $t^* = 0.17$

Figure 8.14 Reynolds number Re and Dean number κ as a function of non-dimensional pulse period t^* and non-dimensional inlet velocity profile u/\bar{u}_{mean} for Womersley entrance condition (—). The bulk velocity \bar{u} corresponds to the uniform entrance condition (---), and the parabolic profile corresponds to the Poiseuille solution (--) obtained using the same bulk flow. The Womersley number is $\alpha = 4.22$. (continued)

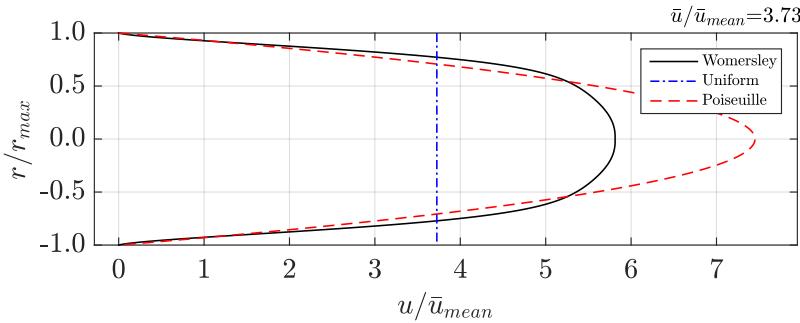
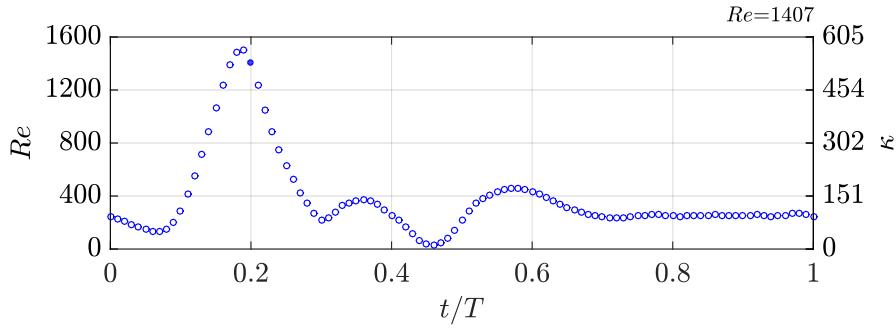


(e) $t^* = 0.18$

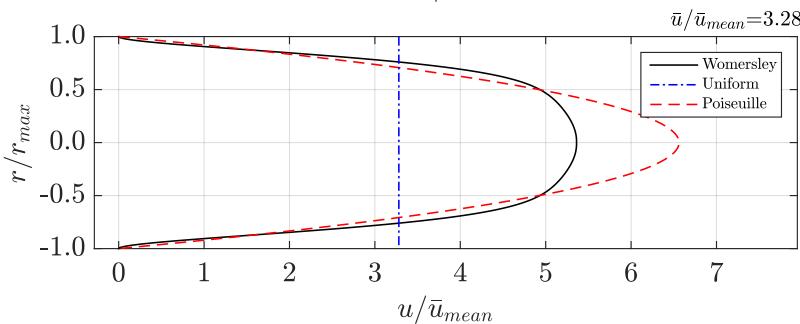
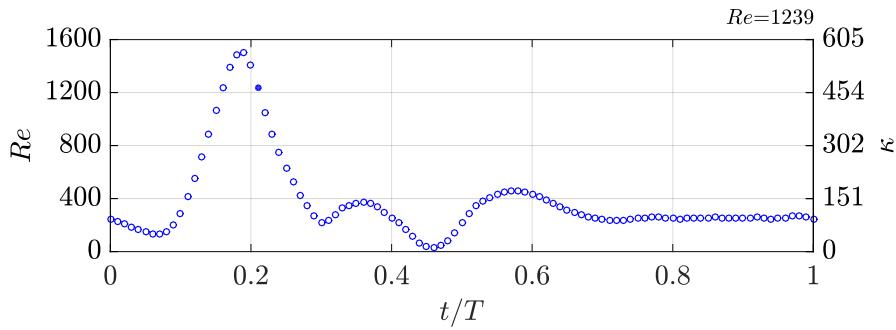


(f) $t^* = 0.19$

Figure 8.14 Reynolds number Re and Dean number κ as a function of non-dimensional pulse period t^* and non-dimensional inlet velocity profile u/\bar{u}_{mean} for Womersley entrance condition (—). The bulk velocity \bar{u} corresponds to the uniform entrance condition (---), and the parabolic profile corresponds to the Poiseuille solution (--) obtained using the same bulk flow. The Womersley number is $\alpha = 4.22$. (continued)

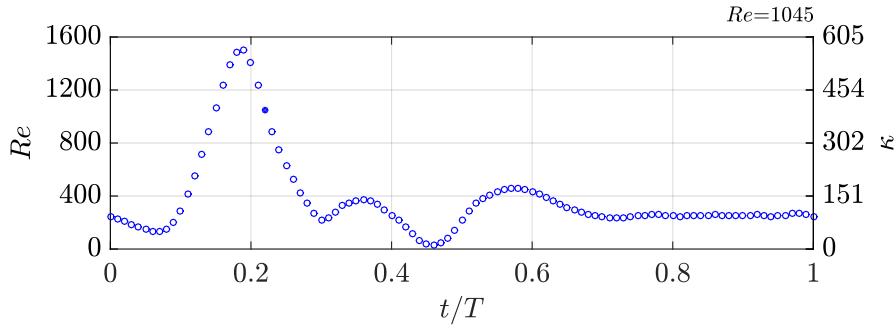


(g) $t^* = 0.20$

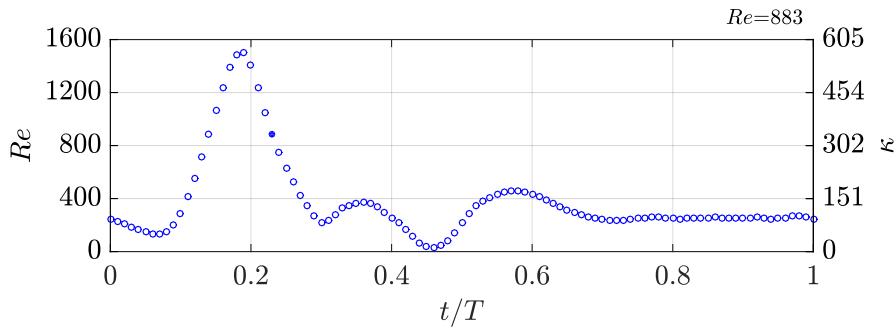


(h) $t^* = 0.21$

Figure 8.14 Reynolds number Re and Dean number κ as a function of non-dimensional pulse period t^* and non-dimensional inlet velocity profile u/\bar{u}_{mean} for Womersley entrance condition (—). The bulk velocity \bar{u} corresponds to the uniform entrance condition (---), and the parabolic profile corresponds to the Poiseuille solution (--) obtained using the same bulk flow. The Womersley number is $\alpha = 4.22$. (continued)

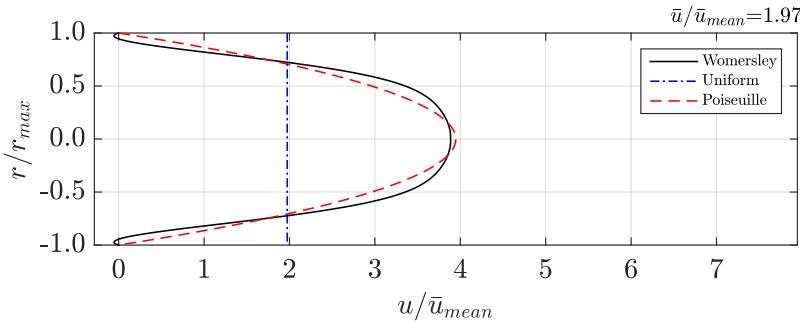
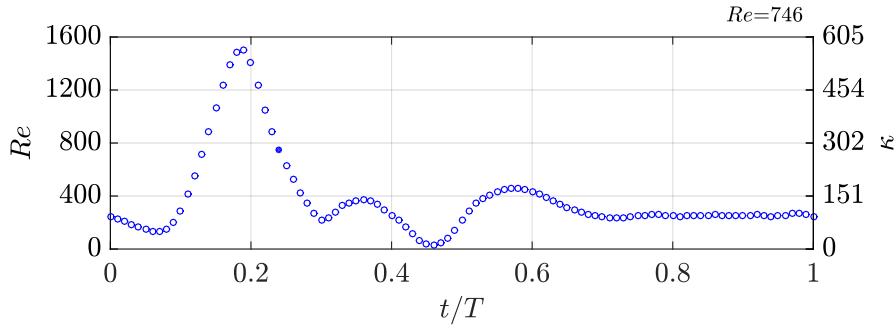


(i) $t^* = 0.22$

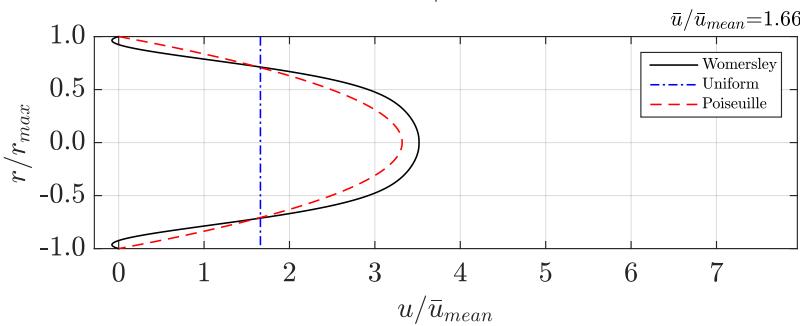
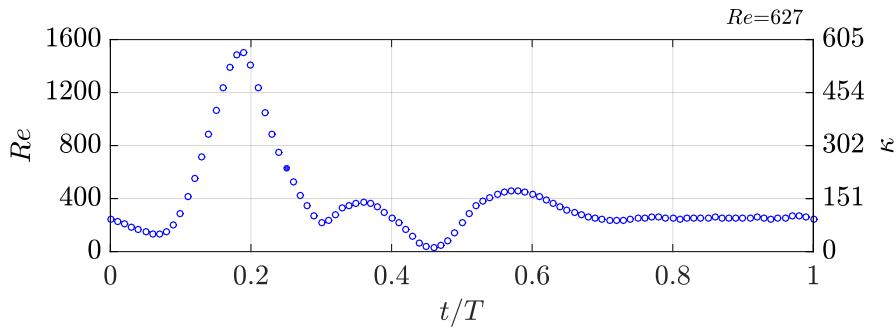


(j) $t^* = 0.23$

Figure 8.14 Reynolds number Re and Dean number κ as a function of non-dimensional pulse period t^* and non-dimensional inlet velocity profile u/\bar{u}_{mean} for Womersley entrance condition (—). The bulk velocity \bar{u} corresponds to the uniform entrance condition (---), and the parabolic profile corresponds to the Poiseuille solution (--) obtained using the same bulk flow. The Womersley number is $\alpha = 4.22$. (continued)

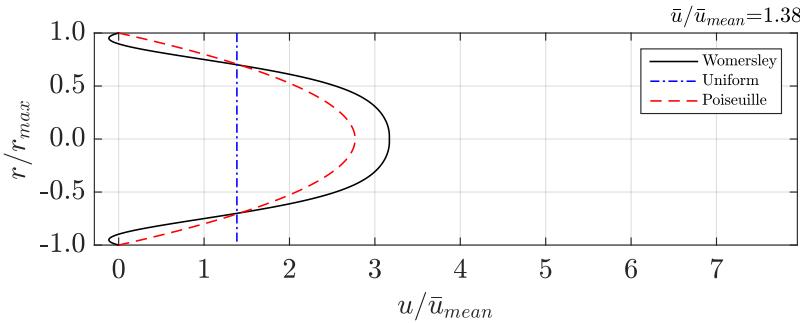
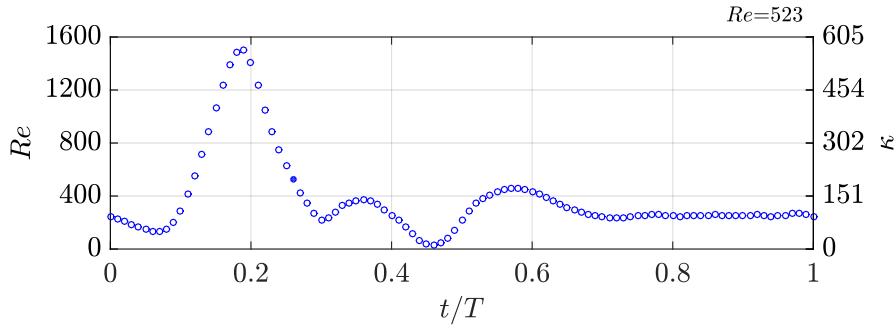


(k) $t^* = 0.24$

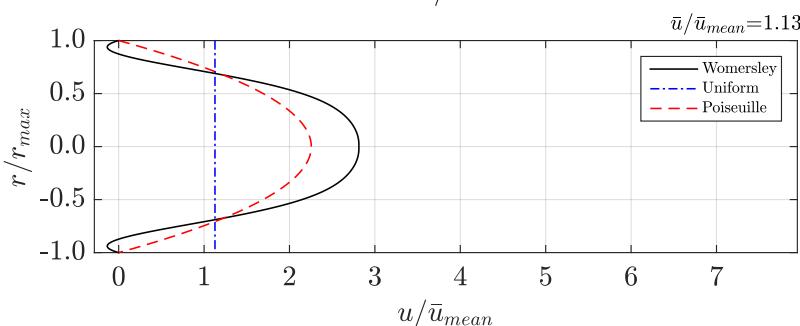
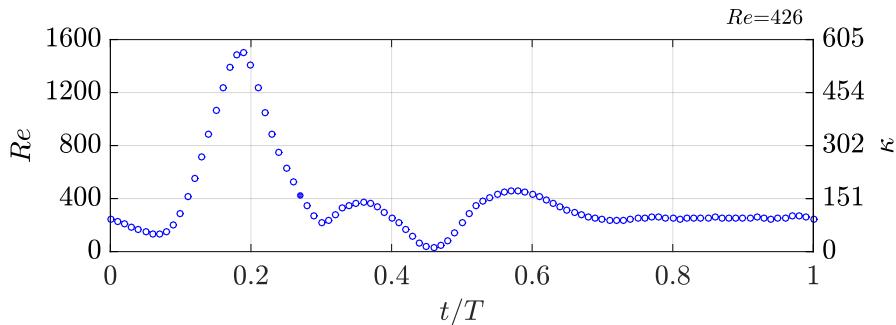


(l) $t^* = 0.25$

Figure 8.14 Reynolds number Re and Dean number κ as a function of non-dimensional pulse period t^* and non-dimensional inlet velocity profile u/\bar{u}_{mean} for Womersley entrance condition (—). The bulk velocity \bar{u} corresponds to the uniform entrance condition (---), and the parabolic profile corresponds to the Poiseuille solution (--) obtained using the same bulk flow. The Womersley number is $\alpha = 4.22$. (continued)

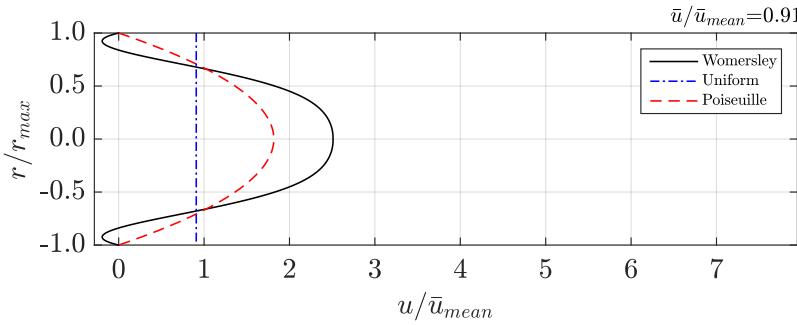
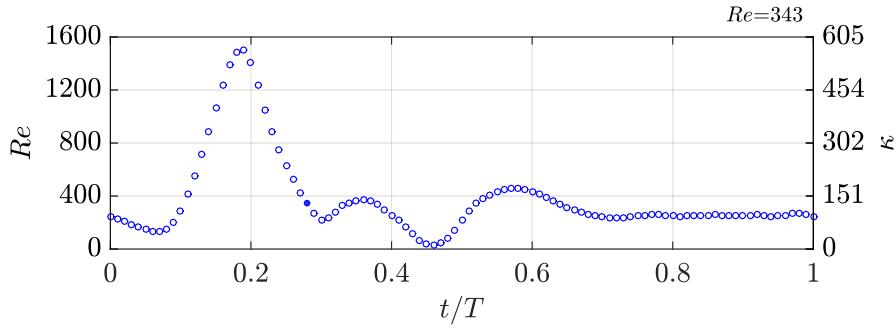


(m) $t^* = 0.26$

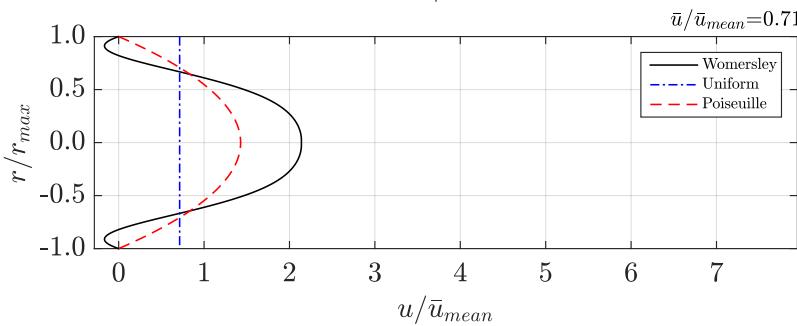
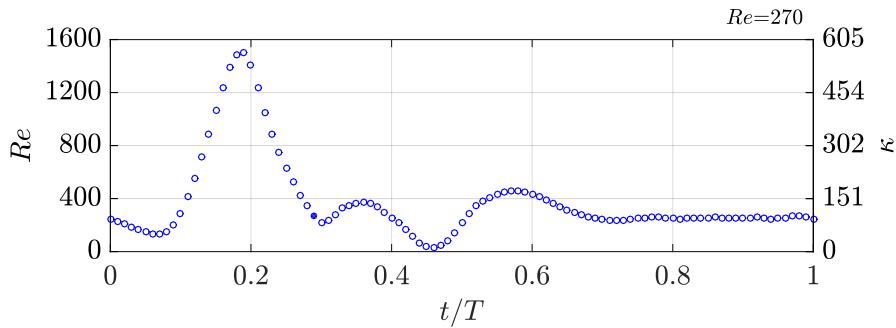


(n) $t^* = 0.27$

Figure 8.14 Reynolds number Re and Dean number κ as a function of non-dimensional pulse period t^* and non-dimensional inlet velocity profile u/\bar{u}_{mean} for Womersley entrance condition (—). The bulk velocity \bar{u} corresponds to the uniform entrance condition (---), and the parabolic profile corresponds to the Poiseuille solution (--) obtained using the same bulk flow. The Womersley number is $\alpha = 4.22$. (continued)



(o) $t^* = 0.28$



(p) $t^* = 0.29$

Figure 8.14 Reynolds number Re and Dean number κ as a function of non-dimensional pulse period t^* and non-dimensional inlet velocity profile u/\bar{u}_{mean} for Womersley entrance condition (—). The bulk velocity \bar{u} corresponds to the uniform entrance condition (---), and the parabolic profile corresponds to the Poiseuille solution (--) obtained using the same bulk flow. The Womersley number is $\alpha = 4.22$. (continued)

8.7.2 Initial and Boundary Conditions

8.7.2.1 Womersley Entrance Condition

Under WEC, the initial velocity field is set equal to the streamwise velocities obtained experimentally from PIV data [118] in the straight section upstream of the curve at the beginning of the waveform where $t^* = 0$. This streamwise velocity profile is prescribed numerically at $t^* = 0$ throughout the entire geometry, where radial and azimuthal components of velocity are all zero. Similar to the Poiseuille entry flow cases in Section 8.6, at the inlet boundary of the numerical domain $\partial\Omega^{inlet}$ the pressure is extrapolated from the interior solution and the velocity is specified. We use the discretely sampled PIV data (see Section 8.7.1) to prescribe the inlet velocity at each time step, which is aligned with the streamwise direction. This inlet condition is written below in Eq. (8.38) as

$$\begin{aligned} p_g^{inlet}(x, y, z, t) &= p_i^{inlet}(x, y, z, t) \\ u_g^{inlet}(x, y, z, t) &= u_{PIV}(x, y, z, t) \\ v_g^{inlet}(x, y, z, t) &= 0 \\ w_g^{inlet}(x, y, z, t) &= 0. \end{aligned} \tag{8.38}$$

8.7.2.2 Uniform Entrance Condition

Under UEC, the initial velocity field is given a uniform value such that all radial and azimuthal components of velocity are zero and all streamwise components of velocity are set equal to the bulk velocity of the pulsatile waveform at $t^* = 0$. The inlet boundary condition for UEC in Eq. (8.39) is applied in the same manner as WEC, except that the u velocity is set equal to the bulk velocity at each phase of the waveform, which is computed from the pulsatile flow rate $Q(t)$. This inlet condition

is prescribed slightly upstream of the entrance to the curve at $x = -d$. Therefore, there is a small length of straight pipe over which the flow develops before entering the pipe curvature at $\phi = 0^\circ$. The inlet condition can be written as

$$\begin{aligned} p_g^{inlet}(x, y, z, t) &= p_i^{inlet}(x, y, z, t) \\ u_g^{inlet}(x, y, z, t) &= \frac{4Q(t)}{\pi d^2} \\ v_g^{inlet}(x, y, z, t) &= 0 \\ w_g^{inlet}(x, y, z, t) &= 0. \end{aligned} \tag{8.39}$$

For both Womersley and uniform entrance conditions, the initial pressure field is given a uniform value of zero. At the outlet boundary of the domain $\partial\Omega^{outlet}$, which is far downstream of the pipe curve, the pressure is given a uniform value of zero for all time and the velocity field at the ghost state is extrapolated from the interior solution such that

$$\begin{aligned} p_g^{outlet} &= 0 \\ u_g^{outlet} &= u_i^{outlet} \\ v_g^{outlet} &= v_i^{outlet} \\ w_g^{outlet} &= w_i^{outlet}. \end{aligned} \tag{8.40}$$

Finally, we apply the no-slip boundary condition at the pipe wall such that

$$u = v = w = 0 \quad \text{at} \quad r = r_{max}. \tag{8.41}$$

8.7.3 Numerical Convergence

We perform an h -convergence test for various meshes consisting of $\Omega^1 = 8,736$, $\Omega^2 = 69,888$ and $\Omega^3 = 559,104$ elements. We evaluate the L^2 -norm of the non-

dimensional wall shear stress τ_w^* for the entire mesh at $t^* = 0.19$ where peak flow rate occurs. At this phase, we find that the difference in $\|\tau_w^*\|_2$ between Ω^2 and Ω^3 is 0.77%. In addition to the grid convergence test, we perform a p -convergence test on Ω^2 for the polynomials $p = 2$, $p = 3$ and $p = 4$. The values of $\|\tau_w^*\|_2$ computed at each time step during acceleration and deceleration for the various polynomial orders are plotted in Figure 8.15 and demonstrate the increase and decrease in overall wall shear stress magnitude during acceleration and deceleration, respectively. Visually, we can see that the lines for $p = 3$ and $p = 4$ are essentially coincident. Quantitatively, this amounts to a mean error between $p = 3$ and $p = 4$ of 0.14%. To further assess p -convergence, we take the velocity field at $t^* = 0.25$ on Ω^2 and compute the non-dimensional velocity magnitude at each node in the mesh and subtract the results from $p = 3$ and $p = 4$. From this data set, we calculate the mean of the velocity magnitude error $\epsilon = |\mathbf{u}_{p3}^*| - |\mathbf{u}_{p4}^*|$ as

$$\epsilon_{mean} = \frac{1}{DOF} \sum_{k=1}^{DOF} \epsilon_k \quad (8.42)$$

to be 2.19E-06, and following Eq. (5.2) the L^1 -norm of the error is $\|\epsilon\|_1 = 2.20E-3$ and the L^2 -norm is $\|\epsilon\|_2 = 3.93E-3$. The formulation given here for $\|\epsilon\|_2$ is equivalent to a root mean square error. Since the non-dimensional bulk velocity at this phase is $\bar{u}^* = 1.66$, we can say that the root mean square of the velocity magnitude error between $p = 3$ and $p = 4$ is approximately 0.24% of the bulk velocity. Therefore, we can conclude that using mesh Ω^2 and order $p = 4$ provides sufficient spatial resolution to resolve the flow physics and that the numerical solution is converged. All pulsatile flow simulations have been generated using an artificial compressibility parameter set to $\beta_o = 2.5$. We use a constant physical time step $\Delta t = 2.5E-5$, producing a maximum *CFL* of 0.04 for a $p = 4$ FR scheme. The explicit RK3 scheme detailed in Section 4.1 was used in all simulations, with a pseudo time step of $\Delta\tau = 5E-6$ and

convergence criterion of $1E - 4$.

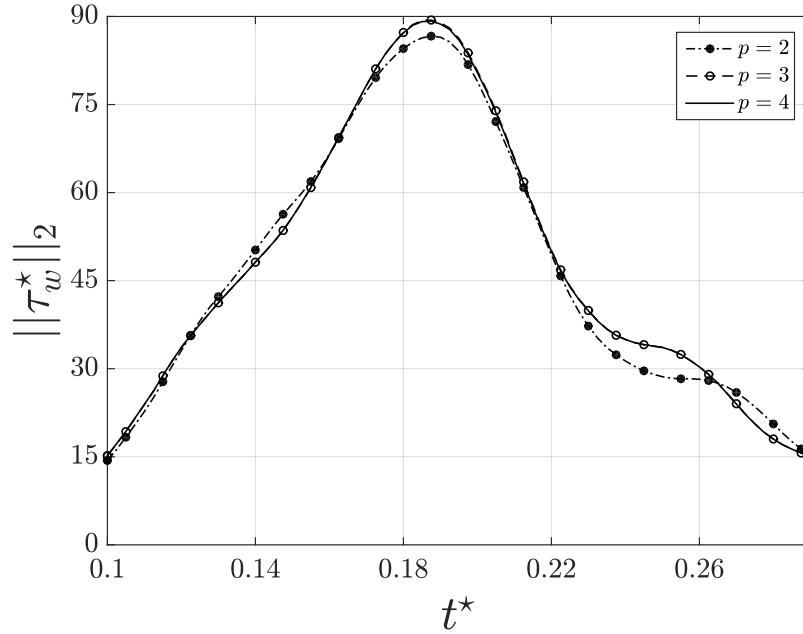


Figure 8.15 Womersley entrance condition: p -convergence of $\|\tau_w^*\|_2$ on Ω^2 during pulse acceleration and deceleration.

8.7.4 Secondary Flow

Cross-sections of non-dimensional secondary velocity magnitude $|\mathbf{u}_{\theta r}^*|$ are shown in Figures 8.22 and 8.23. During acceleration and deceleration under WEC, similar to what was shown under the PEC where the flow is fully developed entering the curve but developing within the curve, we see increased velocities along the upper and lower walls where the velocity vectors are pointing inward. In the interior, the secondary motion of the fluid moves outward (see Appendix D Figure D.6 for velocity vector maps of each cross-section). Generally, this pattern exists during acceleration and deceleration throughout the various cross-sections, although different secondary flow patterns emerge along the streamwise direction due to varying degrees of centrifugal forcing and flow reversal. Comparing results between WEC and UEC at

$\phi = 45^\circ$ and $\phi = 90^\circ$, we see more secondary motion in the interior (i.e. away from the wall and near the pipe axis) under WEC. This means that UEC inhibits secondary motion in the interior, which may ultimately affect the growth of any interior vortices. We will revisit this idea in Section 8.7.7 within the context of vortex identification.

Under WEC, one obvious and distinct feature emerges at $\phi = 45^\circ$ due to strong secondary flow action. To examine this feature more closely, see Figure 8.16 for an image of the secondary velocity vectors $\mathbf{u}_{\theta r}^*$ and streamlines colored by magnitude. The corresponding images from UEC and PEC are shown in Figures 8.17-8.18 for comparison. In Figure 8.16 at $t^* = 0.24$, the secondary motion of the fluid becomes much stronger in the interior of the pipe near the plane of symmetry than along the walls. This increased secondary flow is due to large velocities from the upper and lower half of the pipe competing at the plane of symmetry, causing an outward jet-like motion to appear.

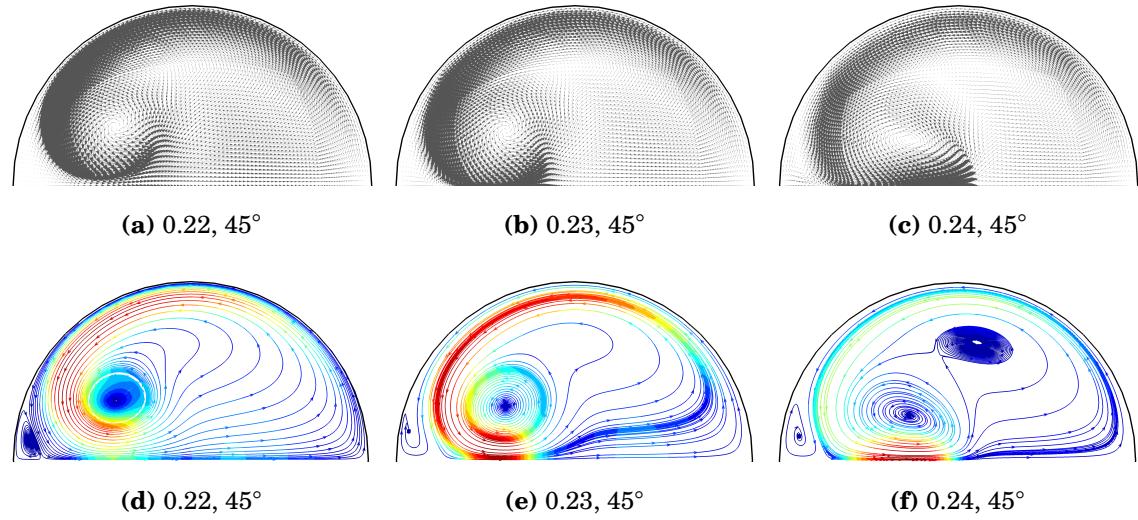


Figure 8.16 Womersley entrance condition: (a)-(c) non-dimensional secondary velocity vectors $\mathbf{u}_{\theta r}^*$ and (d)-(f) streamlines colored by magnitude at $\phi = 45^\circ$ and $0.22 \leq t^* \leq 0.24$.

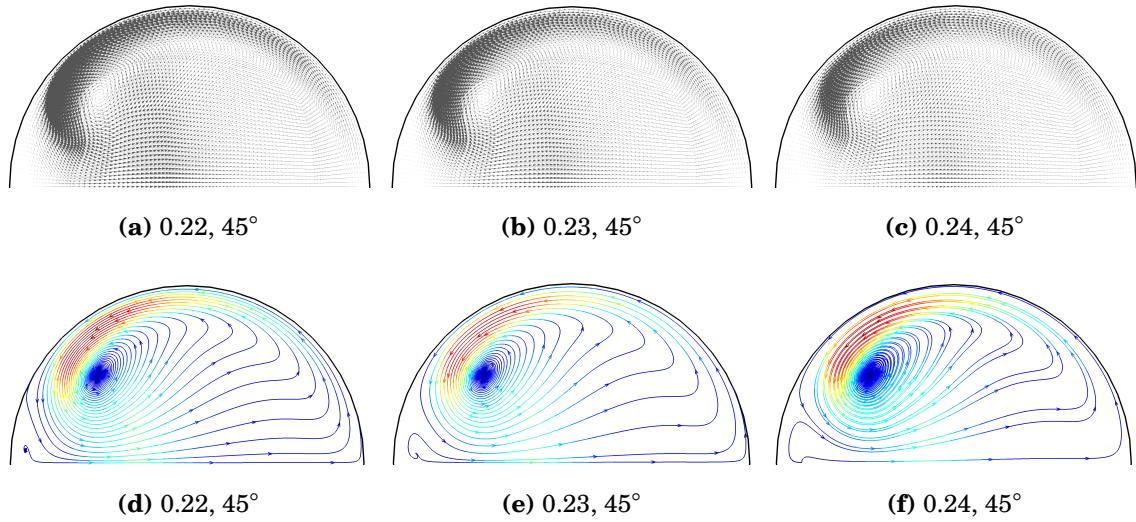


Figure 8.17 Uniform entrance condition: (a)-(c) non-dimensional secondary velocity vectors $\mathbf{u}_{\theta r}^*$ and (d)-(f) streamlines colored by magnitude at $\phi = 45^\circ$ and $0.22 \leq t^* \leq 0.24$.

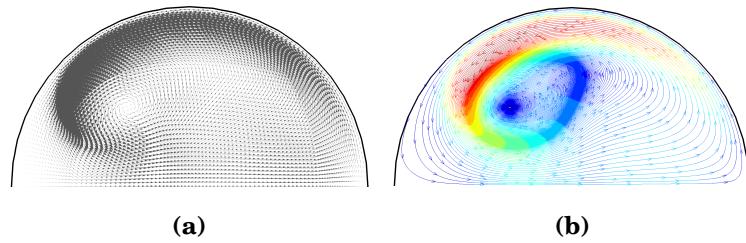


Figure 8.18 Poiseuille entrance condition: (a) non-dimensional secondary velocity vectors $\mathbf{u}_{\theta r}^*$ and (b) streamlines colored by magnitude at $\phi = 45^\circ$ and $Re = 883$. The flow rate at this steady Re corresponds to flow rate at $t^* = 0.23$ under pulsatile conditions.

At this location, two recirculation zones are evident at $t^* = 0.22$ and $t^* = 0.23$, one away from the wall and one near the inner wall, rotating in the opposite direction. At $t^* = 0.24$, a third recirculation zone emerges closer to the upper wall. For UEC, we see one large recirculation zone and a very small recirculation zone near the inner wall. For PEC at $Re = 883$, which corresponds to the bulk flow rate under pulsatile conditions at $t^* = 0.23$, there exists just one secondary recirculation zone that corresponds to the well known Deformed-Dean flow.

Another feature of the flow under WEC at $\phi = 45^\circ$ can be seen at $t^* = 0.24$, where the velocity vectors of the fluid near the pipe origin at $r = 0$ are mainly aligned with the streamwise direction. Thus, the secondary motion is relatively small there, causing the outwardly moving interior cross-flow to deflect away from the plane of symmetry towards the upper and lower walls of the pipe. The small secondary recirculation region near the inner wall, rotating opposite to the larger scale motion in the interior, can be attributed to secondary motion resulting from flow reversal. This feature was also reported by van Wyk et al. [115], who used a similar waveform for studying the non-Newtonian effect on pulsatile blood-analog flows. Our description of this feature above $z = 0$ is that positive primary flow creates counter-clockwise secondary flow and negative primary flow (i.e. flow reversal) creates localized clockwise secondary flow at the inner wall. Throughout the remainder of deceleration, the larger interior recirculation drifts outward and the small inner wall recirculation disappears as deceleration rate decreases and flow reversal diminishes. This feature does occur under UEC (see Figure 8.17) but is not as pronounced due to the combined effect of weaker secondary flow and weak reverse flow at the inner wall. Because this feature appears in the reverse flow region during deceleration, it is considered a pulsatility effect. This phenomenon is important under a fully developed entrance condition because it may provide an explanation for locally increased wall shear stresses, which will be discussed in Section 8.8.3.

Figures 8.19-8.21 show the secondary velocity vectors and streamlines at $\phi = 90^\circ$. At $t^* = 0.23$, four secondary recirculation zones appear under WEC, two under UEC, and three under PEC. Under WEC, quite a bit of secondary motion exists when compared to the results produced from UEC - the secondary pattern from UEC only has two recirculation zones because the secondary flow isn't strong enough. The PEC has one less recirculation zone than WEC because it does not produce any near wall feature as flow reversal does not exist under PEC at Dean number $\kappa = 334$ ($D = 1888$).

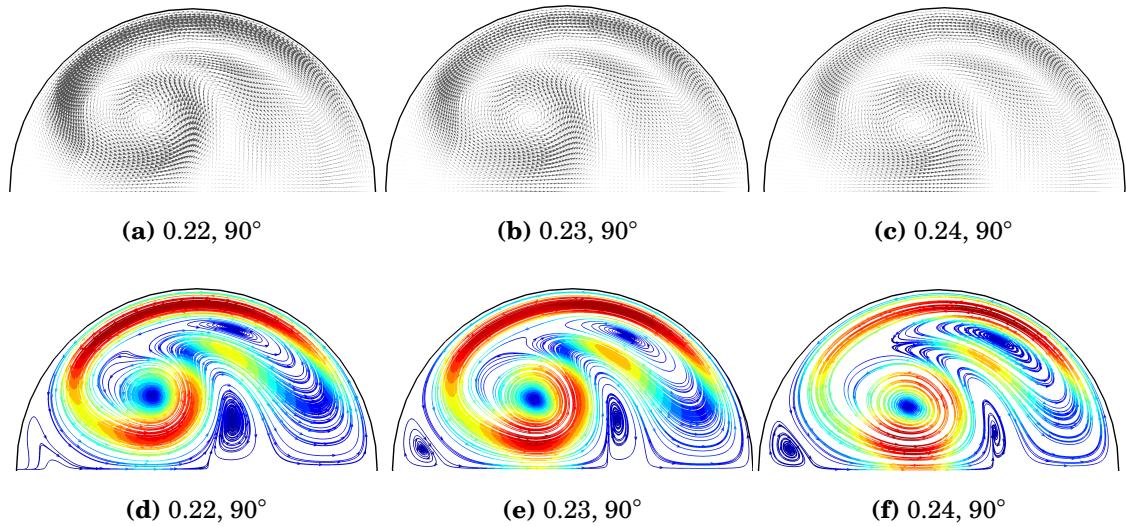


Figure 8.19 Womersley entrance condition: (a)-(c) non-dimensional secondary velocity vectors $\mathbf{u}_{\theta r}^*$ and (d)-(f) streamlines colored by magnitude at $\phi = 90^\circ$ and $0.22 \leq t^* \leq 0.24$.

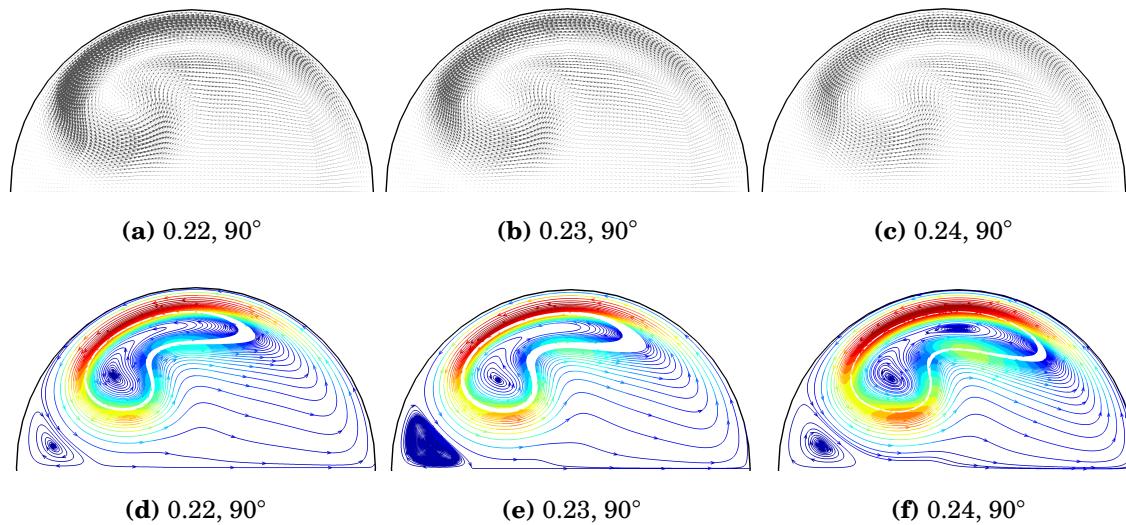


Figure 8.20 Uniform entrance condition: (a)-(c) non-dimensional secondary velocity vectors $\mathbf{u}_{\theta r}^*$ and (d)-(f) streamlines colored by magnitude at $\phi = 90^\circ$ and $0.22 \leq t^* \leq 0.24$.

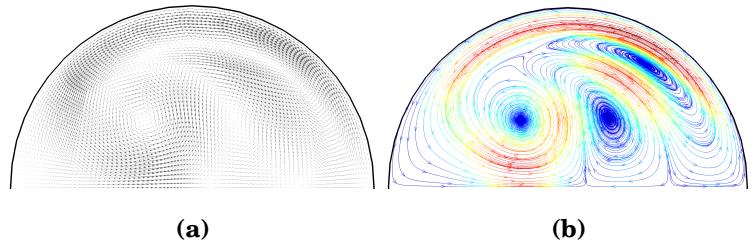


Figure 8.21 Poiseuille entrance condition: (a) non-dimensional secondary velocity vectors $\mathbf{u}_{\theta r}^*$ and (b) streamlines colored by magnitude at $\phi = 90^\circ$ and $Re = 883$. This Re corresponds to the bulk flow at $t^* = 0.23$ under pulsatile conditions.

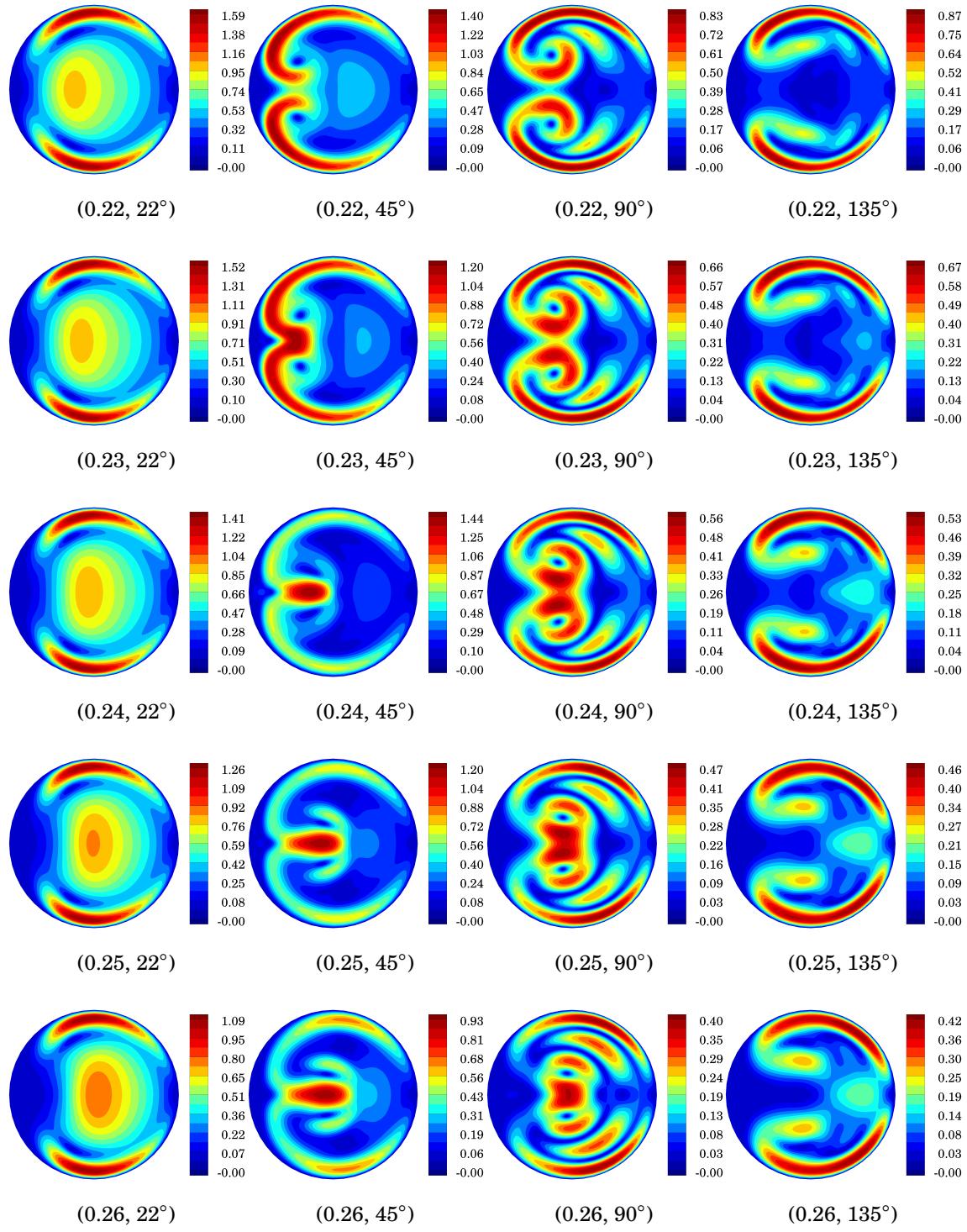


Figure 8.22 Womersley entrance condition: non-dimensional secondary velocity magnitude $|u_{\theta r}^*|$ at (t^*, ϕ) .

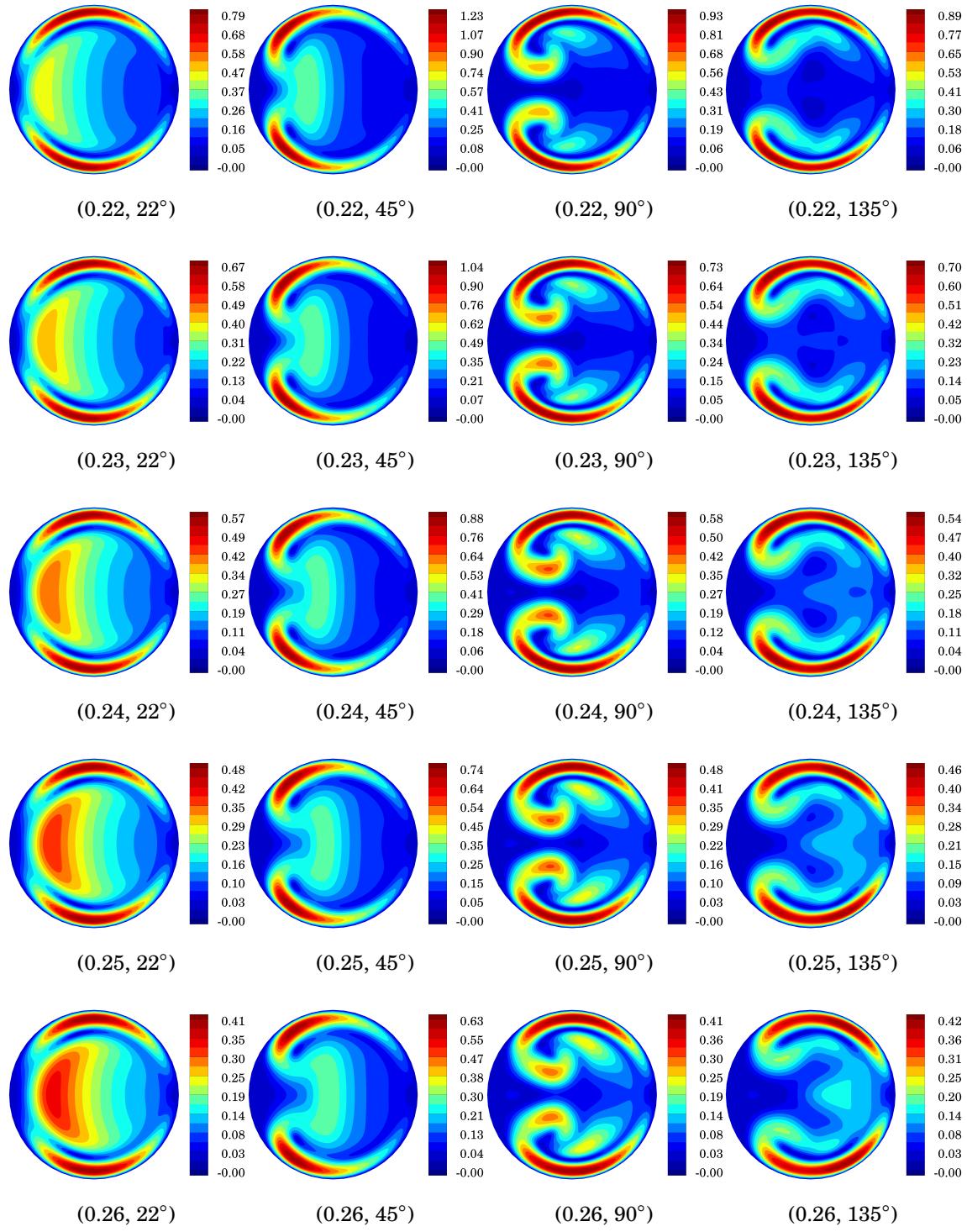


Figure 8.23 Uniform entrance condition: non-dimensional secondary velocity magnitude $|u_{\theta r}^*|$ at (t^*, ϕ) .

8.7.4.1 Comparison with PIV Data

In addition to the numerical convergence tests performed in Section 8.7.3, we validate our numerical solver by comparing secondary velocity magnitudes to the experimental PIV data obtained by Najjari and Plesniak [118]. Figure 8.24 provides a side-by-side comparison of the non-dimensional secondary velocity results for $\phi = \{45^\circ, 90^\circ, 135^\circ\}$ during deceleration at the phase $t^* = 0.25$ where multiple vortical structures exist due to secondary flow (see Figure 8.36). Visually, the results match quite well. Quantitatively, we use the Pearson correlation coefficient, which is a well known statistical measure of the linear correlation between two samples - sample a and sample b - obtained by computing the covariance of the two samples divided by their standard deviations as

$$\rho_{a,b} = \frac{\sum_{m=1}^M a_m b_m}{\sqrt{\sum_{m=1}^M a_m^2} \sqrt{\sum_{m=1}^M b_m^2}} \quad (8.43)$$

where M is the sample size. For our results, $a = |\mathbf{u}_{\theta r,e}^*| - \overline{|\mathbf{u}_{\theta r,e}^*|}$ is the difference between the experimental secondary velocity magnitude and its mean computed at a given radial coordinate in a cross-sectional/toroidal plane and M is the number of coordinates per plane. Similarly, $b = |\mathbf{u}_{\theta r,n}^*| - \overline{|\mathbf{u}_{\theta r,n}^*|}$ is the difference between the numerical secondary velocity magnitude and its mean located at the corresponding coordinate. To obtain matching coordinates, results from the numerical simulation were interpolated onto the Cartesian grid used to process the experimental results. The correlations are computed on the velocity field inside a prescribed circle with radius $r/r_{max} = 0.96$. This radius was chosen to be smaller than the actual pipe radius due to inherent difficulty in obtaining quality PIV data near the wall of an internal flow. The correlations are tabulated in Table 8.2, which shows that $\rho_{a,b} = 0.97$ at $\phi = 45^\circ$, $\rho_{a,b} = 0.86$ at $\phi = 90^\circ$ and $\rho_{a,b} = 0.93$ at $\phi = 135^\circ$. Also, the L^2 -norm of the difference between experimental and numerical velocities $\|\mathbf{u}_{\theta r,e}^* - \mathbf{u}_{\theta r,n}^*\|_2$ for each

plane is 0.0422, 0.0435 and 0.0358. These results correspond to 2.54%, 2.62% and 2.15% of the bulk velocity at this phase.

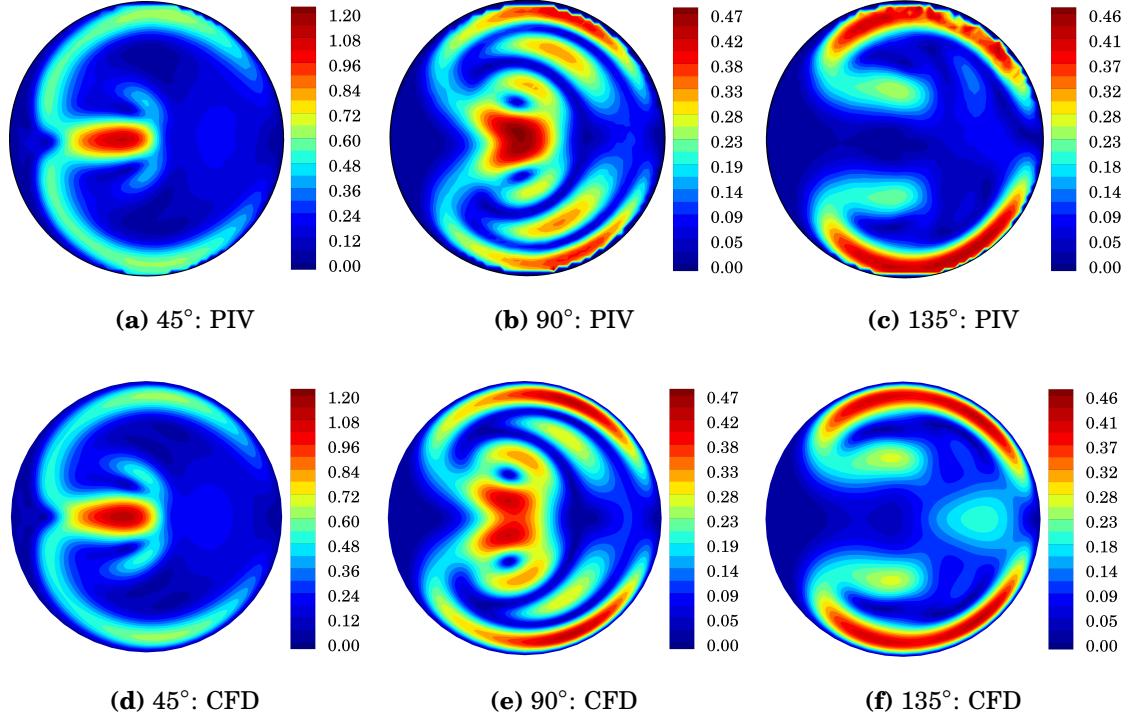


Figure 8.24 Womersley entrance condition: comparison of non-dimensional secondary velocity magnitude $|u_{\theta r}^*|$ with particle image velocimetry data from Najjari and Plesniak (2017) at $t^* = 0.25$ and $\phi = \{45^\circ, 90^\circ, 135^\circ\}$. (a)-(c) PIV, (d)-(f) CFD.

ϕ	$\rho_{a,b}$	$\ u_{\theta r,e}^* - u_{\theta r,n}^*\ _2$
45°	0.97	0.0422
90°	0.86	0.0435
135°	0.93	0.0358

Table 8.2 Pearson correlation coefficient $\rho_{a,b}$ of experimental secondary velocity $u_{\theta r,e}^*$ and numerical secondary velocity $u_{\theta r,n}^*$ and L^2 -norm of the difference $\|u_{\theta r,e}^* - u_{\theta r,n}^*\|_2$ at $t^* = 0.25$ and $\phi = \{45^\circ, 90^\circ, 135^\circ\}$.

8.7.5 Primary Flow

Figure 8.25 shows the component of velocity in the streamwise direction u_s^* under WEC during acceleration and deceleration, which exhibits a crescent-like shape similar to what was seen under PEC. This crescent shape is a typical feature in curved pipes with no torsion, owing to the outwardly shifted location of the maximum velocity. However, there is a stark difference between the Womersley and Poiseuille flow conditions. After peak flowrate of WEC there is a region of reverse flow within the curve along the inner wall that begins near $t^* = 0.22$. This phase corresponds to the same phase at which reverse flow appears in the entrance condition seen in Figure 8.15i. In Figure 8.25, reverse flow in cross-sectional planes is denoted by dashed contour lines, growing with deceleration and becoming largest towards the end of deceleration at $t^* = 0.29$ (see Appendix D Figure D.8). Streamwise velocities from UEC are provided in Figure 8.26, which shows that reverse flow occurs along the inner wall at the same phase as WEC for $\phi = \{45^\circ, 90^\circ, 135^\circ\}$, even though no reverse flow exists in a pulsatile uniform entrance condition. At $\phi = 22^\circ$ flow reversal does not occur until the end of deceleration where $t^* \geq 0.28$ (see Appendix E Figure E.8).

Figures 8.27 and 8.28 show velocity profiles produced from WEC and UEC for $0.14 \leq t^* \leq 0.29$ and $\phi = \{22^\circ, 45^\circ, 90^\circ, 135^\circ\}$ at the $z = 0$ plane of symmetry. In these figures, flowrate acceleration is denoted by solid lines and deceleration is denoted by dashed lines, with the dashed black line highlighting a specific phase of deceleration at $t^* = 0.23$. This phase is significant and will be revisited throughout the remaining sections because it represents the point in time at $\phi = 90^\circ$ where the head of DD vortex splits/separates. A description of this splitting is given in Section 8.7.7.

The results under WEC in Figure 8.27 are skewed slightly inward at $\phi = 22^\circ$ during acceleration and outward during deceleration. On the other hand, for $\phi = \{45^\circ,$

$90^\circ, 135^\circ\}$ the velocity profiles are consistently skewed outward. A double peak in the profile can be seen at $\phi = 45^\circ$ and $t^* = 0.24$, where a local minimum in the velocity occurs near $r = 0$. Throughout deceleration at this toroidal location, the profile remains relatively flat inward of the peak velocity. Maximum velocities occur during peak flow rate at $t^* = 0.19$, where the streamwise velocity is $5.8\bar{u}_{mean}$, which is approximately 72% of the maximum velocity $8\bar{u}_{mean}$ that would be obtained under straight pipe Poiseuille flow with the same bulk flow (see Figure 8.15f for straight pipe Poiseuille profile scaled by the period mean velocity).

The fact that skewness in the velocity profile shifts from the inner wall near the entrance to the outer wall as the fluid moves through the curve was predicted by Singh [101] in his analysis of steady flow development in a curved tube near the entrance. He showed that initial development is influenced by both geometry and entry condition, and that the cross-over of wall shear stress from the inner to outer wall occurs at different toroidal locations downstream of the entrance depending on the entry condition. Results shown here demonstrate that this inner-to-outer shift in profile skewness occurs under both WEC and UEC, although the shift is more visible in the latter due to higher wall shear stress at the inner wall caused by the more uniform entrance velocity condition. The velocity profile results from UEC are provided in Figure 8.28. Singh explains that the effect of secondary velocity near the entrance to the curve is small and the skewness of the velocity profile towards the inner wall stems from the fact that the boundary layer at the outer wall is thicker due to its longer wall length and the boundary layer at the inner wall is thinner due to its shorter wall length, with the fluid in the core accelerating due to the displacement effect caused by the growing boundary layer. The higher wall shear stress seen here under UEC along the inner wall where $\theta = 180^\circ$ near the entrance at $\phi = 0^\circ$ is demonstrated in Figure 8.29.

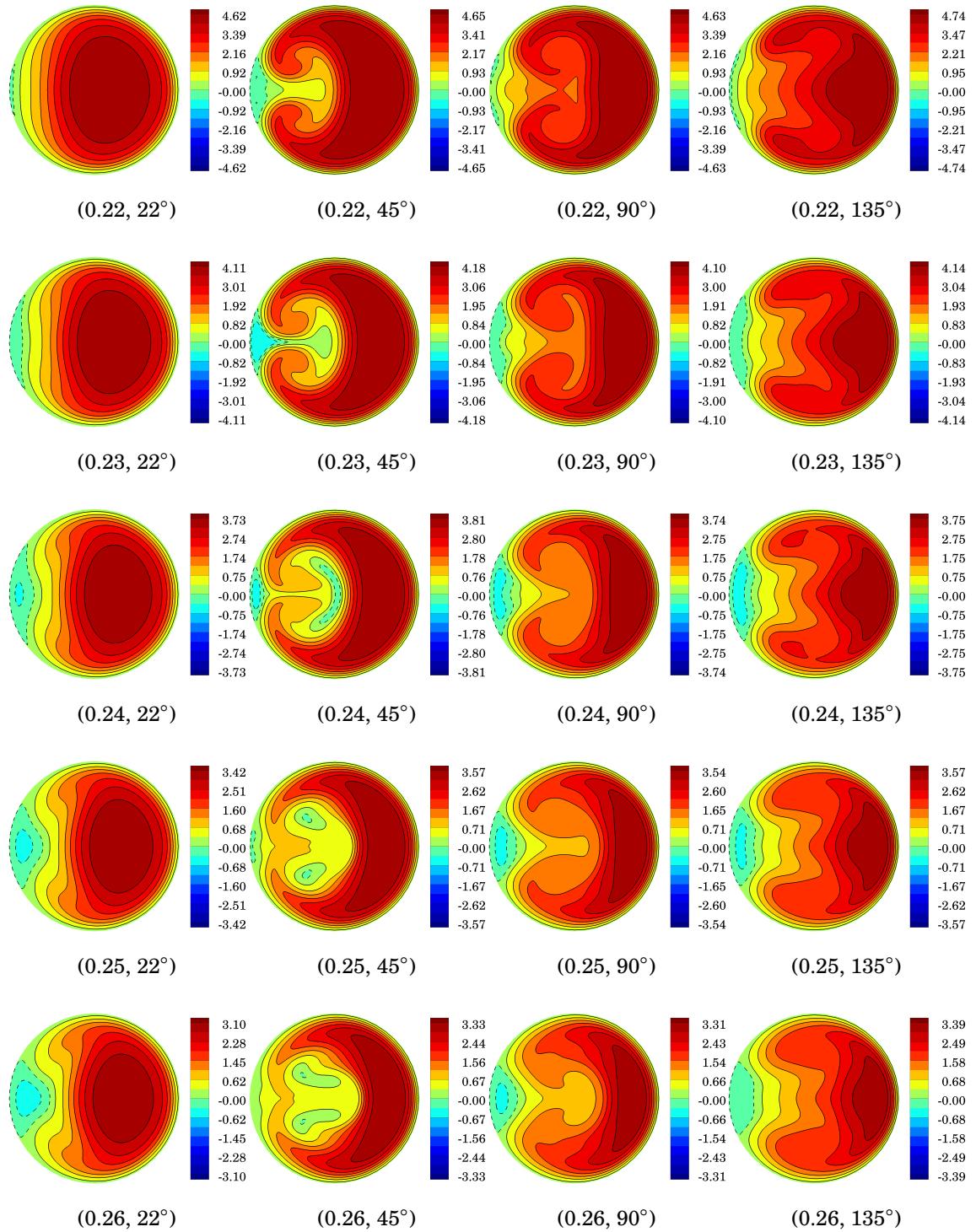


Figure 8.25 Womersley entrance condition: non-dimensional streamwise velocity u_s^* at (t^*, ϕ) .

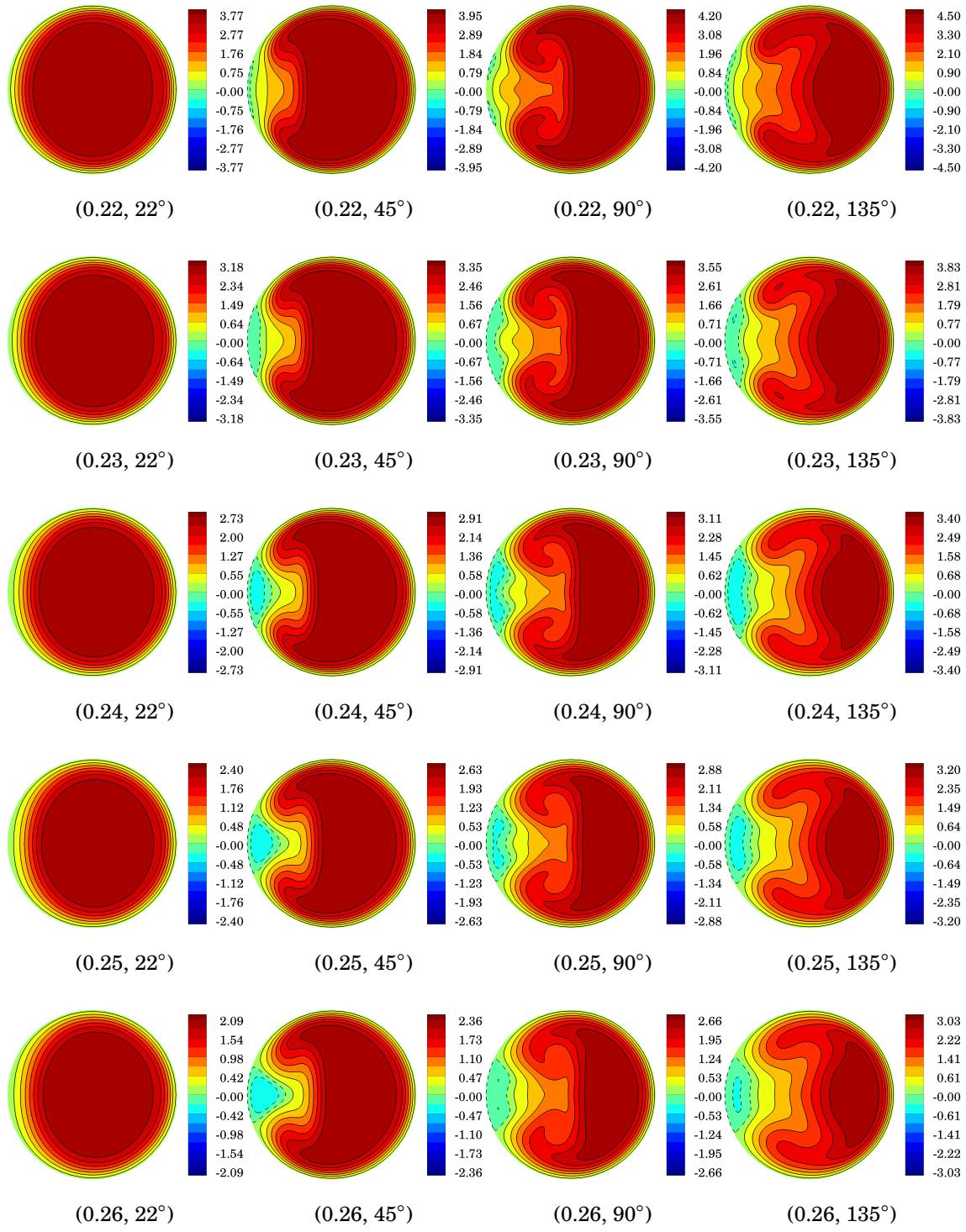


Figure 8.26 Uniform entrance condition: non-dimensional streamwise velocity u_s^* at (t^*, ϕ) .

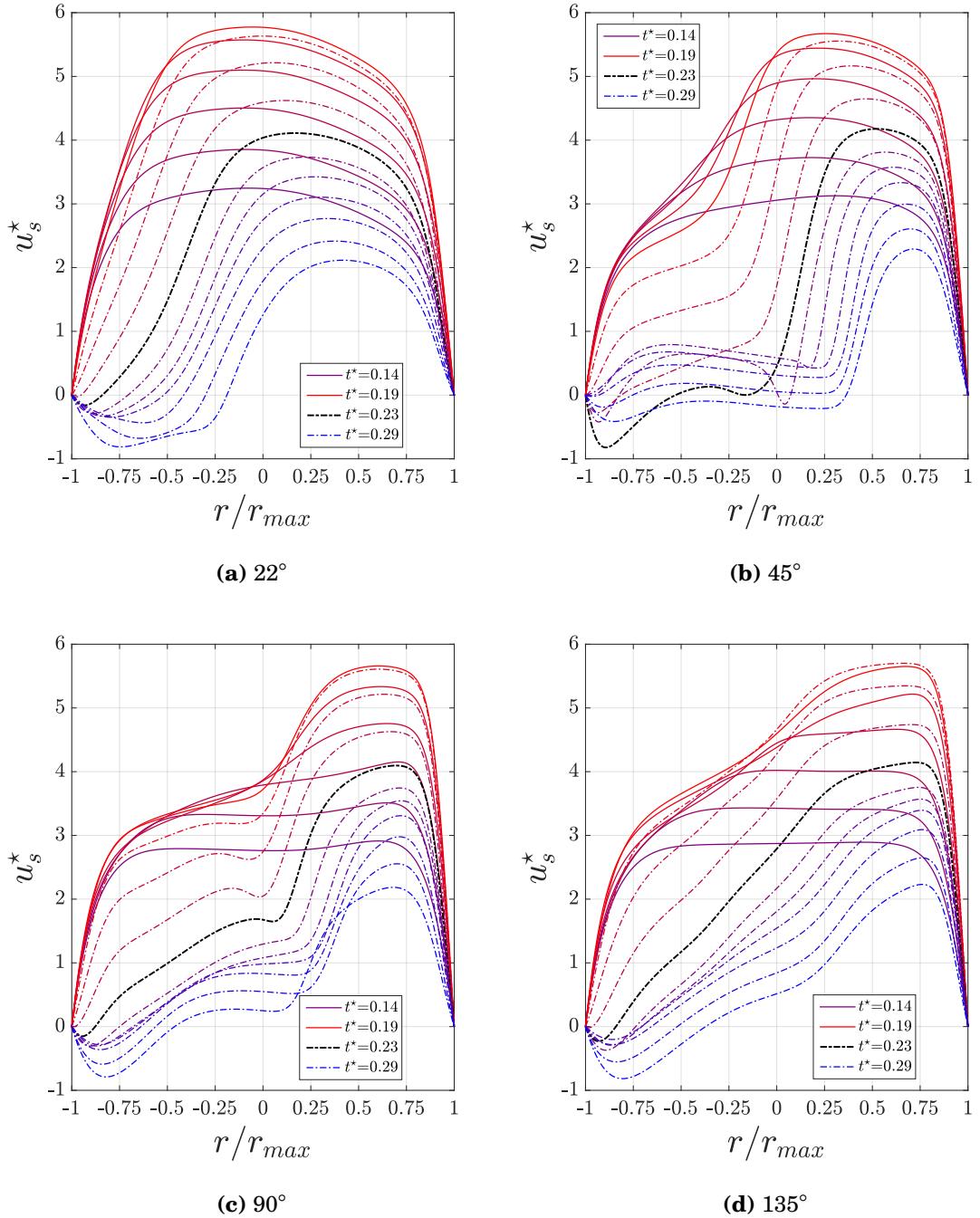


Figure 8.27 Womersley entrance condition: non-dimensional streamwise velocity u_s^* profile at $z = 0$ plane of symmetry for $0.14 \leq t^* \leq 0.29$ showing flow acceleration (solid) and deceleration (dash-dot). $\phi = \{22^\circ, 45^\circ, 90^\circ, 135^\circ\}$.

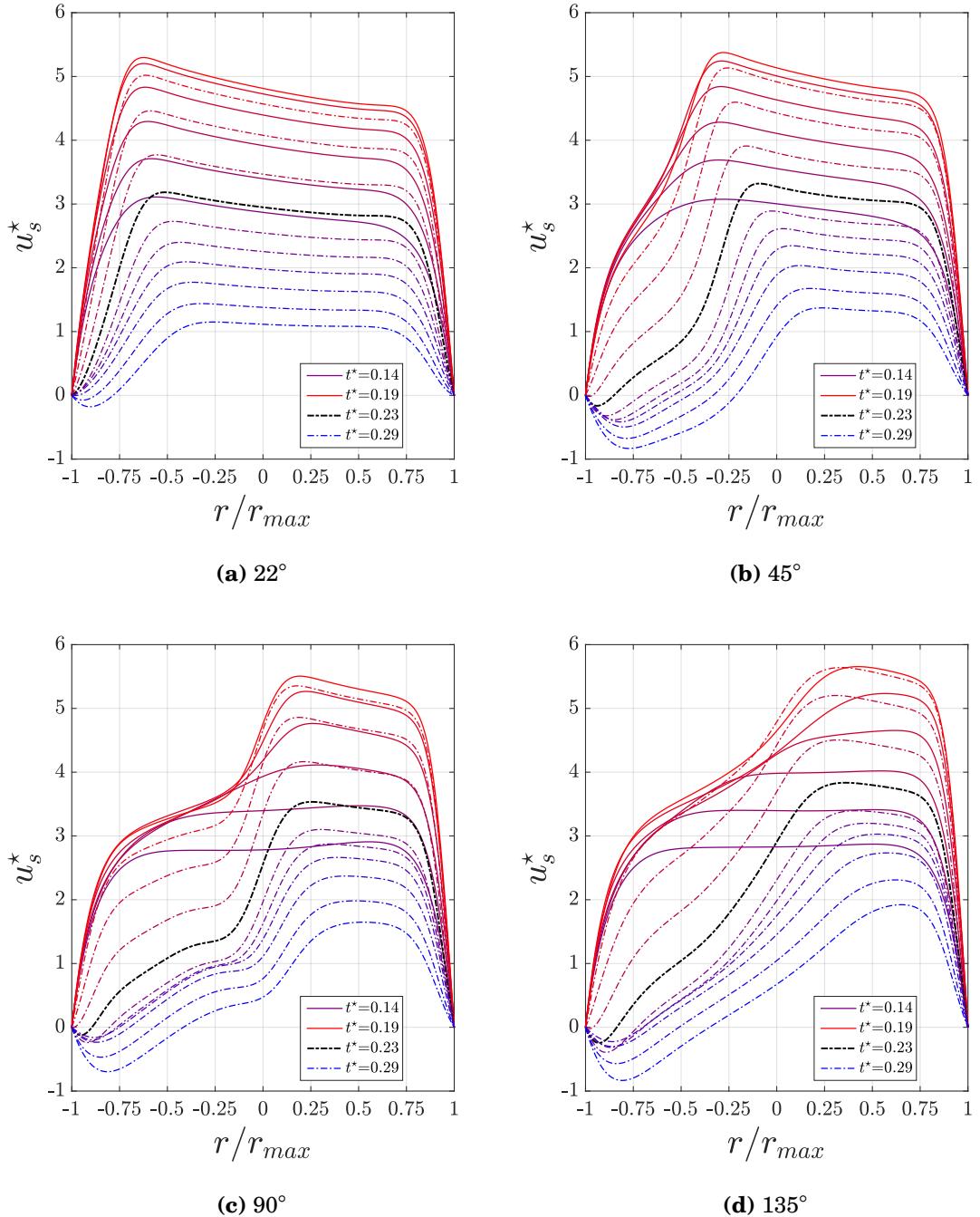


Figure 8.28 Uniform entrance condition: non-dimensional streamwise velocity u_s^* profile at $z = 0$ plane of symmetry for $0.14 \leq t^* \leq 0.29$ showing flow acceleration (solid) and deceleration (dash-dot). $\phi = \{22^\circ, 45^\circ, 90^\circ, 135^\circ\}$.

A comparison of velocity profiles under the various entrance conditions is provided in Figure 8.30. This shows results from Womersley, uniform and Poiseuille conditions at $z = 0$ for the various cross-sections within the curve. The profiles from both WEC and UEC are each plotted from two phases - one during acceleration, one during deceleration - where flow rates are the same; namely, at the point where the bulk velocity is $\bar{u} = 0.247$ m/s. These points in time correspond to $t^* = 0.14$ during acceleration and $t^* = 0.23$ during deceleration. This bulk velocity is equivalent to the bulk velocity under PEC for $Re = 883$. Comparison at these particular phases can be useful for analyzing flow physics that emerge due to fluid inertia and entrance conditions - two pulsatile and one steady - for a given flow rate. All velocity profiles are normalized by the bulk velocity. A straight pipe Poiseuille flow profile where $u_s(r)/\bar{u} = 2 \left(1 - r^2/r_{max}^2\right)$, is also plotted to highlight velocity profile skewness and flatness with respect to a parabolic profile. These profiles demonstrate the variation in streamwise velocity from mid-acceleration to mid-deceleration. For example, under WEC and UEC at $t^* = 0.14$ and $\phi = 22^\circ$ the maximum velocity is 69% and 66%, respectively, of the maximum velocity achieved from straight pipe Poiseuille flow. At $t^* = 0.23$, maximum velocity is at 88% and 68%. This reduction in maximum velocity under pulsatile flow is partly due to the inertia of the fluid associated with the frequency of pulsatility. The effect of curvature alone also reduces the maximum velocity at the plane of symmetry - this was seen earlier under four different steady Poiseuille entrance conditions in Figure 8.5 and is shown here as the dashed red line where the maximum velocity reached is 96% of the maximum velocity achieved under fully developed flow in a straight pipe. Furthermore, at this acceleration phase the profiles from WEC and UEC are rather flattened, with the latter profile even more flattened due to the entrance condition being undeveloped. By the time $t^* = 0.23$, however, the profiles have all skewed, with WEC exhibiting the strongest skewness and larger maximum velocity over UEC due to the fully developed nature

of the entry flow. Under UEC, a flattened region is typically seen outward of the peak as the fluid moves downstream and the profile skews towards the outer wall. This flattened profile causes the crescent shapes seen in Figure 8.26 under UEC to be larger than those in Figure 8.25 under WEC. Ultimately, the reduced peak under UEC produces a smaller centrifugal force and, therefore, a smaller pressure gradient along the radius of curvature than WEC, leading to reduced secondary flows and weaker vortical structures. Flow reversal should be highlighted again here in Figure 8.30 at $\phi = 45^\circ$ near the inner wall at $r/r_{max} = -1$, where reverse flow is quite large under WEC compared to UEC. Also, it shows inward skewness of local reverse flow, causing the clockwise rotation of the small secondary recirculation zone described in Section 8.7.4.

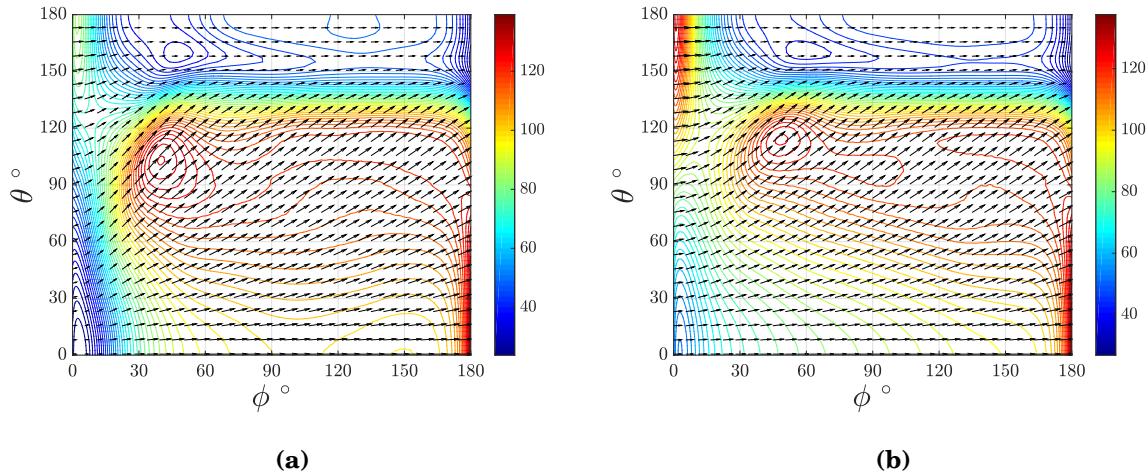


Figure 8.29 Instantaneous non-dimensional wall shear stress vectors τ_w^* with magnitude contours at $t^* = 0.19$ under (a) Womersley entrance condition and (b) Uniform entrance condition. In (b) higher wall shear stress occurs towards the inner wall where $\theta = 180^\circ$ near the entrance at $\phi = 0^\circ$ due to the shorter wall length (i.e. thinner boundary layer) and larger streamwise velocity.

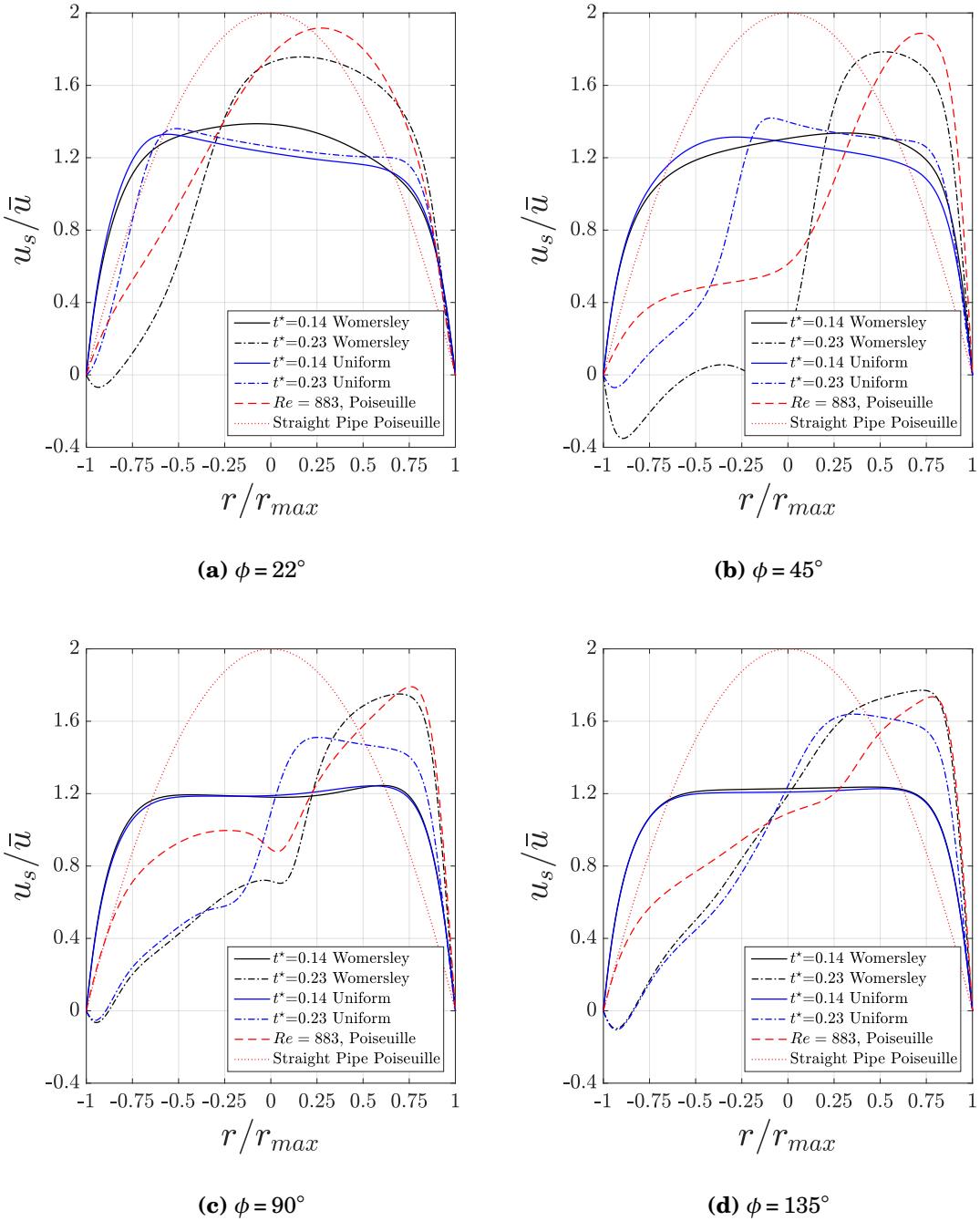


Figure 8.30 Womersley, Uniform and Poiseuille entrance conditions: profiles of streamwise velocity normalized by bulk velocity u_s/\bar{u} at $z = 0$ for $\phi = \{22^\circ, 45^\circ, 90^\circ, 135^\circ\}$. At phases $t^* = 0.14$ and $t^* = 0.23$ the flow is accelerating and decelerating, respectively, at the same bulk velocity of $\bar{u} = 0.247$ m/s. The steady flow result at $Re = 883$ from the Poiseuille entrance condition corresponds to the same value of bulk velocity. A straight pipe Poiseuille flow result is shown to highlight profile flattening and skewness with respect to a parabolic profile, where the maximum non-dimensional velocity equals 2 at $r = 0$ when using \bar{u} as the velocity scale.

8.7.6 Vorticity

Previously defined under steady Poiseuille flow in Section 8.6.5, the streamwise vorticity associated with DD, SD and LT secondary recirculation zones is presented in this section as it pertains to pulsatile viscous flow under Womersley and uniform entrance conditions. The results WEC and UEC from mid-acceleration through deceleration for $0.15 \leq t^* \leq 0.29$ are provided in Appendices D and E Figures D.4 and E.4. This comprehensive set of figures display the spatial and temporal evolution of velocity surfaces and streamwise vorticity at various cross-sections. For discussion in this section, we again extract data from the phase $t^* = 0.23$ and plot results from $\phi = \{22^\circ, 45^\circ, 90^\circ, 135^\circ\}$ in Figures 8.32 and 8.33. In all figures, velocity surfaces are colored by streamwise vorticity where (I), (O), (U) and (L) denote the inner, outer, upper and lower walls, respectively (see Section 8.2 for geometry and orientation definitions). Also, the same right-hand rule convention from Section 8.3 has been adopted here whereby positive vorticity is defined with thumb pointing out of page when viewing cross-sectional data, i.e. pointing upstream and aligned with the pipe axis.

During acceleration under WEC at $\phi = 90^\circ$, we observe mostly DD vorticity. LT vorticity appears just before peak flow rate but after $t^* = 0.17$, when the vorticity of the same sign near the wall erupts into the interior of the pipe. This idea of wall layer vorticity eruption was given by Doorly and Sherwin [108] and the results here confirm their description. At $\phi = 90^\circ$ after peak flow rate at $t^* = 0.19$, the head of the comma-shaped DD vorticity region starts to take shape and by $t^* = 0.23$, the head has peeled off and forms what we have called SD vorticity. At this point, there are now three regions of concentrated vorticity above and below $z = 0$, ignoring vorticity generated at the wall. These are called DD, SD and LT (see Figure 8.32), which were initially identified under PEC at high enough Dean number. The three regions

above the plane of symmetry have opposite sign to those below it. At 45° , vorticity associated with DD separates slightly later at $t^* = 0.25$. However, at $\phi = 22^\circ$ and 135° separation does not occur. Therefore, splitting of DD only occurs locally around the mid-section of the curve between 45° and 135° . Similar to DD and SD, LT streamwise vorticity is most notable at 90° . We observe that at this location and time $t^* = 0.23$, maximum LT streamwise vorticity is 70% of SD vorticity. However, the maximum vorticity magnitude is 125% of SD vorticity magnitude. The reason for this is due to the fact that 99% of SD vorticity is aligned with the streamwise direction, whereas only 36% of LT vorticity is aligned. We plot vortex lines associated with SD and LT in Figure 8.31 to better understand where the three-dimensional vorticity vector points. Streamwise vorticity and vorticity magnitude are also shown. More plots of $|\omega^*|$ are provided in Appendix D Figure D.5. We observe that 64% of total LT vorticity ω^* is distributed among other directions, with 28% along the (negative) radius of curvature direction and 36% in the (positive) z -direction. Therefore, we can conclude that above the plane of symmetry at 90° and $t^* = 0.23$ where splitting occurs, the full three-dimensional vorticity vector associated with SD points directly upstream. On the other hand, LT vorticity vector points downstream and towards the upper and inner walls. Total vorticity is mostly generated along the upper/lower and outer walls while, at the inner wall, vorticity generation is very low due to small local velocities caused by the onset of reversed flow at $t^* = 0.22$ and secondary boundary layer eruption into the mainstream fluid.

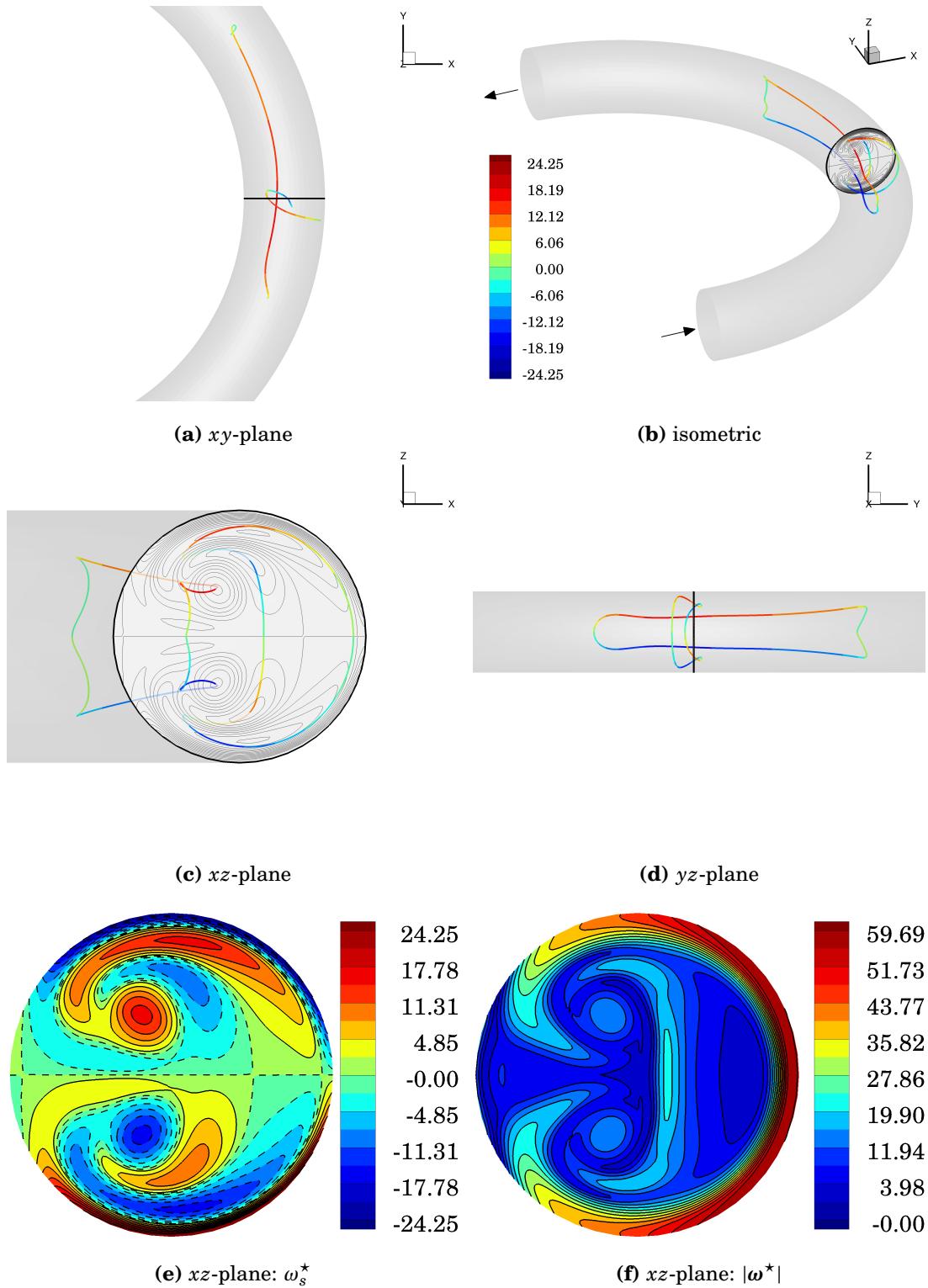


Figure 8.31 Womersley entrance condition: (a)-(d) vortex lines colored by streamwise vorticity ω_s^* at $\phi = 90^\circ$ and $t^* = 0.23$ showing the local direction of the three-dimensional vorticity vector ω^* associated with Split-Dean and Lyne-type regions, (e) streamwise vorticity ω_s^* , and (f) vorticity magnitude $|\omega^*|$.

Under UEC at $\phi = 90^\circ$ in Figure 8.33, the head of DD vorticity does not develop as strongly as it does under WEC and does not fully separate. Furthermore, the separated head does not form at $\phi = 45^\circ$ and all positive streamwise vorticity remains confined to DD. The lack of a Deformed-Dean “head” under UEC at this ϕ can be attributed to the fact that the entrance flow is not developed, producing a skewed but flattened velocity profile (see Figure 8.28), with peak velocity occurring closer to the pipe center and smaller than the result from a fully developed entrance condition. This decreased velocity from UEC produces a smaller centrifugal force and consequently a smaller pressure gradient sets up across the pipe cross-section, thereby driving the secondary motion of the fluid at a slower velocity than that which occurs under a fully developed condition. Lyne-type vorticity is also seen under UEC, but to a lesser extent than WEC.

Since LT vorticity described in this work⁵ appears in both steady and pulsatile entrance conditions, it is considered a curvature effect. It appears once the secondary flow is strong enough, and the slower moving fluid near the walls moves inward and the faster moving fluid away from the wall moves outward causing the streamwise velocity to peak towards the outer wall and depress towards the inner wall. The depressed region of velocity corresponding to DD vorticity (red) induces the formation of LT vorticity (blue). Therefore, a high enough Dean number producing a counter-clockwise rotation of DD circulation is accompanied by clockwise rotation of LT circulation. Figures 8.34 and 8.35 show the changes in streamwise velocity profiles and depression in the pipe interior at the planes $z/r_{max} = 0.38$ for WEC and $z/r_{max} = 0.41$ for UEC. Each z -plane cuts directly through both regions of DD and LT vorticity at $t^* = 0.23$. At $\phi = 90^\circ$, we observe that the depressed velocity in the interior begins

⁵In Section 8.6.5 we loosely defined the term “Lyne-type” under steady flow conditions, highlighting the fact that Lyne circulation was originally described under high-frequency oscillatory viscous flow where the interior core flow was inviscid. We adopt the term “Lyne-type” due to fact that this region of secondary motion rotates in the opposite direction to a Dean/Deformed-Dean cell.

after $t^* = 0.17$ under both WEC and UEC. This is the exact time after which LT vorticity appears in WEC and UEC. Therefore, in steady and pulsatile entrance conditions, LT vorticity appears simultaneously with a double peak in the velocity profile. In Section 8.7.7, we will discuss in more detail the formation of three-dimensional curved vortices associated with DD, SD and LT circulations using the λ_2 -criterion, and we will offer a description for what causes vortex splitting in the ϕ -plane.

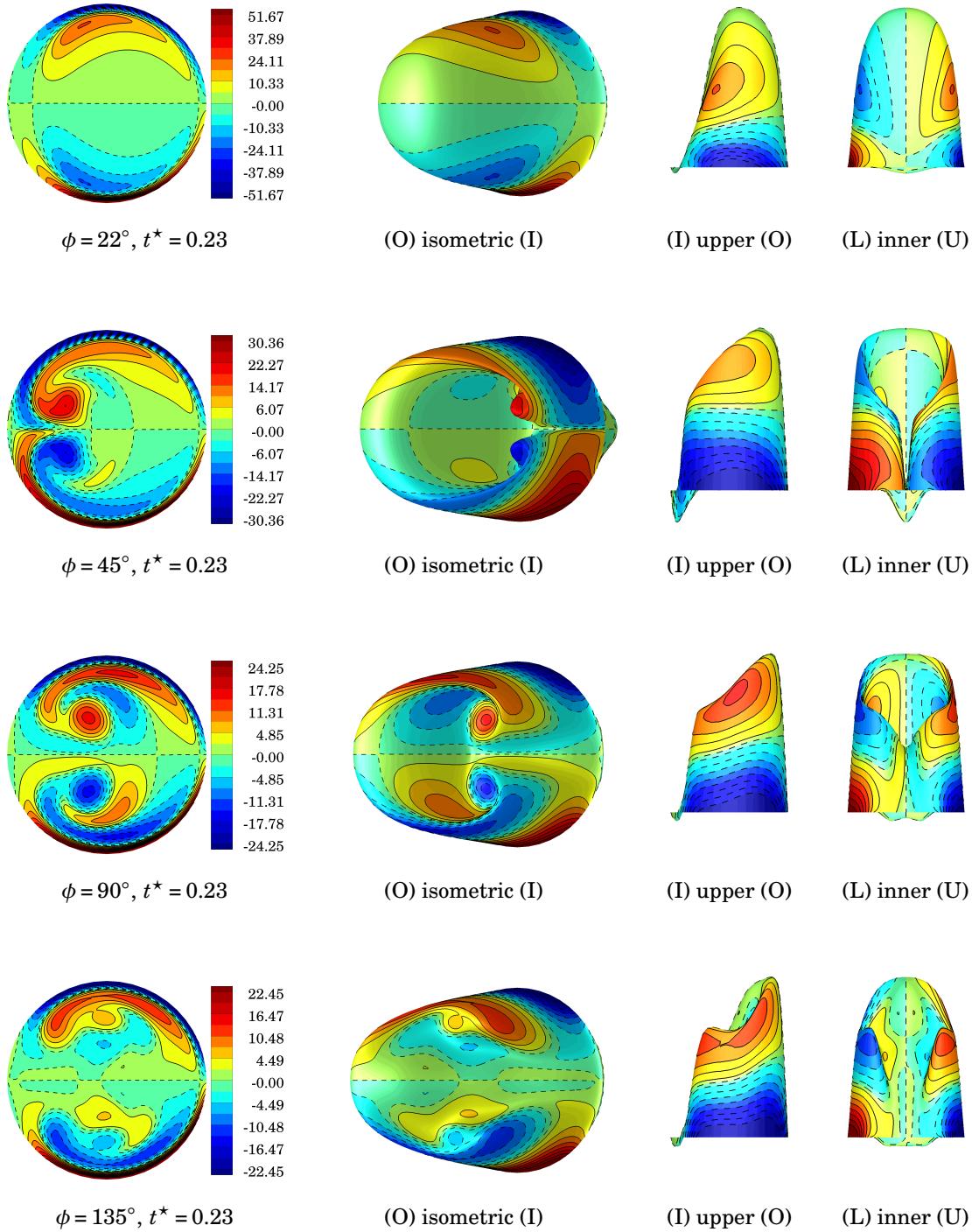


Figure 8.32 Womersley entrance condition: velocity surface of u_s^* at $t^* = 0.23$ colored by non-dimensional streamwise vorticity ω_s^* visualized from three difference views: isometric, upper and inner. ($I \equiv inner$, $O \equiv outer$, $U \equiv upper$, $L \equiv lower$).

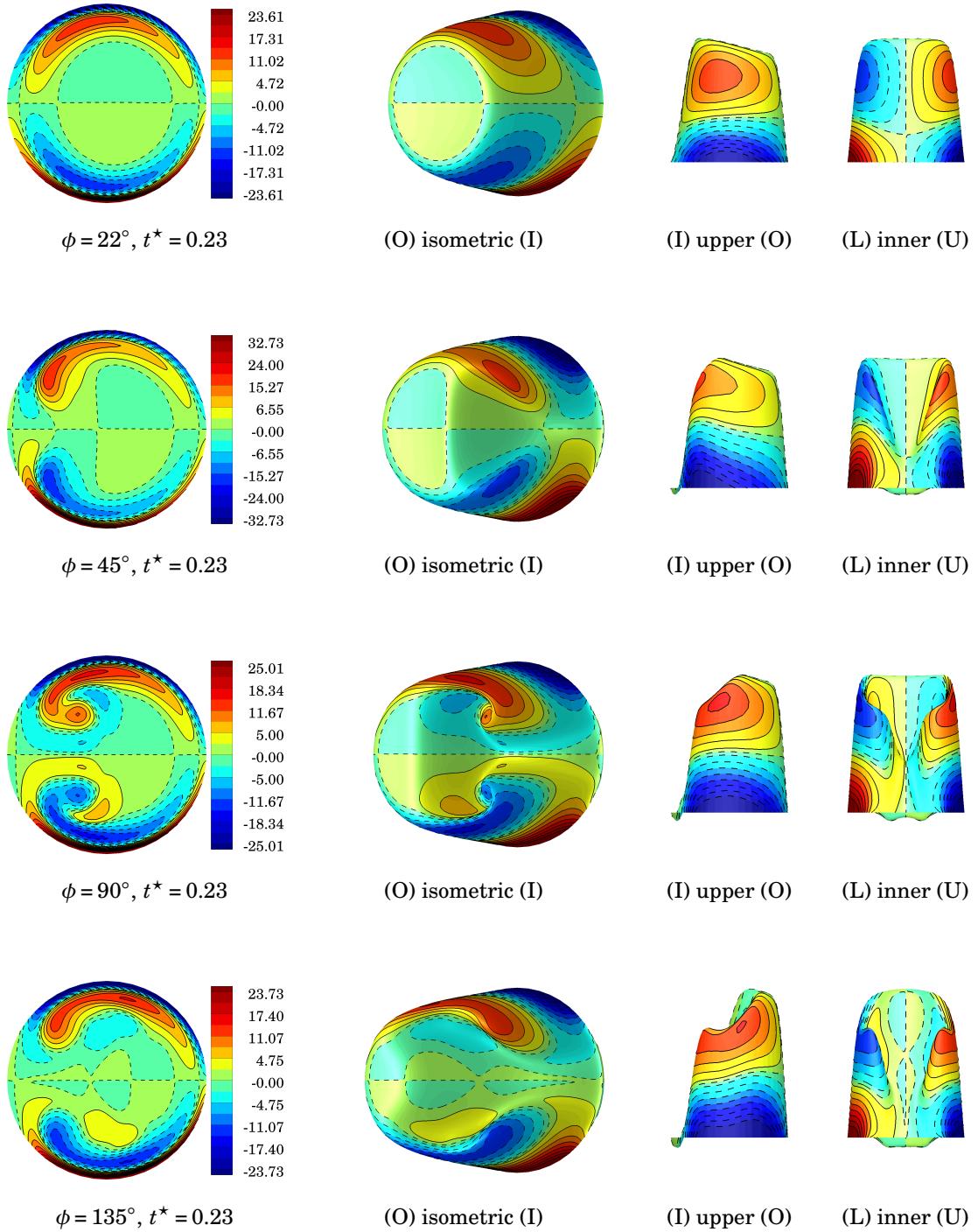
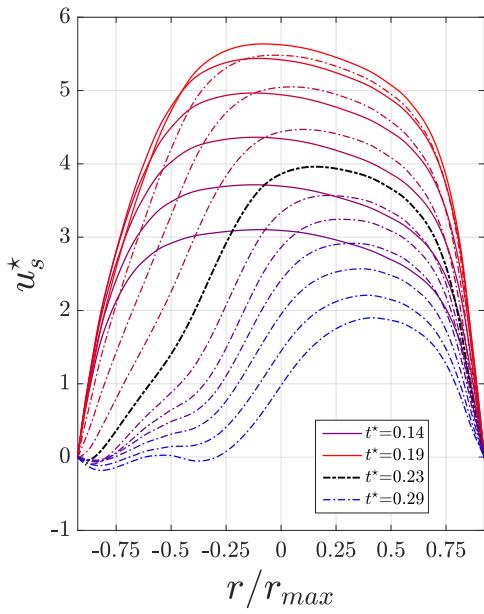
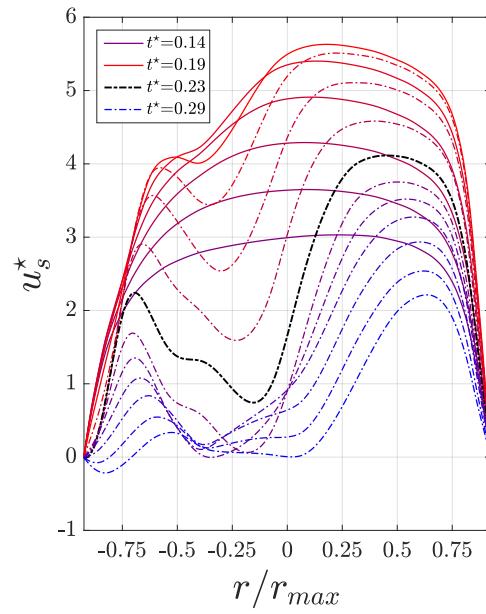


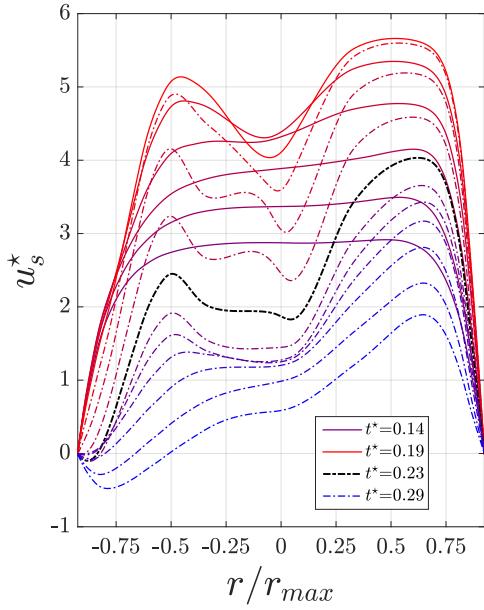
Figure 8.33 Uniform entrance condition: velocity surface of u_s^* at $t^* = 0.23$ colored by non-dimensional streamwise vorticity ω_s^* visualized from three difference views: isometric, upper and inner. ($I \equiv$ inner, $O \equiv$ outer, $U \equiv$ upper, $L \equiv$ lower).



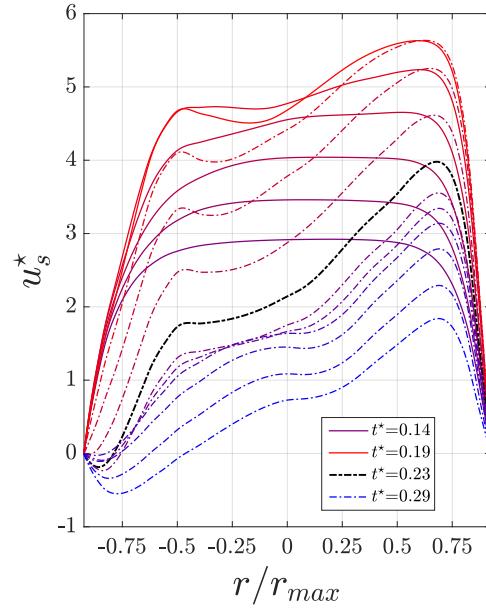
(a) 22°



(b) 45°



(c) 90°



(d) 135°

Figure 8.34 Womersley entrance condition: non-dimensional streamwise velocity, u_s^* , profile at $z/r_{max} = 0.38$ plane for $0.14 \leq t^* \leq 0.29$ showing flow acceleration (solid) and deceleration (dash-dot). $\phi = \{22^\circ, 45^\circ, 90^\circ, 135^\circ\}$.

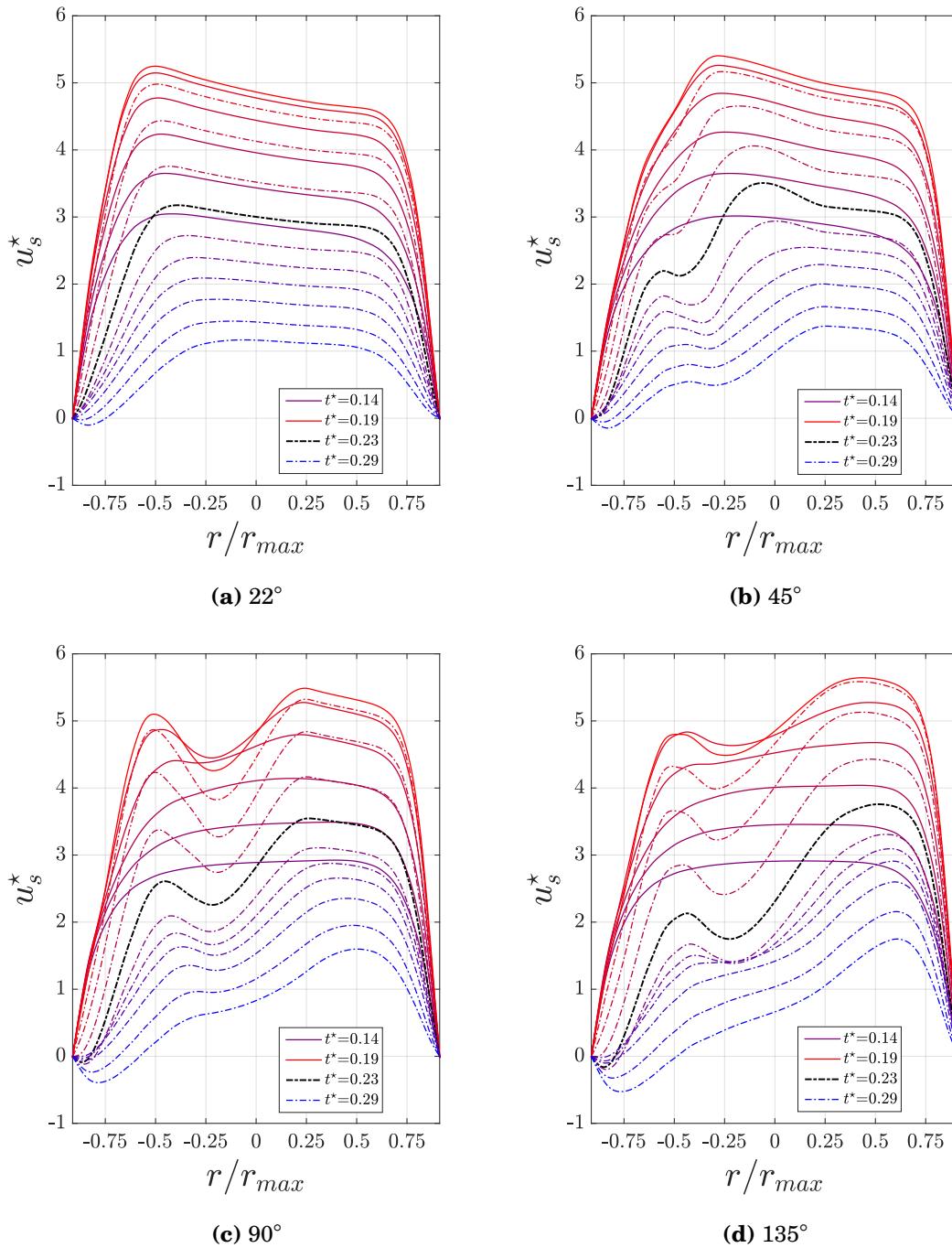


Figure 8.35 Uniform entrance condition: non-dimensional streamwise velocity, u_s^* , profile at $z/r_{max} = 0.41$ plane for $0.14 \leq t^* \leq 0.29$ showing flow acceleration (solid) and deceleration (dash-dot). $\phi = \{22^\circ, 45^\circ, 90^\circ, 135^\circ\}$.

8.7.7 Vortex Identification

8.7.7.1 Deformed/Split-Dean Vortex

In the previous section we described the streamwise vorticity fields of DD, SD and LT - particularly during deceleration - as they related to the two different entrance conditions, WEC and UEC. We compute the λ_2 -criterion from Jeong and Hussain to identify actual vortical structures within the curve, correlate them to the vorticity, and quantify if and when vortex splitting occurs in the cross-section. For results from both WEC and UEC, see Figures 8.36 and 8.37. Regions of large/small negative values of λ_2^* signify strong/weak vortical activity. Although results are somewhat similar between WEC and UEC at 22° and 135° , the results at 45° and 90° are quite different. Under WEC, vortex splitting occurs first at $t^* = 0.23$ and $\phi = 90^\circ$ where two separate regions of λ_2^* exist above and below the plane of symmetry, namely the DD and SD vortices. Most of the vortical activity, however, has been lumped into SD where the value of $\lambda_2^* \approx -61$. The value of DD at this phase and location is about half that at $\lambda_2^* \approx -30$. Also, λ_2^* is strongest at $\phi = 45^\circ$ ranging from $\lambda_2^* = -162$ at $t^* = 0.22$ to $\lambda_2^* = -47$ at $t^* = 0.26$, losing 70% of its strength over this short time interval. At $\phi = 45^\circ$, vortex splitting occurs at $t^* = 0.25$ after the appearance of a swift outward motion of the vortex. The secondary velocity associated with this quick movement of the vortex was first shown in Figure 8.16. This burst of secondary flow is accompanied by a small pair of vortices at the inner wall, seen here using λ_2^* . After vortex splitting at both 45° and 90° , SD vortex drifts towards the outer wall and loses strength while the flow continues to decelerate and the reverse flow region along the inner wall grows. This loss in vortex strength is attributed to viscous diffusion, which plays a larger role as the flow rate drops by a factor of 7 throughout systolic deceleration. This causes the time scale over which convection occurs to increase, ultimately decreasing the ratio of diffusion time scale to convection time

scale $t_d/t_c = (d^2/\nu)/(d/\bar{u})$. Furthermore, SD still appears connected to DD at 22° and 135° ; therefore, splitting of the head of DD is local and confined to the region between 22° and 135° . Under UEC, full separation of the DD vortex at $\phi = 90^\circ$ does not occur. At $\phi = 45^\circ$, only DD exists and LT can only be seen at $\phi = 90^\circ$. All strong vortical activity is confined to DD, and the SD vortex does not fully develop. Under the undeveloped entrance condition, the maximum streamwise velocity is smaller than a fully developed entrance condition and ultimately the secondary flow in the interior of the pipe is smaller. This reduced secondary flow suppresses growth of SD vortex and is accompanied by a weak LT vortex.

In-plane pressure fields are shown in Figures 8.38 and 8.39. These figures demonstrate the pressure gradient that sets up within each cross-section under pulsatile conditions, with high pressures on the outer walls and lower pressures on the inner walls. Also, local pressure minimums can be seen in the regions corresponding to DD in both WEC and UEC. Furthermore, a second local pressure minimum emerges under WEC in the interior once DD splits and forms SD. This pressure minimum indicates the intense vortical motion of SD, which is why λ_2 identifies this as a strong vortex. This can be seen at $\phi = 90^\circ$.

Three-dimensional streamlines associated with DD and SD are shown in Figure 8.40 under both (a) WEC and (b) UEC at $t^* = 0.23$. The streamlines are colored by streamwise vorticity and are chosen such that they pass through regions of DD and SD vorticity. In both cases, DD is apparent throughout the entire curve. It was shown earlier that under WEC at $\phi = 90^\circ$, vortex splitting occurs at this phase and produces SD from DD. Correspondingly, we can see that the streamlines take on a strong helical pattern in the first half of the curve, beginning just before $\phi = 22^\circ$. Vorticity from SD can be seen between 45° and 135° . Under UEC, such a defined region of SD does not form and the streamlines from this entrance condition do not form a helical pattern. This is due to the lack of strong secondary flow action in the

interior of the cross-section. Consequently, splitting does not occur under UEC as it does under WEC.

The temporal and spatial evolution of DD during deceleration can be visualized using isosurfaces of $\lambda_2^* = -24$, which are shown in Figure 8.41. This picture highlights the DD/SD vortical structures, which is colored by streamwise vorticity, before and after the phase where splitting occurs at $t^* = 0.23$. Above the plane of symmetry, ω_s^* shows a counter-clockwise rotation. Below the plane of symmetry the rotation is clockwise. Throughout this deceleration phase interval $0.21 \leq t^* \leq 0.26$ the isosurface shrinks in size, indicating a reduction in vortical activity. At $t^* = 0.21$, the isosurface stretches the length of the curve. The head of DD vortex can be seen rolling up $\phi = 45^\circ$ and 67° while still being connected to the main structure. At $t^* = 0.23$, separation of the head is shown between $\phi = 45^\circ$ and 135° . At $t^* = 0.24$, SD is shown connected to DD, giving credence to the idea that SD emanates from DD near the curve entrance. By $t^* = 0.26$, the remaining structure is confined to the first half of the curve. At this phase, the isosurface occupies the interior at $\phi = 45^\circ$ and 67° (SD) and the region closer to the wall at $\phi = 22^\circ$ (DD). Throughout the remainder of deceleration, the strength of SD subsides and eventually the vortex disappears due to viscous diffusion.

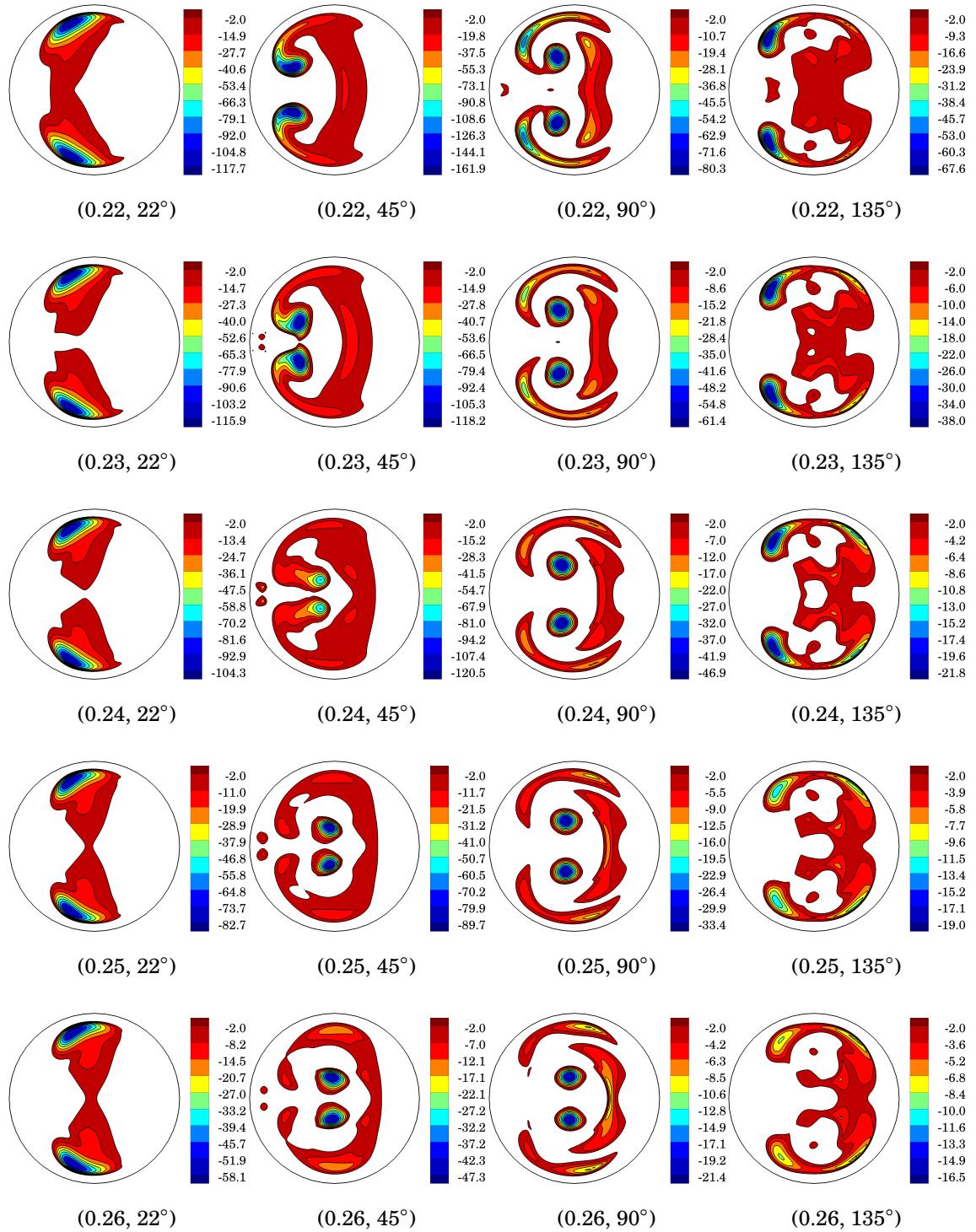


Figure 8.36 Womersley entrance condition: non-dimensional second eigenvalue λ_2^* of $S^2 + R^2$, $\lambda_2^* < 0$ at (t^*, ϕ) .

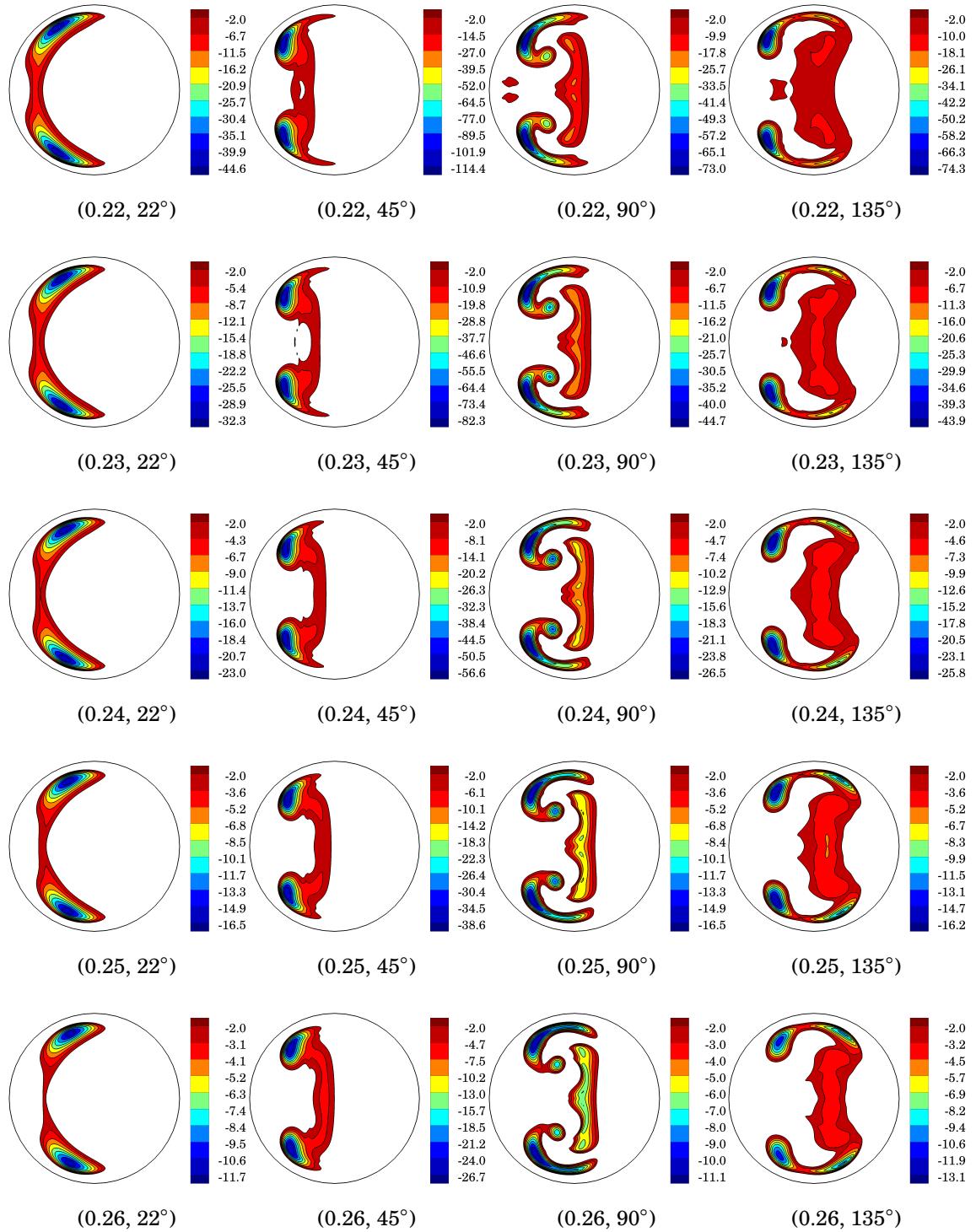


Figure 8.37 Uniform entrance condition: non-dimensional second eigenvalue λ_2^* of $\mathbf{S}^2 + \mathbf{R}^2$, $\lambda_2^* < 0$ at (t^*, ϕ) .

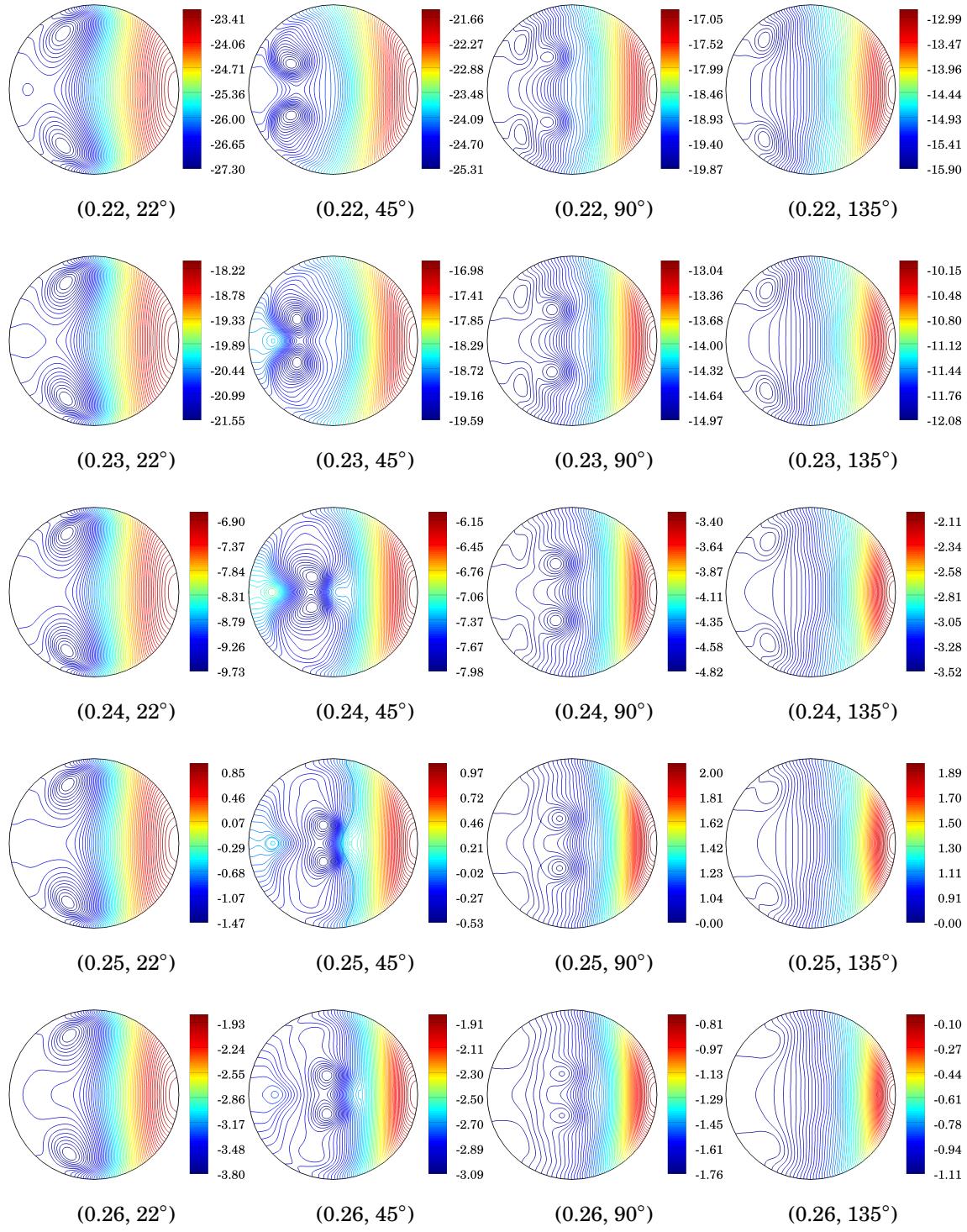


Figure 8.38 Womersley entrance condition: non-dimensional pressure p^* at (t^*, ϕ) (contour levels are rescaled for each cross-section).

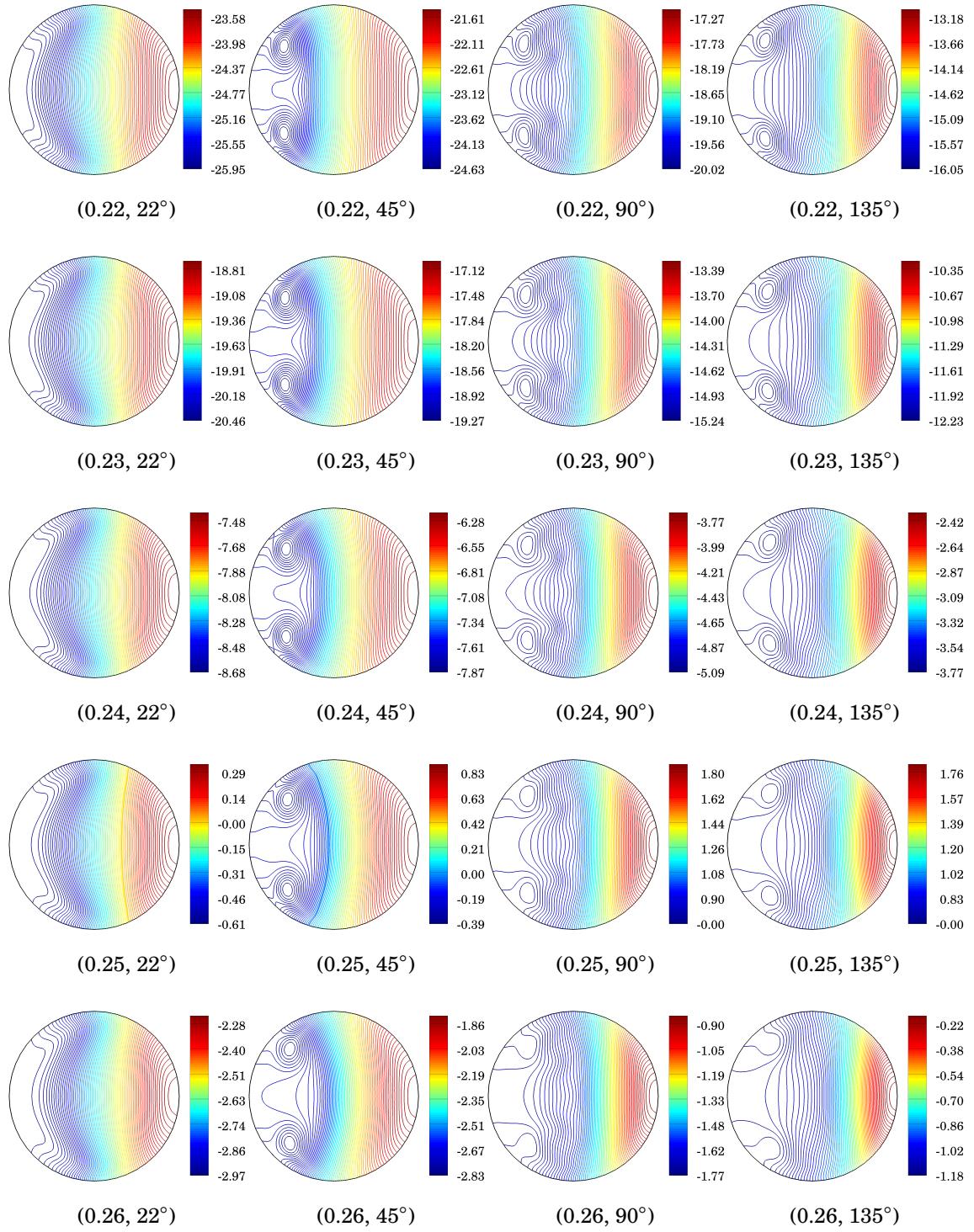


Figure 8.39 Uniform entrance condition: non-dimensional pressure p^* at (t^*, ϕ) (contour levels are rescaled for each cross-section).

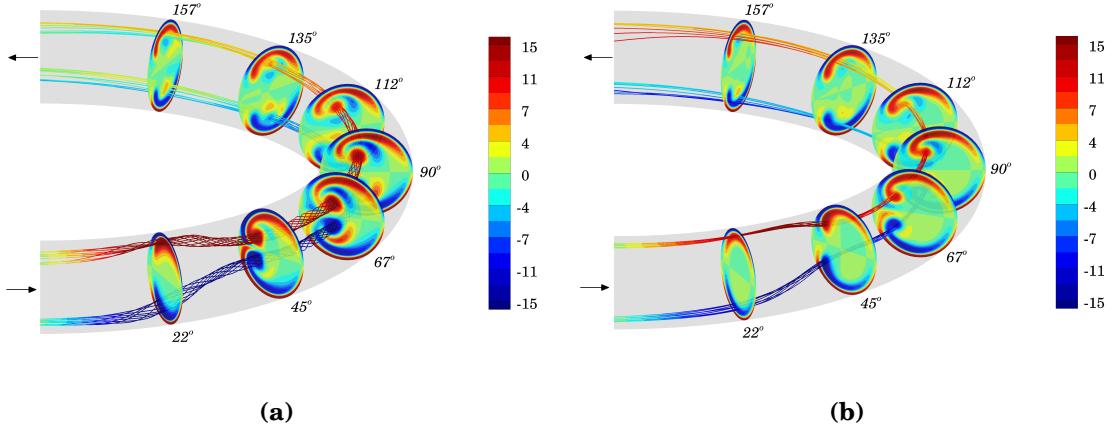


Figure 8.40 Womersley and Uniform entrance conditions: streamlines associated with the “head” of Deformed-Dean colored by non-dimensional streamwise vorticity ω_s^* at $t^* = 0.23$, highlighting the strong helical pattern of the streamlines under WEC in comparison to UEC. Strong helical patterns of streamlines result from strong secondary flow action, which is more prevalent under a fully developed pulsatile entrance condition.

8.7.7.2 Lyne Vortex

By looking at vortex lines in Figure 8.31, which are everywhere tangent to the vorticity vector, we can see in which direction the total vorticity vector is pointing at the 90° plane. Since ω_s is computed from velocity information contained in the ϕ -plane, it can only show vorticity due to the secondary motion. Furthermore, since the flow field is symmetric about $z = 0$, ω_s is zero at the plane of symmetry. On the other hand, λ_2 includes information from all three directions because it is computed based upon the entire velocity gradient tensor. From Figure 8.36, we see that λ_2 can be non-zero at $z = 0$. This indicates that at the plane of symmetry where the streamwise vorticity associated with LT goes to zero, the total vorticity vector must be completely aligned with the z -direction. This is confirmed by the vortex line plotted in Figure 8.31. Overall, λ_2 indicates that LT vortex is weaker than SD/DD vortex under the Womersley/uniform entrance conditions throughout most of the deceleration phase of the waveform. However, the result in Section 8.7.6 showed

that total LT vorticity is greater than SD vorticity. This means that part of the vorticity associated with LT is due to shear, supporting the earlier statement that the existence of vorticity does not imply a vortex and is not capable of distinguishing between pure shearing and swirling motions.

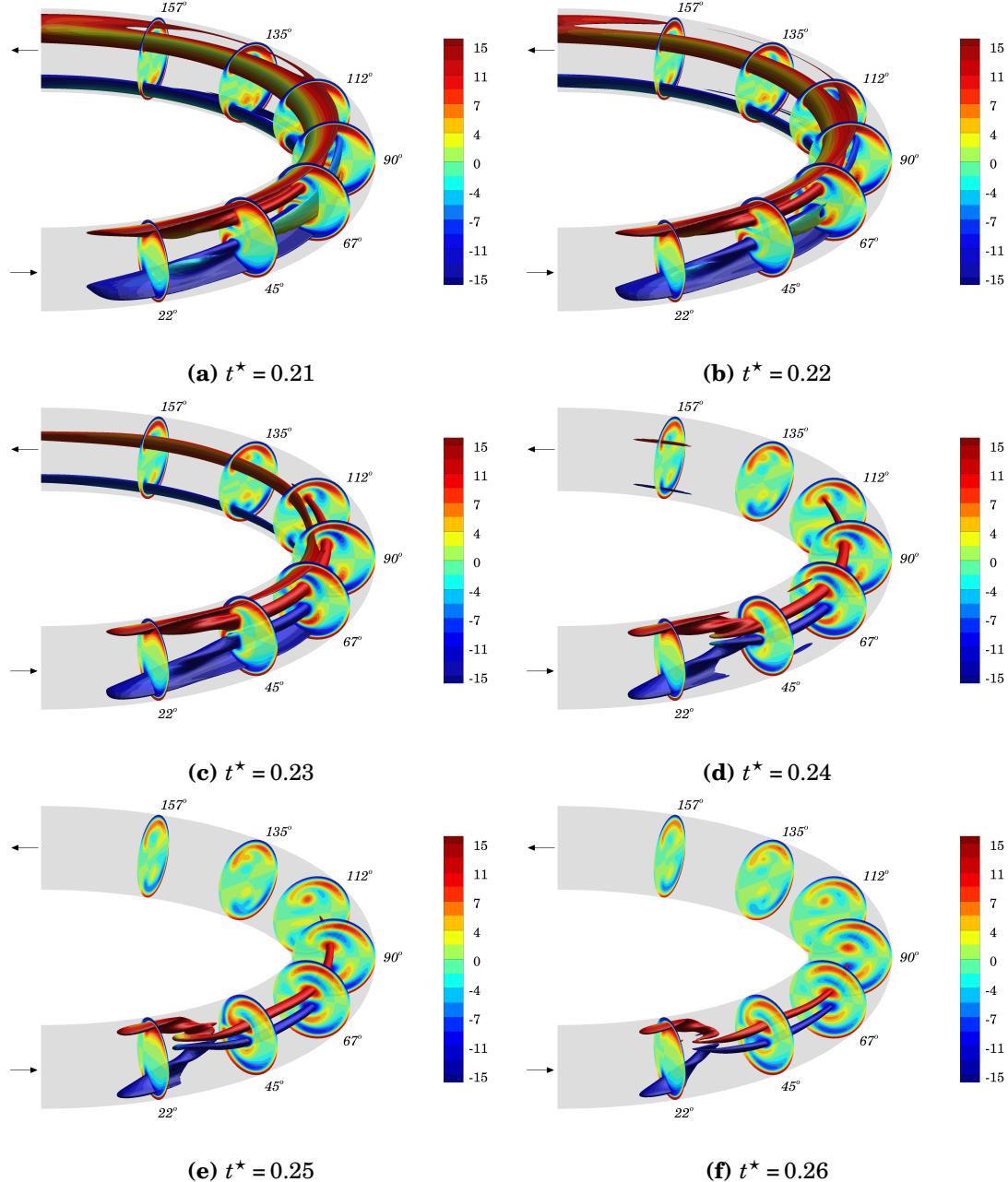


Figure 8.41 Womersley entrance condition: isosurfaces of $\lambda_2^* = -24$ colored by streamwise vorticity ω_s^* , highlighting cross-sectional vortex splitting of Deformed-Dean during deceleration for which $0.21 \leq t^* \leq 0.26$. Vortex splitting occurs at $t^* = 0.23$.

8.7.8 Deformed-Dean Vortex Splitting

One interesting feature of flow through a curved pipe is the potential for vortex splitting⁶ of the head of the DD vortex. We identified this flow feature in previous sections under Poiseuille and Womersley entrance flow conditions by analyzing the velocity and vorticity fields along with the λ_2 -criterion. Under WEC, we identified the time $t^* = 0.23$ to be the phase along the waveform at which splitting initiates for a Womersley number of $\alpha = 4.22$. At this phase, the Reynolds number based on bulk velocity is $Re = 883$ ($\kappa = 334$) and is equivalent to the Reynolds number used to run one of the steady flow cases in Section 8.6. Since vortex splitting was observed under both fully developed steady flow (PEC) and fully developed pulsatile flow (WEC), it is considered a curvature effect. However, the phase at which splitting occurs is a pulsatility effect since a Poiseuille entrance flow is equivalent to the quasi-steady⁷ solution as $\alpha \rightarrow 0$. Therefore, for the current curvature ratio and fluid viscosity, vortex splitting under a pulsatile Poiseuille entrance condition would occur much earlier near $t^* = 0.13$ (corresponding to steady flow at $Re = 883$), which is during the acceleration phase of the waveform. In this quasi-steady case, the pressure and flow rate would be completely in phase. Therefore, the more in phase pressure gradient and flow rate become, the earlier in the pulsatile period that vortex splitting occurs. Considering all results from the Poiseuille, Womersley and uniform entrance flows presented earlier, we attempt to explain the conditions under which splitting/separation of the DD vortex head is possible under the current pulsatile flow conditions (i.e. range of Dean numbers and Womersley number)

In addition to velocity, vorticity and λ_2 , we analyze forces in the cross-section

⁶The term *vortex splitting* is used here to denote the separation of one vortex core region into two vortex core regions as identified by the λ_2 -criterion in the cross-sectional plane perpendicular to the streamwise coordinate.

⁷A quasi-steady result is also known as a pulsatile Poiseuille flow result and is achieved when the frequency of the pulsatile waveform approaches zero.

similar to those shown in Section 8.6.7. As discussed earlier, it is a well known fact that centrifugal and pressure gradient forces play a role in producing secondary motion. In this section, the centrifugal force f_c and pressure gradient force f_{pg} as well as the viscous force f_v are calculated using Eqs. (8.35)-(8.37) with respect to the center of pipe curvature at $(x, y, z) = (0, 0, 0)$ depicted in Figure 8.1. These terms are then summed to give a force balance along the radius of curvature in the cross-section. The force balance is shown in Figure 8.42 under WEC for $0.19 < t^* < 0.23$. This phase interval was chosen because it shows the evolution of forces from peak flow rate at $t^* = 0.19$ to the phase $t^* = 0.23$ where vortex splitting occurs in the 90° cross-section. All forces f_c , f_{pg} and f_v have been normalized by \bar{u}_{mean}^2/d in this figure. Red/blue contours signify positive/negative forcing towards the outer/inner wall. The viscous and pressure gradient forces balance near the wall, where the centrifugal force goes to zero. A distinct feature is that the non-dimensional result $f_c^* + f_{pg}^* + f_v^* = 0$ occurs where the head of DD splits and forms SD at $\phi = 90^\circ$. Similar to steady results shown at $Re = 883$, the SD vortex creates a local pressure gradient with respect to its core at $t^* = 0.23$, where there is a local pressure minimum (see Figure 8.38 at $\phi = 90^\circ$), due to the strong helical motion of the fluid. This local pressure gradient combined with the pressure gradient caused by centrifugal forcing due to positive streamwise velocity creates a force balance at the core of the SD vortex. Unlike steady flow results, under fully developed pulsatile entrance conditions the interior region where $f_c^* + f_{pg}^* + f_v^* = 0$ corresponding to the SD vortex core drifts towards the outer wall as the flow decelerates and the vortex loses its strength (see Appendix D Figure D.14 for remaining phases of deceleration) due to viscous diffusion playing a larger role at lower flow rates. However, under uniform pulsatile entrance conditions the balance between centrifugal, pressure gradient and viscous forces shown in Figure 8.43 is quite different. As we saw in Section 8.7.7, the λ_2 -criterion results from UEC did not indicate creation of a strong SD vortex and

subsequent local splitting from the DD vortex. As a result, contrary to that which was seen under fully developed pulsatile conditions, a local pressure gradient force due to vortical motion does not set up where the SD vortex begins to form under uniform pulsatile entrance conditions.

To more closely analyze these forces at $\phi = 90^\circ$, we plot each term separately in Figure 8.44 under the three difference entrance conditions; PEC, WEC and UEC. All results have been non-dimensionalized using \bar{u} as the velocity scale in order allow for a magnitude comparison of the pulsatile results to the steady results. Results from WEC and UEC are extracted from the pulsatile waveform at $t^* = 0.23$. The flow rates across PEC, WEC and UEC are equal with a bulk velocity $\bar{u} = 0.247$ m/s, corresponding to $Re = 883$. For all entrance conditions, results from centrifugal forcing f_c^* indicate low values along the walls (especially at the inner wall) due to the no slip condition and high values towards the outer wall due to the outward skewness in the streamwise velocity profile. In turn, pressure gradient forces $-f_{pg}^*$ are higher near the outer wall due to the higher centrifugal forces there. Also, for both PEC and WEC there are two distinct high/low pressure gradient regions in the interior, one above and one below $z = 0$, corresponding the vortical motion of the SD vortex; however, the result from WEC is stronger and more noticeable by the contour levels in comparison to the result from PEC. The viscous forces f_v^* calculated in the radius of curvature direction are strongest along the top and bottom walls. Finally, the combination of these forces produces the results shown in Figures 8.44j-8.44l. Under PEC and WEC, the contour picture is similar although the magnitude of the contour levels between the two entrance conditions are very different, with stronger forcing under WEC where both DD and SD form. Under UEC, the balance of forces associated with SD creation does not exist as it does under WEC due to its weak formation and absence of vortex separation.

In Figure 8.45, we plot the non-dimensional streamwise velocity profiles at

$\phi = 90^\circ$ under PEC, WEC and UEC, along with images of various quantities ($u_{\theta r}^*$, $|u_{\theta r}^*|$, w_s^* , λ_2^* , $f_c^* + f_{pg}^* + f_v^*$) superimposed above the profiles. Each superimposed image displays the position of the z/r_{max} plane from which the velocity profiles are extracted. For PEC, WEC and UEC the z/r_{max} planes are located at 0.33, 0.38 and 0.41, respectively. These planes are specifically chosen to cut directly through the region in the cross-section where the SD vortex forms. Once again, data from WEC and UEC are taken from the phase $t^* = 0.23$ and flow rates across PEC, WEC and UEC are equal, where the bulk velocity is $\bar{u} = 0.247$ m/s. Results are non-dimensionalized using \bar{u} as the velocity scale for magnitude comparisons. All velocity profiles in Figures 8.45a-8.45c exhibit a double peak. The peak velocity of PEC and WEC is approximately $u_s/\bar{u} \approx 1.8$ and heavily skewed towards the outer wall at $r/r_{max} \approx 0.65$. The peak velocity of UEC reaches $u_s/\bar{u} \approx 1.5$ but is not as skewed and is farther towards the interior at $r/r_{max} \approx 0.25$. Under PEC and WEC, a small inviscid core in the mainstream flow exists in the SD region of formation. This inviscid core region can be identified where the velocity profile is flattened. Under WEC and UEC, a small region of reverse flow occurs at the inner wall. Furthermore, we stated earlier that stronger forcing occurs under WEC than PEC where the SD vortex forms. This is mainly due to the weaker pressure gradients associated with the formation of SD under PEC because of the weaker secondary velocities and vortical motion in this region. In other words, pulsatility enhances secondary motion during deceleration and creates a stronger SD vortex than a steady entrance condition with the same flow rate. Also, results from λ_2^* in Figure 8.45 indicate that for both PEC and WEC, more vortical activity is associated with SD than DD. Looking at the maximum λ_2^* within each vortex in Table 8.3, $\lambda_{2,SD}^* = 1.26\lambda_{2,DD}^*$ under PEC, $\lambda_{2,SD}^* = 1.95\lambda_{2,DD}^*$ under WEC, and $\lambda_{2,SD}^* = 0.70\lambda_{2,DD}^*$ under UEC. These results demonstrate that the SD vortex is greater under WEC than it is under PEC and UEC by a factor of 3.11 and 1.95, respectively.

Vortex	PEC	WEC	UEC
DD	-2.86	-5.77	-8.17
SD	-3.60	-11.20	-5.75

Table 8.3 Largest negative values of $\lambda_2^* = \lambda_2 d/\bar{u}$ at $\phi = 90^\circ$ and $t^* = 0.23$ within the Deformed-Dean (DD) and Split-Dean (SD) vortex core regions under Poiseuille, Womersley and uniform entrance conditions.

From the results in Figure 8.45, we can also conclude that a larger boundary layer growth at the curved pipe entrance, i.e. a fully developed entrance flow, promotes vortex separation by permitting a larger peak velocity in the streamwise direction during deceleration. As this larger peak in velocity shifts outwards, two secondary stagnation points develop in the cross-section along $z = 0$ and can be seen in the velocity vector images of Figures 8.45a and 8.45b. These stagnation points force the secondary streamlines away from the plane of symmetry toward the upper and lower walls, creating relatively large secondary motions associated with the head of DD. On the other hand, a uniform entrance condition produces a more blunted peak velocity at $\phi = 90^\circ$ during deceleration that is less shifted towards the outer wall than that which is obtained under a fully developed entrance flow. As a result, we can say that boundary layer growth in a curved pipe does affect the development of vortical flow structures. Note that under pulsatile flow the streamwise entrance pressure gradient $\partial p / \partial s$, which “leads” the flow rate, at $t^* = 0.23$ is positive and $-6x$ larger than the pressure gradient required under Poiseuille flow to produce the same flow rate for the current pipe diameter, kinematic viscosity and pulse period. This result was shown in Figure 8.13 in Section 8.7.1. Ultimately, using the results presented herein we can identify flow features that are common among the Poiseuille and Womersley entrance conditions at $\phi = 90^\circ$ where vortex splitting is observed for a Newtonian fluid flowing through a rigid tube with no torsion:

1. Fully developed entrance condition (splitting observed only during deceleration of pulsatile flow).
2. Secondary flow due to curvature.
3. Peak streamwise velocity skewed towards outer wall.
4. Double peak in velocity profile.
5. Locally inviscid region between double peak, where the SD vortex core region forms.

To facilitate the explanation of vortex splitting under the fully developed pulsatile condition, we can track the movement of the SD vortex core region as it begins to take shape in the head of the DD vortex after peak flow rate. Figure 8.46a shows the time evolution of the SD (red) and DD (blue) vortex core region by means of locating the planar coordinate $P(x', z', t)$ ⁸ within each vortex where the largest negative value of λ_2^* occurs at each phase, denoted by $\lambda_2^*|_P$. This coordinate corresponds to the point in the $\phi = 90^\circ$ plane where the fluid incurs the strongest relative rotational acceleration within each SD/DD vortex. Light and dark colored markers signify early and late deceleration. The red markers show that the SD vortex initially moves horizontally towards the outer wall for $0.19 < t^* < 0.23$, vertically towards the plane of symmetry for $0.23 < t^* < 0.28$, and then horizontally towards the inner wall for $0.28 < t^* < 0.30$. The length between each marker is the distance traveled by the vortex in the time increment $\Delta t^* = 0.005$ ($\Delta t = 0.02$ s). From this data, we can estimate the speed of the vortex within each phase of deceleration, which is plotted in Figure 8.46b. The average speed is 8.11 mm/s, which is equivalent to approximately 1.3% of pipe diameter per Δt^* . Also, these results indicate a short pause in SD vortex movement between $0.21 < t^* < 0.22$, where the speed is nearly zero. This pause occurs just before vortex splitting. Finally, in Figure 8.46c we

⁸The coordinates x' and z' represent local coordinates for a given cross-section, with the origin of the $x'z'$ -axis located at the center of the pipe where $r = 0$ (see Figure 8.46a).

superimpose the time evolution plot of $\lambda_2^*|_P$ on top of the flow rate. The important feature is that $\lambda_2^*|_P$ associated with SD continues to increase in magnitude by a factor of ~ 2.5 while the flow rate decreases, and the largest magnitude of $\lambda_2^*|_P$ occurs at the phase where the vortex holds its cross-sectional position in the small inviscid core region described earlier in Figure 8.45b. After this pause, the vortex splits at $t^* = 0.23$ and starts its vertical movement towards the plane of symmetry, during which time vortical motion of SD decreases due to viscous diffusion. At the end of deceleration at $t^* = 0.30$, $\lambda_2^*|_P$ is nearly zero.

Tracking the spatial evolution of the point $P(x', z', t)$ within the DD vortex core region at $\phi = 90^\circ$ in Figure 8.46a indicates movement parallel to the wall and towards the inner wall for $0.15 < t^* < 0.20$, towards the axis of the pipe for $0.20 < t^* < 0.24$ and then reversing direction towards the outer wall for $0.24 < t^* < 0.27$ after creation and subsequent separation of the SD vortex. Tracking the time evolution of the DD vortex in Figure 8.46c indicates that $\lambda_2^*|_P$ reaches its maximum magnitude immediately after peak flow rate and decreases thereafter throughout the entire deceleration phase of the pulsatile waveform. By analyzing the vortex core regions of both DD and SD under fully developed pulsatile entrance conditions, we can conclude that the vortical motion of DD decreases in magnitude while that of SD increases during the deceleration phase $0.19 < t^* < 0.21$. Ultimately, this result combined with that shown in Figure 8.45b, where the SD vortex is sustained by the combination of centrifugal and pressure gradient forces in the small inviscid core region of the flow, produces an environment conducive to the separation of the SD vortex from the DD vortex.

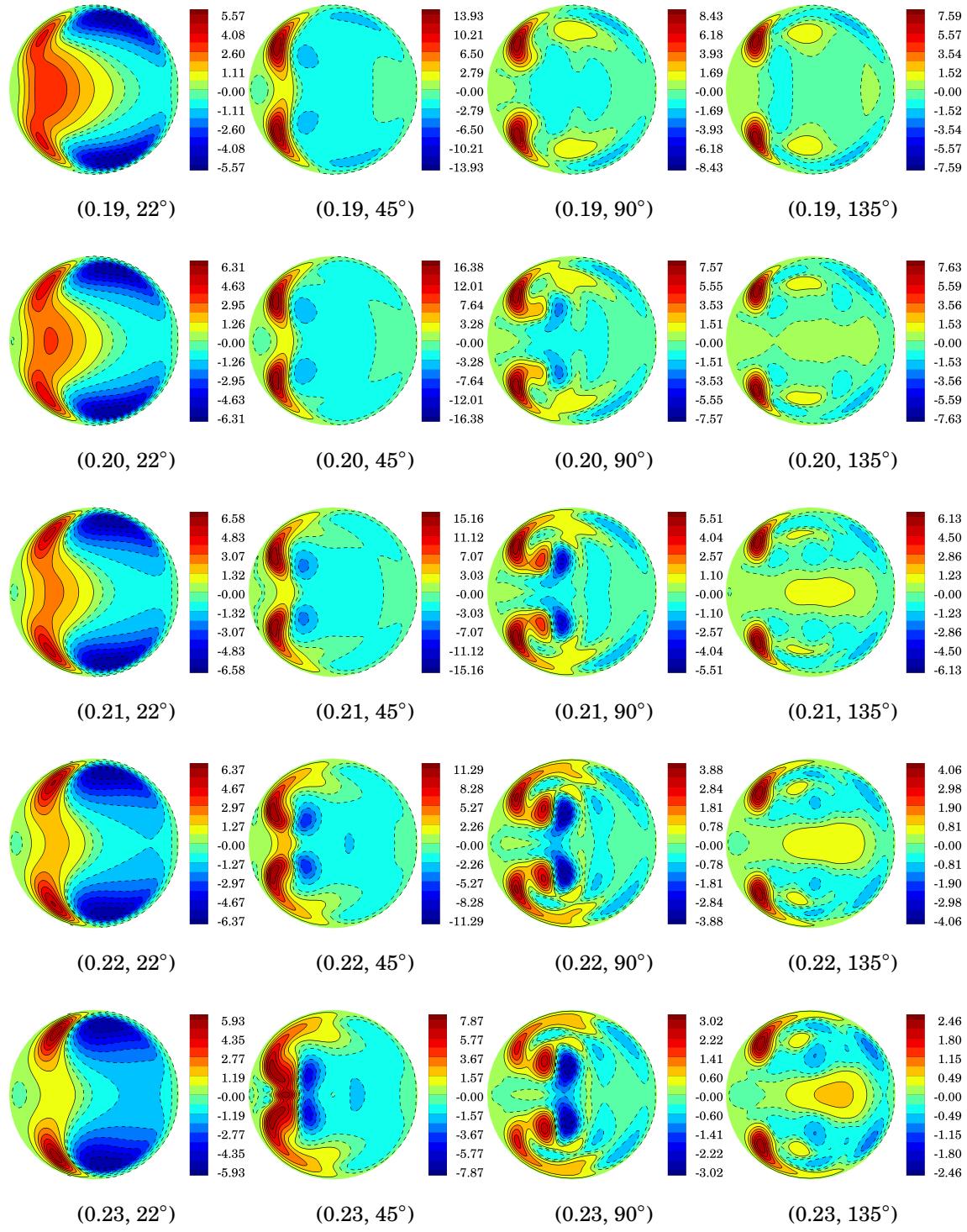


Figure 8.42 Womersley entrance condition: summation of non-dimensional centrifugal, pressure gradient and viscous forces along the radius of curvature direction $f_c^* + f_{pg}^* + f_v^*$ at (t^*, ϕ) .

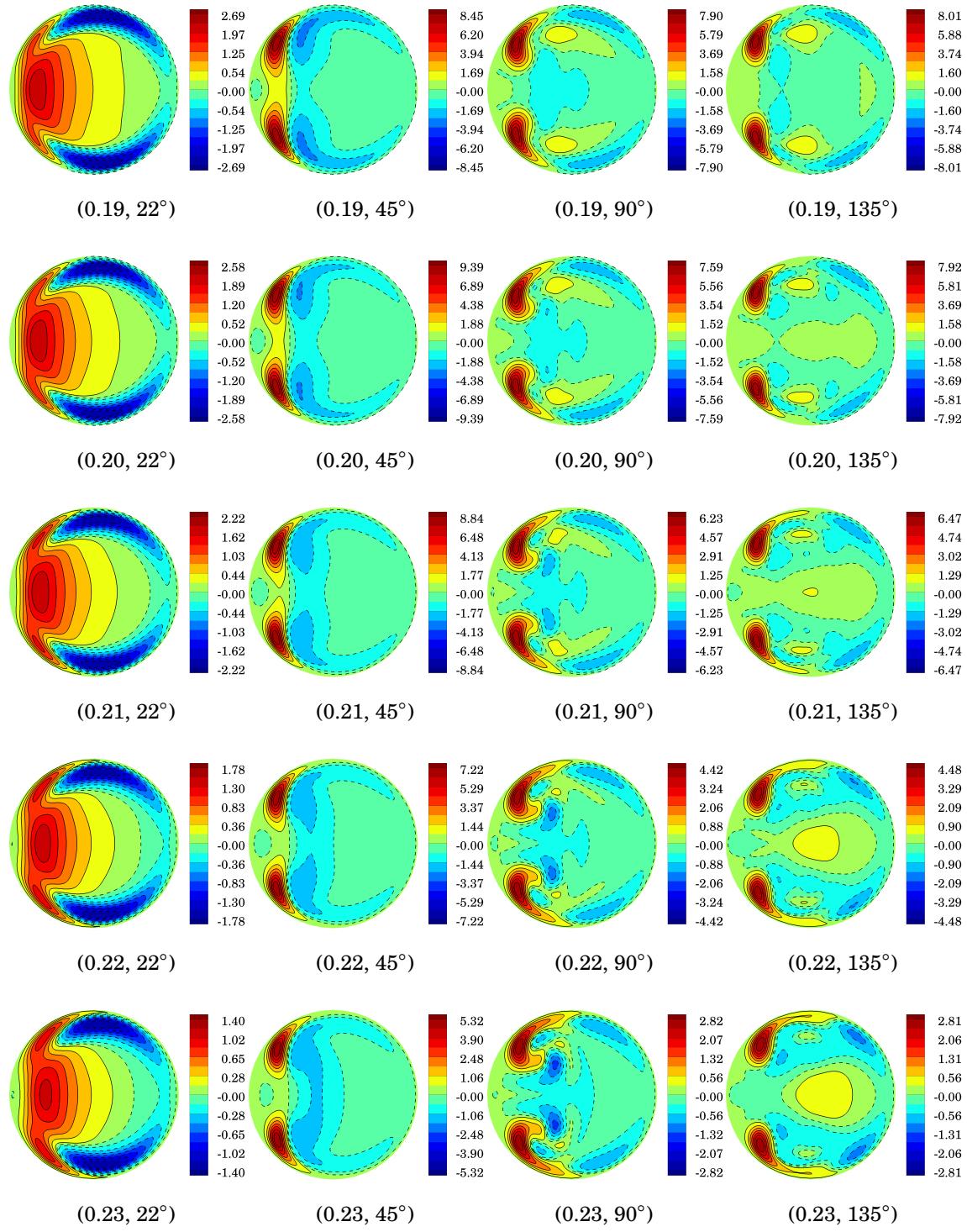


Figure 8.43 Uniform entrance condition: summation of non-dimensional centrifugal, pressure gradient and viscous forces along the radius of curvature direction $f_c^* + f_{pg}^* + f_v^*$ at (t^*, ϕ) .

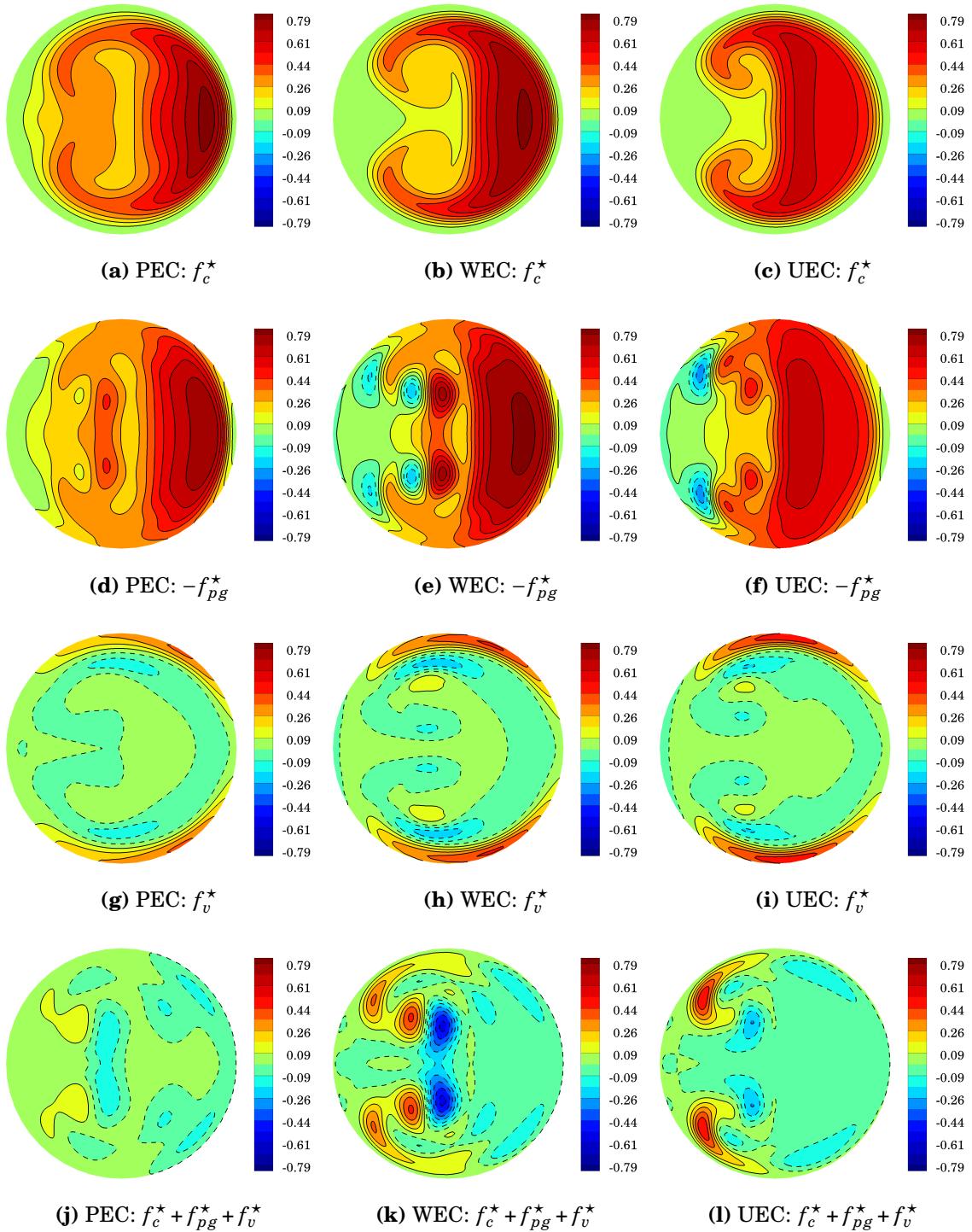


Figure 8.44 Non-dimensional centrifugal forces f_c^* , pressure gradient forces f_{pg}^* and viscous forces f_v^* at $\phi = 90^\circ$. Results from WEC (b,e,h,k) and UEC (c,f,i,l) are extracted from the pulsatile waveform at $t^* = 0.23$. The flow rates across PEC, WEC and UEC are equal with a bulk velocity $\bar{u} = 0.247$ m/s, corresponding to $Re = 883$. All results have been non-dimensionalized using \bar{u} as the velocity scale and contour levels for all images are equal.

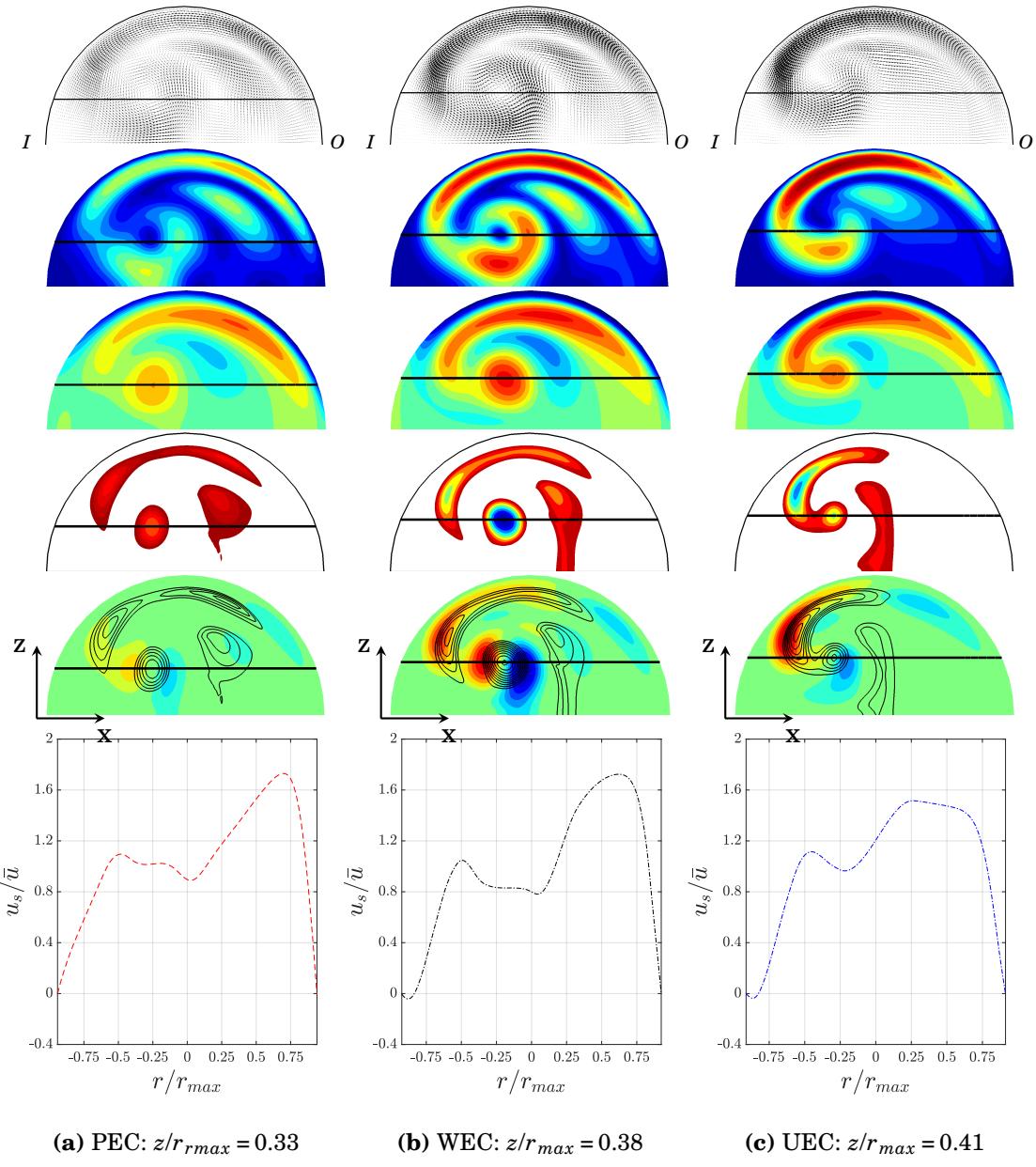


Figure 8.45 Non-dimensional streamwise velocity u_s^* profiles in the given z/r_{max} plane at $\phi = 90^\circ$ under (a) PEC, (b) WEC and (C) UEC. Images superimposed above profiles (top to bottom) are the following: secondary velocity vectors $\mathbf{u}_{\theta r}^*$, secondary velocity magnitude $|\mathbf{u}_{\theta r}^*|$, streamwise vorticity ω_s^* , λ_2^* , and force balance due to centrifugal forces, pressure gradient forces and viscous forces $f_c^* + f_{pg}^* + f_v^*$ (with contours of λ_2^*). Each superimposed image displays the position of the z/r_{max} plane from which the velocity profiles are extracted. Data in both (b) and (c) are extracted from the pulsatile waveform at $t^* = 0.23$. Flow rates of (a), (b) and (c) are equal with a bulk velocity $\bar{u} = 0.247$ m/s, corresponding to $Re = 883$. All results have been non-dimensionalized using \bar{u} as the velocity scale and contour levels for the various entrance conditions are equal for each flow variable. Inner (I) and outer (O) walls are indicated.

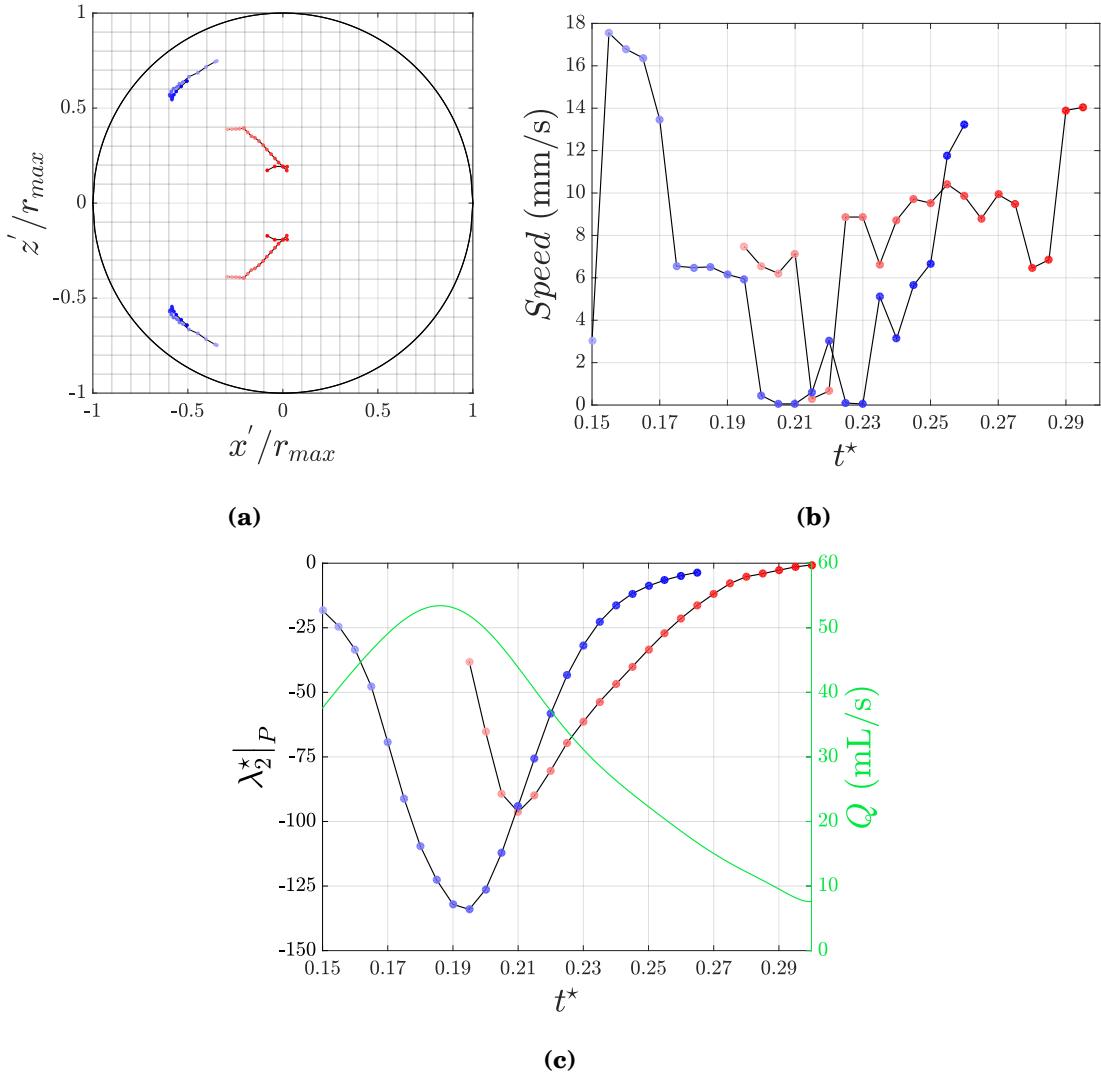


Figure 8.46 Split-Dean (red) and Deformed-Dean (blue) vortex core region trajectory during the phases $0.15 < t^* < 0.30$: (a) vortex trajectory at $\phi = 90^\circ$ of point $P(x', z', t)$ where largest negative value of $\lambda_2^* = \lambda_2 d^2/\bar{u}_{mean}^2$ occurs; (b) time evolution of estimated speed; (c) time evolution of $\lambda_2^*|_P$ superimposed on top of pulsatile flow rate Q (green).

The trajectory of the SD vortex above the plane of symmetry in Figure 8.46a is compared to the trajectory obtained experimentally by Najjari and Plesniak [129]. A comparison between these results is shown in Figure 8.47, where the plus symbols (+) represent the SD vortex trajectory obtained from experimental data. The width of each plus symbol is equal to the resolution of the experiment $\Delta x/d = 0.017$. The

discrepancy between the numerical and experimental data can be attributed to these facts:

1. The numerical results use the full velocity gradient tensor constructed from the three-dimensional velocity field whereas the experimental results use velocity gradients computed from the two-dimensional, secondary velocity field obtained using phase averaged 2C-2D PIV.
2. The numerical results are based upon the λ_2 -criterion while the experimental results are based upon the d_2 -criterion of Vollmers [130].
3. Undesired noise from experimental data can be characteristically problematic for derivative computations.
4. Due to manufacturing and assembly constraints, the experimental curved pipe geometry exhibits slight imperfections, particularly in the alignment and connection of straight and curved sections of pipe. This misalignment can produce slight asymmetries in the velocity field within the curve with respect to the $z = 0$ plane, which are amplified under lower flow rates experienced near the end of deceleration.

Considering items 1-4 explained above, the numerical and experimental results in Figure 8.47 agree extremely well. We analyze the difference in SD vortex trajectories obtained numerically and experimentally for each phase t . The distance Δl between point $P(x'_n, z'_n, t_n)$ obtained numerically, where λ_2 is largest, and point $P(x'_e, z'_e, t_e)$ obtained experimentally, where d_2 is largest, is computed using

$$\Delta l = \sqrt{\left(x'_n - x'_e\right)^2 + \left(z'_n - z'_e\right)^2}. \quad (8.44)$$

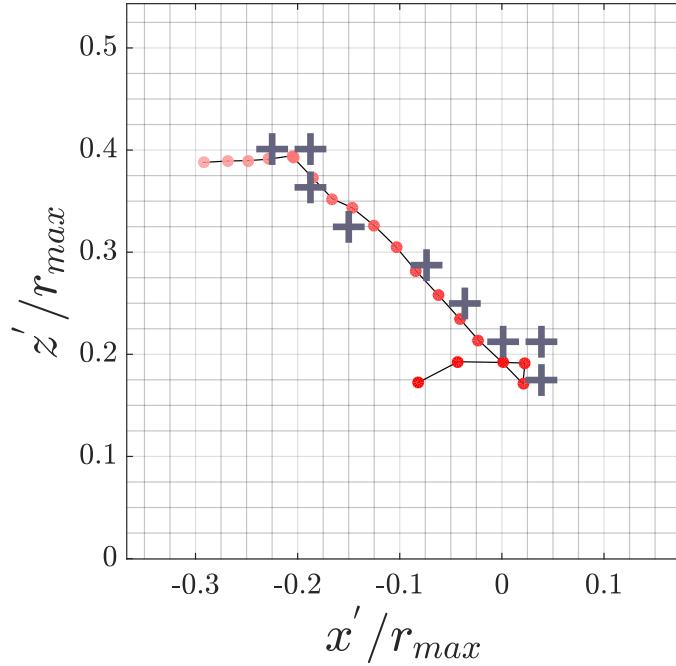


Figure 8.47 Split-Dean (SD) vortex trajectory above $z' = 0$: numerical data from $\lambda_2|_P$ (●), experimental data from $d_2|_P$ (+). Experimental data provided by Najjari and Plesniak (2017).

This distance can be normalized by the diameter of the SD vortex d_{SD} such that

$$\Delta l^* = \frac{\Delta l}{d_{SD}} \quad (8.45)$$

where Δl^* is a non-dimensional value. The size of the SD vortex at $t^* = 0.23$ is $d_{SD}/r_{max} = 0.365$. In other words, the SD vortex is approximately 18% of the pipe diameter when splitting initiates. Values of Δl^* are provided in Table 8.4 for $0.21 \leq t^* \leq 0.29$. These results demonstrate the distance between trajectories predicted numerically and experimentally. Close predictions occur early in the deceleration at $t^* = 0.21$ where Δl^* is 2.8%. At the end of deceleration at $t^* = 0.29$, where slight imperfections in the experimental geometry amplify asymmetries in the velocity field, Δl^* is 11.3%.

t^*	Δl^*	t^*	Δl^*
0.21	0.028	0.26	0.073
0.22	0.053	0.27	0.066
0.23	0.026	0.28	0.123
0.24	0.050	0.29	0.113
0.25	0.093		

Table 8.4 Non-dimensional distance Δl^* between numerical and experimental trajectories of the SD vortex shown in Figure 8.47 for phases $0.21 \leq t^* \leq 0.29$.

8.8 Wall Shear Stress in Pulsatile Flow

8.8.1 Instantaneous Wall Shear Stress

In this section, we compute the instantaneous wall shear stress vector at each solution node on the wall every $\Delta t^* = 0.005$ using the formulation given in Eq. (8.30). This time interval produces 200 data points over the pulsatile waveform from which we can compute the four different wall shear stress metrics described in Section 8.1. Results are generated for both fully developed and uniform entrance conditions. Since the flow is symmetric about $z = 0$, we plot results from the upper surface of the curved pipe only, where the orientation of the geometry is defined in Figure 8.48. To visualize results, we plot the data onto the $\phi\theta$ -axes shown in Figure 8.48c.

A side-by-side comparison of instantaneous wall shear stress obtained from WEC and UEC are plotted in Figure 8.49, where the wall shear stress vectors reflect the secondary flow pattern. Results have been extracted from peak flow rate at $t^* = 0.19$ through the end of deceleration at $t^* = 0.30$. At peak flow rate, the wall shear stress vectors are mostly angled toward the inner wall due to the secondary flow

caused by the curvature. At the inner and outer wall, the vectors are aligned with the streamwise direction. A local maximum in shear stress appears in both entrance conditions near $(\phi, \theta) = (45^\circ, 105^\circ)$, indicating strong secondary flow in this region. At this phase near the entrance, we also observe greater shear stress under UEC than WEC due to the larger velocity near the inner wall caused by the more uniform entrance velocity condition. This feature was explained earlier in Section 8.7.5. We also pointed out the cross-over in maximum wall shear stress from the inner wall to the outer wall and we revisit this concept here. The reason for this cross-over is due to the following explanation from Singh [101]: near the entrance of the curve at a given toroidal cross-section, the fluid experiences less resistance at the outer wall due to longer wall length and smaller streamwise velocity outside of the boundary layer; on the other hand, at the inner wall the fluid experiences more resistance owing to the shorter wall length and larger streamwise velocity. As the fluid moves farther downstream of the curve the situation reverses. Centrifugal forces become more apparent and the secondary flow skews the velocity profile towards the outer wall, thinning the boundary layer there and growing the boundary layer at the inner wall. This effect then causes the fluid to experience more resistance at the outer wall and less resistance at the inner wall, hence the cross-over in the location of maximum wall shear stress.

As systolic deceleration begins, shear stresses decrease globally while altering direction near the $\phi = 30^\circ$ plane such that vectors become less aligned with the streamwise direction and more aligned with the radius of curvature, particularly near the entrance. At $t^* = 0.21$, the fluid has slowed down near the inner wall causing the shear stress vector to decrease in magnitude before reversing direction. After this phase, the flow decelerates further, increasing the amount of reverse flow along the inner wall and causing the shear vectors to point upstream.

For WEC at $t^* = 0.23$, a small circular pocket of relatively large wall shear

stress appears at $\phi = 40^\circ$ and the shear vectors at $\phi = 15^\circ$ point directly towards the inner wall. Throughout the remaining phases of deceleration, the circular pocket of concentrated shear stress moves upstream while decreasing in magnitude. Over the entire systolic deceleration, the spatially averaged shear stress reduces by 86%. In the following sections, the various wall shear stress metrics are computed and results are discussed in the context of entrance conditions and vortex evolution.

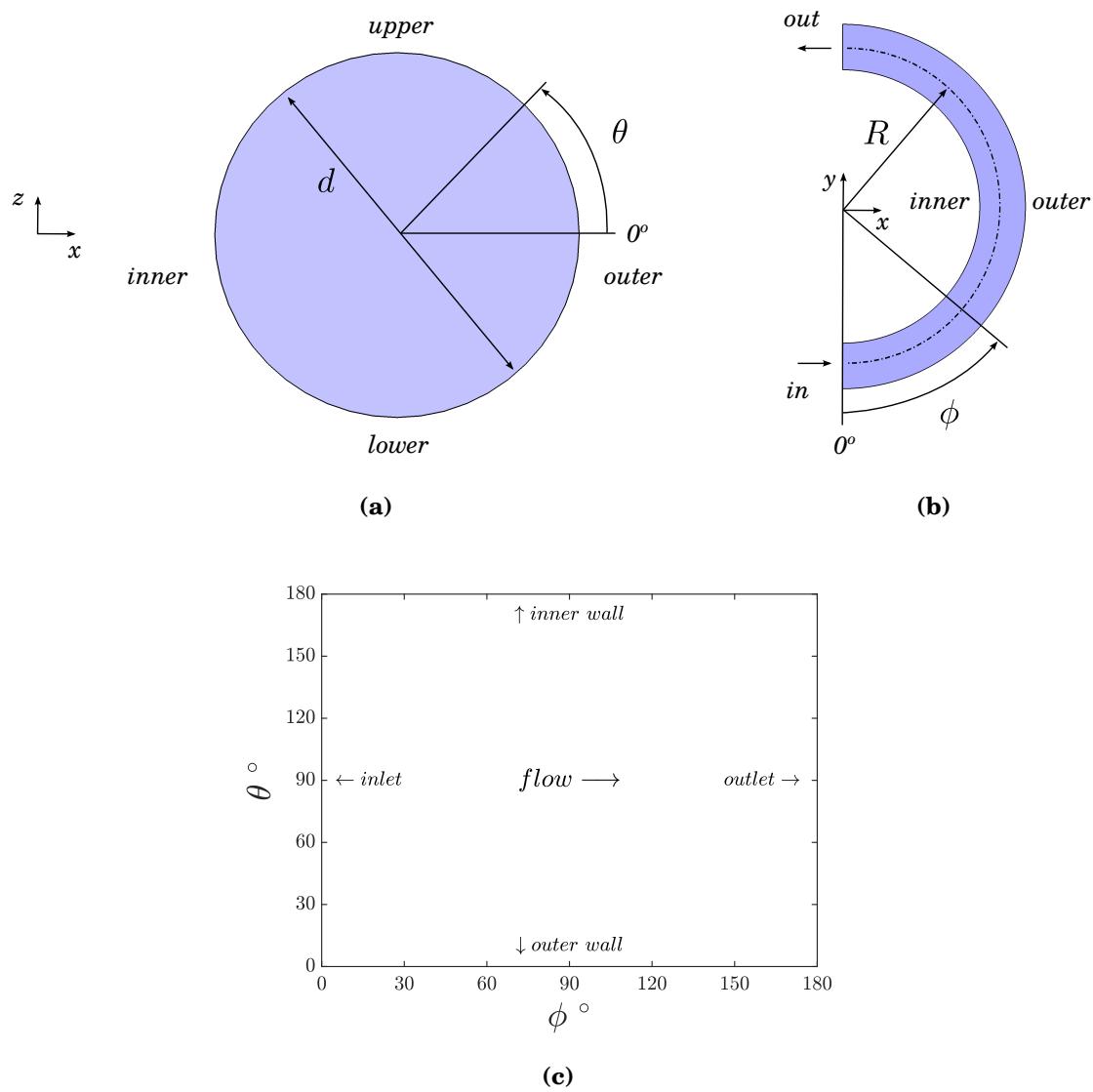


Figure 8.48 Curved pipe orientation and wall shear stress axis description. (a) cross-section planar view, (b) top planar view, (c) WSS axis description.

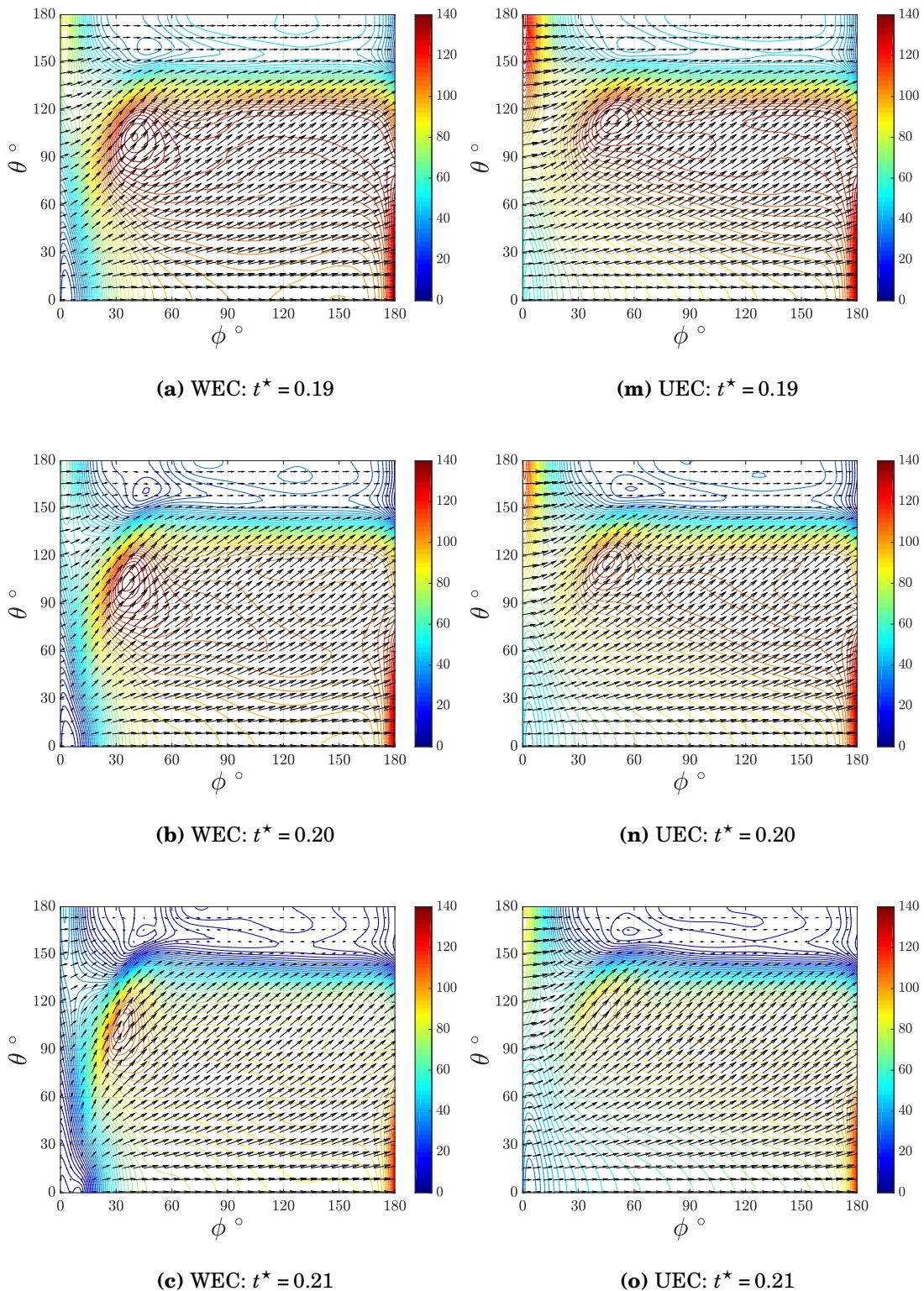


Figure 8.49 Instantaneous non-dimensional wall shear stress vectors τ_w^* with magnitude contours. (a)-(l) WEC, (m)-(x) UEC.

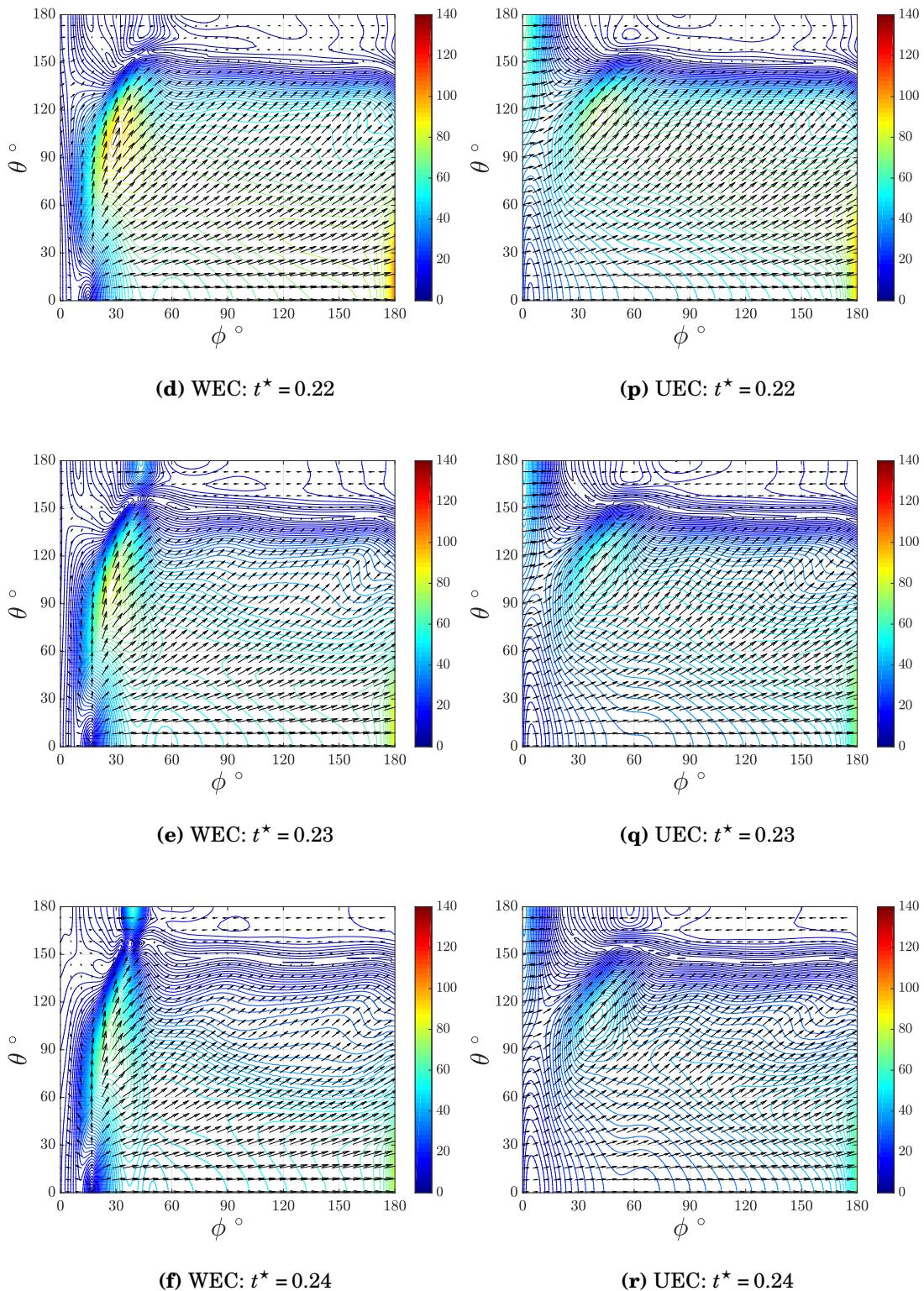


Figure 8.49 Instantaneous non-dimensional wall shear stress vectors τ_w^* with magnitude contours. (a)-(l) WEC, (m)-(x) UEC. (*continued*)

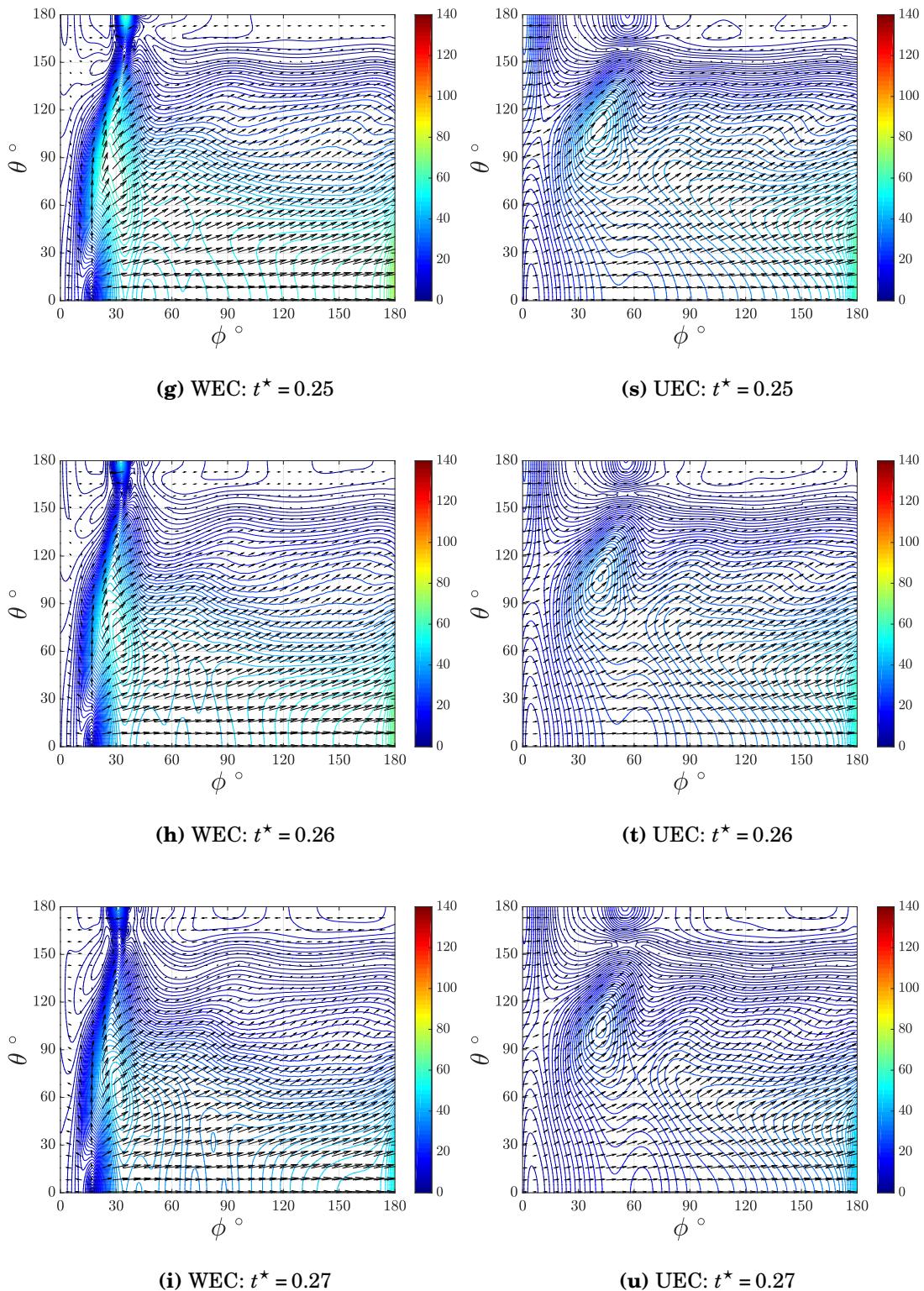


Figure 8.49 Instantaneous non-dimensional wall shear stress vectors τ_w^* with magnitude contours. (a)-(l) WEC, (m)-(x) UEC. (*continued*)

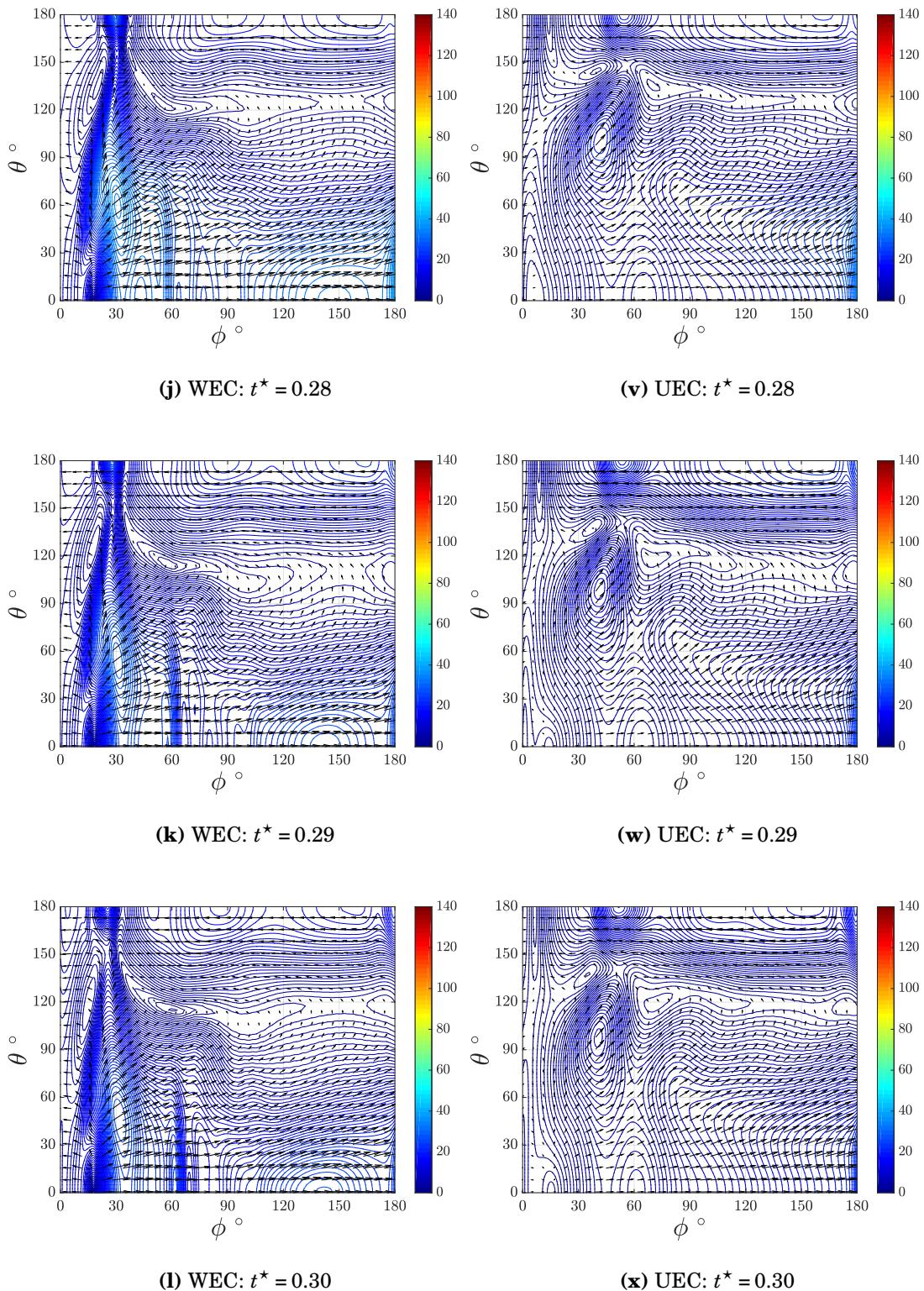


Figure 8.49 Instantaneous non-dimensional wall shear stress vectors τ_w^* with magnitude contours. (a)-(l) WEC, (m)-(x) UEC. (continued)

8.8.2 Time-Averaged Wall Shear Stress

Values of *time-averaged wall shear stress* are computed from the non-dimensional instantaneous wall shear stress vector $\tau_w^* = \tau_w d / \mu \bar{u}_{mean}$ evaluated at each node along the pipe wall by Eq. (8.30) and integrated over the non-dimensional pulsatile waveform period using

$$TAWSS^* = \int_0^1 |\tau_w^*| dt^*. \quad (8.46)$$

Results of $TAWSS^*$ at each wall node are plotted for both WEC and UEC in Figure 8.50. Under WEC, the outer wall experiences higher time-averaged wall shear stress than the inner wall due to the combination of a skewed velocity profile and the absence of reverse flow. For example, a high value of $TAWSS^*$ occurs near the location $(\theta, \phi) = (45^\circ, 45^\circ)$ due to the high wall shear stress resulting from strong secondary flow in that region and no prevalence of reverse flow. Under both WEC and UEC, maximum values occur at the exit for $\theta < 60^\circ$. Low values occur mostly along the inner wall where $15^\circ < \phi < 180^\circ$ and near the entrance for $\theta < 90^\circ$ and $0^\circ < \phi < 15^\circ$. Furthermore, UEC produces higher values of $TAWSS^*$ just downstream of the entrance and towards the inner wall. This is due to higher wall shear stress values produced from higher flow velocities at the inner wall under UEC. The “switching” phenomenon in maximum shear stress that was explained earlier is reflected in the plot of $TAWSS^*$ just downstream of the entrance. The non-dimensional min/max contour levels correspond to 2.50/8.75 dyn/cm², assuming $\rho = 1060$ kg/m³ for the density of blood plasma.

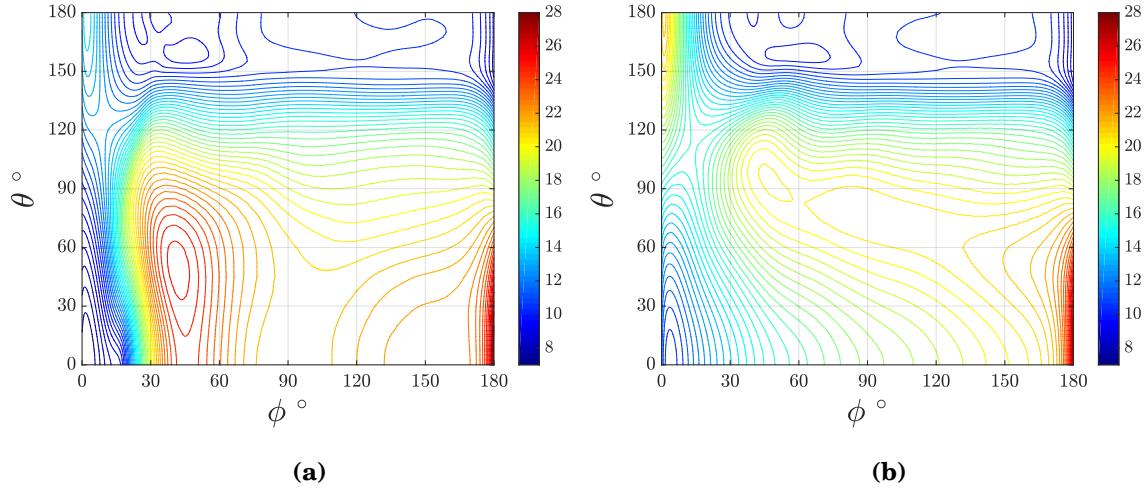


Figure 8.50 Non-dimensional time averaged wall shear stress $TAWSS^*$: (a) Womersley entrance condition, (b) Uniform entrance condition.

8.8.3 Oscillatory Shear Index

The *oscillatory shear index* of He and Ku [95] computed as

$$OSI = \frac{1}{2} \left(1 - \frac{|\tau_{mean}^*|}{TAWSS^*} \right) \quad (8.47)$$

where

$$\tau_{mean}^* = \int_0^1 \tau_w^* dt^* \quad (8.48)$$

is a uniaxial metric that has been used by many authors to identify the oscillatory nature of vascular flows. The theoretical value of OSI can vary from zero to 0.5, the minimum occurring when the mean wall shear vector equals the time-averaged wall shear vector and the maximum occurring when the mean vector is zero. In our results, the maximum OSI obtained is about half the maximum theoretical value. As pointed out by Himborg et al. [96], OSI can identify regions of flow reversal;

however, it is insensitive to shear stress magnitude.

Values of OSI are plotted in Figure 8.51. Results between WEC and UEC are quite similar for $\phi > 60^\circ$. The sharp gradient indicated by the cluster of contour lines at $\theta = 150^\circ$ reflects the higher values near the inner wall that are mainly due to flow reversal during the deceleration phase of the pulsatile waveform. For $\phi < 60^\circ$, the results between WEC and UEC are noticeably different. Under WEC, a pocket of high OSI occurs at the inner wall where $\phi = 33^\circ$. This value reflects the large local flow reversal at this location, indicated by the shear vectors in Figure 8.49 between $0.23 < t^* < 0.27$. Furthermore, large values of OSI are also seen along the outer wall near the entrance where $\phi < 15^\circ$. The value in this region also indicates flow reversal due to the nature of the fully developed entrance condition, which produces reverse flow near the pipe walls. Under UEC, we do not see any increase in OSI near the entrance to the curve because the velocity condition prescribed there is uniform and always streamwise positive. A pocket of increased OSI also occurs along the inner wall; however, it appears further downstream at $\phi = 56^\circ$ and is roughly 75% of the value obtained under WEC.

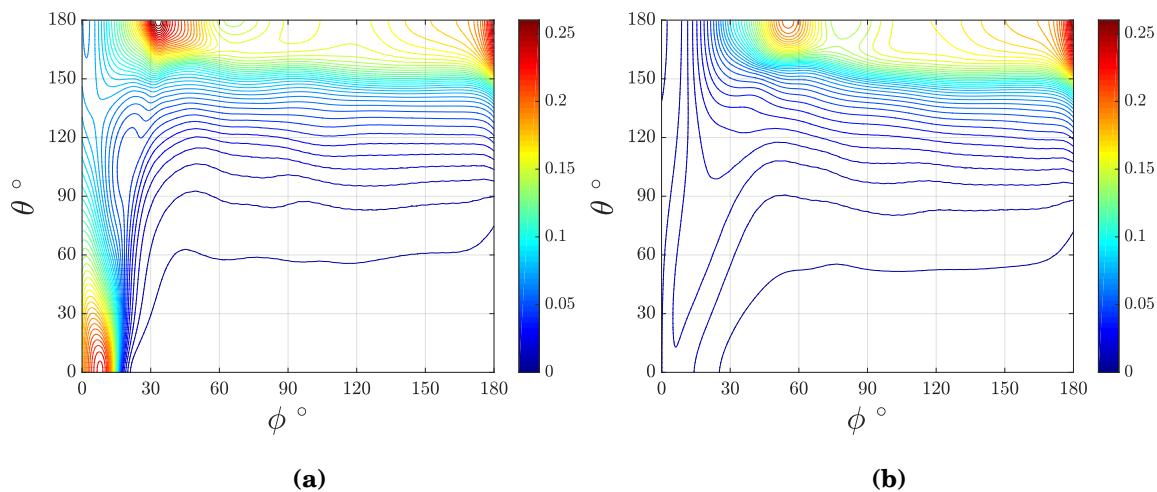


Figure 8.51 Oscillatory shear index OSI : (a) Womersley entrance condition, (b) Uniform entrance condition.

To study more closely the increased *OSI* along the inner wall, we plot the $\lambda_2^* = -15$ isosurface at $t^* = 0.26$ superimposed above the plane of symmetry in Figure 8.52. Also, we plot the wall shear stress and wall pressure in Figure 8.53. Figure 8.52a shows streamlines and ω_z^* in the $z = 0$ plane of symmetry, highlighting the strong shear located along the inner wall at $\phi = 33^\circ$. Figure 8.52b shows the $\lambda_2^* = -15$ isosurface colored by streamwise vorticity ω_s^* and demonstrates proximity of the small vortical structure to the inner wall at this toroidal location where the strong wall shear exists. The coloring of the isosurface by streamwise vorticity indicates the multi-directionality of the streamwise vorticity vector, pointing upstream (red) and downstream (blue). The creation of this small vortical structure (colored in blue) is due to strong reverse flow at this location, creating streamwise vorticity opposite to the larger, Deformed-Dean structure (colored in red).

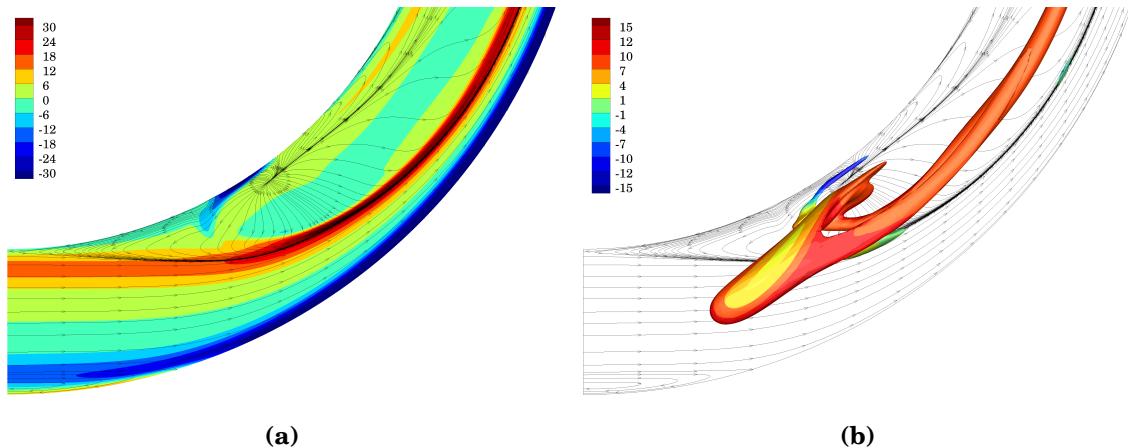


Figure 8.52 Womersley entrance condition at $t^* = 0.26$: (a) streamlines and ω_z^* in the $z = 0$ plane of symmetry, (b) superimposed $\lambda_2^* = -15$ isosurface above $z = 0$ colored by streamwise vorticity ω_s^* (red - ω_s^* points upstream, blue - ω_s^* points downstream).

The effect of the vortical structure on the instantaneous wall shear stress and wall pressure at the inner wall at the phase $t^* = 0.26$ is represented by Figure 8.53. Data has been extracted from the inner wall at $\theta = 180^\circ$ throughout the entire curve

from $0^\circ < \phi < 180^\circ$ for both WEC (black) and UEC (blue). Under WEC at this phase, a maximum value of negative wall shear stress occurs at $\phi = 33^\circ$, indicating locally strong flow reversal. The sharp increase in wall shear stress magnitude at this location is accompanied by a sudden pressure drop. These features are imprinted onto the wall by the vortical structure due to its spatial proximity. Under UEC, such a strong imprint does not occur, although a local maximum value of negative wall shear stress does appear at $\phi = 56^\circ$. This value corresponds to the small pocket of increased *OSI* under UEC.

Three-dimensional streamlines at $t^* = 0.26$ shown in Figure 8.54 depict the skewness in the maximum streamwise velocity towards the outer wall as well as a critical point - encircled by the dashed line - in the $z = 0$ plane at $\phi = 32^\circ$. This critical point is due to strong secondary flow, which is symmetric about $z = 0$ and indicated by the outer-to-inner curvature of streamlines. This critical point in the flow moves upstream as the flow decelerates and causes the streamlines to emanate from this node in all directions, thereby forming another critical point on the inner wall where the streamlines attach. The formation of this critical point on the wall is slightly downstream of the location of increased wall shear shown previously in Figure 8.52a.

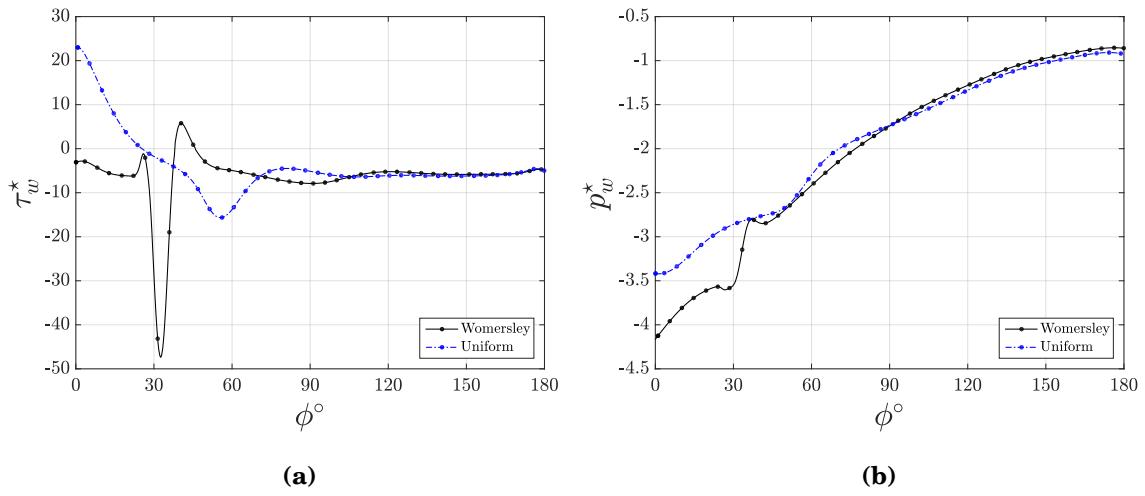


Figure 8.53 (a) non-dimensional wall shear stress vector $\tau_w^*(\phi)$ and (b) non-dimensional wall pressure $p_w^*(\phi)$ along inner wall at $\theta = 180^\circ$ under WEC (—) and UEC (---).

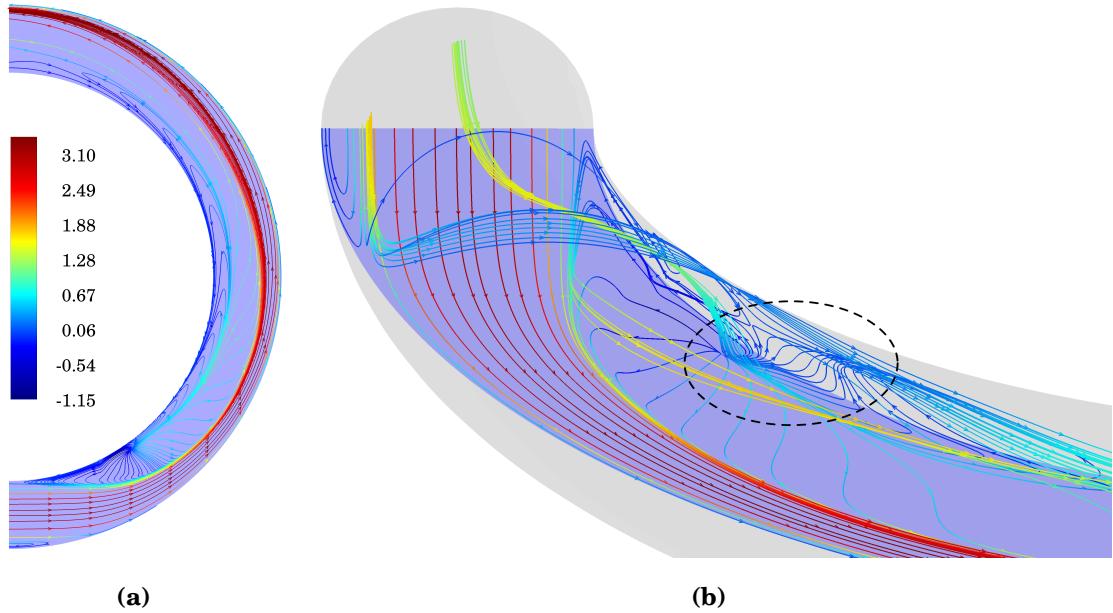


Figure 8.54 Womersley entrance condition at $t^* = 0.26$: (a) streamlines in the $z = 0$ plane of symmetry, (b) streamlines near curve entrance, indicating region of critical points during deceleration near the inner wall, where $25^\circ < \phi < 35^\circ$. Streamlines are colored by the non-dimensional streamwise velocity u_s^* .

8.8.4 Relative Residence Time

The *relative residence time* metric of Himborg et al. [96] is a relative concept since all particles move in the flow and therefore exhibit zero residence time. The formulation of this metric is based upon the idea that an entrained particle located a small distance a from the wall travels a distance $L(a)$ during one cardiac cycle given by

$$L(a) = \frac{T a}{\mu} TAWSS^* (1 - 2 OSI) \quad (8.49)$$

where T is the cardiac cycle period. Since RRT is inversely proportional to L , we can write

$$RRT^* \sim \frac{1}{TAWSS^* (1 - 2 OSI)}. \quad (8.50)$$

Similar to OSI , it is a uniaxial metric whereby the OSI modifies the effect of time-averaged wall shear stress on the relative residence time. As the OSI approaches zero it has little effect on RRT , which becomes inversely proportional to the time-averaged wall shear stress. On the other hand, OSI has an increasingly larger effect on RRT as it approaches the upper limit of 0.5, alluding to the local oscillatory nature of the shear.

Results of RRT for our pulsatile flow rate using WEC and UEC are plotted in Figure 8.55. Since the maximum value of OSI is ~ 0.25 and the minimum value of $TAWSS^*$ is ~ 8 , the maximum value of RRT is also ~ 0.25 . The pattern of RRT looks quite similar to OSI , supporting the description above that higher values of OSI have a larger effect on RRT . Therefore, the vortical structure shown in Figure 8.52b causes a similar effect on RRT as it does on OSI . Comparing the results between WEC and UEC, the former produces much larger RRT values near the entrance along the outer wall due to the flow reversal inherent to that entrance condition.

This feature was also reflected in the plots of *OSI*.

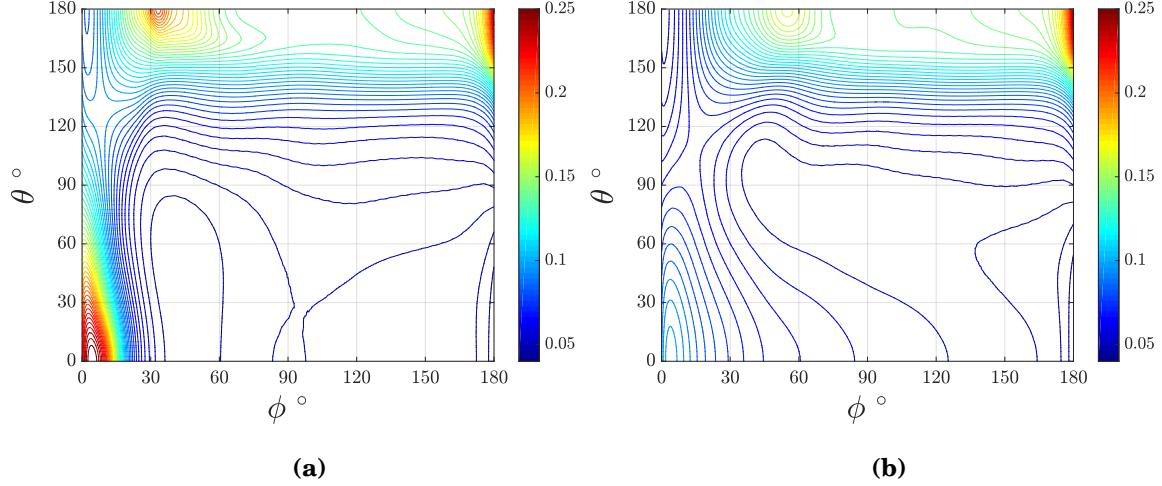


Figure 8.55 Non-dimensional relative residence time RRT^* : (a) Womersley entrance condition, (b) Uniform entrance condition.

8.8.5 Transverse Wall Shear Stress

Although widely popular, the vascular metrics *TAWSS*, *OSI* and *RRT* presented thus far are not designed to distinguish between uniaxial and multidirectional flows. This fact motivated the development of the *transverse wall shear stress* metric by Peiffer et al. [94], which is computed as the time-average of the magnitude of wall shear stress components perpendicular to the mean shear vector at each node on the wall. The formulation for this metric based upon the non-dimensional shear vector is

$$TransWSS^* = \int_0^1 \left| \boldsymbol{\tau}_w^* \cdot \left(\mathbf{n} \times \frac{\boldsymbol{\tau}_{mean}^*}{|\boldsymbol{\tau}_{mean}^*|} \right) \right| dt^* \quad (8.51)$$

where \mathbf{n} is the vector normal to the wall. We can see from Eq. (8.51) that the term $\mathbf{n} \times \boldsymbol{\tau}_{mean}^* / |\boldsymbol{\tau}_{mean}^*|$ represents the unit vector in the plane of the wall that is

perpendicular to mean shear vector τ_{mean}^* . The dot product of the instantaneous shear vector with this unit vector gives the amount of the shear stress projected in the direction perpendicular to τ_{mean}^* . Integrating this value over the cardiac cycle produces the *TransWSS* * metric at each location on the wall, which can theoretically range in value from zero to *TAWSS* * . Low values of *TransWSS* * indicate alignment of the shear vector primarily with a single direction, whereas high values signify multidirectionality. Peiffer et al. note that since this metric cannot distinguish between strictly positive flow and pulsatile flow with reversal, it is not meant to replace *TAWSS* * , *OSI* or *RRT* * but to complement them.

Maps of *TransWSS* * for our pulsatile simulations are shown in Figure 8.56 for both WEC and UEC. Along the inner and outer walls at $\theta = 180^\circ$ and $\theta = 0^\circ$, respectively, *TransWSS* * is zero because the flow is always uniaxial close to the walls at the $z = 0$ plane of symmetry. Downstream of $\phi = 60^\circ$, results appear similar. Upstream of $\phi = 60^\circ$, however, the picture is quite different - a region of high *TransWSS* * is seen under WEC for $15^\circ < \theta < 130^\circ$ and $10^\circ < \phi < 30^\circ$ with a maximum value of 6.1 (1.88 dyn/cm 2) at $(\phi, \theta) = (20^\circ, 78^\circ)$. This increase in *TransWSS* * reflects the multidirectionality of the wall shear stress vector in this region, which in turn is the result of varying degrees of secondary motion. Under UEC, a maximum value of 4.0 (1.25 dyn/cm 2) occurs at $(\phi, \theta) = (40^\circ, 118^\circ)$. From these results, we can conclude that for the current idealized geometry and physiological waveform, a fully developed pulsatile entrance condition produces *TransWSS* * values approximately 50% greater than a uniform pulsatile entrance condition. Since the Deformed-Dean vortex is generated by secondary flow due to curvature and the magnitude of secondary flow varies throughout the pulsatile cycle, we can conclude that alternating strength of the Deformed-Dean vortex near the entrance to the pipe curvature produces high *TransWSS* * in that region and that these results are sensitive to the entrance flow condition. The direct correlation between the evolution

of the Deformed-Dean vortex and $TransWSS^*$ metric aligns with the finding in Mohamied et al. [131] that fluctuating formation of Dean vortices plays an important role in generating $TransWSS^*$.

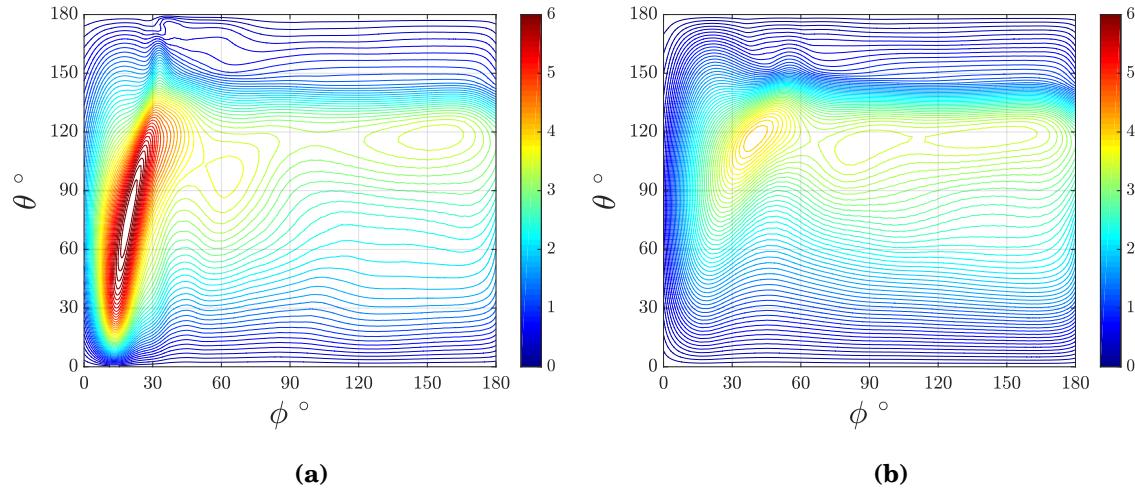


Figure 8.56 Non-dimensional transverse wall shear stress $TransWSS^*$: (a) Womersley entrance condition, (b) Uniform entrance condition.

Chapter 9

Conclusions

Cardiovascular flows are pulsatile and incompressible, and human arteries often follow a path that can curve, twist, taper, bifurcate, and vary in cross-sectional shape. Together, these effects produce a vortex-rich environment that can affect the progression of atherosclerosis by altering wall shear stresses. The wall shear stress is one of the most physiologically relevant factors within the cardiovascular system, affecting endothelial cells via mechanotransduction. Atherosclerotic regions are strongly correlated with curvature and branching, where the flow is both oscillatory and multidirectional. To study the underlying flow physics of pulsatile flow through a curved artery without the added complexity of variable geometry, we use the parallel high-order flux reconstruction Navier-Stokes solver developed in Part I to perform numerical simulations of a Newtonian blood-analog fluid subjected to a physiological waveform in a rigid 180° curved pipe with circular cross-section and constant curvature with zero torsion. Three different inlet conditions to the curve were studied; fully developed steady (i.e. Poiseuille) entrance flow, fully developed pulsatile (i.e. Womersley) entrance flow, and undeveloped (i.e. uniform) pulsatile entrance flow. We characterized both pulsatility and curvature effects on the flow, as well as the temporal and spatial evolution of complex three-dimensional vortex structures and their influence on the wall shear stress.

Pulsatility effects were found to include the reduction in maximum streamwise velocity due to the inertia of the fluid associated with the frequency of pulsatility and the enhanced secondary motion during deceleration of the pulsatile waveform, creating a stronger Split-Dean vortex than the corresponding steady entrance condition with the same flow rate. We also found that the Split-Dean vortex is stronger under the Womersley entrance condition than it is under the Poiseuille or uniform entrance condition, indicating that increased vortical activity results from the combined effect of pulsatility and entrance condition. Furthermore, our results show that above the plane of symmetry positive primary flow creates counter-

clockwise secondary flow, and negative primary flow (or flow reversal) creates localized clockwise secondary flow at the inner wall. This localized secondary flow at the inner wall, in turn, generates a small pair of vortex structures rotating in the opposite sense to the larger Deformed-Dean and Split-Dean vortices. Since reversed flow in this range of Dean numbers only occurs during the main deceleration phase of the pulsatile waveform, the generation of these structures is solely due to pulsatility effects.

The appearance of the aforementioned Deformed-Dean and Split-Dean vortices is an effect of curvature, since we observe both pairs of vortices under Poiseuille, Womersley and uniform entrance conditions. Furthermore, we observe that vorticity associated with the Lyne-type vortex appears for both steady and pulsatile entrance conditions. This vortex appears once the secondary flow is sufficiently strong and the slower moving fluid near the wall moves inward while the faster moving fluid away from the wall moves outward, causing the streamwise velocity to peak towards the outer wall and depress towards the inner wall. The reduced streamwise velocity corresponding to Deformed-Dean streamwise vorticity induces the formation of Lyne-type streamwise vorticity. For a sufficiently high Dean number, a counter-clockwise rotating Deformed-Dean vortex is accompanied by a clockwise rotating Lyne-type vortex. Therefore, the appearance of Lyne-type vortices in this context is considered a curvature effect. Also, since the Deformed-Dean vortex initially splits into two regions halfway downstream of the curve entrance under both fully developed steady flow and fully developed pulsatile flow, Deformed-Dean vortex splitting is considered a curvature effect. However, the phase at which splitting occurs is a pulsatility effect - the more "in phase" pressure gradient and flow rate become, the earlier in the pulsatile period that vortex splitting occurs. Vorticity field analysis indicates that vortex lines associated with the Split-Dean vortex are aligned with the primary flow direction at the 90° location, as opposed to vortex lines associated with the Lyne-

type vortex. This is evidence that Split-Dean streamwise vorticity is due to swirling motions caused by curvature and Lyne-type vorticity is largely due to shear.

A force balance analysis with respect to the radius of curvature direction indicates that the position of the Split-Dean vortex within the cross-section is maintained by the combination of centrifugal and pressure gradient forces. This balance of forces is explained by an analysis of the Split-Dean vortex strength and trajectory, which demonstrates that vortical motion of the Deformed-Dean vortex decreases while that of the Split-Dean vortex increases during the deceleration phase, ultimately leading to vortex splitting. Numerical results of secondary velocity magnitudes and the Split-Dean vortex trajectory during deceleration are in strong agreement with results obtained from experimental PIV data.

Lastly, our results demonstrate that the formation of Deformed-Dean and inner wall vortex structures have a direct effect on common wall shear stress metrics such as the *oscillatory shear index (OSI)* and *transverse wall shear stress (TransWSS)*, particularly when the flow entering the curve is fully developed. A fully developed entrance condition generates larger *OSI* along the inner wall due to local generation of vortical structures during deceleration. We conclude there is an imprint of the vortex on the wall by showing locally increased wall shear stress accompanied by a drop in pressure. Furthermore, we show that the fully developed condition generates larger *TransWSS* near the entrance to the curve due to multidirectionality of the wall shear stress vector caused by strong fluctuation of the Deformed-Dean vortex. These results highlight the importance of the entrance condition to the curved artery model in producing oscillatory and multidirectional flow, its effect on shear stress metrics and its potential role in the progression of atherosclerosis.

9.1 Future Directions for Research

Variable Geometry and Fluid

The are a multitude of alterations that can be made to the current idealized curved pipe from which more detailed analysis of the three-dimensional vortex structures can be made. One such modification involves the addition of taper or torsion to account for realistic variations in the actual geometry of a human curved artery. A second modification is axial variation of the pipe diameter within the curve to understand the effect of stenosed arteries on secondary flow vortical structures. Furthermore, the assumption of Newtonian flow for large arteries in the presence of secondary flows may not be as valid as previously thought [132]. This warrants an investigation of the non-Newtonian effect on secondary flow patterns and a comparison to experimental data obtained by Najjari and Plesniak [117].

Fluid Structure Interaction

Another alteration to the model could involve dynamically changing the radius of curvature as well as the radius of the pipe to study its effect on secondary flow structures and wall shear stress. This may be of interest due to the fact that the coronary arteries, which are subject to atherosclerosis, arise from the aorta and run along the surface of the heart, which alternately contracts and expands to pump blood. The coronary arteries are part of the coronary circulation and are responsible for transporting oxygen-rich blood to the entire heart muscle. Of course, to perform such a simulation a numerical implementation of the fluid-structure interaction is needed.

Appendix A

Two-Dimensional Mapping and Basis Functions

A.1 4-Node Quadrilateral Element

Bilinear ansatz for global coordinate x :

$$x(\xi, \eta) = a_1 + a_2\xi + a_3\eta + a_4\xi\eta \quad (\text{A.1})$$

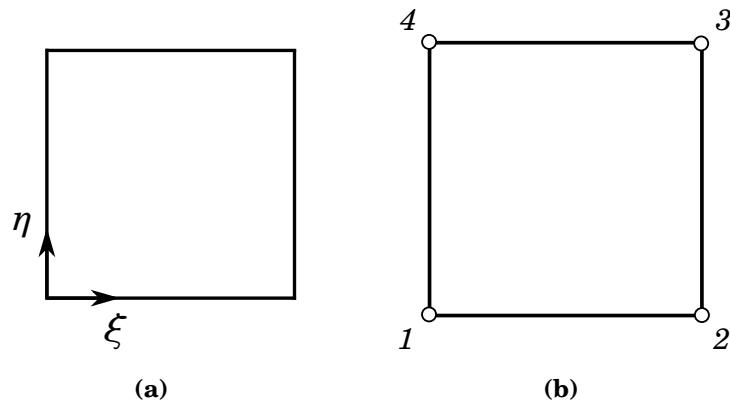


Figure A.1 Orientation of 4-node reference element $\Omega_r = \{\xi, \eta \mid 0 \leq \xi, \eta \leq 1\}$.

Global coordinate of each element node x_i :

$$x_1 = x(0, 0) = a_1 \quad (\text{A.2})$$

$$x_2 = x(1, 0) = a_1 + a_2 \quad (\text{A.3})$$

$$x_3 = x(1, 1) = a_1 + a_2 + a_3 + a_4 \quad (\text{A.4})$$

$$x_4 = x(0, 1) = a_1 + a_3 \quad (\text{A.5})$$

Express in matrix form:

$$\mathbf{x} = \mathbf{B}\mathbf{a} \quad (\text{A.6})$$

Write coefficients a_i as a function of global coordinates x_i :

$$\boldsymbol{a} = \boldsymbol{B}^{-1} \boldsymbol{x} \quad (\text{A.7})$$

Obtain linear basis functions ϕ_i by substituting coefficients from A.7 into A.1:

$$\phi_1 = (\xi - 1)(\eta - 1) \quad (\text{A.8})$$

$$\phi_2 = -\xi(\eta - 1) \quad (\text{A.9})$$

$$\phi_3 = \xi\eta \quad (\text{A.10})$$

$$\phi_4 = -\eta(\xi - 1) \quad (\text{A.11})$$

Map the local coordinate (ξ, η) to the global coordinate (x, y) :

$$x(\xi, \eta) = \sum_{k=1}^4 x_k \phi_k(\xi, \eta) \quad (\text{A.12})$$

$$y(\xi, \eta) = \sum_{k=1}^4 y_k \phi_k(\xi, \eta) \quad (\text{A.13})$$

Evaluate basis function derivatives $\partial\phi_k/\partial\xi$, $\partial\phi_k/\partial\eta$ and the Jacobian matrix:

$$\boldsymbol{J} = \frac{\partial(x, y)}{\partial(\xi, \eta)} = \begin{bmatrix} \frac{\partial x}{\partial \xi} & \frac{\partial x}{\partial \eta} \\ \frac{\partial y}{\partial \xi} & \frac{\partial y}{\partial \eta} \end{bmatrix} \quad (\text{A.14})$$

A.2 8-Node Quadrilateral Element

Biquadratic (serendipity) ansatz for global coordinate x :

$$x(\xi, \eta) = a_1 + a_2\xi + a_3\eta + a_4\xi^2 + a_5\xi\eta + a_6\eta^2 + a_7\xi^2\eta + a_8\xi\eta^2 \quad (\text{A.15})$$

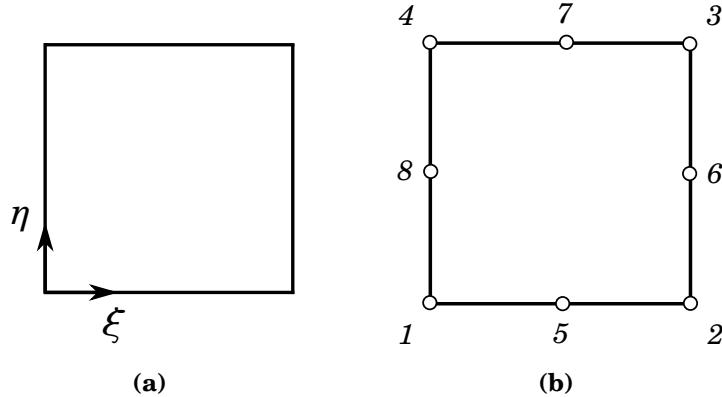


Figure A.2 Orientation of 8-node reference element $\Omega_r = \{\xi, \eta \mid 0 \leq \xi, \eta \leq 1\}$.

Global coordinate of each element node x_i :

$$x_1 = x(0, 0) = a_1 \quad (\text{A.16})$$

$$x_2 = x(1, 0) = a_1 + a_2 + a_4 \quad (\text{A.17})$$

$$x_3 = x(1, 1) = a_1 + a_2 + a_3 + a_4 + a_5 + a_6 + a_7 + a_8 \quad (\text{A.18})$$

$$x_4 = x(0, 1) = a_1 + a_3 + a_6 \quad (\text{A.19})$$

$$x_5 = x\left(\frac{1}{2}, 0\right) = a_1 + \frac{1}{2}a_2 + \frac{1}{4}a_4 \quad (\text{A.20})$$

$$x_6 = x\left(1, \frac{1}{2}\right) = a_1 + a_2 + \frac{1}{2}a_3 + a_4 + \frac{1}{2}a_5 + \frac{1}{4}a_6 + \frac{1}{2}a_7 + \frac{1}{4}a_8 \quad (\text{A.21})$$

$$x_7 = x\left(\frac{1}{2}, 1\right) = a_1 + \frac{1}{2}a_2 + a_3 + \frac{1}{4}a_4 + \frac{1}{2}a_5 + a_6 + \frac{1}{4}a_7 + \frac{1}{2}a_8 \quad (\text{A.22})$$

$$x_8 = x\left(0, \frac{1}{2}\right) = a_1 + \frac{1}{2}a_3 + \frac{1}{4}a_6 \quad (\text{A.23})$$

Express in matrix form:

$$\mathbf{x} = \mathbf{B}\mathbf{a} \quad (\text{A.24})$$

Write coefficients a_i as a function of global coordinates x_i :

$$\boldsymbol{a} = \boldsymbol{B}^{-1} \boldsymbol{x} \quad (\text{A.25})$$

Obtain quadratic basis functions ϕ_i by substituting coefficients from A.25 into A.15:

$$\phi_1 = -(\xi - 1)(\eta - 1)(2\eta + 2\xi - 1) \quad (\text{A.26})$$

$$\phi_2 = \xi(\eta - 1)(2\eta - 2\xi + 1) \quad (\text{A.27})$$

$$\phi_3 = \xi\eta(2\eta + 2\xi - 3) \quad (\text{A.28})$$

$$\phi_4 = \eta(\xi - 1)(2\xi - 2\eta + 1) \quad (\text{A.29})$$

$$\phi_5 = 4\xi(\xi - 1)(\eta - 1) \quad (\text{A.30})$$

$$\phi_6 = -4\xi\eta(\eta - 1) \quad (\text{A.31})$$

$$\phi_7 = -4\xi\eta(\xi - 1) \quad (\text{A.32})$$

$$\phi_8 = 4\eta(\xi - 1)(\eta - 1) \quad (\text{A.33})$$

Map the local coordinate (ξ, η) to the global coordinate (x, y) :

$$x(\xi, \eta) = \sum_{k=1}^8 x_k \phi_k(\xi, \eta) \quad (\text{A.34})$$

$$y(\xi, \eta) = \sum_{k=1}^8 y_k \phi_k(\xi, \eta) \quad (\text{A.35})$$

Evaluate basis function derivatives $\partial\phi_k/\partial\xi$, $\partial\phi_k/\partial\eta$ and the Jacobian matrix:

$$\boldsymbol{J} = \frac{\partial(x, y)}{\partial(\xi, \eta)} = \begin{bmatrix} \frac{\partial x}{\partial \xi} & \frac{\partial x}{\partial \eta} \\ \frac{\partial y}{\partial \xi} & \frac{\partial y}{\partial \eta} \end{bmatrix} \quad (\text{A.36})$$

A.3 12-Node Quadrilateral Element

Bicubic (serendipity) ansatz for global coordinate x :

$$x(\xi, \eta) = a_1 + a_2\xi + a_3\eta + a_4\xi^2 + a_5\xi\eta + a_6\eta^2 + a_7\xi^3 + a_8\xi^2\eta + a_9\xi\eta^2 + a_{10}\eta^3 + a_{11}\xi^3\eta + a_{12}\xi\eta^3 \quad (\text{A.37})$$

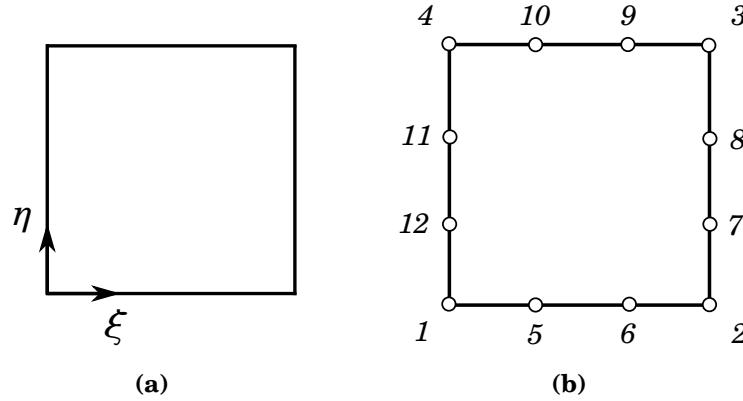


Figure A.3 Orientation of 12-node reference element $\Omega_r = \{\xi, \eta \mid 0 \leq \xi, \eta \leq 1\}$.

Global coordinate of each element node x_i :

$$x_1 = x(0, 0) = a_1 \quad (\text{A.38})$$

$$x_2 = x(1, 0) = a_1 + a_2 + a_4 + a_7 \quad (\text{A.39})$$

$$x_3 = x(1, 1) = a_1 + a_2 + a_3 + a_4 + a_5 + a_6 + a_7 + a_8 + a_9 + a_{10} + a_{11} + a_{12} \quad (\text{A.40})$$

$$x_4 = x(0, 1) = a_1 + a_3 + a_6 + a_{10} \quad (\text{A.41})$$

$$x_5 = x\left(\frac{1}{3}, 0\right) = a_1 + \frac{1}{3}a_2 + \frac{1}{9}a_4 + \frac{1}{27}a_7 \quad (\text{A.42})$$

$$x_6 = x\left(\frac{2}{3}, 0\right) = a_1 + \frac{2}{3}a_2 + \frac{4}{9}a_4 + \frac{8}{27}a_7 \quad (\text{A.43})$$

$$x_7 = x\left(1, \frac{1}{3}\right) = a_1 + a_2 + \frac{1}{3}a_3 + a_4 + \frac{1}{3}a_5 + \frac{1}{9}a_6 + a_7 + \frac{1}{3}a_8 \quad (\text{A.44})$$

$$+ \frac{1}{9}a_9 + \frac{1}{27}a_{10} + \frac{1}{3}a_{11} + \frac{1}{27}a_{12} \quad (\text{A.45})$$

$$x_8 = x(1, \frac{2}{3}) = a_1 + a_2 + \frac{2}{3}a_3 + a_4 + \frac{2}{3}a_5 + \frac{4}{9}a_6 + a_7 + \frac{2}{3}a_8 \quad (\text{A.46})$$

$$+ \frac{4}{9}a_9 + \frac{8}{27}a_{10} + \frac{2}{3}a_{11} + \frac{8}{27}a_{12} \quad (\text{A.47})$$

$$x_9 = x(\frac{2}{3}, 1) = a_1 + \frac{2}{3}a_2 + a_3 + \frac{4}{9}a_4 + \frac{2}{3}a_5 + a_6 + \frac{8}{27}a_7 + \frac{4}{9}a_8 \quad (\text{A.48})$$

$$+ \frac{2}{3}a_9 + a_{10} + \frac{8}{27}a_{11} + \frac{2}{3}a_{12} \quad (\text{A.49})$$

$$x_{10} = x(\frac{1}{3}, 1) = a_1 + \frac{1}{3}a_2 + a_3 + \frac{1}{9}a_4 + \frac{1}{3}a_5 + a_6 + \frac{1}{27}a_7 + \frac{1}{9}a_8 \quad (\text{A.50})$$

$$+ \frac{1}{3}a_9 + a_{10} + \frac{1}{27}a_{11} + \frac{1}{3}a_{12} \quad (\text{A.51})$$

(A.52)

$$x_{11} = x(0, \frac{2}{3}) = a_1 + \frac{2}{3}a_3 + \frac{4}{9}a_6 + \frac{8}{27}a_{10} \quad (\text{A.53})$$

$$x_{12} = x(0, \frac{1}{3}) = a_1 + \frac{1}{3}a_3 + \frac{1}{9}a_6 + \frac{1}{27}a_{10} \quad (\text{A.54})$$

Express in matrix form:

$$\mathbf{x} = \mathbf{B}\mathbf{a} \quad (\text{A.55})$$

Write coefficients a_i as a function of global coordinates x_i :

$$\mathbf{a} = \mathbf{B}^{-1}\mathbf{x} \quad (\text{A.56})$$

Obtain quadratic basis functions ϕ_i by substituting coefficients from A.56 into A.37:

$$\phi_1 = \frac{1}{2}(\xi - 1)(\eta - 1)(9\eta^2 - 9\eta + 9\xi^2 - 9\xi + 2) \quad (\text{A.57})$$

$$\phi_2 = -\frac{1}{2}\xi(\eta - 1)(9\eta^2 - 9\eta + 9\xi^2 - 9\xi + 2) \quad (\text{A.58})$$

$$\phi_3 = \frac{1}{2}\xi\eta(9\eta^2 - 9\eta + 9\xi^2 - 9\xi + 2) \quad (\text{A.59})$$

$$\phi_4 = -\frac{1}{2}\eta(\xi - 1)(9\eta^2 - 9\eta + 9\xi^2 - 9\xi + 2) \quad (\text{A.60})$$

$$\phi_5 = -\frac{9}{2}\xi(\eta-1)(3\xi-2)(\xi-1) \quad (\text{A.61})$$

$$\phi_6 = \frac{9}{2}\xi(\eta-1)(3\xi-1)(\xi-1) \quad (\text{A.62})$$

$$\phi_7 = \frac{9}{2}\xi\eta(3\eta-2)(\eta-1) \quad (\text{A.63})$$

$$\phi_8 = -\frac{9}{2}\xi\eta(3\eta-1)(\eta-1) \quad (\text{A.64})$$

$$\phi_9 = -\frac{9}{2}\xi\eta(3\xi-1)(\xi-1) \quad (\text{A.65})$$

$$\phi_{10} = \frac{9}{2}\xi\eta(3\xi-2)(\xi-1) \quad (\text{A.66})$$

$$\phi_{11} = \frac{9}{2}\eta(\xi-1)(3\eta-1)(\eta-1) \quad (\text{A.67})$$

$$\phi_{12} = -\frac{9}{2}\eta(\xi-1)(3\eta-2)(\eta-1) \quad (\text{A.68})$$

Map the local coordinate (ξ, η) to the global coordinate (x, y) :

$$x(\xi, \eta) = \sum_{k=1}^{12} x_k \phi_k(\xi, \eta) \quad (\text{A.69})$$

$$y(\xi, \eta) = \sum_{k=1}^{12} y_k \phi_k(\xi, \eta) \quad (\text{A.70})$$

Evaluate basis function derivatives $\partial\phi_k/\partial\xi$, $\partial\phi_k/\partial\eta$ and the Jacobian matrix:

$$\mathbf{J} = \frac{\partial(x, y)}{\partial(\xi, \eta)} = \begin{bmatrix} \frac{\partial x}{\partial \xi} & \frac{\partial x}{\partial \eta} \\ \frac{\partial y}{\partial \xi} & \frac{\partial y}{\partial \eta} \end{bmatrix} \quad (\text{A.71})$$

Appendix B

Three-Dimensional Mapping and Basis Functions

B.1 8-Node Hexahedral Element

Trilinear ansatz for global coordinate x :

$$x(\xi, \eta, \beta) = a_1 + a_2\xi + a_3\eta + a_4\beta + a_5\xi\eta + a_6\xi\beta + a_7\eta\beta + a_8\xi\eta\beta \quad (\text{B.1})$$

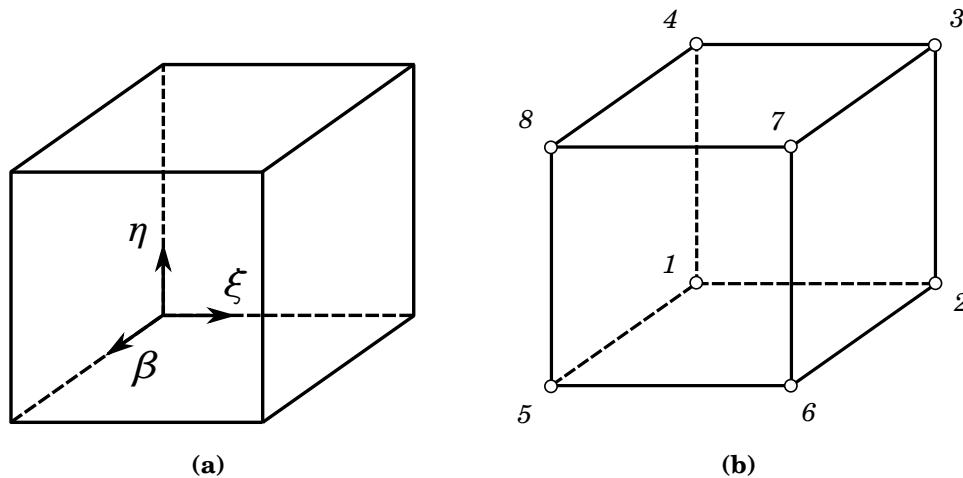


Figure B.1 Orientation of 8-node reference element $\Omega_r = \{\xi, \eta, \beta \mid 0 \leq \xi, \eta, \beta \leq 1\}$.

Global coordinate of each element node x_i :

$$x_1 = x(0, 0, 0) = a_1 \quad (\text{B.2})$$

$$x_2 = x(1, 0, 0) = a_1 + a_2 \quad (\text{B.3})$$

$$x_3 = x(1, 1, 0) = a_1 + a_2 + a_3 + a_5 \quad (\text{B.4})$$

$$x_4 = x(0, 1, 0) = a_1 + a_3 \quad (\text{B.5})$$

$$x_5 = x(0, 0, 1) = a_1 + a_4 \quad (\text{B.6})$$

$$x_6 = x(1, 0, 1) = a_1 + a_2 + a_4 + a_6 \quad (\text{B.7})$$

$$x_7 = x(1, 1, 1) = a_1 + a_2 + a_3 + a_4 + a_5 + a_6 + a_7 + a_8 \quad (\text{B.8})$$

$$x_8 = x(0, 1, 1) = a_1 + a_3 + a_4 + a_7 \quad (\text{B.9})$$

Express in matrix form:

$$\mathbf{x} = \mathbf{B}\mathbf{a} \quad (\text{B.10})$$

Write coefficients a_i as a function of global coordinates x_i :

$$\mathbf{a} = \mathbf{B}^{-1}\mathbf{x} \quad (\text{B.11})$$

Obtain linear basis functions ϕ_i by substituting coefficients from B.11 into B.1:

$$\phi_1 = -(\xi - 1)(\eta - 1)(\beta - 1) \quad (\text{B.12})$$

$$\phi_2 = \xi(\eta - 1)(\beta - 1) \quad (\text{B.13})$$

$$\phi_3 = -\xi\eta(\beta - 1) \quad (\text{B.14})$$

$$\phi_4 = \eta(\xi - 1)(\beta - 1) \quad (\text{B.15})$$

$$\phi_5 = \beta(\xi - 1)(\eta - 1) \quad (\text{B.16})$$

$$\phi_6 = -\xi\beta(\eta - 1) \quad (\text{B.17})$$

$$\phi_7 = \xi\eta\beta \quad (\text{B.18})$$

$$\phi_8 = -\eta\beta(\xi - 1) \quad (\text{B.19})$$

Map the local coordinate (ξ, η, β) to the global coordinate (x, y, z) :

$$x(\xi, \eta, \beta) = \sum_{k=1}^8 x_k \phi_k(\xi, \eta, \beta) \quad (\text{B.20})$$

$$y(\xi, \eta, \beta) = \sum_{k=1}^8 y_k \phi_k(\xi, \eta, \beta) \quad (\text{B.21})$$

$$z(\xi, \eta, \beta) = \sum_{k=1}^8 z_k \phi_k(\xi, \eta, \beta) \quad (\text{B.22})$$

Evaluate basis function derivatives $\partial\phi_k/\partial\xi$, $\partial\phi_k/\partial\eta$, $\partial\phi_k/\partial\beta$ and the Jacobian matrix:

$$\mathbf{J} = \frac{\partial(x, y, z)}{\partial(\xi, \eta, \beta)} = \begin{bmatrix} \frac{\partial x}{\partial \xi} & \frac{\partial x}{\partial \eta} & \frac{\partial x}{\partial \beta} \\ \frac{\partial y}{\partial \xi} & \frac{\partial y}{\partial \eta} & \frac{\partial y}{\partial \beta} \\ \frac{\partial z}{\partial \xi} & \frac{\partial z}{\partial \eta} & \frac{\partial z}{\partial \beta} \end{bmatrix} \quad (\text{B.23})$$

B.2 20-Node Hexahedral Element

Triquadratic (serendipity) ansatz for global coordinate x :

$$\begin{aligned} x(\xi, \eta, \beta) = & a_1 + a_2\xi + a_3\eta + a_4\beta + a_5\xi\eta + a_6\xi\beta + a_7\eta\beta + a_8\xi^2 \\ & + a_9\xi^2\eta + a_{10}\xi^2\beta + a_{11}\eta^2 + a_{12}\eta^2\xi + a_{13}\eta^2\beta + a_{14}\beta^2 \\ & + a_{15}\beta^2\xi + a_{16}\beta^2\eta + a_{17}\xi^2\eta\beta + a_{18}\eta^2\xi\beta + a_{19}\beta^2\xi\eta \\ & + a_{20}\xi\eta\beta \end{aligned} \quad (\text{B.24})$$

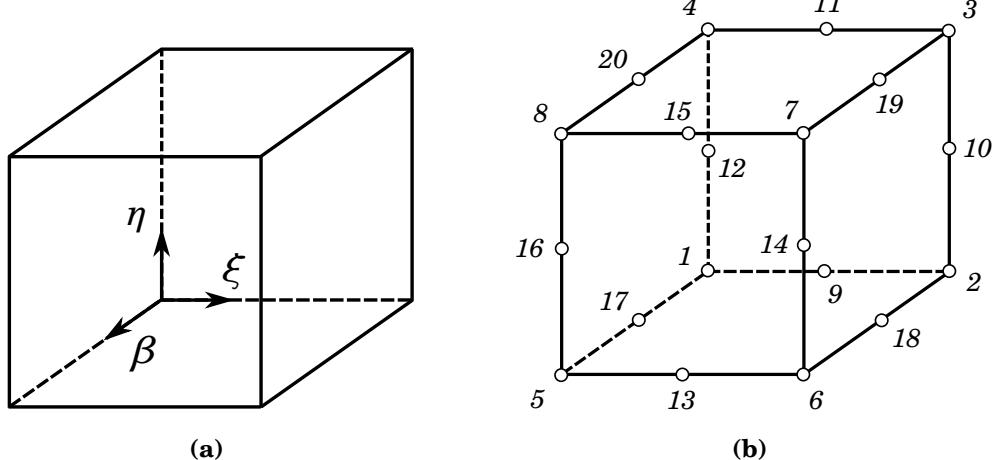


Figure B.2 Orientation of 20-node reference element $\Omega_r = \{\xi, \eta, \beta \mid 0 \leq \xi, \eta, \beta \leq 1\}$.

Global coordinate of each element node x_i :

$$x_1 = x(0, 0, 0) = a_1 \quad (\text{B.25})$$

$$x_2 = x(1, 0, 0) = a_1 + a_2 + a_8 \quad (\text{B.26})$$

$$x_3 = x(1, 1, 0) = a_1 + a_2 + a_3 + a_5 + a_8 + a_9 + a_{11} + a_{12} \quad (\text{B.27})$$

$$x_4 = x(0, 1, 0) = a_1 + a_3 + a_{11} \quad (\text{B.28})$$

$$x_5 = x(0, 0, 1) = a_1 + a_4 + a_{14} \quad (\text{B.29})$$

$$x_6 = x(1, 0, 1) = a_1 + a_2 + a_4 + a_6 + a_8 + a_{10} + a_{14} + a_{15} \quad (\text{B.30})$$

$$x_7 = x(1, 1, 1) = a_1 + a_2 + a_3 + a_4 + a_5 + a_6 + a_7 + a_8 \quad (\text{B.31})$$

$$+ a_9 + a_{10} + a_{11} + a_{12} + a_{13} + a_{14} + a_{15} + a_{16} \quad (\text{B.32})$$

$$+ a_{17} + a_{18} + a_{19} + a_{20} \quad (\text{B.33})$$

$$x_8 = x(0, 1, 1) = a_1 + a_3 + a_4 + a_7 + a_{11} + a_{13} + a_{14} + a_{16} \quad (\text{B.34})$$

$$x_9 = x\left(\frac{1}{2}, 0, 0\right) = a_1 + \frac{1}{2}a_2 + \frac{1}{4}a_8 \quad (\text{B.35})$$

$$x_{10} = x\left(1, \frac{1}{2}, 0\right) = a_1 + a_2 + \frac{1}{2}a_3 + \frac{1}{2}a_5 + a_8 + \frac{1}{2}a_9 + \frac{1}{4}a_{11} + \frac{1}{4}a_{12} \quad (\text{B.36})$$

$$x_{11} = x\left(\frac{1}{2}, 1, 0\right) = a_1 + \frac{1}{2}a_2 + a_3 + \frac{1}{2}a_5 + \frac{1}{4}a_8 + \frac{1}{4}a_9 + a_{11} + \frac{1}{2}a_{12} \quad (\text{B.37})$$

$$x_{12} = x\left(0, \frac{1}{2}, 0\right) = a_1 + \frac{1}{2}a_3 + \frac{1}{4}a_{11} \quad (\text{B.38})$$

$$x_{13} = x\left(\frac{1}{2}, 0, 1\right) = a_1 + \frac{1}{2}a_2 + a_4 + \frac{1}{2}a_6 + \frac{1}{4}a_8 + \frac{1}{4}a_{10} + a_{14} + \frac{1}{2}a_{15} \quad (\text{B.39})$$

$$x_{14} = x\left(1, \frac{1}{2}, 1\right) = a_1 + a_2 + \frac{1}{2}a_3 + a_4 + \frac{1}{2}a_5 + a_6 + \frac{1}{2}a_7 + a_8 \quad (\text{B.40})$$

$$+ \frac{1}{2}a_9 + a_{10} + \frac{1}{4}a_{11} + \frac{1}{4}a_{12} + \frac{1}{4}a_{13} + a_{14} + a_{15} + \frac{1}{2}a_{16} \quad (\text{B.41})$$

$$+ \frac{1}{2}a_{17} + \frac{1}{4}a_{18} + \frac{1}{2}a_{19} + \frac{1}{2}a_{20} \quad (\text{B.42})$$

$$x_{15} = x\left(\frac{1}{2}, 1, 1\right) = a_1 + \frac{1}{2}a_2 + a_3 + a_4 + \frac{1}{2}a_5 + \frac{1}{2}a_6 + a_7 + \frac{1}{4}a_8 \quad (\text{B.43})$$

$$+ \frac{1}{4}a_9 + \frac{1}{4}a_{10} + a_{11} + \frac{1}{2}a_{12} + a_{13} + a_{14} + \frac{1}{2}a_{15} + a_{16} \quad (\text{B.44})$$

$$+ \frac{1}{4}a_{17} + \frac{1}{2}a_{18} + \frac{1}{2}a_{19} + \frac{1}{2}a_{20} \quad (\text{B.45})$$

$$x_{16} = x\left(0, \frac{1}{2}, 1\right) = a_1 + \frac{1}{2}a_3 + a_4 + \frac{1}{2}a_7 + \frac{1}{4}a_{11} + \frac{1}{4}a_{13} + a_{14} + \frac{1}{2}a_{16} \quad (\text{B.46})$$

$$x_{17} = x(0, 0, \frac{1}{2}) = a_1 + \frac{1}{2}a_4 + \frac{1}{4}a_{14} \quad (\text{B.47})$$

$$x_{18} = x(1, 0, \frac{1}{2}) = a_1 + a_2 + \frac{1}{2}a_4 + \frac{1}{2}a_6 + a_8 + \frac{1}{2}a_{10} + \frac{1}{4}a_{14} + \frac{1}{4}a_{15} \quad (\text{B.48})$$

$$x_{19} = x(1, 1, \frac{1}{2}) = a_1 + a_2 + a_3 + \frac{1}{2}a_4 + a_5 + \frac{1}{2}a_6 + \frac{1}{2}a_7 + a_8 \quad (\text{B.49})$$

$$+ a_9 + \frac{1}{2}a_{10} + a_{11} + a_{12} + \frac{1}{2}a_{13} + \frac{1}{4}a_{14} + \frac{1}{4}a_{15} + \frac{1}{4}a_{16} \quad (\text{B.50})$$

$$+ \frac{1}{2}a_{17} + \frac{1}{2}a_{18} + \frac{1}{4}a_{19} + \frac{1}{2}a_{20} \quad (\text{B.51})$$

$$x_{20} = x(0, 1, \frac{1}{2}) = a_1 + a_3 + \frac{1}{2}a_4 + \frac{1}{2}a_7 + a_{11} + \frac{1}{2}a_{13} + \frac{1}{4}a_{14} + \frac{1}{4}a_{16} \quad (\text{B.52})$$

Express in matrix form:

$$\mathbf{x} = \mathbf{B}\mathbf{a} \quad (\text{B.53})$$

Write coefficients a_i as a function of global coordinates x_i :

$$\mathbf{a} = \mathbf{B}^{-1}\mathbf{x} \quad (\text{B.54})$$

Obtain quadratic basis functions ϕ_i by substituting coefficients from B.54 into B.24:

$$\phi_1 = (\beta - 1)(\eta - 1)(\xi - 1)(2\beta + 2\eta + 2\xi - 1) \quad (\text{B.55})$$

$$\phi_2 = -\xi(\beta - 1)(\eta - 1)(2\beta + 2\eta - 2\xi + 1) \quad (\text{B.56})$$

$$\phi_3 = \eta\xi(\beta - 1)(2\beta - 2\eta - 2\xi + 3) \quad (\text{B.57})$$

$$\phi_4 = -\eta(\beta - 1)(\xi - 1)(2\beta - 2\eta + 2\xi + 1) \quad (\text{B.58})$$

$$\phi_5 = -\beta(\eta - 1)(\xi - 1)(2\eta - 2\beta + 2\xi + 1) \quad (\text{B.59})$$

$$\phi_6 = -\beta\xi(\eta - 1)(2\beta - 2\eta + 2\xi - 3) \quad (\text{B.60})$$

$$\phi_7 = \beta\eta\xi(2\beta + 2\eta + 2\xi - 5) \quad (\text{B.61})$$

$$\phi_8 = -\beta\eta(\xi - 1)(2\beta + 2\eta - 2\xi - 3) \quad (\text{B.62})$$

$$\phi_9 = -4\xi(\beta - 1)(\eta - 1)(\xi - 1) \quad (\text{B.63})$$

$$\phi_{10} = 4\eta\xi(\beta-1)(\eta-1) \quad (\text{B.64})$$

$$\phi_{11} = 4\eta\xi(\beta-1)(\xi-1) \quad (\text{B.65})$$

$$\phi_{12} = -4\eta(\beta-1)(\eta-1)(\xi-1) \quad (\text{B.66})$$

$$\phi_{13} = 4\beta\xi(\eta-1)(\xi-1) \quad (\text{B.67})$$

$$\phi_{14} = -4\beta\eta\xi(\eta-1) \quad (\text{B.68})$$

$$\phi_{15} = -4\beta\eta\xi(\xi-1) \quad (\text{B.69})$$

$$\phi_{16} = 4\beta\eta(\eta-1)(\xi-1) \quad (\text{B.70})$$

$$\phi_{17} = -4\beta(\beta-1)(\eta-1)(\xi-1) \quad (\text{B.71})$$

$$\phi_{18} = 4\beta\xi(\beta-1)(\eta-1) \quad (\text{B.72})$$

$$\phi_{19} = -4\beta\eta\xi(\beta-1) \quad (\text{B.73})$$

$$\phi_{20} = 4\beta\eta(\beta-1)(\xi-1) \quad (\text{B.74})$$

Map the local coordinate (ξ, η, β) to the global coordinate (x, y, z) :

$$x(\xi, \eta, \beta) = \sum_{k=1}^{20} x_k \phi_k(\xi, \eta, \beta) \quad (\text{B.75})$$

$$y(\xi, \eta, \beta) = \sum_{k=1}^{20} y_k \phi_k(\xi, \eta, \beta) \quad (\text{B.76})$$

$$z(\xi, \eta, \beta) = \sum_{k=1}^{20} z_k \phi_k(\xi, \eta, \beta) \quad (\text{B.77})$$

Evaluate basis function derivatives $\partial\phi_k/\partial\xi$, $\partial\phi_k/\partial\eta$, $\partial\phi_k/\partial\beta$ and the Jacobian matrix:

$$\mathbf{J} = \frac{\partial(x, y, z)}{\partial(\xi, \eta, \beta)} = \begin{bmatrix} \frac{\partial x}{\partial \xi} & \frac{\partial x}{\partial \eta} & \frac{\partial x}{\partial \beta} \\ \frac{\partial y}{\partial \xi} & \frac{\partial y}{\partial \eta} & \frac{\partial y}{\partial \beta} \\ \frac{\partial z}{\partial \xi} & \frac{\partial z}{\partial \eta} & \frac{\partial z}{\partial \beta} \end{bmatrix} \quad (\text{B.78})$$

Appendix C

**Curved Pipe Entrance Condition:
Fully Developed Steady (Poiseuille)
Flow**

Supplemental steady flow results are provided $Re = 220, 430, 640$ and 883 at the various cross-section $\phi = 22^\circ, 45^\circ, 90^\circ$ and 135° for the non-dimensional vorticity magnitude $|\omega^*|$, centrifugal force f_c^* , pressure gradient force f_{pg}^* , viscous force f_v^* and wall shear stress magnitude $|\tau_w^*|$. The centrifugal, pressure gradient and viscous force terms are defined in Section 8.6.7.

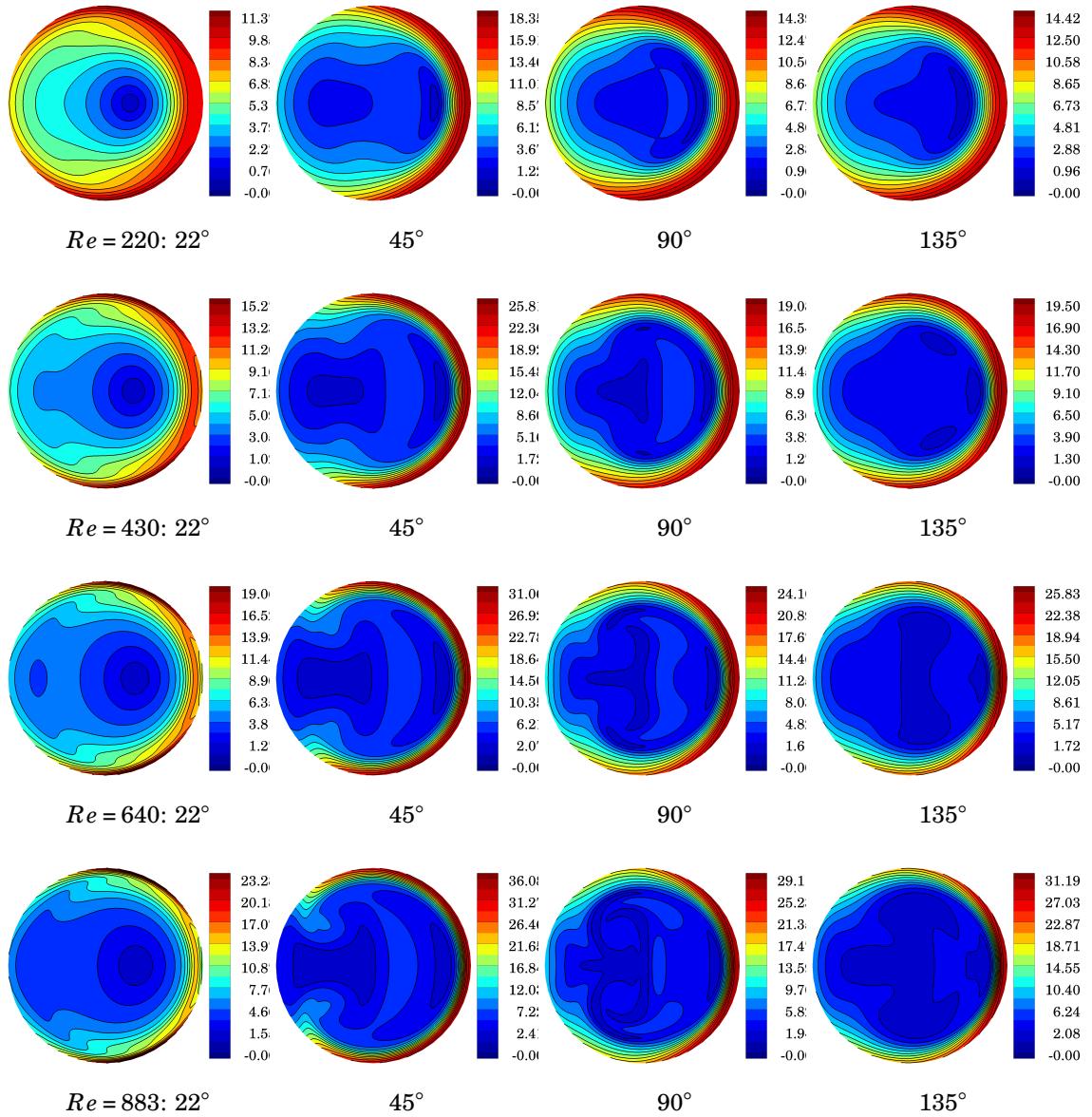


Figure C.1 Poiseuille entrance condition: non-dimensional vorticity magnitude $|\omega^*|$. $Re = \{220, 430, 640, 883\}$, $\phi = \{22^\circ, 45^\circ, 90^\circ, 135^\circ\}$.

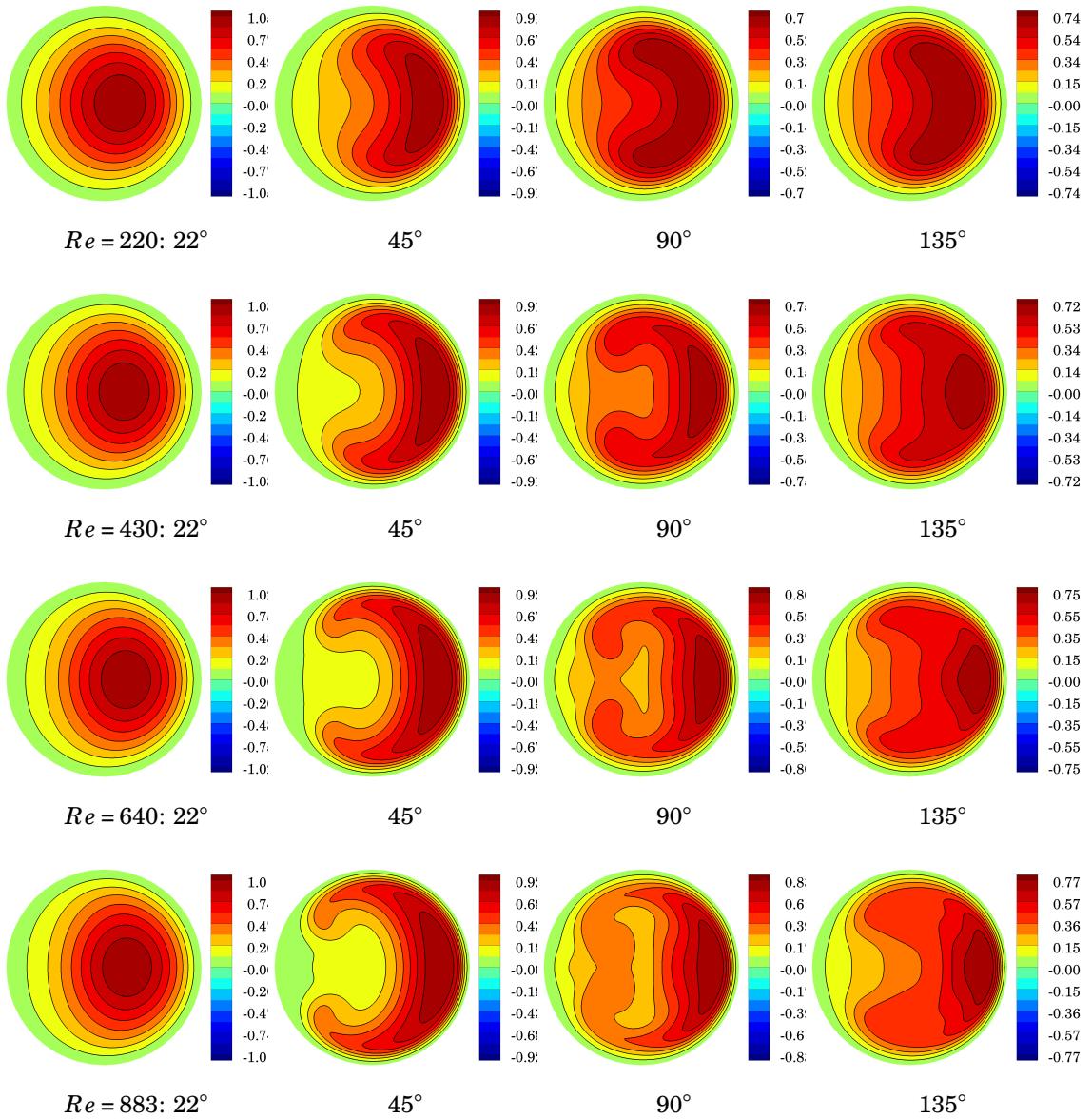


Figure C.2 Poiseuille entrance condition: non-dimensional centrifugal force f_c^* . $Re = \{220, 430, 640, 883\}$, $\phi = \{22^\circ, 45^\circ, 90^\circ, 135^\circ\}$.

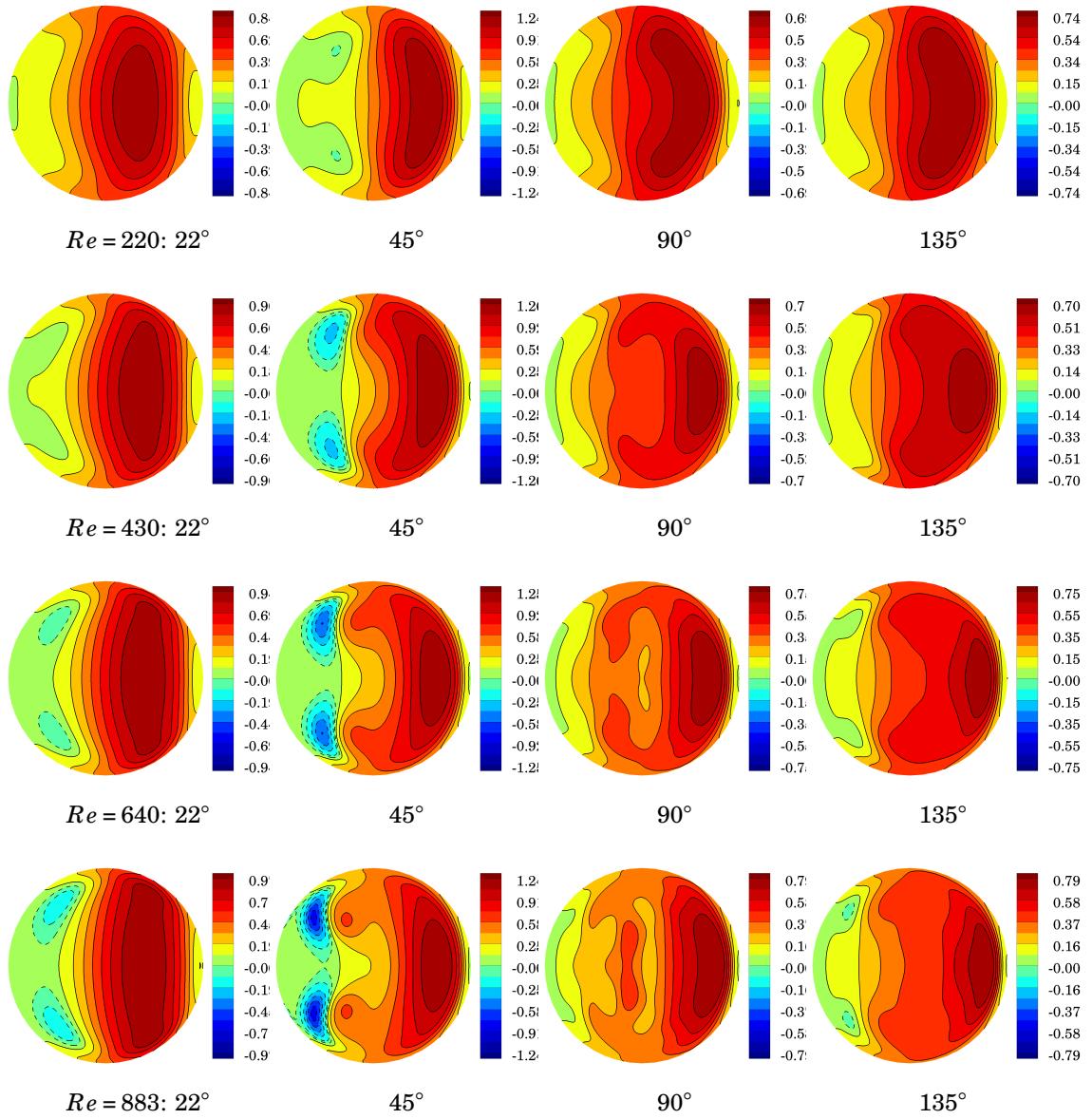


Figure C.3 Poiseuille entrance condition: non-dimensional pressure gradient force $-f_{pg}^*$.
 $Re = \{220, 430, 640, 883\}$, $\phi = \{22^\circ, 45^\circ, 90^\circ, 135^\circ\}$.

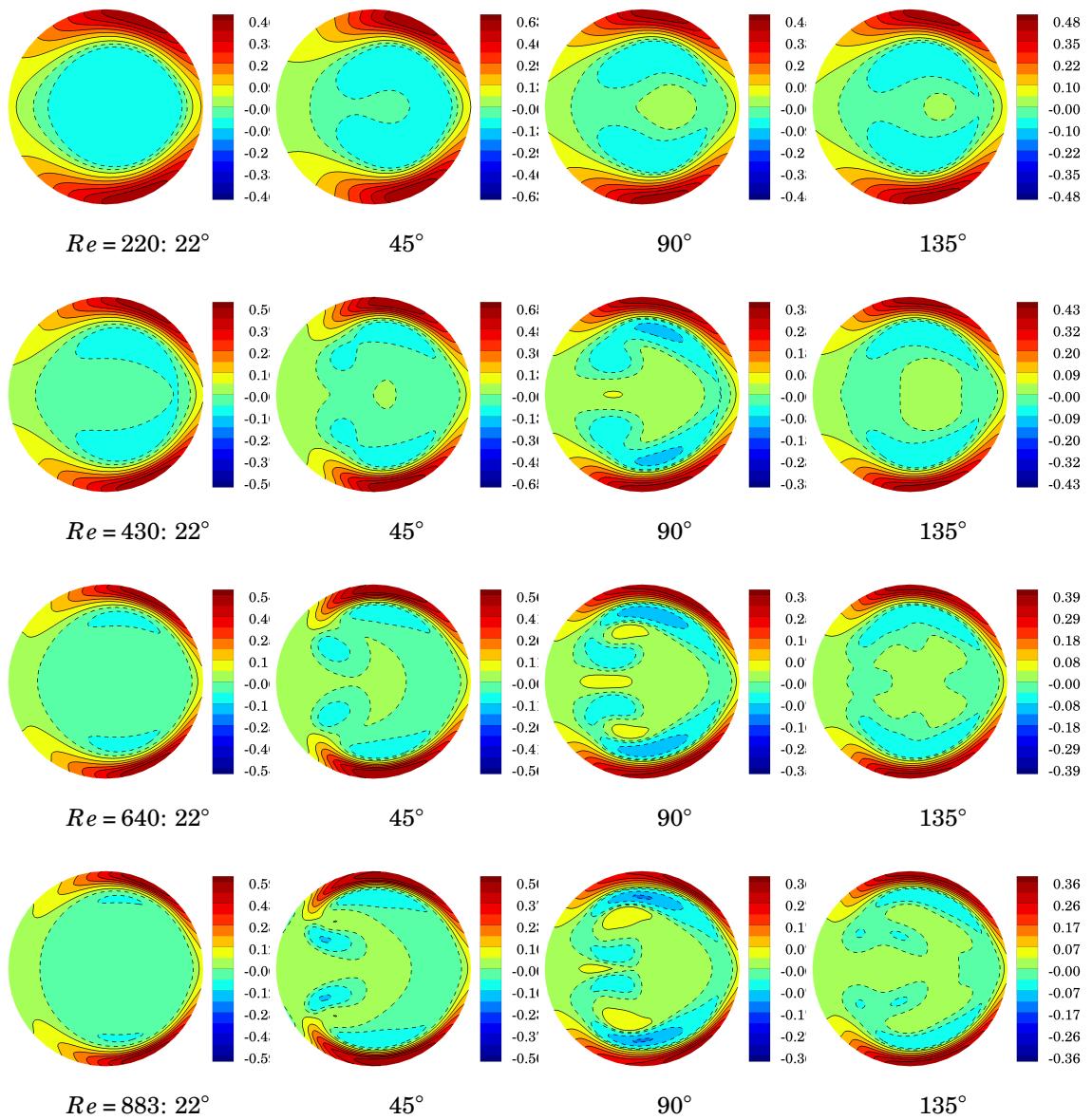


Figure C.4 Poiseuille entrance condition: non-dimensional viscous force f_v^* . $Re = \{220, 430, 640, 883\}$, $\phi = \{22^\circ, 45^\circ, 90^\circ, 135^\circ\}$.

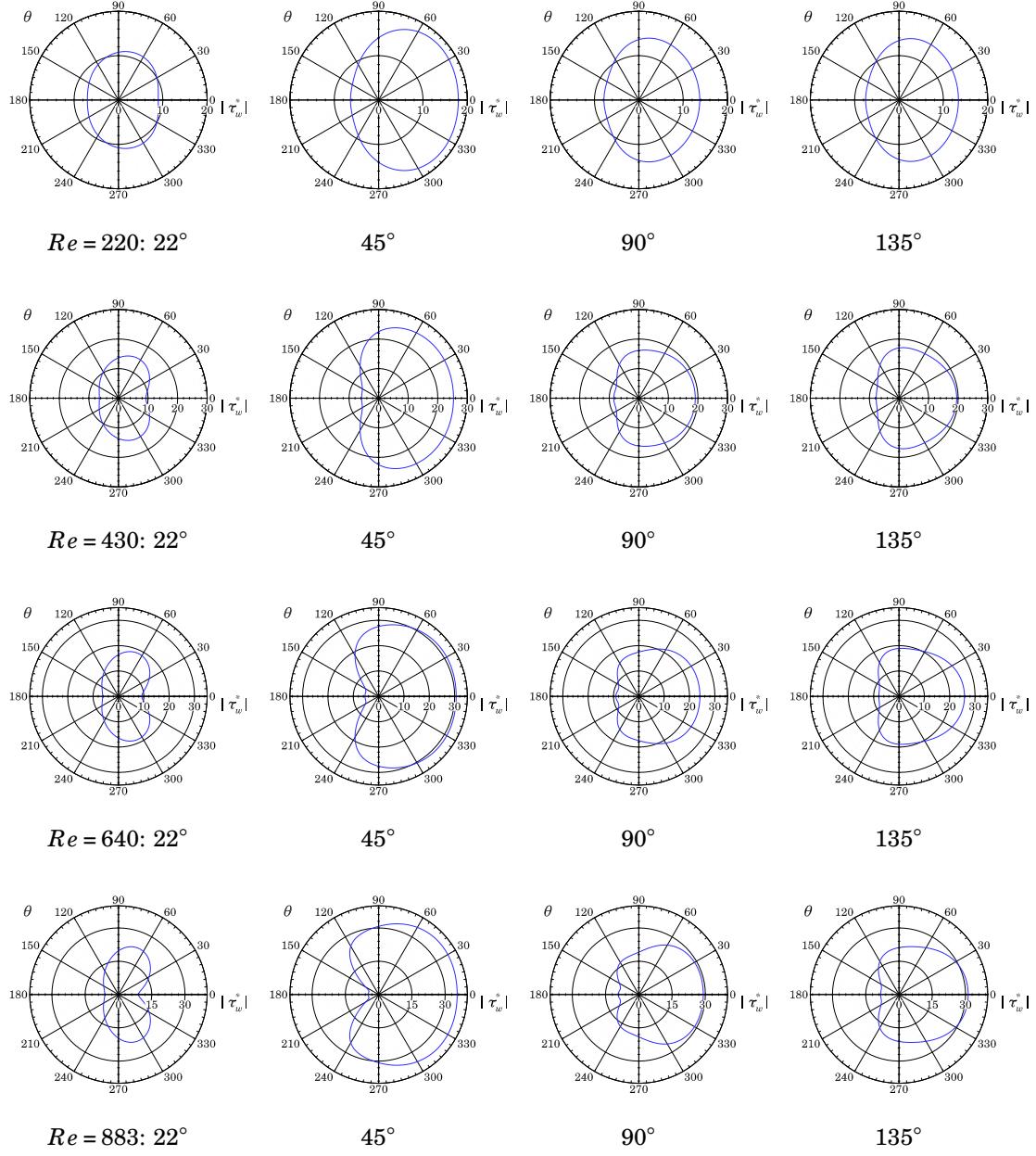


Figure C.5 Poiseuille entrance condition: non-dimensional wall shear stress magnitude $|\tau_w^*|$. $Re = \{220, 430, 640, 883\}$, $\phi = \{22^\circ, 45^\circ, 90^\circ, 135^\circ\}$.

Appendix D

**Curved Pipe Entrance Condition:
Fully Developed Pulsatile
(Womersley) Flow**

Supplemental fully developed pulsatile entrance flow results are provided for mid-acceleration ($t^* = 0.15$) through end of deceleration ($t^* = 0.29$) at the various cross-section $\phi = 22^\circ, 45^\circ, 90^\circ$ and 135° for the non-dimensional streamwise vorticity ω_s^* , vorticity magnitude $|\boldsymbol{\omega}^*|$, secondary velocity vectors $\boldsymbol{u}_{\theta r}^*$, streamwise velocity u_s^* , second eigenvalue λ_2^* of $\mathbf{S}^2 + \mathbf{R}^2$, pressure p^* , centrifugal force f_c^* , pressure gradient force f_{pg}^* , viscous force f_v^* and wall shear stress magnitude $|\boldsymbol{\tau}_w^*|$. The centrifugal, pressure gradient and viscous force terms are defined in Section 8.6.7.

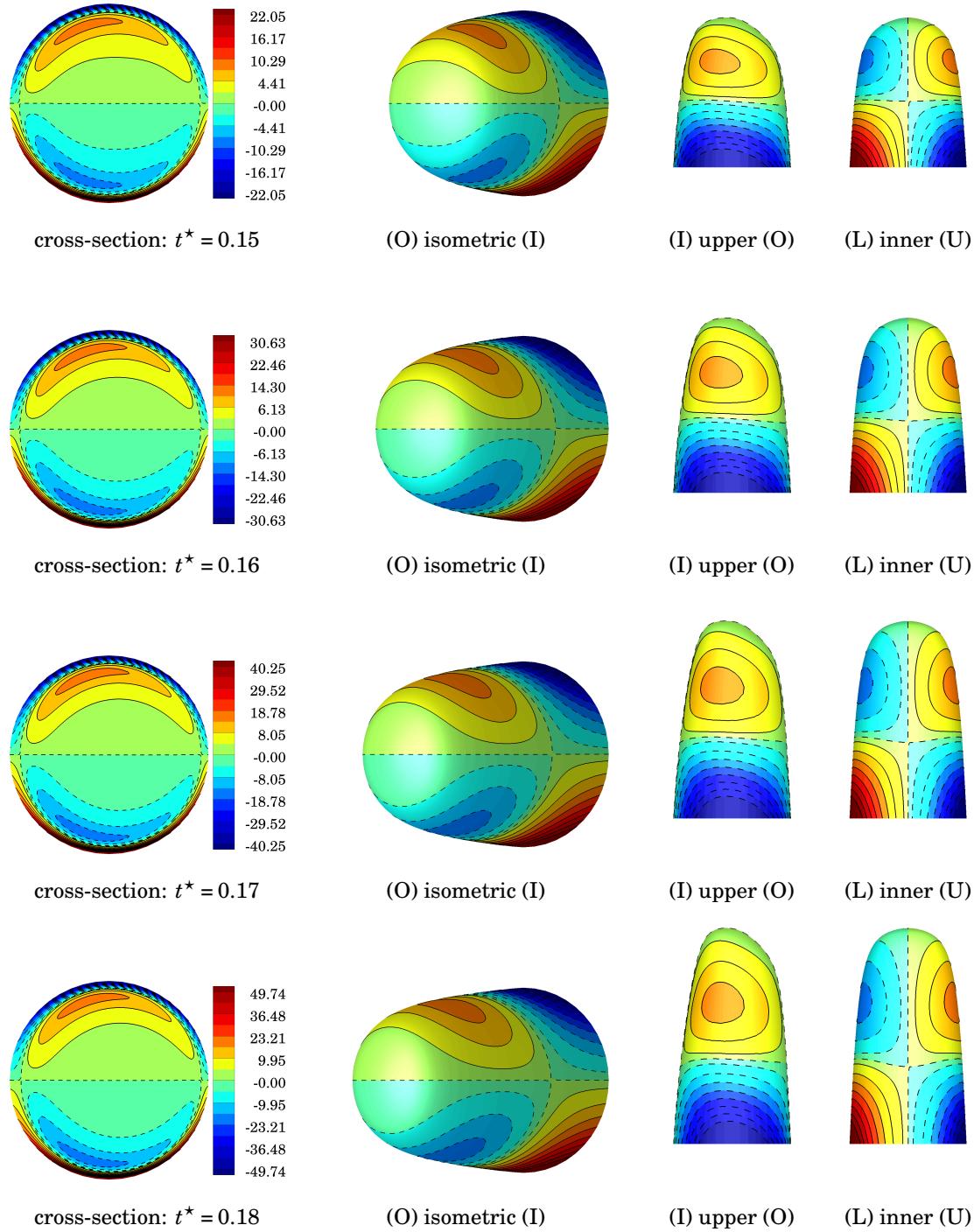


Figure D.1 Womersley entrance condition: velocity surface of u_s^* at $\theta = 22^\circ$ colored by non-dimensional streamwise vorticity ω_s^* visualized from three difference views: isometric, upper and inner. ($I \equiv$ inner, $O \equiv$ outer, $U \equiv$ upper, $L \equiv$ lower).

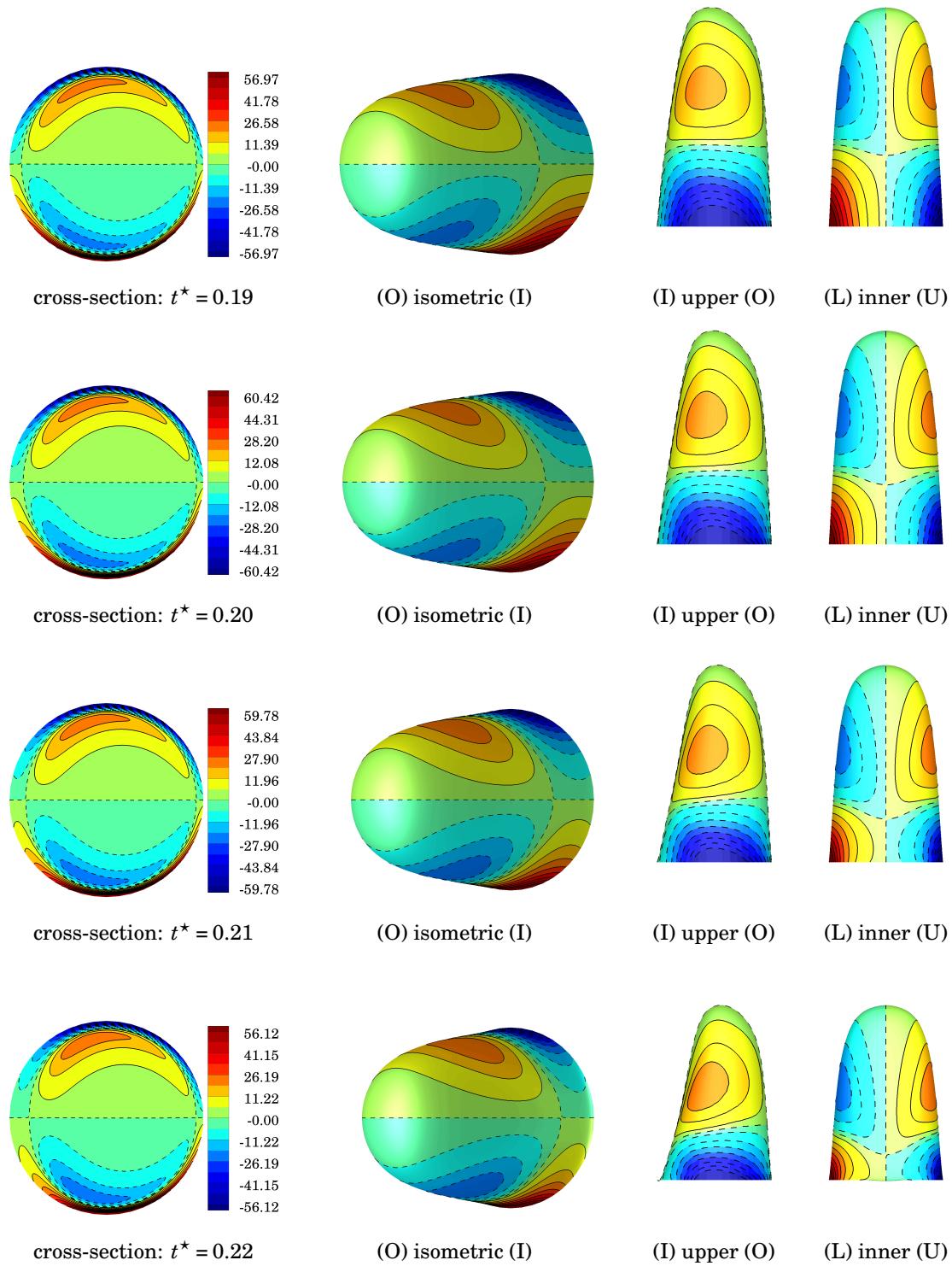


Figure D.1 Womersley entrance condition: velocity surface of u_s^* at $\theta = 22^\circ$ colored by non-dimensional streamwise vorticity ω_s^* visualized from three difference views: isometric, upper and inner. ($I \equiv$ inner, $O \equiv$ outer, $U \equiv$ upper, $L \equiv$ lower). (continued)

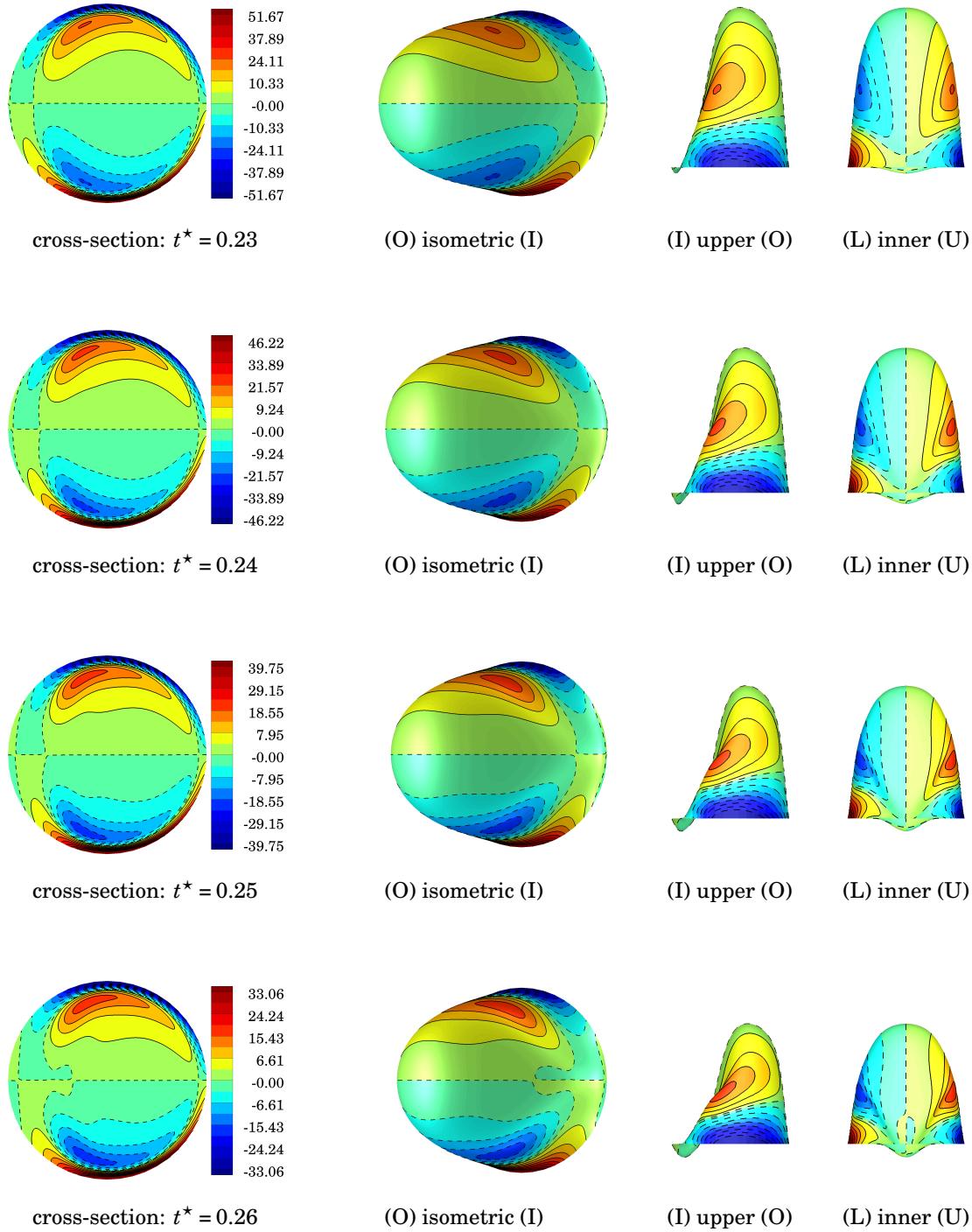


Figure D.1 Womersley entrance condition: velocity surface of u_s^* at $\theta = 22^\circ$ colored by non-dimensional streamwise vorticity ω_s^* visualized from three difference views: isometric, upper and inner. ($I \equiv inner$, $O \equiv outer$, $U \equiv upper$, $L \equiv lower$). (continued)

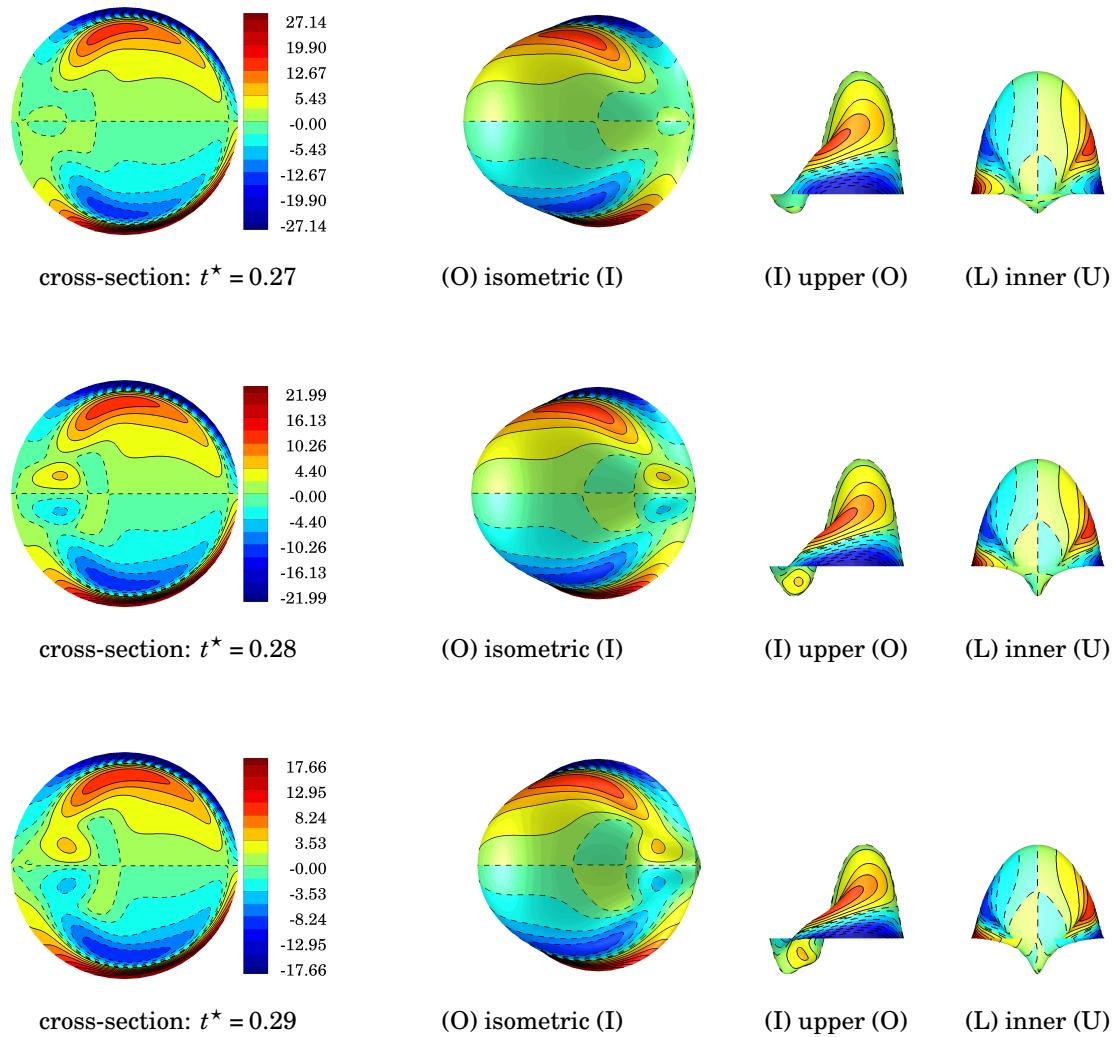


Figure D.1 Womersley entrance condition: velocity surface of u_s^* at $\theta = 22^\circ$ colored by non-dimensional streamwise vorticity ω_s^* visualized from three difference views: isometric, upper and inner. ($I \equiv inner$, $O \equiv outer$, $U \equiv upper$, $L \equiv lower$). (continued)

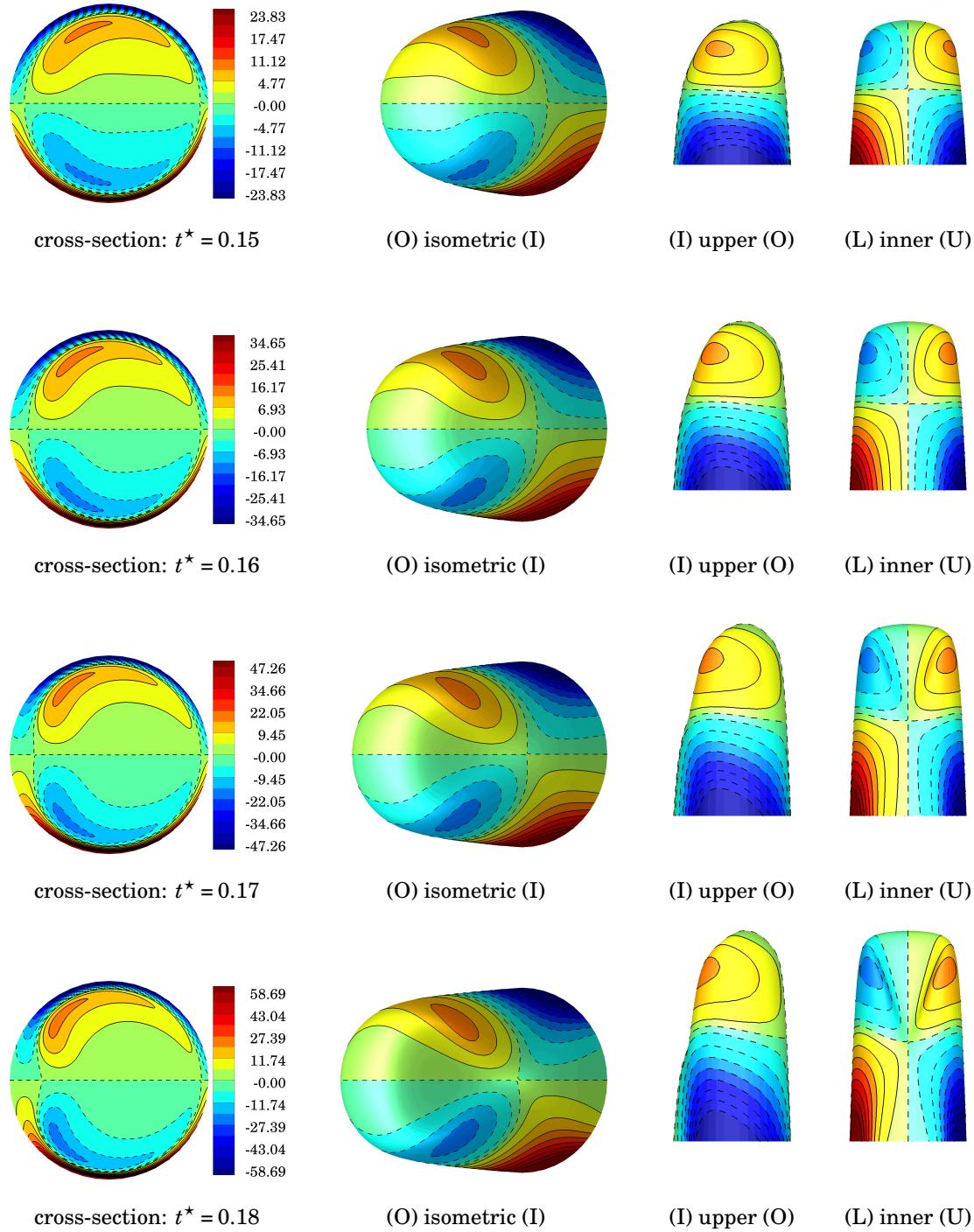


Figure D.2 Womersley entrance condition: velocity surface of u_s^* at $\theta = 45^\circ$ colored by non-dimensional streamwise vorticity ω_s^* visualized from three difference views: isometric, upper and inner. ($I \equiv inner$, $O \equiv outer$, $U \equiv upper$, $L \equiv lower$).

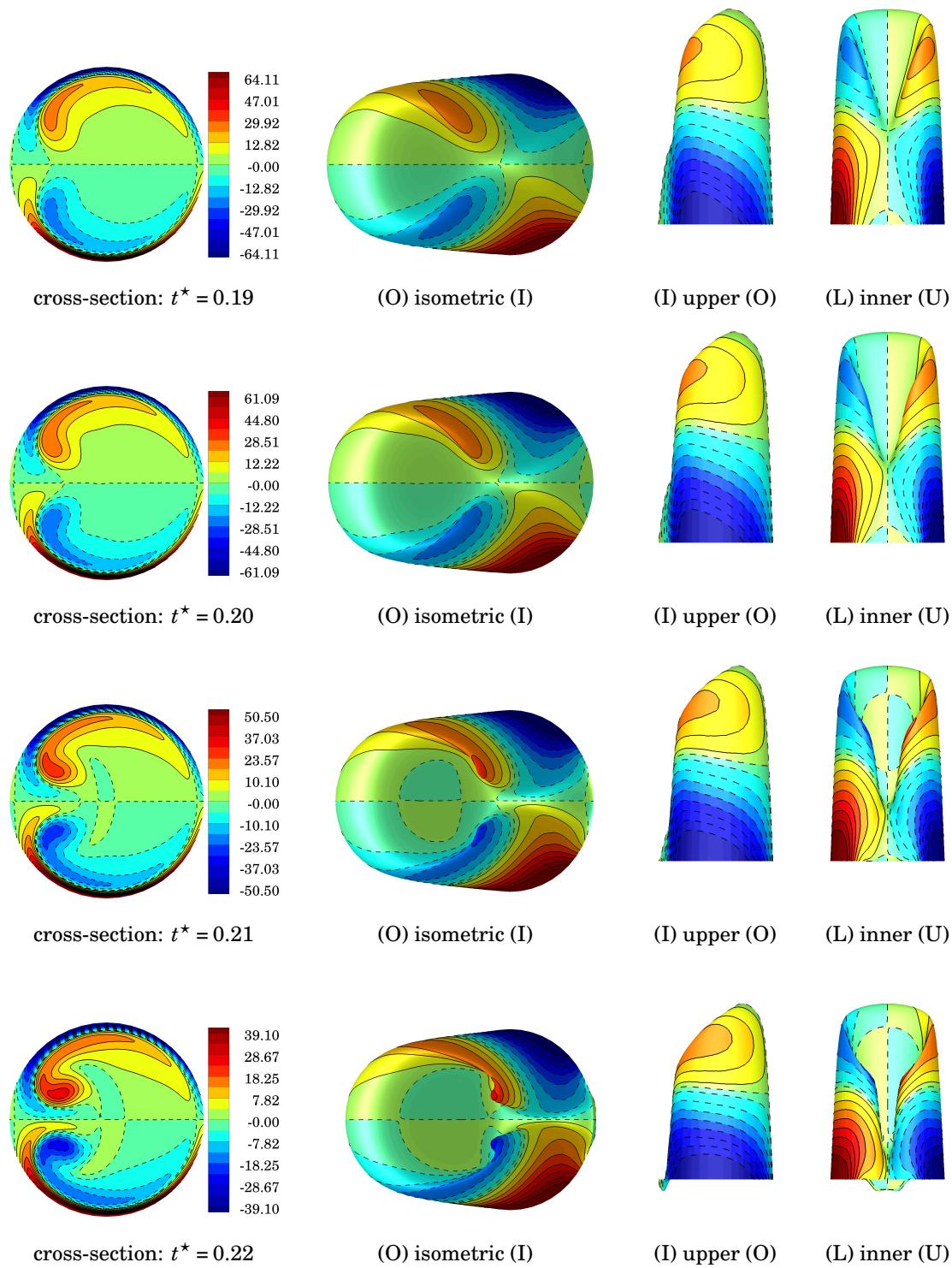


Figure D.2 Womersley entrance condition: velocity surface of u_s^* at $\theta = 45^\circ$ colored by non-dimensional streamwise vorticity ω_s^* visualized from three difference views: isometric, upper and inner. ($I \equiv inner$, $O \equiv outer$, $U \equiv upper$, $L \equiv lower$). (continued)

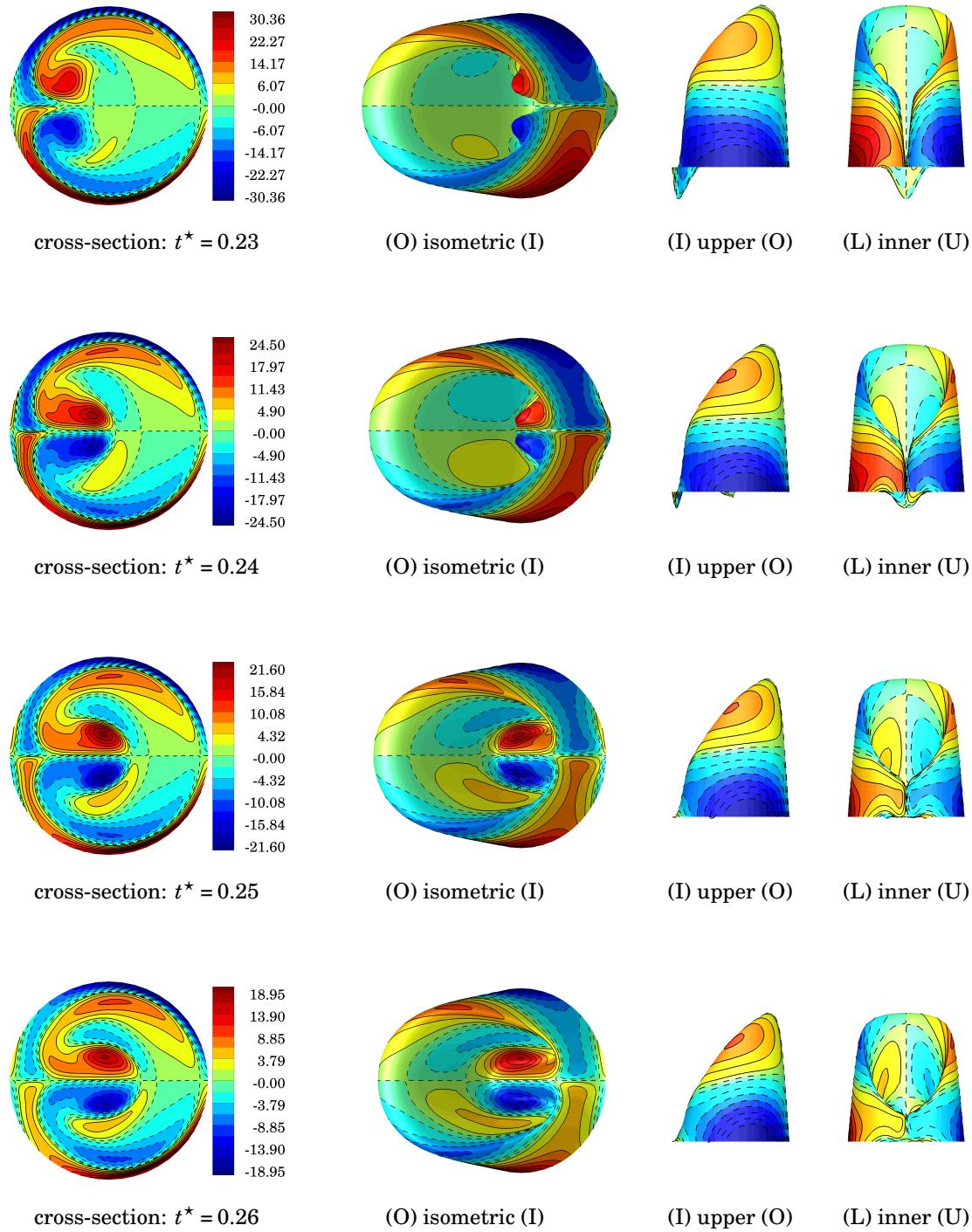


Figure D.2 Womersley entrance condition: velocity surface of u_s^* at $\theta = 45^\circ$ colored by non-dimensional streamwise vorticity ω_s^* visualized from three difference views: isometric, upper and inner. ($I \equiv$ inner, $O \equiv$ outer, $U \equiv$ upper, $L \equiv$ lower). (continued)

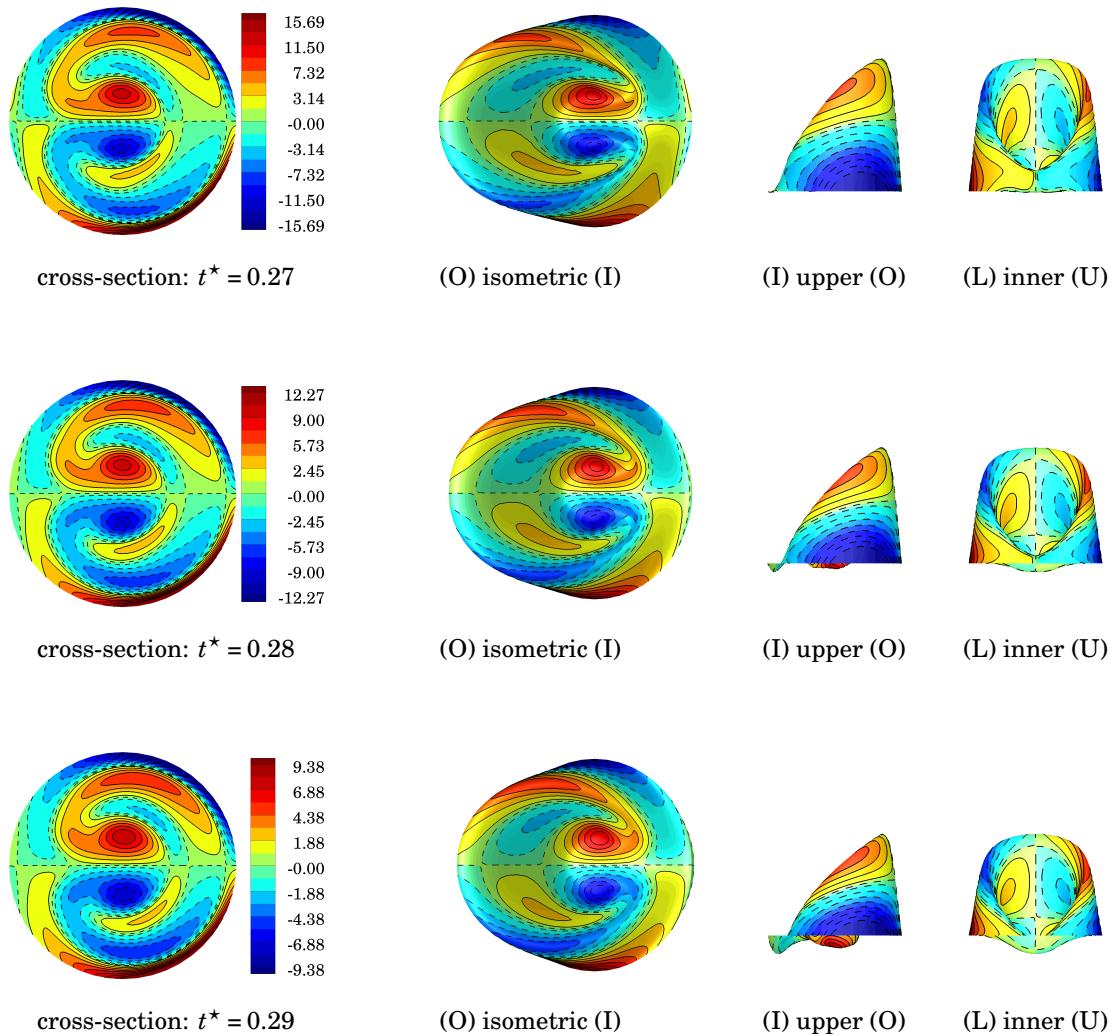


Figure D.2 Womersley entrance condition: velocity surface of u_s^* at $\theta = 45^\circ$ colored by non-dimensional streamwise vorticity ω_s^* visualized from three difference views: isometric, upper and inner. ($I \equiv \text{inner}$, $O \equiv \text{outer}$, $U \equiv \text{upper}$, $L \equiv \text{lower}$). (continued)

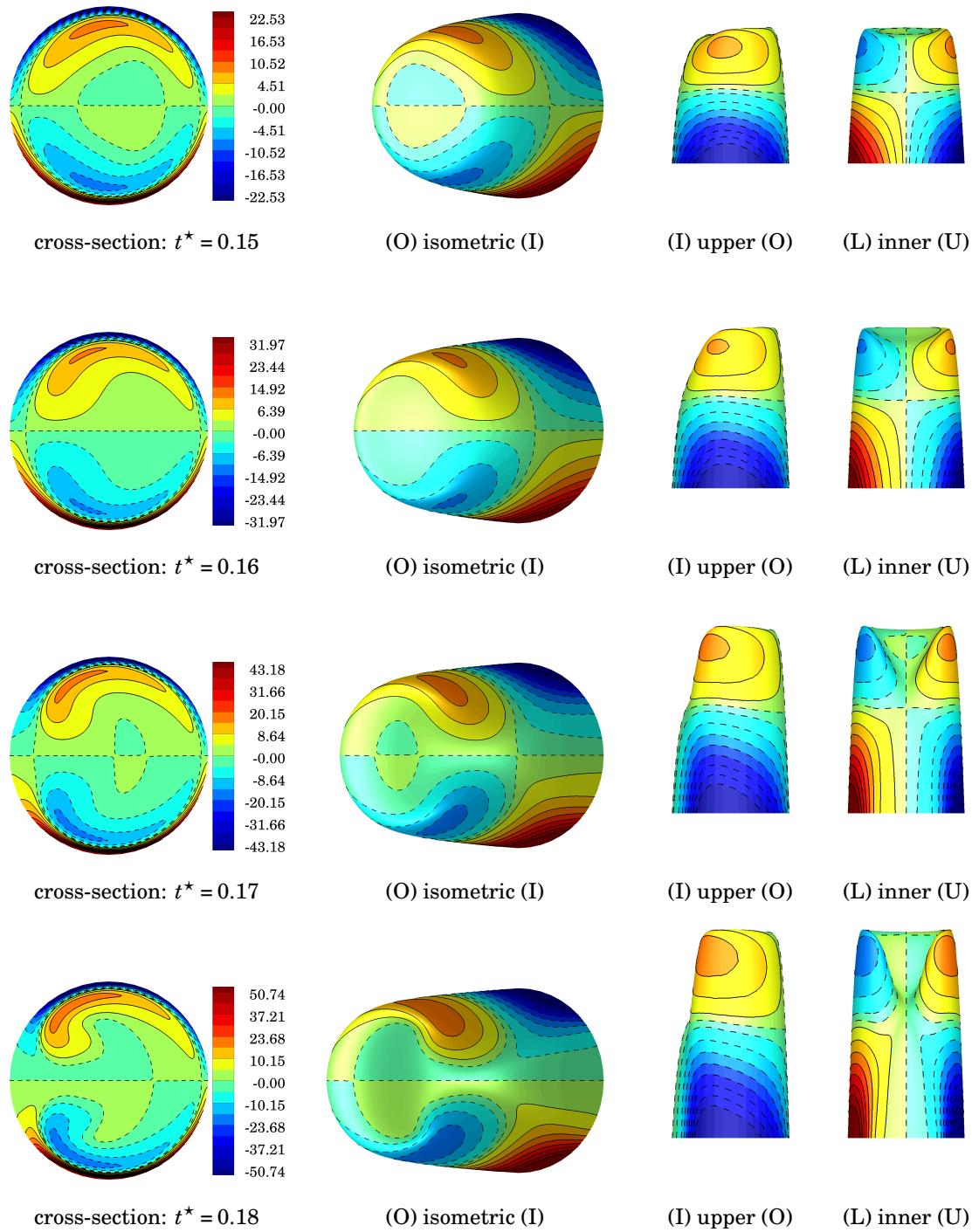


Figure D.3 Womersley entrance condition: velocity surface of u_s^* at $\theta = 90^\circ$ colored by non-dimensional streamwise vorticity ω_s^* visualized from three difference views: isometric, upper and inner. ($I \equiv inner$, $O \equiv outer$, $U \equiv upper$, $L \equiv lower$).

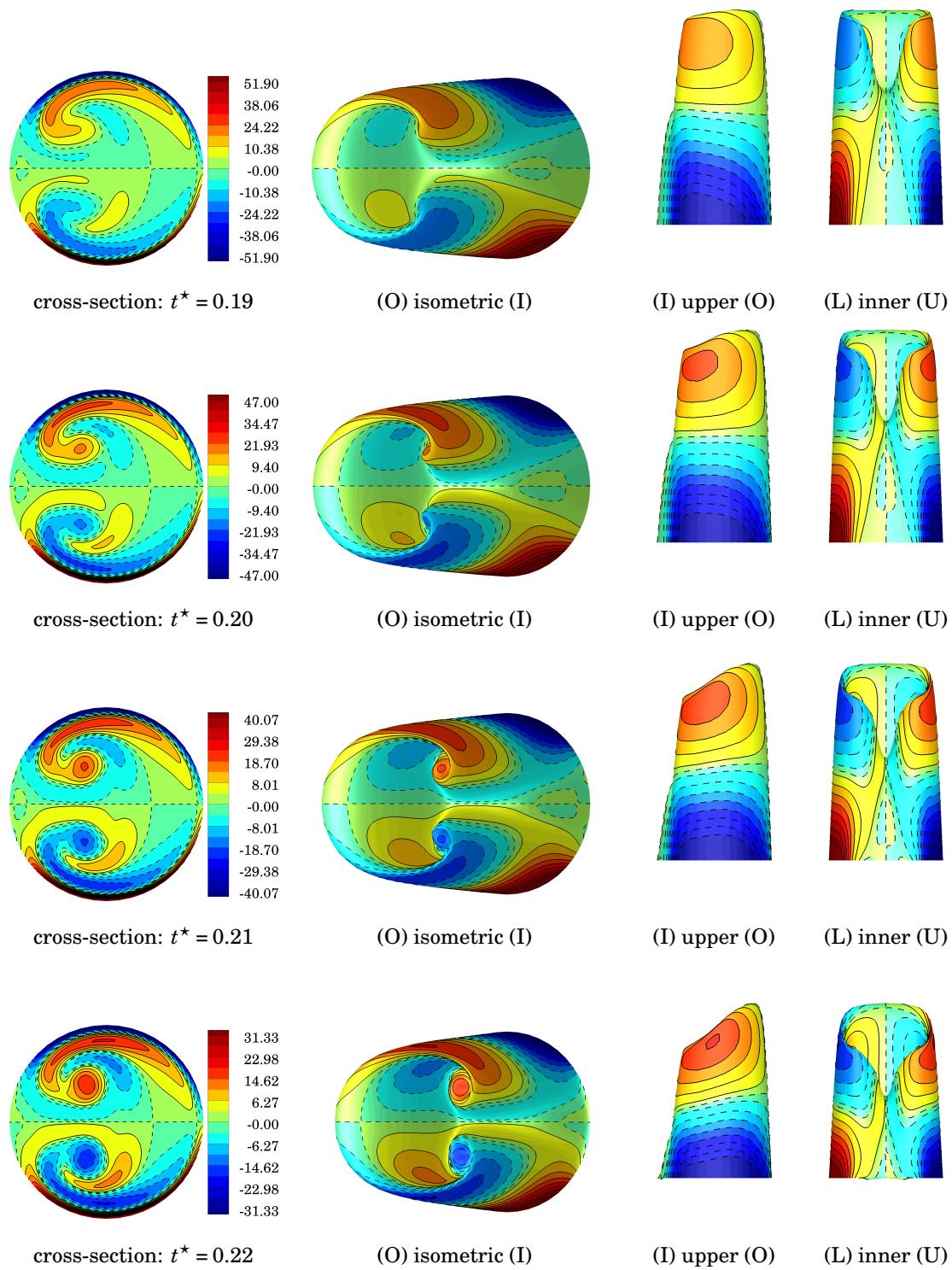


Figure D.3 Womersley entrance condition: velocity surface of u_s^* at $\theta = 90^\circ$ colored by non-dimensional streamwise vorticity ω_s^* visualized from three difference views: isometric, upper and inner. ($I \equiv inner$, $O \equiv outer$, $U \equiv upper$, $L \equiv lower$). (continued)

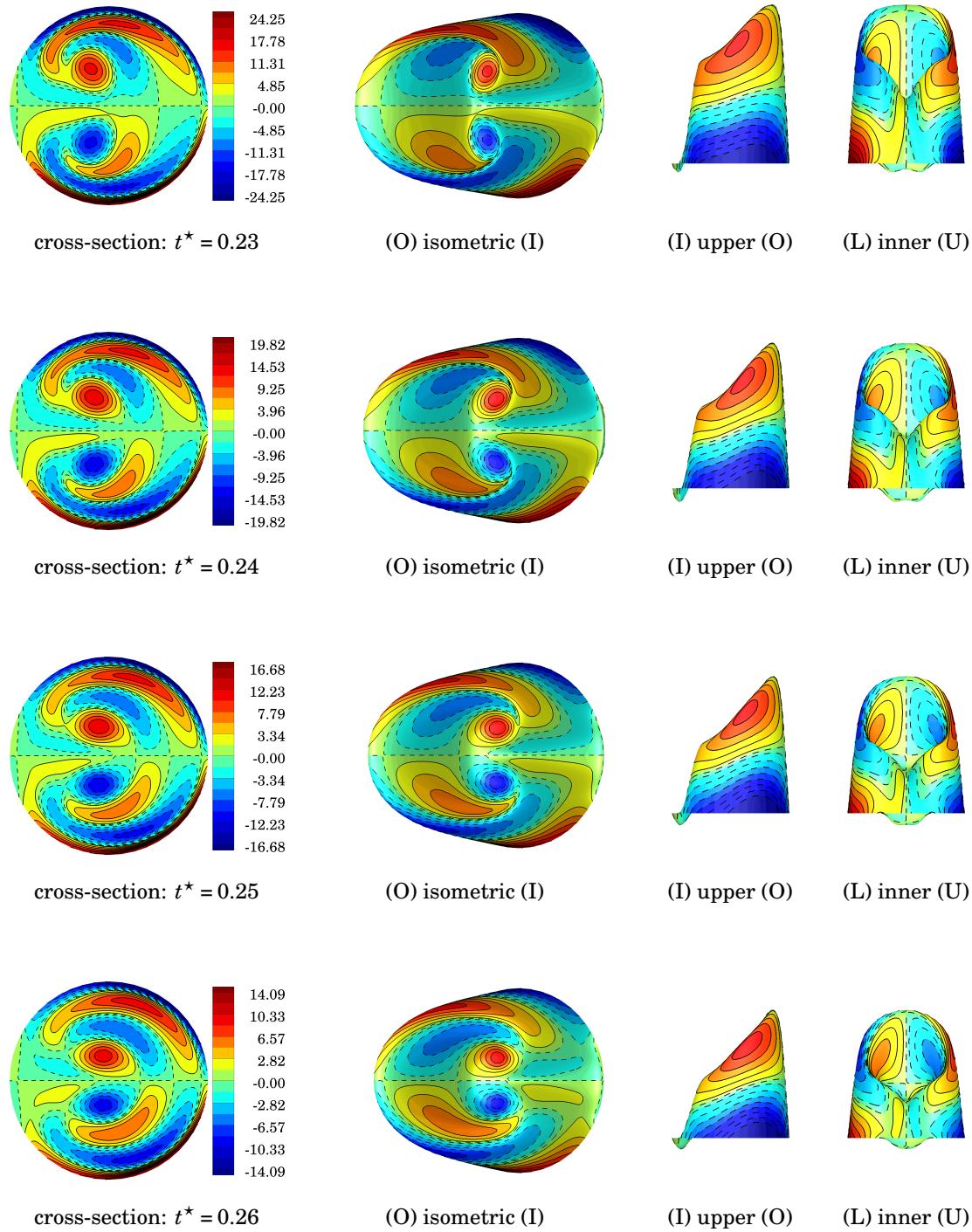


Figure D.3 Womersley entrance condition: velocity surface of u_s^* at $\theta = 90^\circ$ colored by non-dimensional streamwise vorticity ω_s^* visualized from three difference views: isometric, upper and inner. ($I \equiv inner$, $O \equiv outer$, $U \equiv upper$, $L \equiv lower$). (continued)

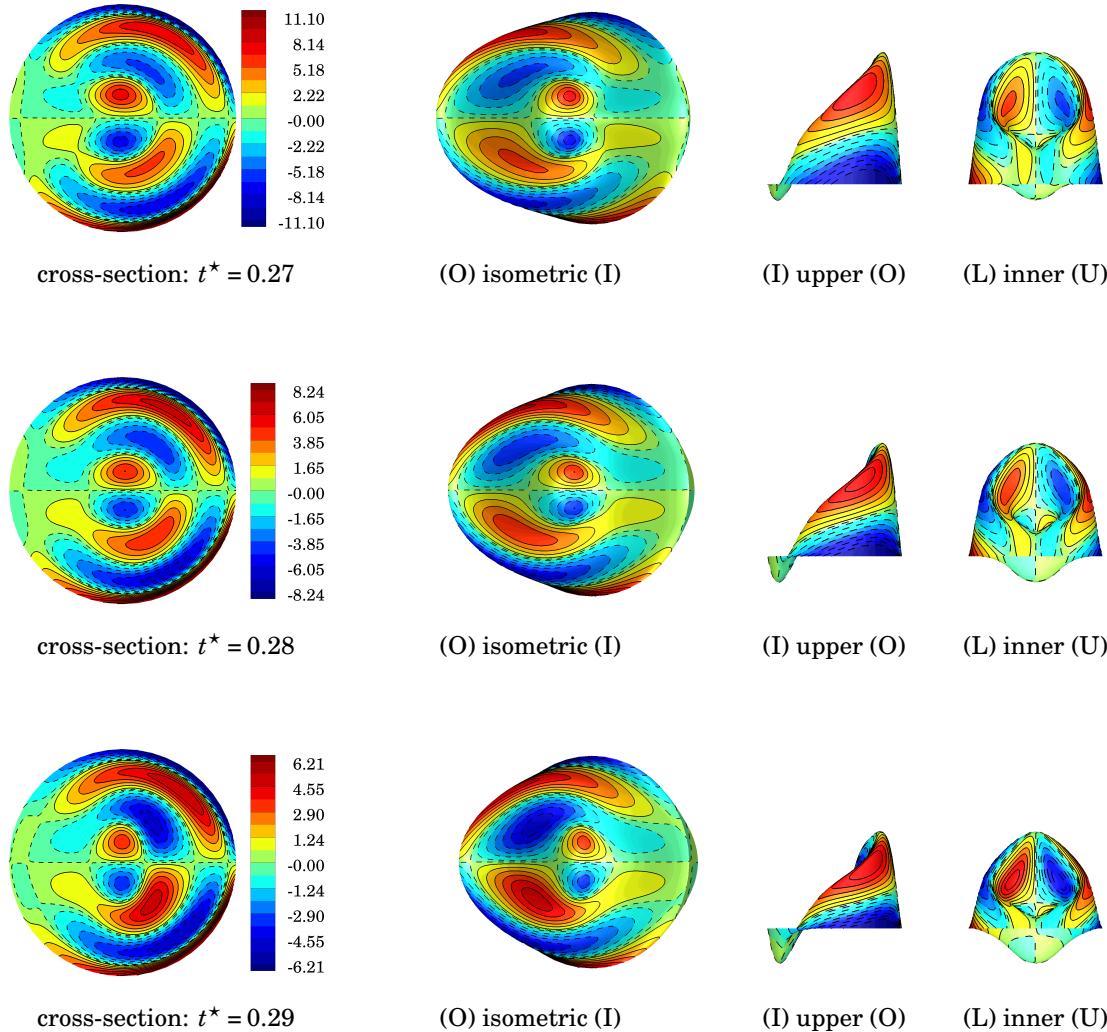


Figure D.3 Womersley entrance condition: velocity surface of u_s^* at $\theta = 90^\circ$ colored by non-dimensional streamwise vorticity ω_s^* visualized from three difference views: isometric, upper and inner. ($I \equiv inner$, $O \equiv outer$, $U \equiv upper$, $L \equiv lower$). (continued)

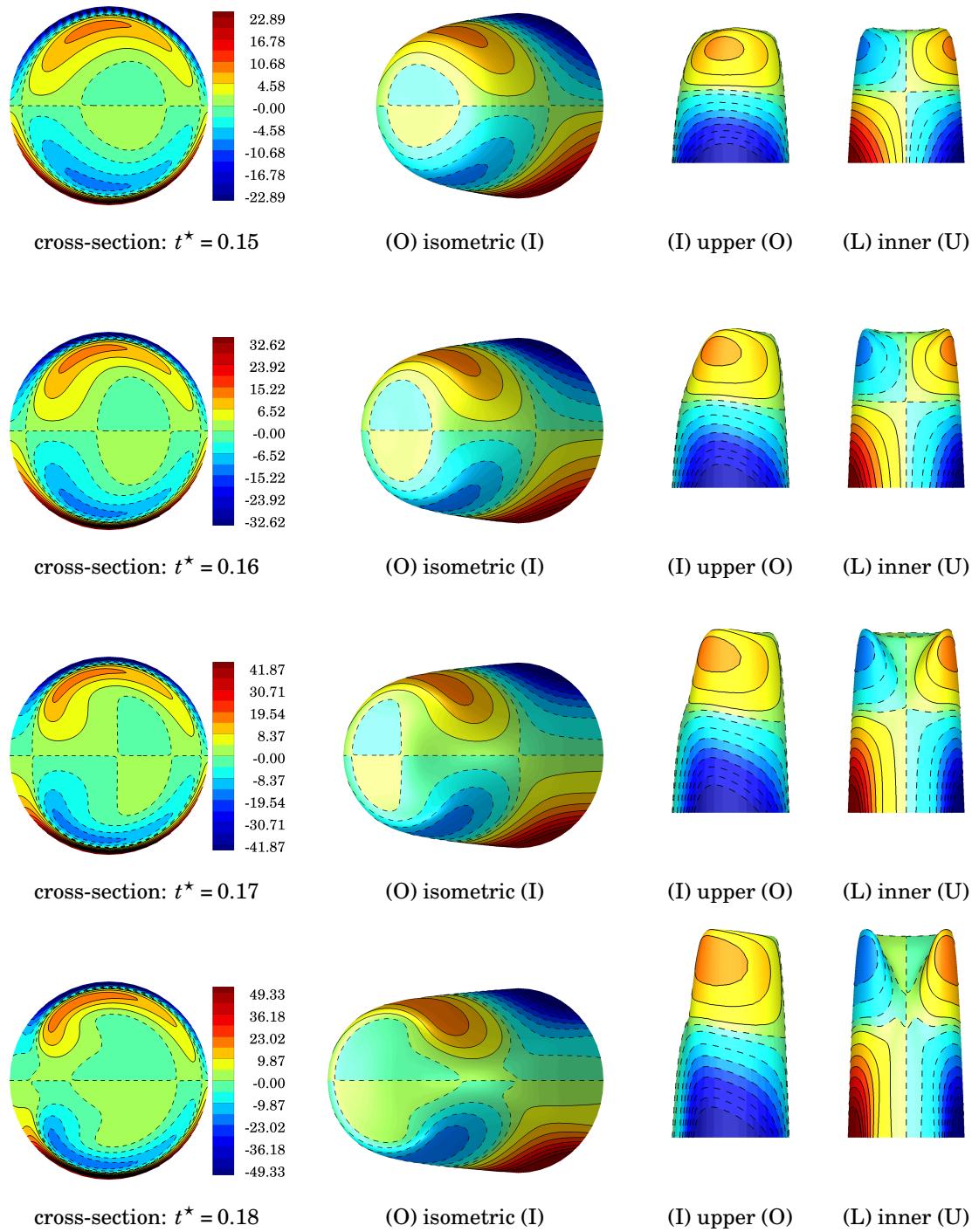


Figure D.4 Womersley entrance condition: velocity surface of u_s^* at $\theta = 135^\circ$ colored by non-dimensional streamwise vorticity ω_s^* visualized from three difference views: isometric, upper and inner. ($I \equiv$ inner, $O \equiv$ outer, $U \equiv$ upper, $L \equiv$ lower).

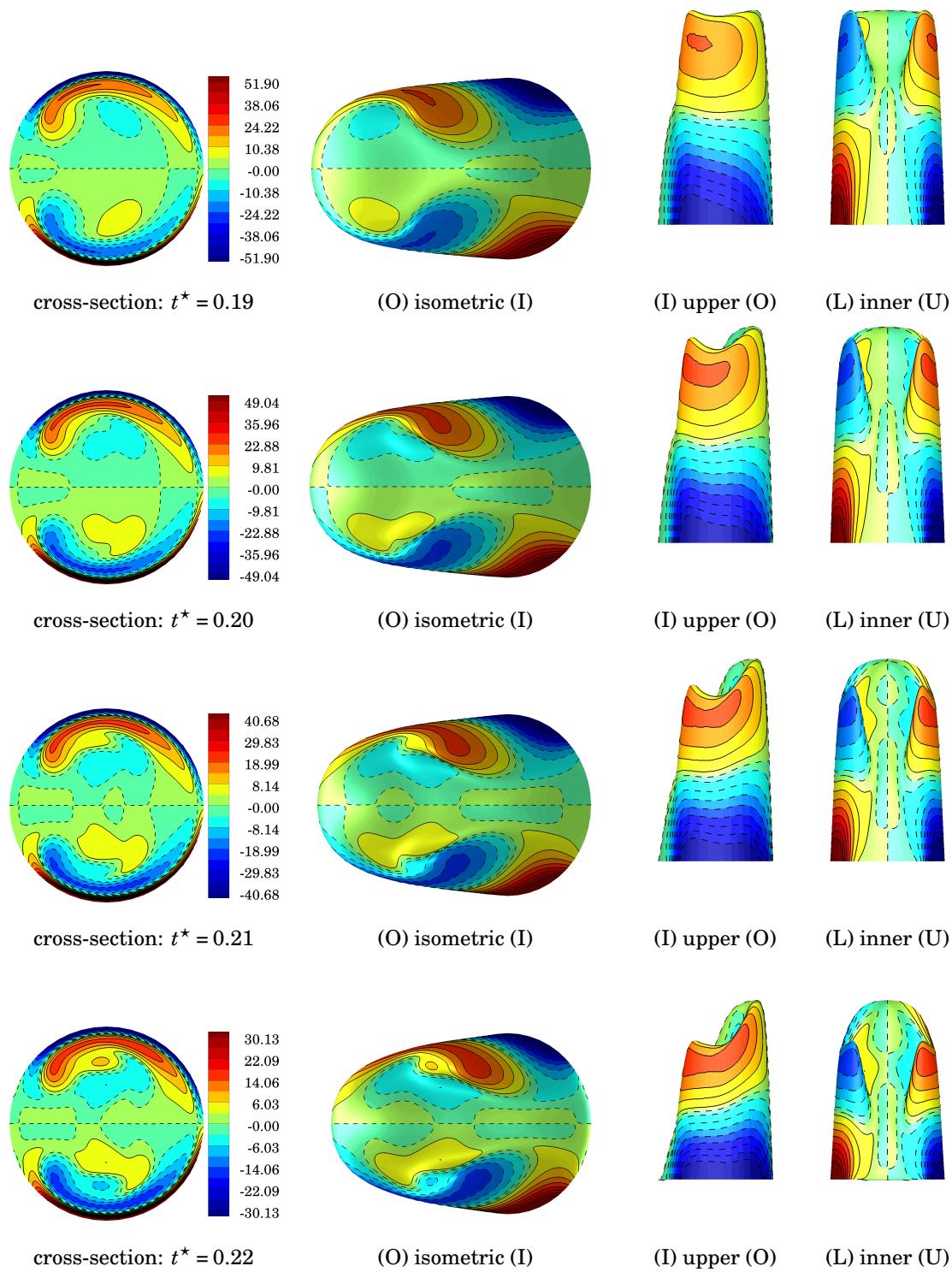


Figure D.4 Womersley entrance condition: velocity surface of u_s^* at $\theta = 135^\circ$ colored by non-dimensional streamwise vorticity ω_s^* visualized from three difference views: isometric, upper and inner. ($I \equiv$ inner, $O \equiv$ outer, $U \equiv$ upper, $L \equiv$ lower). (continued)

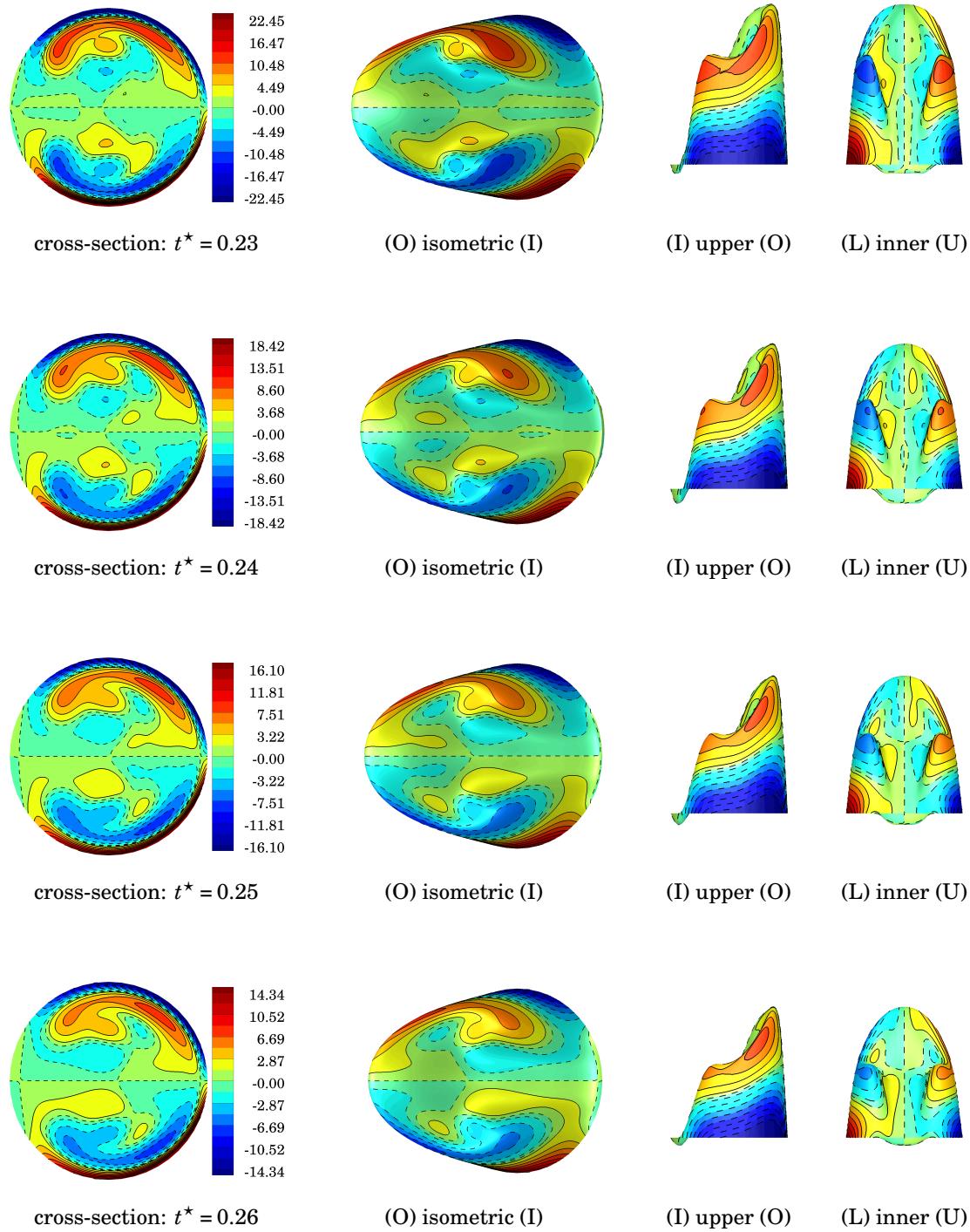


Figure D.4 Womersley entrance condition: velocity surface of u_s^* at $\theta = 135^\circ$ colored by non-dimensional streamwise vorticity ω_s^* visualized from three difference views: isometric, upper and inner. ($I \equiv inner$, $O \equiv outer$, $U \equiv upper$, $L \equiv lower$). (continued)

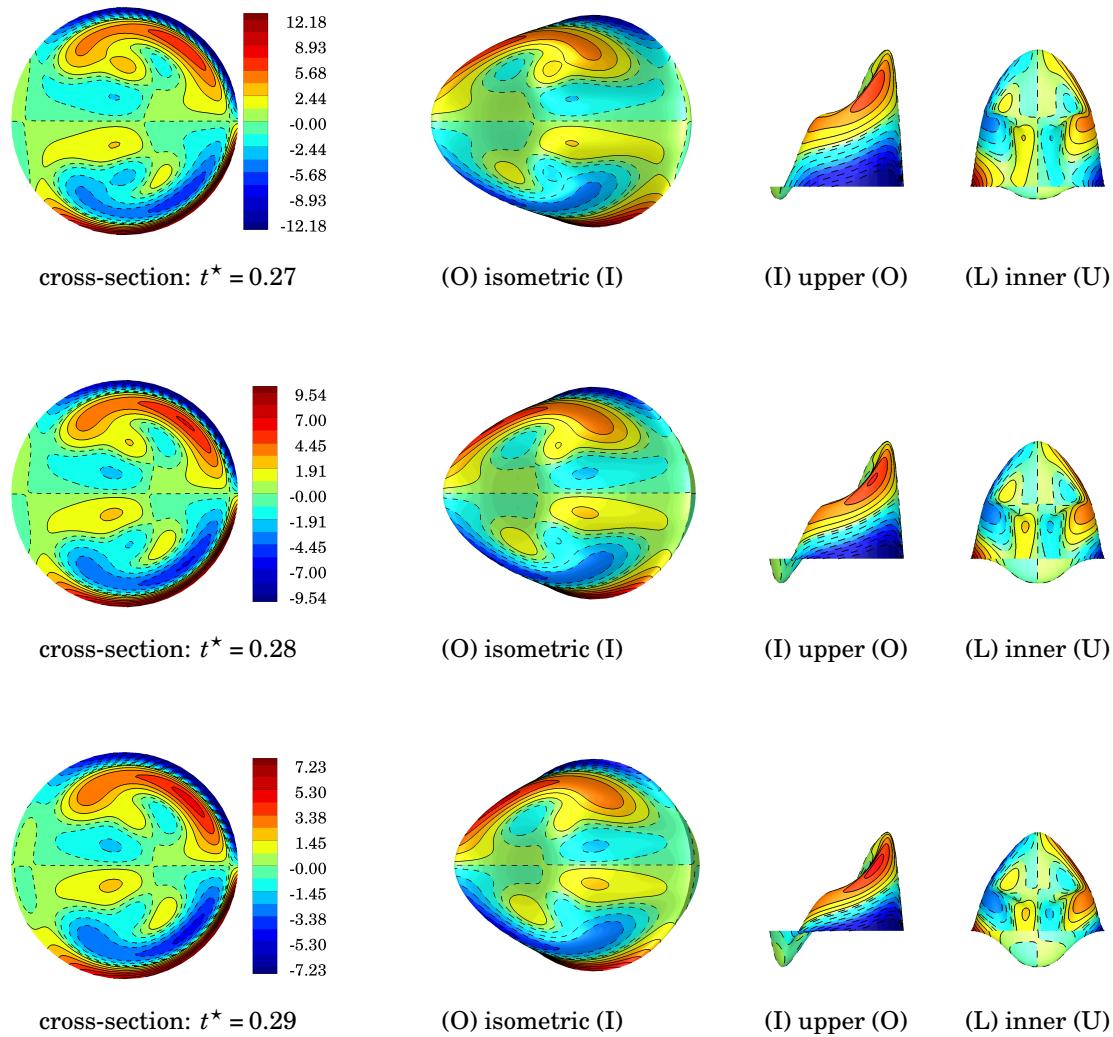


Figure D.4 Womersley entrance condition: velocity surface of u_s^* at $\theta = 135^\circ$ colored by non-dimensional streamwise vorticity ω_s^* visualized from three difference views: isometric, upper and inner. ($I \equiv inner$, $O \equiv outer$, $U \equiv upper$, $L \equiv lower$). (continued)

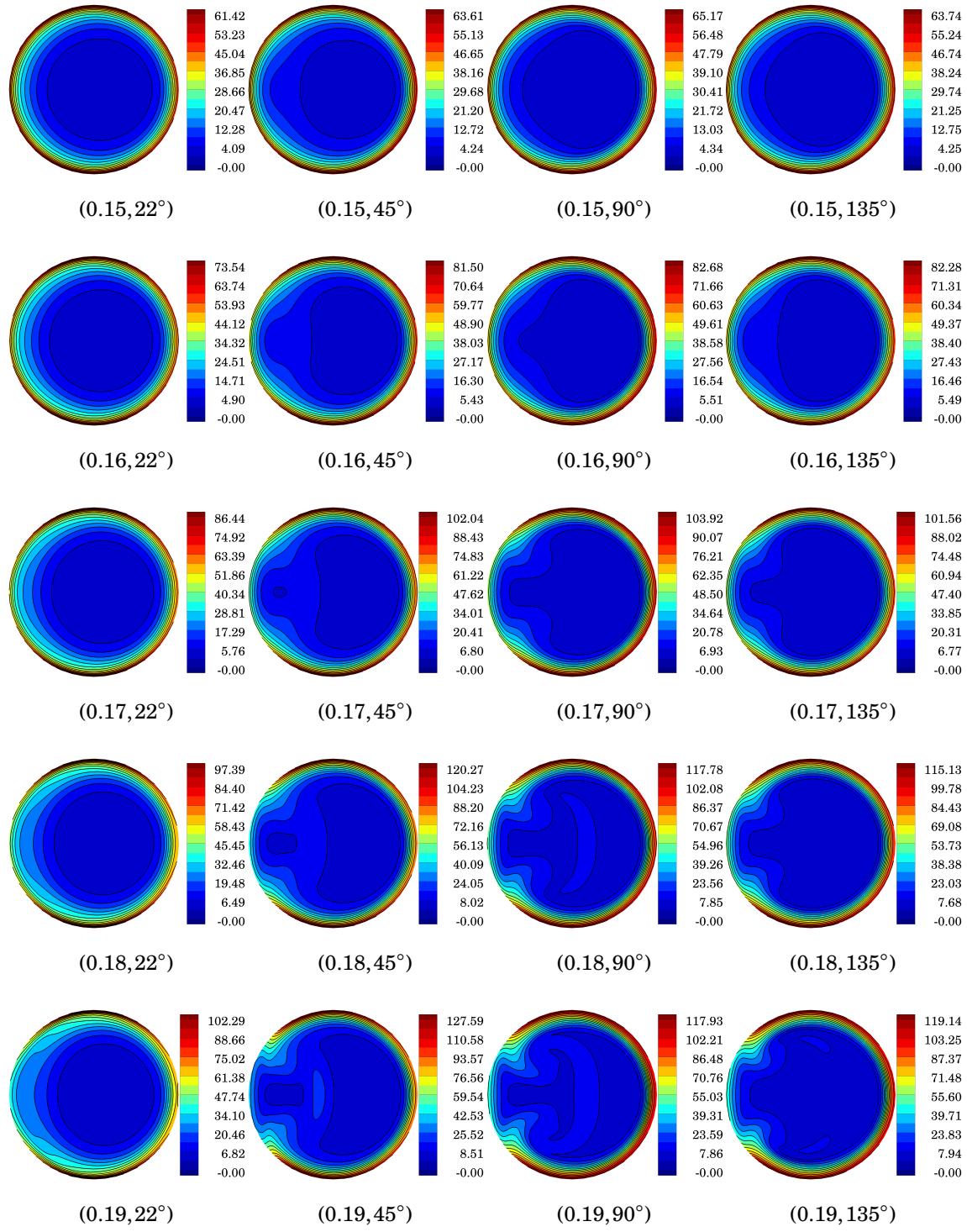


Figure D.5 Womersley entrance condition: non-dimensional vorticity magnitude $|\omega^*|$ at (t^*, ϕ) .

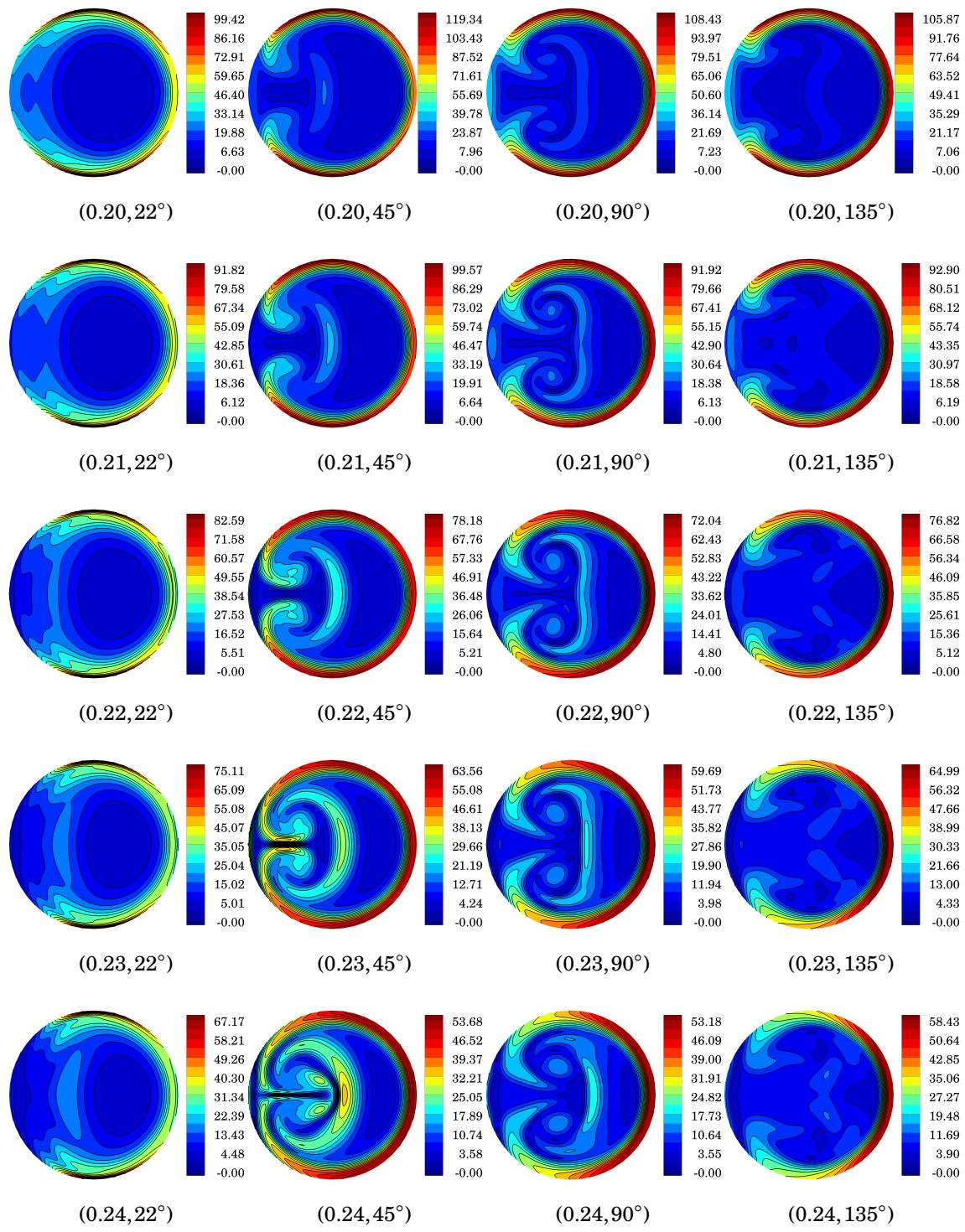


Figure D.5 Womersley entrance condition: non-dimensional vorticity magnitude $|\omega^*|$ at (t^*, ϕ) . (*continued*)

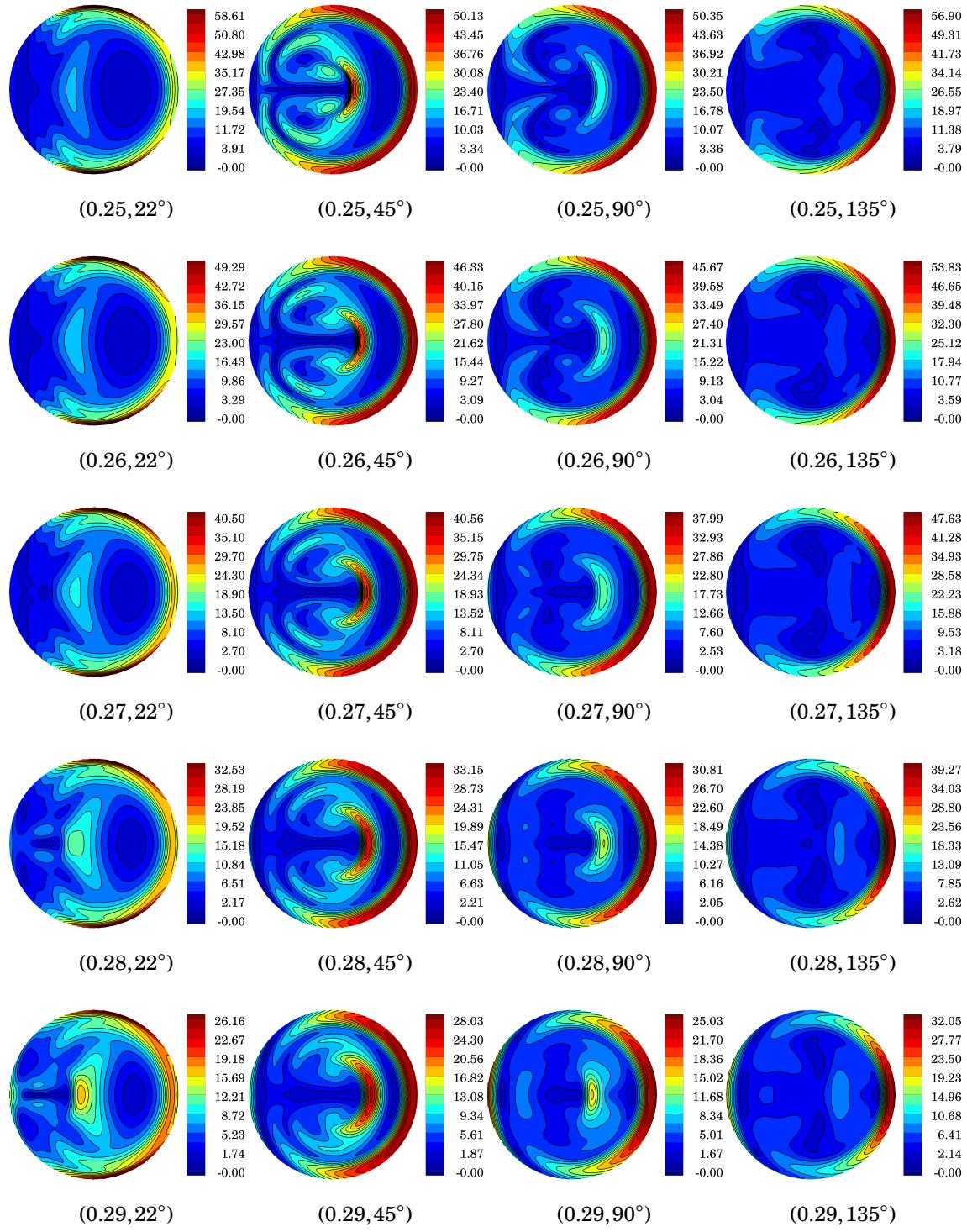


Figure D.5 Womersley entrance condition: non-dimensional vorticity magnitude $|\omega^*|$ at (t^*, ϕ) . (continued)

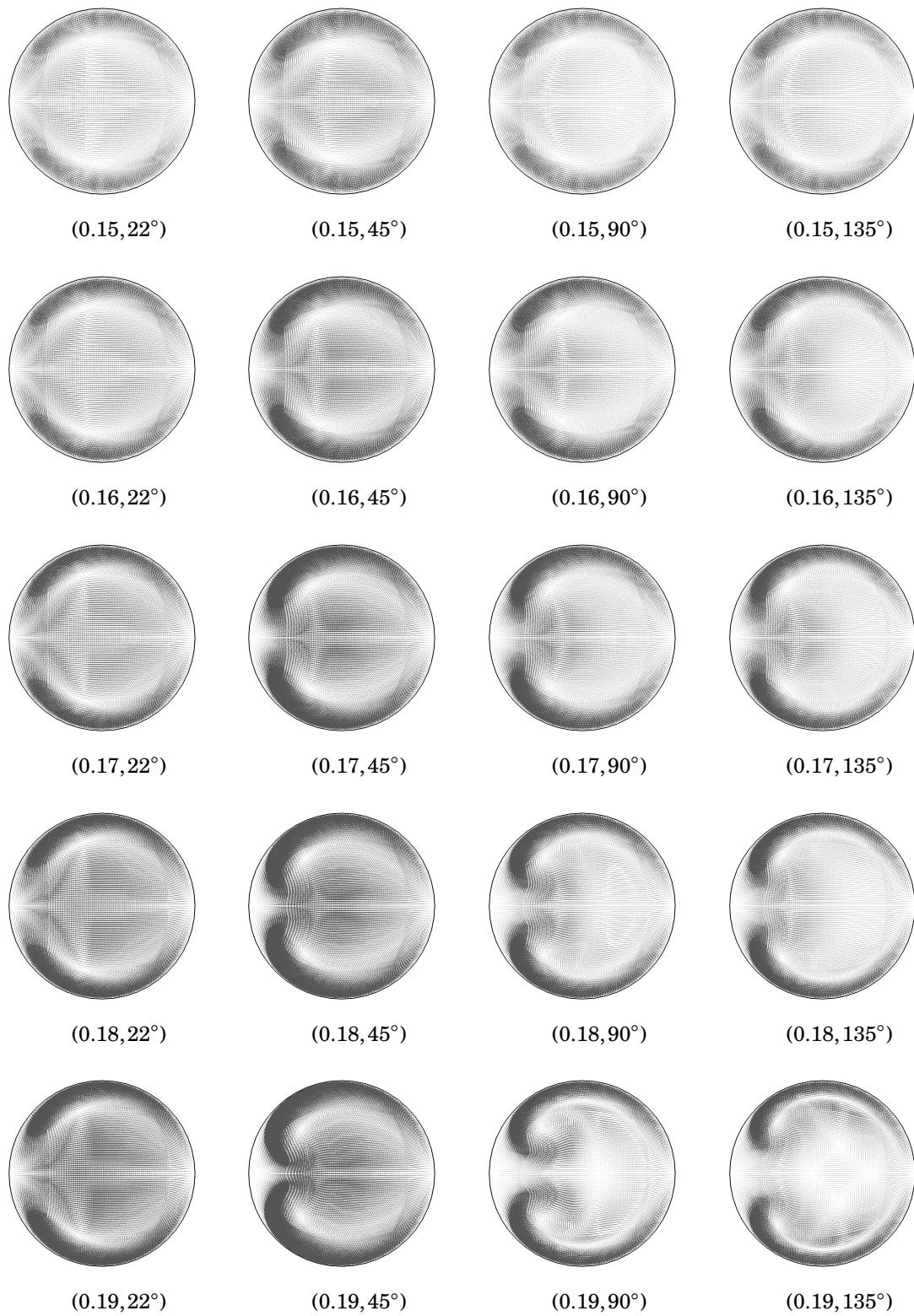


Figure D.6 Womersley entrance condition: non-dimensional secondary velocity vectors $\mathbf{u}_{\theta r}^*$ at (t^*, ϕ) .

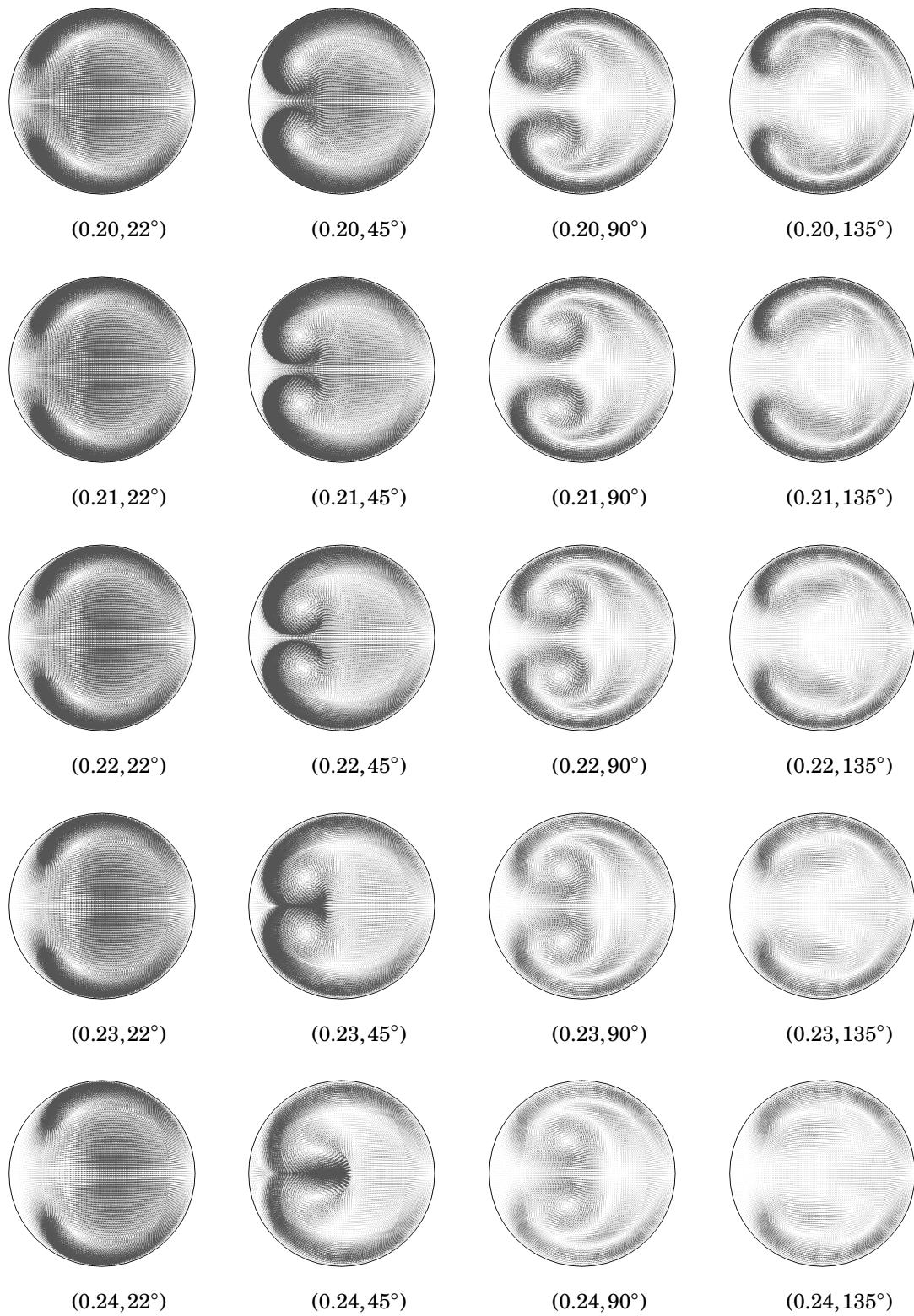


Figure D.6 Womersley entrance condition: non-dimensional secondary velocity vectors $\mathbf{u}_{\theta r}^*$ at (t^*, ϕ) . (*continued*)

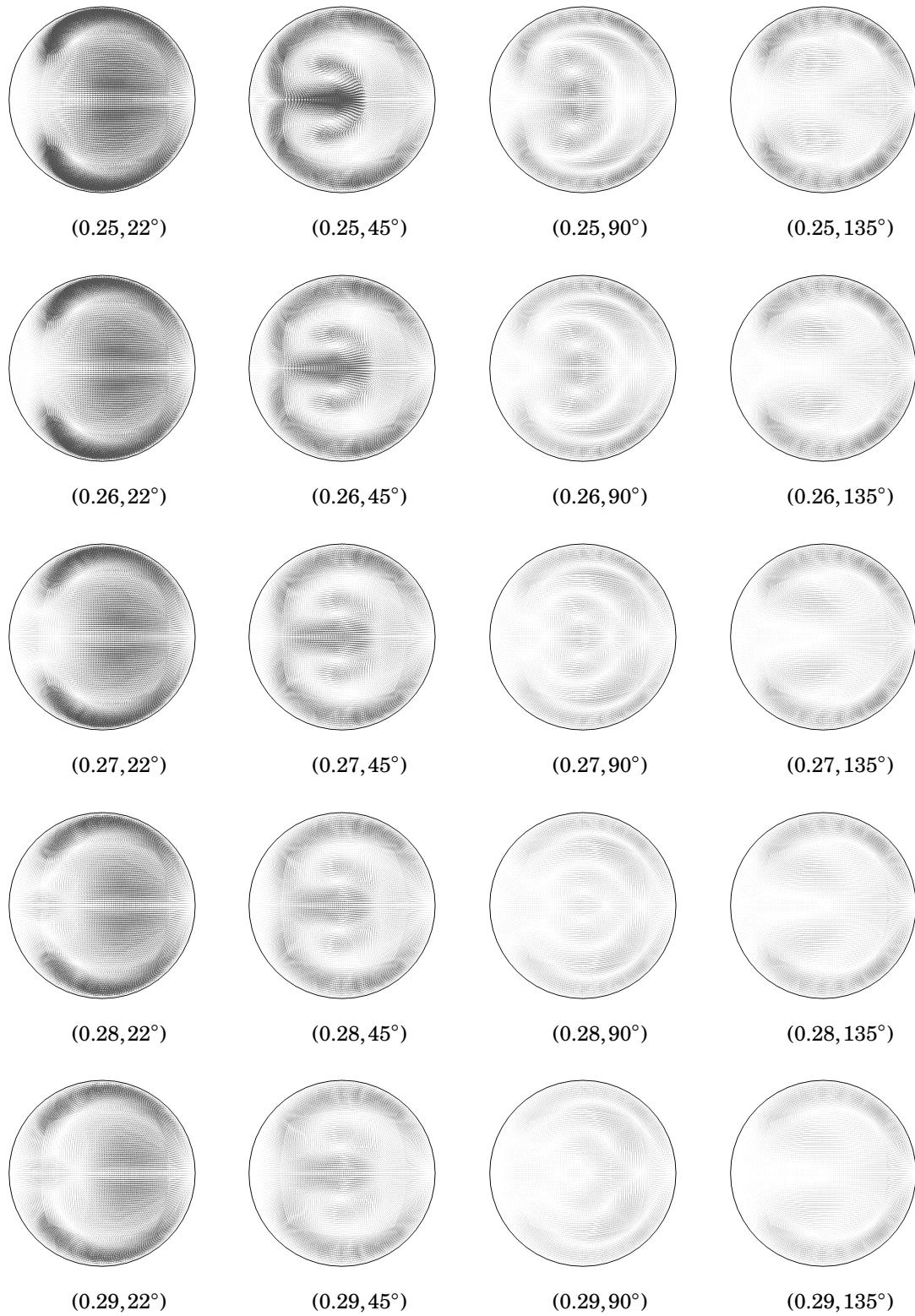


Figure D.6 Womersley entrance condition: non-dimensional secondary velocity vectors $\mathbf{u}_{\theta r}^*$ at (t^*, ϕ) . (*continued*)

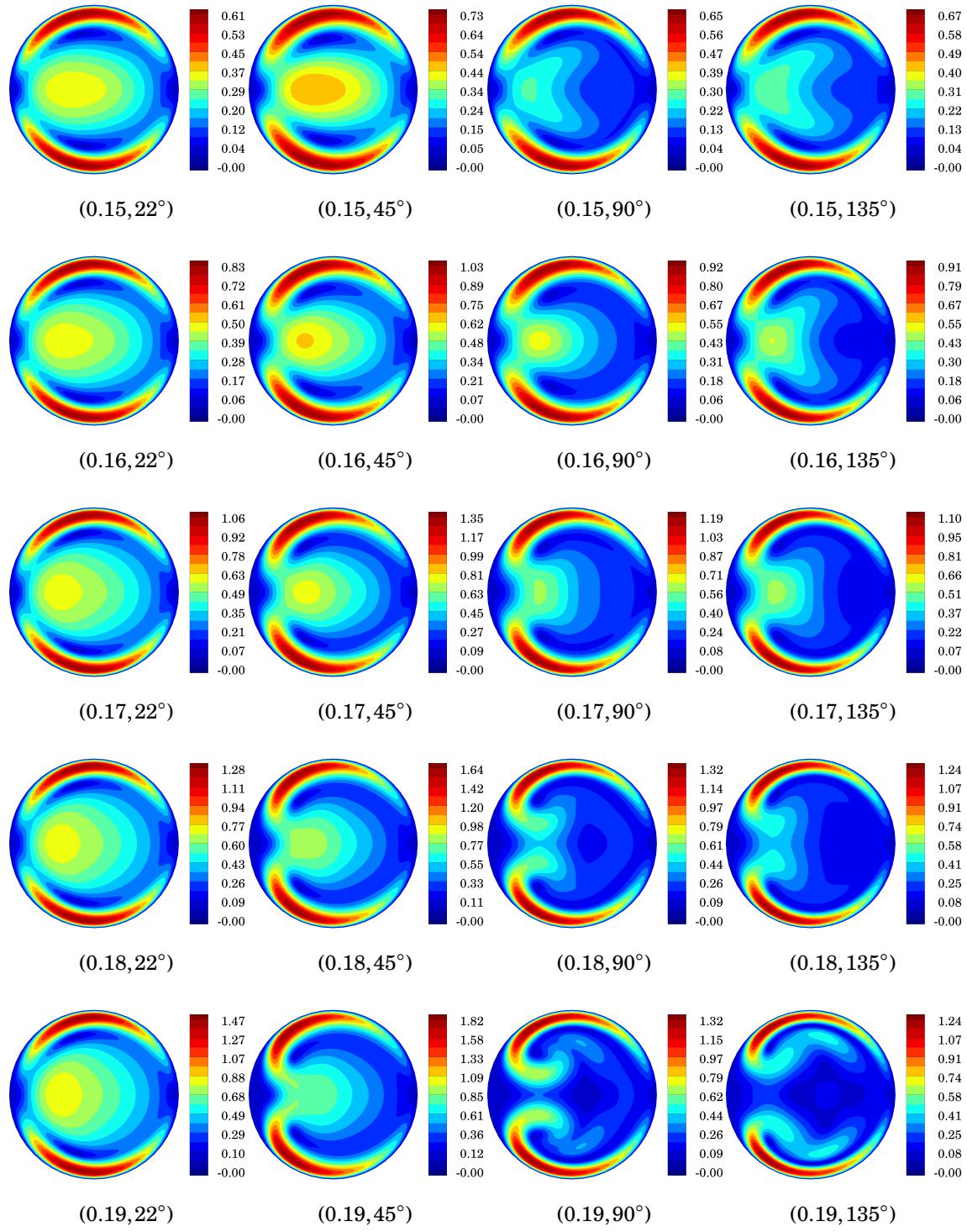


Figure D.7 Womersley entrance condition: non-dimensional secondary velocity magnitude $|u_{\theta r}^*|$ at (t^*, ϕ) .

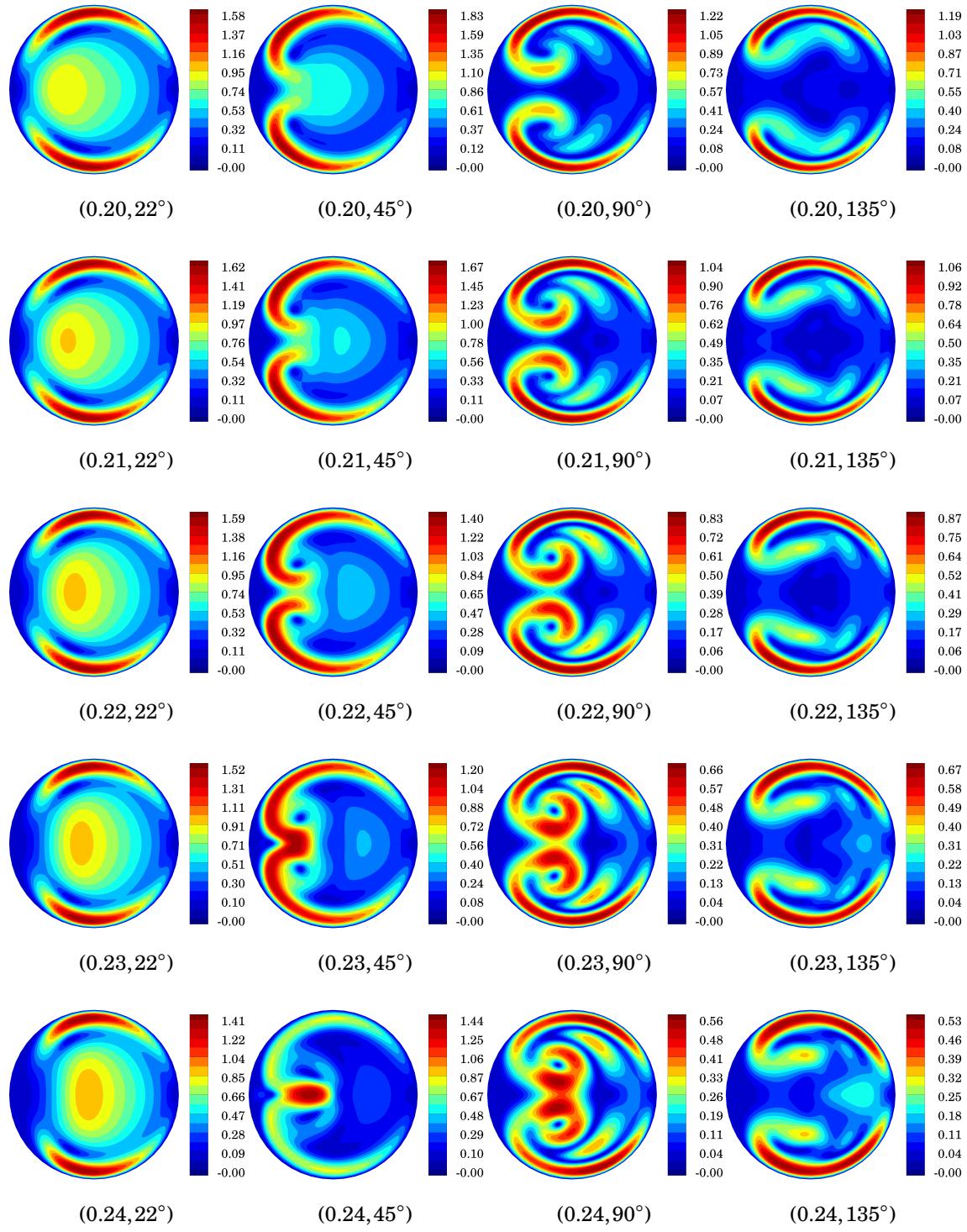


Figure D.7 Womersley entrance condition: non-dimensional secondary velocity magnitude $|u_{\theta r}^*|$ at (t^*, ϕ) . (continued)

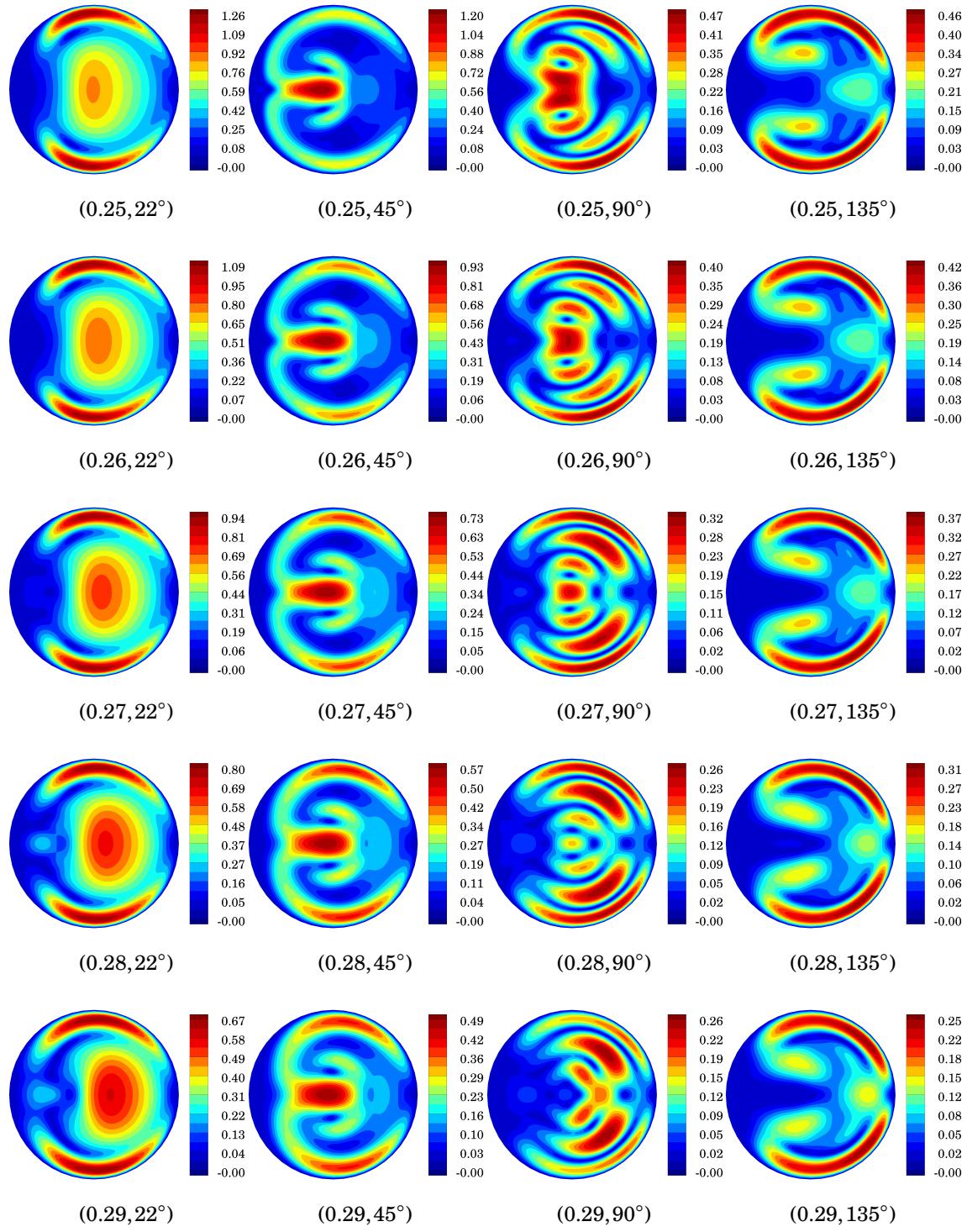


Figure D.7 Womersley entrance condition: non-dimensional secondary velocity magnitude $|u_{\theta r}^*|$ at (t^*, ϕ) . (continued)

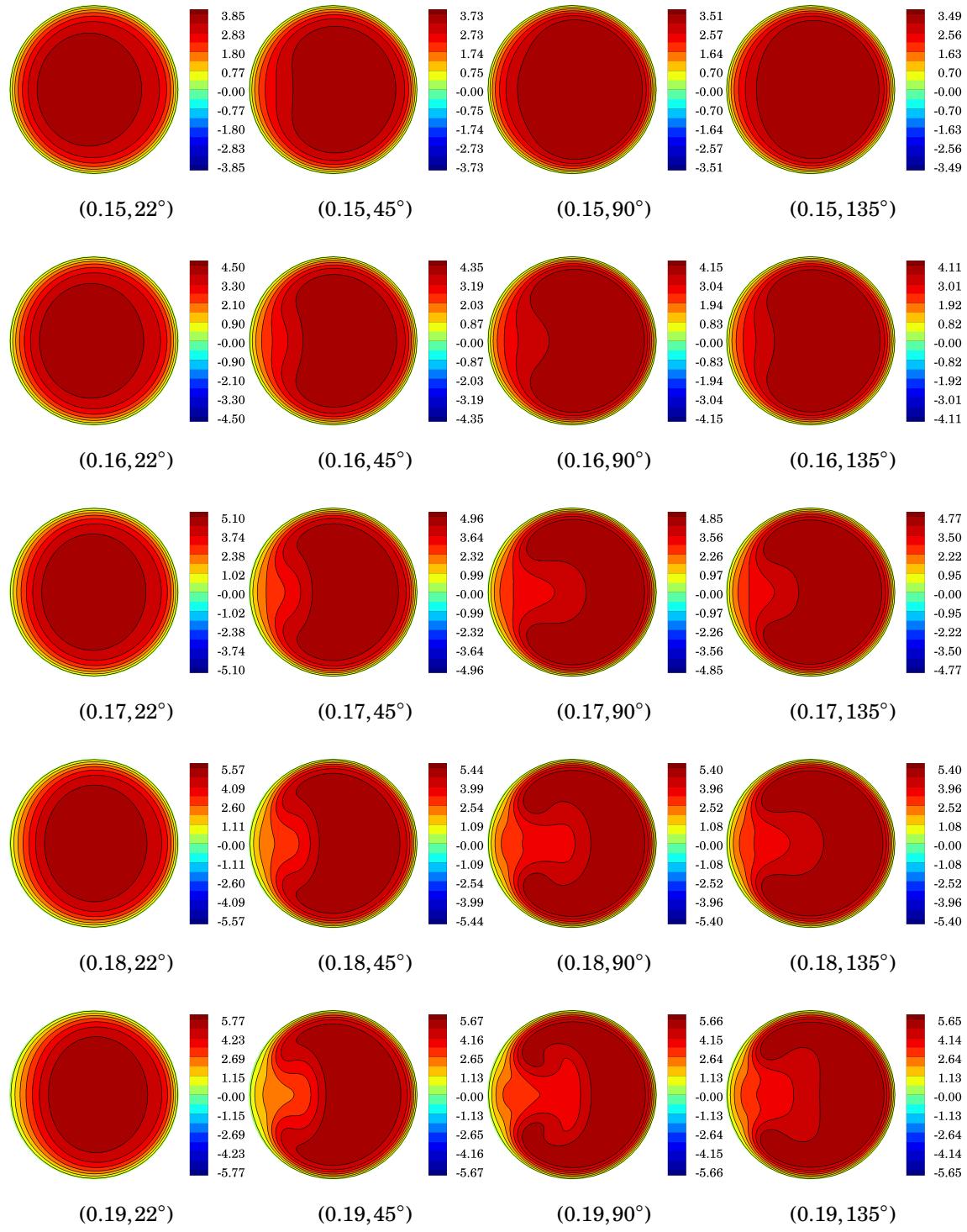


Figure D.8 Womersley entrance condition: non-dimensional streamwise velocity u_s^* at (t^*, ϕ) .

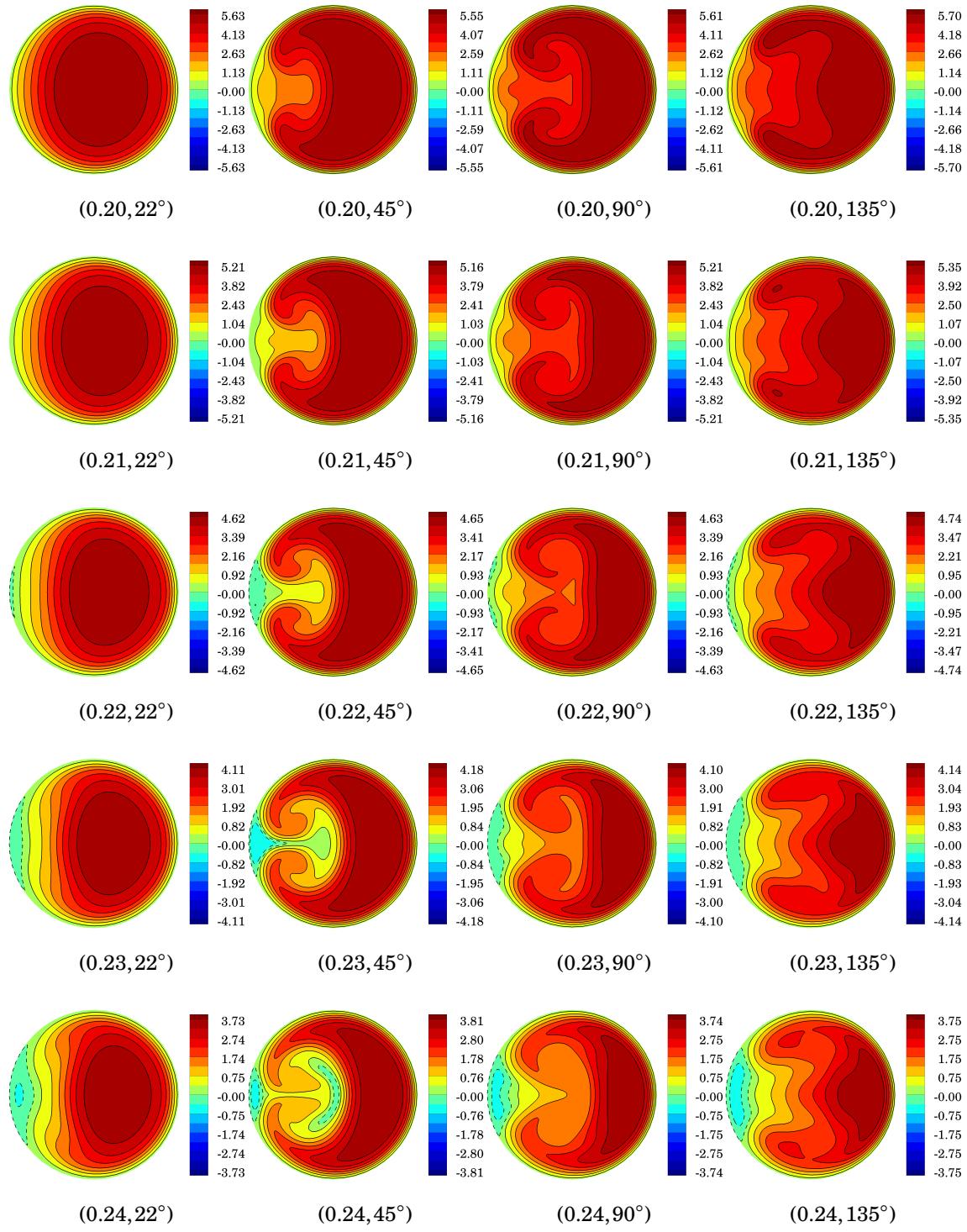


Figure D.8 Womersley entrance condition: non-dimensional streamwise velocity u_s^* at (t^*, ϕ) . (continued)

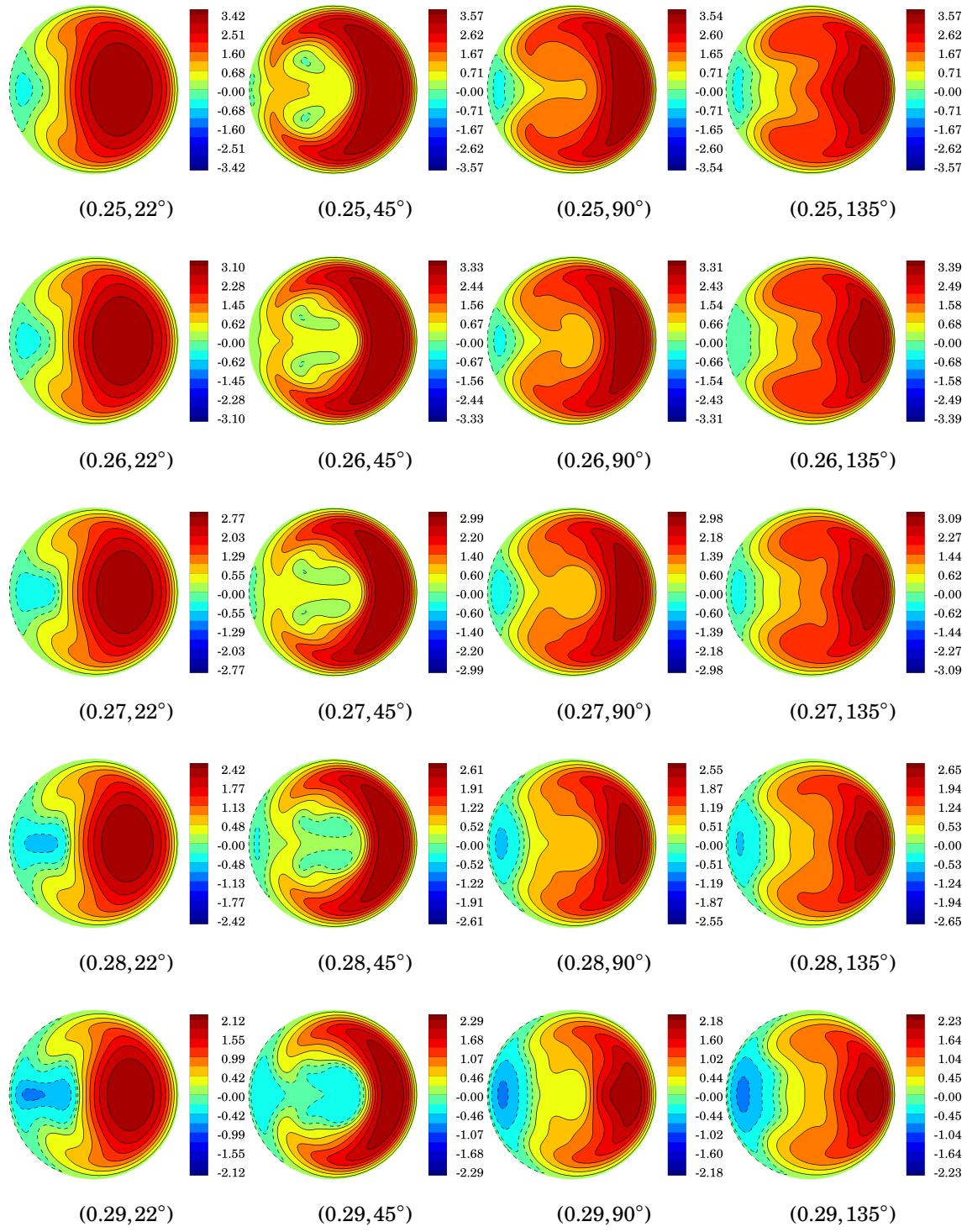


Figure D.8 Womersley entrance condition: non-dimensional streamwise velocity u_s^* at (t^*, ϕ) . (*continued*)

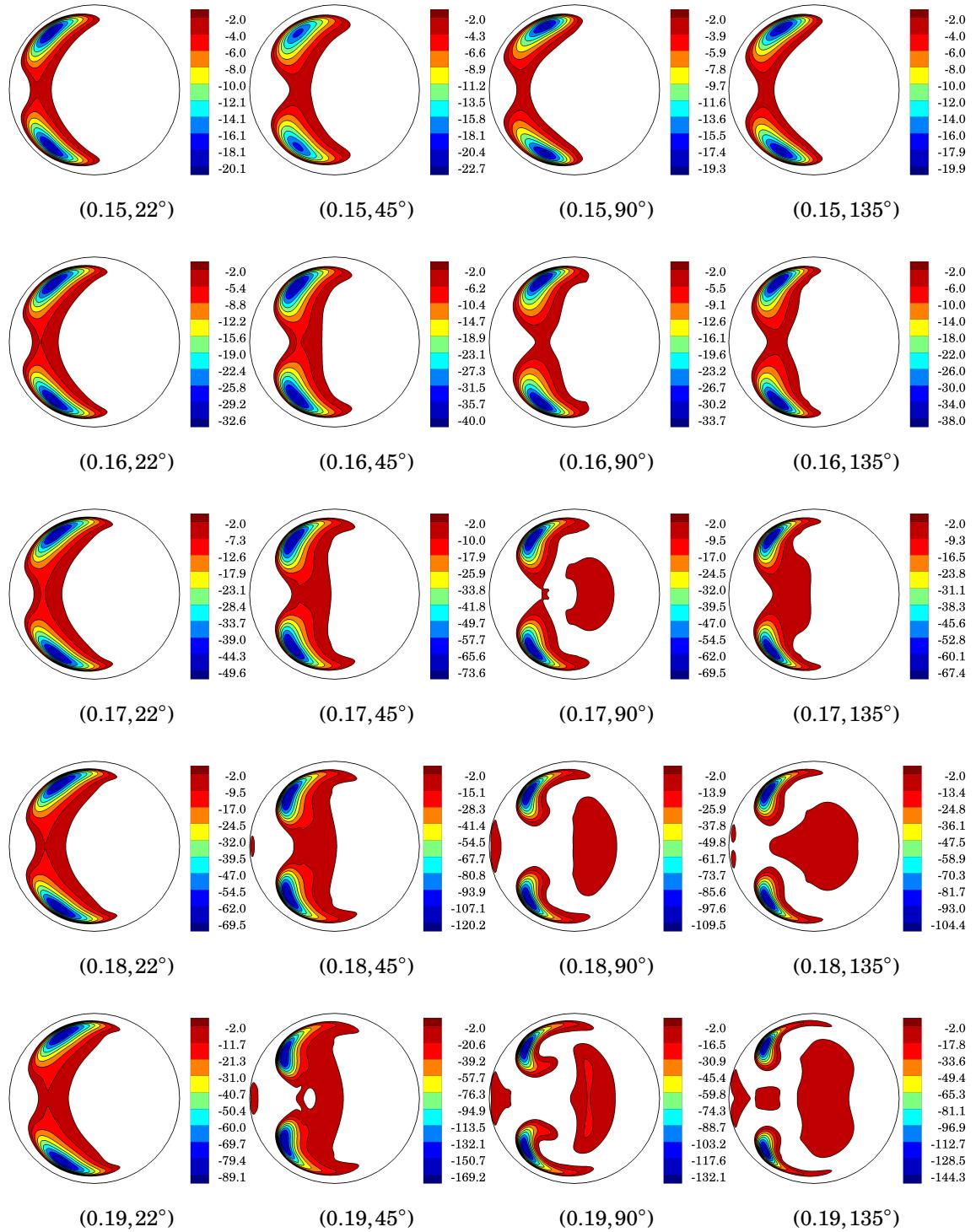


Figure D.9 Womersley entrance condition: non-dimensional second eigenvalue λ_2^* of $S^2 + R^2$, $\lambda_2^* < 0$ at (t^*, ϕ) .

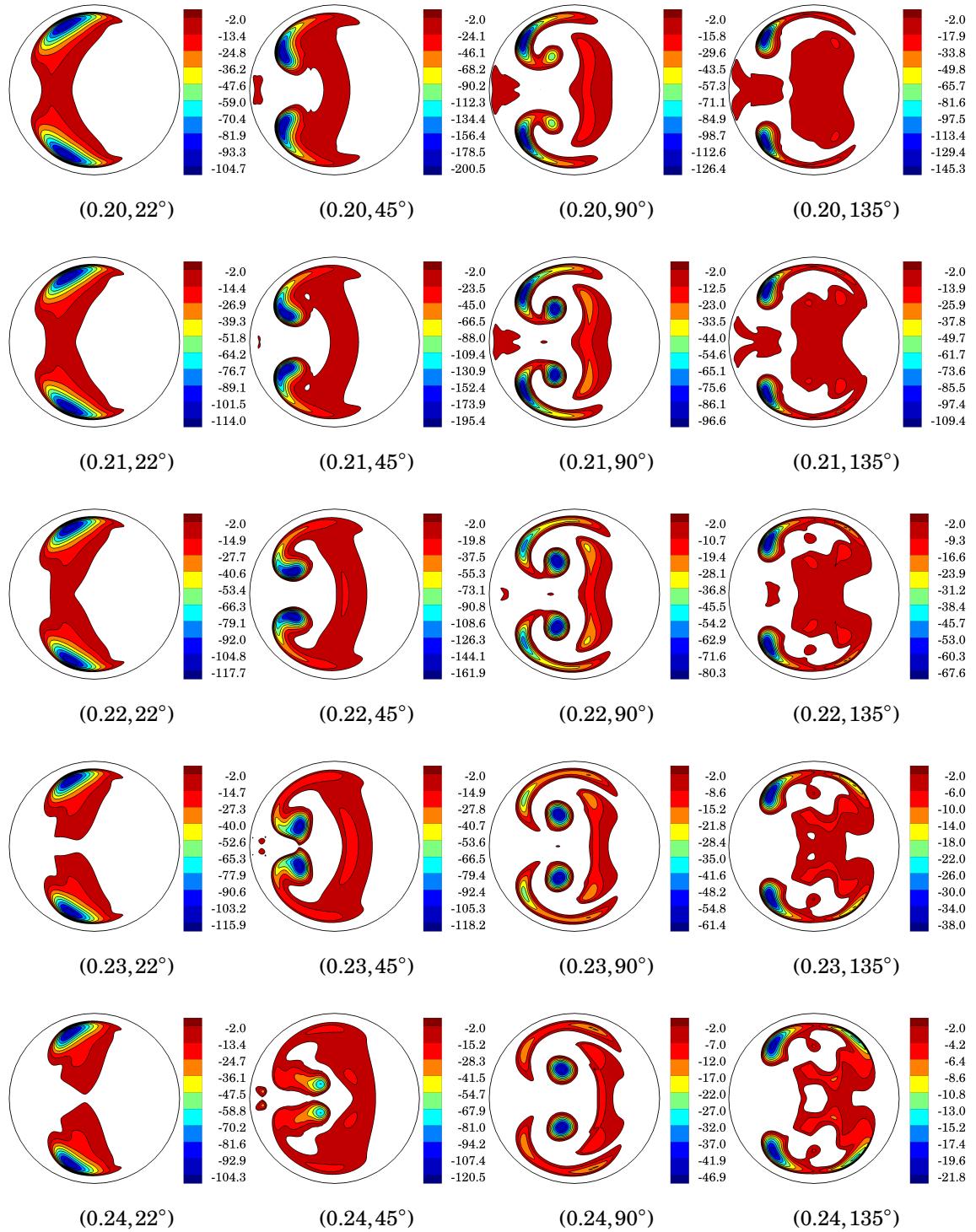


Figure D.9 Womersley entrance condition: non-dimensional second eigenvalue λ_2^* of $S^2 + R^2$, $\lambda_2^* < 0$ at (t^*, ϕ) . (*continued*)

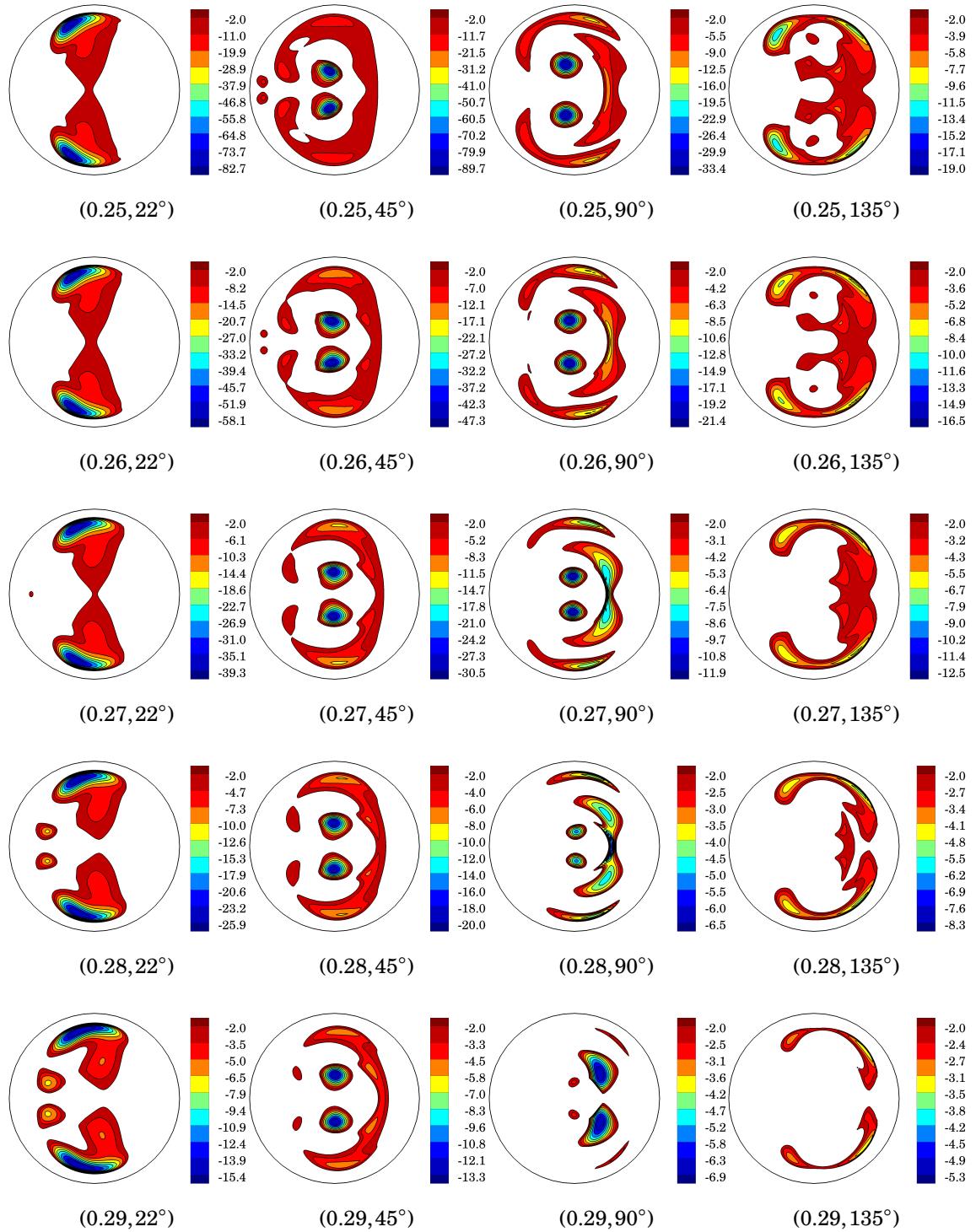


Figure D.9 Womersley entrance condition: non-dimensional second eigenvalue λ_2^* of $S^2 + R^2$, $\lambda_2^* < 0$ at (t^*, ϕ) . (*continued*)

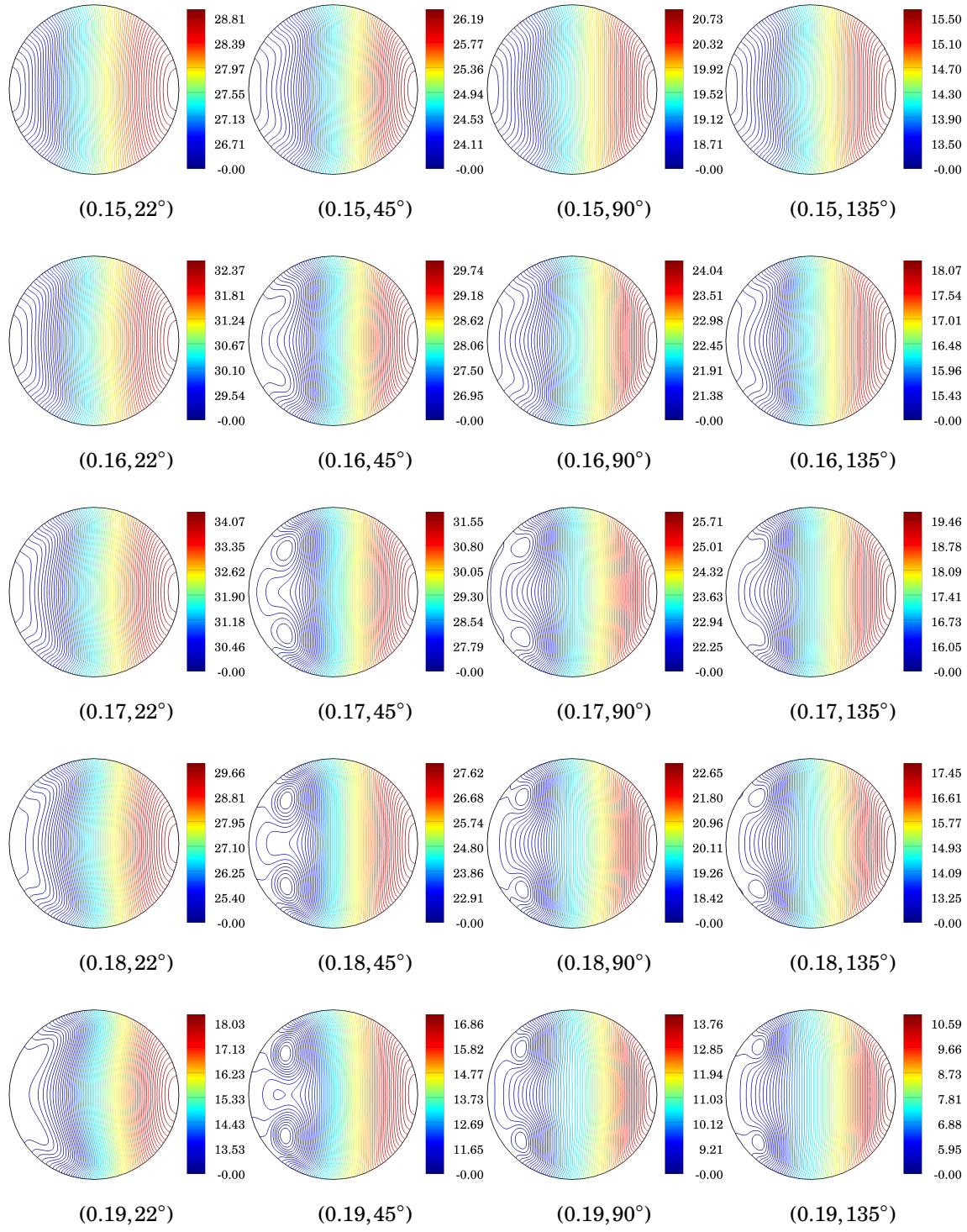


Figure D.10 Womersley entrance condition: non-dimensional pressure p^* at (t^*, ϕ) .

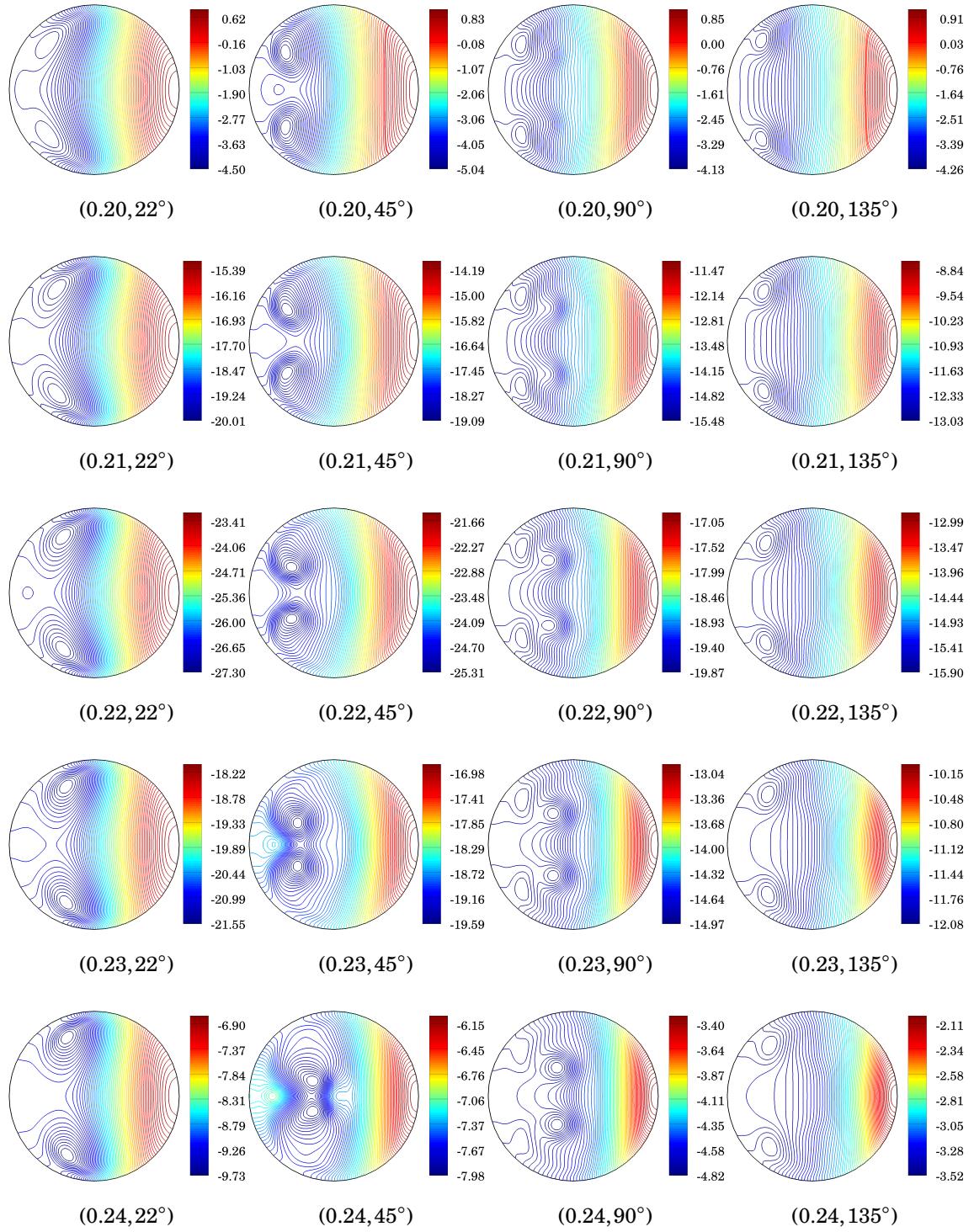


Figure D.10 Womersley entrance condition: non-dimensional pressure p^* at (t^*, ϕ) .
(continued)

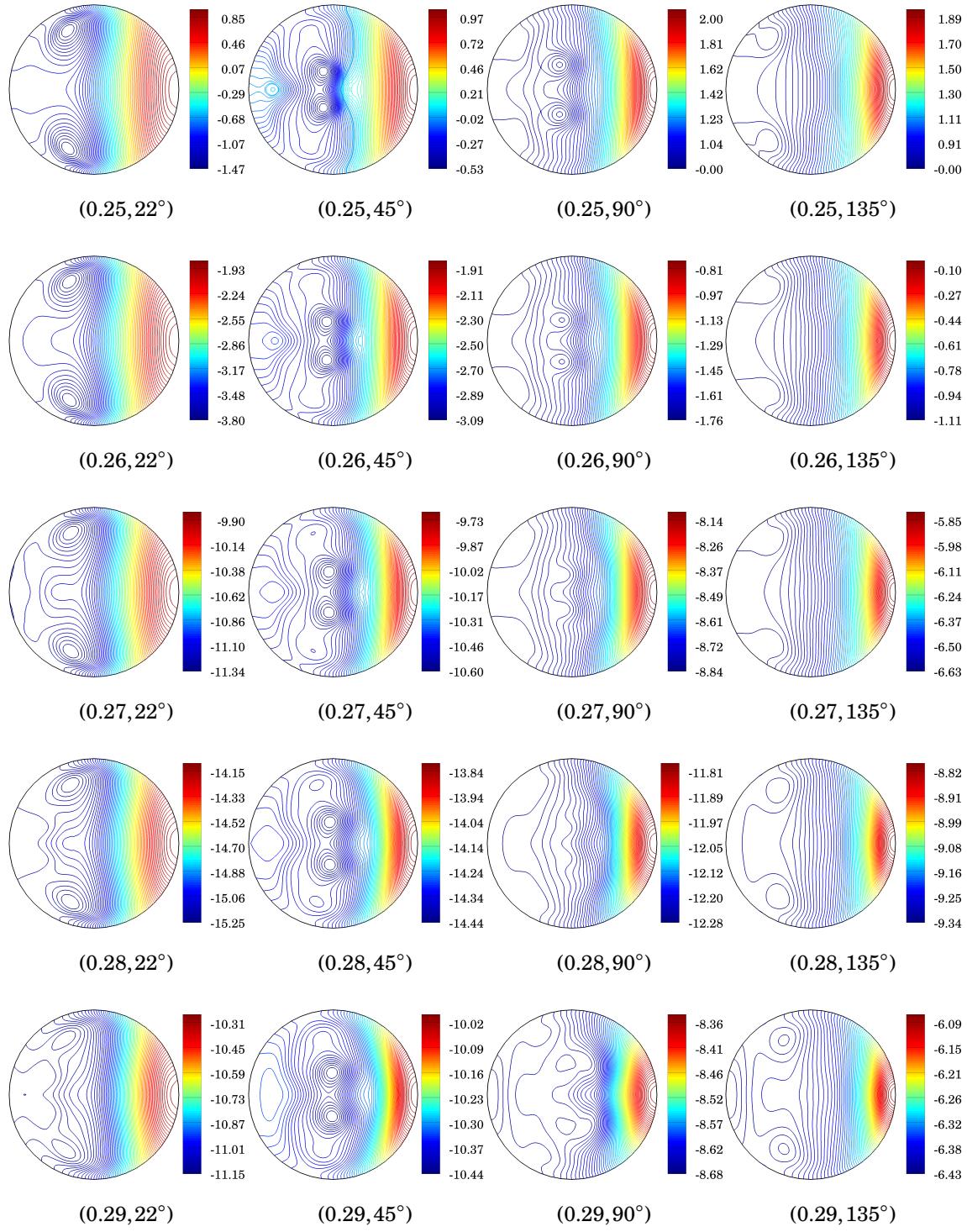


Figure D.10 Womersley entrance condition: non-dimensional pressure p^* at (t^*, ϕ) .
(continued)

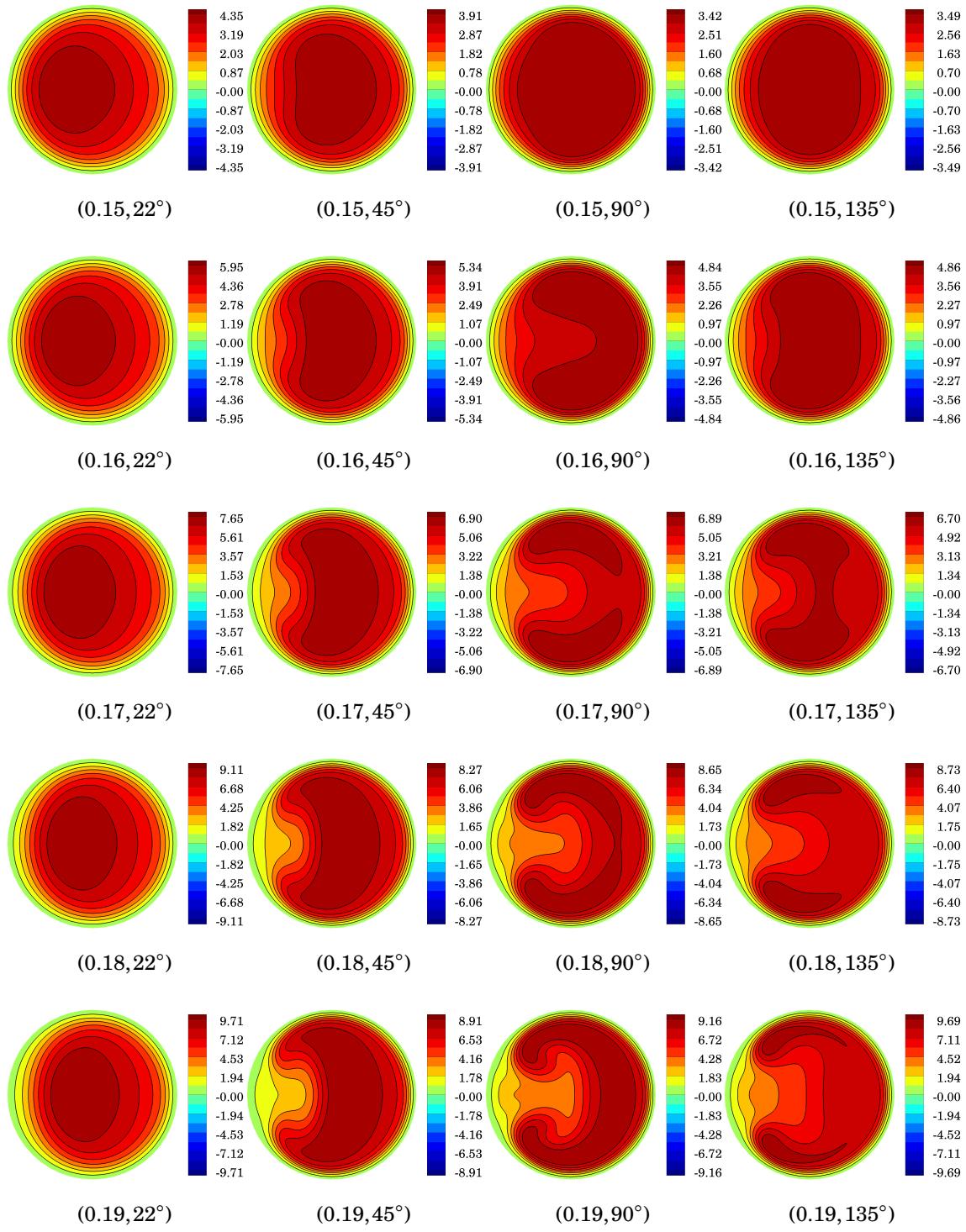


Figure D.11 Womersley entrance condition: non-dimensional centrifugal force f_c^* at (t^*, ϕ) .

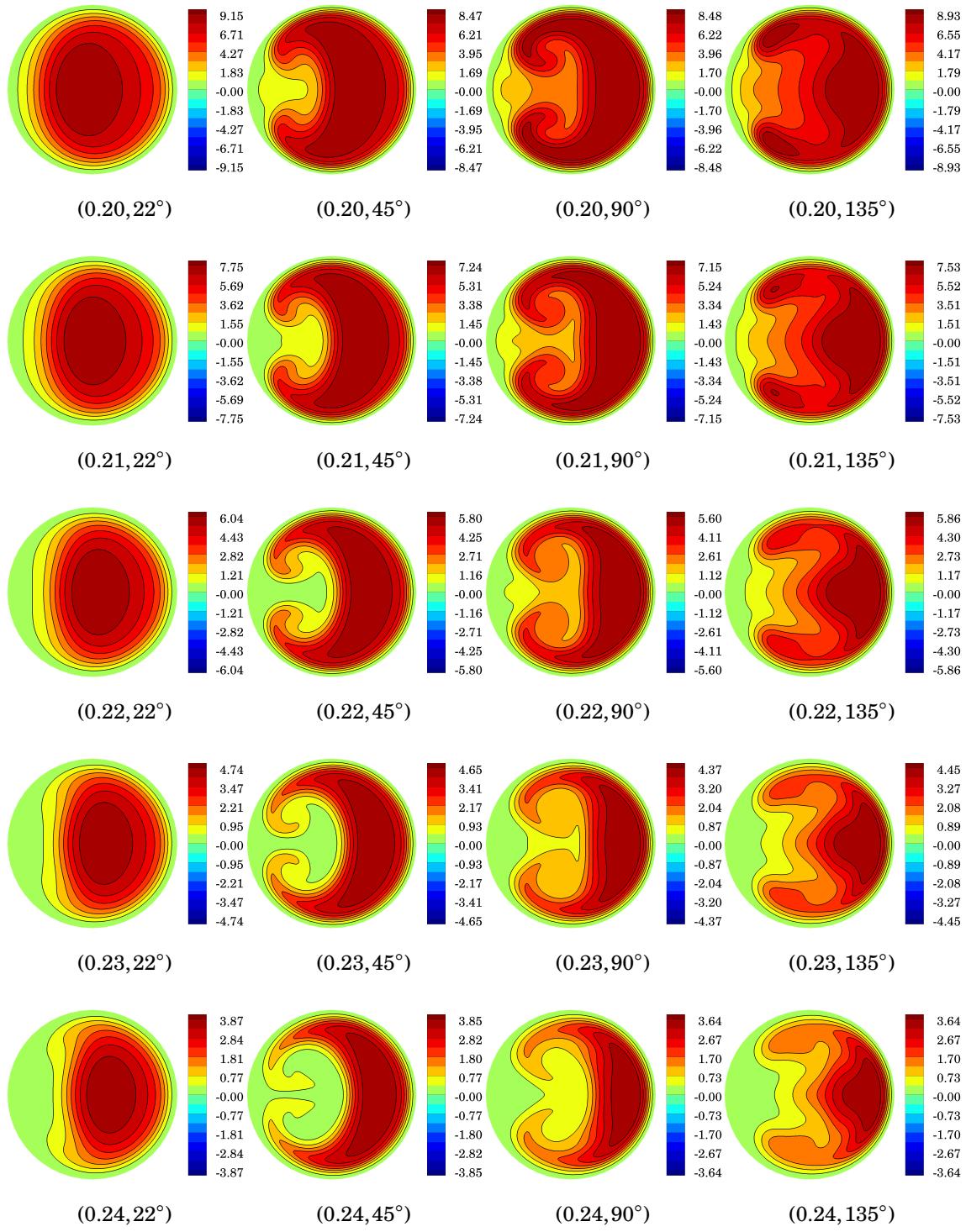


Figure D.11 Womersley entrance condition: non-dimensional centrifugal force f_c^* at (t^*, ϕ) .
(continued)

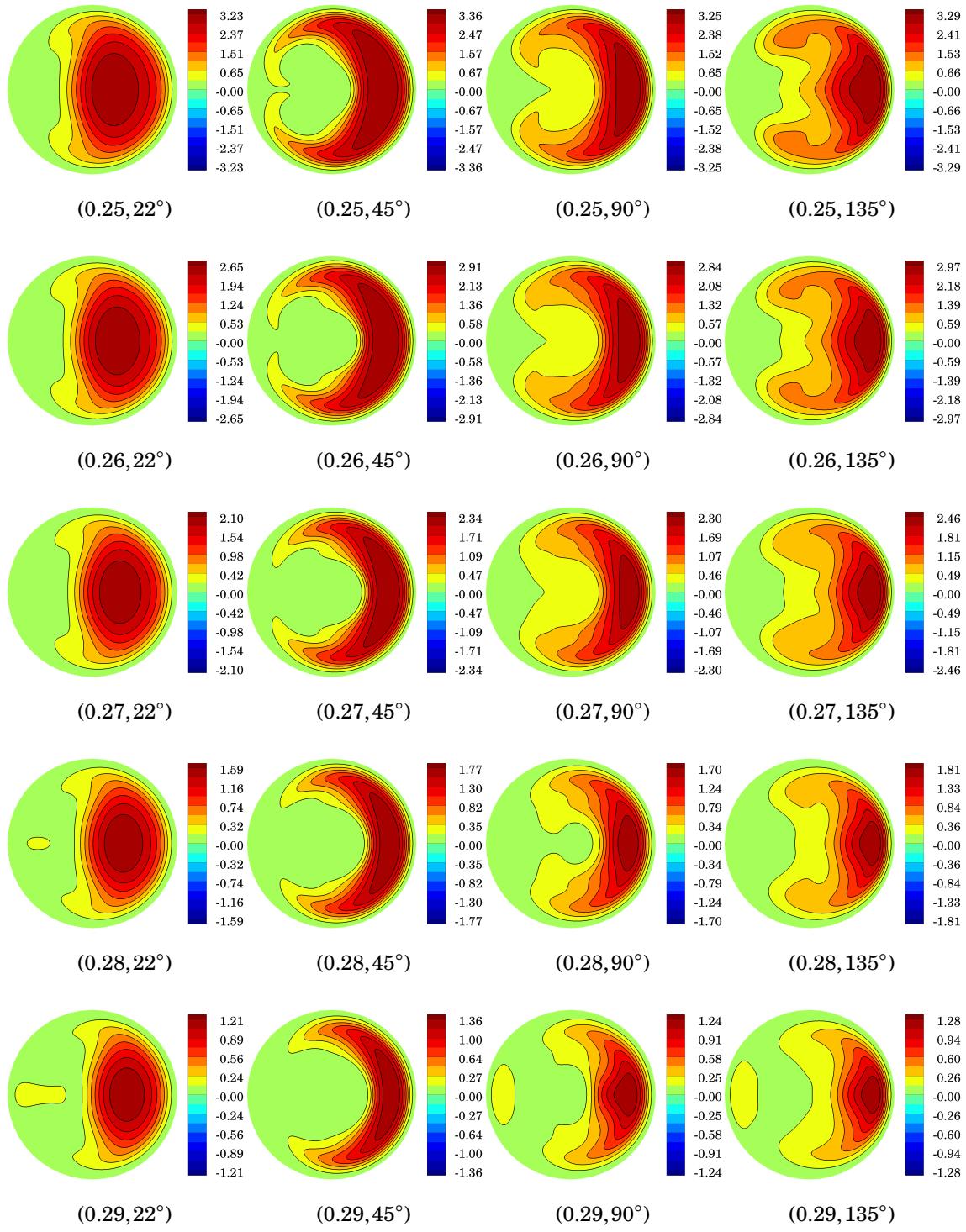


Figure D.11 Womersley entrance condition: non-dimensional centrifugal force f_c^* at (t^*, ϕ) .
(continued)

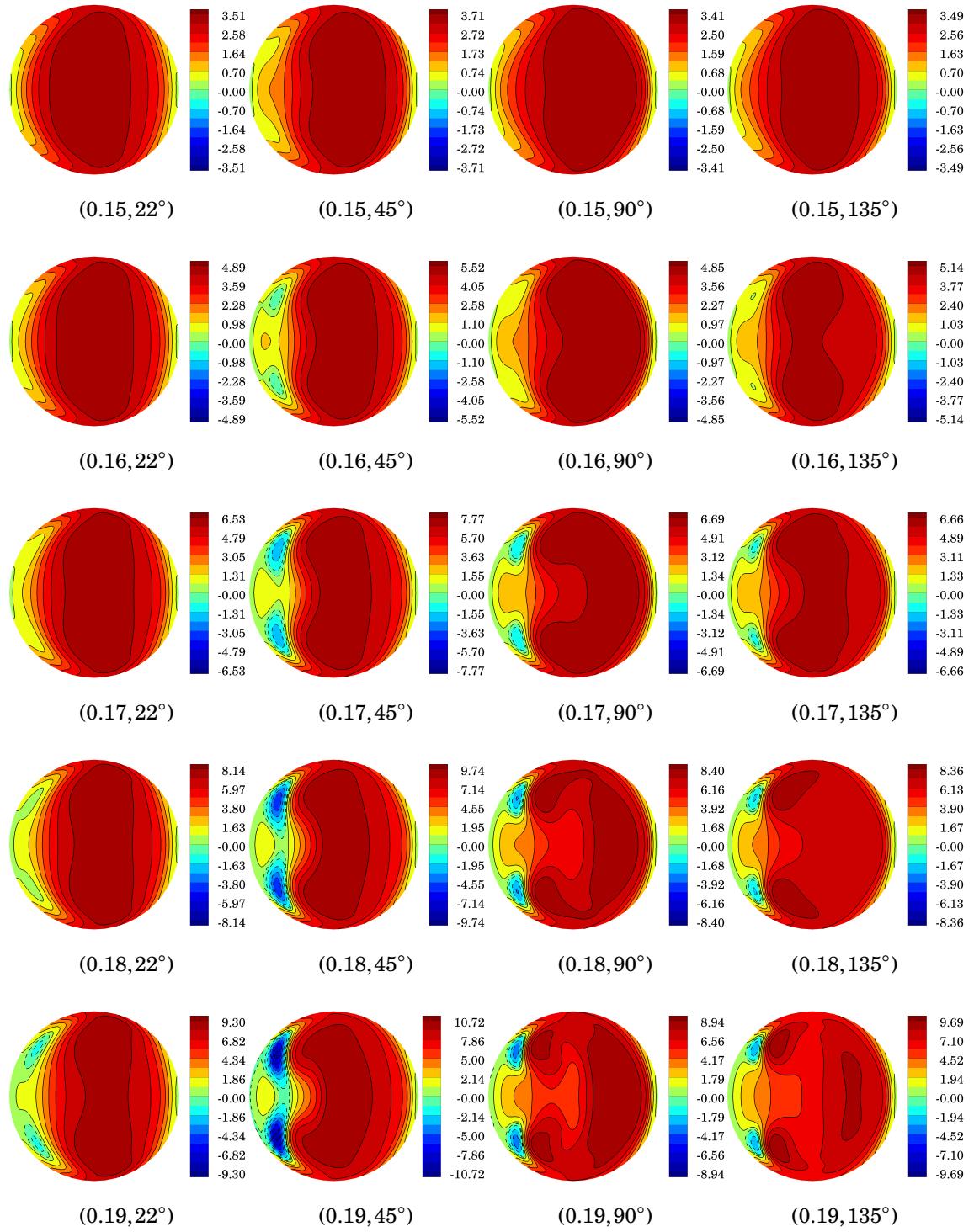


Figure D.12 Womersley entrance condition: non-dimensional pressure gradient force $-f_{pg}^*$ at (t^*, ϕ) .

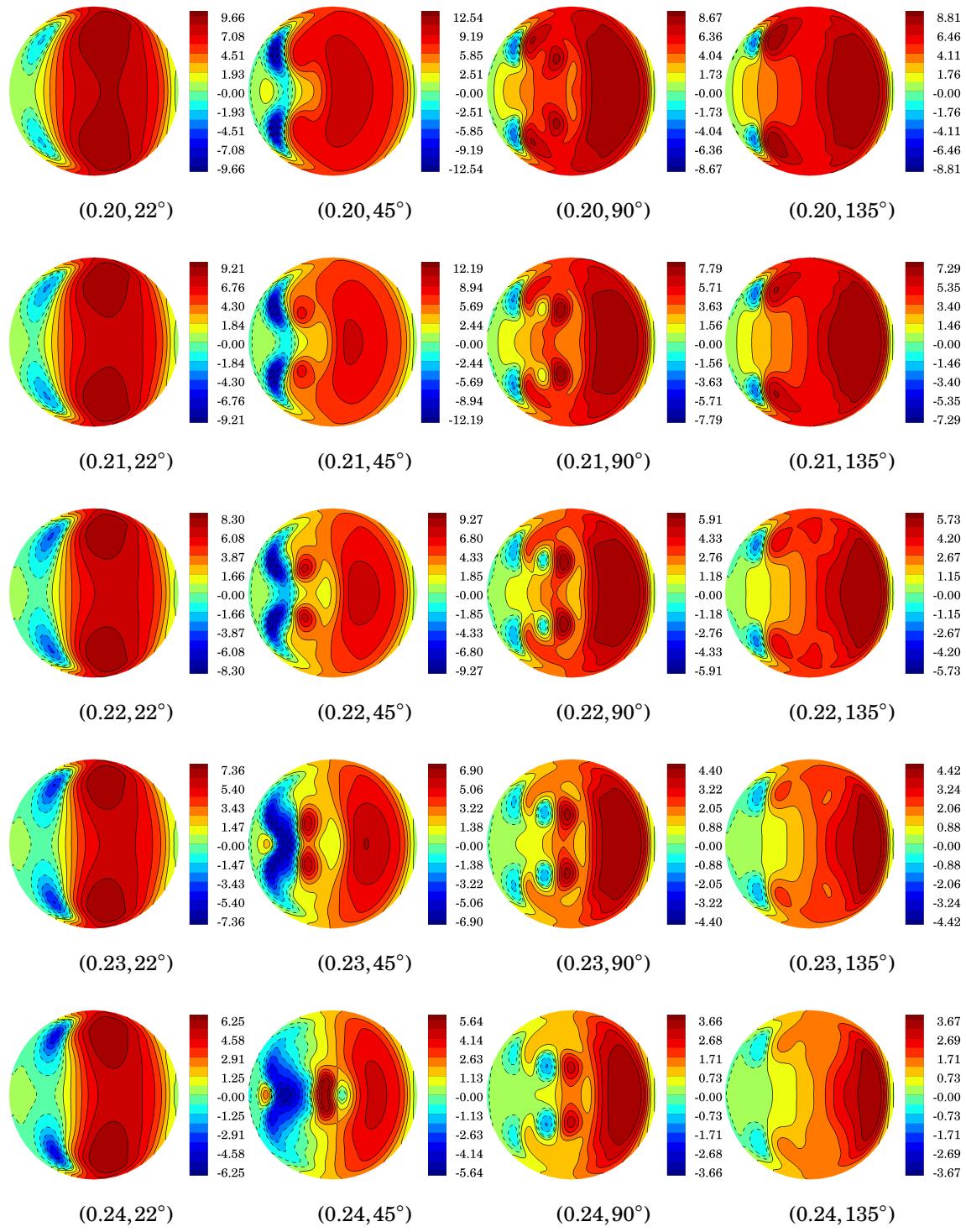


Figure D.12 Womersley entrance condition: non-dimensional pressure gradient force $-f_{pg}^*$ at (t^*, ϕ) . (continued)

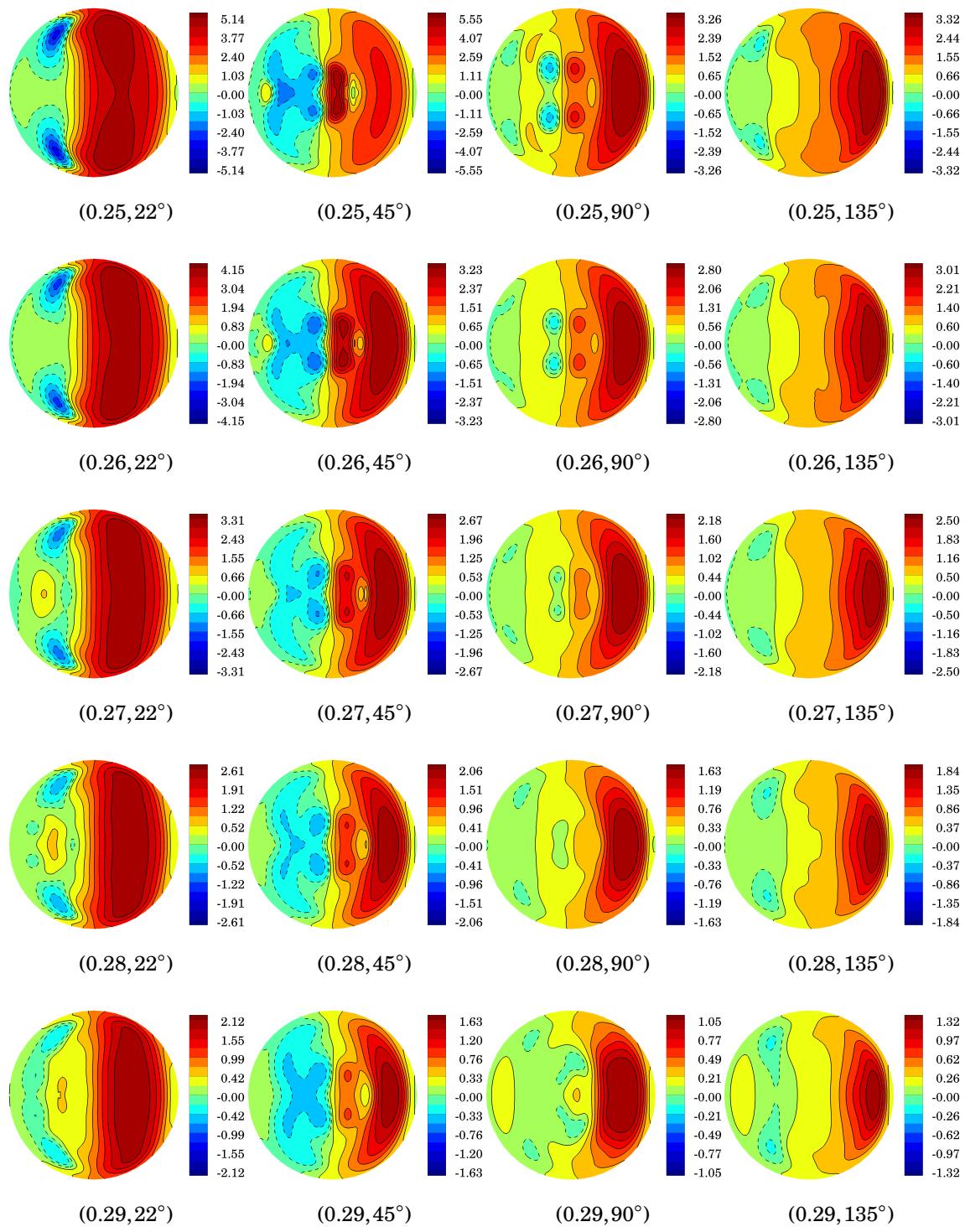


Figure D.12 Womersley entrance condition: non-dimensional pressure gradient force $-f_{pg}^*$ at (t^*, ϕ) . (continued)

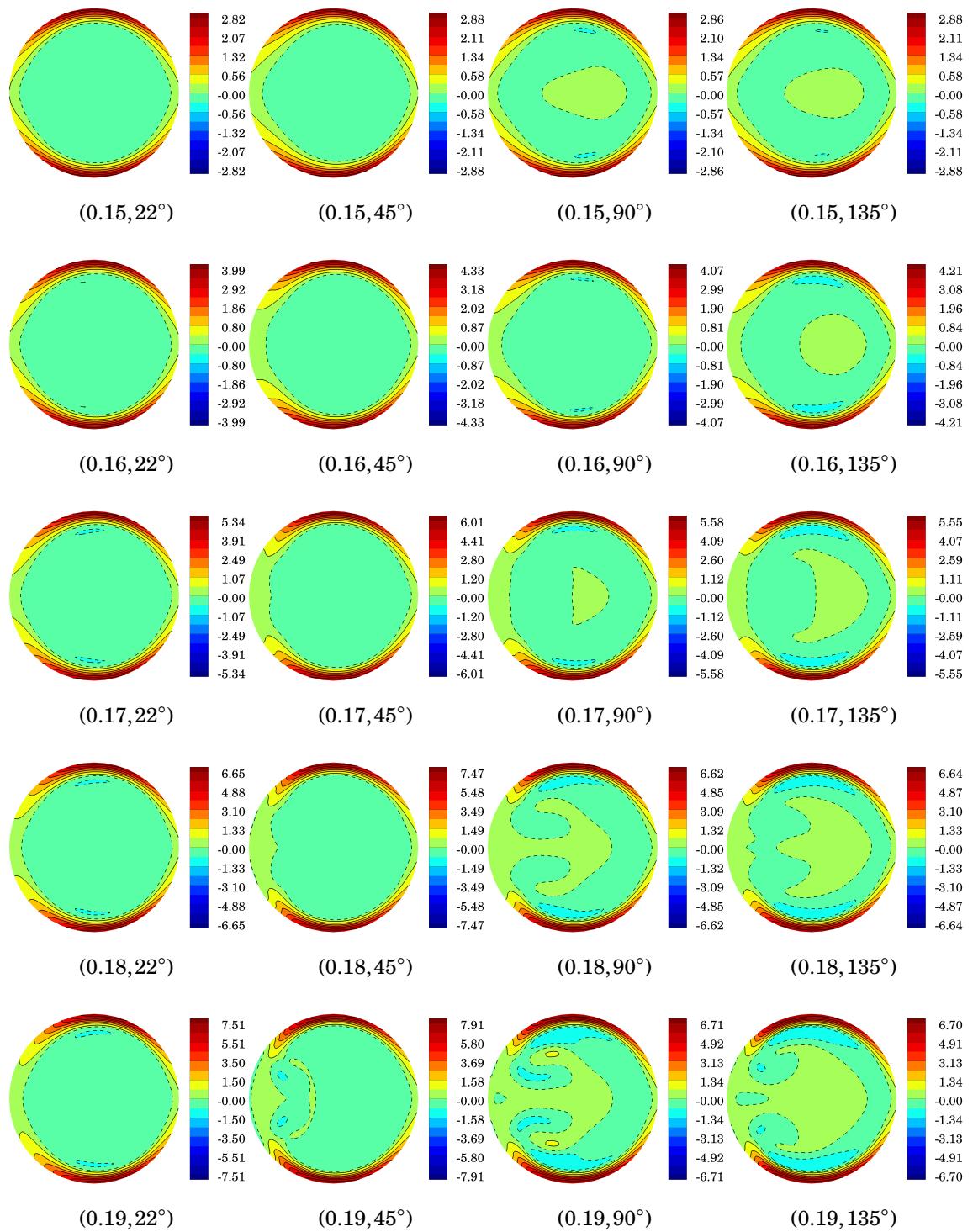


Figure D.13 Womersley entrance condition: non-dimensional viscous force f_v^* at (t^*, ϕ) .

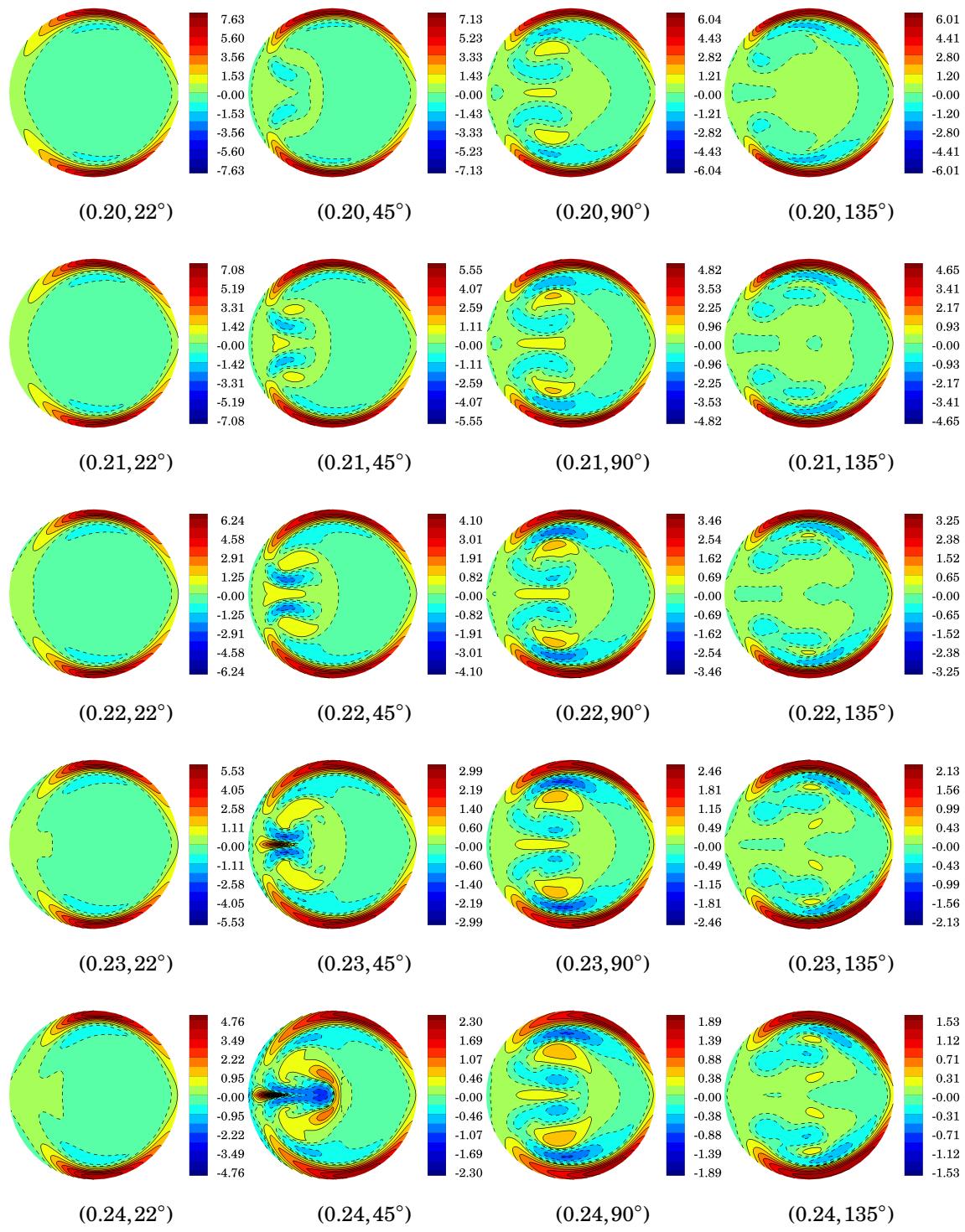


Figure D.13 Womersley entrance condition: non-dimensional viscous force f_v^* at (t^*, ϕ) .
(continued)

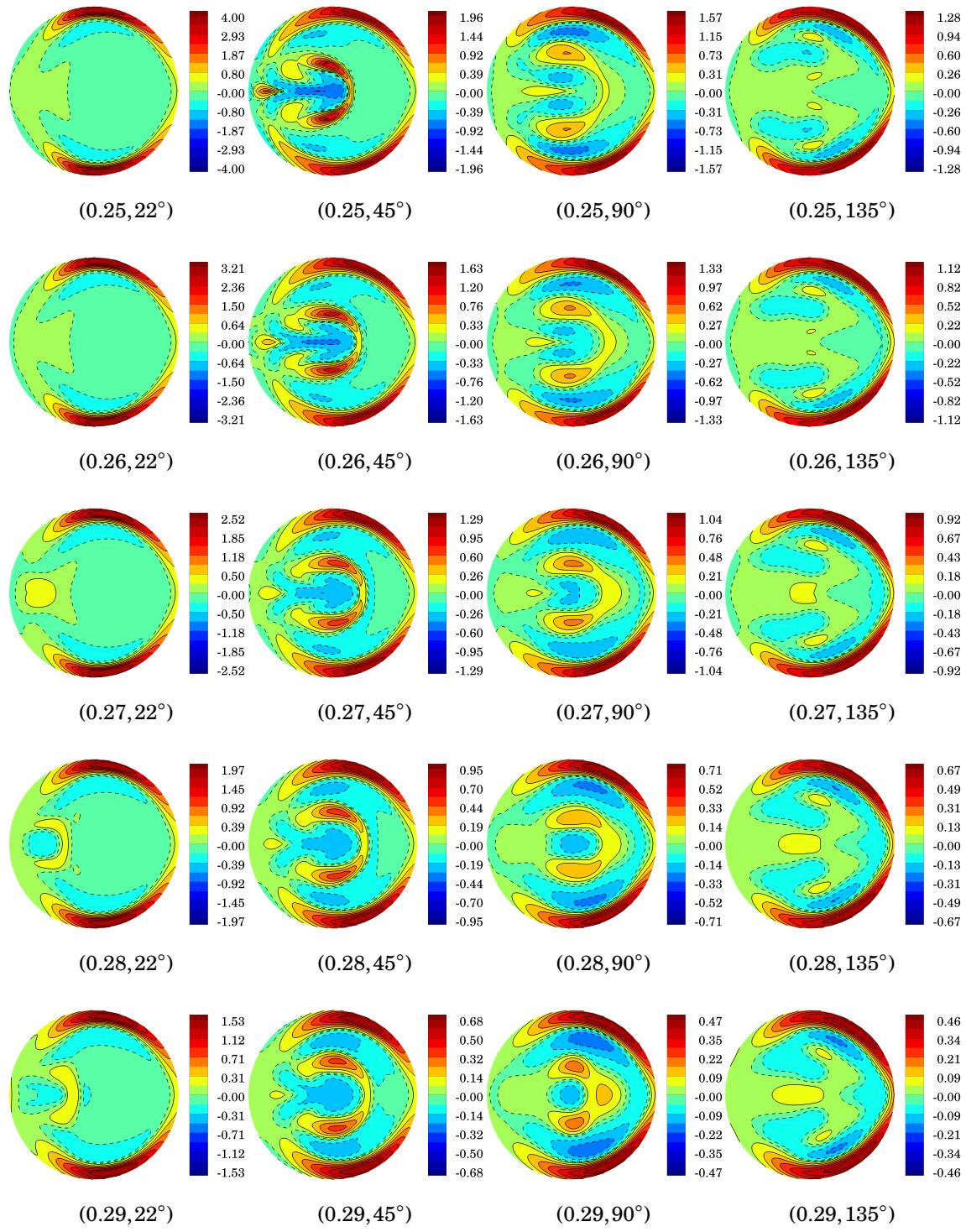


Figure D.13 Womersley entrance condition: non-dimensional viscous force f_v^* at (t^*, ϕ) .
(continued)

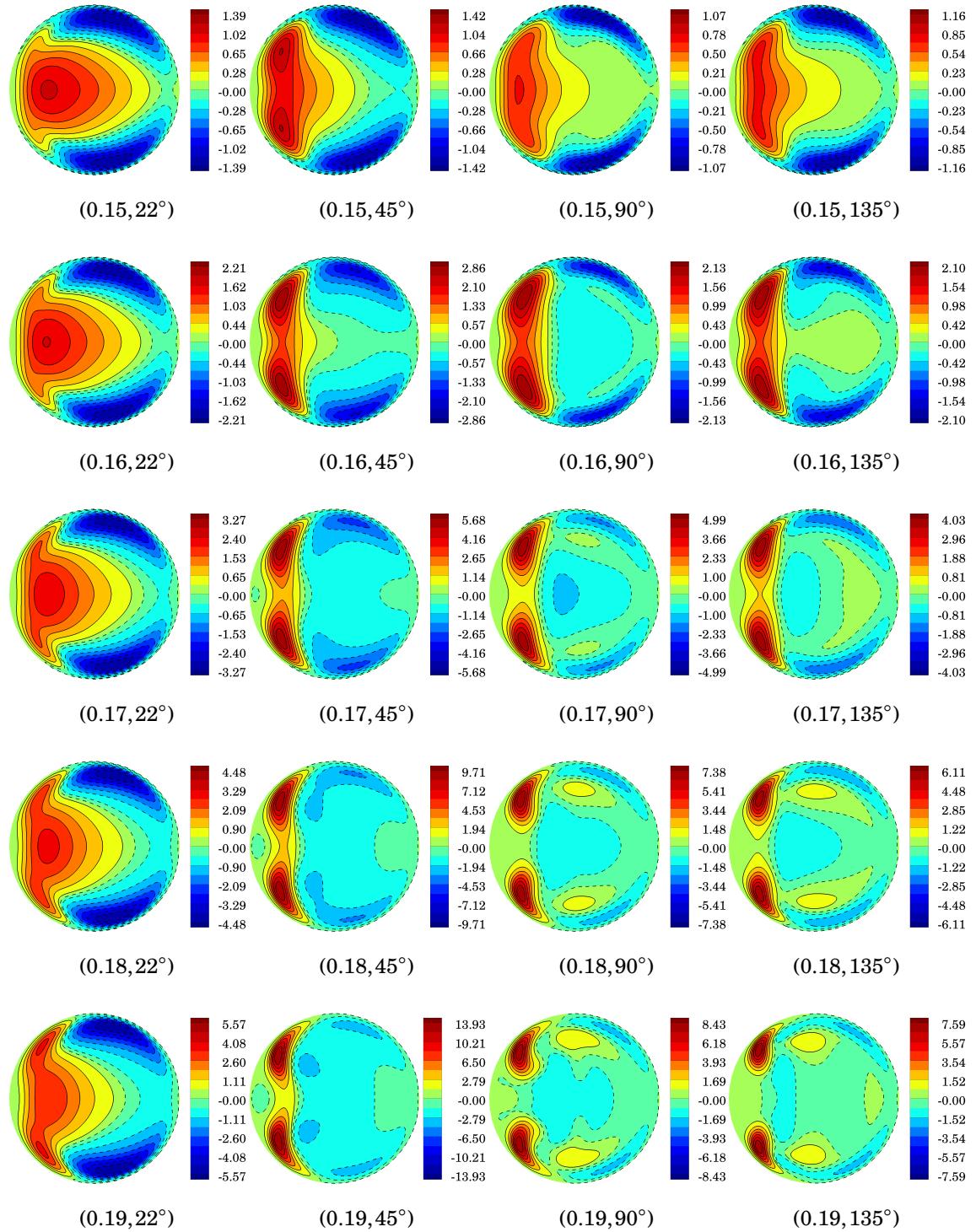


Figure D.14 Womersley entrance condition: non-dimensional centrifugal, pressure gradient and viscous forces along the radius of curvature direction $f_c^* + f_{pg}^* + f_v^*$ at (t^*, ϕ) .

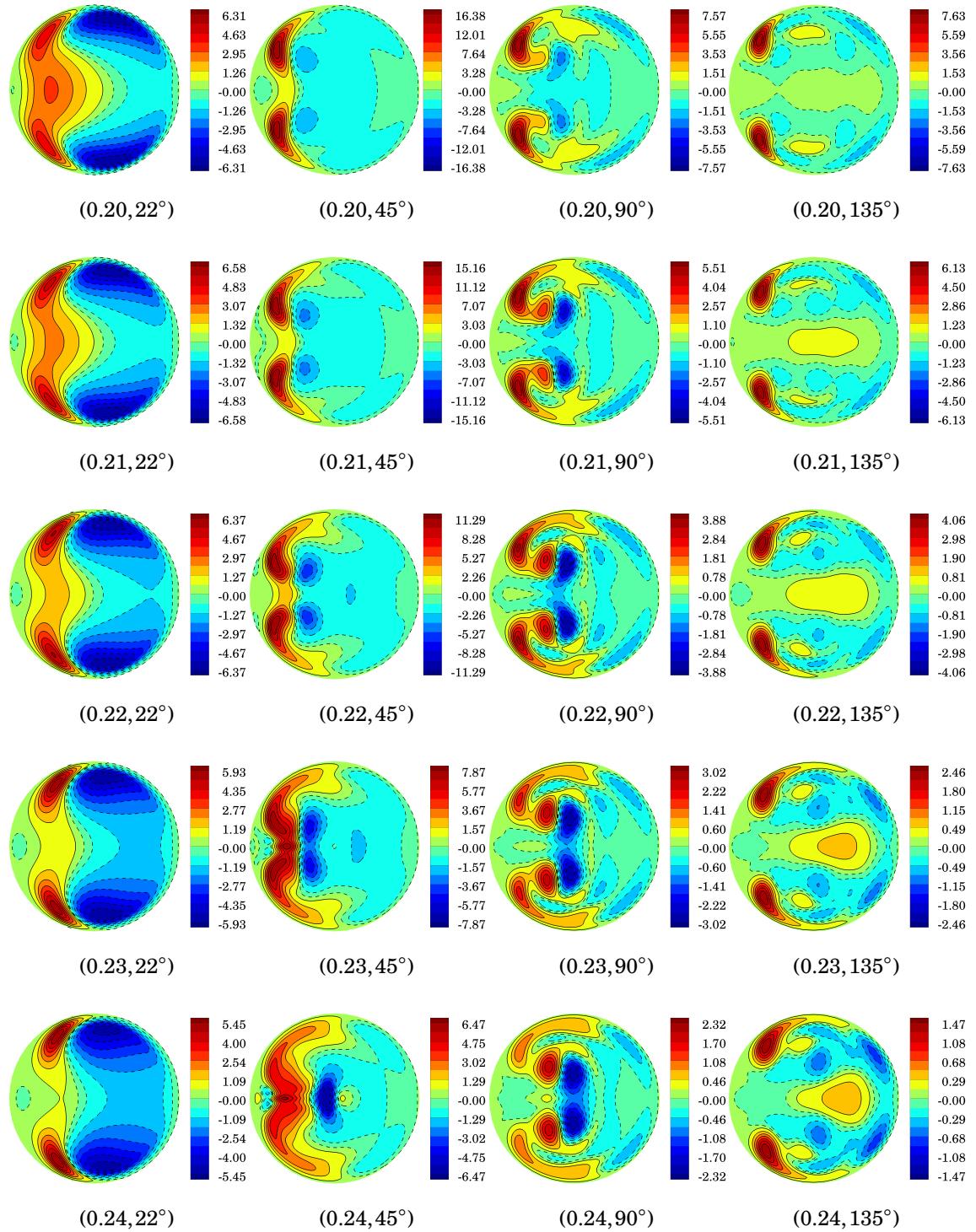


Figure D.14 Womersley entrance condition: non-dimensional centrifugal, pressure gradient and viscous forces along the radius of curvature direction $f_c^* + f_{pg}^* + f_v^*$ at (t^*, ϕ) . (continued)

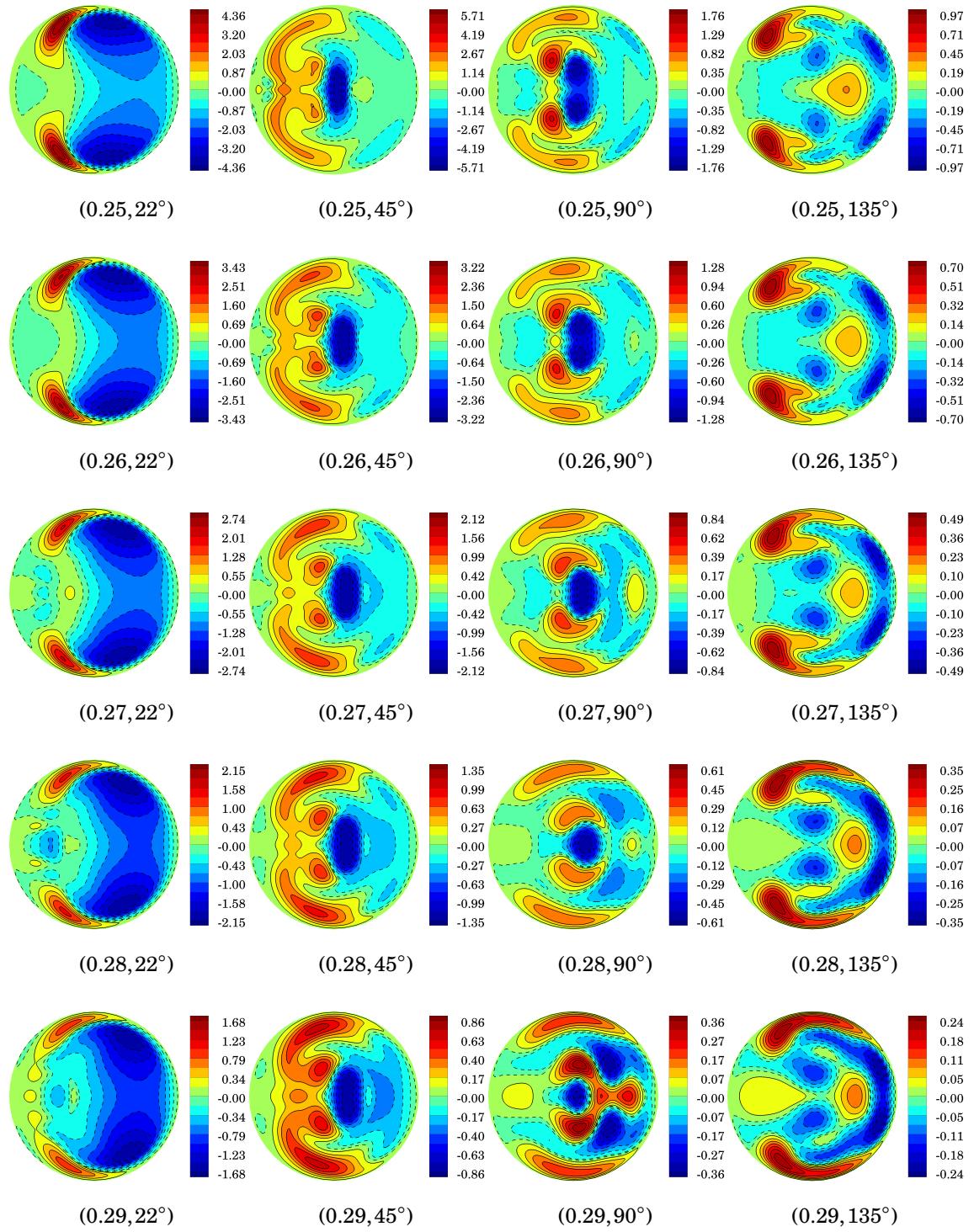


Figure D.14 Womersley entrance condition: non-dimensional centrifugal, pressure gradient and viscous forces along the radius of curvature direction $f_c^* + f_{pg}^* + f_v^*$ at (t^*, ϕ) . (continued)

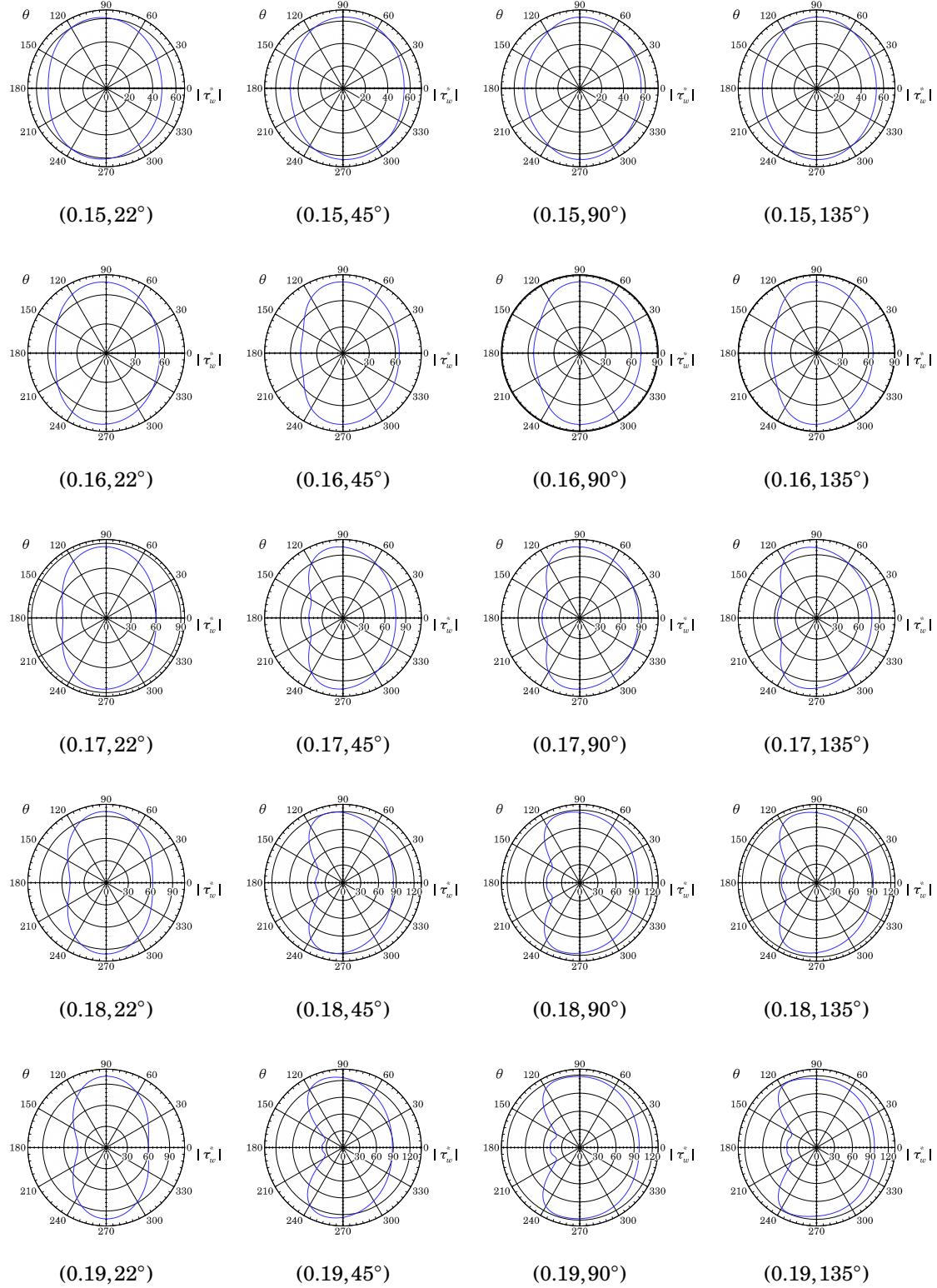


Figure D.15 Womersley entrance condition: non-dimensional wall shear stress magnitude $|\tau_w^*|$ at (t^*, ϕ) .

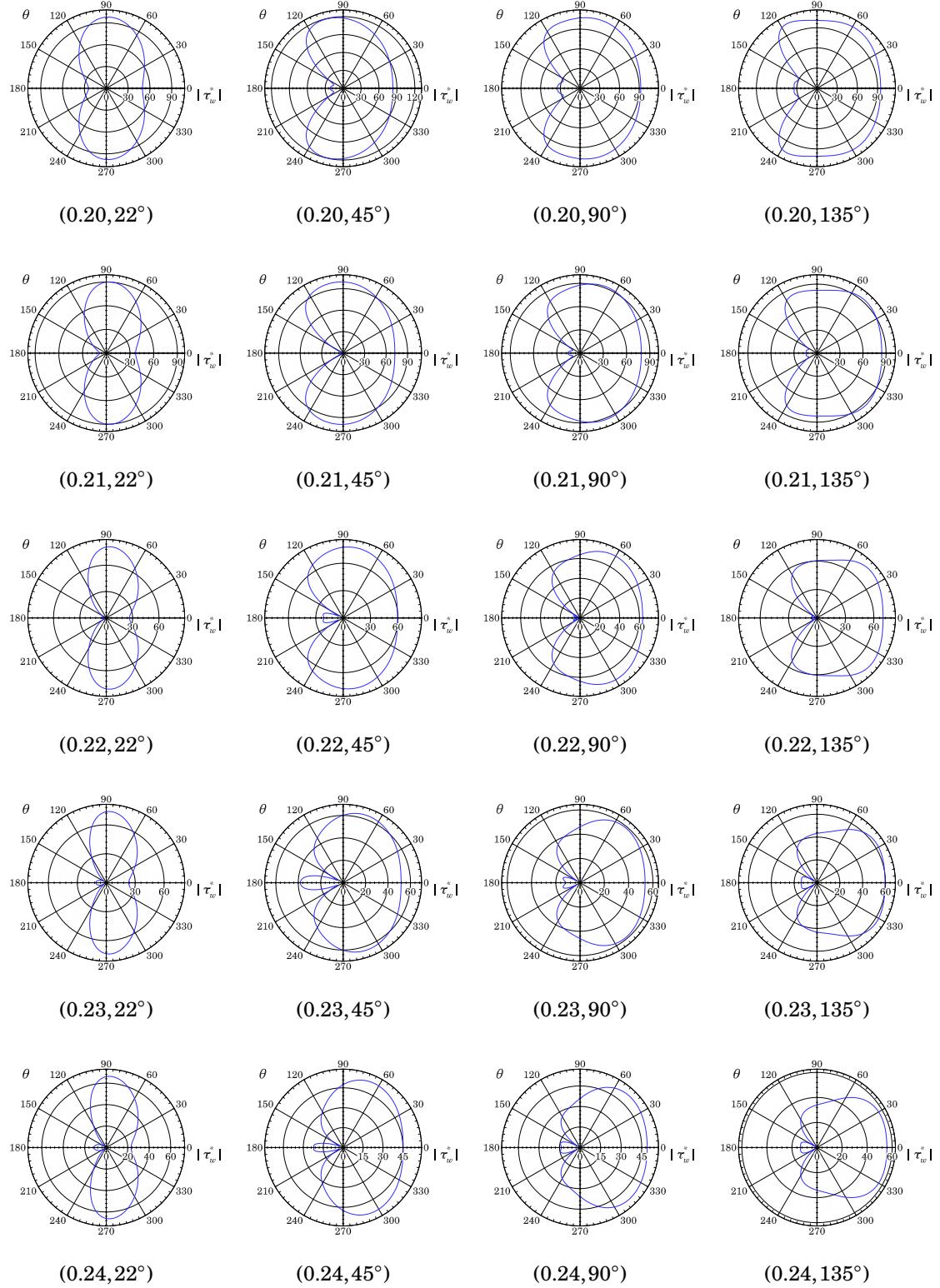


Figure D.15 Womersley entrance condition: non-dimensional wall shear stress magnitude $|\tau_w^*|$ at (t^*, ϕ) . (continued)

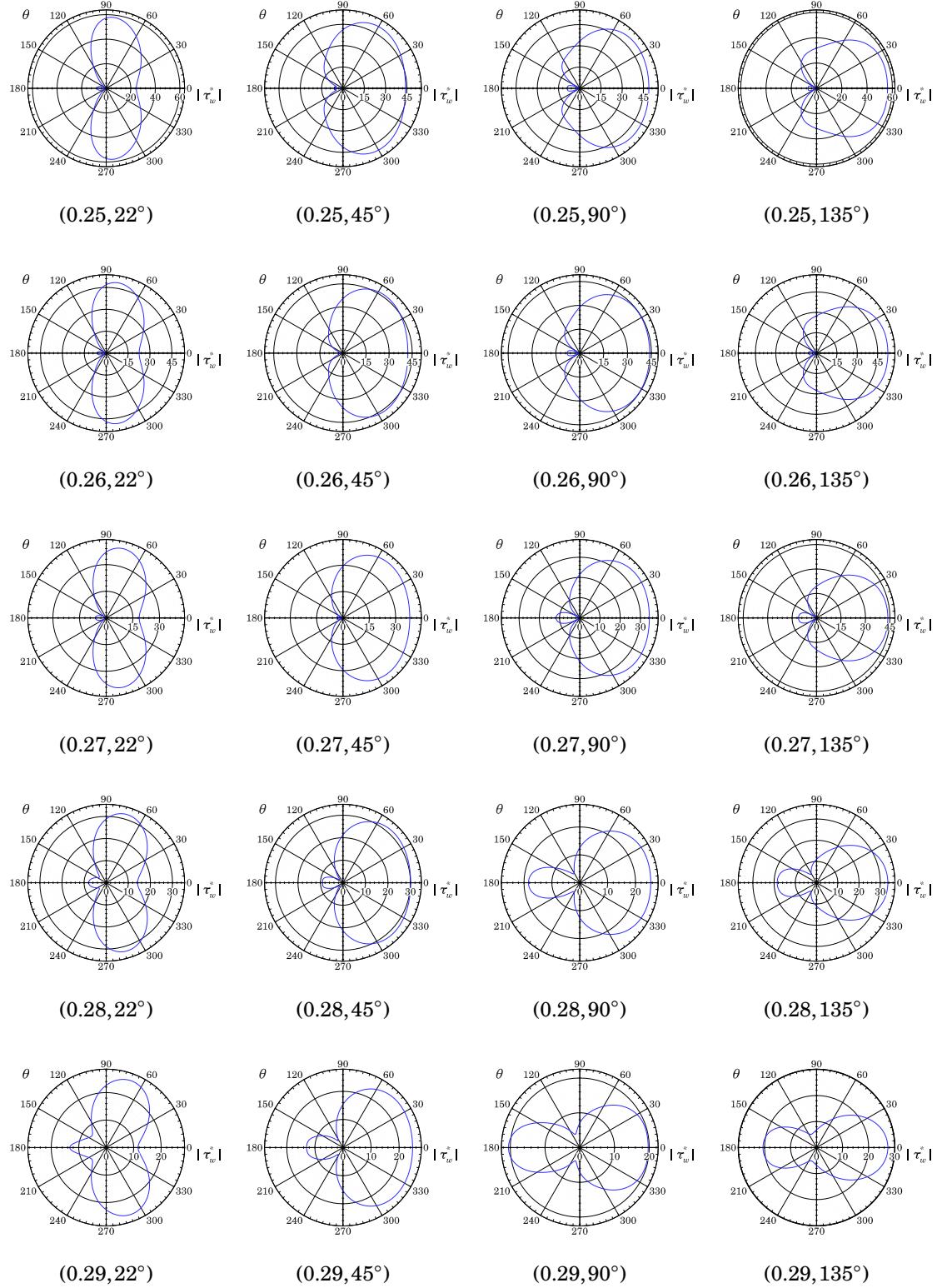


Figure D.15 Womersley entrance condition: non-dimensional wall shear stress magnitude $|\tau_w^*|$ at (t^*, ϕ) . (continued)

Appendix E

Curved Pipe Entrance Condition: Undeveloped (Uniform) Pulsatile Flow

Supplemental uniform pulsatile entrance flow results are provided for mid-acceleration ($t^* = 0.15$) through end of deceleration ($t^* = 0.29$) at the various cross-section $\phi = 22^\circ, 45^\circ, 90^\circ$ and 135° for the non-dimensional streamwise vorticity ω_s^* , vorticity magnitude $|\boldsymbol{\omega}^*|$, secondary velocity vectors $\boldsymbol{u}_{\theta r}^*$, streamwise velocity u_s^* , second eigenvalue λ_2^* of $\mathbf{S}^2 + \mathbf{R}^2$, pressure p^* , centrifugal force f_c^* , pressure gradient force f_{pg}^* , viscous force f_v^* and wall shear stress magnitude $|\boldsymbol{\tau}_w^*|$. The centrifugal, pressure gradient and viscous force terms are defined in Section 8.6.7.

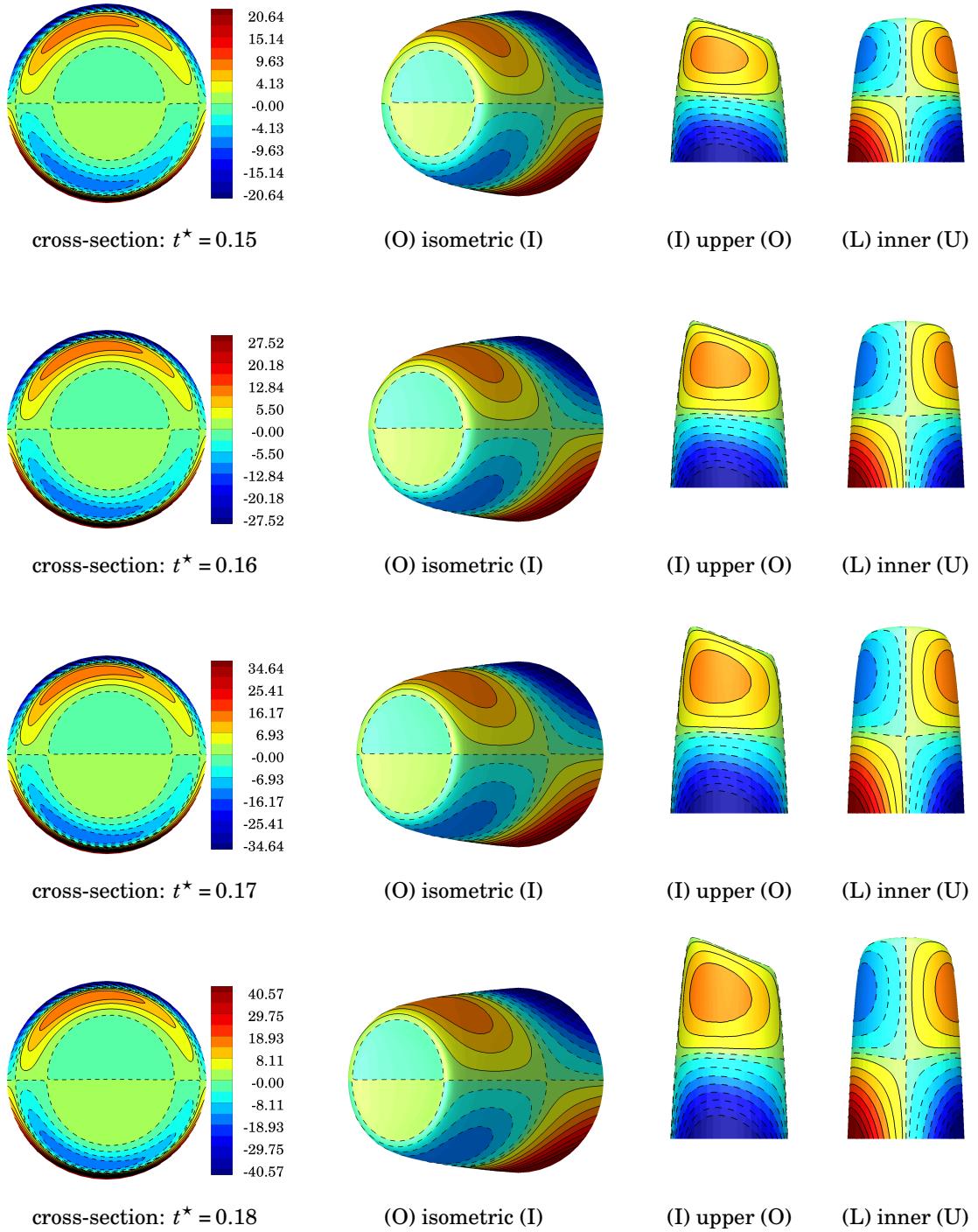


Figure E.1 Uniform entrance condition: velocity surface of u_s^* at $\theta = 22^\circ$ colored by non-dimensional streamwise vorticity ω_s^* visualized from three difference views: isometric, upper and inner. ($I \equiv inner$, $O \equiv outer$, $U \equiv upper$, $L \equiv lower$).

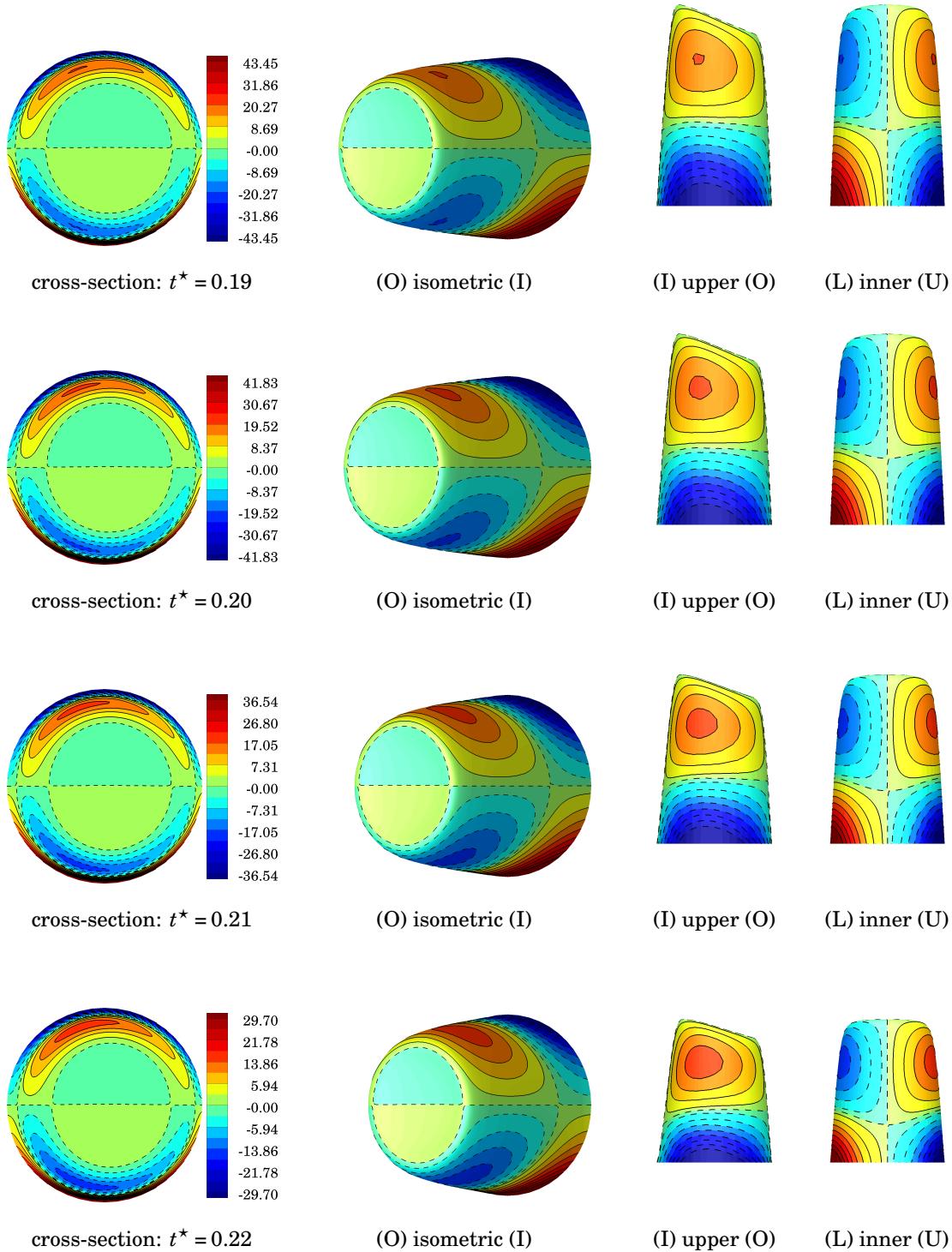


Figure E.1 Uniform entrance condition: velocity surface of u_s^* at $\theta = 22^\circ$ colored by non-dimensional streamwise vorticity ω_s^* visualized from three difference views: isometric, upper and inner. ($I \equiv inner$, $O \equiv outer$, $U \equiv upper$, $L \equiv lower$). (continued)

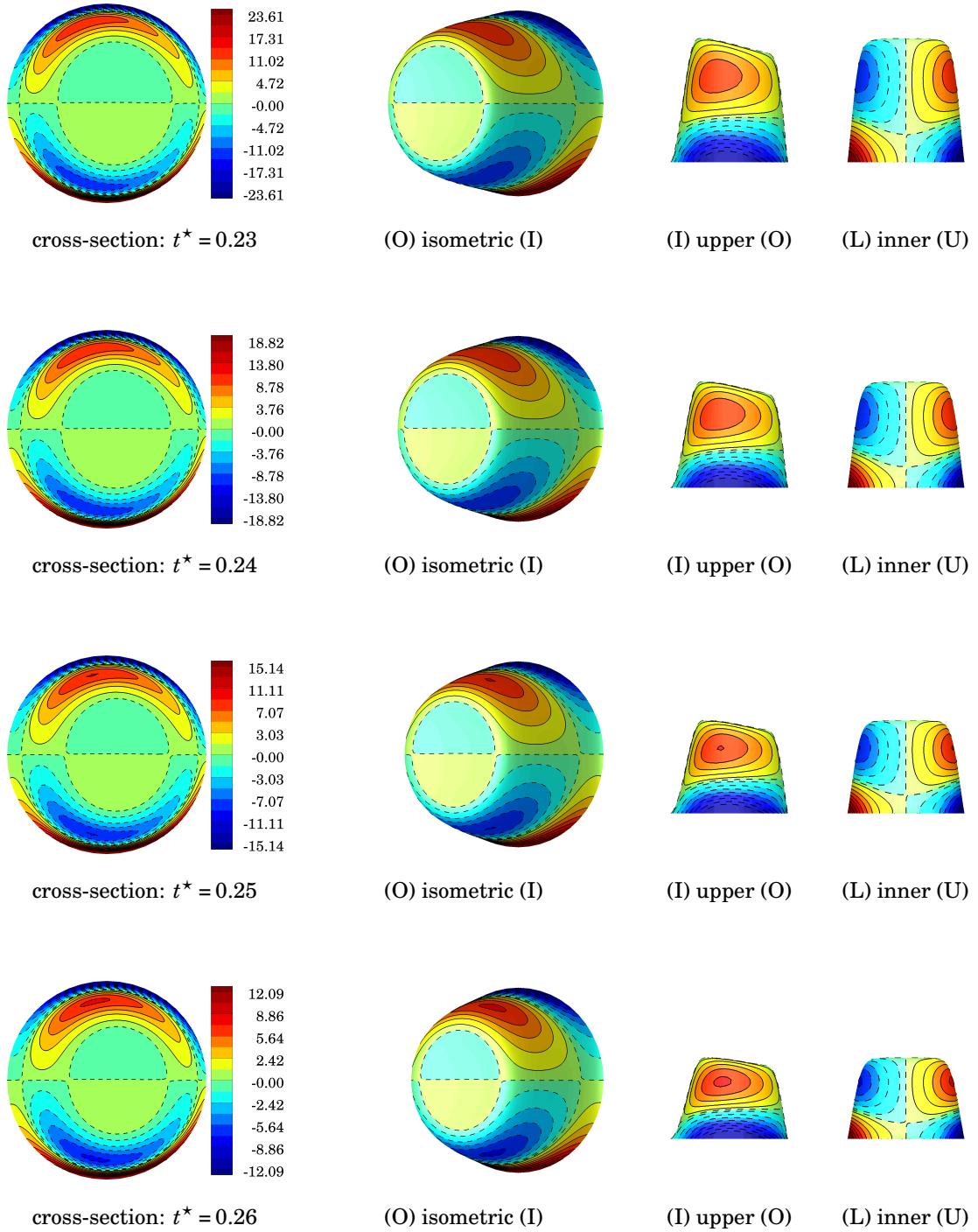


Figure E.1 Uniform entrance condition: velocity surface of u_s^* at $\theta = 22^\circ$ colored by non-dimensional streamwise vorticity ω_s^* visualized from three difference views: isometric, upper and inner. ($I \equiv inner$, $O \equiv outer$, $U \equiv upper$, $L \equiv lower$). (continued)

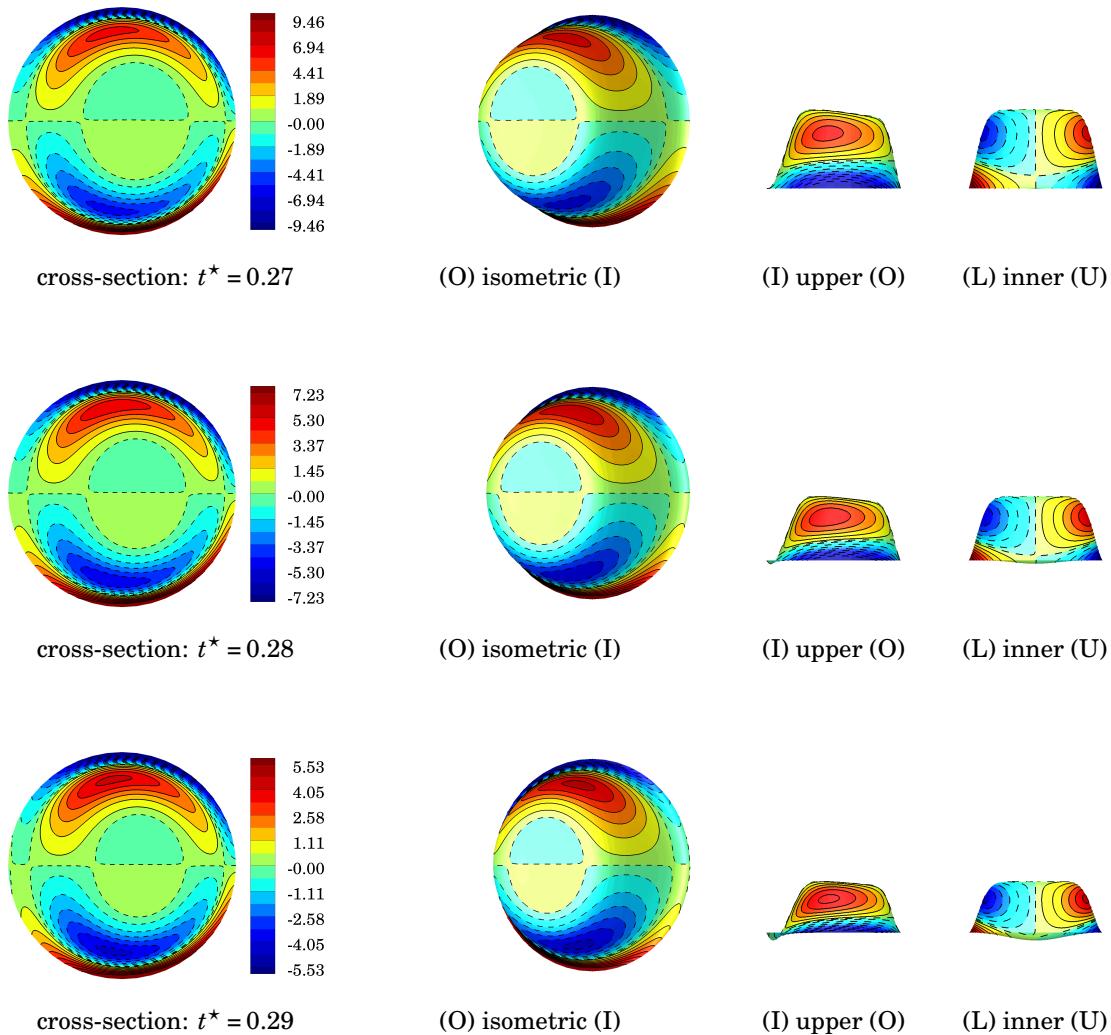


Figure E.1 Uniform entrance condition: velocity surface of u_s^* at $\theta = 22^\circ$ colored by non-dimensional streamwise vorticity ω_s^* visualized from three difference views: isometric, upper and inner. ($I \equiv \text{inner}$, $O \equiv \text{outer}$, $U \equiv \text{upper}$, $L \equiv \text{lower}$). (continued)

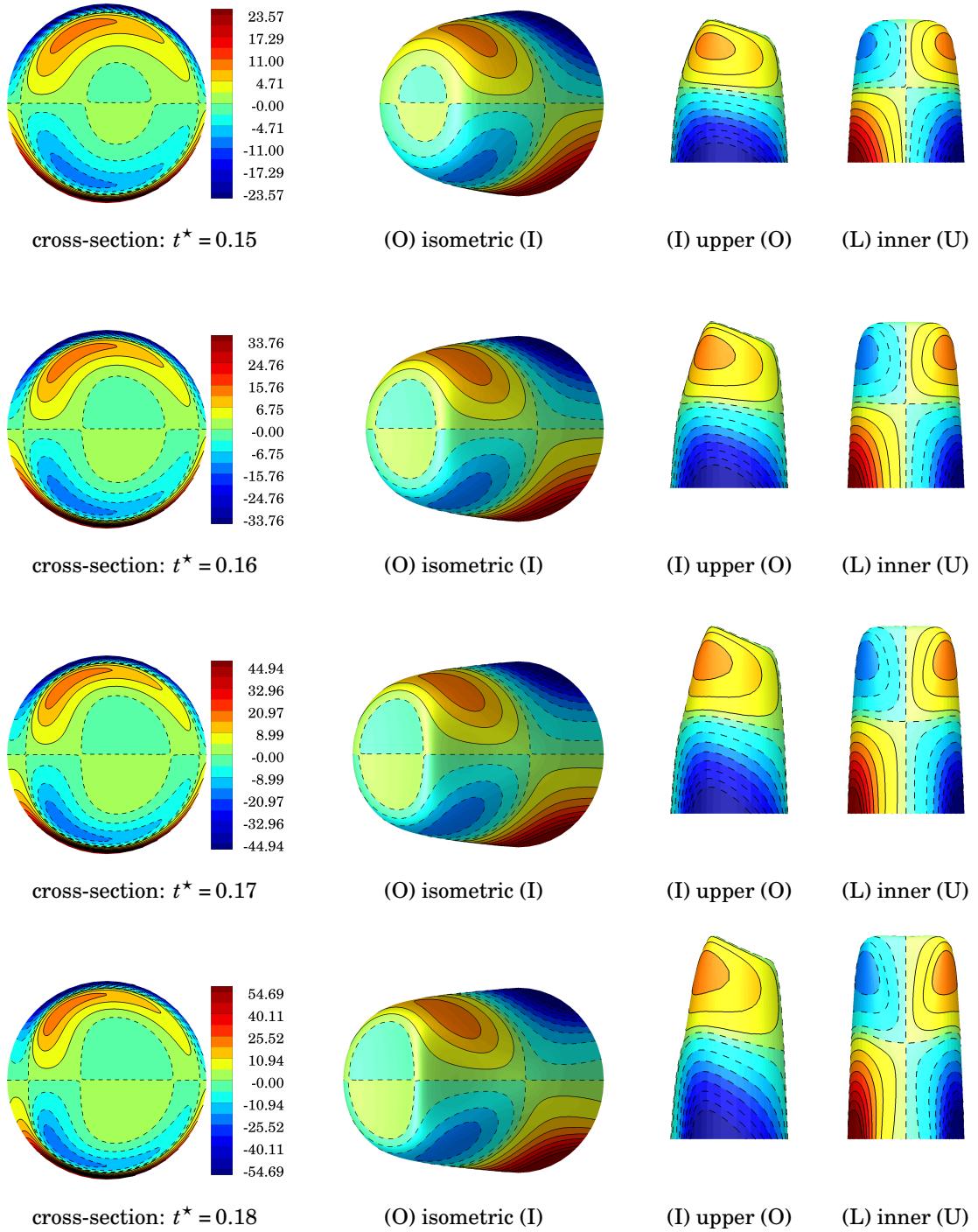


Figure E.2 Uniform entrance condition: velocity surface of u_s^* at $\theta = 45^\circ$ colored by non-dimensional streamwise vorticity ω_s^* visualized from three difference views: isometric, upper and inner. ($I \equiv$ inner, $O \equiv$ outer, $U \equiv$ upper, $L \equiv$ lower).

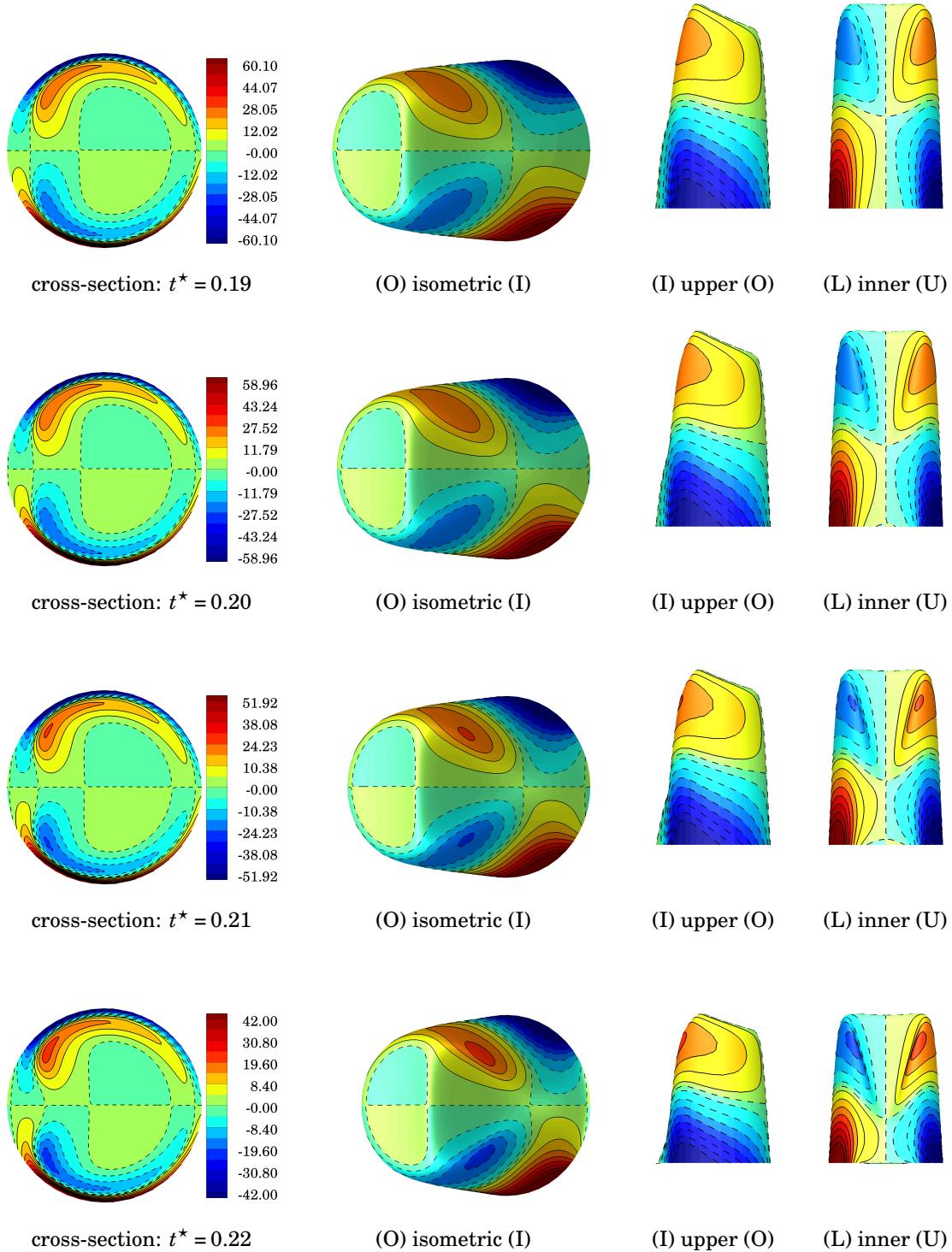


Figure E.2 Uniform entrance condition: velocity surface of u_s^* at $\theta = 45^\circ$ colored by non-dimensional streamwise vorticity ω_s^* visualized from three difference views: isometric, upper and inner. ($I \equiv inner$, $O \equiv outer$, $U \equiv upper$, $L \equiv lower$). (continued)

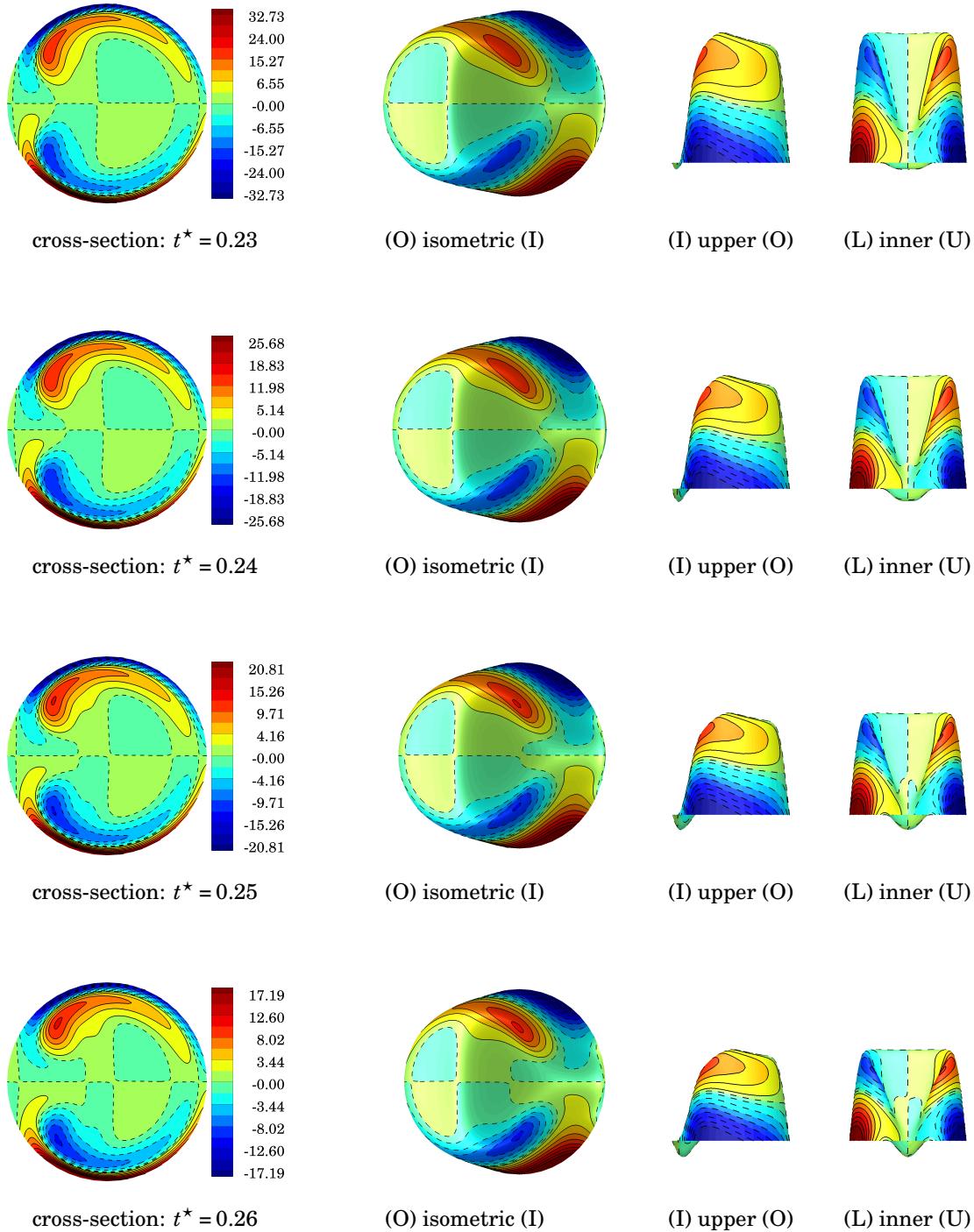


Figure E.2 Uniform entrance condition: velocity surface of u_s^* at $\theta = 45^\circ$ colored by non-dimensional streamwise vorticity ω_s^* visualized from three difference views: isometric, upper and inner. ($I \equiv inner$, $O \equiv outer$, $U \equiv upper$, $L \equiv lower$). (continued)

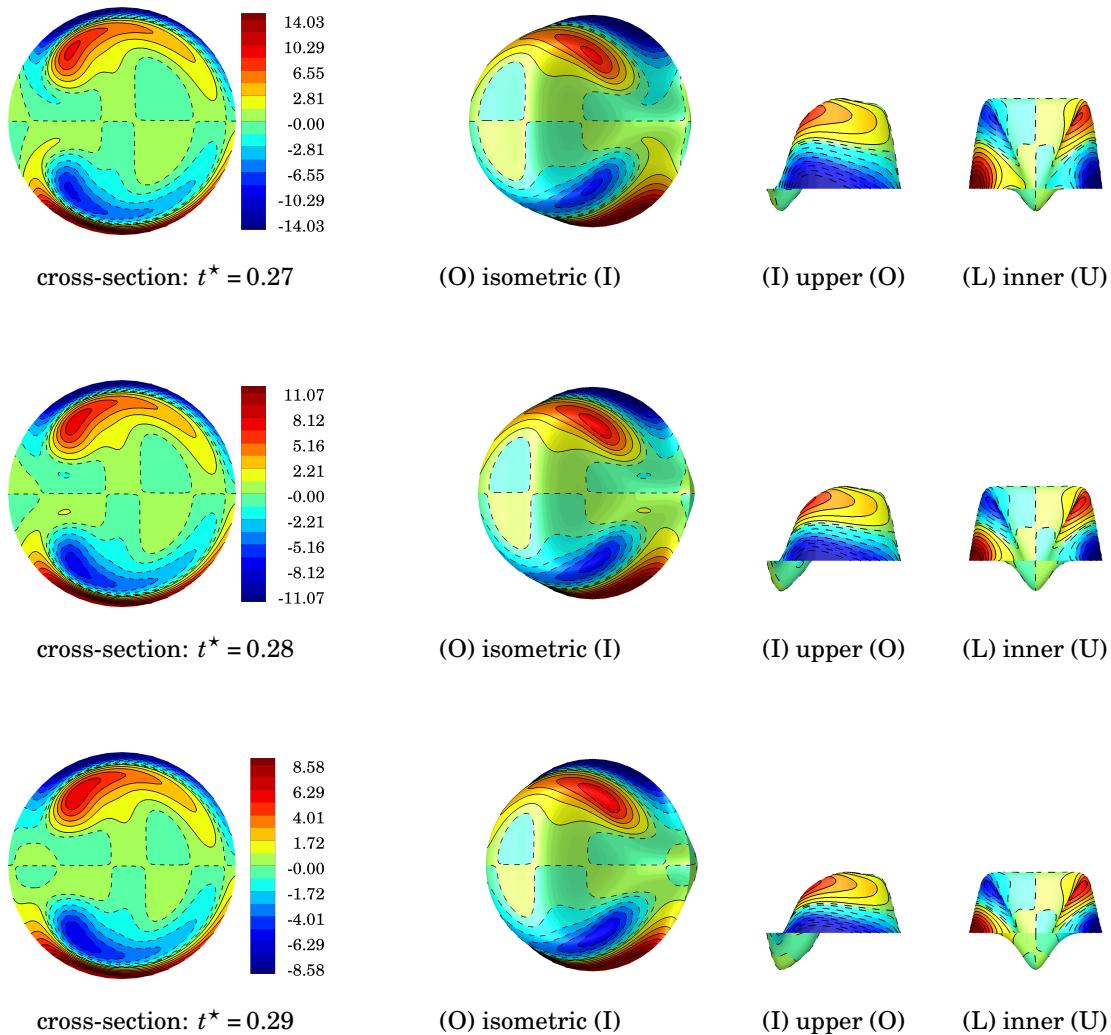


Figure E.2 Uniform entrance condition: velocity surface of u_s^* at $\theta = 45^\circ$ colored by non-dimensional streamwise vorticity ω_s^* visualized from three difference views: isometric, upper and inner. ($I \equiv \text{inner}$, $O \equiv \text{outer}$, $U \equiv \text{upper}$, $L \equiv \text{lower}$). (continued)

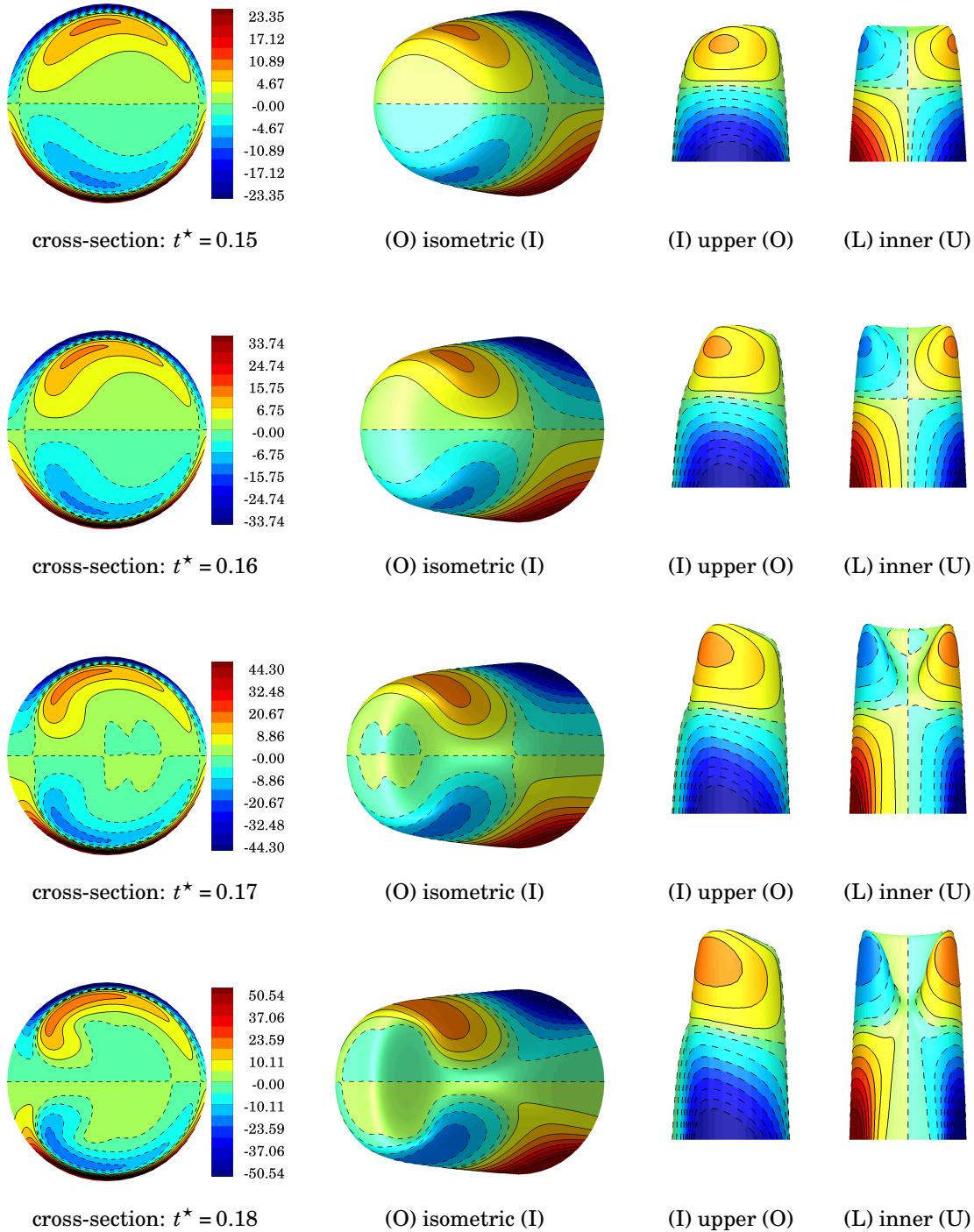


Figure E.3 Uniform entrance condition: velocity surface of u_s^* at $\theta = 90^\circ$ colored by non-dimensional streamwise vorticity ω_s^* visualized from three difference views: isometric, upper and inner. ($I \equiv inner$, $O \equiv outer$, $U \equiv upper$, $L \equiv lower$).

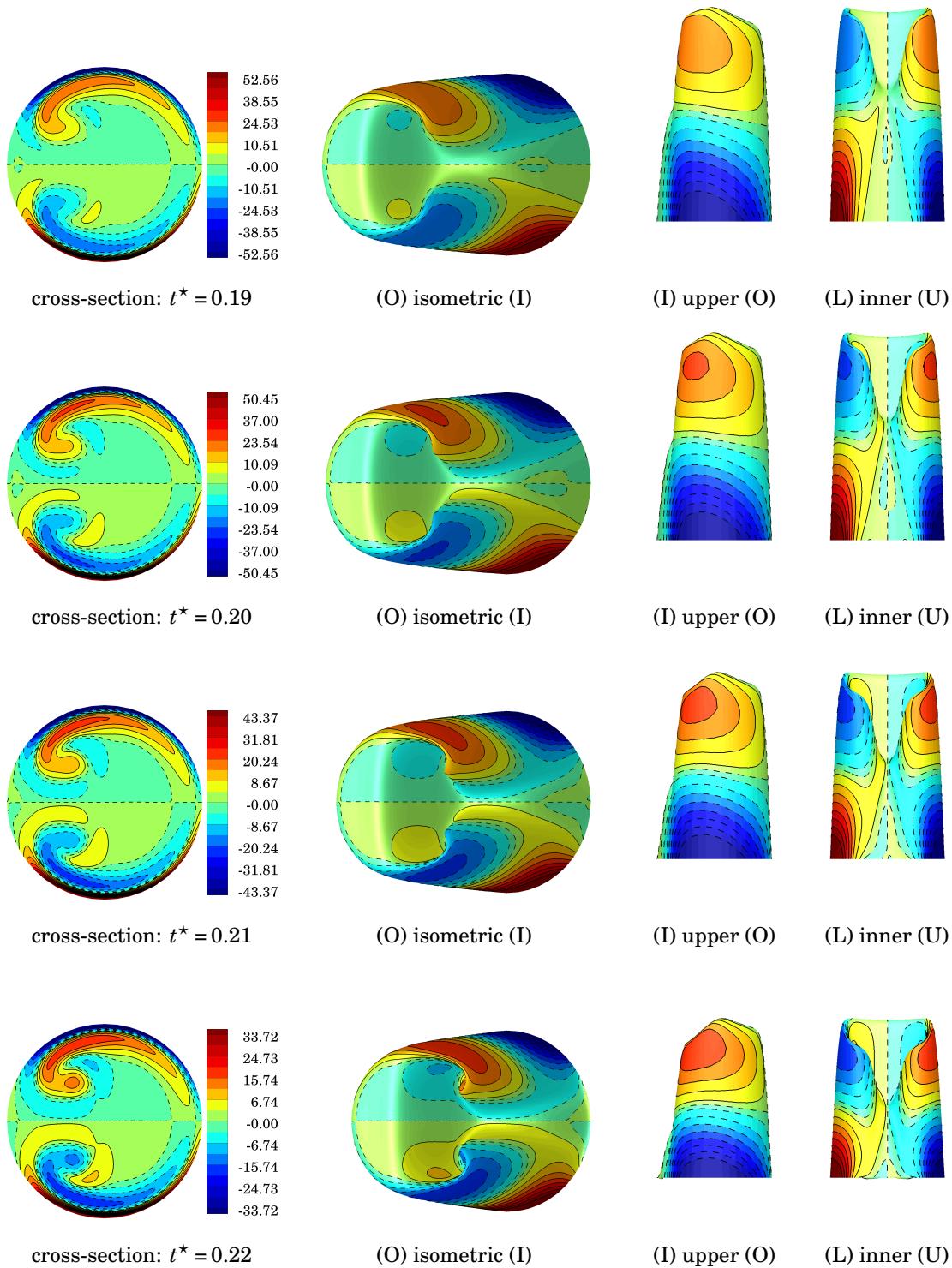


Figure E.3 Uniform entrance condition: velocity surface of u_s^* at $\theta = 90^\circ$ colored by non-dimensional streamwise vorticity ω_s^* visualized from three difference views: isometric, upper and inner. ($I \equiv$ inner, $O \equiv$ outer, $U \equiv$ upper, $L \equiv$ lower). (continued)

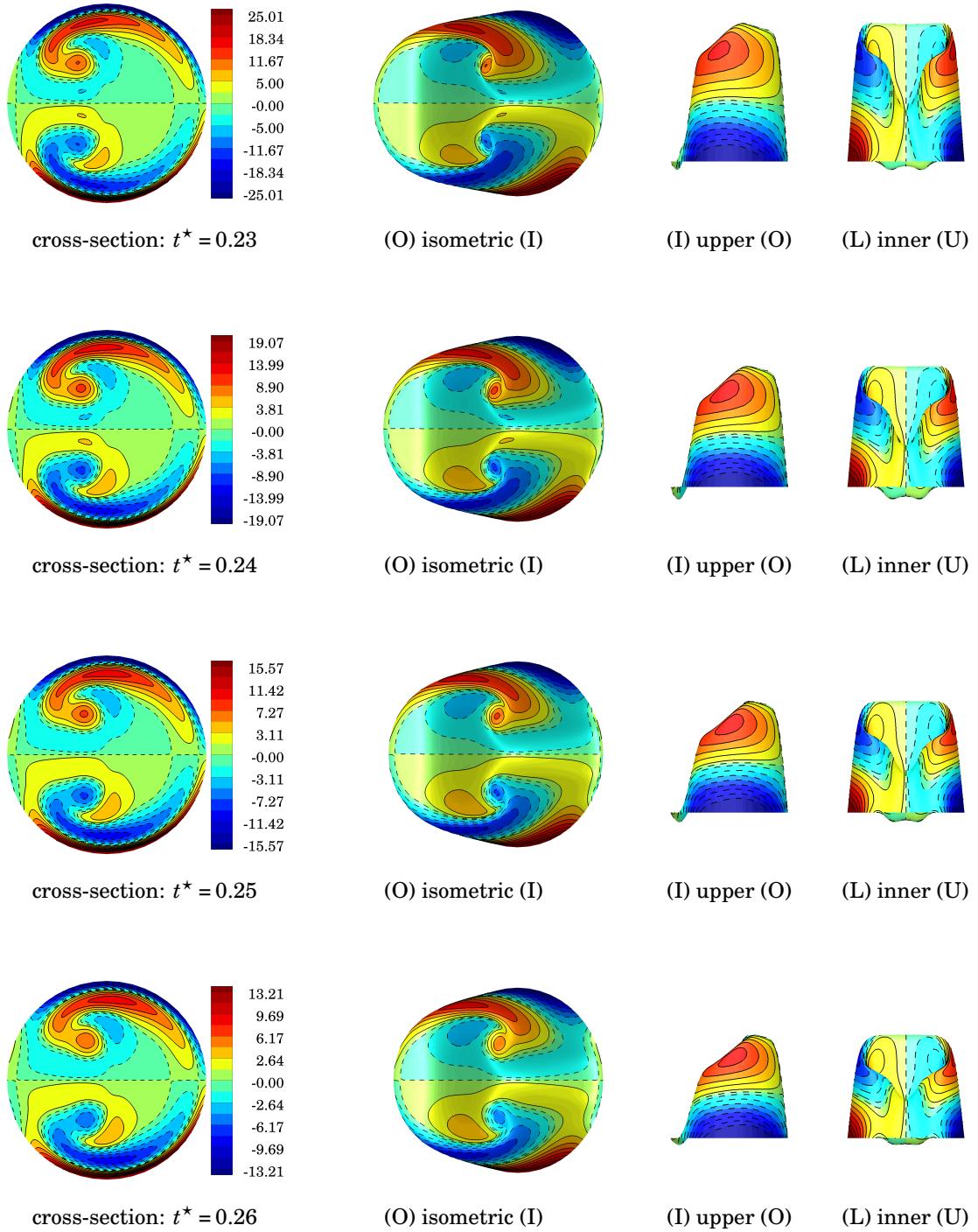


Figure E.3 Uniform entrance condition: velocity surface of u_s^* at $\theta = 90^\circ$ colored by non-dimensional streamwise vorticity ω_s^* visualized from three difference views: isometric, upper and inner. ($I \equiv inner$, $O \equiv outer$, $U \equiv upper$, $L \equiv lower$). (continued)

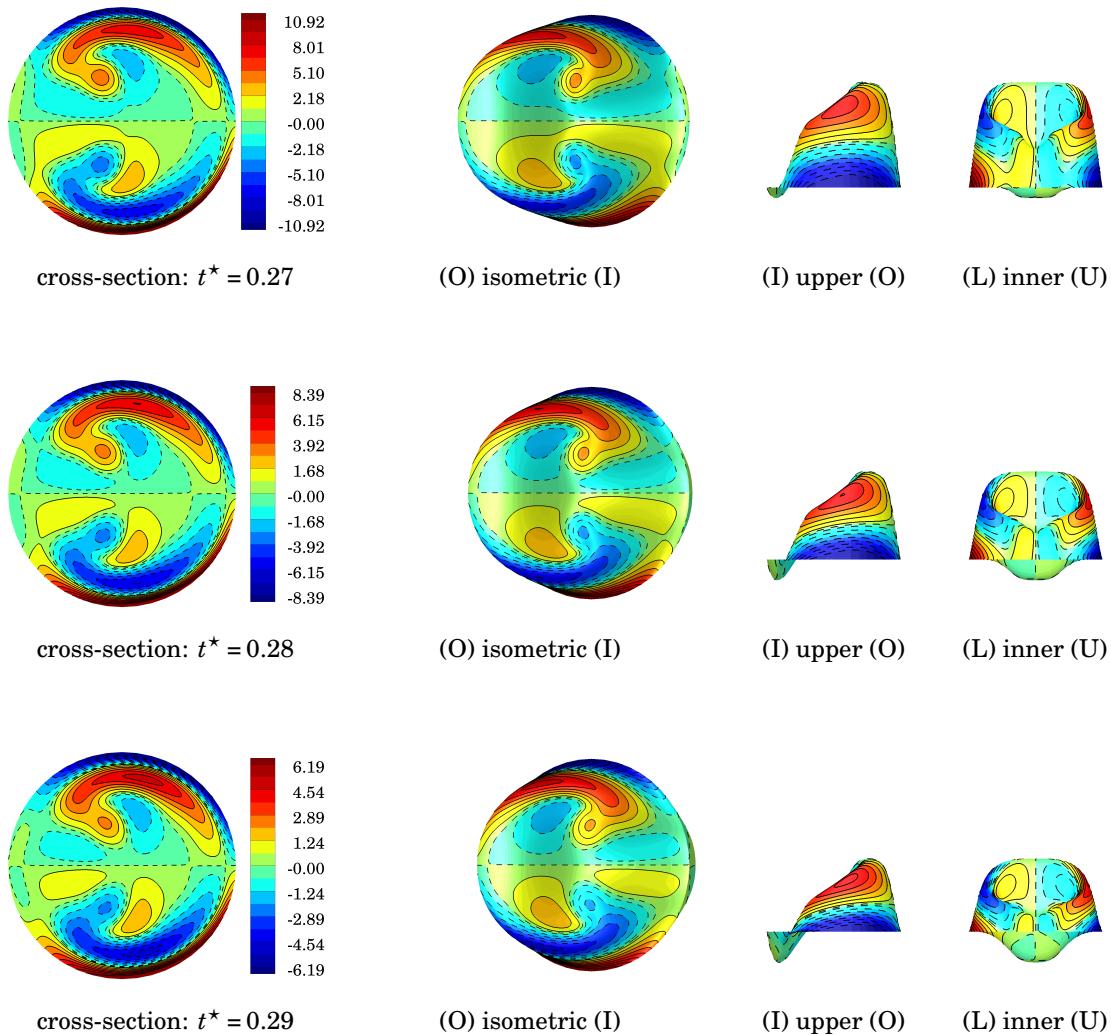


Figure E.3 Uniform entrance condition: velocity surface of u_s^* at $\theta = 90^\circ$ colored by non-dimensional streamwise vorticity ω_s^* visualized from three difference views: isometric, upper and inner. ($I \equiv \text{inner}$, $O \equiv \text{outer}$, $U \equiv \text{upper}$, $L \equiv \text{lower}$). (continued)

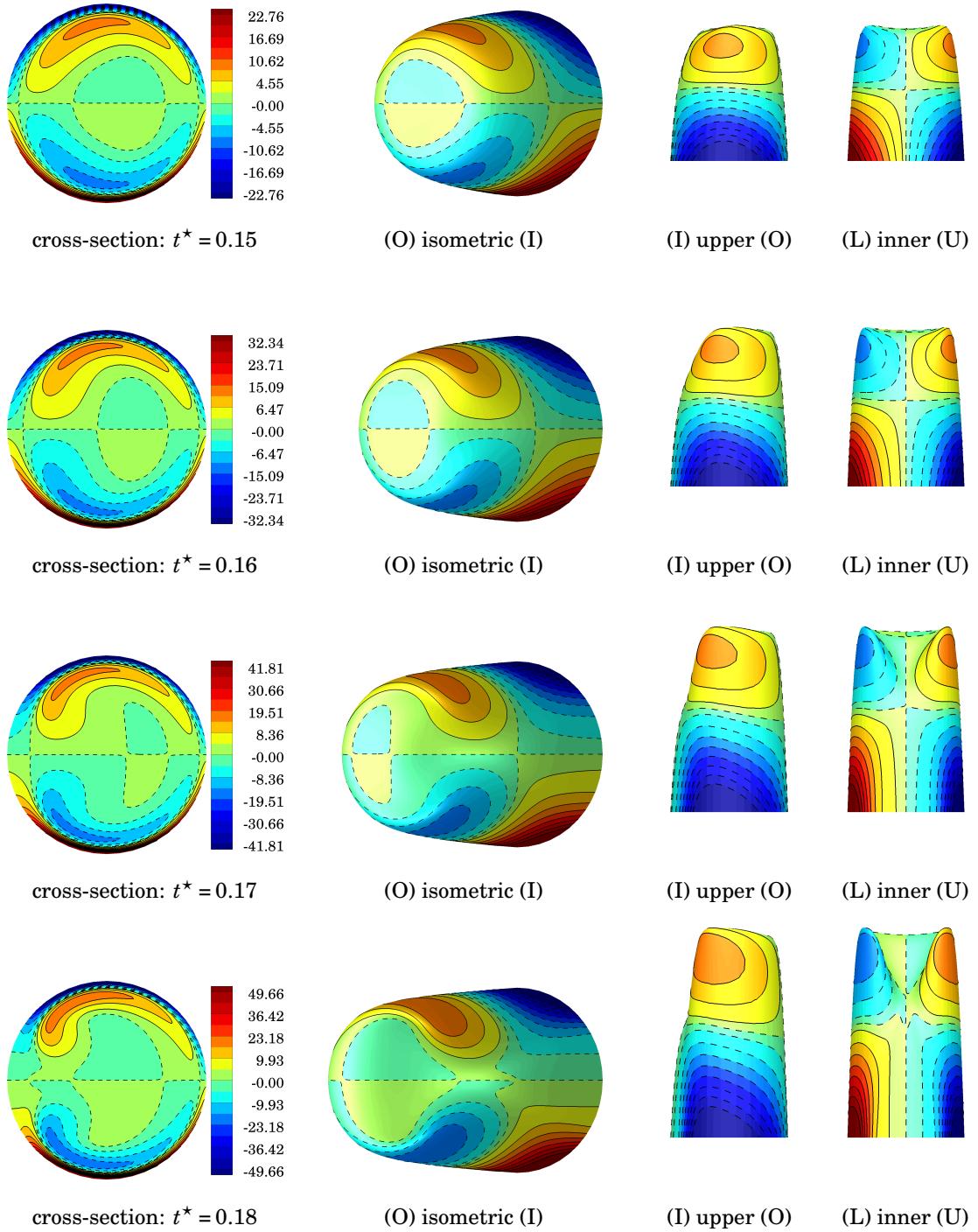


Figure E.4 Uniform entrance condition: velocity surface of u_s^* at $\theta = 135^\circ$ colored by non-dimensional streamwise vorticity ω_s^* visualized from three difference views: isometric, upper and inner. ($I \equiv inner$, $O \equiv outer$, $U \equiv upper$, $L \equiv lower$).

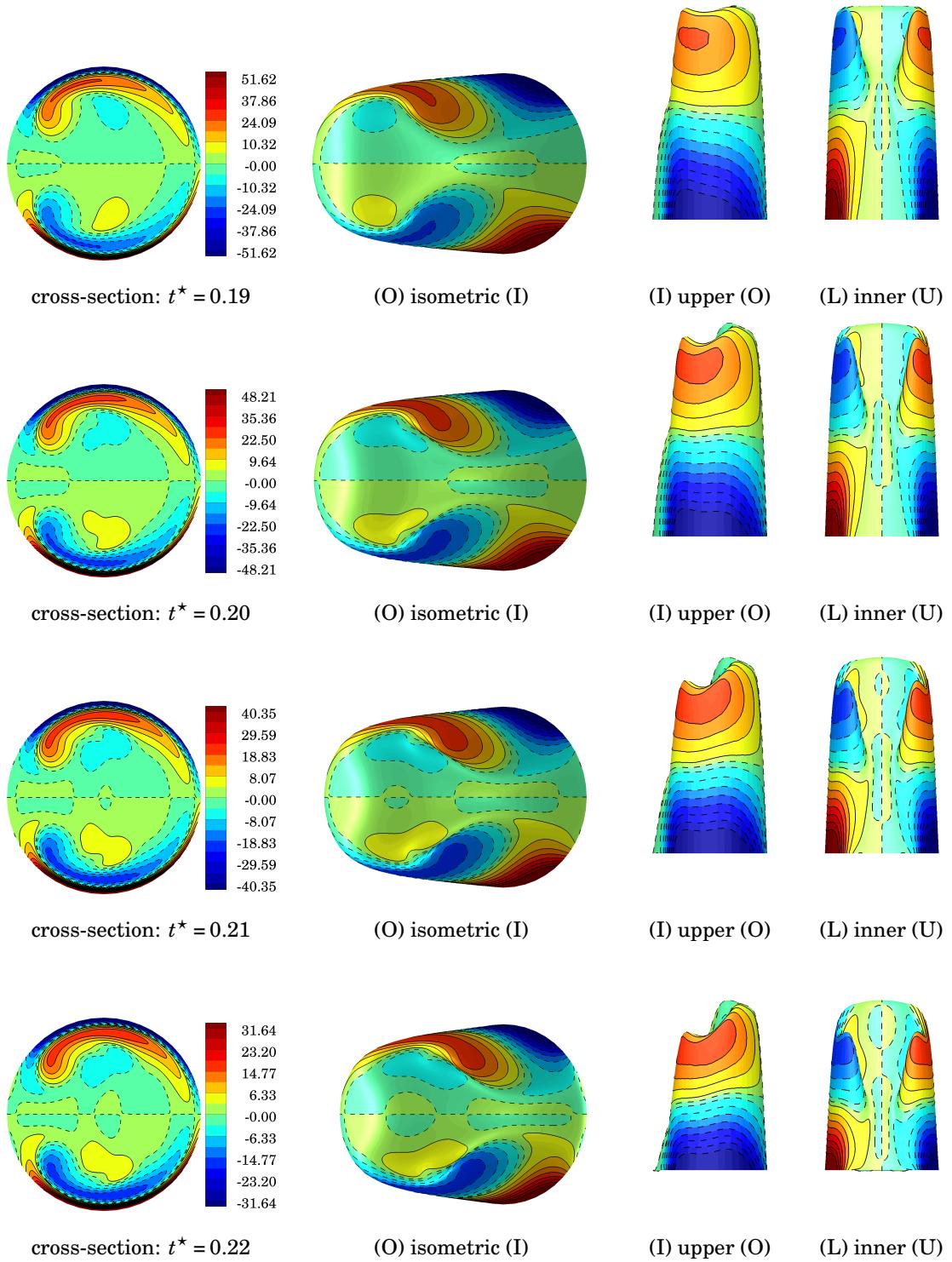


Figure E.4 Uniform entrance condition: velocity surface of u_s^* at $\theta = 135^\circ$ colored by non-dimensional streamwise vorticity ω_s^* visualized from three difference views: isometric, upper and inner. ($I \equiv inner$, $O \equiv outer$, $U \equiv upper$, $L \equiv lower$). (continued)

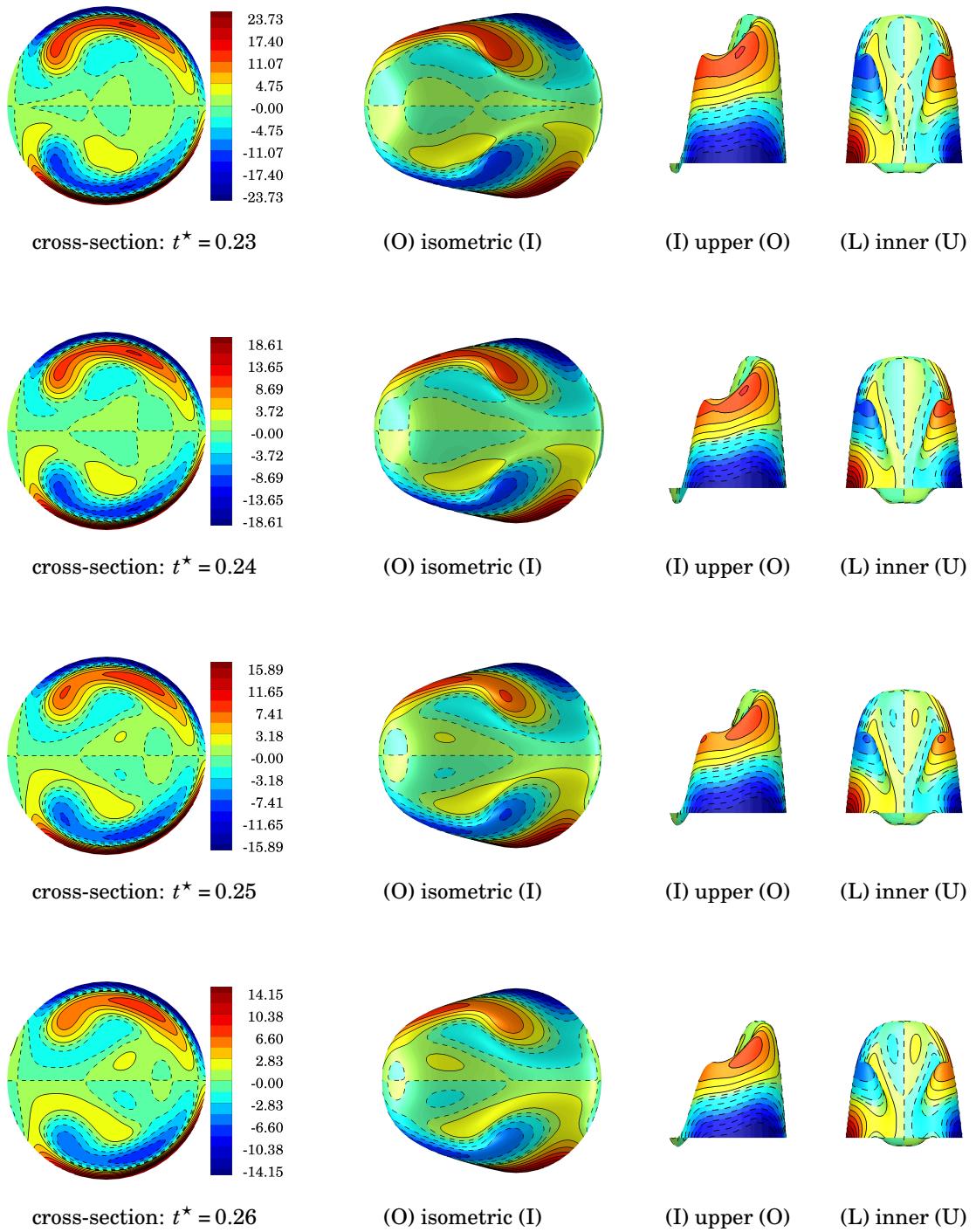


Figure E.4 Uniform entrance condition: velocity surface of u_s^* at $\theta = 135^\circ$ colored by non-dimensional streamwise vorticity ω_s^* visualized from three difference views: isometric, upper and inner. ($I \equiv inner$, $O \equiv outer$, $U \equiv upper$, $L \equiv lower$). (continued)

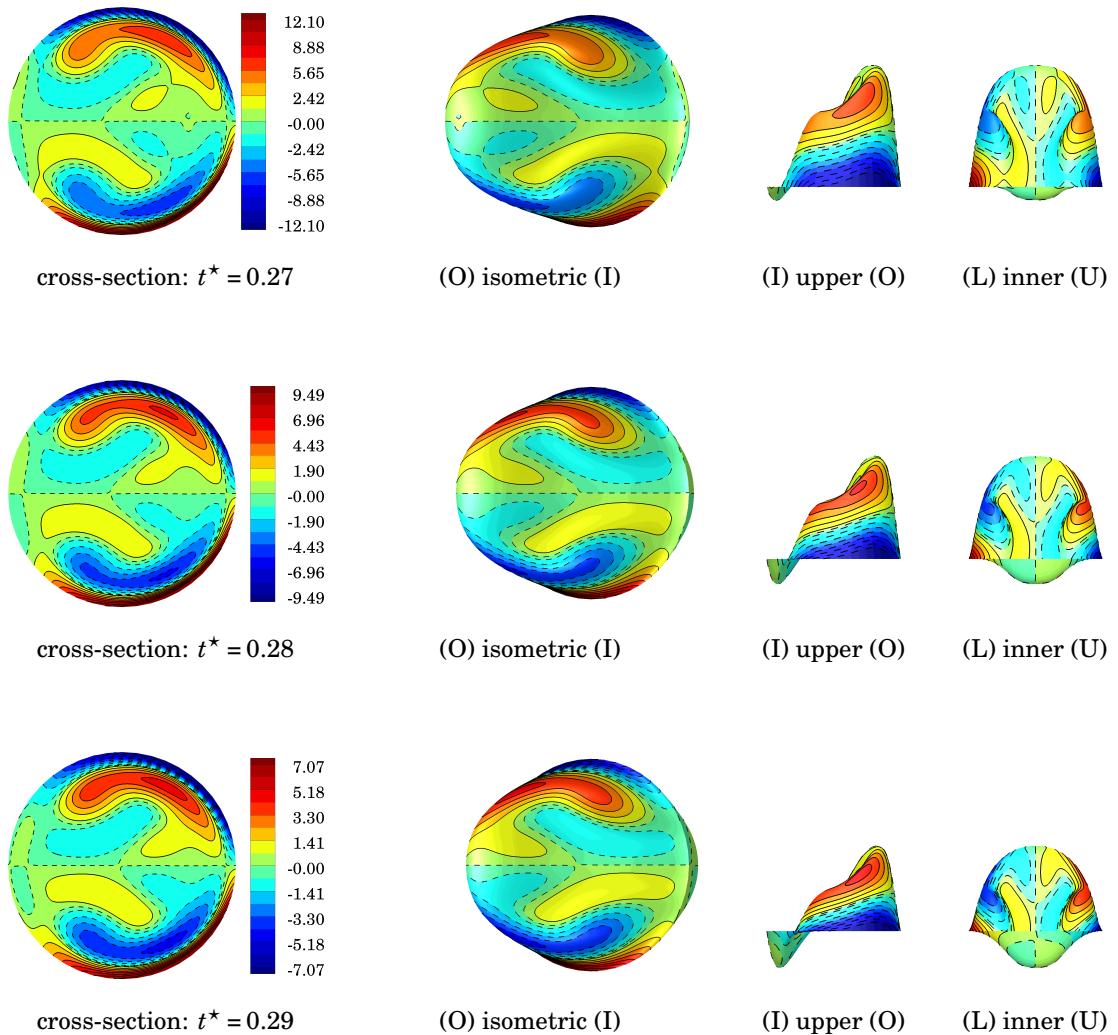


Figure E.4 Uniform entrance condition: velocity surface of u_s^* at $\theta = 135^\circ$ colored by non-dimensional streamwise vorticity ω_s^* visualized from three difference views: isometric, upper and inner. ($I \equiv \text{inner}$, $O \equiv \text{outer}$, $U \equiv \text{upper}$, $L \equiv \text{lower}$). (continued)

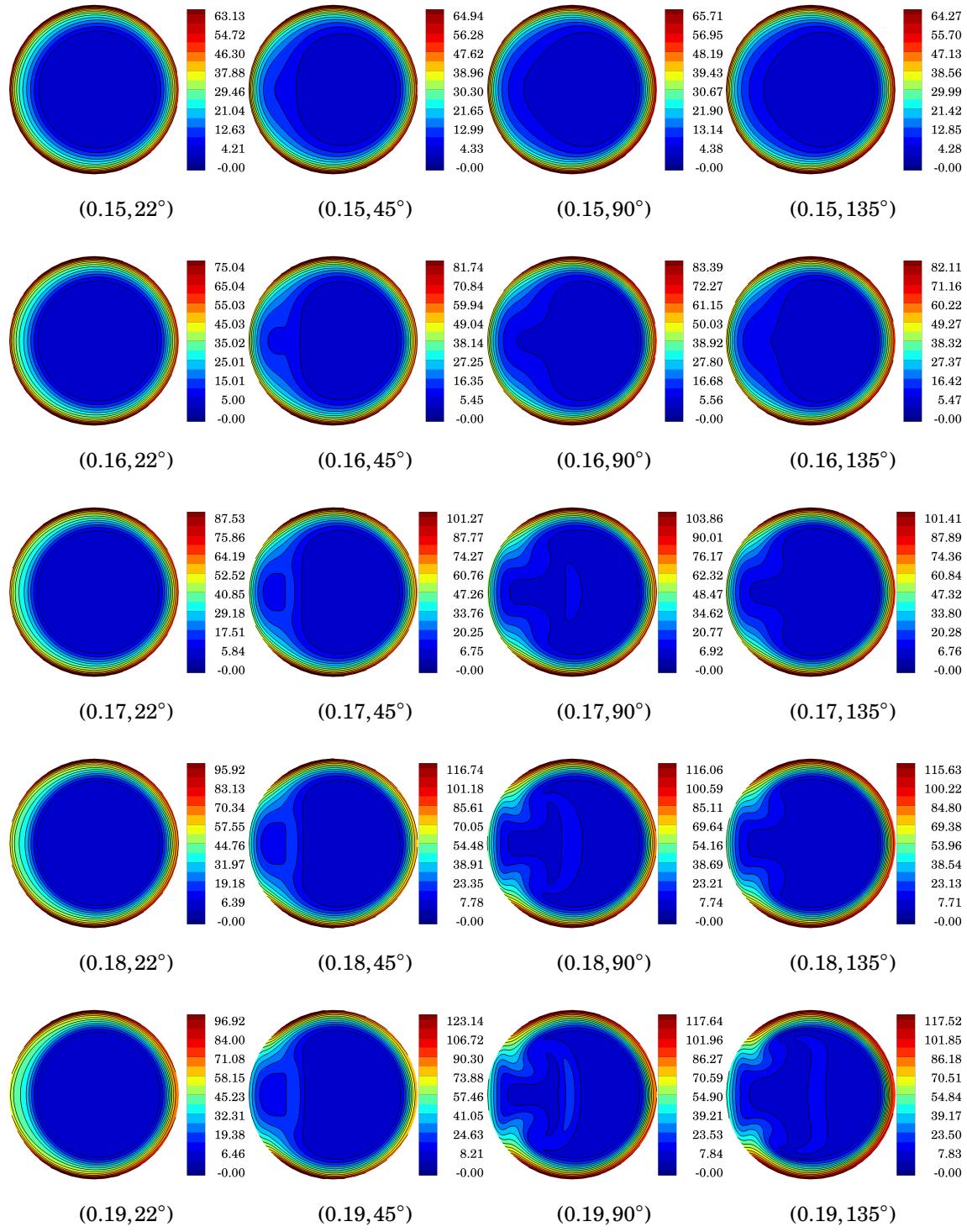


Figure E.5 Uniform entrance condition: non-dimensional vorticity magnitude $|\omega^*|$ at (t^*, ϕ) .

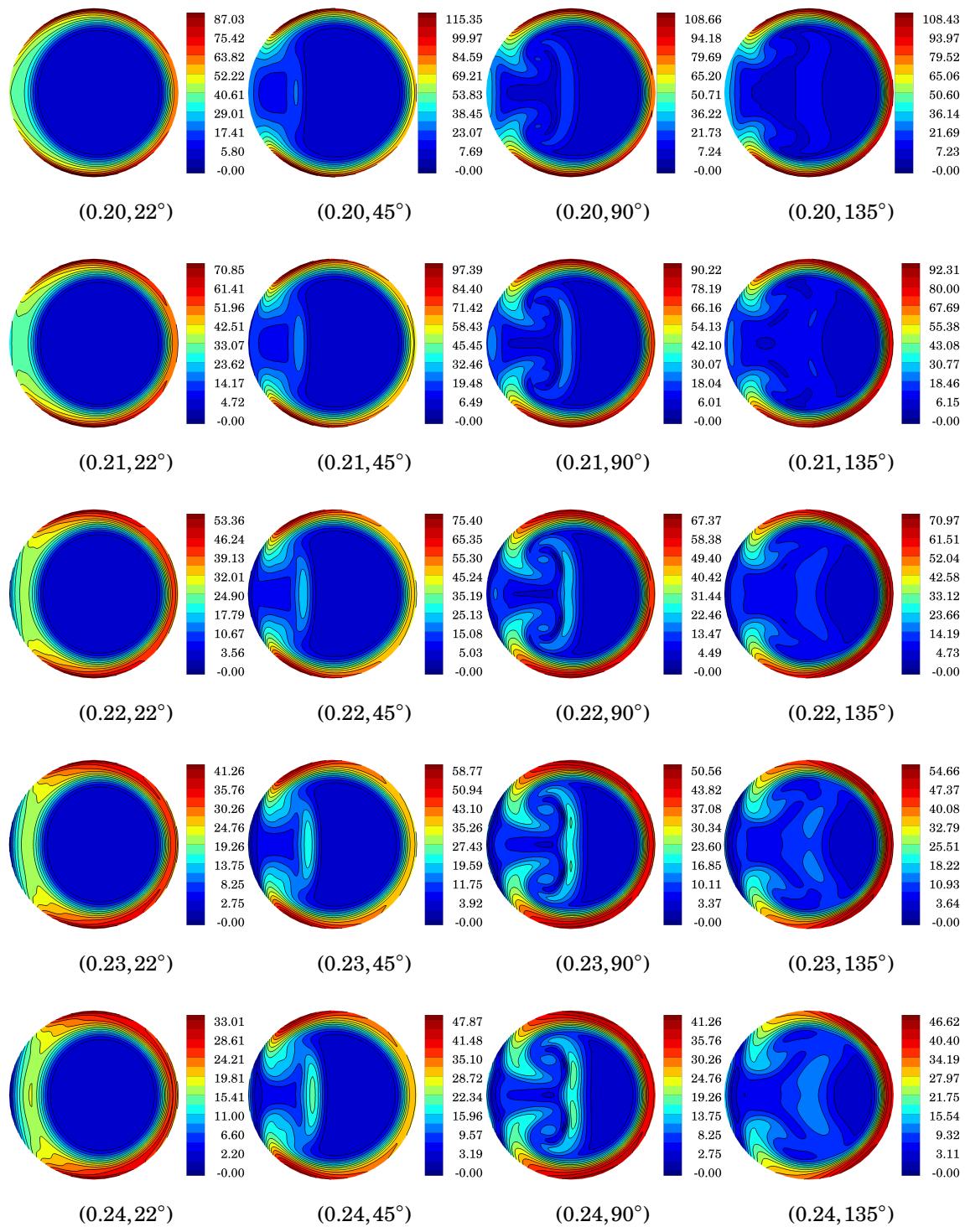


Figure E.5 Uniform entrance condition: non-dimensional vorticity magnitude $|\omega^*|$ at (t^*, ϕ) . (*continued*)

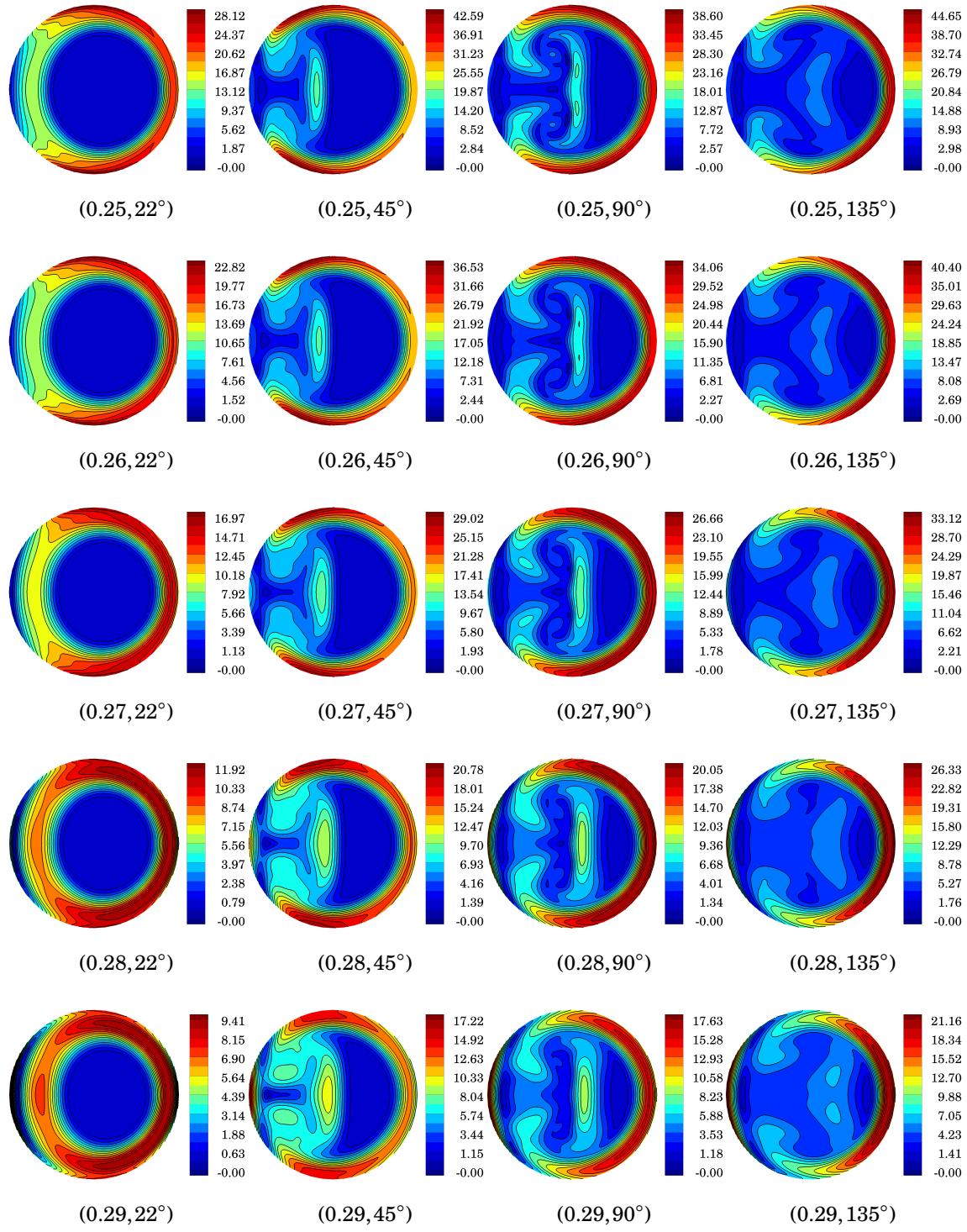


Figure E.5 Uniform entrance condition: non-dimensional vorticity magnitude $|\omega^*|$ at (t^*, ϕ) . (*continued*)

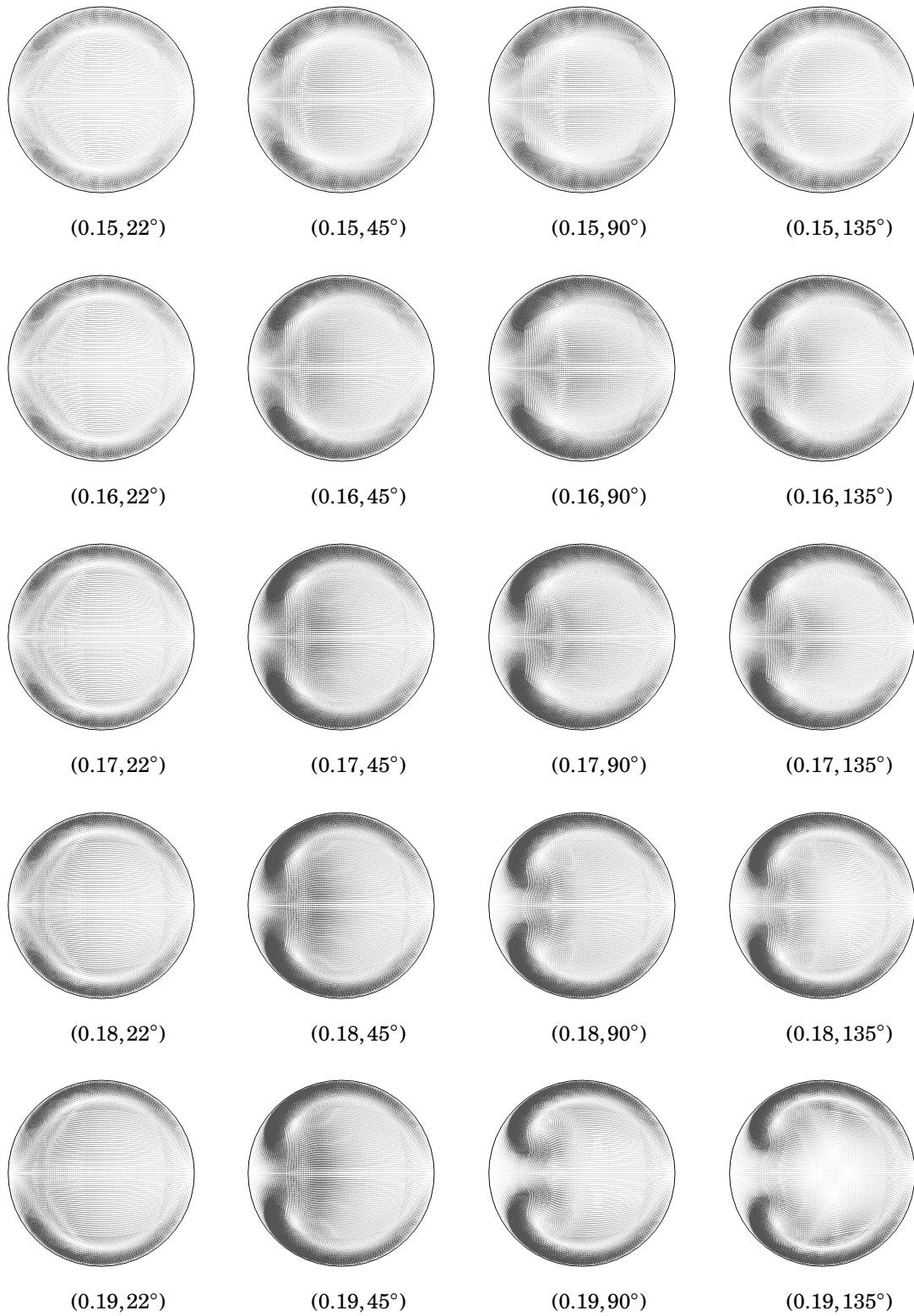


Figure E.6 Uniform entrance condition: non-dimensional secondary velocity vectors $\mathbf{u}_{\theta r}^*$ at (t^*, ϕ) .

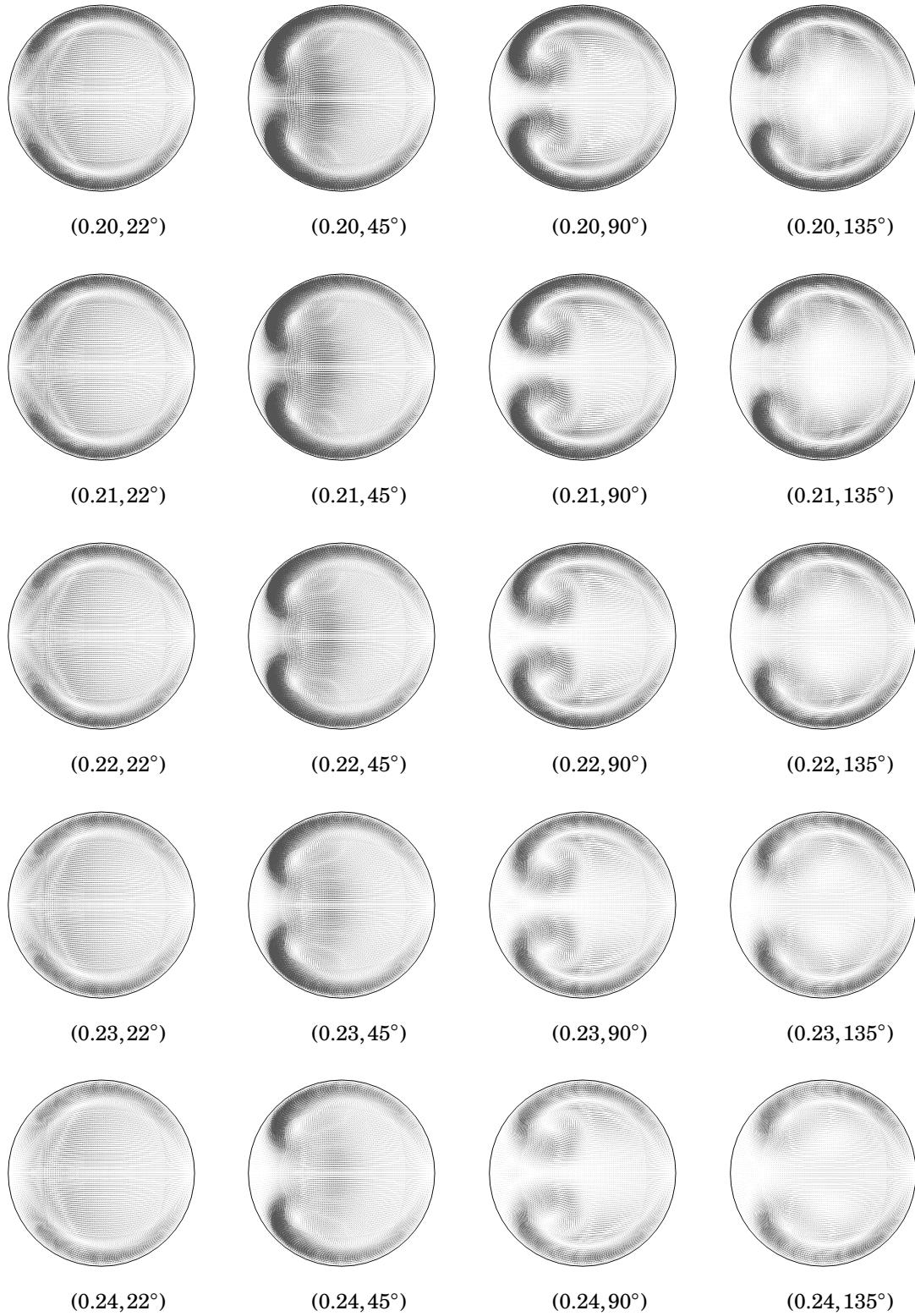


Figure E.6 Uniform entrance condition: non-dimensional secondary velocity vectors $\mathbf{u}_{\theta r}^*$ at (t^*, ϕ) . (*continued*)

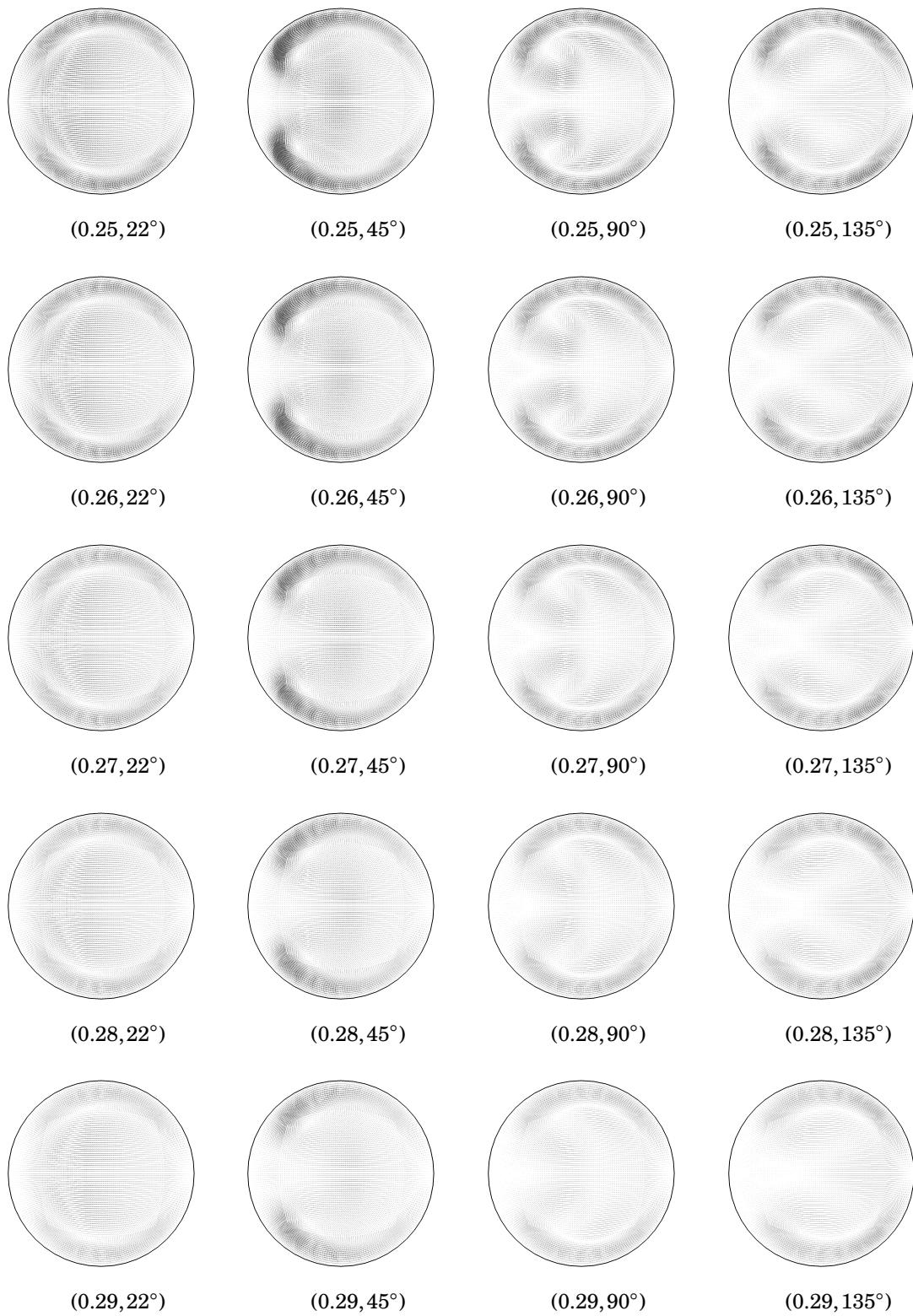


Figure E.6 Uniform entrance condition: non-dimensional secondary velocity vectors $\mathbf{u}_{\theta r}^*$ at (t^*, ϕ) . (*continued*)

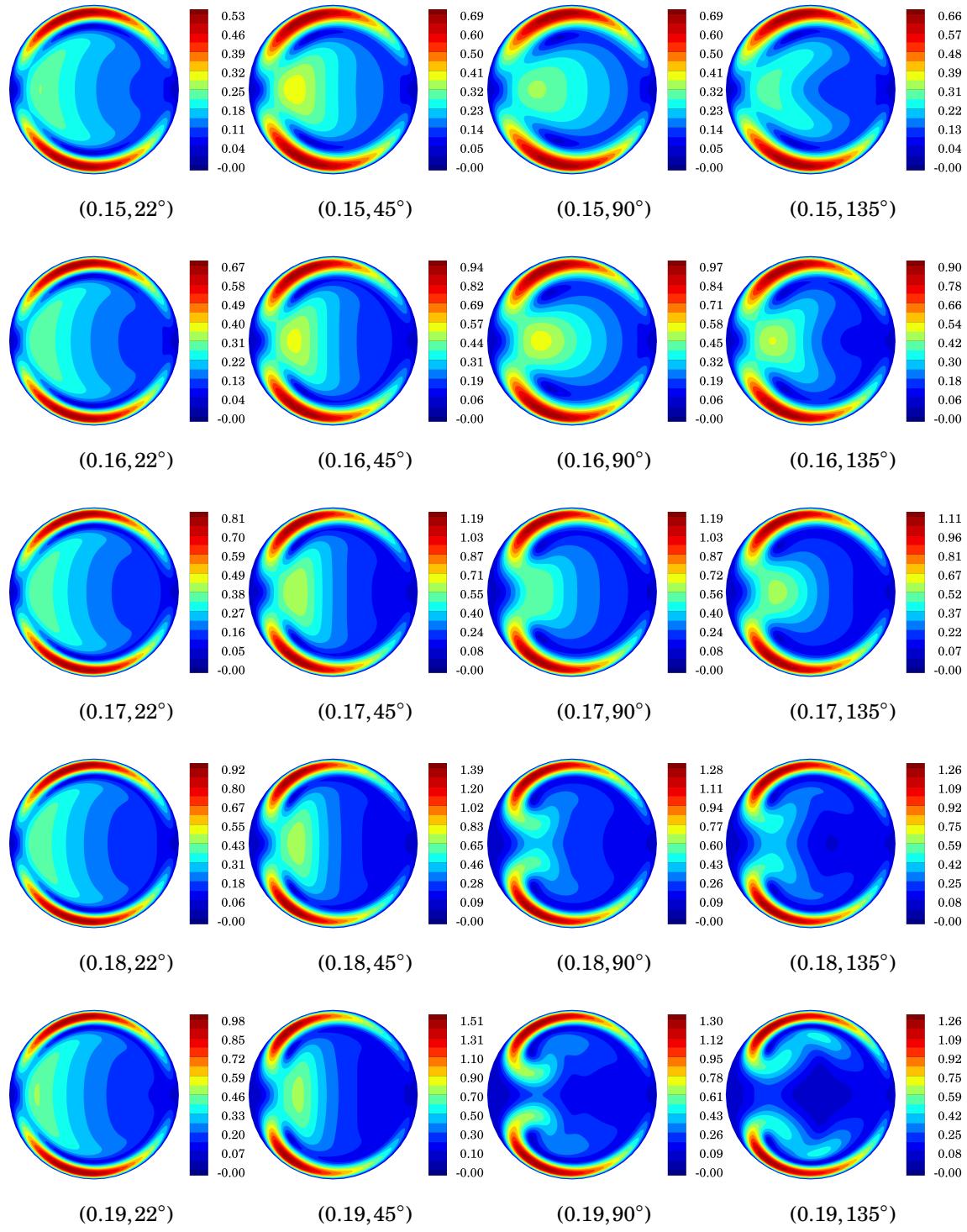


Figure E.7 Uniform entrance condition: non-dimensional secondary velocity magnitude $|u_{\theta_r}^*|$ at (t^*, ϕ) .

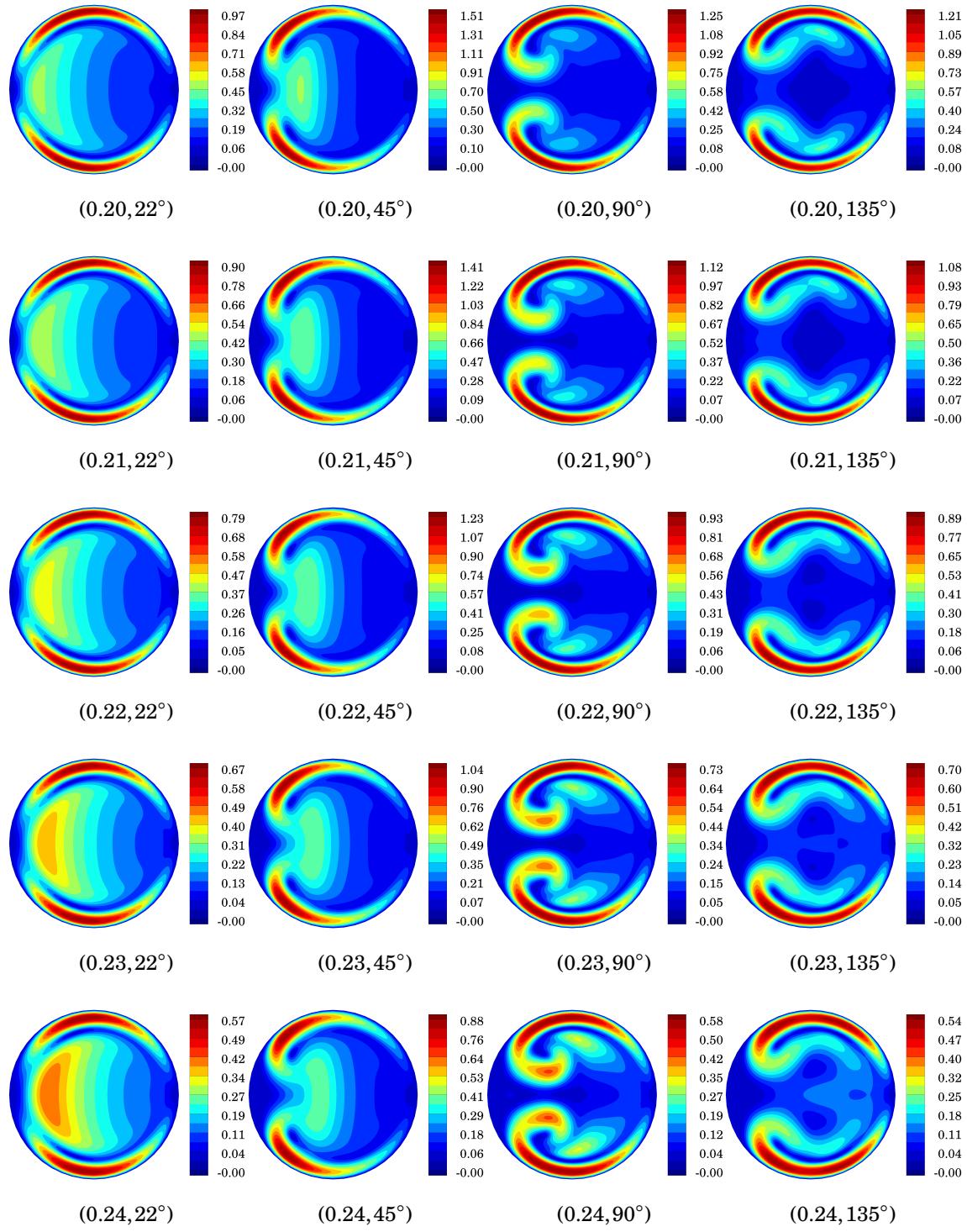


Figure E.7 Uniform entrance condition: non-dimensional secondary velocity magnitude $|u_{\theta r}^*|$ at (t^*, ϕ) . (continued)

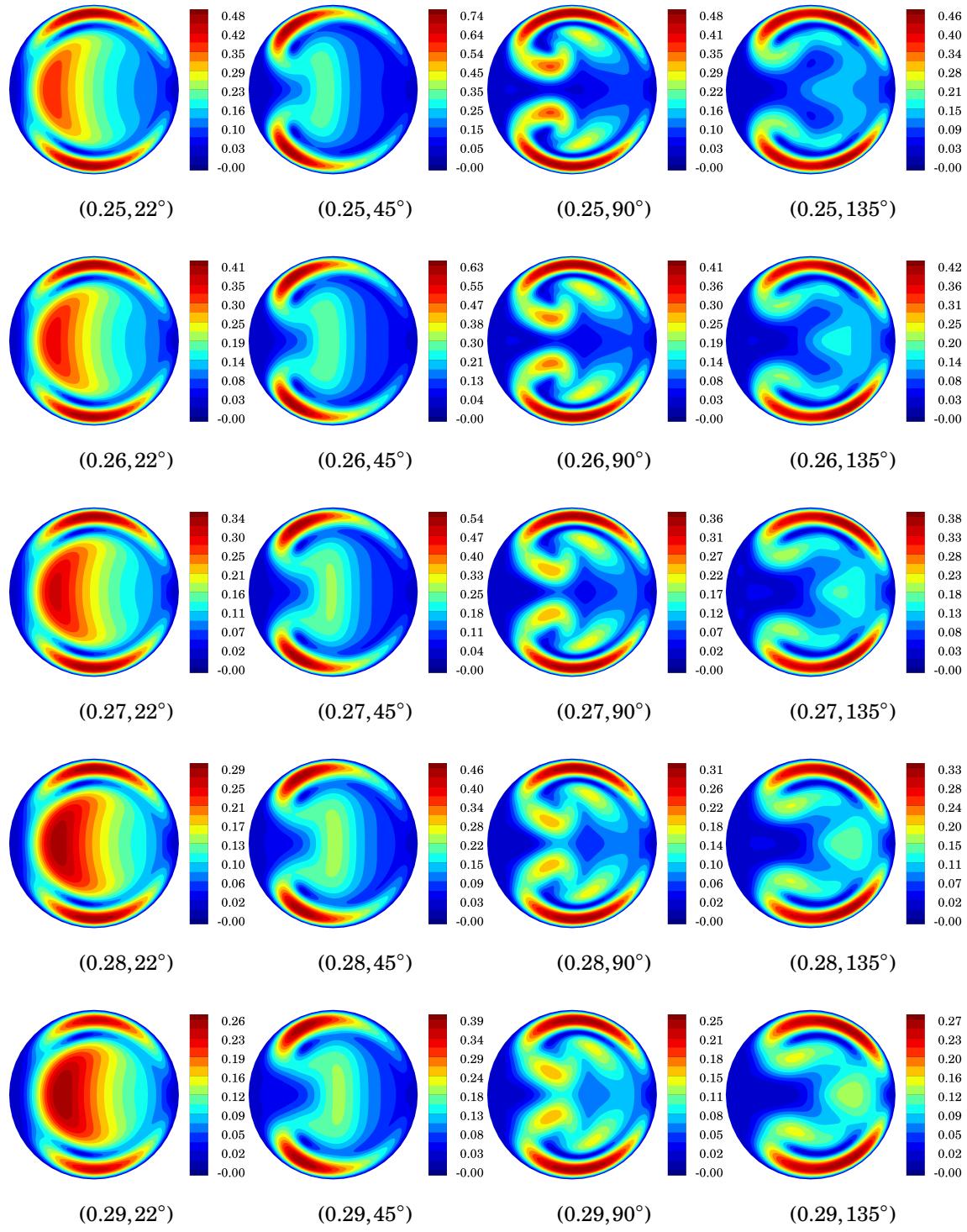


Figure E.7 Uniform entrance condition: non-dimensional secondary velocity magnitude $|u_{\theta r}^*|$ at (t^*, ϕ) . (*continued*)

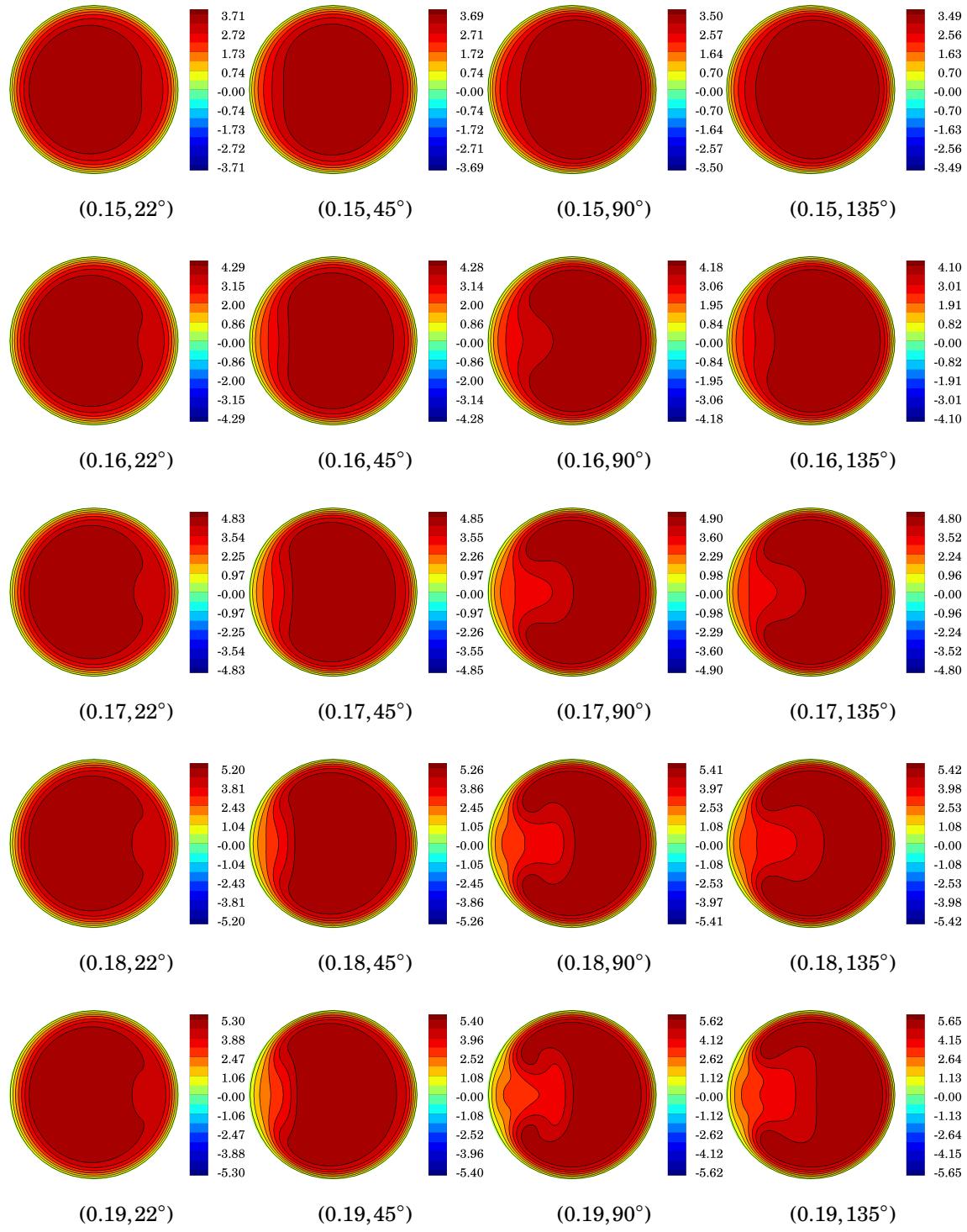


Figure E.8 Uniform entrance condition: non-dimensional streamwise velocity u_s^* at (t^*, ϕ) .

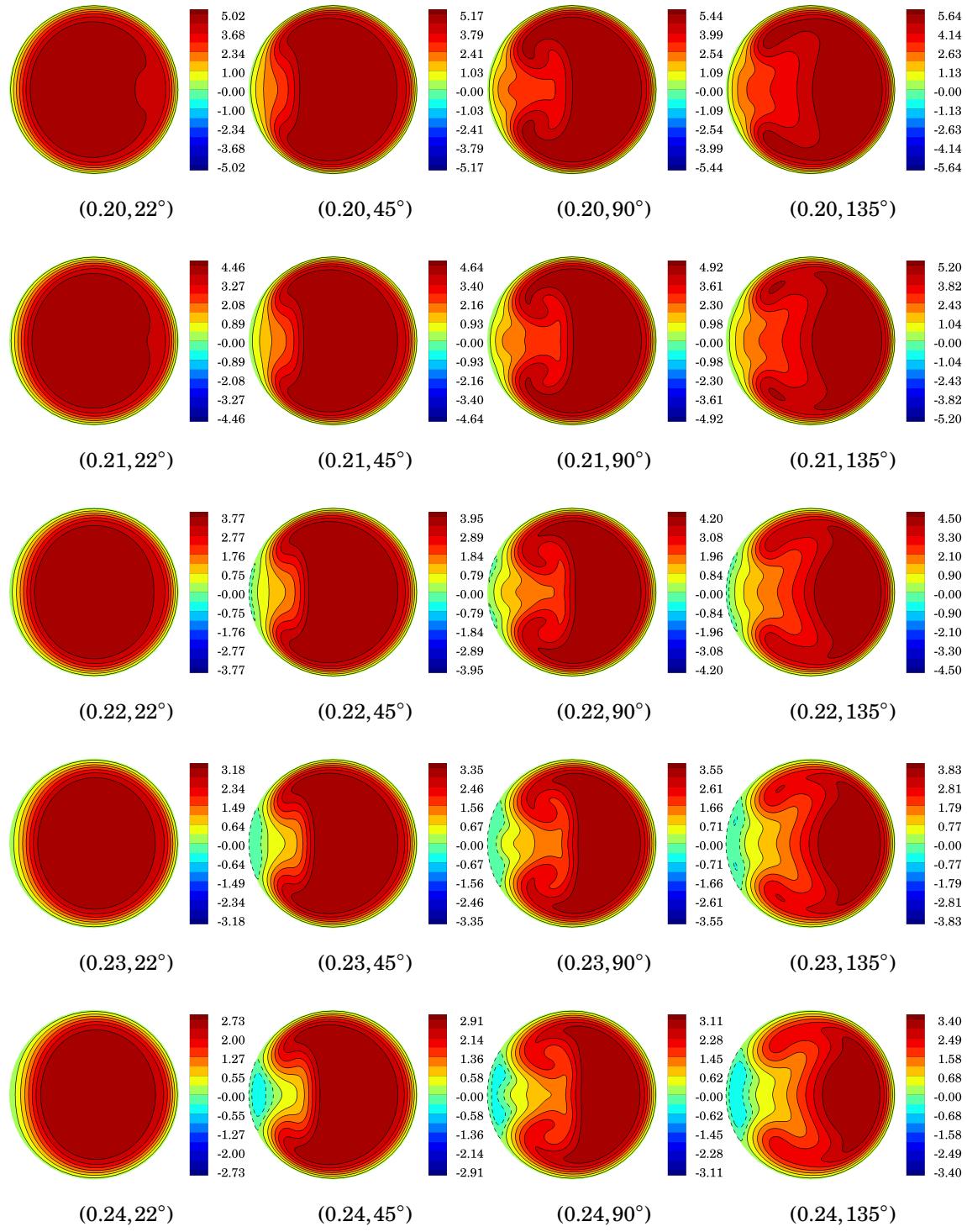


Figure E.8 Uniform entrance condition: non-dimensional streamwise velocity u_s^* at (t^*, ϕ) .
(continued)

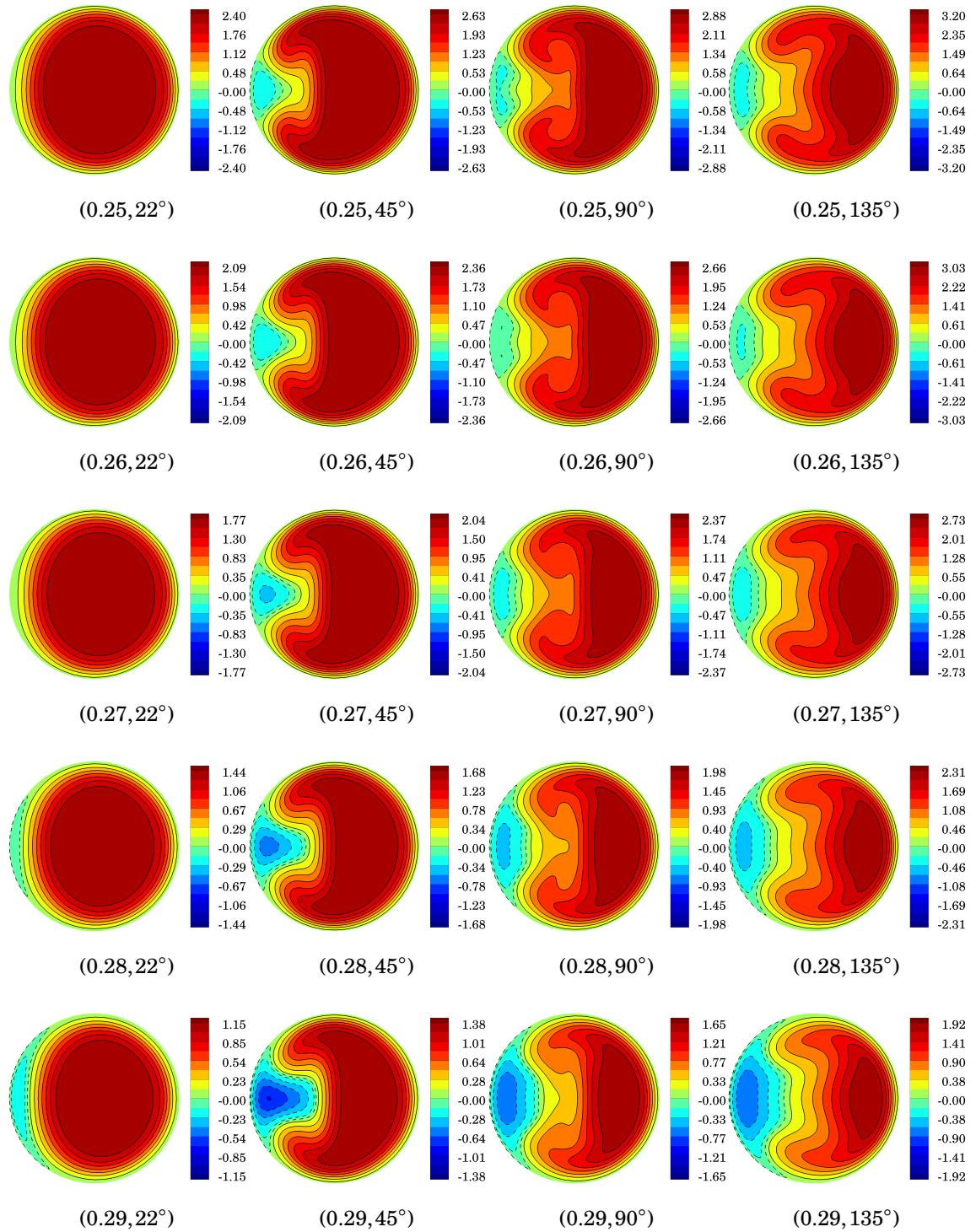


Figure E.8 Uniform entrance condition: non-dimensional streamwise velocity u_s^* at (t^*, ϕ) .
(continued)

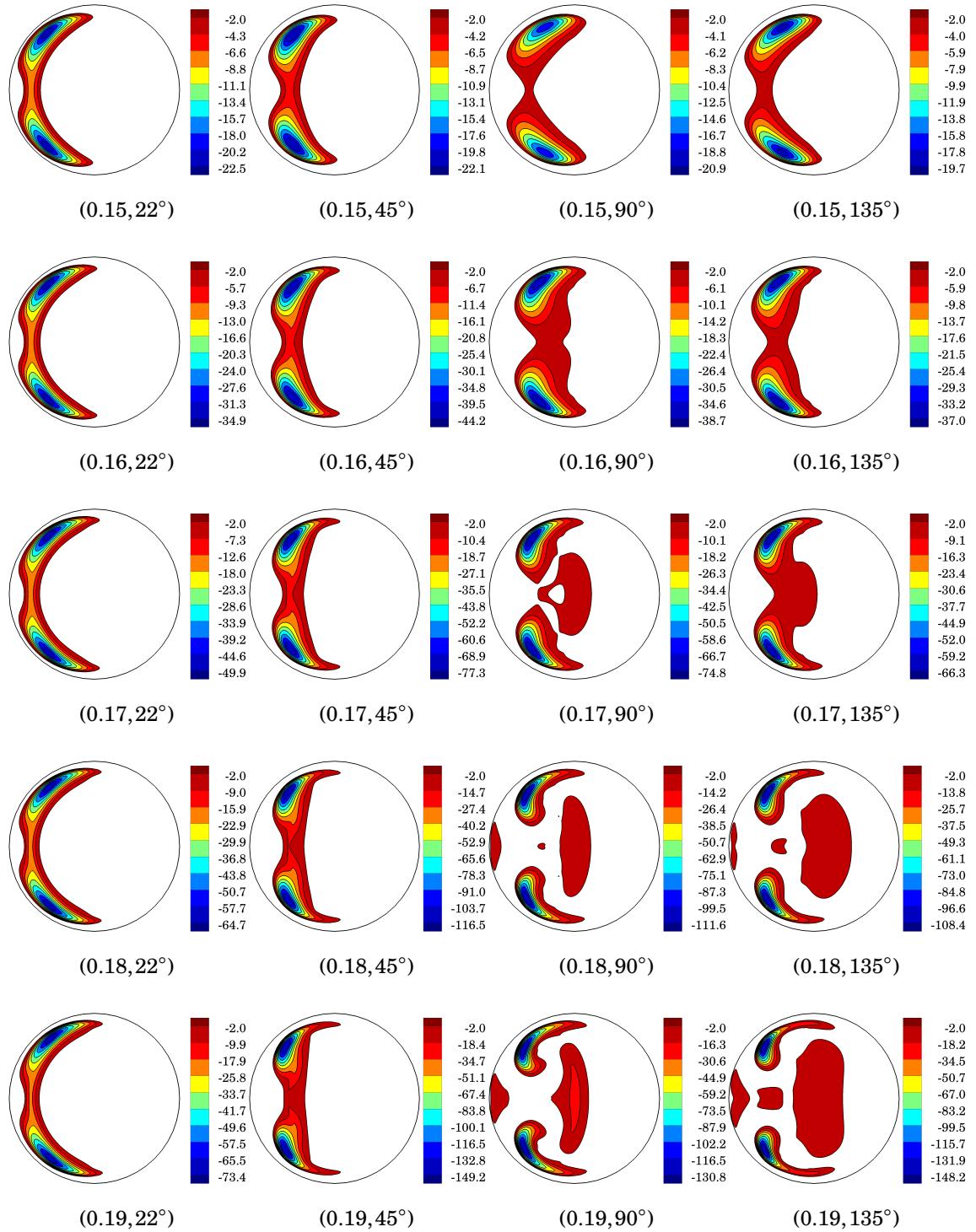


Figure E.9 Uniform entrance condition: non-dimensional second eigenvalue λ_2^* of $\mathbf{S}^2 + \mathbf{R}^2$, $\lambda_2^* < 0$ at (t^*, ϕ) .

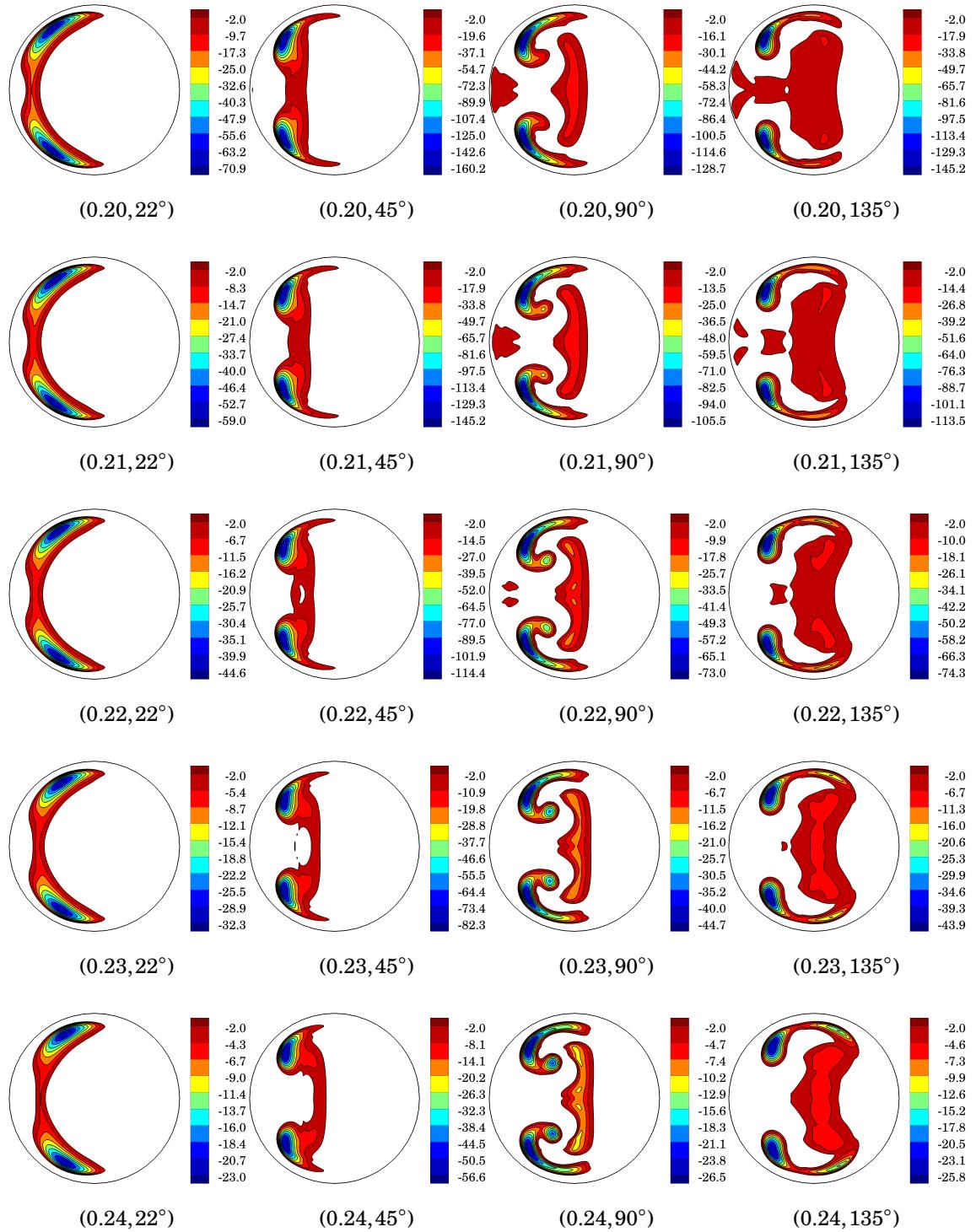


Figure E.9 Uniform entrance condition: non-dimensional second eigenvalue λ_2^* of $\mathbf{S}^2 + \mathbf{R}^2$, $\lambda_2^* < 0$ at (t^*, ϕ) . (*continued*)

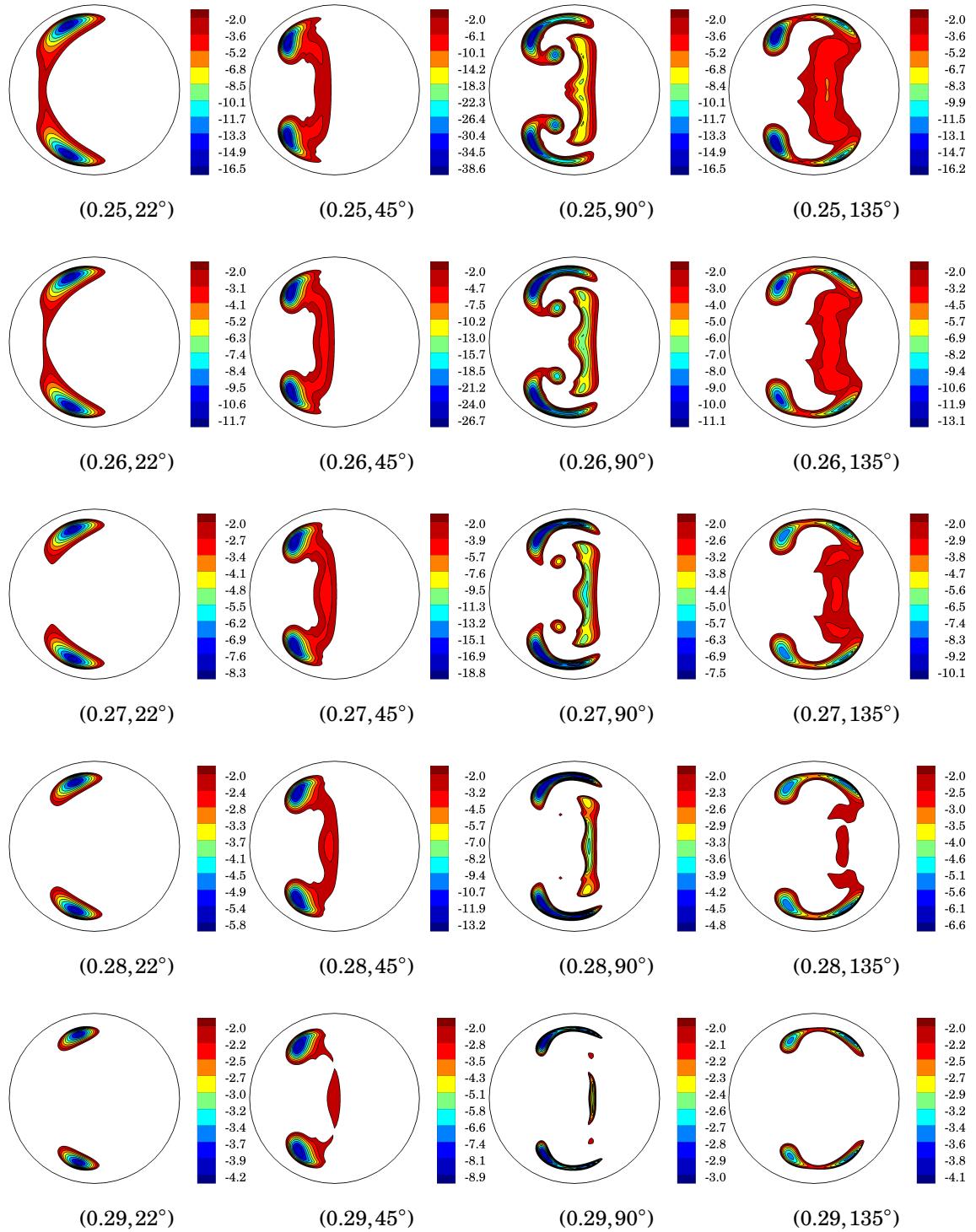


Figure E.9 Uniform entrance condition: non-dimensional second eigenvalue λ_2^* of $\mathbf{S}^2 + \mathbf{R}^2$, $\lambda_2^* < 0$ at (t^*, ϕ) . (*continued*)

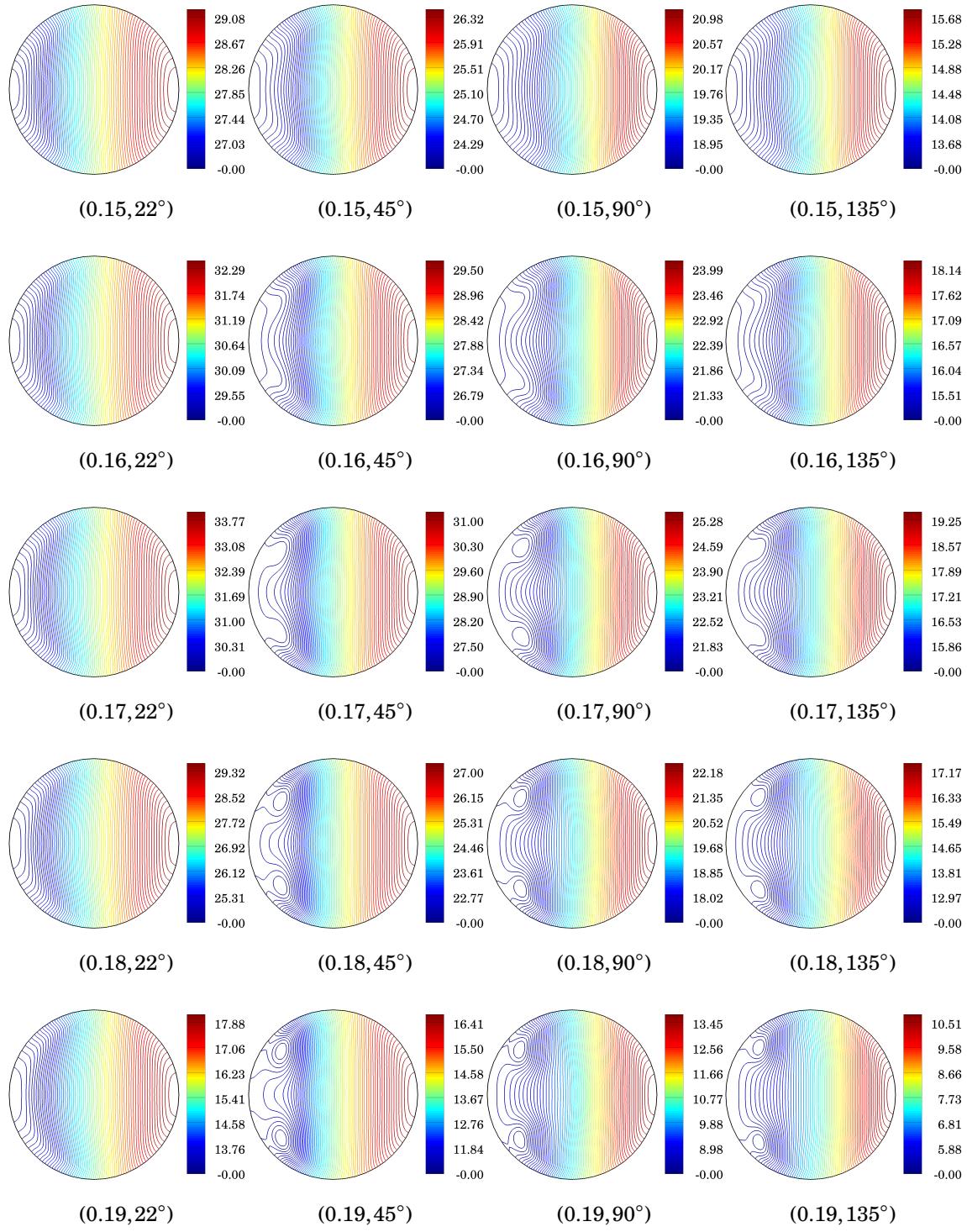


Figure E.10 Uniform entrance condition: non-dimensional pressure p^* at (t^*, ϕ) .

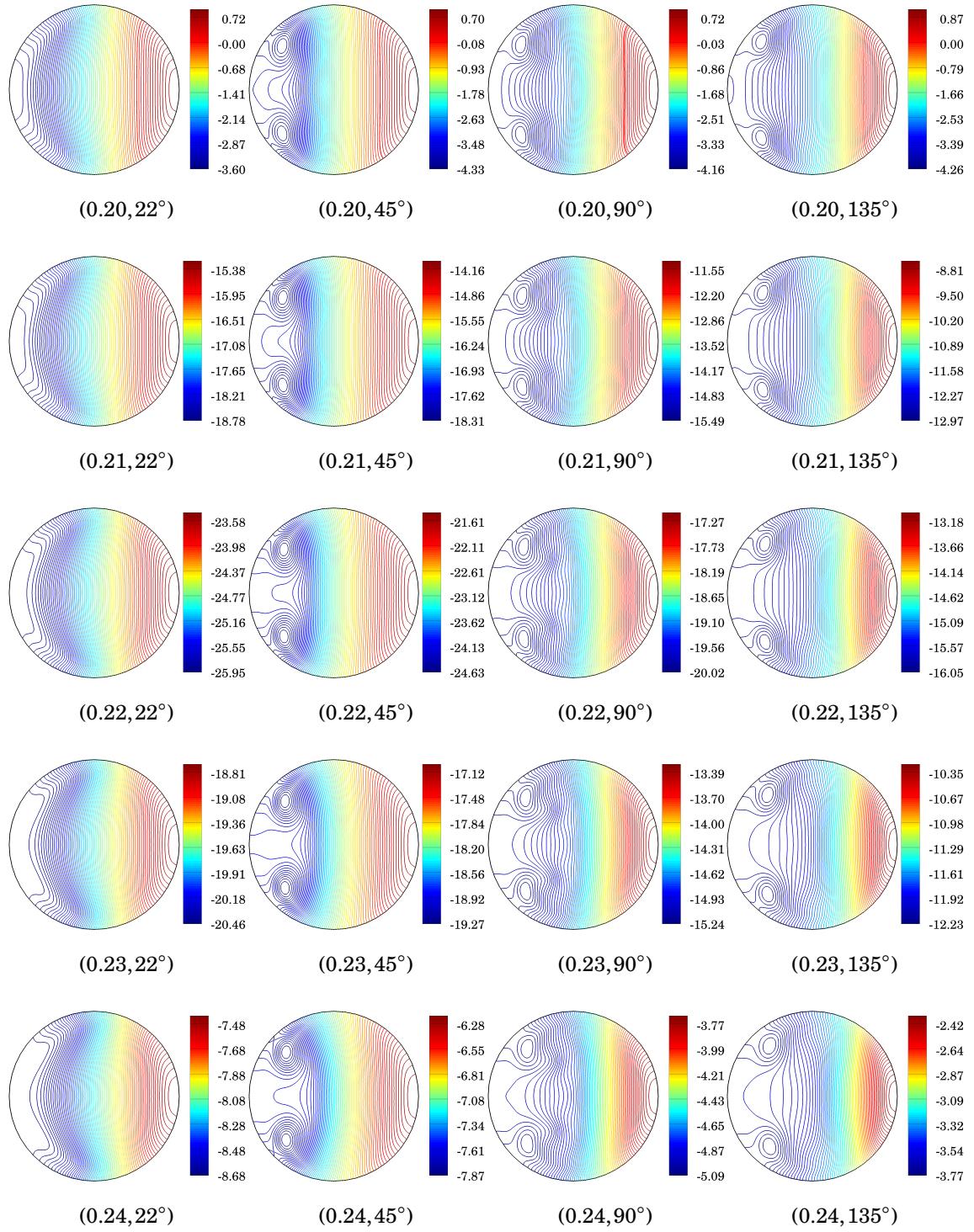


Figure E.10 Uniform entrance condition: non-dimensional pressure p^* at (t^*, ϕ) .
(continued)

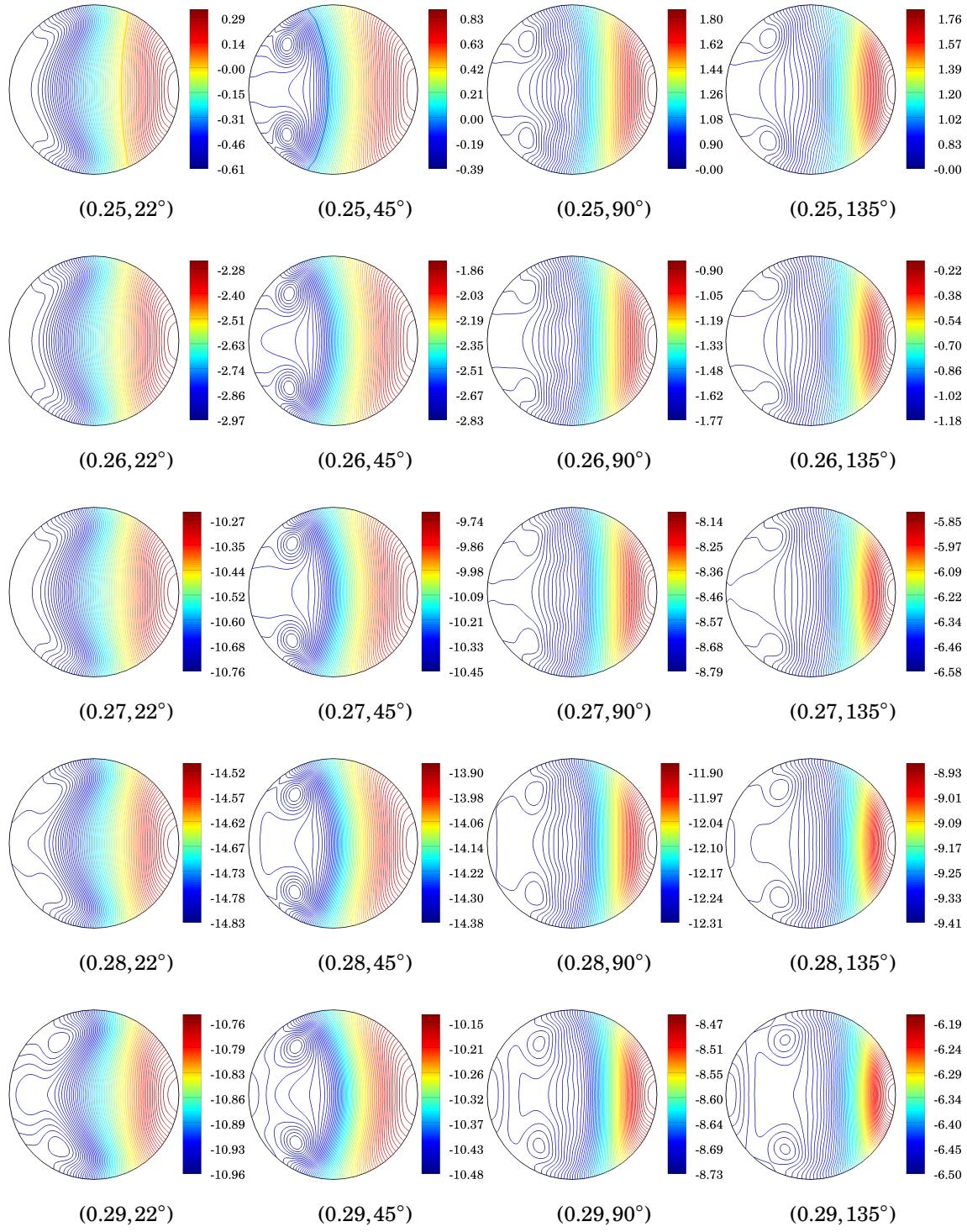


Figure E.10 Uniform entrance condition: non-dimensional pressure p^* at (t^*, ϕ) .
(continued)

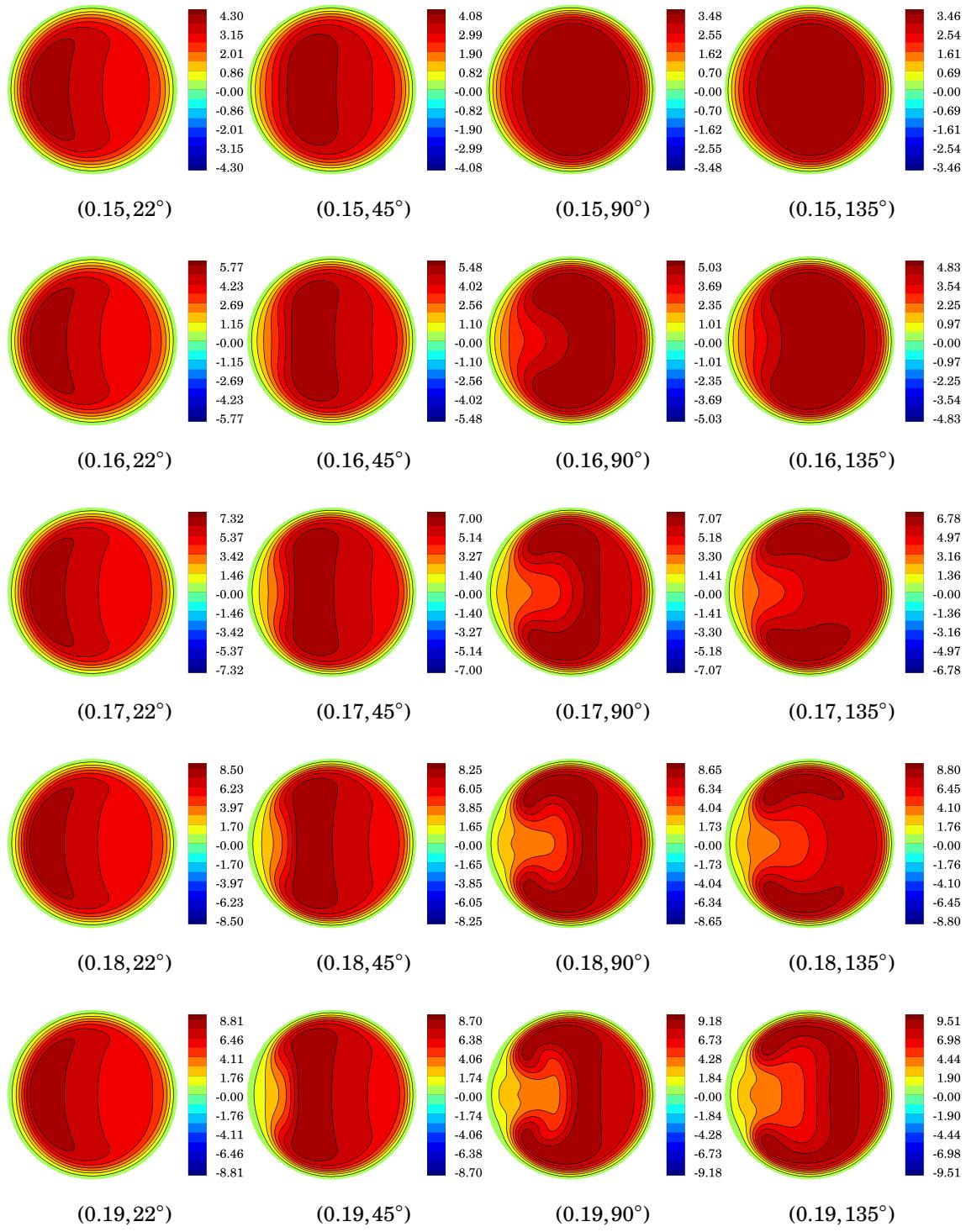


Figure E.11 Uniform entrance condition: non-dimensional centrifugal force f_c^* at (t^*, ϕ) .

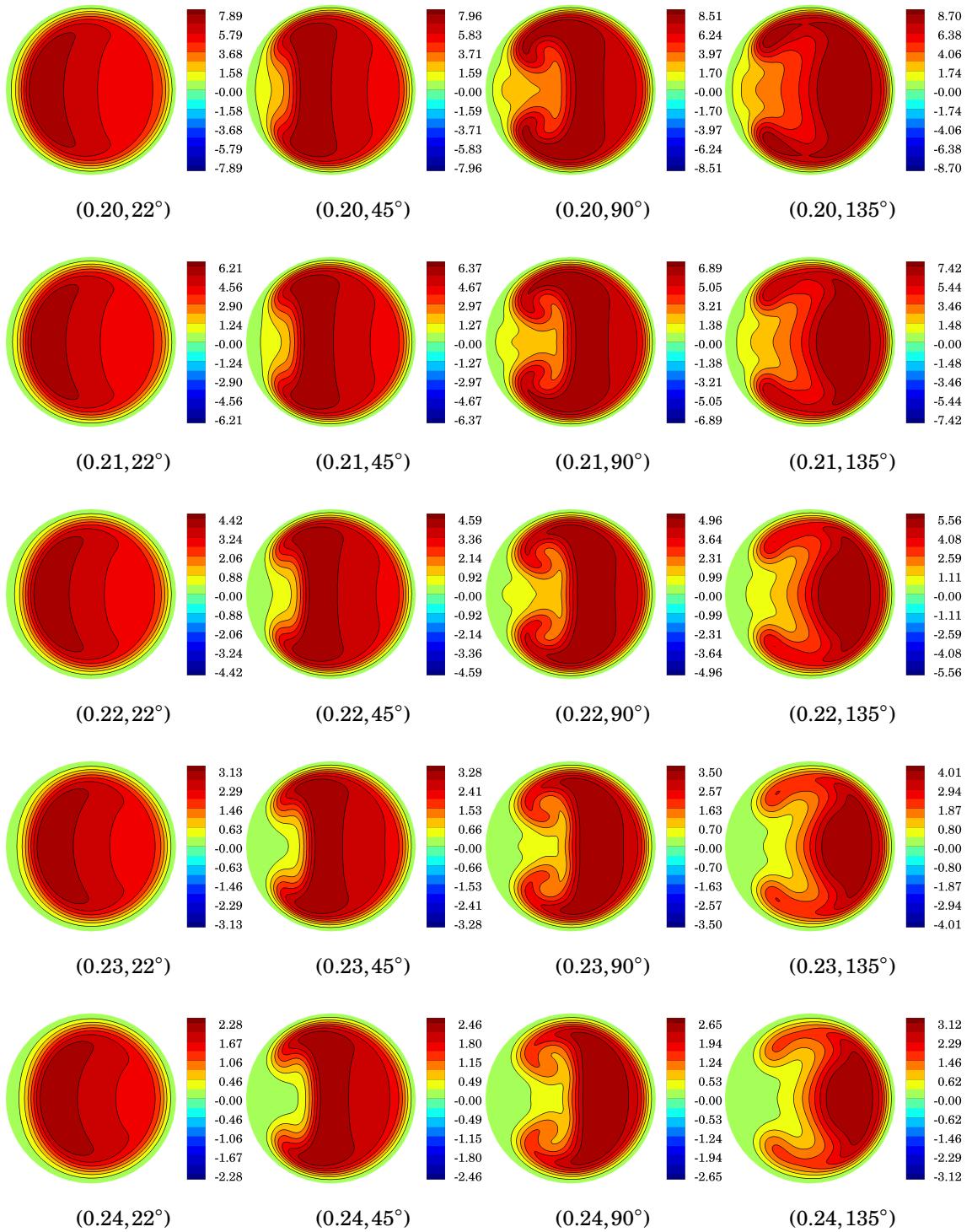


Figure E.11 Uniform entrance condition: non-dimensional centrifugal force f_c^* at (t^*, ϕ) .
(continued)

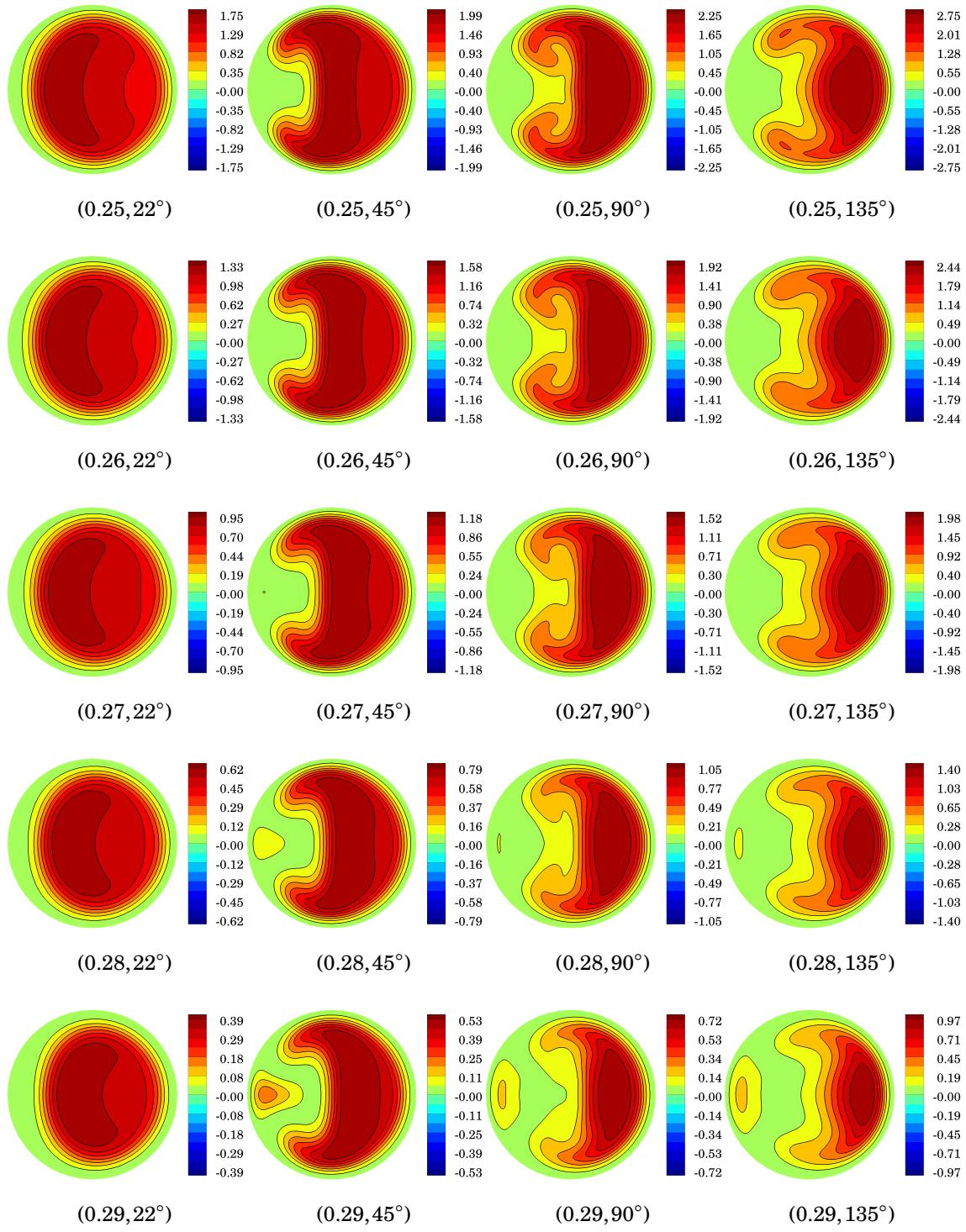


Figure E.11 Uniform entrance condition: non-dimensional centrifugal force f_c^* at (t^*, ϕ) .
(continued)

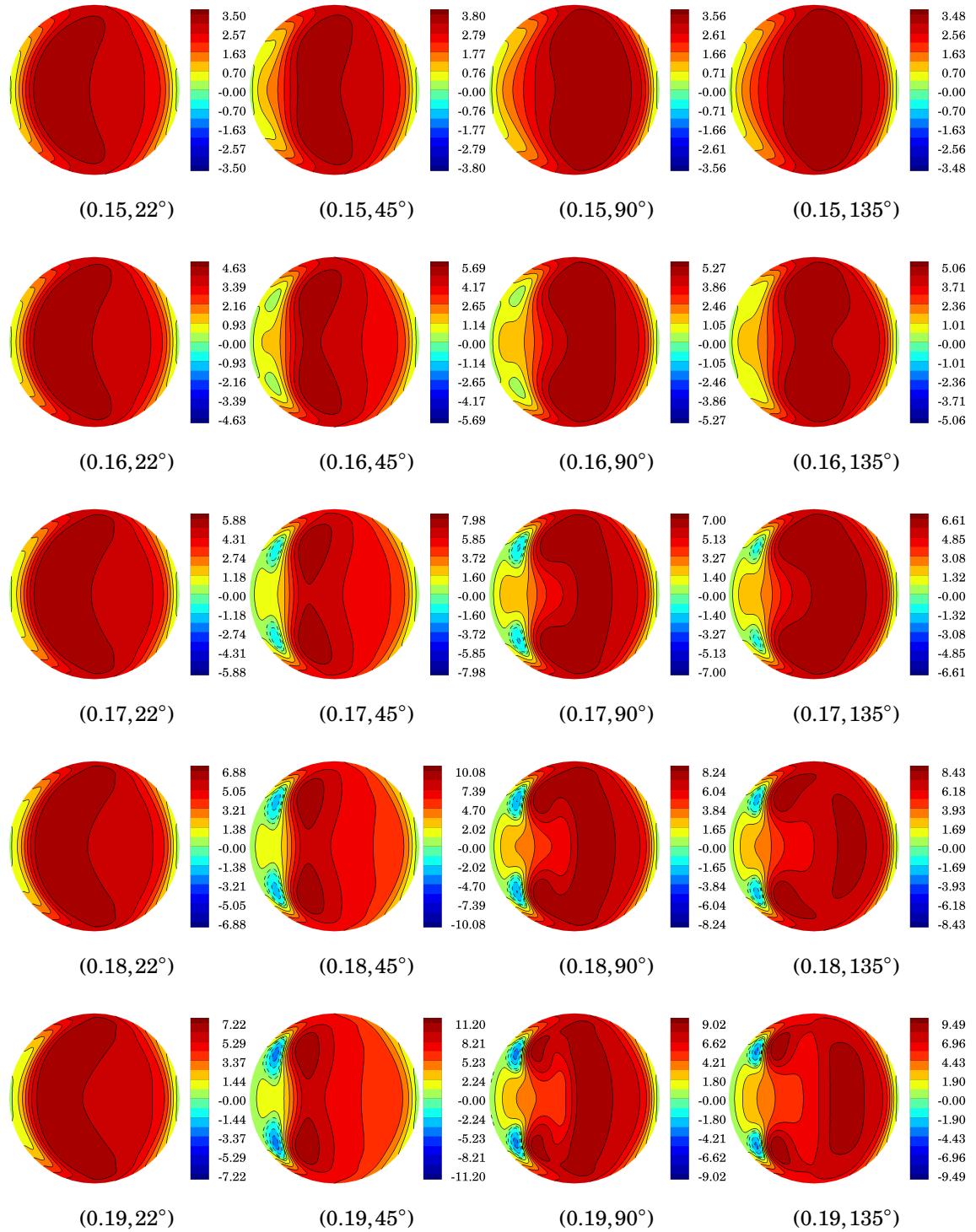


Figure E.12 Uniform entrance condition: non-dimensional pressure gradient force $-f_{pg}^*$ at (t^*, ϕ) .

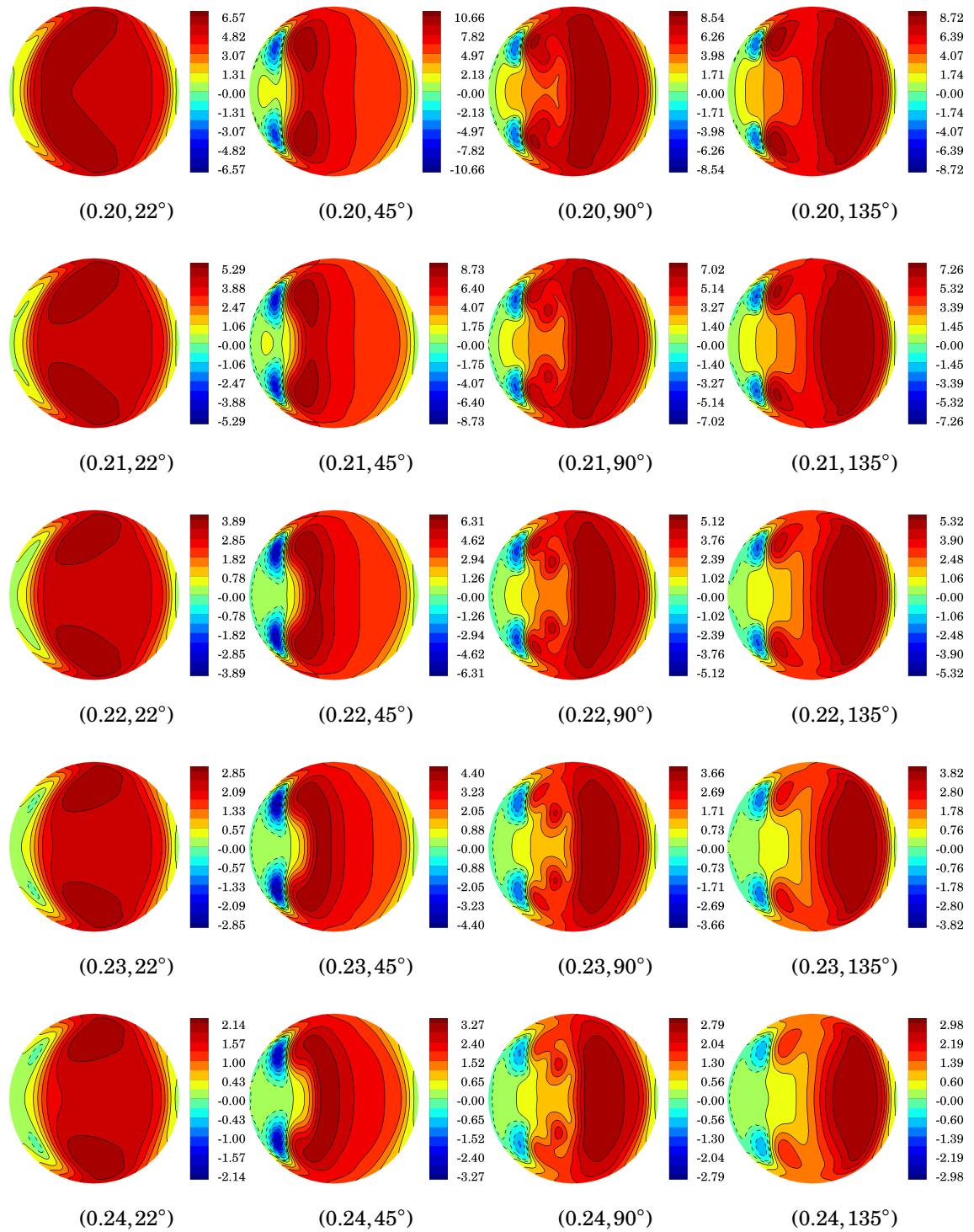


Figure E.12 Uniform entrance condition: non-dimensional pressure gradient force $-f_{pg}^*$ at (t^*, ϕ) . (*continued*)

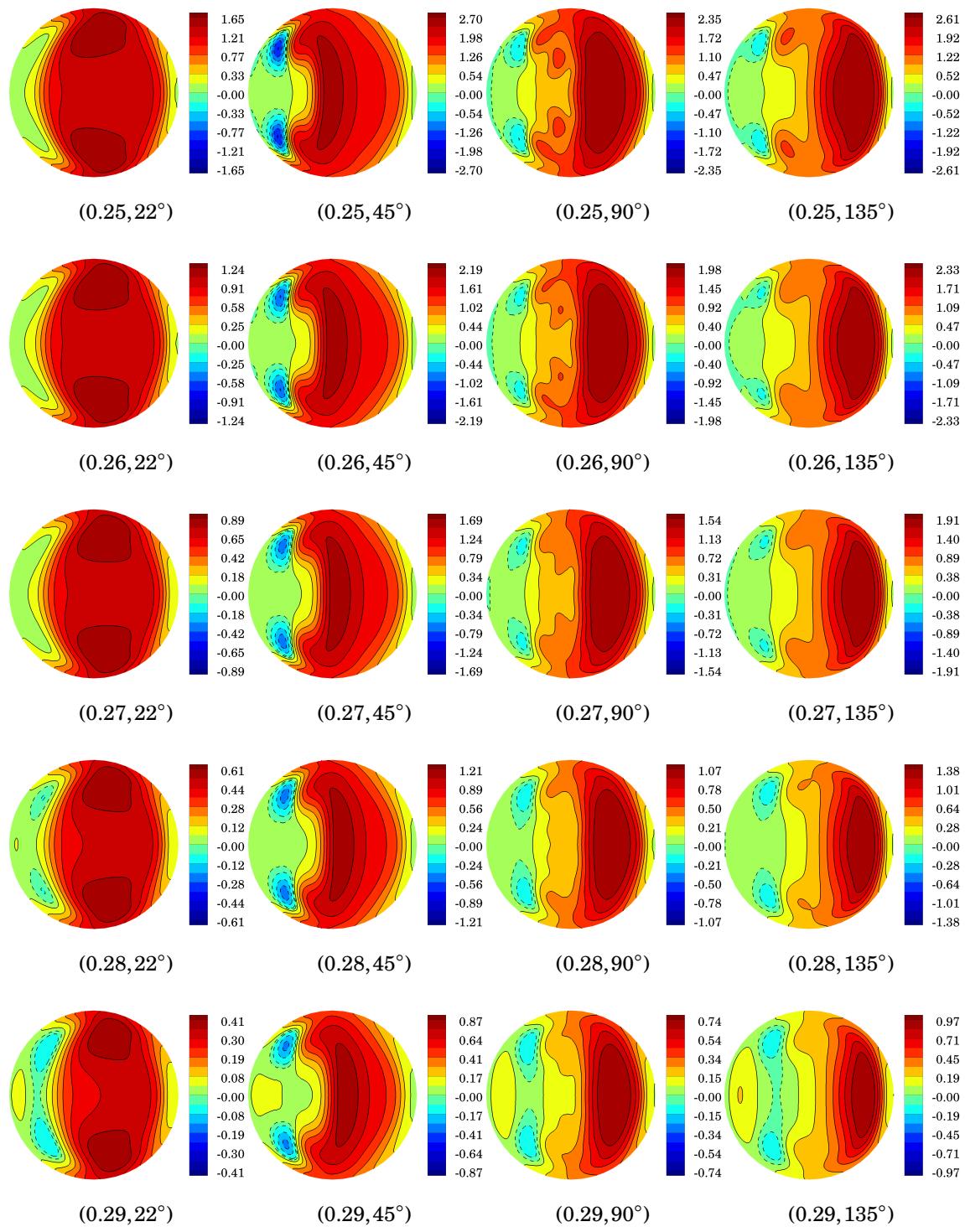


Figure E.12 Uniform entrance condition: non-dimensional pressure gradient force $-f_{pg}^*$ at (t^*, ϕ) . (*continued*)

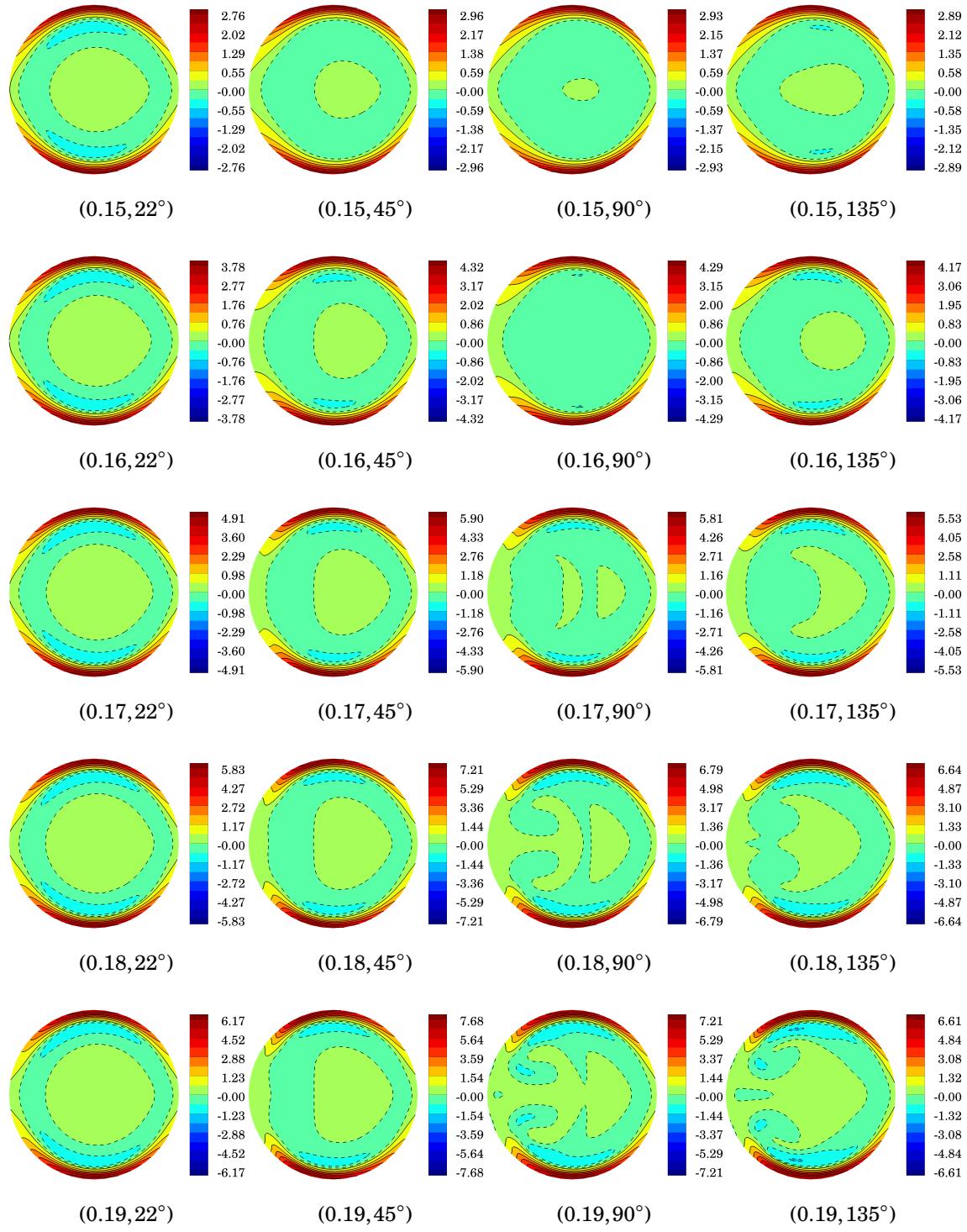


Figure E.13 Uniform entrance condition: non-dimensional viscous force f_v^* at (t^*, ϕ) .

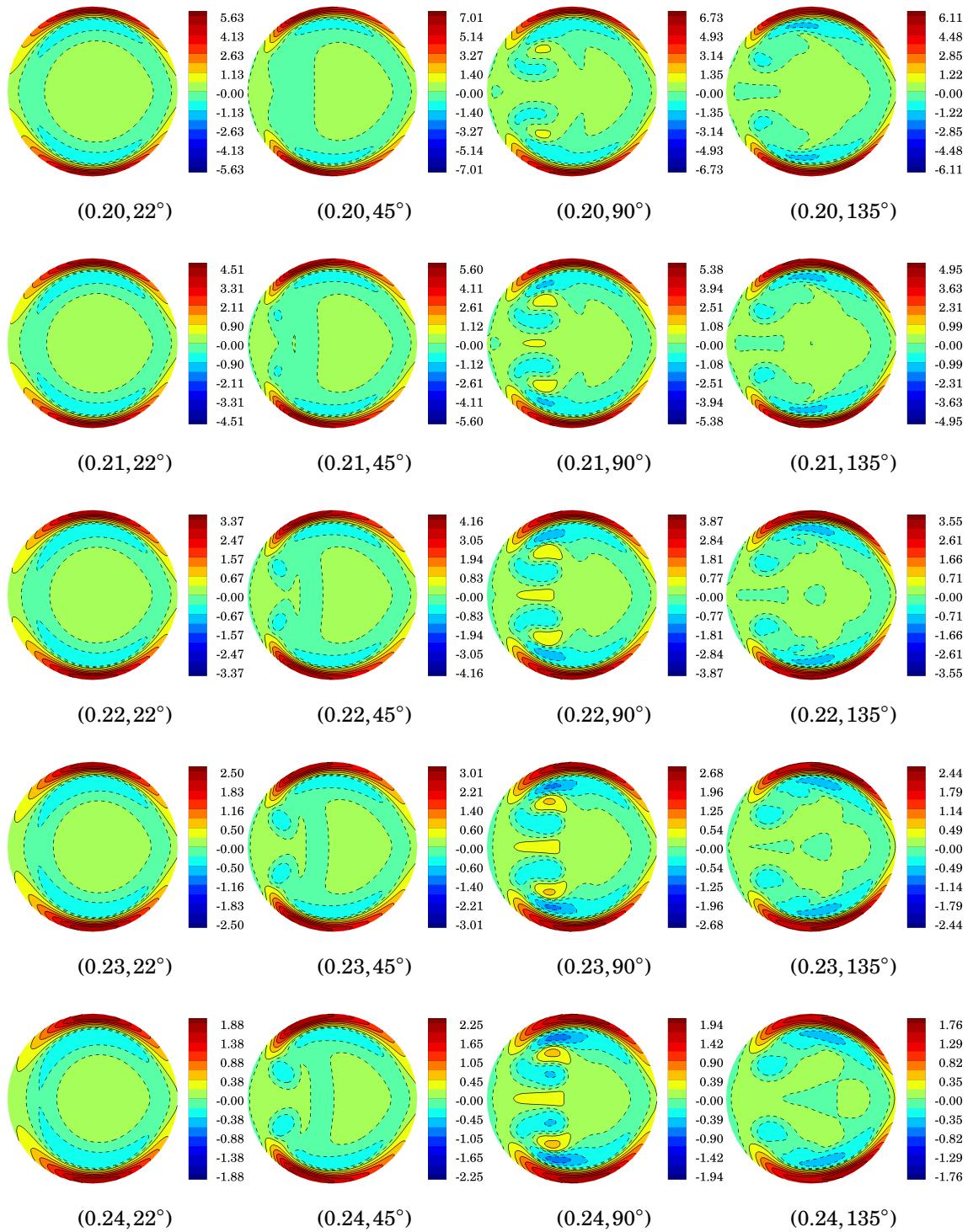


Figure E.13 Uniform entrance condition: non-dimensional viscous force f_v^* at (t^*, ϕ) .
(continued)

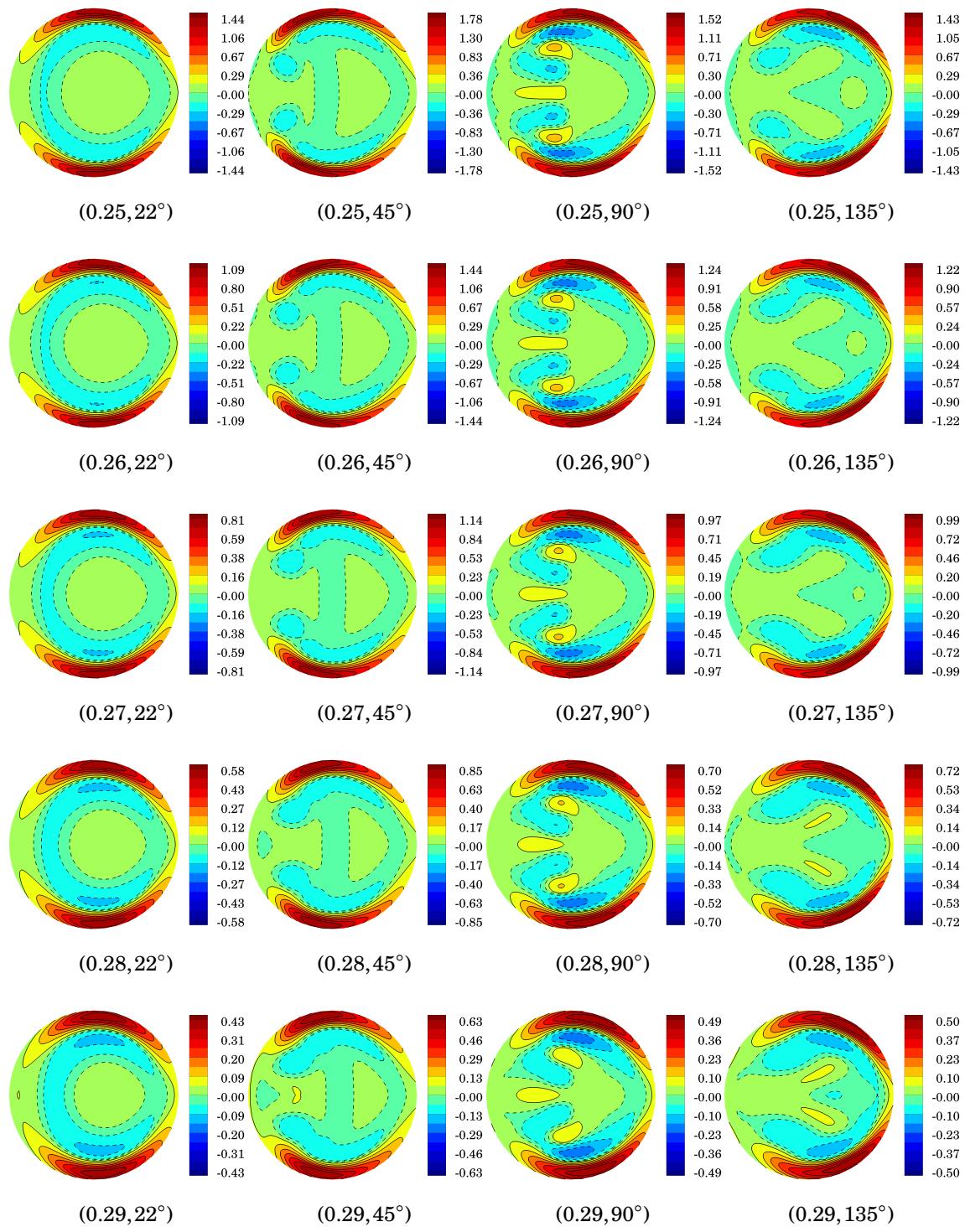


Figure E.13 Uniform entrance condition: non-dimensional viscous force f_v^* at (t^*, ϕ) .
(continued)

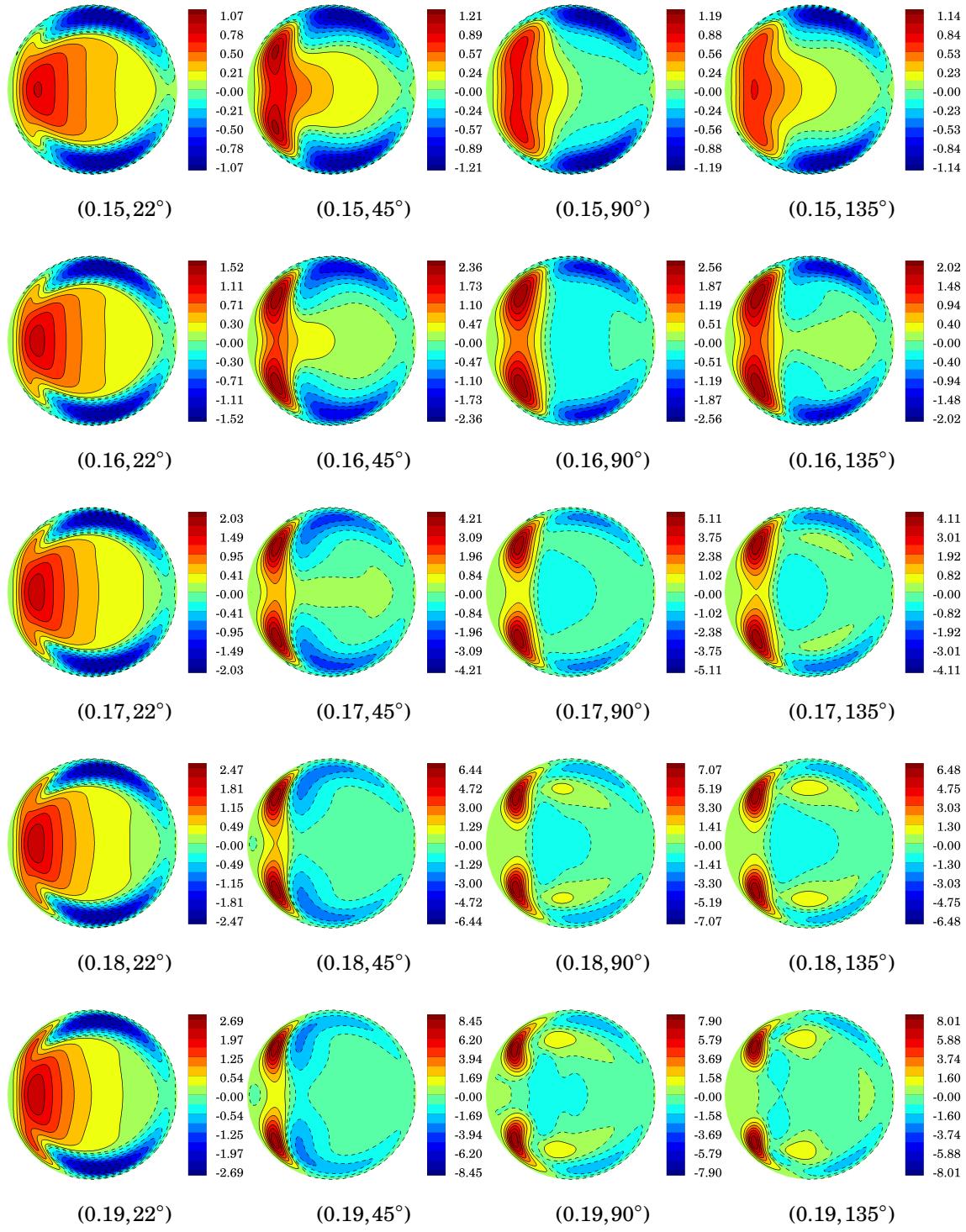


Figure E.14 Uniform entrance condition: non-dimensional centrifugal, pressure gradient and viscous forces along the radius of curvature direction $f_c^* + f_{pg}^* + f_v^*$ at (t^*, ϕ) .

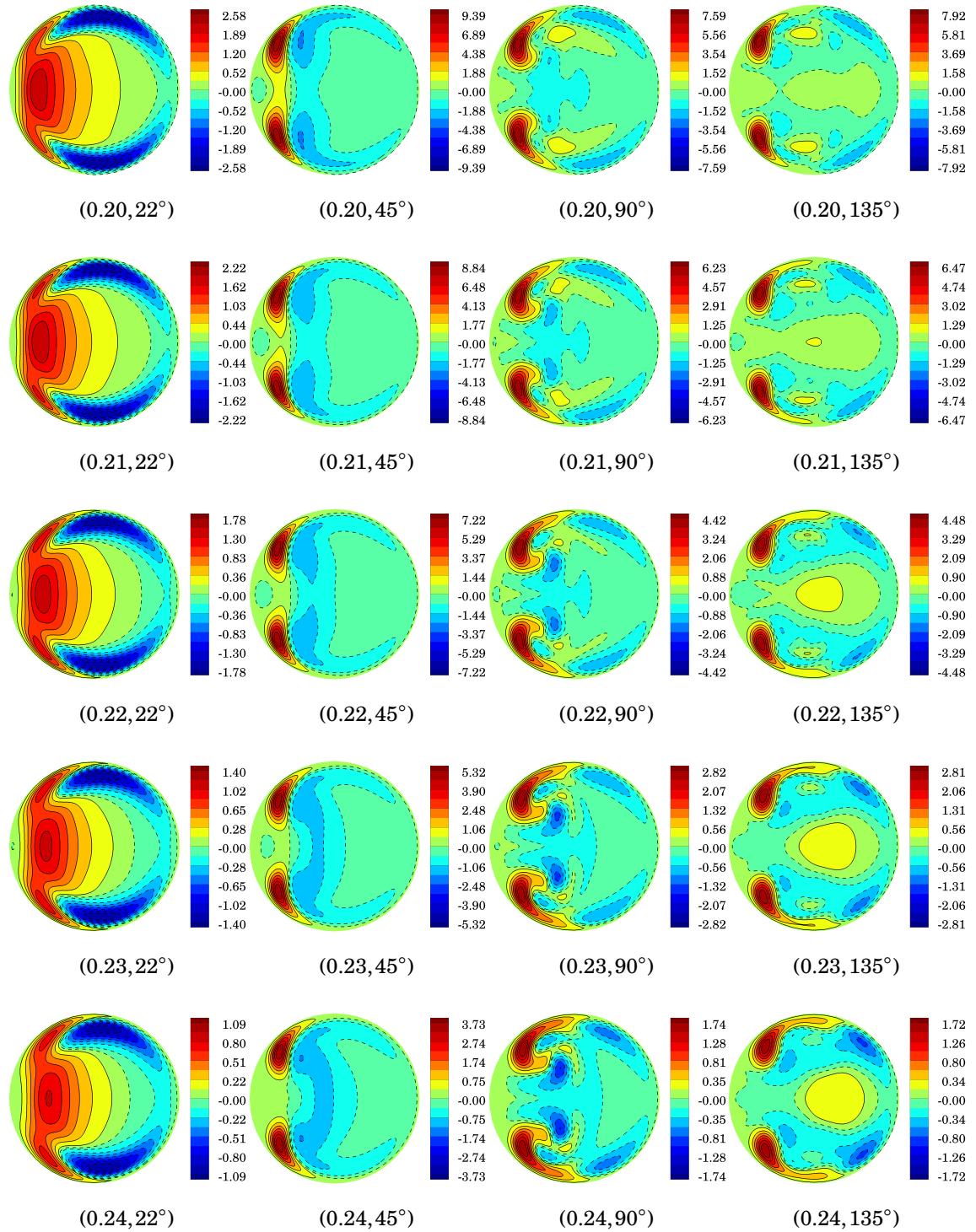


Figure E.14 Uniform entrance condition: non-dimensional centrifugal, pressure gradient and viscous forces along the radius of curvature direction $f_c^* + f_{pg}^* + f_v^*$ at (t^*, ϕ) . (continued)

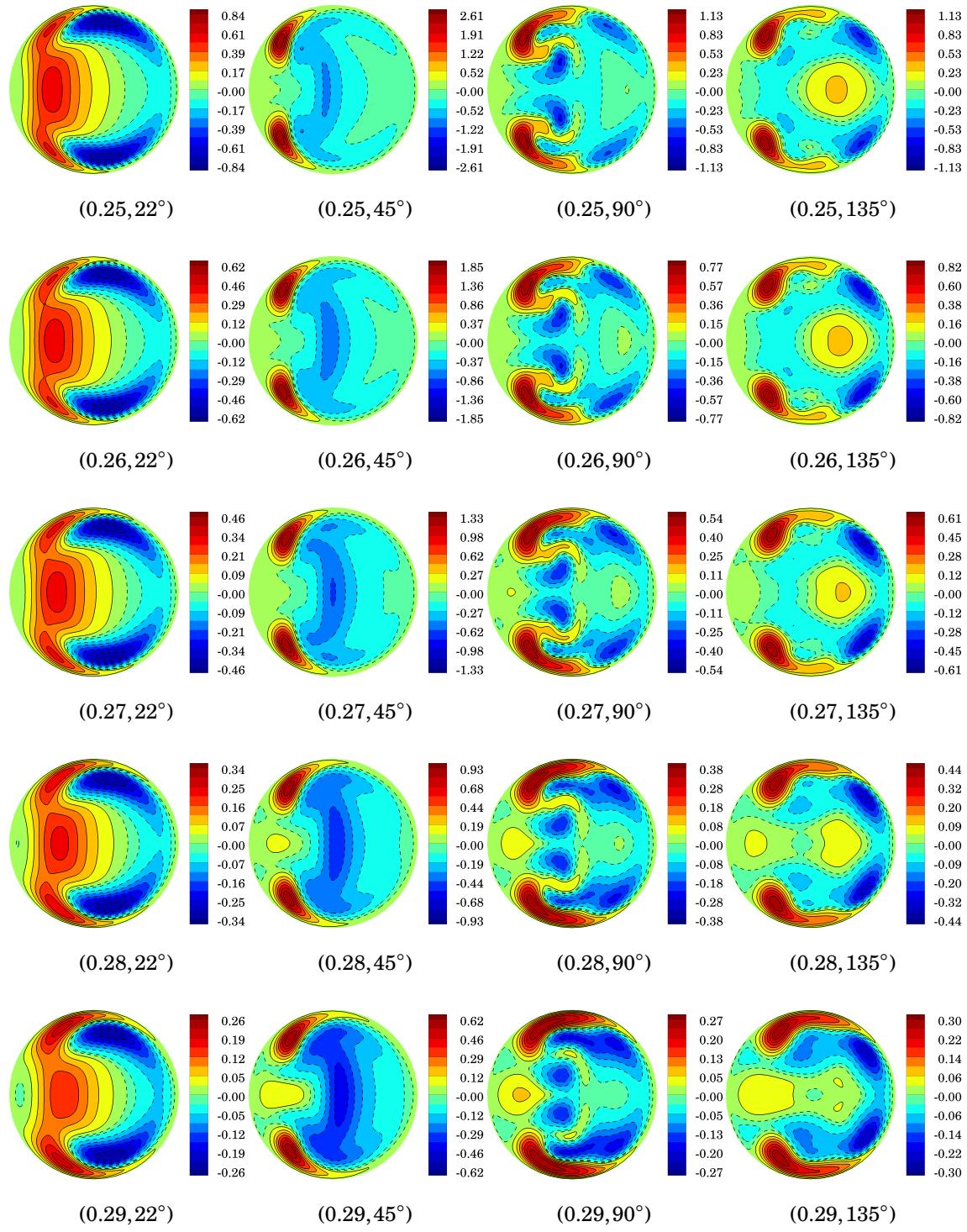


Figure E.14 Uniform entrance condition: non-dimensional centrifugal, pressure gradient and viscous forces along the radius of curvature direction $f_c^* + f_{pg}^* + f_v^*$ at (t^*, ϕ) . (continued)

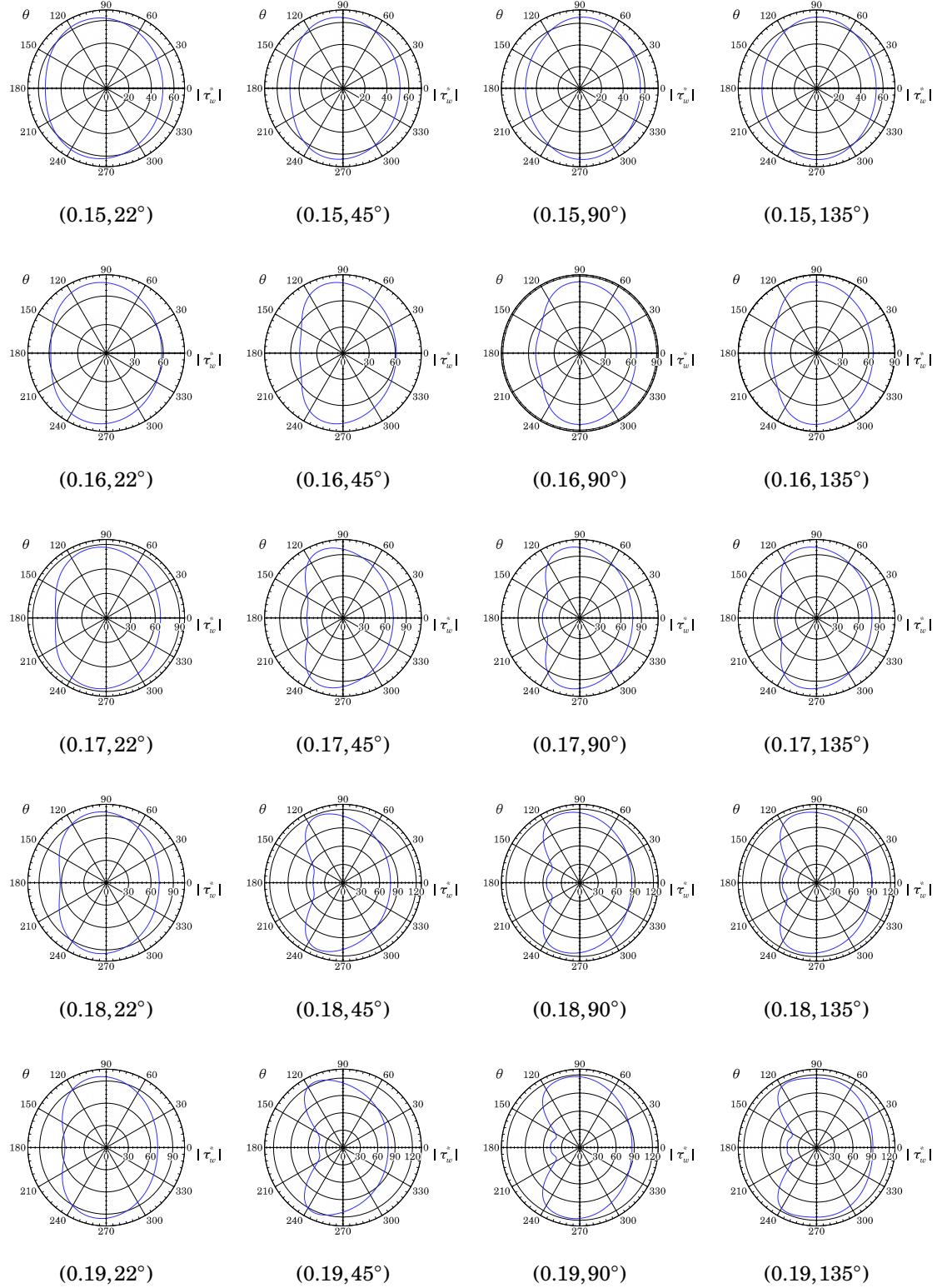


Figure E.15 Uniform entrance condition: non-dimensional wall shear stress magnitude $|\tau_w^*|$ at (t^*, ϕ) .

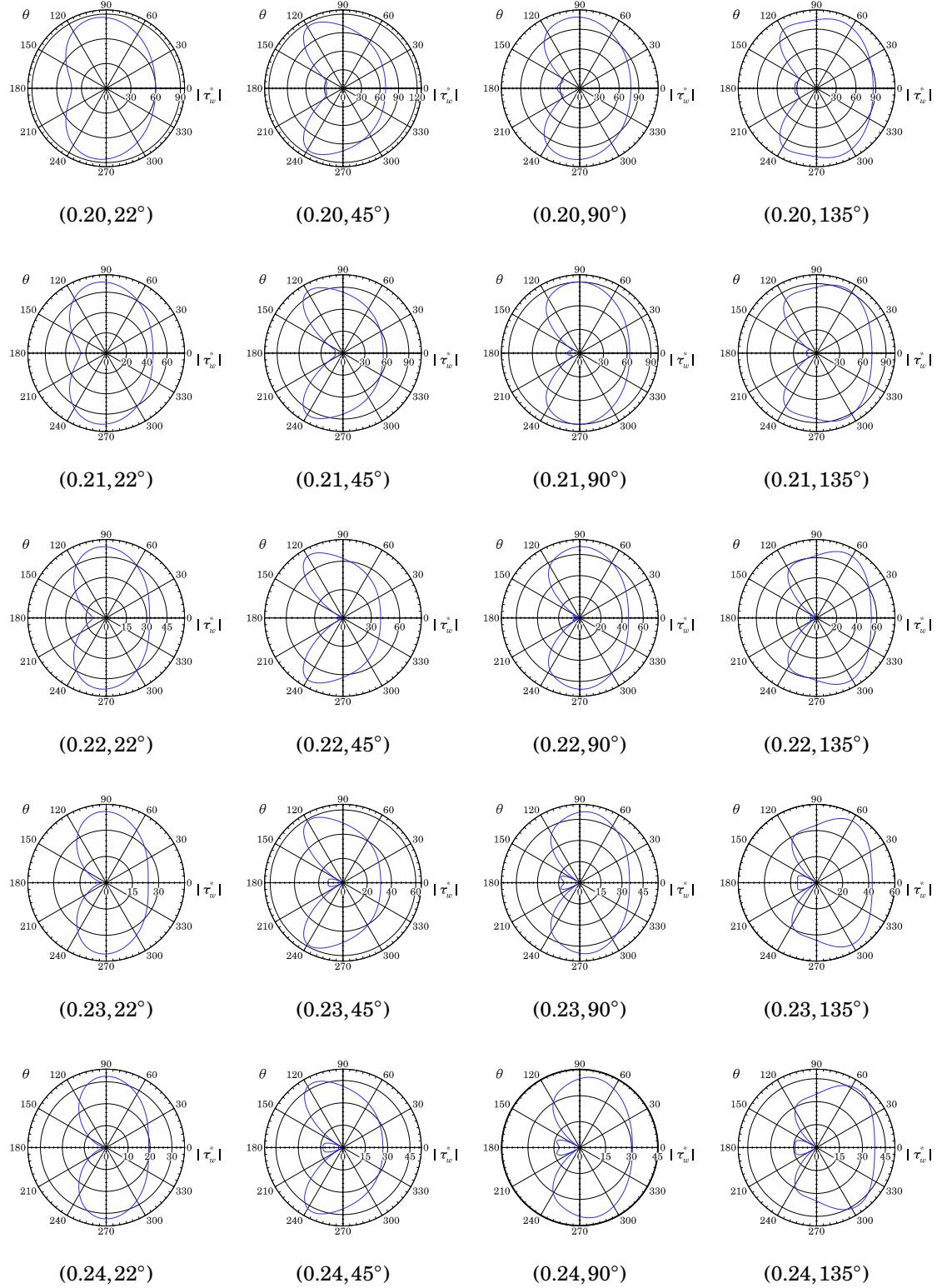


Figure E.15 Uniform entrance condition: non-dimensional wall shear stress magnitude $|\tau_w^*|$ at (t^*, ϕ) . (*continued*)

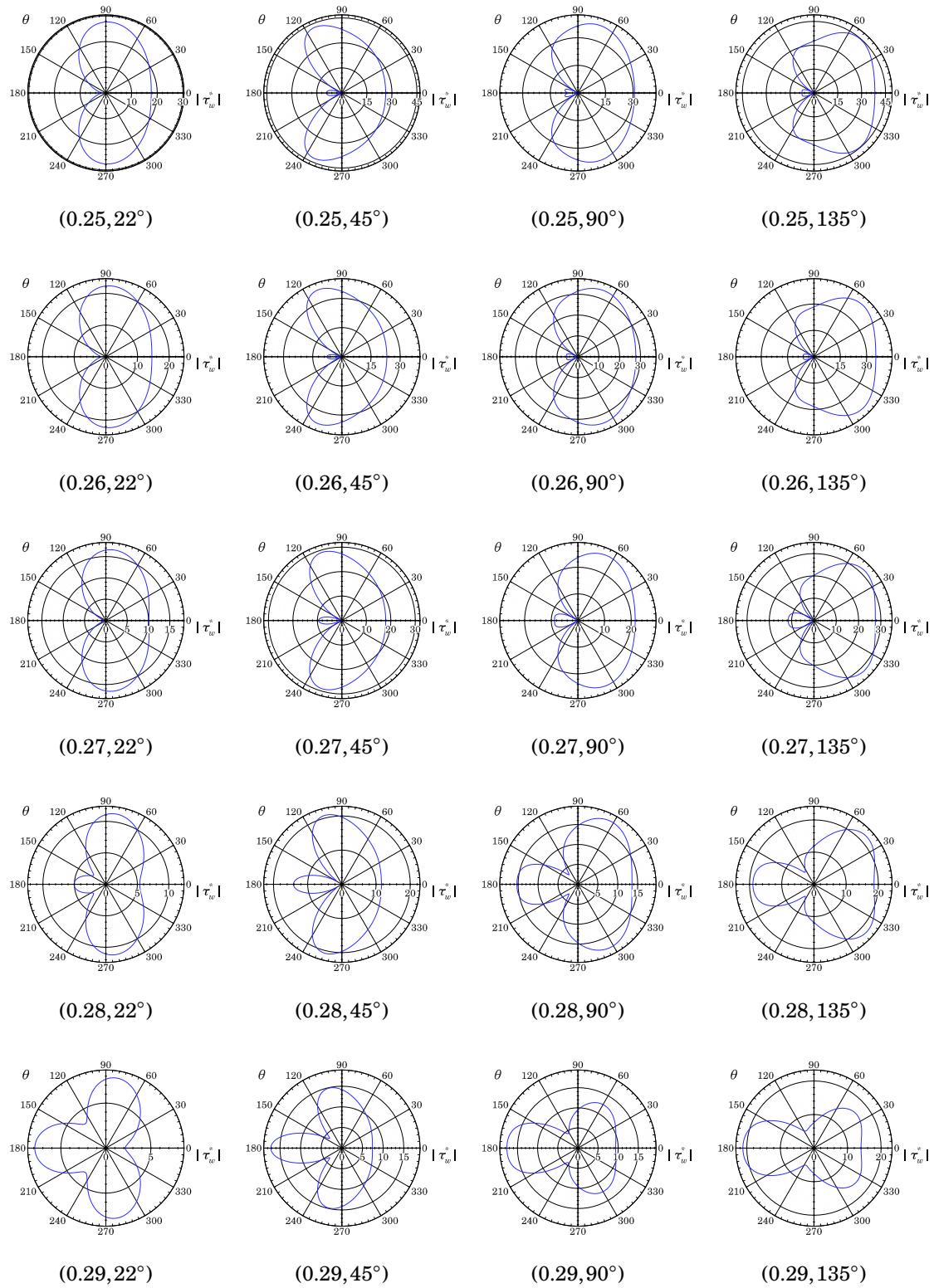


Figure E.15 Uniform entrance condition: non-dimensional wall shear stress magnitude $|\tau_w^*|$ at (t^*, ϕ) . (*continued*)

Bibliography

- [1] F.T. Johnson, E.N. Tinoco, and N. Jong Yu. Thirty years of development and application of cfd at boeing commercial airplanes, seattle. *34:1115–1151*, 2005.
- [2] Z.J. Wang, K. Fidkowski, R. Abgrall, F. Bassi, D. Caraeni, A. Cary, H. Deconinck, R. Hartmann, K. Hillewaert, H.T. Huynh, N. Kroll, G. May, P.-O. Persson, B. van Leer, and M. Visbal. High-order CFD methods: current status and perspective. *International Journal for Numerical Methods in Fluids*, 72:811–845, 2013.
- [3] W.H. Reed and T.R. Hill. Triangular mesh methods for the neutron transport equation. Technical Report LA-UR-73-479, Los Alamos Scientific Laboratory, 1973.
- [4] D.N. Arnold, F. Brezzi, B. Cockburn, and L.D. Marini. Unified analysis of discontinuous Galerkin methods for elliptic problems. *SIAM Journal of Numerical Analysis*, 39(5):1749–1779, 2002.
- [5] B. Cockburn and C.-W. Shu. The local discontinuous Galerkin method for time-dependent convection-diffusion systems. *SIAM Journal of Numerical Analysis*, 35(6):2440–2463, 1998.
- [6] J.S. Hesthaven and T. Warburton. *Nodal Discontinuous Galerkin Methods - Algorithms, Analysis, and Applications*. Springer-Berlin, 2008.

- [7] B. Cockburn, J. Gopalakrishnan, and R. Lazarov. Unified hybridization of discontinuous Galerkin, mixed and continuous Galerkin method for second order elliptic problems. *SIAM Journal of Numerical Analysis*, 47(2):1319–1365, 2009.
- [8] Z.J. Wang, L. Zhang, and Y. Liu. Spectral (finite) volume method for conservation laws on unstructured grids iv: Extension to two-dimensional Euler equations. *Journal of Computational Physics*, 194(2):716–741, 2004.
- [9] D.A. Kopriva. A staggered-grid multidomain spectral method for the compressible Navier-Stokes equations. *Journal of Computational Physics*, 143:125–158, 1998.
- [10] Y. Liu, M. Vinokur, and Z.J. Wang. Spectral difference method for unstructured grids i: Basic formulation. *Journal of Computational Physics*, 216:780–801, 2006.
- [11] H.T. Huynh. A flux reconstruction approach to high-order schemes including discontinuous Galerkin methods. In *18th AIAA Computational Fluid Dynamics Conference*, Miami, FL, 2007.
- [12] H.T. Huynh. A reconstruction approach to high-order schemes including discontinuous Galerkin for diffusion. In *47th AIAA Aerospace Sciences Meeting*, Orlando, FL, 2009.
- [13] Z.J. Wang and H. Gao. A unifying lifting collocation penalty formulation including the discontinuous Galerkin, spectral volume/difference methods for conservation laws on mixed grids. *Journal of Computational Physics*, 228(21):8161–8186, 2009.
- [14] T. Haga, H. Gao, and Z.J. Wang. A high-order unifying discontinuous

formulation for the Navier-Stokes equations on 3D mixed grids. *Mathematical Modelling of Natural Phenomena*, 6(3):28–56, 2011.

- [15] C. Liang, C. Cox, and M.W. Plesniak. A comparison of computational efficiencies of spectral difference method and correction procedure via reconstruction. *Journal of Computational Physics*, 239:138–146, 2013.
- [16] P.E. Vincent, P. Castonguay, and A. Jameson. A new class of high-order energy stable flux reconstruction schemes. *Journal of Scientific Computing*, 47(1):50–72, 2011.
- [17] P. Castonguay, P.E. Vincent, and A. Jameson. A new class of high-order energy stable flux reconstruction schemes for triangular elements. *Journal of Scientific Computing*, 51(1):224–256, 2012.
- [18] D.M. Williams, P. Castonguay, P.E. Vincent, and A. Jameson. Energy stable flux reconstruction schemes for advection-diffusion problems on triangles. *Journal of Computational Physics*, 250:53–76, 2013.
- [19] A. Jameson, P. Castonguay, and P.E. Vincent. On the non-linear stability of flux reconstruction schemes. *Journal of Scientific Computing*, 50(2):434–445, 2012.
- [20] S.C. Spiegel, H.T. Huynh, and J.R. DeBonis. De-aliasing through over-integration applied to the flux reconstruction and discontinuous Galerkin methods. In *22nd AIAA Aviation Forum*, Dallas, TX, 2015.
- [21] Z.J. Wang. High-order methods for the Euler and Navier-Stokes equations on unstructured grids. *Progress in Aerospace Sciences*, 43(1-3):1–41, 2007.
- [22] P.E. Vincent and A. Jameson. Facilitating the adoption of unstructured high-

order methods amongst a wider community of fluid dynamicists. *Mathematical Modelling of Natural Phenomena*, 6(3):97–140, 2011.

- [23] H.T. Huynh, Z.J. Wang, and P.E. Vincent. High-order methods for computational fluid dynamics: A brief review of compact differential formulations on unstructured grids. *Computers and Fluids*, 98:209–220, 2014.
- [24] D. De Grazia, G. Mengaldo, D. Moxey, P.E. Vicent, and S.J. Sherwin. Connections between the discontinuous Galerkin method and high-order flux reconstruction schemes. *International Journal for Numerical Methods in Fluids*, 75(12):860–877, 2014.
- [25] G. Mengaldo, D. De Grazia, P.E. Vincent, and S.J. Sherwin. On the connections between discontinuous Galerkin and flux reconstruction schemes: extension to curvilinear meshes. *Journal of Scientific Computing*, 67(3):1272–1292, 2016.
- [26] C. Liang, A. Chan, X. Liu, and A. Jameson. An artificial compressibility method for the spectral difference solution of unsteady incompressible Navier-Stokes equations on multiple grids. In *49th AIAA Aerospace Sciences Meeting*, Orlando, FL, 2011.
- [27] A.J. Chorin. A numerical method for solving incompressible viscous flow problems. *Journal of Computational Physics*, 135(2):118–125, 1997. reprinted from Vol. 2(1), 1967, 12-26.
- [28] F. Bassi, A. Crivellini, D.A. Di Pietro, and S. Rebay. An artificial compressibility flux for the discontinuous Galerkin solution of the incompressible Navier-Stokes equations. *Journal of Computational Physics*, 218(2):794–815, 2006.
- [29] K. Shahbazi, P.F. Fischer, and C.R. Ethier. A high-order discontinuous

Galerkin method for the unsteady incompressible Navier-Stokes equations.
Journal of Computational Physics, 222(1):391–407, 2007.

- [30] N.C. Nguyen, J. Peraire, and B. Cockburn. An implicit hybridizable discontinuous Galerkin method for the incompressible Navier-Stokes equations. *Journal of Computational Physics*, 230(4):1147–1170, 2011.
- [31] A. Jameson and S. Yoon. Lower-upper implicit schemes with multiple grids for the Euler equations. *AIAA Journal*, 25(7):929–935, 1987.
- [32] C. Liang, R. Kannan, and Z.J. Wang. A p-multigrid spectral difference method with explicit and implicit smoothers on unstructured triangular grids. *Computers and Fluids*, 38:254–265, 2009.
- [33] Y. Sun, Z.J. Wang, and Y. Liu. Efficient implicit non-linear LU-SGS approach for compressible flow computation using high-order spectral difference method. *Communications in Computational Physics*, 5(2-4):760–778, 2009.
- [34] M. Parsani, G. Ghorbaniasl, C. Lacor, and E. Turkel. An implicit high-order spectral difference approach for large eddy simulation. *Journal of Computational Physics*, 229:5373–5393, 2010.
- [35] T. Haga, K. Sawada, and Z.J. Wang. An implicit LU-SGS scheme for the spectral volume method on unstructured tetrahedral grids. *Communications in Computational Physics*, 6(5):978–996, 2009.
- [36] MATLAB. *version 8.4.0 (R2014b)*. The MathWorks, Inc., Natick, Massachusetts, 2014.
- [37] C. Geuzaine and J.-F. Remacle. Gmsh: a three-dimensional finite element mesh generator with built-in pre- and post-processing facilities. *International Journal for Numerical Methods in Engineering*, 79(11):1309–1331, 2009.

- [38] Tecplot 360. *version 14.2.0 (EX 2014 Release 2)*. Tecplot, Inc., Bellevue, WA, 2014.
- [39] D.T. Elsworth and E.F. Toro. Riemann solvers for solving the incompressible Navier-Stokes equations using the artificial compressibility method. Technical Report 9208, Cranfield Institute of Technology, June 1992.
- [40] S.E. Rogers, D. Kwak, and U. Kaul. On the accuracy of the pseudocompressibility method in solving the incompressible Navier-Stokes equations. *Applied Mathematical Modelling*, 11:35–44, 1987.
- [41] E. Turkel. Preconditioned methods for solving the incompressible and low speed compressible equations. *Journal of Computational Physics*, 72:277–298, 1987.
- [42] B.T. Helenbrook. Artificial compressibility preconditioning for incompressible flows under all conditions. In *44th AIAA Aerospace Sciences Meeting*, Reno, NV, 2006.
- [43] A. Belov, L. Martinelli, and A. Jameson. A new implicit algorithm with multigrid for unsteady incompressible flow calculations. In *33rd Aerospace Sciences Meeting*, Reno, NV, 1995.
- [44] D. Drikakis, O.P. Iliev, and D.P. Vassileva. A nonlinear multigrid method for the three-dimensional incompressible Navier-Stokes equations. *Journal of Computational Physics*, 146:301–321, 1998.
- [45] C.L. Merkle and M. Athavale. Time accurate unsteady incompressible flow algorithms based on artificial compressibility. In *8th Computational Fluid Dynamics Conference*, Honolulu, HI, 1987.

- [46] W.Y. Soh and J.W. Goodrich. Unsteady solution of incompressible Navier-Stokes equations. *Journal of Computational Physics*, 79(1):113–134, 1988.
- [47] S.E. Rogers and D. Kwak. Upwind-differencing scheme for the time-accurate incompressible Navier-Stokes equations. *AIAA Journal*, 28(2):253–262, 1990.
- [48] S.E. Rogers, D. Kwak, and C. Kiris. Steady and unsteady solutions of the incompressible Navier-Stokes equations. *AIAA Journal*, 29(4):603–610, 1991.
- [49] D. Kwak, C. Kiris, and J. Housman. Implicit methods for viscous incompressible flows. *Computers and Fluids*, 41:51–64, 2011.
- [50] D.T. Elsworth and E.F. Toro. A numerical investigation of the artificial compressibility method for the solution of the Navier-Stokes equations. Technical Report 9213, Cranfield Institute of Technology, November 1992.
- [51] D. Drikakis and W. Rider. *High-resolution methods for incompressible and low-speed flows*. Springer, 2005.
- [52] A. Jameson. A proof of the stability of the spectral difference method for all orders of accuracy. *Journal of Scientific Computing*, 45:348–358, 2010.
- [53] H. Gao, Z.J. Wang, and Y. Liu. A study of curved boundary representations for 2D high-order Euler solvers. *Journal of Scientific Computing*, 44:323–336, 2010.
- [54] V.V. Rusanov. Calculation of interaction of non-steady shock waves with obstacles. *Journal of Computational and Mathematical Physics USSR*, 1:267–279, 1961.
- [55] L. Krivodonova and M. Berger. High-order accurate implementation of solid wall boundary conditions in curved geometries. *Journal of Computational Physics*, 211:492–512, 2006.

- [56] F. Bassi and S. Rebay. High-order accurate discontinuous finite element solution of the 2D Euler equations. *Journal of Computational Physics*, 138:251–285, 1997.
- [57] J. Peraire and P.-O. Persson. The compact discontinuous Galerkin method for elliptic problems. *SIAM Journal of Scientific Computing*, 30:1806–1824, 2009.
- [58] B. Cockburn and C.-W. Shu. The local discontinuous Galerkin method for time-dependent convection-diffusion systems. *SIAM Journal of Numerical Analysis*, 35:2440–2463, 1998.
- [59] F. Bassi and S. Rebay. A high-order discontinuous Galerkin method for compressible turbulent flows. In G. Karniadakis B. Cockburn and C.-W. Shu, editors, *Discontinuous Galerkin methods: Theory, Computation, and Application. Lecture notes in Computational Science and Engineering*, volume 11, pages 77–88. Springer, 2000.
- [60] C.-W. Shu and S. Osher. Efficient implementation of essentially non-oscillatory shock-capturing schemes. *Journal of Computational Physics*, 77(2):439–471, 1988.
- [61] A. Jameson. Time dependent calculations using multigrid with applications to unsteady flows past airfoils and wings. In *10th Computational Fluid Dynamics Conference*, Honolulu, HI, 1991.
- [62] R. Kannan and Z.J. Wang. A study of viscous flux formulations for a p-multigrid spectral volume Navier-Stokes solver. *Journal of Scientific Computing*, 41:165–199, 2009.
- [63] G.I. Taylor. Stability of a viscous liquid contained between two rotating cylinders. *Philosophical Transactions of the Royal Society of London. Series*

A, Containing Papers of a Mathematical or Physical Character, 223:289–343, 1923.

- [64] J.B. Bell, P. Colella, and H.M. Glaz. A second-order projection method for the incompressible Navier-Stokes equations. *Journal of Computational Physics*, 85:257–283, 1989.
- [65] M.L. Minion and D.L. Brown. Performance of under-resolved two-dimensional incompressible flow simulations, ii. *Journal of Computational Physics*, 138:734–765, 1997.
- [66] J. Park, K. Kwon, and H. Choi. Numerical solutions of flow past a circular cylinder at Reynolds number up to 160. *KSME International Journal*, 12(6):1200–1205, 1998.
- [67] B. Sharman, F.S. Lian, L. Davidson, and C. Norberg. Numerical predictions of low Reynolds number flows over two tandem circular cylinders. *International Journal for Numerical Methods in Fluids*, 47:423–447, 2005.
- [68] H. Choi and P. Moin. Effects of the computational time step on numerical solutions of turbulent flow. *Journal of Computational Physics*, 113(1):1–4, 1994.
- [69] L.S. Caretto, A.D. Gosman, S.V. Patankar, and D.B. Spalding. Two calculation procedures for steady, three-dimensional flows with recirculation. In *Proceedings of the Third International Conference on Numerical Methods in Fluid Mechanics*, volume 19 of *Lecture Notes in Physics*, pages 60–68. Springer, 1973.
- [70] O. Posdziech and R. Grundmann. Technical report, Technische Universitat Dresden, Germany, 2000.

- [71] A. Chan, P. Dewey, A. Jameson, C. Liang, and A. Smits. Vortex suppression and drag reduction in the wake of counter-rotating cylinders. *Journal of Fluid Mechanics*, 679:343–382, 2011.
- [72] C. Liu, X. Zheng, and C. Sung. Preconditioned multigrid methods for unsteady incompressible flows. *Journal of Computational Physics*, 139:35–57, 1998.
- [73] H. Ding, C. Shu, K.S. Yeo, and D. Xu. Simulation of incompressible viscous flows past a circular cylinder by hybrid FD scheme and meshless least square-based finite difference method. *Computational Methods in Applied Mechanics and Engineering*, 193:727–744, 2004.
- [74] H. Ding, C. Shu, K.S. Yeo, and D. Xu. Numerical simulation of flows around two circular cylinders by mesh-free least square-based finite difference methods. *International Journal of Numerical Methods in Fluids*, 53:305–332, 2007.
- [75] C.H.K. Williamson. Vortex dynamics in the cylinder wake. *Annual Review of Fluid Mechanics*, 28:477–539, 1996.
- [76] P. Castonguay. *High-order energy stable flux reconstructions schemes for fluid flow simulations on unstructured grids*. PhD thesis, Stanford University, Stanford, CA, 2012.
- [77] S. Taneda. Experimental investigation of the wake behind a sphere at low reynolds numbers. *Journal of the Physical Society of Japan*, 11(10):1104–1108, 1956.
- [78] M. Van Dyke. *An Album of Fluid Motion*. The Parabolic Press, Stanford, CA, 1982.
- [79] Y. Sun, Z.J. Wang, and Y. Liu. High-order multidomain spectral difference

method for the Navier-Stokes equations on unstructured hexahedral grids.
Communications in Computational Physics, 2(2):310–333, 2007.

- [80] T.A. Johnson and V.C. Patel. Flow past a sphere up to a reynolds number of 300. *Journal of Fluid Mechanics*, 378(17):19–70, 1999.
- [81] A. Tomboulides and S.A. Orszag. Numerical investigation of transitional and weak turbulent flow past a sphere. *Journal of Fluid Mechanics*, 416(1):45–73, 2000.
- [82] J. Jeong and F. Hussain. On the identification of a vortex. *Journal of Fluid Mechanics*, 285:69–94, 1995.
- [83] G.J. Gassner, F. Lorcher, C.D. Munz, and J.S. Hesthaven. Polymorphic nodal elements and their application in discontinuous Galerkin methods. *Journal of Computational Physics*, 228(5):1573–1590, 2009.
- [84] G. Karypis and V. Kumar. A fast and high quality multilevel scheme for partitioning irregular graphs. *SIAM Journal of Scientific Computing*, 20(1):359–392, 1999.
- [85] MPICH: a high performance and widely portable implementation of the Message Passing Interface standard. <https://www.mpich.org/>.
- [86] F.D. Witherden, B.C. Vermeire, and P.E. Vincent. Heterogeneous computing on mixed unstructured grids with pyfr. *Computers and Fluids*, 120:173–186, 2015.
- [87] Open MPI: a high performance message passing library. <https://www.open-mpi.org/>.
- [88] C. Cox, C. Liang, and M.W. Plesniak. Spectral difference solution of incompressible flow over an inline tube bundle with oscillating cylinder. In

ASME Pressure Vessels and Piping Conference, pages 9–20, Toronto, Ontario, Canada, 2012.

- [89] C. Liang, A.S. Chan, and A. Jameson. A p-multigrid spectral difference method for incompressible Navier-Stokes equations. *Computers and Fluids*, 51:127–135, 2011.
- [90] P.F. Davies. Endothelial transcriptome profiles In Vivo in complex arterial flow fields. *Annals of Biomedical Engineering*, 36(4):563–570, 2008.
- [91] S. Glagov, C. Zarins, D. Giddens, and D.N. Ku. Hemodynamics and Atherosclerosis: insights and perspectives gained from studies of human arteries. *Archives of Pathology and Laboratory Medicine*, 112:1018–1031, 1988.
- [92] A. Mantha, C. Karmonik, G. Benndorf, C. Strother, and R. Metcalfe. Hemodynamics in a cerebral artery before and after the formation of an aneurysm. *American Journal of Neuroradiology*, 27(5):1113–1118, 2006.
- [93] A. Chakraborty, S. Chakraborty, V.R. Jala, B. Haribabu, M.K. Sharp, and R.E. Berson. Effects of biaxial oscillatory shear stress on endothelial cell proliferation and morphology. *Biotechnology and Bioengineering*, 109(3):695–707.
- [94] V. Peiffer, S.J. Sherwin, and P.D. Weinberg. Computation in the rabbit aorta of a new metric - the transverse wall shear stress - to quantify the multidirectional character of disturbed blood flow. *Journal of Biomechanics*, 46:2651–2658, 2013.
- [95] X. He and D.N. Ku. Pulsatile flow in the human left coronary artery bifurcation: average conditions. *Journal of Biomechanical Engineering*, 118:74–82, 1996.

- [96] H.A. Himborg, D.M. Grzybowski, A.L. Hazel, J.A. LaMack, X.-M. Li, and M.H. Friedman. Spatial comparisons between wall shear stress measures and porcine arterial endothelial permeability. *American Journal of Physiology, Heart and Circulatory Physiology*, 286:H1916–H1922, 2004.
- [97] V. Peiffer, S.J. Sherwin, and P.D. Weinberg. Does low and oscillatory wall shear stress correlate spatially with early atherosclerosis? A systematic review. *Cardiovascular Research*, 99:242–250, 2013.
- [98] G.S. Williams, C.W. Hubbell, and G.H. Fenkell. Experiments at detroit, mich., on the effect of curvature upon the flow of water in pipes. *Transactions of the American Society of Civil Engineers*, 47(911):1–196, 1902.
- [99] J. Eustice. Flow of water in curved pipes. *Proceedings of the Royal Society A: Mathematical, Physical and Engineering Sciences*, 84(568):107–118, 1910.
- [100] J. Eustice. Experiments of streamline motion in curved pipes. *Proceedings of the Royal Society A: Mathematical, Physical and Engineering Sciences*, 85(576):119–131, 1911.
- [101] M.P. Singh. Entry flow in a curved pipe. *Journal of Fluid Mechanics*, 65(3):517–539, 1974.
- [102] W.Y. Soh and S.A. Berger. Laminar entrance flow in a curved pipe. *Journal of Fluid Mechanics*, 148:109–135, 1984.
- [103] W.R. Dean. Note on the motion of fluid in a curved pipe. *The London, Edinburgh, and Dublin Philosophical Magazine and Journal of Science: Series 7*, 4(20):208–223, 1927.
- [104] W.R. Dean. The stream-line motion of a fluid in a curved pipe. *The London, Edinburgh, and Dublin Philosophical Magazine and Journal of Science: Series 7*, 4(21):233–247, 1927.

Edinburgh, and Dublin Philosophical Magazine and Journal of Science: Series 7, 5(30):673–695, 1928.

- [105] D.J. McConalogue and R.R. Srivastava. Motion of a fluid in a curved tube. *Proceedings of the Royal Society of London A: Mathematical, Physical and Engineering Sciences*, 307(1488):37–53, 1968.
- [106] S.A. Berger, L. Talbot, and L.-S. Yao. Flow in curved pipes. *Annual Reviews of Fluid Mechanics*, 15:461–512, 1983.
- [107] J.R. Womersley. Method for the calculation of velocity, rate of flow and viscous drag in arteries when the pressure gradient is unknown. *Journal of Physiology*, 127(3):553–563, 1955.
- [108] D. Doorly and S. Sherwin. Geometry and Flow. In L. Formaggia, A. Quarteroni, and A. Veneziani, editors, *Cardiovascular Mathematics, modeling and simulation of the circulatory system*, volume 1 of *Modeling, Simulation and Applications*, chapter 5, pages 177–209. Springer, 2009.
- [109] W.H. Lyne. Unsteady viscous flow in a curved pipe. *Journal of Fluid Mechanics*, 45(1):13–31, 1970.
- [110] J.H. Siggers and S.L. Waters. Unsteady flow in pipes with finite curvature. *Journal of Fluid Mechanics*, 600:133–165, 2008.
- [111] F.T. Smith. Pulsatile flow in curved pipes. *Journal of Fluid Mechanics*, 71(1):15–42, 1975.
- [112] K. Sudo, M. Sumida, and R. Yamane. Secondary motion of fully developed oscillatory flow in a curved pipe. *Journal of Fluid Mechanics*, 237:189–208, 1992.

- [113] O. Boiron, V. Deplano, and R. Pelissier. Experimental and numerical studies on the starting effect on the secondary flow in a bend. *Journal of Fluid Mechanics*, 574:109–129, 2007.
- [114] B. Timate, C. Castelain, and H. Peerhossaini. Pulsatile viscous flow in a curved pipe: effects of pulsation on the development of secondary flow. *International Journal of Heat and Fluid Flow*, 31:879–896, 2010.
- [115] S. van Wyk, L.P. Wittberg, K.V. Bulusu, L. Fuchs, and M.W. Plesniak. Non-Newtonian perspectives on pulsatile blood-analog flows in a 180° curved artery model. *Physics of Fluids*, 27(071901), 2015.
- [116] D.N. Ku. Blood flow in arteries. *Annual Reviews of Fluid Mechanics*, 29:399–434, 1997.
- [117] M.R. Najjari and M.W. Plesniak. Evolution of vortical structures in a curved artery model with non-Newtonian blood-analog fluid under pulsatile inflow conditions. *Experiments in Fluids*, 57(100), 2016.
- [118] M.R. Najjari and M.W. Plesniak. Secondary flow vortical structures in a 180° elastic curved vessel with torsion under steady and pulsatile inflow conditions. *Submitted for Publication*, 2017.
- [119] R.L. Panton. *Incompressible Flow*. John Wiley & Sons, Inc., 3rd edition, 2005.
- [120] P.G. Saffman. *Vortex Dynamics*. Cambridge University Press, 1992.
- [121] H. Helmholtz. Über integrale der hydrodynamischen gleichungen, welche den wirbelbewegungen entsprechen. *Journal für die reine und angewandte Mathematik*, 55:25–55, 1858.
- [122] H.J. Lugt. The dilemma of defining a vortex. In U. Müller, K.G. Roesner, and B. Schmidt, editors, *Recent Developments in Theoretical and Experimental*

Fluid Mechanics: Compressible and Incompressible Flows, pages 309–321. Springer Berlin Heidelberg, Berlin, Heidelberg, 1979.

- [123] P. Chakraborty, S. Balachandar, and R. Adrian. On the relationships between local vortex identification schemes. *Journal of Fluid Mechanics*, 535:189–214, 2005.
- [124] D.J. Doorly, S.J. Sherwin, P.T. Franke, and J. Peiró. Vortical flow structure identification and flow transport in arteries. *Computational Methods in Biomechanics and Biomedical Engineering*, 5(3):261–275, 2002.
- [125] P. Pustějovská L. John and O. Steinbach. Computation in the rabbit aorta of a new metric - the transverse wall shear stress - to quantify the multidirectional character of disturbed blood flow. *Journal of Biomechanics*, 46:2651–2658, 2013.
- [126] D.W. Holdsworth, C.J.D. Norley, R. Frayne, D.A. Steinman, and B.K. Rutt. Characterization of common carotid artery blood-flow waveforms in normal human subjects. *Physiological Measurement*, 20(3):219–240, 1999.
- [127] M. Zamir. *The physics of pulsatile flow*. Biological Physics. Springer, 2000.
- [128] M. Zamir. *Hemo-Dynamics*. Biological and Medical Physics, Biomedical Engineering. Springer, 2016.
- [129] M.R. Najjari and M.W. Plesniak. Private communication. The George Washington University, Washington, DC, 2017.
- [130] H. Vollmers. Detection of vortices and quantitative evaluation of their main parameters from experimental velocity data. *Measurement Science and Technology*, 12(8):1199–1207, 2001.

- [131] Y. Mohamied, S.J. Sherwin, and P.D. Weinberg. Understanding the fluid mechanics behind transverse wall shear stress. *Journal of Biomechanics*, 50:102–109, 2017.
- [132] E.M. Cherry and J.K. Eaton. Shear thinning effects on blood flow in straight and curved tubes. *Physics of Fluids*, 25(073104), 2013.